Available online at www.sciencedirect.com
SCIENCE DIRECT®
Optics Communications 215 (2003) 79–92
OPTICS COMMUNICATIONS
www.elsevier.com/locate/optcom

Specular and nonspecular, thickness-dependent, spectral holes in a slanted chiral sculptured thin film with a central twist defect

Fei Wang[1], Akhlesh Lakhtakia[*,1]

CATMAS – Computational and Theoretical Materials Sciences Group, Department of Engineering Science and Mechanics, Pennsylvania State University, 212 EES Building, University Park, PA 16802–6812, USA

Received 20 August 2002; accepted 18 November 2002

Abstract

We demonstrate analytically that two types of spectral holes located approximately in the center of the Bragg regime could be exhibited by a slanted chiral sculptured thin film (STF) containing a 90° twist defect midway through its thickness. One is a nonspecular spectral reflection hole excited by an incident circularly polarized plane wave of the same handedness as the chiral slanted STF, and the other a specular transmission hole excited by an incident circularly polarized plane wave of the opposite handedness. The occurrences of these holes depend on the device thickness, and a crossover thickness can be defined. The existence of both types of spectral holes is sensitive to the dual-periodicity of the slanted chiral STF, and can be completely subverted by the Rayleigh–Wood phenomenon.

PACS: 42.25.Fx; 42.40.Eq; 42.79.Dj; 77.55.+f; 78.20.Fm

Keywords: Chirality; Circular Bragg phenomenon; Rayleigh–Wood anomaly; Sculptured thin films; Spectral reflection hole; Specular transmission hole; Structural handedness

1. Introduction

Volume gratings are commonly used as dielectric mirrors in optics. Such gratings are either ...HLHLHL... multilayers [1] (where H stands for a high-permittivity layer and L for a low-permittivity layer) or the permittivity varies sinusoidally in the thickness direction [2]. Being periodic systems, volume gratings exhibit the Bragg phenomenon – which manifests itself as a high-reflectance wavelength-regime, provided the grating thickness spans a sufficient number of permittivity periods.

Haus and Shank [3] proposed the creation of a spectral hole in the reflection spectrum by inserting

* Corresponding author. Tel.: +1-814-863-4319; fax: +1-814-865-9974.
E-mail addresses: fuw101@psu.edu (F. Wang), axl4@psu.edu (A. Lakhtakia).
[1] Fax: +1-814-863-7967.

0030-4018/02/$ - see front matter
PII: S0030-4018(02)02204-6

a phase defect half-way along a volume grating. The spectral hole is a narrow transmission feature in the center of the Bragg wavelength-regime, and is useful for narrowband filtering. The proposal is implemented chiefly in quarter-wavelength-shifted distributed feedback lasers [4].

When normally illuminated, so that the wave propagation vector inside a volume grating is parallel to the thickness direction, the Bragg phenomenon is insensitive to the polarization state of the incident light. This is because the described volume gratings are made of isotropic dielectric substances. But periodically nonhomogeneous materials can possess structural handedness; and if they do, the Bragg phenomenon turns to be polarization-sensitive.

Cholesteric liquid crystals (CLCs) [5,6] as well as chiral sculptured thin films (STFs) [7,8] are periodically nonhomogeneous in the thickness direction, as their permittivity dyadics vary helicoidally in that direction. Accordingly, the high-reflectance characteristic of the Bragg regime is observed only when the circular polarization state of incident light matches the structural handedness of the material; otherwise, low reflectance is observed. Liquid-crystalline as well as thin-film chiral mirrors are available for circular-polarization-sensitive reflection [9,10]. The introduction of a phase defect half-way inside a structurally chiral structure also gives rise to a spectral hole – but only when the circular polarization state of the incident light matches the structural handedness [11–13].

The polarization-sensitivity of structurally chiral spectral-hole filters cannot, of course, be exhibited by isotropic spectral-hole filters. Very recently, Kopp and Genack [14] reported an even more interesting feature. As a CLC with a phase defect becomes thicker, but with its period fixed, the spectral hole in the co-handed reflectance spectrum diminishes steadily and eventually vanishes. Simultaneously, a spectral hole appears and grows in the transmittance spectrum for incident light of the other circular polarization state. The bandwidth of the second spectral hole is a few thousandths of the bandwidth of the initial spectral hole, according to theoretical calculations. Although these conclusions were reported for CLCs, in this paper we have verified the results to qualitatively hold for chiral STFs as well.

Reflection and transmission for all structures discussed heretofore are purely specular [15,16]. Spectral-hole filters implemented with these structures, therefore, cannot be used for nonspecular applications [17]. If, however, the direction of nonhomogeneity were inclined with respect to the thickness direction, then the structure would be periodic in the thickness direction as well as in a direction perpendicular to it [18]. The specular nature of the Bragg phenomenon and the nonspecular nature of the Rayleigh–Wood phenomenon (generally observed with surface-relief gratings [19,20]) can be expected to interact with each other.

With this motivation, slanted chiral STFs were recently proposed by us [21]. Several physical vapor deposition techniques have emerged for manufacturing STFs [10,22–26]. Normally, the helical microcolumns of a chiral STF grow upright on the substrate. However, it is possible to grow the microcolumns slanted at angle $\alpha \neq 0^\circ$ with respect to the substrate normal [25,27], which should lead to the fabrication of slanted chiral STFs.

The interactions of the two orthogonal periodicities of slanted chiral STFs have been researched [21]. In particular, the circular Bragg phenomenon for slanted chiral STFs ($\alpha \neq 0^\circ$) is *partially* nonspecular, in contrast to that for an unslanted chiral STF ($\alpha = 0^\circ$), and is highly affected or even totally subverted at large $|\alpha|$ by the Rayleigh–Wood anomalies that occur due to the transverse periodicity.

In this paper, we examine the optical response of a slanted chiral STF with a phase defect inserted midway through its thickness. The chosen defect is a twist defect characterized by an angle $\phi_t \neq 0^\circ$ [12–14]. The plan of this paper is as follows: Section 2 provides a detailed description of the theoretical treatment of the boundary value problem to be solved. First, the geometry of the boundary value problem, the constitutive relations of the two halves of the slanted chiral STF, and the field representations above and below the central twist defect are presented. Then, coupled wave theory [28,29] is used to formulate a matrix ordinary differential equation [16] for the fields excited in

both the halves. Finally, the numerical solution procedure adopted for the boundary value problem is briefly described, the details being available elsewhere [21]. Section 3 is devoted to the presentation and discussion of the numerical results obtained. An $\exp(-i\omega t)$ time-dependence is implicit, with ω as the angular frequency of the incident plane wave, and t as the time. Vectors are in boldface, while dyadics are double-underlined.

2. Theoretical analysis

Let the region $0 \leqslant z \leqslant 2L$ be occupied by the slanted chiral STF with a twist of angle ϕ_t between the upper and the lower halves about their common axis of nonhomogeneity, as shown in Fig. 1, while the half-spaces $z \leqslant 0$ and $z \geqslant 2L$ are vacuous. A plane wave is incident from the lower half-space $z \leqslant 0$ on to the plane $z = 0$. As a result, reflection and transmission into the two half-spaces occur.

2.1. Constitutive relations

The relative permittivity dyadic $\underline{\underline{\epsilon}}(\mathbf{r}, \lambda_0)$ of the slanted chiral STF of thickness $2L$ is factorable as

$$\underline{\underline{\epsilon}}(\mathbf{r}, \lambda_0) = \underline{\underline{S}}_y(-\alpha) \cdot \underline{\underline{S}}_z(\mathbf{r}) \cdot \underline{\underline{S}}_y(\chi_s) \cdot \underline{\underline{\epsilon}}_{ref}(\lambda_0) \cdot \underline{\underline{S}}_y^T(\chi_s) \cdot \underline{\underline{S}}_z^T(\mathbf{r}) \cdot \underline{\underline{S}}_y^T(-\alpha), \quad 0 \leqslant z \leqslant 2L, \tag{1}$$

where the position vector $\mathbf{r} = x\mathbf{u}_x + y\mathbf{u}_y + z\mathbf{u}_z$, λ_0 is the free-space wavelength, and the superscript T denotes the transpose. As most STFs are locally biaxial [24,30], the reference relative permitivity dyadic is given by [31]

$$\underline{\underline{\epsilon}}_{ref}(\lambda_0) = \epsilon_a(\lambda_0)\mathbf{u}_z\mathbf{u}_z + \epsilon_b(\lambda_0)\mathbf{u}_x\mathbf{u}_x + \epsilon_c(\lambda_0)\mathbf{u}_y\mathbf{u}_y. \tag{2}$$

The wavelength-dependences of the scalars $\epsilon_{a,b,c}$ are assumed to emerge from a single-resonance Lorentzian model [32,33] as

$$\epsilon_{a,b,c}(\lambda_0) = 1 + \frac{p_{a,b,c}}{\left[1 + \left(N_{a,b,c}^{-1} - i\lambda_{a,b,c}\lambda_0^{-1}\right)^2\right]}, \tag{3}$$

where $p_{a,b,c}$ are the oscillator strengths. The parameters $\lambda_{a,b,c}$ and $N_{a,b,c}$ determine the resonance wavelengths and absorption linewidths. Based on the local columnarity of the STFs, we surmise that $|\epsilon_b(\lambda_0)| \geqslant |\epsilon_c(\lambda_0)| \geqslant |\epsilon_a(\lambda_0)|$ away from the resonance wavelengths of the bulk material deposited as the thin film [31,34].

The rotational nonhomogeneity of the chosen thin film is captured by the dyadic

$$\underline{\underline{S}}_z(\mathbf{r}) = \left(\mathbf{u}_x\mathbf{u}_x + \mathbf{u}_y\mathbf{u}_y\right)\cos\left[\frac{\pi}{\Omega}(\mathbf{r}\cdot\mathbf{u}_\ell) + \phi\right] + h\left(\mathbf{u}_y\mathbf{u}_x - \mathbf{u}_x\mathbf{u}_y\right)\sin\left[\frac{\pi}{\Omega}(\mathbf{r}\cdot\mathbf{u}_\ell) + \phi\right] + \mathbf{u}_z\mathbf{u}_z, \tag{4}$$

the axis of rotational nonhomogeneity (i.e., the helical axis) being parallel to the unit vector $\mathbf{u}_\ell = \sin\alpha\mathbf{u}_x + \cos\alpha\mathbf{u}_z$. The structural period along the helical axis is denoted by 2Ω. The parameter $h = 1$ for structural right-handedness, while $h = -1$ for structural left-handedness. The central twist defect is described through the angle

$$\phi = \begin{cases} 0^\circ, & 0 \leqslant z \leqslant L, \\ \phi_t, & L \leqslant z \leqslant 2L. \end{cases} \tag{5}$$

Finally, the dyadic

$$\underline{\underline{S}}_y(\gamma) = (\mathbf{u}_x\mathbf{u}_x + \mathbf{u}_z\mathbf{u}_z)\cos\gamma + (\mathbf{u}_z\mathbf{u}_x - \mathbf{u}_x\mathbf{u}_z)\sin\gamma + \mathbf{u}_y\mathbf{u}_y \tag{6}$$

serves two different roles. Whereas $\underline{\underline{S}}_y(\chi_s)$ delineates the role of the growth process with $90^\circ - \chi_s$ being the angle of declination from the helical axis, $\underline{\underline{S}}_y(-\alpha)$ represents the slanted orientation of the helical axis. Since STFs are generally fabricated using physical vapor deposition [22,26], the

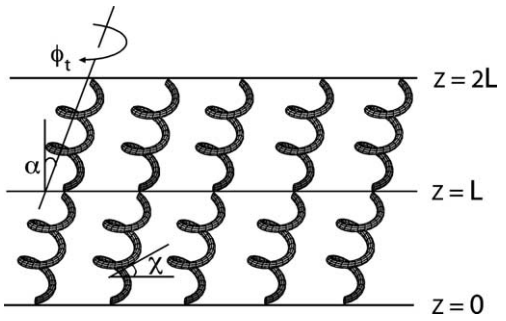

Fig. 1. Schematic of the boundary value problem involving the slanted chiral sculptured thin film with a twist angle of ϕ_t introduced between the upper and lower halves about the axis of nonhomogeneity. Nonspecular reflection and transmission can occur because $\alpha \neq 0^\circ$.

growing microcolumns of an STF must be oriented at some angle to the substrate plane such that the so-called angle of rise $\chi = \chi_s - |\alpha|$. Hence, $\chi \in (0°, 90°]$ for the ideal helical microcolumns of a slanted chiral STF to always grow upwards in relation to the substrate plane, while $0° < \chi_s < 90°$ is mandated by the equation of a helix. Thus, α is restricted to the range $(-\chi_s, \chi_s)$. When $\alpha = 0°$, the slant is absent and the usual chiral STFs are represented by $\underline{\underline{\epsilon}}(\mathbf{r}, \lambda_0) \equiv \underline{\underline{\epsilon}}(z, \lambda_0)$.

2.2. Incident, reflected and transmitted plane waves

Clearly, $\underline{\underline{\epsilon}}(\mathbf{r}, \lambda_0) \equiv \epsilon(x, z, \lambda_0)$ is periodic along the x and the z axes, but is independent of y. Therefore, the field representation in the two half-spaces must be periodic with respect to x. It must also comprise both specular and nonspecular plane-wave components, in accordance with the Floquet–Bloch theorem [28,35,36].

Let the incident plane wave propagate at an angle $\theta_{\rm inc}$ to the $+z$ axis and at an angle $\psi_{\rm inc}$ to the $+x$ axis (in the xy plane), in the lower half-space $z \leqslant 0$. Hence, the incident, the reflected and the transmitted electromagnetic field phasors are best expressed in a set of Floquet harmonics [29] respectively, as follows:

$$\mathbf{E}_i = \sum_{n=0,\pm1,\pm2,\ldots} \left[\frac{(\mathrm{i}s_n - \mathbf{p}_n^+)}{\sqrt{2}} a_{\rm L}^{(n)} - \frac{(\mathrm{i}s_n + \mathbf{p}_n^+)}{\sqrt{2}} a_{\rm R}^{(n)} \right] \times \exp\left[\mathrm{i}\left(k_{xn}x + k_{y0}y + k_{zn}z\right)\right], \quad z \leqslant 0, \tag{7}$$

$$\mathbf{H}_i = \sum_{n=0,\pm1,\pm2,\ldots} \frac{-\mathrm{i}}{\eta_0} \left[\frac{(\mathrm{i}s_n - \mathbf{p}_n^+)}{\sqrt{2}} a_{\rm L}^{(n)} + \frac{(\mathrm{i}s_n + \mathbf{p}_n^+)}{\sqrt{2}} a_{\rm R}^{(n)} \right] \times \exp\left[\mathrm{i}\left(k_{xn}x + k_{y0}y + k_{zn}z\right)\right], \quad z \leqslant 0, \tag{8}$$

$$\mathbf{E}_r = \sum_{n=0,\pm1,\pm2,\ldots} \left[-\frac{(\mathrm{i}s_n - \mathbf{p}_n^-)}{\sqrt{2}} r_{\rm L}^{(n)} + \frac{(\mathrm{i}s_n + \mathbf{p}_n^-)}{\sqrt{2}} r_{\rm R}^{(n)} \right] \times \exp\left[\mathrm{i}\left(k_{xn}x + k_{y0}y - k_{zn}z\right)\right], \quad z \leqslant 0, \tag{9}$$

$$\mathbf{H}_r = \sum_{n=0,\pm1,\pm2,\ldots} \frac{-\mathrm{i}}{\eta_0} \left[-\frac{(\mathrm{i}s_n - \mathbf{p}_n^-)}{\sqrt{2}} r_{\rm L}^{(n)} - \frac{(\mathrm{i}s_n + \mathbf{p}_n^-)}{\sqrt{2}} r_{\rm R}^{(n)} \right] \times \exp\left[\mathrm{i}\left(k_{xn}x + k_{y0}y - k_{zn}z\right)\right], \quad z \leqslant 0, \tag{10}$$

$$\mathbf{E}_t = \sum_{n=0,\pm1,\pm2,\ldots} \left[\frac{(\mathrm{i}s_n - \mathbf{p}_n^+)}{\sqrt{2}} t_{\rm L}^{(n)} - \frac{(\mathrm{i}s_n + \mathbf{p}_n^+)}{\sqrt{2}} t_{\rm R}^{(n)} \right] \times \exp\left\{\mathrm{i}\left[k_{xn}x + k_{y0}y + k_{zn}(z - 2L)\right]\right\}, \quad z \geqslant 2L, \tag{11}$$

$$\mathbf{H}_t = \sum_{n=0,\pm1,\pm2,\ldots} \frac{-\mathrm{i}}{\eta_0} \left[\frac{(\mathrm{i}s_n - \mathbf{p}_n^+)}{\sqrt{2}} t_{\rm L}^{(n)} + \frac{(\mathrm{i}s_n + \mathbf{p}_n^+)}{\sqrt{2}} t_{\rm R}^{(n)} \right] \times \exp\left\{\mathrm{i}\left[k_{xn}x + k_{y0}y + k_{zn}(z - 2L)\right]\right\}, \quad z \geqslant 2L. \tag{12}$$

In (7)–(12) and thereafter, $\eta_0 = \sqrt{\mu_0/\epsilon_0}$ is the intrinsic impedance, while μ_0 and ϵ_0 are the permittivity and the permeability, of free space. The transverse wavenumbers

$$\begin{aligned} k_{xn} &= k_0 \sin\theta_{\rm inc}\cos\psi_{\rm inc} + n\kappa_x, \\ k_{y0} &= k_0 \sin\theta_{\rm inc}\sin\psi_{\rm inc}, \\ n &= 0, \pm1, \pm2, \ldots, \end{aligned} \tag{13}$$

where $k_0 = \omega\sqrt{\mu_0\epsilon_0} = 2\pi/\lambda_0$ is the free-space wavenumber, and

$$\kappa_x = (\pi/\Omega)|\sin\alpha| \tag{14}$$

because the slanted chiral STF has a period $L_x = 2\Omega/|\sin\alpha|$ along the x axis. The vertical wavenumbers,

$$k_{zn} = \begin{cases} +\left(k_0^2 - k_{xn}^2 - k_{y0}^2\right)^{1/2} & \text{if } k_0^2 \geqslant k_{xn}^2 + k_{y0}^2, \\ +\mathrm{i}\left(k_{xn}^2 + k_{y0}^2 - k_0^2\right)^{1/2} & \text{otherwise,} \end{cases} \tag{15}$$

are either real-valued (for propagating harmonics) or imaginary (for evanescent harmonics).

The nth-order Floquet harmonic in any of the fields (7)–(12) involves left and right circularly polarized (LCP and RCP) components with amplitudes $a_{\rm L}^{(n)}$ and $a_{\rm R}^{(n)}$ for the incident plane wave, $r_{\rm L}^{(n)}$ and $r_{\rm R}^{(n)}$ for the reflected field, and $t_{\rm L}^{(n)}$ and $t_{\rm R}^{(n)}$ for the transmitted field. As the incident plane wave is a Floquet harmonic of order $n = 0$, the coefficients $a_{\rm L}^{(n)} = a_{\rm R}^{(n)} = 0\ \forall n \neq 0$. The vectors,

$$\begin{aligned} \mathbf{s}_n &= \frac{-k_{y0}\mathbf{u}_x + k_{xn}\mathbf{u}_y}{k_{xyn}}, \\ \mathbf{p}_n^{\pm} &= \mp\left(\frac{k_{xn}\mathbf{u}_x + k_{y0}\mathbf{u}_y}{k_{xyn}}\right)\frac{k_{zn}}{k_0} + \frac{k_{xyn}}{k_0}\mathbf{u}_z, \\ n &= 0, \pm1, \pm2, \ldots, \end{aligned} \tag{16}$$

individually denote linear polarization of the perpendicular and the parallel types in electromagnetics literature [37], respectively, with respect to the direction vectors $\mathbf{d}_n^{\pm} = \left(k_{xn}\mathbf{u}_x + k_{y0}\mathbf{u}_y \pm k_{zn}\mathbf{u}_z\right)/k_0$; whilst

$$k_{xyn} = +\sqrt{k_{xn}^2 + k_{y0}^2} \tag{17}$$

is defined for convenience.

Since $\{a_{\mathrm{L}}^{(n)}\}$ and $\{a_{\mathrm{R}}^{(n)}\}$ are supposedly known, the amplitude sets $\{r_{\mathrm{L}}^{(n)}\}$, $\{r_{\mathrm{R}}^{(n)}\}$, $\{t_{\mathrm{L}}^{(n)}\}$ and $\{t_{\mathrm{R}}^{(n)}\}$, $(n = 0, \pm1, \pm2, \ldots)$, have to be determined by solving a boundary value problem.

2.3. Coupled wave equations

Each of the nine components $\epsilon_{pq}(x,z)$, $(p,q = x,y,z)$, of the relative permittivity dyadic $\underline{\underline{\epsilon}}(\mathbf{r})$ of (1) is represented as

$$\epsilon_{pq}(x,z) = \sum_{n=0,\pm1,\pm2} \epsilon_{pq}^{(n)}(z)\exp\left(\mathrm{i}n\kappa_x x\right), \quad p,q = x,y,z, \;\; 0 \leqslant z \leqslant 2L, \tag{18}$$

where $\epsilon_{pq}^{(n)}(z)$ are the Fourier amplitudes; we have dropped explicitly mention of wavelength-dependences at this point. The Floquet–Bloch theorem entails the decompositions

$$\mathbf{E}(\mathbf{r}) = \sum_{n=0,\pm1,\pm2,\ldots} \left[E_x^{(n)}(z)\mathbf{u}_x + E_y^{(n)}(z)\mathbf{u}_y + E_z^{(n)}(z)\mathbf{u}_z\right] \times \exp\left[\mathrm{i}\left(k_{xn}x + k_{y0}y\right)\right], \quad 0 \leqslant z \leqslant 2L, \tag{19}$$

$$\mathbf{H}(\mathbf{r}) = \sum_{n=0,\pm1,\pm2,\ldots} \left[H_x^{(n)}(z)\mathbf{u}_x + H_y^{(n)}(z)\mathbf{u}_y + H_z^{(n)}(z)\mathbf{u}_z\right] \times \exp\left[\mathrm{i}\left(k_{xn}x + k_{y0}y\right)\right], \quad 0 \leqslant z \leqslant 2L, \tag{20}$$

for the electromagnetic field phasors within the chosen thin-film device. Parenthetically, we note that Rokushima and Yamakita [18] also used the Floquet–Bloch theorem for locally uniaxial chiral liquid crystals; however, their representation is periodic with respect to the helical axis.

On substituting (18)–(20) in the frequency-domain Maxwell curl postulates

$$\nabla \times \mathbf{E}(\mathbf{r}) = \mathrm{i}\omega\mu_0\mathbf{H}(\mathbf{r}), \quad \nabla \times \mathbf{H}(\mathbf{r}) = -\mathrm{i}\omega\epsilon_0\underline{\underline{\epsilon}}(\mathbf{r})\cdot\mathbf{E}(\mathbf{r}), \quad 0 < z < 2L, \tag{21}$$

and exploiting the orthogonalities of the functions $\exp[\mathrm{i}(k_{xn}x + k_{y0}y)]$ across any plane $z =$ constant, we derive the following set of coupled wave equations:

$$\frac{\mathrm{d}}{\mathrm{d}z}E_x^{(n)}(z) - \mathrm{i}k_{xn}E_z^{(n)}(z) = \mathrm{i}k_0\eta_0 H_y^{(n)}(z), \tag{22}$$

$$\frac{\mathrm{d}}{\mathrm{d}z}E_y^{(n)}(z) - \mathrm{i}k_{y0}E_z^{(n)}(z) = -\mathrm{i}k_0\eta_0 H_x^{(n)}(z), \tag{23}$$

$$k_{y0}E_x^{(n)}(z) - k_{xn}E_y^{(n)}(z) = -k_0\eta_0 H_z^{(n)}(z), \tag{24}$$

$$\frac{\mathrm{d}}{\mathrm{d}z}H_x^{(n)}(z) - \mathrm{i}k_{xn}H_z^{(n)}(z) = -\frac{\mathrm{i}k_0}{\eta_0}\sum_{\tilde{n}=0,\pm1,\pm2,\ldots}\left[\epsilon_{yx}^{(n-\tilde{n})}(z)E_x^{(\tilde{n})}(z) + \epsilon_{yy}^{(n-\tilde{n})}(z)E_y^{(\tilde{n})}(z) + \epsilon_{yz}^{(n-\tilde{n})}(z)E_z^{(\tilde{n})}(z)\right], \tag{25}$$

$$\frac{\mathrm{d}}{\mathrm{d}z}H_y^{(n)}(z) - \mathrm{i}k_{y0}H_z^{(n)}(z) = \frac{\mathrm{i}k_0}{\eta_0}\sum_{\tilde{n}=0,\pm1,\pm2,\ldots}\left[\epsilon_{xx}^{(n-\tilde{n})}(z)E_x^{(\tilde{n})}(z) + \epsilon_{xy}^{(n-\tilde{n})}(z)E_y^{(\tilde{n})}(z) + \epsilon_{xz}^{(n-\tilde{n})}(z)E_z^{(\tilde{n})}(z)\right], \tag{26}$$

$$k_{y0}H_x^{(n)}(z) - k_{xn}H_y^{(n)}(z) = \frac{k_0}{\eta_0}\sum_{\tilde{n}=0,\pm1,\pm2,\ldots}\left[\epsilon_{zx}^{(n-\tilde{n})}(z)E_x^{(\tilde{n})}(z) + \epsilon_{zy}^{(n-\tilde{n})}(z)E_y^{(\tilde{n})}(z) + \epsilon_{zz}^{(n-\tilde{n})}(z)E_z^{(\tilde{n})}(z)\right]. \tag{27}$$

These six equations hold for all $n = 0, \pm1, \pm2, \ldots$

The solution procedure for (22)–(27) is described in detail in a predecessor paper [21], to which we refer the interested readers. It suffices to mention here that both n and $\tilde{n}$ are restricted to the range $[-N_T, N_T]$, $N_T > 0$, and a system of $4(2N_T + 1)$ ordinary differential equations is solved numerically, with (7)–(12) providing the necessary boundary conditions.

Finally, reflectances ($R^{(n)}_{\mathrm{LL}}$, etc.) and the transmittances ($T^{(n)}_{\mathrm{LL}}$, etc.) are defined as

$$\begin{bmatrix} R^{(n)}_{\mathrm{LL}} & R^{(n)}_{\mathrm{LR}} \\ R^{(n)}_{\mathrm{RL}} & R^{(n)}_{\mathrm{RR}} \end{bmatrix} = \frac{\mathrm{Im}(\xi_n\zeta_n)}{\mathrm{Im}(\xi_0\zeta_0)} \begin{bmatrix} \frac{|r^{(n)}_{\mathrm{L}}|^2}{|a^0_L|^2} & \frac{|r^{(n)}_{\mathrm{L}}|^2}{|a^0_R|^2} \\ \frac{|r^{(n)}_{\mathrm{R}}|^2}{|a^0_L|^2} & \frac{|r^{(n)}_{\mathrm{R}}|^2}{|a^0_R|^2} \end{bmatrix},$$

$$\begin{bmatrix} T^{(n)}_{\mathrm{LL}} & T^{(n)}_{\mathrm{LR}} \\ T^{(n)}_{\mathrm{RL}} & T^{(n)}_{\mathrm{RR}} \end{bmatrix} = \frac{\mathrm{Im}(\xi_n\zeta_n)}{\mathrm{Im}(\xi_0\zeta_0)} \begin{bmatrix} \frac{|t^{(n)}_{\mathrm{L}}|^2}{|a^0_L|^2} & \frac{|t^{(n)}_{\mathrm{L}}|^2}{|a^0_R|^2} \\ \frac{|t^{(n)}_{\mathrm{R}}|^2}{|a^0_L|^2} & \frac{|t^{(n)}_{\mathrm{R}}|^2}{|a^0_R|^2} \end{bmatrix}, \quad (28)$$

$$n \in [-N_T, N_T],$$

where $\mathrm{Im}()$ denotes the imaginary part, and

$$\xi_n = \frac{1}{\sqrt{2}}\left(\frac{k_{xn}k_{zn}}{k_0 k_{xyn}} - \mathrm{i}\frac{k_{y0}}{k_{xyn}}\right),$$

$$\zeta_n = \frac{1}{\sqrt{2}}\left(\frac{k_{y0}k_{zn}}{k_0 k_{xyn}} - \mathrm{i}\frac{k_{xn}}{k_{xyn}}\right), \quad (29)$$

$$n \in [-N_T, N_T].$$

Co-polarized remittances (i.e., reflectances and transmittances) have both subscripts identical, while cross-polarized remittances have both subscripts different. The principle of conservation of energy mandates the inequalities

$$\sum_{n\in[-N_T,N_T]} \left[R^{(n)}_{\mathrm{LL}} + R^{(n)}_{\mathrm{RL}} + T^{(n)}_{\mathrm{LL}} + T^{(n)}_{\mathrm{RL}}\right] \leqslant 1, \quad (30)$$

$$\sum_{n\in[-N_T,N_T]} \left[R^{(n)}_{\mathrm{LR}} + R^{(n)}_{\mathrm{RR}} + T^{(n)}_{\mathrm{LR}} + T^{(n)}_{\mathrm{RR}}\right] \leqslant 1, \quad (31)$$

which reduce to equalities for nondissipative thin films. The sums on the left sides of (30) and (31) are denoted by $1 - A_{\mathrm{L}}$ and $1 - A_{\mathrm{R}}$, where A_{L} and A_{R} are the absorbances for incident LCP and RCP plane waves, respectively.

3. Results and discussion

3.1. Preliminaries

The solution procedure was implemented using double-precision arithmetic in Fortran 90 on a Solaris computer. The following constitutive and structural parameters were chosen: $p_a = 2.0$, $p_b = 2.6$ and $p_c = 2.1$; $\lambda_a = \lambda_c = 140$ nm and $\lambda_b = 150$ nm; $N_a = N_b = N_c = 40{,}000$; $\Omega = 300$ nm; $\chi_{\mathrm{s}} = 30°$; $h = 1$. These constitutive parameters are potentially realizable using silicon dioxide, and are thus likely to be compatible with semiconductor and optical technologies. The half-thickness L varied from 25Ω to 100Ω in our study, the minimum value of L chosen to let the circular Bragg phenomenon develop fully [16,21]. The slant angle α was set to be positive and less than χ_{s}. The twist angle ϕ_{t} was generally assumed equal to 90°, in order to produce a spectral hole roughly in the center of the Bragg regime. For compatibility with the commonplace planar structures in electronics and optics, we examined only the normal-incidence case (i.e., $\theta_{\mathrm{inc}} = 0°$) with $\psi_{\mathrm{inc}} = 0°$; hence, $\sin\psi_n = 0\ \forall n$. We focused on the wavelength-regime $\lambda_0 \in [1000, 1110]$ nm.

The maximum order parameter for the Floquet harmonics was fixed at $N_T = 3$ for the chosen wavelength-regime, after ensuring that every reflectance and transmittance greater than 0.001 converged to 1% accuracy. All propagating harmonics and some evanescent harmonics were thereby covered. Moreover, we ensured that the left sides of both (30) and (31) converged, and that neither condition was violated by more than 1 ppm.

3.2. Unslanted chiral STF device

Let us begin with $\alpha = 0°$, which provides the STF analog of the CLC devices considered by Kopp and Genack [14]. The center-wavelength of the Bragg regime is then estimated as 1090 nm, and the full-width-at-half-maximum bandwidth as 72 nm [21].

Fig. 2 shows a narrow spectral hole (about 2 nm bandwidth) in the total co-polarized reflectance $R_{\mathrm{RR}} = \sum_n R^{(n)}_{\mathrm{RR}}$ and, correspondingly, a peak in the total co-polarized transmittance $T_{\mathrm{RR}} = \sum_n T^{(n)}_{\mathrm{RR}}$, excited by a normally incident RCP plane wave when $L = 27\Omega$. The plots in Fig. 2 are similar to those discussed by Hodgkinson et al. [12]. However, on extrapolating from Kopp and Genack [14], a spectral hole must also be generated by an incident LCP plane wave, provided the ratio L/Ω is sufficiently large.

Indeed, Fig. 3 shows an ultra-narrow (about 0.02 nm bandwidth) spectral hole in the total co-polarized transmittance $T_{\mathrm{LL}} = \sum_n T^{(n)}_{\mathrm{LL}}$ and a corre-

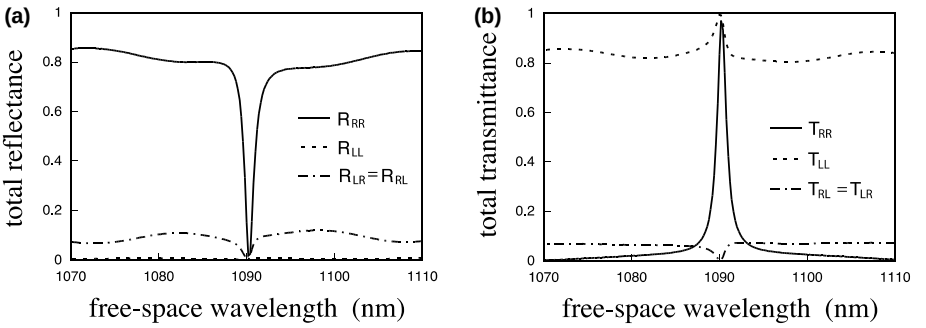

Fig. 2. (a) Total reflectances $R_{RR} = \sum_n R_{RR}^{(n)}$, etc., and (b) total transmittances $T_{RR} = \sum_n T_{RR}^{(n)}$, etc., computed for the unslanted chiral STF device with the following parameters: $\alpha = 0°$, $\chi_s = 30°$, $p_a = 2.0$, $p_b = 2.6$, $p_c = 2.1$, $\lambda_a = \lambda_c = 140$ nm, $\lambda_b = 150$ nm, $N_a = N_b = N_c = 40{,}000$, $\Omega = 300$ nm, $h = 1$, $\phi_t = 90°$, $L = 27\Omega$ and $\theta_{inc} = \psi_{inc} = 0°$.

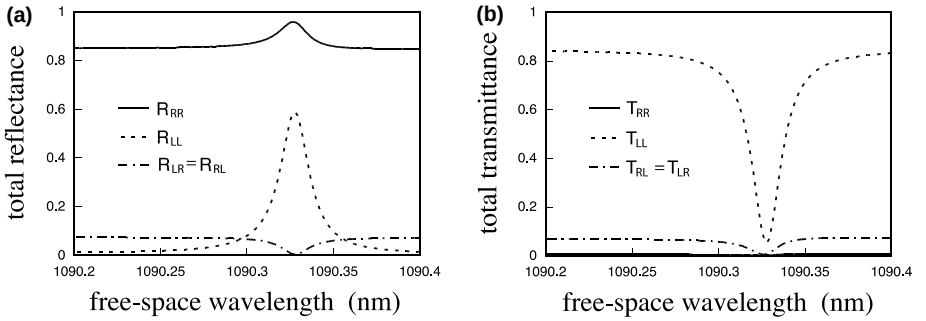

Fig. 3. Same as Fig. 2, but for $L = 91\Omega$.

sponding peak in the total co-polarized reflectance $R_{LL} = \sum_n R_{LL}^{(n)}$ excited by an incident LCP plane wave when $L = 91\Omega$. Therefore, there are two types of spectral holes of opposite circular polarization states, depending on different values of L/Ω. Furthermore, one type of hole is found in co-handed reflectance – when the handedness of the incident circularly polarized plane wave is the same as the structural handedness of the chosen thin film – and the second in cross-handed transmittance (when the handednesses of the incident plane wave and the chiral STF do not coincide).

Fig. 4 shows the plots of T_{RR} and R_{LL} versus the ratio L/Ω at the peak wavelength $\lambda_p = 1090.328$ nm, which is the center-wavelength of the 0.02 nm spectral hole of Fig. 3. If L_{co} is defined as the crossover thickness at which $T_{RR} = R_{LL}$, spectral holes of the second type appear only for $L > L_{co}$. The crossover thickness is seen in Fig. 4 to be $L_{co} \approx 54.5\Omega$. As L increases above L_{co}, the spectral reflection hole wanes and the spectral transmission hole enhances to steady state.

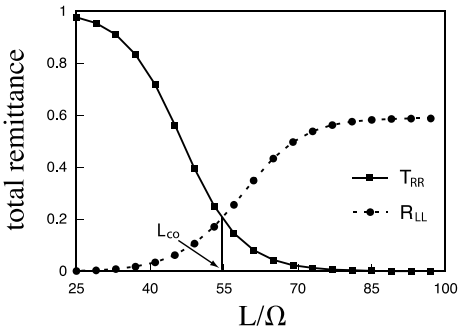

Fig. 4. Total transmittance $T_{RR} = \sum_n T_{RR}^{(n)}$ and total reflectance $R_{LL} = \sum_n R_{LL}^{(n)}$ versus L/Ω at the peak wavelength $\lambda_p = 1090.328$ nm. See Fig. 2 for other parameters. The crossover thickness $L_{co} \approx 54.5\Omega$.

3.3. Slanted chiral STF device

There is no distinction in the direction of propagation of Floquet harmonics of orders $n = 0$ and $n \neq 0$, when $\alpha = 0°$ [21]. But a distinction appears for $\alpha \neq 0°$ between Floquet harmonics of orders $n = 0$ and $n \neq 0$, the former being classified as *specular* and the latter as *nonspecular* in the literature on diffraction gratings [38]. Regardless of the value of α in our studies, non-negligible remittances were found to be only of orders $n = \pm 2$ (nonspecular) and $n = 0$ (specular). The remittances of other orders turned out to be negligible (<0.01) in the wavelength-regime focused on. Plots of only the non-negligible remittances are presented in this paper. All presented results apply for negative values of α, provided all remittances of order n are considered as the remittances of order $-n$.

Let us commence with $\alpha = 15°$. The center-wavelength of the Bragg regime can be *estimated* as the solution of the equation [21]

$$\lambda_0^{\mathrm{Br}} = (\Omega \cos\alpha)\left[\sqrt{\epsilon_c\left(\lambda_0^{\mathrm{Br}}\right)} + \sqrt{\tilde{\epsilon}_d\left(\lambda_0^{\mathrm{Br}}\right)}\right], \tag{32}$$

where

$$\tilde{\epsilon}_d(\lambda_0) = \frac{\epsilon_a(\lambda_0)\epsilon_b(\lambda_0)}{\epsilon_a(\lambda_0)\cos^2\chi + \epsilon_a(\lambda_0)\sin^2\chi}. \tag{33}$$

In comparison with Figs. 2 and 3 therefore, Figs. 5 and 6 display a blue-shifted Bragg regime with $\lambda_0^{\mathrm{Br}} \approx 1053$ nm, while $\lambda_0^{\mathrm{Br}} \approx 1090$ nm in Figs. 2 and 3.

Fig. 5 shows the remittance spectrums for $L = 27\Omega$. A hole centered at λ_0^{Br} in the spectrum of $R_{\mathrm{RR}}^{(-2)}$, and a corresponding peak in the spectrum of $T_{\mathrm{RR}}^{(0)}$, are clearly evident therein. The bandwidth of the hole is still about 2 nm. Thus, a major effect of $\alpha \neq 0°$ is to produce a nonspecular spectral reflection hole.

That reflection hole is absent in the remittance spectrums of Fig. 6, for which $L = 91\Omega$. Instead, a hole appears in the spectrum of $T_{\mathrm{LL}}^{(0)}$, which is purely specular; and it is accompanied by signifi-

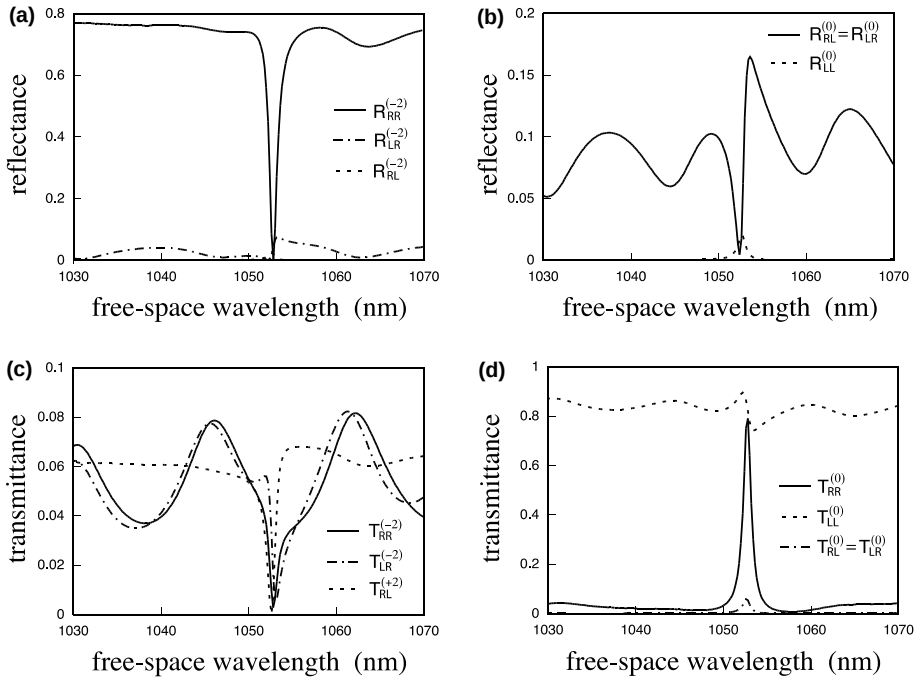

Fig. 5. (a,b) Nonspecular and specular reflectances and (c,d) nonspecular and specular transmittances of order n, computed for the slanted chiral STF device with the following parameters: $\alpha = 15°$, $\chi_s = 30°$, $p_a = 2.0$, $p_b = 2.6$, $p_c = 2.1$, $\lambda_a = \lambda_c = 140$ nm, $\lambda_b = 150$ nm, $N_a = N_b = N_c = 40{,}000$, $\Omega = 300$ nm, $h = 1$, $\phi_t = 90°$, $L = 27\Omega$ and $\theta_{\mathrm{inc}} = \psi_{\mathrm{inc}} = 0°$. Remittances of maximum magnitudes less than 0.01 are not shown.

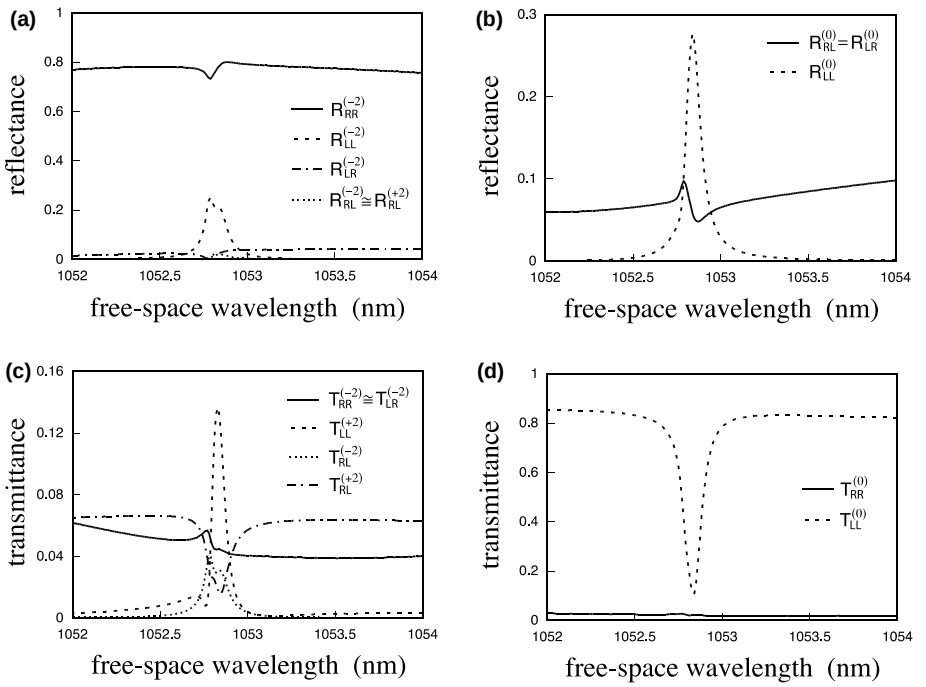

Fig. 6. Same as Fig. 5, but for $L = 91\Omega$.

cant peaks in the spectrums of $R_{\mathrm{LL}}^{(-2)}$, $R_{\mathrm{LL}}^{(0)}$ and $T_{\mathrm{LL}}^{(-2)}$. The peak wavelength $\lambda_{\mathrm{p}} = 1052.80$ nm and the bandwidth is $\sim$0.15 nm.

The crossover thickness of the slanted chiral STF device can be estimated from the plots of various remittances against L/Ω in Fig. 7. Actually, the peak wavelength turns out to be a function of both α and L. For $\alpha = 0°$, $\lambda_{\mathrm{p}} = 1090.328$ nm for all L. In contrast, λ_{p} varies from 1052.65 to 1053.75 nm as L changes from 25Ω to 100Ω, when $\alpha = 15°$. The remittances at the peak wavelengths seem to be varying somewhat irregularly with L in Fig. 7, in contrast to that in Fig. 4 for the unslanted chiral STF device. However, the values of $T_{\mathrm{RR}}^{(0)}$ and $R_{\mathrm{LL}}^{(-2)} + R_{\mathrm{LL}}^{(0)} + T_{\mathrm{LL}}^{(+2)}$ at 1052.80 nm do vary quite smoothly with L. From their plots therefore, the crossover thickness is determined as $L_{\mathrm{co}} = 42.0\Omega$ for $\alpha = 15°$. Only for $L < L_{\mathrm{co}}$ does the spectral reflection hole exist in $R_{\mathrm{RR}}^{(-2)}$; when $L > L_{\mathrm{co}}$, the spectral transmission hole in $T_{\mathrm{LL}}^{(0)}$ takes over just as for the unslanted chiral STF device.

Though the chiral STF device, whether slanted or unslanted, is very weakly dissipative, significant absorption occurs only for LCP incidence in the wavelength-regime of the spectral transmission hole ($L > L_{\mathrm{co}}$). In contrast, the absorbance for RCP incidence first increases to a small value (< 0.1) as L increases to L_{co}, and then drops to a minuscule value (< 0.01). Fig. 8 shows the absorbance spectrums for LCP incidence in both the unslanted and the slanted chiral STF devices when $L = 91\Omega$. Clearly, absorbance is higher for the unslanted chiral STF device than for the slanted one, in their respective spectral transmission hole regimes.

When dissipation in the chiral slanted STF is enhanced – for example, by choosing smaller $N_{a,b,c}$ in (3) – the spectral hole in $T_{\mathrm{LL}}^{(0)}$ for $L > L_{\mathrm{co}}$ fades away, although the spectral hole in $R_{\mathrm{RR}}^{(-2)}$ for $L < L_{\mathrm{co}}$ still exists. We concluded thus from several calculations not reported here. This conclusion is not surprising because the transmission hole is affected by the entire thickness $2L$ of the thin film, whereas the reflection hole is affected only by the first few thickness periods [39,40].

While the transmission hole always occurs in the spectrum of $T_{\mathrm{LL}}^{(0)}$ for $L > L_{\mathrm{co}}$, the corresponding reflectance peaks appear in different Floquet harmonics as the slant angle α changes. Fig. 9 shows

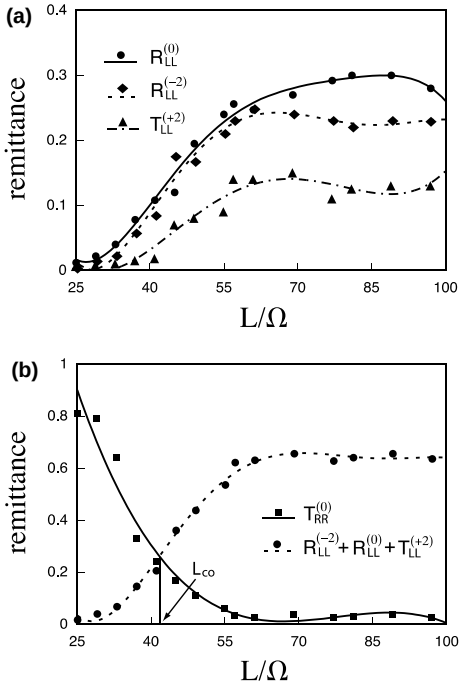

Fig. 7. (a) Reflectances $R_{LL}^{(-2)}$ and $R_{LL}^{(0)}$ as well as transmittance $T_{LL}^{(+2)}$, and (b) transmittance $T_{RR}^{(0)}$ and the sum $R_{LL}^{(-2)}+R_{LL}^{(0)}+T_{LL}^{(+2)}$, versus L/Ω at the peak wavelength $\lambda_p = 1052.80$ nm. The curves are obtained by least-squares fitting of fifth-order polynomials to the computed data (shown by heavy dots).

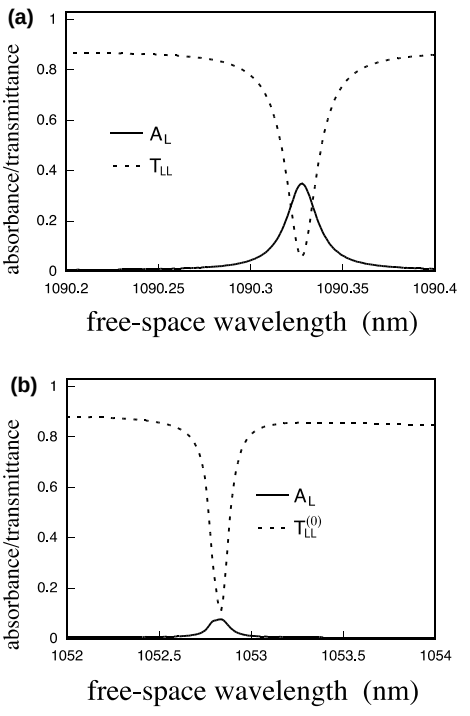

Fig. 8. Absorbance $A_L = 1 - \sum_n [R_{RL}^{(n)} + R_{LL}^{(n)} + T_{RL}^{(n)} + T_{LL}^{(n)}]$ for LCP incidence for (a) the unlanted chiral STF device and (b) the slanted chiral STF device ($\alpha = 15°$), when $L = 91\Omega$. See Fig. 2 for other parameters. For comparison, T_{LL} and $T_{LL}^{(0)}$, respectively, are also plotted.

the peaks in the co-polarized reflectances of different orders for $\alpha = 5°, 10°, 15°$ and 16.7°, respectively, excited by an incident LCP plane wave when $L = 91\Omega$. The spectral hole in $T_{LL}^{(0)}$ shown in Fig. 9 is nearly unaffected by α, though its bandwidth increases with α (with the exception of $\alpha = 16.7°$). But the reflectance peak first shifts from a nonspecular mode ($R_{LL}^{(+2)}$) to the specular mode ($R_{LL}^{(0)}$), and then is shared by the specular and the other nonspecular modes ($R_{LL}^{(0)}$ and $R_{LL}^{(-2)}$), as α increases up to 15°. A further increase of α returns the peak in Fig. 9 to the specular mode.

In fact, as α increases beyond 15°, the circular Bragg phenomenon is subverted by a Rayleigh–Wood anomaly, which is the conversion of the nth-order Floquet harmonic from propagating to evanescent, or vice versa. This conversion occurs at the wavelength [21]

$$\lambda_{0_n}^{RW} = \frac{2\Omega}{|n|\sin\alpha}. \tag{34}$$

At a fixed α, the nth-order Floquet harmonic is evanescent along the z axis for $\lambda_0 > \lambda_{0_n}^{RW}$.

As α increases from 0°, in the present instance, $\lambda_{0_{-2}}^{RW}$ decreases from "infinity" and begins to approach the center-wavelength λ_0^{Br} of the Bragg regime predicted by (32). Both $\lambda_{0_{-2}}^{RW}$ and λ_0^{Br} blue-shift as α increases, but $\lambda_{0_{-2}}^{RW}$ decreases more rapidly than λ_0^{Br}, and the Rayleigh–Wood anomaly eventually wipes out the circular Bragg phenomenon. No wonder, the spectral hole in $R_{RR}^{(-2)}$ is absent in Fig. 10 for $\alpha = 16.7°$ and $L = 27\Omega$. But the spectral hole in $T_{LL}^{(0)}$ survives at about $\lambda_p = 1043.98$ nm when $L = 91\Omega$; see Fig. 9(d). For $\alpha > 17.1°$, the circular Bragg phenomenon vanishes completely, and in consequence, neither of the two types of spectral holes exists.

Finally, the twist angle $\phi_t \neq 90°$ affects the spectral holes too. Most significantly, the spectral holes are not located roughly in the center of the

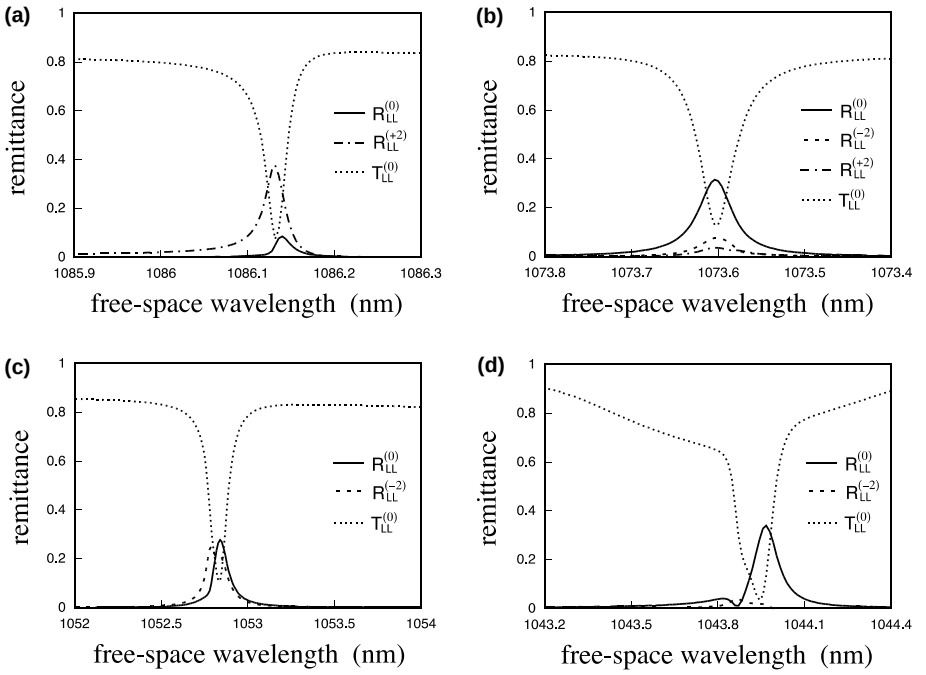

Fig. 9. Reflectances $R_{LL}^{(n)}$ ($n = 0, \pm 2$) and transmittance $T_{LL}^{(0)}$, computed for the slanted chiral STF device with (a) $\alpha = 5°$, (b) $\alpha = 10°$, (c) $\alpha = 15°$ and (d) $\alpha = 16.7°$. See Fig. 6 for other parameters. Reflectances of maximum magnitude less than 0.01 are not shown.

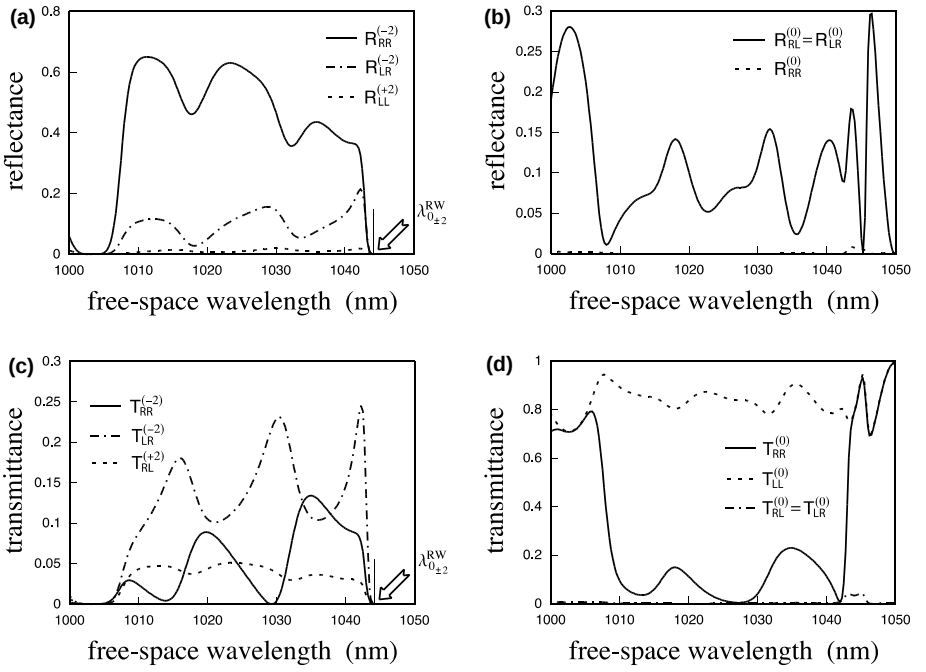

Fig. 10. Same as Fig. 5, but for $\alpha = 16.7°$.

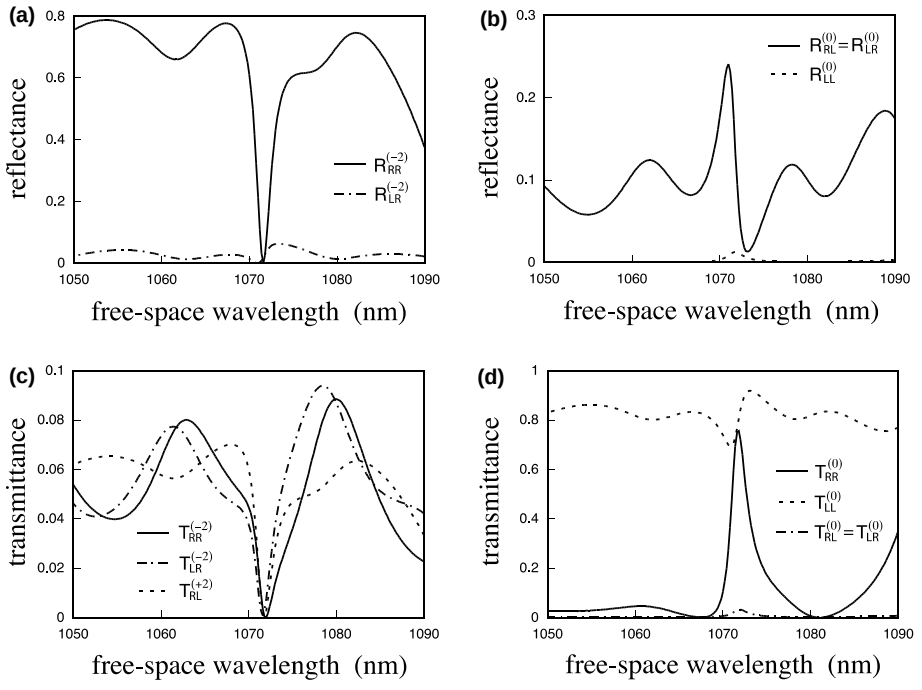

Fig. 11. Same as Fig. 5, but for $\phi_t = 45°$.

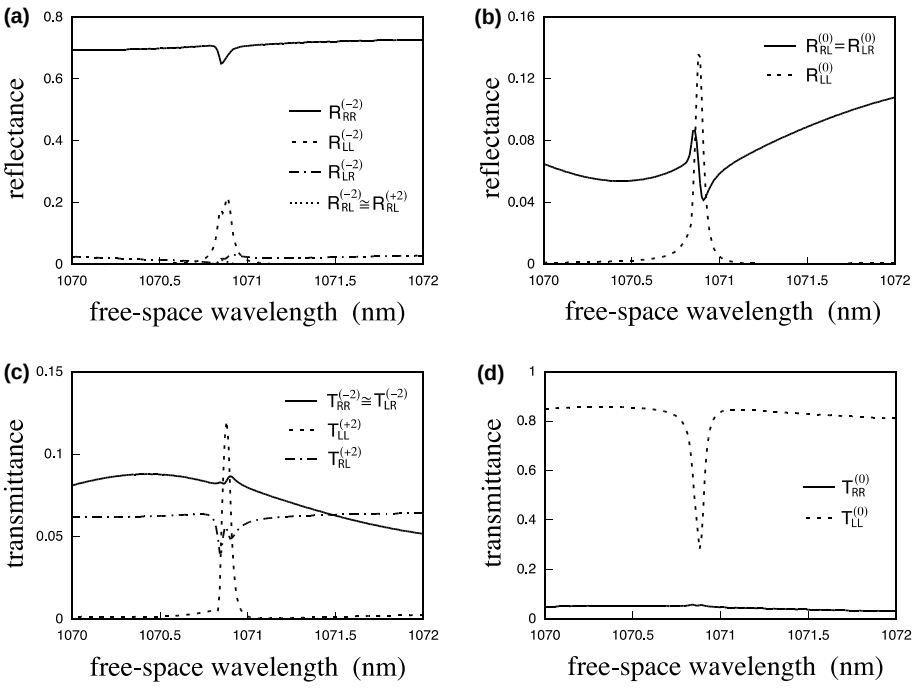

Fig. 12. Same as Fig. 6, but for $\phi_t = 45°$.

Bragg regime as for $\phi_t = 90°$, but are shifted towards the edges of the Bragg regime when $\phi \neq 90°$. This is illustrated by Figs. 11 and 12 – which show the spectral holes of the chiral slanted STF device as before, but with $\phi_t = 45°$. Evidently, the spectral holes, located close to 1071 nm, are blue-shifted in the Bragg regime.

4. Concluding remarks

In this paper, we have theoretically analyzed an optical device made by introducing a central twist defect in a slanted chiral sculptured thin film. A slanted chiral STF is periodically nonhomogenous in two directions: normal and parallel to the substrate plane. The normal and transverse periodicities are intimately coupled by the slant angle $\alpha \neq 0°$.

A coupled wave theory was employed for the planewave response of the slanted chiral STF device of finite thickness. The twist angle ϕ_t, if equal to 90°, gives rise to two types of spectral holes roughly centered in the Bragg regime: one is in the nonspecular reflectance excited by an incident RCP plane wave, and the other in the specular transmittance excited by an incident LCP plane wave. The thickness of the device determines which of the two hole is observed. Both types of holes eventually disappear – as the Bragg regime also does – as α increases, having been subverted completely by the Rayleigh–Wood phenomenon.

Corresponding to the spectral reflection hole, a peak occurs in the co-handed and specular transmittance for all α. However, a reflectance peak accompanying the spectral transmission hole turns out to be cross-handed and can be evinced in specular and/or nonspecular directions. The spectral reflection hole is less susceptible than the spectral transmission hole to the dissipative properties of the chiral STF.

References

[1] A. Thelen, J. Opt. Soc. Am. 56 (1966) 1533.
[2] W.H. Southwell, J. Opt. Soc. Am. A 5 (1988) 1558.
[3] H.A. Haus, C.V. Shank, IEEE J. Quantum Electron. 12 (1976) 532.
[4] G.P. Agrawal, N.K. Dutta, Semiconductor Lasers, Van Nostrand Reinhold, New York, NY, USA, 1993.
[5] S. Chandrasekhar, Liquid Crystals, second ed., Cambridge University Press, Cambridge, UK, 1992 (Chapter 4).
[6] P.G. de Gennes, J. Prost, The Physics of Liquid Crystals, second ed., Clarendon Press, Oxford, UK, 1993 (Chapter 6).
[7] A. Lakhtakia, Mater. Sci. Eng. C 19 (2002) 427.
[8] A. Lakhtakia, R. Messier, Opt. Photon. News 12 (9) (2001) 26.
[9] S.D. Jacobs, K.A. Cerqua, K.L. Marshall, A. Schmid, M.J. Guardalben, K.J. Skerrett, J. Opt. Soc. Am. B 5 (1988) 1962.
[10] I.J. Hodgkinson, Q.h. Wu, Adv. Mater. 13 (2001) 889.
[11] A. Lakhtakia, M.W. McCall, Opt. Commun. 160 (1999) 457.
[12] I.J. Hodgkinson, Q.H. Wu, K.E. Thorn, A. Lakhtakia, M.W. McCall, Opt. Commun. 184 (2000) 57.
[13] V.I. Kopp, A.Z. Genack, U.S. Patent 6 396 859, 2002.
[14] V.I. Kopp, A.Z. Genack, Phys. Rev. Lett. 89 (2002) 033901.
[15] A. Lakhtakia, W.S. Weiglhofer, Proc. R. Soc. Lond. A 453 (1997) 93, erratum: 454 (1998) 3275.
[16] V.C. Venugopal, A. Lakhtakia, Proc. R. Soc. Lond. A 456 (2000) 125.
[17] A. Lakhtakia, V.C. Venugopal, M.W. McCall, Opt. Commun. 177 (2000) 57.
[18] K. Rokushima, J. Yamakita, J. Opt. Soc. Am. A 4 (1987) 27.
[19] K.C. Chang, V. Shah, T. Tamir, J. Opt. Soc. Am. 70 (1980) 804.
[20] R. Petit (Ed.), Electromagnetic Theory of Gratings, Springer, Heidelberg, Germany, 1980.
[21] F. Wang, A. Lakhtakia, R. Messier, Eur. Phys. J. AP 20 (2002) 91.
[22] K. Robbie, M.J. Brett, A. Lakhtakia, J. Vac. Sci. Technol. A 12 (1995) 2991.
[23] F. Liu, M.T. Umlor, L. Shen, J. Weston, W. Eads, J.A. Barnard, G.J. Mankey, J. Appl. Phys. 85 (1999) 5486.
[24] I.J. Hodgkinson, Q.H. Wu, B. Knight, A. Lakhtakia, K. Robbie, Appl. Opt. 39 (2000) 642.
[25] R. Messier, V.C. Venugopal, P.D. Sunal, J. Vac. Sci. Technol. B 18 (2000) 1538.
[26] M. Suzuki, Y. Taga, Jpn. J. Appl. Phys. Pt. 2 40 (2001) L358.
[27] R. Messier, A. Lakhtakia, V.C. Venugopal, P.D. Sunal, Vac. Technol. Coating 2 (10) (2001) 40.
[28] K. Rokushima, J. Yamakita, J. Opt. Soc. Am. 73 (1983) 901.
[29] J.M. Jarem, P.P. Banerjee, Computational Methods for Electromagnetic and Optical Systems, Marcel Dekker, New York, NY, USA, 2000 (Chapter 3).
[30] I.J. Hodgkinson, Q.H. Wu, Appl. Opt. 38 (1999) 3621.
[31] V.C. Venugopal, A. Lakhtakia, in: O.N. Singh, A. Lakhtakia (Eds.), Electromagnetic Fields in Unconventional Materials and Structures, Wiley, New York, NY, USA, 2000 (Chapter 5).

[32] C. Kittel, Introduction to Solid State Physics, fourth ed., Wiley Eastern, New Delhi, India, 1974 (Chapter 13).
[33] A. Lakhtakia, Eur. Phys. J. AP 8 (1999) 129.
[34] I.J. Hodgkinson, Q.h. Wu, Birefingent Thin Films and Polarizing Elements, World Scientific, Singapore, 1997 (Chapter 16).
[35] T.K. Gaylord, M.G. Moharam, Proc. IEEE 73 (1985) 894.
[36] A. Lakhtakia, V.K. Varadan, V.V. Varadan, J. Opt. Soc. Am. A 6 (1989) 1675, erratum: 7 (1990) 951.
[37] J.D. Jackson, Classical Electrodynamics, third ed., Wiley, New York, NY, USA, 1999 (Section 7.3).
[38] D. Maystre (Ed.), Selected Papers on Diffraction Gratings, SPIE Optical Engineering Press, Bellingham, WA, USA, 1993.
[39] J.B. Geddes III, A. Lakhtakia, Eur. Phys. J. AP 14 (2001) 97, erratum: 16 (2001) 247.
[40] I.J. Hodgkinson, Q.h. Wu, L. De Silva, Proc. SPIE 4806 (2002) 118.

Available online at www.sciencedirect.com
SCIENCE DIRECT®
Optics Communications 250 (2005) 105–110
OPTICS COMMUNICATIONS
www.elsevier.com/locate/optcom

Third method for generation of spectral holes in chiral sculptured thin films

Fei Wang *, Akhlesh Lakhtakia

CATMAS – Computational and Theoretical Materials Sciences Group, Department of Engineering Science and Mechanics, Pennsylvania State University, 212 EES Building, University Park, PA 16802–6812, USA

Received 21 November 2004; accepted 31 January 2005

Abstract

The introduction of either a central layer defect or a central twist defect in a periodic structurally chiral material generates circular-polarization-sensitive spectral holes in the remittance spectrums for normally incident plane waves. We propose and theoretically establish here the third method to generate such spectral holes using two-section chiral sculptured thin films (STFs). Both sections of the proposed device have the same periodicity and handedness, but their dielectric properties are different and related in a specific way. The concept of pseudoisotropy is highly relevant for the production of the proposed device.

PACS: 42.70.−a; 42.79.−e; 78.20.−e; 78.66.−w; 61.30.Jf

Keywords: Cholesteric liquid crystals; Layer defects; Pseudoisotropy; Sculptured thin films; Structural chirality; Spectral holes; Twist defects

1. Introduction

The generation of an intra-band spectral hole was first demonstrated by inserting a phase defect in the center of a scalar Bragg grating [1]. The scalar Bragg grating, without the central phase defect, has a spectral regime of high reflectance for normally incident plane waves. This regime is called the Bragg regime. When the central phase defect is inserted, the Bragg regime is punctured by a much narrower high-transmittance regime. This second regime is called a spectral (reflection) hole and is widely employed in laser optics [2] as well as in optical-fiber communication [3,4].

* Corresponding author. Tel.: +1 814 863 4319; fax: +1 814 863 7967.
E-mail addresses: fuw101@psu.edu (F. Wang), akhlesh@psu.edu (A. Lakhtakia).

0030-4018/$ - see front matter © 2005 Elsevier B.V. All rights reserved.
doi:10.1016/j.optcom.2005.01.055

As a scalar Bragg grating is insensitive to the polarization state of the incident plane wave, the incorporation of a central phase defect gives rise to a reflection hole regardless of the polarization state. In order to generate circular-polarization-sensitive reflection holes, periodic structurally chiral materials – exemplified by chiral sculptured thin films (STFs) and cholesteric liquid crystals (CLCs) [5–9] – are used in lieu of scalar Bragg gratings. In general, these materials discriminate between incident plane waves of different circular polarization states in the Bragg regime. Periodic structurally chiral materials and circularly polarized plane waves possess handedness. In the Bragg regime, the reflectance is very high for a co-handed normally incident plane wave, but not for the cross-handed one – leading to the term *circular Bragg phenomenon*. As the high reflectance in the Bragg regime is co-handed only, so is the reflection hole in the Bragg regime generated by the insertion of a central phase defect in the periodic structurally chiral material.

Theoretical analysis has recently engendered another spectral hole – i.e., a cross-handed transmission hole – in a periodic structurally chiral material by the introduction of a central phase defect [10–12]. The thickness of the periodic structurally chiral material is crucial to the exhibition of the two types of spectral holes. When the thickness is relatively small, the co-handed reflection hole occurs. As the thickness increases, the co-handed reflection hole diminishes to vanish eventually and it is gradually replaced by the cross-handed transmission hole. The bandwidth of the second type of spectral holes is a tiny fraction of that of the first type. However, even modest dissipation can be deleterious to the second type of spectral holes [11,13]. Needless to add, the second type cannot be generated using scalar Bragg gratings.

The central phase defects investigated thus far are of two types:

(i) *Layer defect*: A homogeneous layer, whether isotropic [5,6] or anisotropic [14], is inserted in the center of the periodic structurally chiral material. The thickness of the homogeneous layer determines the center wavelength of the spectral hole, with a quarter-wave layer positioning the spectral hole quite accurately in the center of the Bragg regime [15].

(ii) *Twist defect*: One half of the periodic structurally chiral material is rotated about the thickness axis with respect to the other half by a certain angle [8,10,11,16]. The amount of rotation determines the center-wavelength of the spectral hole, with a 90°-twist positioning the spectral hole in the center of the Bragg regime.

Combinations of the two types of phase defects are likely to offer superior performance than either alone [12].

We propose here a third method to generate both types of spectral holes in periodic structurally chiral materials. This method can be implemented with chiral STFs but not with CLCs. It is based on the selection of a two-section chiral STF with the two sections having different dielectric properties but the same periodicity and the same handedness. The relevant boundary value problem for normally incident plane waves is briefly described in Section 2, while the proposed method and its possible implementation are examined in Section 3. The concept of pseudoisotropy is highly relevant to the implementation of our proposal [17,18].

2. Theory

Suppose the region $0 < z < D$ is occupied by a two-section chiral STF, while the half-spaces $z \leqslant 0$ and $z \geqslant D$ are vacuous, as shown in Fig. 1. The relative permittivity dyadic of the chiral STF is stated as follows

$$\underline{\underline{\epsilon}}(\underline{r}) = \begin{cases} \underline{\underline{S}}_z(z) \cdot \underline{\underline{S}}_y(\chi_1) \cdot \left[\epsilon_{a_1}\underline{u}_z\underline{u}_z + \epsilon_{b_1}\underline{u}_x\underline{u}_x + \epsilon_{c_1}\underline{u}_y\underline{u}_y\right] \\ \quad \cdot \underline{\underline{S}}_y^{-1}(\chi_1) \cdot \underline{\underline{S}}_z^{-1}(z), \quad 0 < z < D/2, \\ \underline{\underline{S}}_z(z - D/2) \cdot \underline{\underline{S}}_y(\chi_2) \cdot \left[\epsilon_{a_2}\underline{u}_z\underline{u}_z + \epsilon_{b_2}\underline{u}_x\underline{u}_x + \epsilon_{c_2}\underline{u}_y\underline{u}_y\right] \\ \quad \cdot \underline{\underline{S}}_y^{-1}(\chi_2) \cdot \underline{\underline{S}}_z^{-1}(z - D/2), \quad D/2 < z < D. \end{cases} \tag{1}$$

Here and hereafter, ϵ_{a_j,b_j,c_j}, $(j = 1, 2)$, are the reference relative permittivity scalars of the jth section; $\{\underline{u}_x, \underline{u}_y, \underline{u}_z\}$ are the unit cartesian vectors with $\underline{u}_z$ parallel to the axis of nonhomogeneity of the chiral STF; the rotational dyadic

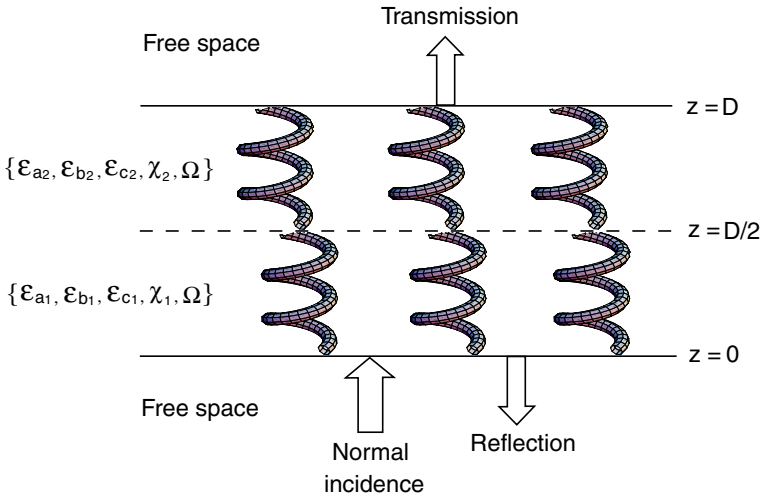

Fig. 1. Schematic of the boundary value problem involving a two-section chiral STF whose lower and upper sections have different reference relative permittivity scalars $\epsilon_{a,b,c}$ and tilt angle χ. The structural half-period Ω and handedness are uniform throughout the chiral STF.

$$\underline{\underline{S}}_z(z) = \underline{u}_z\underline{u}_z + \left(\underline{u}_x\underline{u}_x + \underline{u}_y\underline{u}_y\right)\cos pz + h\left(\underline{u}_y\underline{u}_x - \underline{u}_x\underline{u}_y\right)\sin pz, \tag{2}$$

where $p = \pi/\Omega$, 2Ω is the structural period, and the parameter $h = 1$ for structural right-handedness and $h = -1$ for structural left-handedness; and the tilt dyadic

$$\underline{\underline{S}}_y(\chi_j) = \underline{u}_y\underline{u}_y + (\underline{u}_x\underline{u}_x + \underline{u}_z\underline{u}_z)\cos\chi_j + (\underline{u}_z\underline{u}_x - \underline{u}_x\underline{u}_z)\sin\chi_j, \quad j = 1,2, \tag{3}$$

represents the *locally* aciculate morphology of the STF with χ_j as the tilt angle. The scalars ϵ_{a_j,b_j,c_j}, $(j = 1,2)$, are implicitly dependent on the free-space wavelength λ_0, and $\chi_j > 0$ for chiral STFs. The ratio $D/2\Omega$ is set as a positive integer. For convenience, we define

$$\tilde{\epsilon}_{d_j} = \frac{\epsilon_{a_j}\epsilon_{b_j}}{\epsilon_{a_j}\cos^2\chi_j + \epsilon_{b_j}\sin^2\chi_j}, \quad j = 1,2. \tag{4}$$

Parenthetically, the relative permittivity dyadic of CLCs can be described by (1) as well, but with the restrictions $\chi_j \equiv 0$ and $\epsilon_{a_j} \equiv \epsilon_{c_j}$.

The two-section chiral STF is axially excited by a normally incident, circularly polarized plane wave from the half-space $z \leqslant 0$. The procedure to obtain the planewave reflectances and transmittances is devised from the solution of a boundary value problem detailed elsewhere [15,19]. Let us content ourselves here by stating that 4×4 algebraic matrix equation [5]

$$[f_{\text{exit}}] = [\underline{\underline{M}}][f_{\text{entry}}] \tag{5}$$

eventually emerges, where the column-4 vectors $[f_{\text{entry}}]$ and $[f_{\text{exit}}]$ contain the x- and the y-components of the electromagnetic field phasors at the entry and the exit pupils, respectively. The 4×4 matrix

$$[\underline{\underline{M}}] = \exp\left(\mathrm{i}[\underline{\underline{P}}_2]D/2\right)\exp\left(\mathrm{i}[\underline{\underline{P}}_1]D/2\right) \tag{6}$$

relating $[f_{\text{entry}}]$ and $[f_{\text{exit}}]$ is computed using the matrixes

$$[\underline{\underline{P}}_j] = \begin{bmatrix} 0 & -\mathrm{i}hp & 0 & \frac{2\pi\eta_0}{\lambda_0} \\ ihp & 0 & -\frac{2\pi\eta_0}{\lambda_0} & 0 \\ 0 & -\frac{2\pi}{\lambda_0\eta_0}\epsilon_{c_j} & 0 & -\mathrm{i}hp \\ \frac{2\pi}{\lambda_0\eta_0}\tilde{\epsilon}_{d_j} & 0 & \mathrm{i}hp & 0 \end{bmatrix}, \quad j = 1,2, \tag{7}$$

where η_0 is the intrinsic impedance of free space. The derivation of (6) does not account for the possible excitation of Voigt waves [20]; but that

possibility is remote, and can occur only for highly dissipative chiral STFs [21].

3. Proposed method

The planewave remittances (i.e., reflectances and transmittances) can be easily computed after solving (5). But our interest was in finding relationships between ϵ_{c_j} and $\tilde{\epsilon}_{d_j}$, $(j = 1, 2)$ for the generation of the two types of spectral holes.

We determined that the relationships

$$\begin{cases} \epsilon_{c_1} = \tilde{\epsilon}_{d_2}, \\ \tilde{\epsilon}_{d_1} = \epsilon_{c_2}, \end{cases} \tag{8}$$

lead to the identity

$$[\underline{\underline{P}}_2] = [\underline{\underline{B}}(\pi/2)][\underline{\underline{P}}_1][\underline{\underline{B}}(\pi/2)]^{-1}. \tag{9}$$

Therefore, satisfaction of the conditions (8) implies that (6) converts to

$$[\underline{\underline{M}}] = [\underline{\underline{B}}(\pi/2)] \exp\left(\mathrm{i}[\underline{\underline{P}}_1]D/2\right)[\underline{\underline{B}}(\pi/2)]^{-1} \times \exp\left(\mathrm{i}[\underline{\underline{P}}_1]D/2\right), \tag{10}$$

where

$$[\underline{\underline{B}}(\phi)] = \begin{bmatrix} \cos\phi & -h\sin\phi & 0 & 0 \\ h\sin\phi & \cos\phi & 0 & 0 \\ 0 & 0 & \cos\phi & -h\sin\phi \\ 0 & 0 & h\sin\phi & \cos\phi \end{bmatrix}. \tag{11}$$

The matrix $[\underline{\underline{M}}]$ of (10) is identical to that formulated for an axially excited chiral STF with a central 90°-twist defect [8]. Therefore, the two-section chiral STF satisfying the conditions (8) should resemble a chiral STF with a central 90°-twist defect in terms of the response to normally incident plane waves.[1] Accordingly, both types of spectral holes must emerge in the optical remittance spectrums of a two-section chiral STF obeying (8) as the thickness D changes; see the spectrums of the co–polarized remittances in Figs. 2 and 3 for an illustrative example. The bandwidths of the spectral holes are so small that dispersion of the constitutive scalars ϵ_{a_j,b_j,c_j} can be ignored in most instances.

The theoretical underpinnings of the proposed method having been thus established, let us turn our attention to the feasibility of fabricating the described device. Chiral STFs are fabricated by directional physical vapor deposition, whereby the vapor of an inorganic material is directed towards a substrate at an angle $\chi^{\mathrm{v}} \in (0, \pi/2]$ to the substrate plane [15,24]. Optical characterization experiments on (nonchiral) columnar thin films [23] indicate that $\epsilon_{a,b,c}$ and χ are all monotonically increasing functions of χ^{v}. From the collected data, it has been shown that there exists a value χ^{pi} (called the pseudoisotropic value) of χ such that $\epsilon_c = \tilde{\epsilon}_d$ [25]. Furthermore, $\epsilon_c \gtrless \tilde{\epsilon}_d$ for $\chi \gtrless \chi^{\mathrm{pi}}$; thus, the local birefringence changes sign as the pseudoisotropic value of χ is crossed. The value of χ^{pi} is dependent on the type of evaporant [23] and most likely on the deposition conditions as well [26].

It follows that the two sections of the proposed device must be deposited with vapors of different materials (or combinations of materials). For example, suppose $\tilde{\epsilon}_{d_1} > \epsilon_{c_1}$, and therefore $\tilde{\epsilon}_{d_2} < \epsilon_{c_2}$. Then the section labeled $j = 1$ must be deposited at a low enough value of χ_1^{v} such that $\chi_1 < \chi_1^{\mathrm{pi}}$, whereas the section labeled $j = 2$ must be deposited at a high enough value of χ_2^{v} such that $\chi_2 > \chi_2^{\mathrm{pi}}$. Furthermore, the two materials should be properly selected such that $\epsilon_{c_1} + \tilde{\epsilon}_{d_1} = \epsilon_{c_2} + \tilde{\epsilon}_{d_2}$.

Could the proposed device be made by depositing vapor of a single material? Based on the limited experimental data reported for columnar thin films [23], the answer is in the negative. Since the sum $\epsilon_c + \tilde{\epsilon}_d$ increases monotonically with χ^{v}, (8) cannot be fulfilled with just one material being deposited first with vapor directed at angle χ_1^{v} and then at $\chi_2^{\mathrm{v}} \neq \chi_1^{\mathrm{v}}$.

Could a pair of CLCs be made to satisfy the conditions (8)? The answer to this question is in the negative as well, because (i) $\chi = 0$ for CLCs

[1] It is worth mentioning that, although the responses to normally incident plane waves are the same for the two-section chiral STF satisfying (8) and for a chiral STF with a central 90°-twist defect, the z-directed components of the electric fields in the region $0 < z < D$ are different in general. Therefore, the two types of devices, although functioning equivalently in terms of the generation of spectral holes, are not identical electromagnetically.

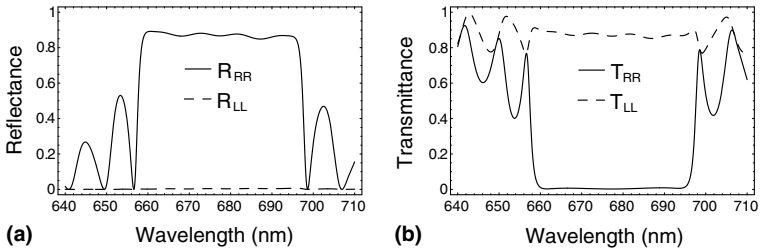

Fig. 2. Spectrums of: (a) reflectances R_{RR} and R_{LL} and (b) transmittances T_{RR} and T_{LL}, computed for a structurally right-handed, defect-free chiral STF with $\epsilon_{c_1} = \epsilon_{c_2} = 2.72$, $\tilde{\epsilon}_{d_1} = \tilde{\epsilon}_{d_2} = 3.02$, $\Omega = 200$ nm, and $D = 60\Omega$. The Bragg regime of the chiral STF is estimated as $600 < \lambda_0 < 695$ nm. The circular Bragg phenomenon is evident as a high co-handed reflectance (R_{RR}) and a high cross-handed transmittance (T_{LL}) in the Bragg regime. (The double subscript LL in T_{LL} indicates that the incident and the transmitted plane waves are Left circularly polarized. Likewise, T_{RR} is the transmittance of an incident Right circularly polarized plane wave as a Right circularly polarized plane wave. The cross–polarized remittances, such as R_{LR}, etc., can be minimized by using index-matching layers [22], which was not implemented for this figure.)

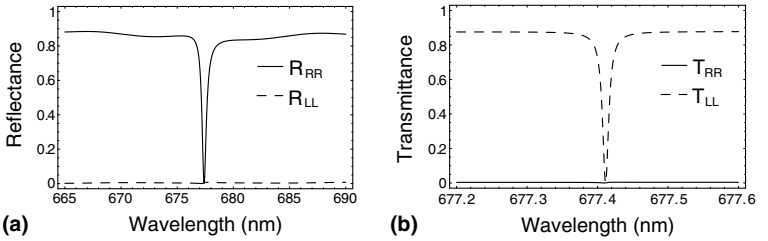

Fig. 3. Spectrums of: (a) reflectances R_{RR} and R_{LL} and (b) transmittances T_{RR} and T_{LL}, computed for a structurally right-handed, two-section chiral STF with $\epsilon_{c_1} = \tilde{\epsilon}_{d_2} = 2.72$, $\tilde{\epsilon}_{d_1} = \epsilon_{c_2} = 3.02$, and $\Omega = 200$ nm. The thickness of the device is (a) $D = 60\Omega$ and (b) $D = 180\Omega$. Compared with the remittance spectrums in Fig. 2 for the defect-free chiral STF, the remittance spectrums of the two-section chiral STF exhibit two types of spectral holes in the center of the Bragg regime. A co-handed reflection hole in the spectrum of R_{RR} emerges in the center of the Bragg regime when D is relatively small. As D increases, the co-handed reflection hole vanishes and is replaced by a cross-handed transmission hole in the spectrum of T_{LL} when D is sufficiently large.

and (ii) the rodlike shapes of molecules [27] impose the restriction $\tilde{\epsilon}_d > \epsilon_c$. In other words, neither a single-material, two-section chiral STF nor a combination of two CLCs can be utilized to implement the proposed third method for the generation of the two types of spectral holes. However, with the choice of a single-material chiral STF for one section and a CLC for the second section, it could, in principle, be possible to satisfy (8).

To conclude, we have theoretically established here the third method (in addition to the ones calling for the insertion of layer and twist defects) to generate circular-polarization-sensitive spectral holes using STF technology. The proposed device is optically similar to a chiral STF with a central 90°-twist defect. Finally, we have assessed the technological feasibility of implementing the proposed method.

Acknowledgments

This work was supported in part by a US National Science Foundation grant. F.W. thanks Prof. J. A. Todd (Penn State) for continued support.

References

[1] H.A. Haus, C.V. Shank, IEEE J. Quantum Electron. 12 (1976) 352.
[2] G.P. Agrawal, N.K. Dutta, Semiconductor Lasers, Van Nostrand Reinhold, New York, 1993 (Chapter 7).
[3] G.P. Agrawal, S. Radic, IEEE Photon. Technol. Lett. 6 (1994) 995.
[4] F. Bakhti, P. Sansonetti, J. Lightwave Technol. 15 (1997) 1433.
[5] A. Lakhtakia, M. McCall, Opt. Commun. 168 (1999) 457.

[6] I.J. Hodgkinson, Q.h. Wu, A. Lakhtakia, M.W. McCall, Opt. Commun. 177 (2000) 79.
[7] Y.-C. Yang, C.-S. Kee, J.-E. Kim, H.Y. Park, J.-C. Lee, Y.-J. Jeon, Phys. Rev. B 60 (1999) 6852.
[8] I.J. Hodgkinson, Q.H. Wu, K.E. Thorn, A. Lakhtakia, M.W. McCall, Opt. Commun. 184 (2000) 57.
[9] V.I. Kopp, A.Z. Genack, US Patent 6 396 859, 2002.
[10] V.I. Kopp, A.Z. Genack, Phys. Rev. Lett. 89 (2002) 033901.
[11] F. Wang, A. Lakhtakia, Opt. Commun. 215 (2003) 79.
[12] I.J. Hodgkinson, Q.h. Wu, L. De Silva, M. Arnold, M.W. McCall, A. Lakhtakia, Phys. Rev. Lett. 91 (2003) 223903.
[13] M. Becchi, S. Ponti, J.A. Reyes, C. Oldano, Phys. Rev. B 70 (2004) 033103.
[14] A. Lakhtakia, V.C. Venugopal, M.W. McCall, Opt. Commun. 177 (2003) 57.
[15] A. Lakhtakia, R. Messier, Sculptured Thin Films: Nanoengineered Morphology and Optics, SPIE Press, Bellingham, WA, USA, 2005, Chapter 10.
[16] J. Schmidtke, W. Stille, Eur. Phys. J. E 12 (2003) 553.
[17] I. Abdulhalim, Europhys. Lett. 48 (1999) 177.
[18] A. Lakhtakia, W.S. Weiglhofer, J. Opt. A: Pure Appl. Opt. 2 (2000) 107.
[19] V.C. Venugopal, A. Lakhtakia, Proc. R. Soc. Lond. A 454 (1998) 1535.
[20] A. Lakhtakia, Opt. Commun. 157 (1998) 193.
[21] A. Lakhtakia, J. Phys. D: Appl. Phys. 31 (1998) 235.
[22] I.J. Hodgkinson, Q.h. Wu, M. Arnold, M.W. McCall, A. Lakhtakia, Opt. Commun. 210 (2002) 201.
[23] I.J. Hodgkinson, Q.H. Wu, J. Hazel, Appl. Opt. 37 (1998) 2653.
[24] R. Messier, A. Lakhtakia, Mater. Res. Innov. 2 (1999) 217.
[25] A. Lakhtakia, Microw. Opt. Technol. Lett. 34 (2002) 367.
[26] R. Messier, Personal communication to A. Lakhtakia, 2004.
[27] P.G. de Gennes, J. Prost, The Physics of Liquid Crystals, Clarendon Press, Oxford, UK, 1993 (Chapter 4).

1 July 2001

ELSEVIER

Optics Communications 194 (2001) 33–46

OPTICS COMMUNICATIONS

www.elsevier.com/locate/optcom

Sculptured-thin-film spectral holes for optical sensing of fluids

Akhlesh Lakhtakia [a], Martin W. McCall [b,*], Joseph A. Sherwin [a], Qi Hong Wu [c], Ian J. Hodgkinson [c]

[a] *Computational and Theoretical Materials Sciences Group (CATMAS), Department of Engineering Science and Mechanics, Pennsylvania State University, University Park, PA 16802-6812, USA*

[b] *Department of Physics, The Blackett Laboratory, Imperial College of Science, Technology and Medicine, Prince Consort Road, London SW7 2BZ, UK*

[c] *Department of Physics, University of Otago, Private Bag 56, Dunedin, New Zealand*

Received 14 November 2000; received in revised form 13 March 2001; accepted 21 March 2001

Abstract

A novel class of fluid sensors is proposed based on monitoring the optical properties of multi-section chiral sculptured thin films (STFs) that function as spectral reflection holes. Using a nominal model that treats a chiral STF as a two-phase composite material with locally biaxial dielectric properties, we predict that the presence of a fluid in the porous film results in a red-shift of the spectral holes. Several device operation modes are proposed, and their relative merits are compared. Proof-of-concept experiments with both circularly polarized and unpolarized incident light confirm the red-shift of the spectral holes, and demonstrate operation in a practical situation. © 2001 Elsevier Science B.V. All rights reserved.

Keywords: Fluid concentration sensors; Sculptured thin films; Spectral reflection holes

1. Introduction

The porosity of sculptured thin films (STFs) makes them attractive for fluid concentration sensing applications [1–3], because their optical response properties must change in accordance with the number density of molecules intruding into the void regions. In particular, theoretical research has shown that the Bragg wavelength regime of a chiral STF – which is periodically nonhomogeneous along the so-called helicoidal axis of its microstructure – must shift accordingly, thereby providing a measure of the fluid concentration [2].

The sensitivity of a chiral STF-based fluid concentration sensor can be improved if the shift in a spectral feature narrower than the Bragg regime can be exploited. Very recently, we have shown experimentally as well as theoretically that, by cascading two identical chiral STF sections with one section twisted with respect to the other by 90° about their common helicoidal axis, a spectral reflection hole can be realized [4].

* Corresponding author. Tel.: +44-171-594-7749; fax: +44-171-594-7714.
E-mail address: m.mccall@ic.ac.uk (M.W. McCall).

PII: S0030-4018(01)01225-1

For instance, the full-width half-maximum (FWHM) of the Bragg regime in a particular instance was experimentally determined as ~80 nm, whereas the FWHM of the spectral hole turned out to be ~10 nm – a dramatic reduction indeed. The 90°-twist between the two sections serves as a discontinuity in the phase of the effective grating [5] seen by circularly polarized light of handedness same as the structural handedness of the chiral STF [4]. Theory shows that the incorporation of $M > 1$ such phase discontinuities in periodic structures generally results in M spectral holes occurring within the Bragg regime [6], the occurrence of which was studied recently [7,8]. Moreover, if the number of structural periods of each layer is maintained, then increasing M also has the effect of making each spectral hole even narrower. Besides serving as a multi-band, ultranarrow-bandpass filter, such a STF-based device with $M > 1$ phase discontinuities could act as a sensitive fluid concentration sensor also. A theoretical demonstration of the latter possibility motivated the work reported here.

In a parallel vein, a spectral-hole filter may be realized by cascading two slightly different chiral STF sections, whose periodicities are in a definite relationship with respect to their thicknesses [9]. Only one of the two sections is supposed to be exposed to the fluid being sensed. The spectral location as well as the depth of the spectral hole would change with fluid concentration.

The plan of this paper is as follows: In Section 2, we describe the two proposed devices in terms of frequency-domain constitutive relations. In Section 3, an ellipsoidal model is exploited to obtain the so-called reference permittivity dyadic of the chiral STF. Numerical results are provided in Section 4. Proof-of-concept experiments with water as the fluid to be sensed are presented in Section 5. An $\exp(-i\omega t)$ time-dependence is implicit; vectors are underlined and dyadics are double-underlined, while four-component column vectors as well as 4×4 matrixes are additionally enclosed in square brackets; $\underline{u}_x$, $\underline{u}_y$ and $\underline{u}_z$ are cartesian unit vectors; and the helicoidal axis is parallel to the z-axis.

2. Description of the devices

Suppose a material of bulk refractive index n_s is deposited as a chiral STF of thickness L, while the void regions of the thin film are occupied by a fluid of molar refractivity $A_{\rm mf}$ and molar density $\rho_{\rm mf}$ [10,11]. We assume here that the fluid does not react chemically with the deposited material, that the internal temperature of the film is constant in time and spatially uniform, and that the solid–fluid composite medium has purely dielectric response characteristics. We also assume that the film is essentially a two-phase composite material, but the nominal model provided here is robust enough to incorporate a more realistic multi-phase description if needed.

2.1. First device

The nonhomogeneous permittivity dyadic of the first device may be stated as follows:

$$\underline{\underline{\epsilon}}_{\rm dev1}(\underline{r}) = \epsilon_0 \underline{\underline{S}}_z(z,\Omega,\psi) \cdot \underline{\underline{S}}_y(\chi) \cdot \left[\epsilon_a \underline{u}_z\underline{u}_z + \epsilon_b \underline{u}_x\underline{u}_x + \epsilon_c \underline{u}_y\underline{u}_y\right] \cdot \underline{\underline{S}}_y^{-1}(\chi) \cdot \underline{\underline{S}}_z^{-1}(z,\Omega,\psi), \quad 0 \leqslant z \leqslant L. \tag{1}$$

In this equation, $\epsilon_0 = 8.854 \times 10^{-12}$ F m^{-1} is the free-space permittivity, and the tilt dyadic

$$\underline{\underline{S}}_y(\chi) = \underline{u}_y\underline{u}_y + (\underline{u}_x\underline{u}_x + \underline{u}_z\underline{u}_z)\cos\chi + (\underline{u}_z\underline{u}_x - \underline{u}_x\underline{u}_z)\sin\chi \tag{2}$$

represents the *locally* aciculate microstructure of any chiral STF with $\chi > 0°$ [12,13]. The rotation dyadic

$$\underline{\underline{S}}_z(z,\Omega,\psi) = \underline{u}_z\underline{u}_z + \left(\underline{u}_x\underline{u}_x + \underline{u}_y\underline{u}_y\right)\cos\left(\psi + \frac{h\pi\zeta}{\Omega}\right) + (\underline{u}_y\underline{u}_x - \underline{u}_x\underline{u}_y)\sin\left(\psi + \frac{h\pi\zeta}{\Omega}\right) \tag{3}$$

contains the remaining information emanating from the microstructure of the chosen device, with

$$\left.\begin{array}{l}\psi = m\dfrac{\pi}{2} \\ \zeta = z - m\dfrac{L}{M+1}\end{array}\right\}, \qquad m\frac{L}{M+1} \leqslant z \leqslant (m+1)\frac{L}{M+1}, \quad m = 0, 1, 2, \ldots, M. \tag{4}$$

Thus, the proposed device is a STF comprising $M+1$ identical sections. Each section of thickness $D = L/(M+1)$ is helicoidally nonhomogeneous about the z-axis with 2Ω as the structural period. The mth section is twisted with respect to the $(m-1)$th section by 90°, $(m = 1, 2, \ldots, M+1)$. Finally, the parameter $h = 1$ for structural right-handedness and $h = -1$ for structural left-handedness.

We have not yet related $\underline{\underline{\epsilon}}_{\rm dev}(\underline{r})$ to n_s, $A_{\rm mf}$ and $\rho_{\rm mf}$. As the chosen film is definitely a two-phase composite material, $\underline{\underline{\epsilon}}_{\rm dev}(\underline{r})$ must emerge from the microstructural details. The mathematical process describing the necessary transition is called homogenization. It is commonly implemented in various fashions for random distributions of electrically small particles in a homogeneous host medium [14], the constitutive properties after homogenization being independent of position. In contrast, a chiral STF amounts to a unidirectionally nonhomogeneous continuum at visible and infra-red wavelengths.

Therefore, Sunal et al. [15] adopted the following local homogenization process: In a thin slice of a chiral STF, the deposited material is distributed in the form of similarly oriented, identical, electrically small inclusions. Each slice can be homogenized using the Bruggeman formalism, and the dyadic

$$\underline{\underline{\epsilon}}_{\rm ref} = \underline{\underline{S}}_y(\chi) \cdot \left[\epsilon_a \underline{u}_z \underline{u}_z + \epsilon_b \underline{u}_x \underline{u}_x + \epsilon_c \underline{u}_y \underline{u}_y\right] \cdot \underline{\underline{S}}_y^{-1}(\chi) \tag{5}$$

is predicted from n_s, $A_{\rm mf}$ and $\rho_{\rm mf}$. The parameters Ω and χ are assumed known for a chiral STF, as they are controlled during the deposition process. The shape of the electrically small inclusions provides variables that can be chosen to fit limited experimental data.

Early homogenization research [2,3,15] considered the electrically small inclusions to be needles whose length is u times their cross-sectional radius, the shape parameter $u > 1$ being fixed by reference to experimental data. One limitation of this simple model is that $\epsilon_a = \epsilon_c$. But, chiral STFs are locally biaxial (i.e., $\epsilon_a \neq \epsilon_b \neq \epsilon_c$) in general [16]. Therefore, more recently, the inclusions have been chosen to be of ellipsoidal shape [17].

Let us define $\breve{\underline{r}} = \underline{\underline{S}}_y(\chi) \cdot \underline{r}$. With respect to its centroid, the surface of an ellipsoid may be described in cartesian coordinates by the relation

$$\breve{z}^2 + \left(\frac{\breve{y}}{\gamma_2}\right)^2 + \left(\frac{\breve{x}}{\gamma_3}\right)^2 = \delta^2, \tag{6}$$

where δ is a linear measure of the absolute size, while the transverse aspect ratio $\gamma_2 > 1$ and the slenderness ratio $\gamma_3 \gg 1$ relate the three principal axes. The longest principal axes of all ellipsoidal inclusions are aligned parallel to the unit vector $\underline{u}_{\breve{x}} = \underline{\underline{S}}_y(\chi) \cdot \underline{u}_x$, while the smaller of the two remaining principal axes is aligned parallel to the unit vector $\underline{u}_{\breve{z}} = \underline{\underline{S}}_y(\chi) \cdot \underline{u}_z$.

The Bruggeman formalism involves the solution of the dyadic equation

$$f\underline{\underline{a}}_s + (1-f)\underline{\underline{a}}_{\rm f} = \underline{\underline{0}}, \tag{7}$$

where $\underline{\underline{0}}$ is the null dyadic, and f $(0 \leqslant f \leqslant 1)$ is the volume fraction of the film occupied by the deposited material. The polarizability dyadic

$$\underline{\underline{a}}_s = \epsilon_0 \left(n_s^2 \underline{\underline{I}} - \underline{\underline{\epsilon}}_{\rm ref}\right) \cdot \left[\underline{\underline{I}} + {\rm i}\omega\epsilon_0 \underline{\underline{D}}_s \cdot \left(n_s^2 \underline{\underline{I}} - \underline{\underline{\epsilon}}_{\rm ref}\right)\right]^{-1} \tag{8}$$

involves the unit dyadic $\underline{\underline{I}}$ and the depolarization dyadic, $\underline{\underline{D}}_s$, is given by

$$\underline{\underline{D}}_s = \underline{\underline{S}}_y(\chi)\cdot\left[\frac{1}{\mathrm{i}\omega\epsilon_0}\frac{2}{\pi}\int_{\phi=0}^{\pi/2}\mathrm{d}\phi\int_{\theta=0}^{\pi/2}\mathrm{d}\theta\sin\theta\frac{\dfrac{\cos^2\theta}{\gamma_3^2}\underline{u}_x\underline{u}_x+\sin^2\theta\left(\cos^2\phi\,\underline{u}_z\underline{u}_z+\dfrac{\sin^2\phi}{\gamma_2^2}\underline{u}_y\underline{u}_y\right)}{\epsilon_b\dfrac{\cos^2\theta}{\gamma_3^2}+\sin^2\theta\left(\epsilon_a\cos^2\phi+\epsilon_c\dfrac{\sin^2\phi}{\gamma_2^2}\right)}\right]\cdot\underline{\underline{S}}_y^{-1}(\chi). \tag{9}$$

The calculation of $\underline{\underline{a}}_f$ is similar, except that it involves a spherical topology rather than an ellipsoidal topology, as we take the fluid molecules to be spherical here. Thus,

$$\underline{\underline{a}}_f = \epsilon_0\left(n_f^2\underline{\underline{I}}-\underline{\underline{\epsilon}}_{ref}\right)\cdot\left[\underline{\underline{I}}+\mathrm{i}\omega\epsilon_0\underline{\underline{D}}_f\cdot\left(n_f^2\underline{\underline{I}}-\underline{\underline{\epsilon}}_{ref}\right)\right]^{-1}, \tag{10}$$

where

$$n_f = \left(\frac{1+2\rho_{mf}A_{mf}}{1-\rho_{mf}A_{mf}}\right)^{1/2} \tag{11}$$

is the bulk refractive index of the fluid, and

$$\underline{\underline{D}}_f = \underline{\underline{D}}_s\Big|_{\gamma_2=1,\gamma_3=1}. \tag{12}$$

Eq. (7) has to be solved numerically in order to determine $\underline{\underline{\epsilon}}_{ref}$. This is readily accomplished using iterative techniques [18,19].

2.2. Second device

The permittivity dyadic of the second device is best stated sectionwise, as follows:

$$\underline{\underline{\epsilon}}_{dev2}(\underline{r}) = \epsilon_0 \tag{13}$$

$$\times\begin{cases}\underline{\underline{S}}_z(z,\Omega',0)\cdot\underline{\underline{S}}_y(\chi)\cdot\left[\epsilon'_a\underline{u}_z\underline{u}_z+\epsilon'_b\underline{u}_x\underline{u}_x+\epsilon'_c\underline{u}_y\underline{u}_y\right]\cdot\underline{\underline{S}}_y^{-1}(\chi)\cdot\underline{\underline{S}}_z^{-1}(z,\Omega',0), & 0\leqslant z\leqslant L',\\ \underline{\underline{S}}_z(z,\Omega,0)\cdot\underline{\underline{S}}_y(\chi)\cdot\left[\epsilon_a\underline{u}_z\underline{u}_z+\epsilon_b\underline{u}_x\underline{u}_x+\epsilon_c\underline{u}_y\underline{u}_y\right]\cdot\underline{\underline{S}}_y^{-1}(\chi)\cdot\underline{\underline{S}}_z^{-1}(z,\Omega,0), & L'\leqslant z\leqslant L.\end{cases} \tag{14}$$

The ratio $q = L'/L$ $(0 < q < 1)$ is a design variable that is best kept somewhat in excess of 0.5. As the lower section is not to be exposed to the fluid to be sensed, the relative permittivity scalars $\epsilon'_{a,b,c}$ are computed just as $\epsilon_{a,b,c}$ are in the previous subsection but with $\rho_{mf} = 0$; i.e.,

$$\epsilon'_{a,b,c} = \epsilon_{a,b,c}\Big|_{\rho_{mf}=0}. \tag{15}$$

Finally, the structural periods of the two sections satisfy the relationship [9]

$$\frac{1}{\Omega}-\frac{1}{\Omega'}=\frac{1}{L}. \tag{16}$$

Since the section thickness of a chiral STF is kept much larger than its structural period for the Bragg phenomenon to develop fully [1], Ω and Ω' are quite close in magnitude – which is desirable for ease of fabrication.

3. Boundary value problem

Let the halfspaces $z \leqslant 0$ and $z \geqslant L$ be vacuous. An arbitrarily polarized plane wave is normally incident on the chosen chiral STF from the lower halfspace $z \leqslant 0$. As a result, a plane wave is reflected into the lower halfspace and another is transmitted into the upper halfspace. The electric field phasors associated with the two plane waves in the lower halfspace are stated as [20]

$$\underline{E}_{\rm inc}(\underline{r}) = (a_{\rm L}\underline{u}_{+} + a_{\rm R}\underline{u}_{-})\exp(\mathrm{i}k_0 z); \quad z \leqslant 0, \tag{17}$$

$$\underline{E}_{\rm ref}(\underline{r}) = (r_{\rm L}\underline{u}_{-} + r_{\rm R}\underline{u}_{+})\exp(-\mathrm{i}k_0 z); \quad z \leqslant 0, \tag{18}$$

where $\underline{u}_{\pm} = (\underline{u}_x \pm \mathrm{i}\underline{u}_y)/\sqrt{2}$ and k_0 is the free-space wave number. Likewise, the electric field phasor in the upper halfspace is represented as

$$\underline{E}_{\rm trs}(\underline{r}) = (t_{\rm L}\underline{u}_{+} + t_{\rm R}\underline{u}_{-})\exp[\mathrm{i}k_0(z-L)]; \quad z \geqslant L. \tag{19}$$

Here, $a_{\rm L}$ and $a_{\rm R}$ are the known amplitudes of the left- and the right-circularly polarized (LCP and RCP) components of the incident plane wave; $r_{\rm L}$ and $r_{\rm R}$ are the unknown amplitudes of the reflected plane wave components; while $t_{\rm L}$ and $t_{\rm R}$ are the unknown amplitudes of the transmitted plane wave components.

The procedure to obtain the unknown amplitudes leads to the 4×4 matrix relation [4,20]

$$[\underline{f}_{\rm exit}] = [\underline{\underline{M}}_{\rm dev}][\underline{f}_{\rm entry}], \tag{20}$$

where the four-component column vectors

$$[\underline{f}_{\rm entry}] = \frac{1}{\sqrt{2}}\begin{bmatrix} (r_{\rm L}+r_{\rm R}) + (a_{\rm L}+a_{\rm R}) \\ \mathrm{i}[-(r_{\rm L}-r_{\rm R}) + (a_{\rm L}-a_{\rm R})] \\ -\mathrm{i}[(r_{\rm L}-r_{\rm R}) + (a_{\rm L}-a_{\rm R})]/\eta_0 \\ -[(r_{\rm L}+r_{\rm R}) - (a_{\rm L}+a_{\rm R})]/\eta_0 \end{bmatrix}, \tag{21}$$

$$[\underline{f}_{\rm exit}] = \frac{1}{\sqrt{2}}\begin{bmatrix} t_{\rm L}+t_{\rm R} \\ \mathrm{i}(t_{\rm L}-t_{\rm R}) \\ -\mathrm{i}(t_{\rm L}-t_{\rm R})/\eta_0 \\ (t_{\rm L}+t_{\rm R})/\eta_0 \end{bmatrix} \tag{22}$$

denote the electromagnetic fields at the entry and the exit pupils, respectively, and η_0 is the intrinsic impedance of free space.

3.1. First device

The 4×4 system matrix

$$[\underline{\underline{M}}_{\rm dev1}] = \left[\underline{\underline{B}}\left(D, \Omega, M\frac{\pi}{2}\right)\right]\exp(\mathrm{i}[\underline{\underline{P}}]D)\left\{\left[\underline{\underline{B}}\left(D, \Omega, -\frac{\pi}{2}\right)\right]\exp(\mathrm{i}[\underline{\underline{P}}]D)\right\}^{M} \tag{23}$$

relating the two four-component column vectors characterizes the axial excitation response of the device, and is computed using the matrixes

$$[\underline{\underline{B}}(z, \Omega, \psi)] = \begin{bmatrix} \cos(\psi + h\frac{\pi z}{\Omega}) & -\sin(\psi + h\frac{\pi z}{\Omega}) & 0 & 0 \\ \sin(\psi + h\frac{\pi z}{\Omega}) & \cos(\psi + h\frac{\pi z}{\Omega}) & 0 & 0 \\ 0 & 0 & \cos(\psi + h\frac{\pi z}{\Omega}) & -\sin(\psi + h\frac{\pi z}{\Omega}) \\ 0 & 0 & \sin(\psi + h\frac{\pi z}{\Omega}) & \cos(\psi + h\frac{\pi z}{\Omega}) \end{bmatrix}, \tag{24}$$

$$[\underline{\underline{P}}] = \begin{bmatrix} 0 & -\mathrm{i}h\pi/\Omega & 0 & \frac{2\pi\eta_0}{\lambda_0} \\ \mathrm{i}h\pi/\Omega & 0 & -\frac{2\pi\eta_0}{\lambda_0} & 0 \\ 0 & -\frac{2\pi}{\lambda_0\eta_0}\,\epsilon_c & 0 & -\mathrm{i}h\pi/\Omega \\ \frac{2\pi}{\lambda_0\eta_0}\,\tilde{\epsilon}_d & 0 & \mathrm{i}h\pi/\Omega & 0 \end{bmatrix}, \tag{25}$$

where λ_0 is the free-space wavelength and

$$\tilde{\epsilon}_d = \frac{\epsilon_a\epsilon_b}{\epsilon_a\cos^2\chi + \epsilon_b\sin^2\chi}. \tag{26}$$

3.2. Second device

The system matrix for the second device is given by

$$[\underline{\underline{M}}_{\mathrm{dev2}}] = [\underline{\underline{B}}(L-L',\Omega,0)]\exp\{\mathrm{i}[\underline{\underline{P}}](L-L')\}[\underline{\underline{B}}(L',\Omega',0)]\exp(\mathrm{i}[\underline{\underline{P}}']L'), \tag{27}$$

where

$$[\underline{\underline{P}}'] = [\underline{\underline{P}}]\Big|_{\epsilon_{a,b,c}\to\epsilon'_{a,b,c}}. \tag{28}$$

4. Numerical results and discussion

The reflection amplitudes $r_{\mathrm{L,R}}$ and the transmission amplitudes $t_{\mathrm{L,R}}$ can be computed for specified incident amplitudes (a_{L} and a_{R}) by solving Eq. (20). Our interests lie in determining the reflection and transmission coefficients entering the 2×2 matrixes in the following two relations:

$$\begin{bmatrix} r_{\mathrm{L}} \\ r_{\mathrm{R}} \end{bmatrix} = \begin{bmatrix} r_{\mathrm{LL}} & r_{\mathrm{LR}} \\ r_{\mathrm{RL}} & r_{\mathrm{RR}} \end{bmatrix}\begin{bmatrix} a_{\mathrm{L}} \\ a_{\mathrm{R}} \end{bmatrix}, \tag{29}$$

$$\begin{bmatrix} t_{\mathrm{L}} \\ t_{\mathrm{R}} \end{bmatrix} = \begin{bmatrix} t_{\mathrm{LL}} & t_{\mathrm{LR}} \\ t_{\mathrm{RL}} & t_{\mathrm{RR}} \end{bmatrix}\begin{bmatrix} a_{\mathrm{L}} \\ a_{\mathrm{R}} \end{bmatrix}. \tag{30}$$

Both 2×2 matrixes are defined phenomenologically. The co-polarized transmission coefficients are denoted by t_{LL} and t_{RR}, and the cross-polarized ones by t_{LR} and t_{RL}; and similarly for the reflection coefficients in Eq. (29). Reflectances and transmittances are denoted, e.g., as $T_{\mathrm{LR}} = |t_{\mathrm{LR}}|^2$.

The foregoing procedure was implemented for several different sets of variables, and only a few results are shown here. A glance at tables of refractive index data for organic substances – see, e.g., Ref. [21] – that $n_{\mathrm{f}} \sim 1.5$ is quite typical at room temperature, which means that the product $\rho_{\mathrm{mf}}A_{\mathrm{mf}} \sim 0.3$. Thus, higher is the value of A_{mf} of a fluid, the lower is the smallest detectable value of its ρ_{mf}. For all results shown in Figs. 1–6, we set $n_s = 2.3$, $A_{\mathrm{mf}} = 10^{-3}\ \mathrm{m^3\,mol^{-1}}$ and $\chi = 60^\circ$. The porosity was chosen at 40% so that $f = 0.6$. Finally, we set $\gamma_2 = 3$ and $\gamma_3 = 15$ for the shape parameters, in accordance with experience gained from several local homogenization studies [17]. We also chose the chiral STF sections to be structurally left-handed (i.e, $h = -1$). Dispersion and dissipation were neglected over the selected wavelength regime $\lambda_0 \in [500, 525]$ nm, as we assumed that the material resonances lie far away in the ultraviolet regime.

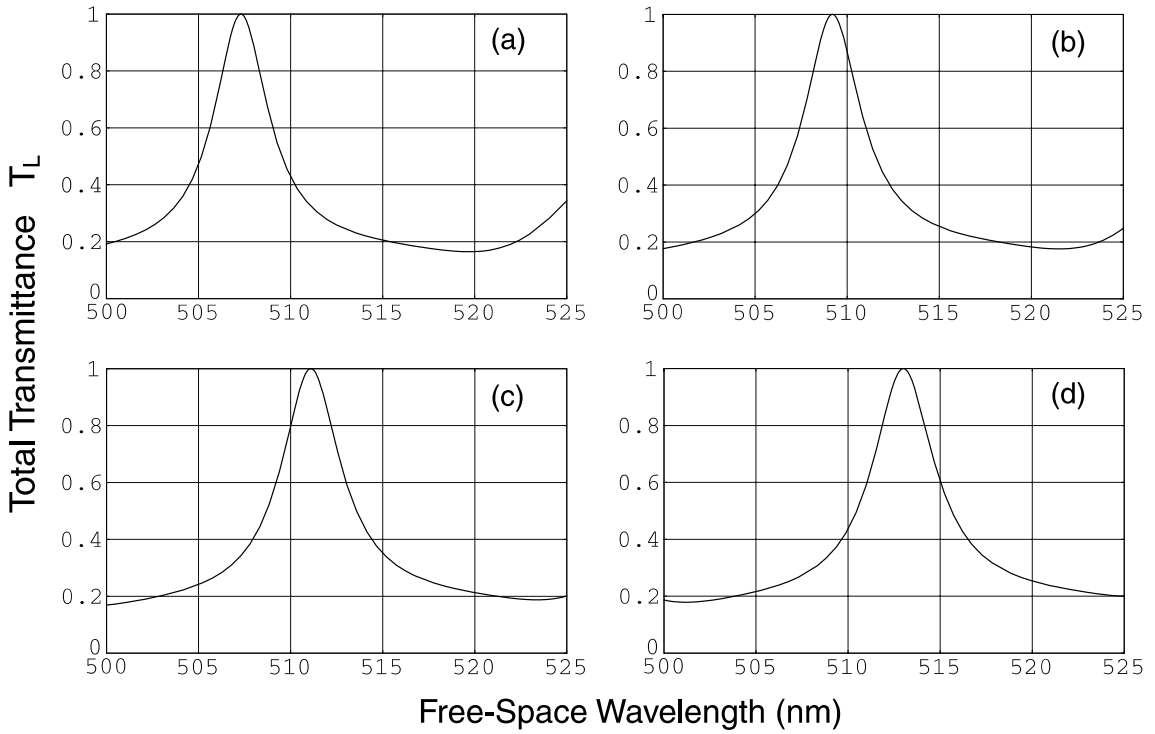

Fig. 1. Computed spectrum of the total transmittance $T_L = |t_{LL}|^2 + |t_{RL}|^2$ for a LCP plane wave normally incident on a two-section device ($M = 1$). (a) $\rho_{mf} = 0$ mol m^{-3}, (b) $\rho_{mf} = 10$ mol m^{-3}, (c) $\rho_{mf} = 20$ mol m^{-3}, (d) $\rho_{mf} = 30$ mol m^{-3}. See the text for other parameters.

4.1. First device

Three modes of operating the first device appear feasible. The first mode takes advantage of the spectral shift of the spectral hole due to the presence of the fluid in the device. The second and the third modes have a fixed operating wavelength. In all three modes, the overall transmittance $T_L = T_{LL} + T_{RL}$ is to be measured.

All calculations were made using $D = 20\Omega$ for each section and $\Omega = 146$ nm. The best results were obtained for odd values of M. Shown in Fig. 1 are the spectrums of T_L for a two-section device when the molar density $\rho_{mf} = 0$, 10, 20 and 30 mol m^{-3}. As $M = 1$, only one spectral hole is evident. As the fluid intrusion increases, the spectral hole shifts towards higher wavelengths. Its FWHM is roughly 5 nm, and it shifts $\sim$0.21 nm/(mol m^{-3}) with ρ_{mf}.

The spectrums plotted in Fig. 2 are for a four-section device. Three spectral holes are evident in each spectrum, with the middle one being the best. The FWHM of the middle hole is $\sim$2.6 nm and it shifts $\sim$0.21 nm/(mol m^{-3}) with ρ_{mf}. The FWHM of the middle hole in Fig. 3 for a six-section device is $\sim$1.67 nm, but its red-shift per unit molar density is the virtually identical with that in Figs. 1 and 2. Thus, an increase in M makes the spectral holes narrower, but the shift sensitivity to fluid intrusion remains virtually constant, in the first operating mode.

For the second operating mode, a fixed wavelength of operation is chosen such that T_L is minimum when no fluid is present. As the fluid intrusion increases, T_L increases to a maximum (of unity). Before the maximum is reached, however, the sensor sounds an alarm (or initiates some control action) as T_L crosses a

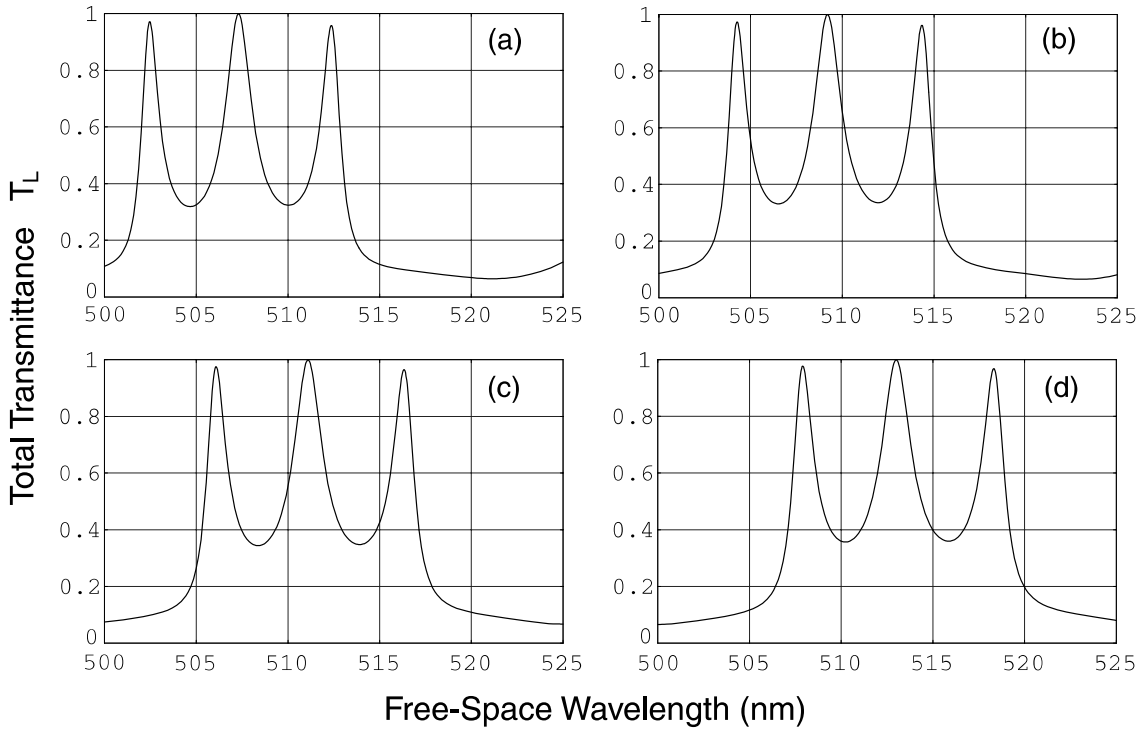

Fig. 2. Same as Fig. 1, but for a four-section device ($M = 3$).

threshold value. The possibility of this operation mode is evident from the plot of T_L versus ρ_{mf} in Fig. 4, for a four-section device operating at $\lambda_0 = 510$ nm.

For very high sensitivity to fluid intrusion, a third mode of operation may be better: to choose an operating wavelength at which T_L is maximum (≈ 1) when no fluid is present. Any deviation of ρ_{mf} from a null value would cause T_L to fall and control actions would be triggered thereby. This mode can be established from the plot of T_L versus ρ_{mf} in Fig. 5, for a six-section device operating at $\lambda_0 = 507.335$ nm.

4.2. Second device

Only the co-polarized transmittance T_{LL} is to be measured when operating the second device. The spectrums of this quantity are plotted in Fig. 6 for $\rho_{mf} = 0$, 10, 20, and 30 mol m^{-3}, when $\Omega = 146$ nm, $L = 80\Omega$, and $\Omega' = 147.85$ nm. Five mid-range values of q were selected for the presented spectrums. In all of these instances, the spectral peak of T_{LL} clearly shifts to lower wavelengths as ρ_{mf} increases – so that the second device can function similarly to the first device in the first operating mode. The peak values of T_{LL} diminish as either $q \to 0$ or $q \to 1$, because the thickness (and, hence, the relative importance) of one of the two sections in creating the narrowband feature diminishes. Indeed, the spectral hole must vanish when either $q = 0$ or 1. Furthermore, the sensitivity to fluid intrusion declines readily as $q \to 1$, because the fluid-impregnated section reduces in thickness.

For values of q somewhat higher than 0.5, the second device offers another exploitable feature: the spectral peak not only shifts but also diminishes with increasing ρ_{mf}. Two channels for initiating control action are thus feasible.

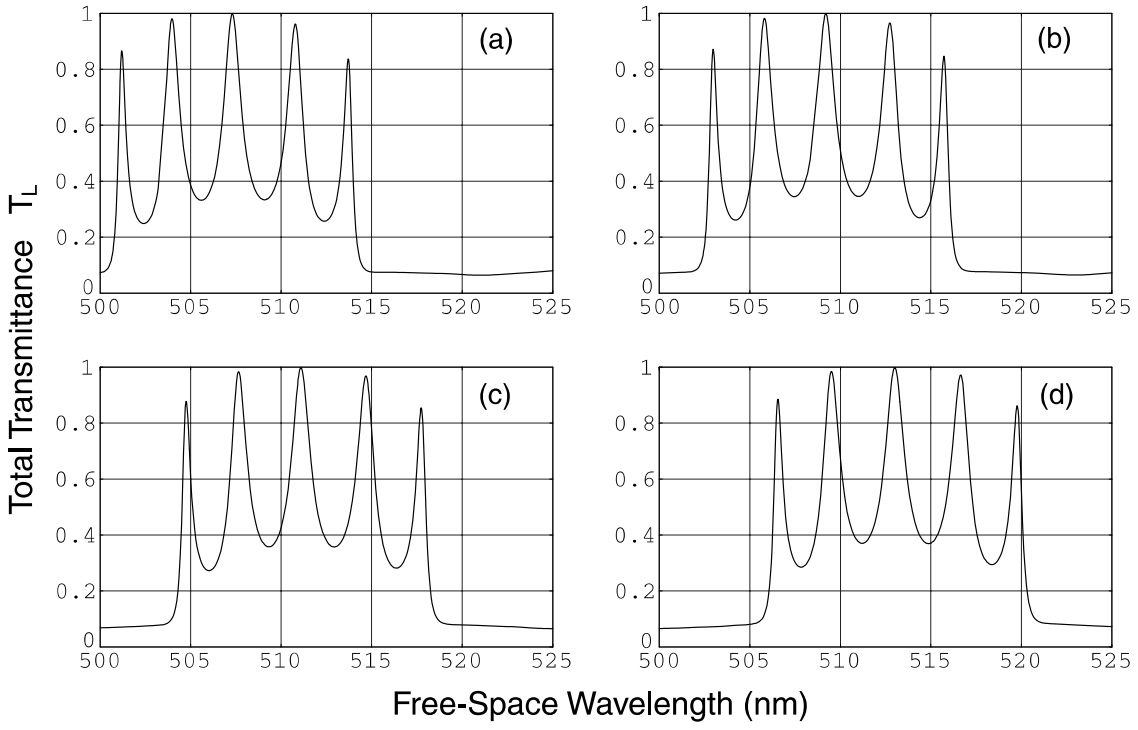

Fig. 3. Same as Fig. 1, but for a six-section device ($M = 5$).

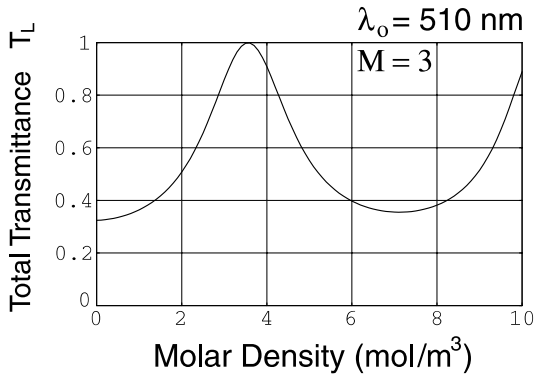

Fig. 4. Plot of T_L versus ρ_{mf} for a four-section device ($M = 3$) operating at $\lambda_0 = 510$ nm. See the text for other parameters.

5. Proof-of-concept experiments for the first device

Proof-of-concept experiments were undertaken to confirm the predicted red-shift of spectral holes with fluid uptake in the proposed first device, as discussed in Sections 2.1 and 4.1. The filter used in these experiments was the one used in Ref. [4] (sp011299). It is a two-section ($M = 1$) left-handed ($h = -1$) structure. Each section has six structural turns ($D = 12\Omega$) and a thickness of 3.5 μm.

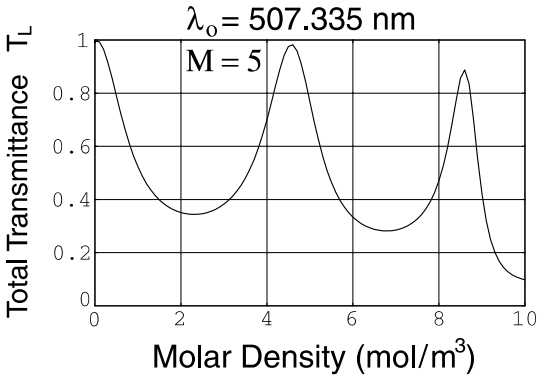

Fig. 5. Plot of T_L versus ρ_{mf} for for a six-section device ($M = 5$) operating at $\lambda_0 = 507.335$ nm. See the text for other parameters.

Fig. 7 shows the three experimental configurations that were implemented. These all employ an Ocean Optics [22] PC plug-in ccd spectrometer [22] for detection of the light transmitted or reflected by the filter. They differ in that either circularly polarized (Fig. 7a) or unpolarized (Fig. 7b), (Fig. 7c) incident light was used. The filter was flooded with water via a puff of saturated air from a bottle containing water at a temperature of approximately 40°C, and then the filter was allowed to recover by evaporation at room temperature. During a typical wetting and evaporation cycle, about 100 spectrums were recorded.

In the configuration of Fig. 7a, the incident light is LCP, and the total transmittance $T_L = T_{LL} + T_{RL}$ is monitored. The subset of frames in Fig. 8, in which the original transmittance spectrum is shown as a broken line, and the plot in Fig. 9 together show the optical changes that accompanied the wetting and drying operation. After 5 s the filter was saturated and the spectral hole was red-shifted by about 26 nm. As well the figures confirm that (i) wetting reduces the depth of the circular Bragg resonance, (ii) the spectral hole remains intact and centred on the circular Bragg resonance, and (iii) the original spectral properties are recovered after evaporation. Simulations show that the red-shift of the hole is attributable to increase in $n_{av} \equiv (\tilde{\epsilon}_d^{1/2} + \epsilon_c^{1/2})/2$ due to the uptake of water, and the smaller depth of the circular Bragg resonance is due to reduction in the form birefringence $\Delta n \equiv |\tilde{\epsilon}_d^{1/2} - \epsilon_c^{1/2}|$.

The wavelength displacement curve shown in Fig. 9 indicates a fast wetting transient and a much slower recovery time of about 30 s. These may be compared with similarly fast wetting times and recovery times of about 5 s measured earlier for the linear birefringence of a 1.1 μm wave plate with a normal-columnar nanostructure, and about 20 s recorded for the optical rotation of a 4.4 μm single-section chiral STF (at a wavelength λ_0 considerably less than the Bragg wavelength) [23].

In practice, it is convenient to operate an optical sensor with a bifurcated fiber optic, with one arm delivering unpolarized light to the sensor and the other arm delivering the remitted light to the spectrometer. With this type of operation in mind, we also investigated spectral hole filters illuminated with unpolarized light.

In transmission mode with unpolarized incident light, $T = (T_{LL} + T_{RL} + T_{LR} + T_{RR})/2$ was monitored. Here T_{LL} holds the prominent signature of the spectral hole, the cross-polarized terms T_{RL} and T_{LR} are small at all wavelengths, and $T_{RR} \approx 1$. Thus T was expected to have, more or less, the spectrally significant form of T_{LL} but with a transmittance offset. Fig. 10a confirms both the expected form of T and the integrity of the spectral shape during flooding and drying of the nanostructure.

In the same vein, the reflectance R_{LL} holds a prominant signature of the spectral hole, whereas the terms R_{RL}, R_{LR} and R_{RR} are all small; hence $R = (R_{LL} + R_{RL} + R_{LR} + R_{RR})/2$ was expected to appear as an inverted version of T_{LL}. This prediction is confirmed by Fig. 10b in which the non-normalized value of R is plotted for unpolarized light incident at a small angle with respect to the z-axis. In an earlier publication [4],

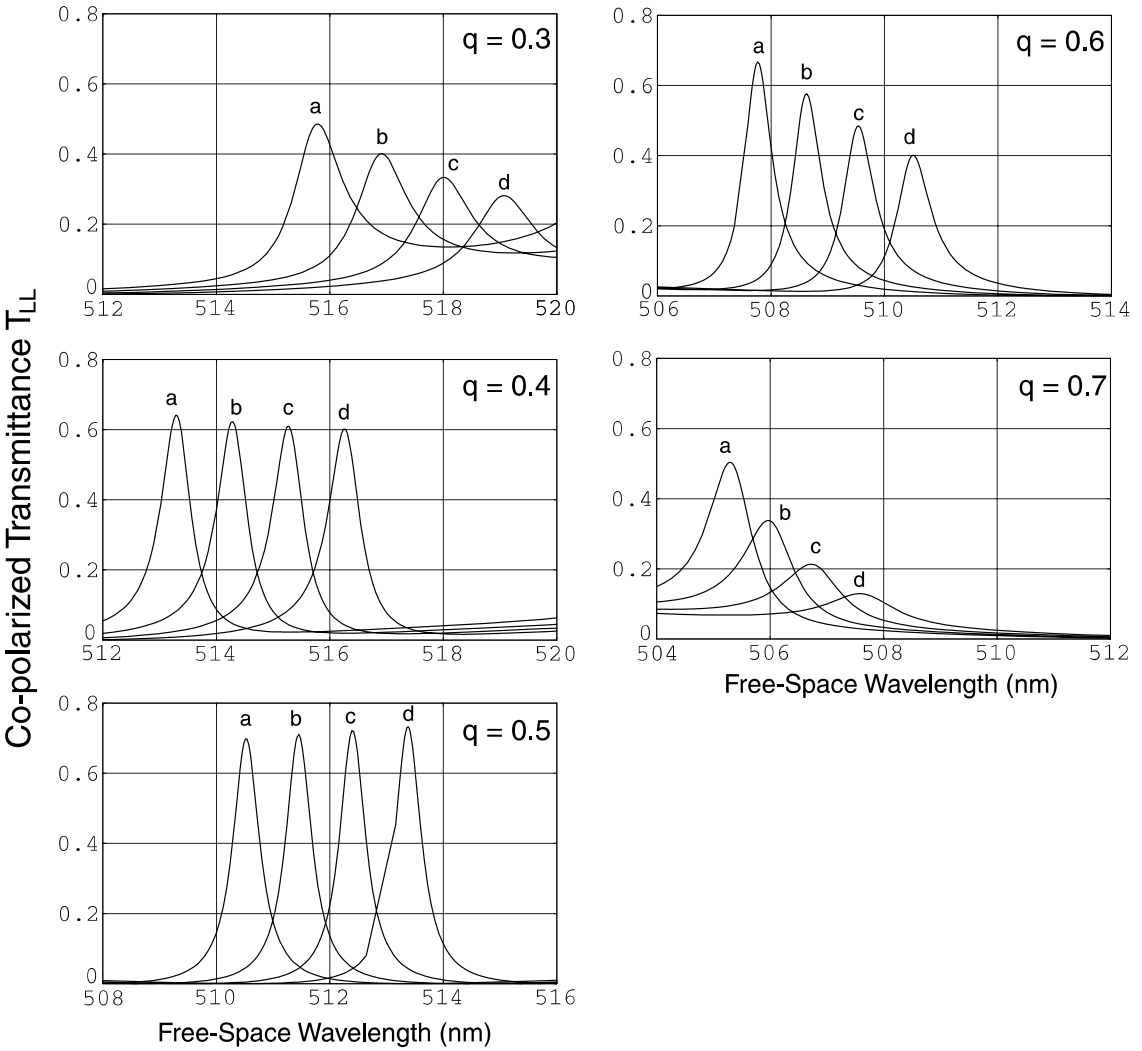

Fig. 6. Computed spectrum of the total transmittance $|t_{LL}|^2$ for five mid-range values of ρ. (a) $\rho_{mf} = 0\ \mathrm{mol\,m^{-3}}$, (b) $\rho_{mf} = 10\ \mathrm{mol\,m^{-3}}$, (c) $\rho_{mf} = 20\ \mathrm{mol\,m^{-3}}$, (d) $\rho_{mf} = 30\ \mathrm{mol\,m^{-3}}$. See the text for other parameters.

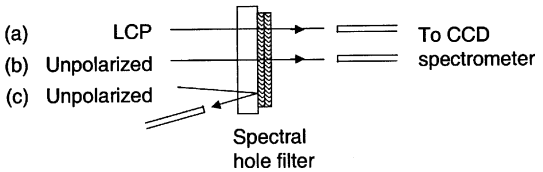

Fig. 7. Experimental configurations in which a structurally left-handed filter is illuminated with (a) LCP light, (b) and (c) unpolarized light.

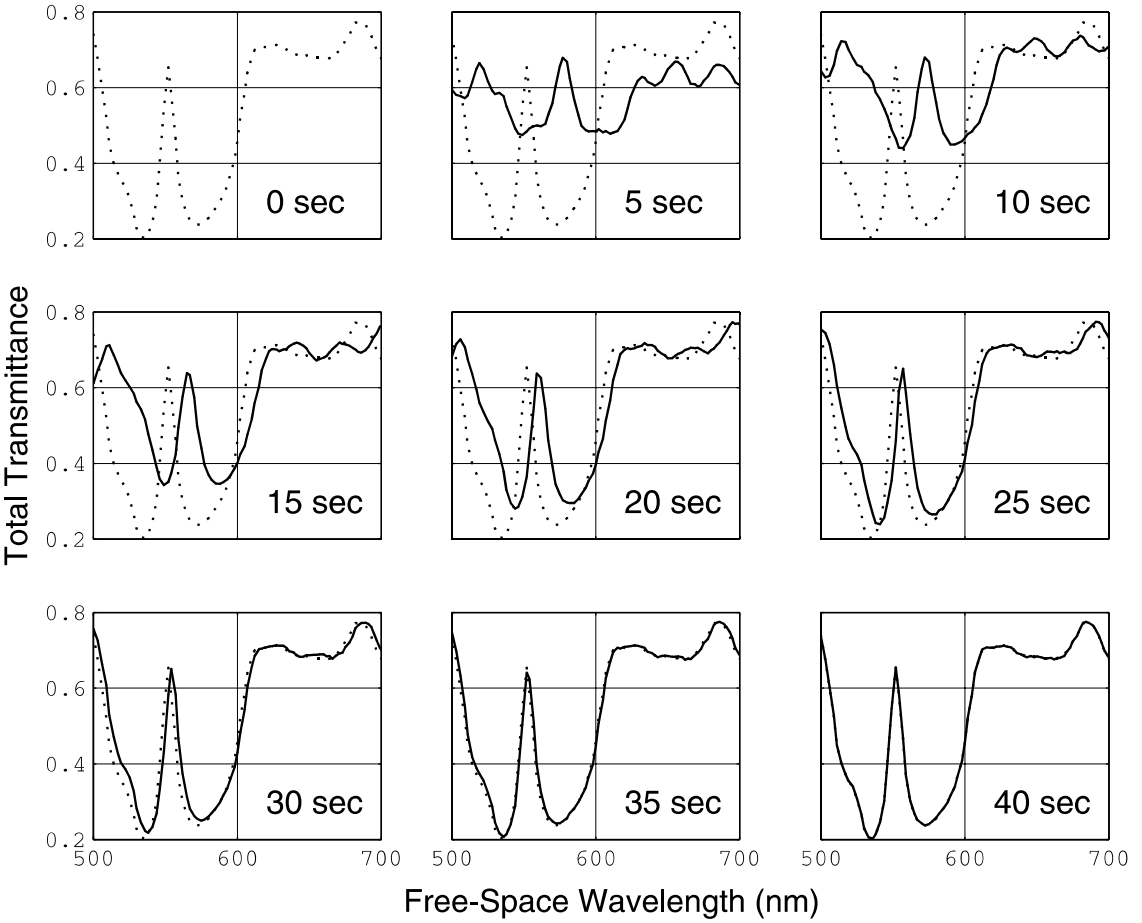

Fig. 8. Subset of spectrums recorded as the filter was flooded with water, and then allowed to recover by evaporation in air.

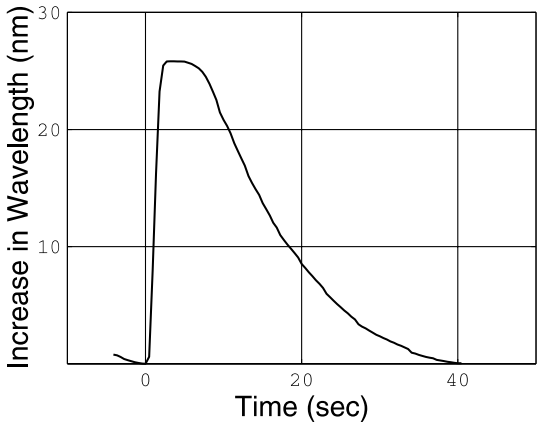

Fig. 9. Increase in the wavelength of the spectral hole recorded during wetting and subsequent evaporation.

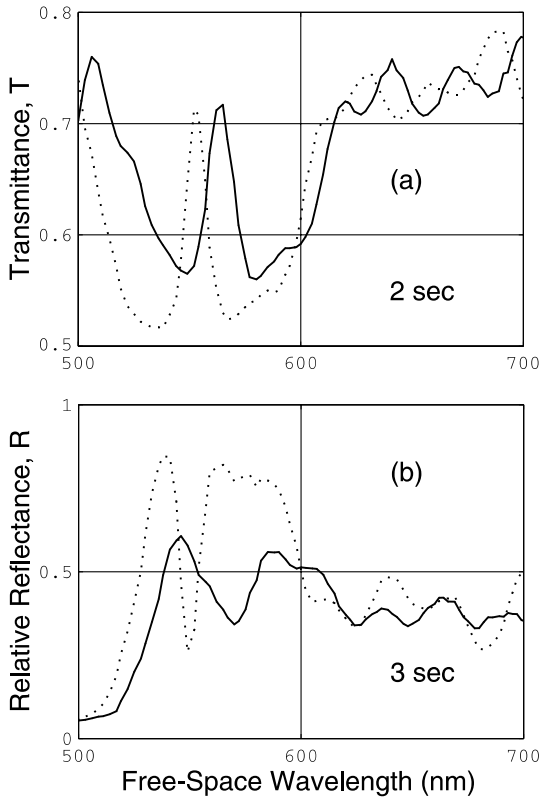

Fig. 10. Original and displaced spectrums recorded in (a) transmission and (b) reflection modes of operation, but for the filter illuminated with unpolarized light.

we showed that a similar filter could be tilted by 10° without deterioration of the spectral-hole line shape and with only a small (≈2 nm) blue-shift of the hole.

Finally we note that, for both reflection and transmission modes of operation using unpolarized light, the sensor was operated continuously during flooding and drying of the filter, and time-evolving spectrums and displacement curves equivalent to those shown in Figs. 8 and 9 were obtained.

6. Concluding remarks

Using a nominal model which treats a chiral sculptured thin film as a two-phase composite material, as well as proof-of-concept experiments, we have shown that spectral-hole filters realizable with STF technology may be used as fluid concentration sensors. A variety of operating modes appears possible. The nominal model employed here may be enhanced by modeling different solid–fluid interaction products as additional material phases.

One feature of the optical behavior of the sensor has not been mentioned so far: even though no spectral hole appears when the handedness of the incident circularly polarized light is the opposite of the structural handedness of the chosen STF [4,9], the presence of a fluid in the void regions does affect the transmission spectrum. This feature may therefore be used to normalize the sensor in the presence of source fluctuations.

Three cautionary notes are in order. First, the value of $\rho_{\rm mf}A_{\rm mf}$ must exceed 0.1 or thereabouts in order for a significant spectral shift to be observed, indicating that the proposed sensor is more suitable for vapors emanating from volatile solids and liquids than for gases. Second, care must also be taken to ensure that the inclusion of the fluid to be detected does not reduce the local linear birefringence $\Delta n = |\tilde{\epsilon}_d^{1/2} - \epsilon_c^{1/2}|$ of the chiral STF – implying that n_s and $n_{\rm f}$ must be far apart, and f must be significantly different from both 0 and 1 – since it is this parameter which principally determines the circular Bragg phenomenon upon which the sensor is based [1]. Finally, fluids comprising large organic molecules may be unsuitable for penetrating the columnar structure of the STF. Despite these potential limitations, we believe that the proposed sensor technology is feasible for a large class of fluids.

References

[1] V.C. Venugopal, A. Lakhtakia, in: O.N. Singh, A. Lakhtakia (Eds.), Electromagnetic Fields in Unconventional Materials and Structures, Wiley, New York, 2000 (Chapter 5).
[2] A. Lakhtakia, Sensors and Actuators B: Chem. 52 (1998) 243.
[3] E. Ertekin, A. Lakhtakia, Eur. Phys. J. Appl. Phys. 5 (1999) 45.
[4] I.J. Hodgkinson, Q.H. Wu, K.E. Thorn, A. Lakhtakia, M.W. McCall, Opt. Commun. 184 (2000) 57.
[5] M.W. McCall, A. Lakhtakia, J. Mod. Opt. 47 (2000) 973.
[6] G.P. Agrawal, S. Radic, IEEE Photon. Technol. Lett. 6 (1994) 995.
[7] M. McCall, J. Lightwave Technol. 18 (2000) 236.
[8] M. Zeller, V. Dupray, M.W. McCall, Opt. Commun., submitted for publication.
[9] M.W. McCall, A. Lakhtakia, J. Mod. Opt. 47 (2000) 743.
[10] M. Born, E. Wolf, Principles of Optics, Pergamon Press, Oxford, 1987, p. 88.
[11] K. Kerl, U. Hohm, H. Varchmin, Ber. Bunsenges. Phys. Chem. 96 (1992) 728.
[12] R. Messier, A. Lakhtakia, Mater. Res. Innov. 2 (1999) 217.
[13] R. Messier, V.C. Venugopal, P.D. Sunal, J. Vac. Sci. Technol. A 18 (2000) 1538.
[14] P.S. Neelakanta, Handbook of Electromagnetic Materials, CRC Press, Boca Raton, FL, 1995 (Chapters 4–6).
[15] P.D. Sunal, A. Lakhtakia, R. Messier, Opt. Commun. 158 (1998) 119.
[16] I. Hodgkinson, Q.H. Wu, B. Knight, A. Lakhtakia, K. Robbie, Appl. Opt. 39 (2000) 642.
[17] J.A. Sherwin, A. Lakhtakia, Proc. SPIE 4097 (2000) 250.
[18] J.A. Sherwin, A. Lakhtakia, B. Michel, Opt. Commun. 178 (2000) 267.
[19] T.G. Mackay, W.S. Weiglhofer, J. Opt. A: Pure Appl. Opt. 2 (2000) 426.
[20] A. Lakhtakia, M. McCall, Opt. Commun. 168 (1999) 457.
[21] R.C. Weast (Ed.), CRC Handbook of Chemistry and Physics, CRC Press, Boca Raton, FL, USA, 1981, pp. C-65–575.
[22] Ocean Optics Inc., 1237 Lady Marion Lane, Dunedin, FL, USA.
[23] I.J. Hodgkinson, Q.H. Wu, K.M. McGrath, Proc. SPIE 3790 (1999) 184.

15 February 2001

ELSEVIER

Optics Communications 188 (2001) 313–320

OPTICS COMMUNICATIONS

www.elsevier.com/locate/optcom

On bioluminescent emission from chiral sculptured thin films

Akhlesh Lakhtakia *

CATMAS – Computational and Theoretical Materials Sciences Group, Department of Engineering Science and Mechanics, Pennsylvania State University, 212 Earth-Engineering Sciences Building, University Park, PA 16802-6812, USA

Received 14 September 2000; received in revised form 20 November 2000; accepted 24 November 2000

Abstract

The theory of bioluminescent emission from a chiral sculptured thin film (STF) of finite width but infinite lateral extent is formulated. The photon source filaments embedded in the chiral STF are modelled as either co-wound or contra-wound. The structural handedness as well as the periodicity of the chiral STF are shown to critically control the emission spectrum and intensity, while the polarization state of the emitted light is strongly correlated with the structural handedness of the source filaments. © 2001 Elsevier Science B.V. All rights reserved.

Keywords: Thin film sensors; Bioluminescence; Chiralty; Structural handedness; DNA sensing

1. Introduction

The last few years have seen the emergence of locally columnar, porous, solid, thin films which can be created from a wide range of materials that can be evaporated or sputter deposited by ion bombardment in vacuum. These films have been dubbed sculptured thin films (STFs). The columns of an ideal STF are all parallel but bent and twisted – either continuously (as helixes, S's, C's, etc.) or sectionwise in the thickness/growth direction. The initial conception of STFs as well as their optical properties and applications have recently been reviewed elsewhere [1]. Fabrication methods continue to improve, as discussed in detail by Brett et al. [2] and Messier et al. [3]; and the serial bideposition technique pioneered by Hodgkinson and colleagues [4] must be singled out for special mention. Finally, optical devices such as circular polarization filters and spectral hole filters have been designed exploiting the STF concept, and fabricated as well as tested [5,6].

The hallmark of a STF is a precisely controlled porosity with 10–300 nm void regions between columns of similar cross-sectional dimensions. The porosity can be engineered to lie within the 10–90% range [3]. Being porous, a STF can function as a nanoreactor. This capability can be harnessed for a variety of chemical and biochemical applications, one of which motivated this communication in the following manner.

Intercalation of an appropriate ruthenium complex with double-stranded DNA is known to generate luminescence [7]. The bioluminescent signal, essentially the rate of photon emission [8], is an indication of the volumetric concentration of the DNA present in the reactor. The chemical mechanisms underlying the

* Tel.: +1-814-863-4319; fax: +1-814-863-7967.
E-mail address: axl4@psu.edu (A. Lakhtakia).

PII: S0030-4018(00)01144-5

photon-production process can be made specific enough to identify a specific gene in a particular sample of biological matter. For instance, suppose that identical single-strand DNA molecules – each containing a particular gene sequence matched to *E. coli* – are dispersed as probe molecules in a reactor. An aqueous solution contaminated with DNA fragments from exploded *E. coli* is introduced in the reactor. Single-strand DNA fragments with the appropriate gene sequence couple with the probe molecules to form double-stranded DNA filaments. The subsequent introduction of the ruthenium complex [7,9,10] in the reactor initiates photon production from those filaments.

Bioluminescent emission is bound to be affected by the reactor characteristics. If the reactor is a chiral STF, also called a thin-film helicoidal bianisotropic medium (TFHBM), the possibility of exploiting the circular Bragg phenomenon [1,11] exhibited by it offers attractive possibilities. This is indeed borne out by the theoretical analysis and numerical results presented here.

In the following sections, the theory of bioluminescent emission from a chiral STF of finite width but infinite lateral extent is presented. An $\exp(-i\omega t)$ time dependence is implicit; vectors are underlined and dyadics are double underlined, while column 4 vectors as well as 4×4 matrices are additionally enclosed in square brackets; $\underline{r} = x\underline{u}_x + y\underline{u}_y + z\underline{u}_z$ is the position vector with $\underline{u}_x$, $\underline{u}_y$ and $\underline{u}_z$ as the cartesian unit vectors; and the z axis is parallel to the thickness direction.

2. Theoretical analysis

The canonical boundary value problem in the present context is that of a chiral STF which occupies the region $0 \leqslant z \leqslant L$, while the half-spaces $z \leqslant 0$ and $z \geqslant L$ are vacuous. The photon source filaments are distributed uniformly in any xy plane, but their distribution can be a function of z. The duration of photon production and emission is assumed to be far in excess of $2\pi/\omega$, which permits the use of frequency-domain analysis.

2.1. Matrix ordinary differential equation

The nonhomogeneous, frequency-dependent permittivity dyadic of the chosen chiral STF is expressed as follows [1]:

$$\underline{\underline{\epsilon}}(\underline{r}) = \epsilon_0 \underline{\underline{S}}_z(z,h) \cdot \underline{\underline{S}}_y(\chi) \cdot \left[\epsilon_a \underline{u}_z\underline{u}_z + \epsilon_b \underline{u}_x\underline{u}_x + \epsilon_c \underline{u}_y\underline{u}_y\right] \cdot \underline{\underline{S}}_y^{-1}(\chi) \cdot \underline{\underline{S}}_z^{-1}(z,h). \tag{1}$$

In this equation, the relative permittivity scalars $\epsilon_{a,b,c}$ are functions of ω; $\epsilon_0 = 8.854 \times 10^{-12}$ F m^{-1} is the free-space permittivity; the tilt dyadic

$$\underline{\underline{S}}_y(\chi) = \underline{u}_y\underline{u}_y + (\underline{u}_x\underline{u}_x + \underline{u}_z\underline{u}_z)\cos\chi + (\underline{u}_z\underline{u}_x - \underline{u}_x\underline{u}_z)\sin\chi \tag{2}$$

represents the locally columnar microstructure of any chiral STF with $\chi > 0°$; while the rotation dyadic

$$\underline{\underline{S}}_z(z,h) = \underline{u}_z\underline{u}_z + \left(\underline{u}_x\underline{u}_x + \underline{u}_y\underline{u}_y\right)\cos\left(\frac{\pi z}{\Omega}\right) + h\left(\underline{u}_y\underline{u}_x - \underline{u}_x\underline{u}_y\right)\sin\left(\frac{\pi z}{\Omega}\right) \tag{3}$$

contains 2Ω as the structural period. The structural handedness parameter h, $h^2 \equiv 1$, can take one of only two values: $h = 1$ for right handedness and $h = -1$ for left handedness.

Frequency-domain electromagnetic fields inside the chiral STF must satisfy the Maxwell curl postulates

$$\nabla \times \underline{E}(\underline{r}) = i\omega\mu_0 \underline{H}(\underline{r}), \tag{4}$$

$$\nabla \times \underline{H}(\underline{r}) = -i\omega \underline{\underline{\epsilon}}(\underline{r}) \cdot \underline{E}(\underline{r}) + \underline{J}^{so}(\underline{r}), \tag{5}$$

wherein $\mu_0 = 4\pi \times 10^{-7}$ H m^{-1} is the permeability of free space and $\underline{J}^{so}(\underline{r})$ is the source current density phasor indicative of bioluminescence. As the lateral extent of the chiral STF is infinite and the source

current density distribution is independent of both x and y, the electromagnetic field phasors $\underline{E}(\underline{r}) \equiv \underline{E}(z)$ and $\underline{H}(\underline{r}) \equiv \underline{H}(z)$.

Making use of the foregoing assumptions and their consequences in Eqs. (4) and (5), and after considerable algebraic manipulations, one gets the following 4×4 matrix differential equation:

$$\frac{\mathrm{d}}{\mathrm{d}z}[\underline{f}'(z)] = \mathrm{i}[\underline{\underline{P}}'][\underline{f}'(z)] + [\underline{\gamma}'(z)]. \tag{6}$$

The column 4 vector $[\underline{f}'(z)] = [\underline{\underline{B}}(-z,h)][\underline{f}(z)]$, where

$$[\underline{\underline{B}}(z,h)] = \begin{bmatrix} \cos(\pi z/\Omega) & -h\sin(\pi z/\Omega) & 0 & 0 \\ h\sin(\pi z/\Omega) & \cos(\pi z/\Omega) & 0 & 0 \\ 0 & 0 & \cos(\pi z/\Omega) & -h\sin(\pi z/\Omega) \\ 0 & 0 & h\sin(\pi z/\Omega) & \cos(\pi z/\Omega) \end{bmatrix}, \qquad [\underline{f}(z)] = \begin{bmatrix} E_x(z) \\ E_y(z) \\ H_x(z) \\ H_y(z) \end{bmatrix}; \tag{7}$$

the 4×4 matrix

$$[\underline{\underline{P}}'] = \begin{bmatrix} 0 & -\mathrm{i}h\pi/\Omega & 0 & \omega\mu_0 \\ \mathrm{i}h\pi/\Omega & 0 & -\omega\mu_0 & 0 \\ 0 & -\omega\epsilon_0\epsilon_c & 0 & -\mathrm{i}h\pi/\Omega \\ \omega\epsilon_0\tilde{\epsilon}_d & 0 & \mathrm{i}h\pi/\Omega & 0 \end{bmatrix}, \tag{8}$$

where $\tilde{\epsilon}_d = \epsilon_a\epsilon_b/\left(\epsilon_a\cos^2\chi + \epsilon_b\sin^2\chi\right)$; while the source 4 vector

$$[\underline{\gamma}'(z)] = \begin{bmatrix} 0 \\ 0 \\ J_y^{\mathrm{so}}(z)\cos(\pi z/\Omega) - hJ_x^{\mathrm{so}}(z)\sin(\pi z/\Omega) \\ -J_x^{\mathrm{so}}(z)\cos(\pi z/\Omega) - hJ_y^{\mathrm{so}}(z)\sin(\pi z/\Omega) + J_z^{\mathrm{so}}(z)(\tilde{\epsilon}_d/\epsilon_a\epsilon_b)(\epsilon_b - \epsilon_a)\sin\chi\cos\chi \end{bmatrix}. \tag{9}$$

As the matrix $[\underline{\underline{P}}']$ is independent of z, the solution of Eq. (6) is straightforward; thus [1,12],

$$[\underline{f}(z)] = [\underline{\underline{B}}(z,h)]\mathrm{e}^{\mathrm{i}[\underline{\underline{P}}']z}\left\{[\underline{f}(0)] + \int_0^z \mathrm{e}^{-\mathrm{i}[\underline{\underline{P}}']z_s}[\underline{\gamma}'(z_s)]\,\mathrm{d}z_s\right\}. \tag{10}$$

2.2. Helicoidal source filaments

The morphology of chiral STFs being helicoidal – to which one expects the photon source filaments would conform – a helicoidal representation for the source current density phasor is appropriate. The tangential, the normal, and the binormal unit vectors in a helicoidal coordinate system conformal with the chosen chiral STF are denoted by $\underline{\underline{S}}_z(z,h)\cdot\underline{u}_{\tau,n,b}$, respectively, where the unit vectors

$$\underline{u}_\tau = \underline{u}_x\cos\chi + \underline{u}_z\sin\chi, \qquad \underline{u}_n = -\underline{u}_x\sin\chi + \underline{u}_z\cos\chi, \qquad \underline{u}_b = -\underline{u}_y. \tag{11}$$

The handedness of the embedded photon source filaments may be either the same as that of the chiral STF or the opposite. A co-wound filamentary source current density is best expressed as

$$\underline{J}_{\mathrm{co}}^{\mathrm{so}}(z) = \underline{\underline{S}}_z(z,h)\cdot[J_n(z)\underline{u}_n + J_\tau(z)\underline{u}_\tau + J_b(z)\underline{u}_b]; \tag{12}$$

accordingly,

$$[\underline{\gamma}'(z)]_{\mathrm{co}} = \begin{bmatrix} 0 \\ 0 \\ -J_b(z) \\ [J_n(z)\epsilon_b\sin\chi - J_\tau(z)\epsilon_a\cos\chi](\tilde{\epsilon}_d/\epsilon_a\epsilon_b) \end{bmatrix}. \tag{13}$$

A contra-wound filamentary source current density is denoted by

$$\underline{J}^{\mathrm{so}}_{\mathrm{contra}}(z) = \underline{S}_{\tau}(z,-h)\cdot[J_n(z)\underline{u}_n + J_\tau(z)\underline{u}_\tau + J_b(z)\underline{u}_b]. \tag{14}$$

The corresponding expression for the source 4 vector in Eq. (6) is now more complicated than Eq. (13); thus,

$$[\underline{\gamma}'(z)]_{\mathrm{contra}} = \left[\begin{array}{c} 0 \\ 0 \\ h[J_n(z)\sin\chi - J_\tau(z)\cos\chi]\sin(2\pi z/\Omega) - J_b(z)\cos(2\pi z/\Omega) \\ \Big\{[J_n(z)\cos\chi + J_\tau(z)\sin\chi](\epsilon_b-\epsilon_a)(\tilde{\epsilon}_d/\epsilon_a\epsilon_b)\sin\chi\cos\chi \\ +[J_n(z)\sin\chi - J_\tau(z)\cos\chi]\cos(2\pi z/\Omega) + hJ_b(z)\sin(2\pi z/\Omega)\Big\} \end{array}\right]. \tag{15}$$

2.3. Boundary value problem

As a result of photon production inside the chiral STF, light is emitted into the upper and the lower half-spaces. The electric field phasor of the emitted light is stated as

$$\underline{E}(\underline{z}) = \begin{cases} \left(b_{\mathrm{L}}\underline{u}_- + b_{\mathrm{R}}\underline{u}_+\right)\exp(-\mathrm{i}k_0 z), & z \leqslant 0, \\ \left(c_{\mathrm{L}}\underline{u}_+ + c_{\mathrm{R}}\underline{u}_-\right)\exp\left[\mathrm{i}k_0(z-L)\right], & z \geqslant L, \end{cases} \tag{16}$$

where $\underline{u}_\pm = (\underline{u}_x \pm \mathrm{i}\underline{u}_y)/\sqrt{2}$ and $k_0 = \omega\sqrt{\epsilon_0\mu_0}$ is the free-space wave number. Whereas b_{L} and c_{L} are the amplitudes of the left-circularly polarized (LCP) components, b_{R} and c_{R} are the amplitudes of the right-circularly polarized (RCP) components, of the emitted plane waves.

Accordingly, the boundary values

$$[\underline{f}(0)] = \frac{1}{\sqrt{2}}\left[\begin{array}{c} b_{\mathrm{L}} + b_{\mathrm{R}} \\ -\mathrm{i}(b_{\mathrm{L}} - b_{\mathrm{R}}) \\ -\mathrm{i}(b_{\mathrm{L}} - b_{\mathrm{R}})/\eta_0 \\ -(b_{\mathrm{L}} + b_{\mathrm{R}})/\eta_0 \end{array}\right], \qquad [\underline{f}(L)] = \frac{1}{\sqrt{2}}\left[\begin{array}{c} c_{\mathrm{L}} + c_{\mathrm{R}} \\ \mathrm{i}(c_{\mathrm{L}} - c_{\mathrm{R}}) \\ -\mathrm{i}(c_{\mathrm{L}} - c_{\mathrm{R}})/\eta_0 \\ (c_{\mathrm{L}} + c_{\mathrm{R}})/\eta_0 \end{array}\right] \tag{17}$$

of $[\underline{f}(z)]$ emerge, with $\eta_0 = \sqrt{\mu_0/\epsilon_0}$ as the intrinsic impedance of free space. These boundary values are substituted in Eq. (10) to get the matrix algebraic relation

$$[\underline{f}(L)] = [\underline{\underline{B}}(L,h)]\mathrm{e}^{\mathrm{i}[\underline{\underline{P}}']L}\left\{[\underline{f}(0)] + \int_0^L \mathrm{e}^{-\mathrm{i}[\underline{\underline{P}}']z_{\mathrm{s}}}[\underline{\gamma}'(z_{\mathrm{s}})]\,\mathrm{d}z_{\mathrm{s}}\right\}. \tag{18}$$

Provided the source current density phasor is known and the relative remote possibility of Voigt wave propagation [13] at the frequency of interest is discounted, Eq. (18) can be solved using standard techniques in order to determine the four amplitudes $b_{\mathrm{L,R}}$ and $c_{\mathrm{L,R}}$.

3. Numerical results and discussion

A variety of results can be obtained using the formulation developed in the preceding section. The photon source filaments are likely to either stick to or wrap around the helicoidal columns. Therefore, at this initial stage of research on bioluminescence in STFs, let the source current density be entirely tangential, i.e., $J_{n,b}(z) \equiv 0$, $\forall z \in [0,L]$. For illustrative results, let it also be independent of z in the bottom part and null valued in the top part of the chiral STF, as per

$$J_\tau(z) = \begin{cases} J_{\tau 0}, & 0 \leqslant z \leqslant fL \\ 0, & fL < z \leqslant L \end{cases}, \quad 0 \leqslant f \leqslant 1. \tag{19}$$

Eq. (18) simplifies greatly for co-wound source filaments, leading to the following equation:

$$[\underline{f}(L)] = [\underline{\underline{B}}(L,h)]\mathrm{e}^{\mathrm{i}[\underline{\underline{P}}']L} \left\{ [\underline{f}(0)] - J_{\tau 0}\frac{\tilde{\epsilon}_d}{\epsilon_b}\cos\chi[\underline{\underline{\widetilde{F}}}_{\mathrm{c}}(0,-\mathrm{i}[\underline{\underline{P}}'];fL,0)] \begin{bmatrix} 0 \\ 0 \\ 0 \\ 1 \end{bmatrix} \right\}. \tag{20}$$

The 4×4 matrix $[\underline{\underline{\widetilde{F}}}_{\mathrm{c}}(q,[\underline{\underline{A}}];z,\zeta)]$ on the right side of Eq. (20) – and later on the right side of Eq. (23) – is a function of the wave number q, the matrix $[\underline{\underline{A}}]$, as well as the distances z and ζ. This matrix function is best computed after diagonalizing the matrix $[\underline{\underline{A}}]$; thus, $[\underline{\underline{A}}] = [\underline{\underline{T}}][\underline{\underline{Q}}][\underline{\underline{T}}]^{-1}$, with the diagonal matrix $[\underline{\underline{Q}}]$ containing the eigenvalues of $[\underline{\underline{A}}]$ and the orthogonal matrix $[\underline{\underline{T}}]$ comprising the eigenvectors of $[\underline{\underline{A}}]$ [14]. Then,

$$[\underline{\underline{\widetilde{F}}}_{\mathrm{c}}(q,[\underline{\underline{A}}];z,\zeta)] = [\underline{\underline{F}}_{\mathrm{c}}(q,[\underline{\underline{A}}];z)] - [\underline{\underline{F}}_{\mathrm{c}}(q,[\underline{\underline{A}}];\zeta)], \tag{21}$$

where the matrix

$$[\underline{\underline{F}}_{\mathrm{c}}(q,[\underline{\underline{A}}];z)] = [\underline{\underline{T}}]\left\{[\underline{\underline{I}}] + q^2[\underline{\underline{Q}}]^{-2}\right\}^{-1}\left\{[\underline{\underline{I}}]\cos qz + q[\underline{\underline{Q}}]^{-1}\sin qz\right\}[\underline{\underline{Q}}]^{-1}\mathrm{e}^{[\underline{\underline{Q}}]z}[\underline{\underline{T}}]^{-1} \tag{22}$$

is a function q, $[\underline{\underline{A}}]$ and z; while $[\underline{\underline{I}}]$ is the 4×4 identity matrix.

The final expression is not as simple as Eq. (20) for contra-wound source current filaments; instead, the counterpart of Eq. (20) is the expression

$$\begin{aligned}[\underline{f}(L)] = [\underline{\underline{B}}(L,h)]\mathrm{e}^{\mathrm{i}[\underline{\underline{P}}']L} \Bigg\{ & [\underline{f}(0)] + J_{\tau 0}(\epsilon_b - \epsilon_a)\frac{\tilde{\epsilon}_d}{\epsilon_a\epsilon_b}\sin^2\chi\cos\chi[\underline{\underline{\widetilde{F}}}_{\mathrm{c}}(0,-\mathrm{i}[\underline{\underline{P}}'];fL,0)] \begin{bmatrix} 0 \\ 0 \\ 0 \\ 1 \end{bmatrix} \\ & - J_{\tau 0}\cos\chi \left(\left[\underline{\underline{\widetilde{F}}}_{\mathrm{c}}\left(\frac{2\pi}{\Omega},-\mathrm{i}[\underline{\underline{P}}'];fL,0\right)\right] \begin{bmatrix} 0 \\ 0 \\ 0 \\ 1 \end{bmatrix} + h\left[\underline{\underline{\widetilde{F}}}_{\mathrm{s}}\left(\frac{2\pi}{\Omega},-\mathrm{i}[\underline{\underline{P}}'];fL,0\right)\right] \begin{bmatrix} 0 \\ 0 \\ 1 \\ 0 \end{bmatrix} \right) \Bigg\}. \end{aligned} \tag{23}$$

The 4×4 matrix function $[\underline{\underline{\widetilde{F}}}_{\mathrm{s}}(q,[\underline{\underline{A}}];z,\zeta)]$ is defined similarly to $[\underline{\underline{\widetilde{F}}}_{\mathrm{c}}(q,[\underline{\underline{A}}];z,\zeta)]$; thus,

$$[\underline{\underline{\widetilde{F}}}_{\mathrm{s}}(q,[\underline{\underline{A}}];z,\zeta)] = [\underline{\underline{F}}_{\mathrm{s}}(q,[\underline{\underline{A}}];z)] - [\underline{\underline{F}}_{\mathrm{s}}(q,[\underline{\underline{A}}];\zeta)], \tag{24}$$

where

$$[\underline{\underline{F}}_{\mathrm{s}}(q,[\underline{\underline{A}}];z)] = [\underline{\underline{T}}]\left\{[\underline{\underline{I}}] + q^2[\underline{\underline{Q}}]^{-2}\right\}^{-1}\left\{[\underline{\underline{I}}]\sin qz - q[\underline{\underline{Q}}]^{-1}\cos qz\right\}[\underline{\underline{Q}}]^{-1}\mathrm{e}^{[\underline{\underline{Q}}]z}[\underline{\underline{T}}]^{-1}. \tag{25}$$

Calculations of the emission efficiencies

$$\mathscr{B}_{\mathrm{R,L}} = \frac{1}{2\eta_0 J_{\tau 0}}|b_{\mathrm{R,L}}|^2, \qquad \mathscr{C}_{\mathrm{R,L}} = \frac{1}{2\eta_0 J_{\tau 0}}|c_{\mathrm{R,L}}|^2, \tag{26}$$

were made as functions of the fraction f of the chiral STF occupied by the photon source filaments and the free-space wavelength $\lambda_0 = 2\pi/k_0$ for a variety of dielectric parameters. The relative permittivity scalars $\epsilon_{a,b,c}$ were modelled as single-resonance Lorentzian functions of λ_0 as per [15]

$$\epsilon_{a,b,c} = 1 + p_{a,b,c}\left[1 + \left(N_{a,b,c}^{-1} - \mathrm{i}\lambda_{a,b,c}\lambda_0^{-1}\right)^2\right]^{-1}, \tag{27}$$

where the oscillator strengths are denoted by $p_{a,b,c}$, while the parameters $\lambda_{a,b,c}$ and $N_{a,b,c}$ assist in the delineation of resonances and absorption bands, respectively. According to these expressions,

$$\lambda_{a,b,c}^{\mathrm{res}} = \lambda_{a,b,c}\left(1 + N_{a,b,c}^{-2}\right)^{-1/2} \tag{28}$$

are the three resonance wavelengths of the chosen STF, while

$$\lambda_{a,b,c}^{\mathrm{lw}} = \lambda_{a,b,c}N_{a,b,c}^{-1} \tag{29}$$

are defined as the respective resonance linewidths. The dissipative nature of the chosen material is manifested in the imaginary parts of $\epsilon_{a,b,c}$. The larger the values of the parameters $N_{a,b,c}$, the narrower are the absorption bands. All calculations were made for structurally right-handed films (i.e., $h = 1$).

Figs. 1 and 2 show the calculated emission efficiencies as functions of f and λ_0 for co- and contra-wound source filaments, respectively. The values $p_a = 1.6$, $p_b = 2.0$, $p_c = 1.7$, $\lambda_{a,b,c} = 180$ nm and $N_{a,b,c} = 100$ were selected so that the resonance wavelengths of $\epsilon_{a,b,c}$ lie in the ultraviolet regime [15], while dissipation is moderate in the $\lambda_0 \in [400, 800]$ nm regime. The chosen values of the tilt angle $\chi = 30^\circ$ and $\Omega = 150$ nm ensure that the Bragg regime is delineated by $\lambda_0 \in [513.4, 531.8]$ nm. The thickness ratio $L/\Omega = 60$ was selected so that the circular Bragg phenomenon is fully developed [1].

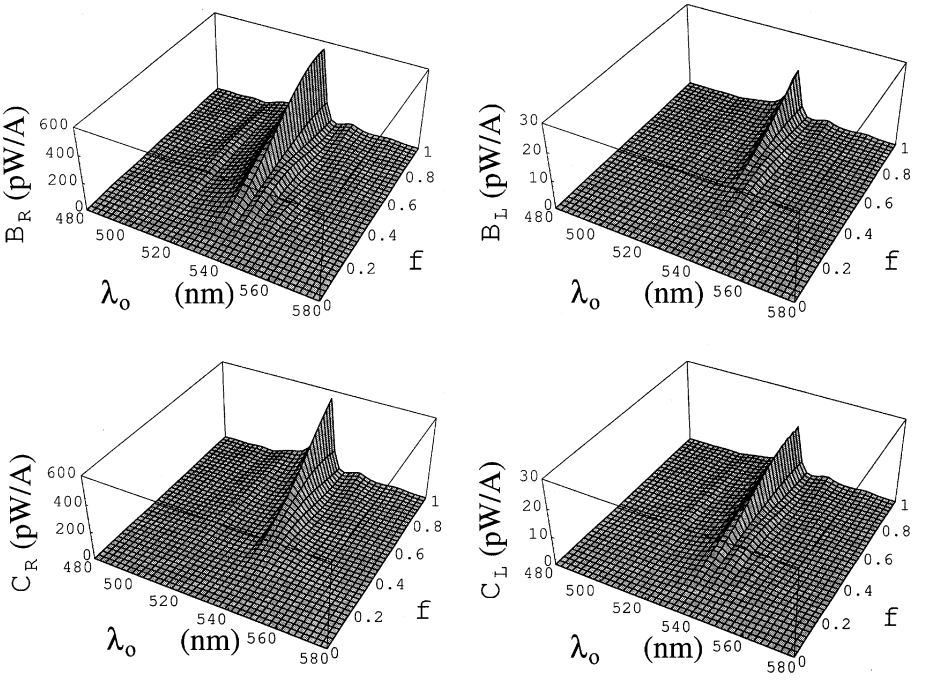

Fig. 1. Computed spectrums of the emission efficiencies $\mathscr{B}_{\mathrm{R,L}}$ and $\mathscr{C}_{\mathrm{R,L}}$ as functions of the fraction f of a chiral STF occupied by co-wound photon source filaments and the free-space wavelength λ_0. See the text for the constitutive and other parameters used. The Bragg regime for the selected parameters is $\lambda_0 \in [513.4, 531.8]$ nm.

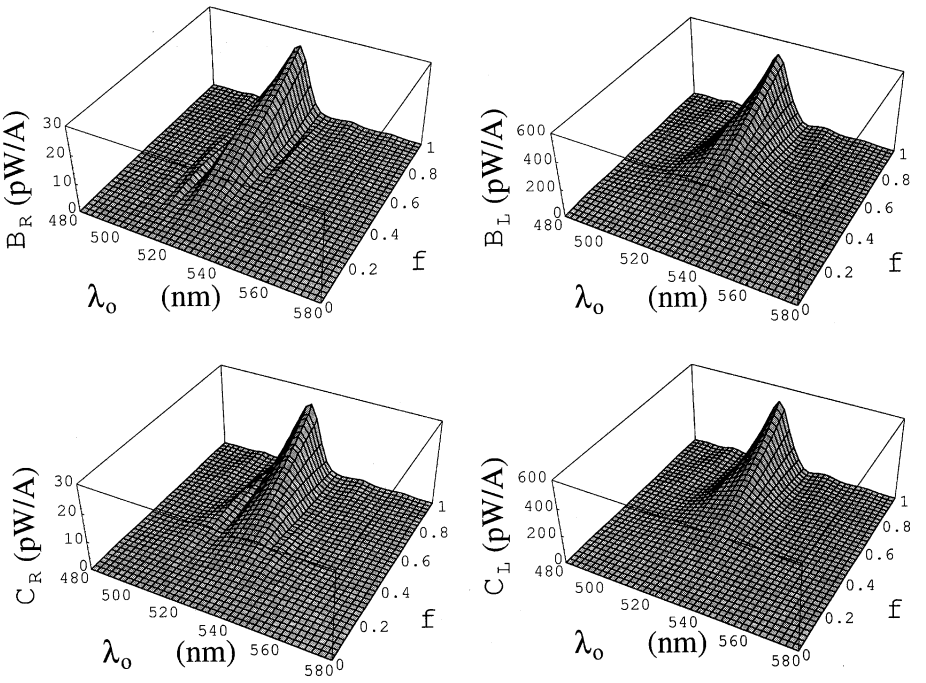

Fig. 2. Same as Fig. 1, except that the photon source filaments are contra-wound.

A comparison of Figs. 1 and 2, as well as of similar pairs of figures for other constitutive parameters, yields the following conclusions:

(1) Emission is strongest in intensity when the entire film is impregnated with the source filaments (i.e., $f = 1$). This stands to reason, because more photon sources must lead to stronger emission.

(2) Light is equally emitted into the upper and the lower half-spaces when the source filaments are present throughout the film (i.e., $f = 1$). Even when $0.5 < f < 1$, light is emitted in the two half-spaces in almost equal proportions. Clearly, the use of mirrors for chiral STF bioluminescence sensors is recommended for signal enhancement. The mirrors can be either dielectric multilayers [16,17] or chiral STF bilayers [18], the latter prospect being specially attractive for integrated fabrication technologies.

(3) The emission spectrums are highly localized with respect to the wavelength λ_0. The emitted light is virtually monochromatic (with a half-power bandwidth not exceeding 5 nm in Fig. 1) for co-wound source filaments, but the bandwidth is three to four times larger for contra-wound source filaments. This distinction is a significant effect of the structural handedness of chiral STFs.

(4) Emission is strongest on the long-wavelength side of the Bragg regime for co-wound, and in the Bragg regime for contra-wound, source filaments. This is a major effect of the periodicity of chiral STFs. Significantly, the location of the Bragg regime can be substantially controlled by choosing Ω properly during fabrication [3,6], other factors being the same.

(5) Emission is stronger in intensity for co-wound than for contra-wound source filaments, also an important consequence of the structural handedness of chiral STFs.

(6) The polarization state of the emitted light is virtually circular for both types of source filaments. Furthermore, the handedness of the emitted light is identical to the structural handedness of the source filaments, regardless of the structural handedness of the chiral STF.

The foregoing conclusions derived in this preliminary study amply indicate the promise of chiral STFs as biosensor platforms, particularly for genomic sensing applications. Research on the possible use of chiral STFs for optical emitters such as light emitting diodes also appears warranted [19], and will be reported in forthcoming publications.

Acknowledgements

The author thanks his colleagues Russell Messier and Erwin Vogler for several stimulating discussions. This work is affectionately dedicated to Craig Frederick Bohren, distinguished Professor Emeritus of Meteorology, Pennsylvania State University, on the occasion of his 60th birthday.

References

[1] V.C. Venugopal, A. Lakhtakia, in: O.N. Singh, A. Lakhtakia (Eds.), Electromagnetic Fields in Unconventional Materials and Structures, Wiley, New York, 2000 (Chapter 5).
[2] M.J. Brett, M.W. Seto, J.C. Sit, K.D. Harris, D. Vick, K. Robbie, Proc. SPIE 3097 (1999) 114.
[3] R. Messier, V.C. Venugopal, P.D. Sunal, J. Vac. Sci. Technol. A 18 (2000) 1538.
[4] I.J. Hodgkinson, Proc. SPIE 3097 (1999) 119.
[5] Q. Wu, I.J. Hodgkinson, A. Lakhtakia, Opt. Eng. 39 (2000) 1863.
[6] I.J. Hodgkinson, Q.h. Wu, A. Lakhtakia, M.W. McCall, Opt. Commun. 177 (2000) 79.
[7] X.-H. Xu, A.J. Bard, J. Am. Chem. Soc. 117 (1995) 2627.
[8] K. Van Dyke (Ed.), Bioluminescence and Chemiluminescence: Instruments and Applications, CRC Press, Boca Raton, FL, USA, 1985.
[9] A. Islam, N. Ikeda, A. Yoshimura, T. Ohno, Inorg. Chem. 37 (1998) 3093.
[10] E.S. Handy, A.J. Pal, M.F. Rubner, J. Am. Chem. Soc. 121 (1999) 3525.
[11] M.W. McCall, A. Lakhtakia, J. Mod. Opt. 47 (2000) 973.
[12] A. Lakhtakia, W.S. Weiglhofer, IEE Proc. – Microw. Antennas Propag. 144 (1997) 57.
[13] A. Lakhtakia, Opt. Commun. 157 (1998) 193.
[14] H. Hochstadt, Differential Equations, Dover Press, New York, 1975, p. 56.
[15] C. Kittel, Introduction to Solid State Physics, Wiley Eastern, New Delhi, 1974.
[16] I. Abdulhalim, Opt. Commun. 174 (2000) 43.
[17] M.F. Weber, C.A. Stover, L.R. Gilbert, T.J. Nevitt, A.J. Ouderkirk, Nature 287 (2000) 2451.
[18] A. Lakhtakia, V.C. Venugopal, Microw. Opt. Technol. Lett. 17 (1998) 135.
[19] J.A.E. Wasey, A. Safonov, I.D.W. Samuel, W.L. Barnes, Opt. Commun. 183 (2000) 109.

1 February 2002

ELSEVIER

Optics Communications 202 (2002) 103–111

OPTICS COMMUNICATIONS

www.elsevier.com/locate/optcom

Local inclination angle: a key structural factor in emission from chiral sculptured thin films

Akhlesh Lakhtakia *

CATMAS – Computational and Theoretical Materials Sciences Group, Department of Engineering Science and Mechanics, Pennsylvania State University, University Park, PA 16802-6812, USA

Received 24 August 2001; received in revised form 6 November 2001; accepted 12 November 2001

Abstract

Sculptured thin films (STFs) are unidirectionally nonhomogeneous, anisotropic, porous, nanoengineered materials possessing morphological features of optically significant dimensions. Light emission efficiencies of chiral STFs are examined to establish the role of a key structural factor: the local inclination angle χ of the morphology. The centrality of its so-called pseudo-isotropic value χ^{pi} is identified. When the source configuration has the same handedness as the chiral STF, the emission spectrum is spread over the Bragg regime if χ is in the neighborhood of χ^{pi}; otherwise, the emission spectrum is highly localized in the short-wavelength (resp. long-wavelength) vicinity of the Bragg regime for $\chi > \chi^{pi}$ (resp. $\chi < \chi^{pi}$). In contrast, the emission spectrum is spread over the entire Bragg regime for the contra-wound source configuration, regardless of the value of χ. High emission efficiencies require that χ be considerably less than χ^{pi}.

1. Introduction

The characteristics of radiation emitted by a source depend not only on the source itself but also on the medium into which radiation is emitted. This becomes clear from even a cursory inspection of the dyadic Green functions for different classes of mediums, a dyadic Green function being – in effect – the field emitted by a point source into a particular medium at a specific frequency [1,2]. Most theoretical analyses are confined to radiation from a concentrated source, whether or not of infinitesimal dimensions, which is contiguous to a homogeneous medium that completely surrounds the source and is of non-zero extent in all directions. Analyses for a source interpenetrating the microscopic interstices of a nonhomogeneous medium are extremely rare, because they are difficult to implement – except for plane-stratified mediums [3].

The situation is obviously more complicated for unidirectionally and continuously nonhomogeneous mediums than for unidirectionally piecewise nonhomogeneous mediums. The one exception this author knows is furnished by the Green functions for helicoidal bianisotropic mediums, by virtue of the Oseen transformation [4,5]. Those Green functions provide the analytical basis for treating second harmonic emission [6,7] and bioluminescence from chiral sculptured thin films (STFs).

* Fax: +1-814-863-7967.
E-mail address: AXL4@psu.edu (A. Lakhtakia).

0030-4018/02/$ - see front matter
PII: S0030-4018(01)01696-0

A chiral STF can be morphologically likened to a bed of microscopic springs, being essentially a collection of parallel upright helical columns deposited on a substrate [9], as shown schematically in Fig. 1. The optical response of a chiral STF is controlled by three phenomenological factors and three structural factors. The first three are the relative permittivity scalars – denoted by ϵ_a, ϵ_b and ϵ_c – arising from the local orthorhombic symmetry of the thin film, and are functions of the free-space wavelength λ_0. The latter three are the handedness parameter h, the half-period Ω, and the local inclination angle χ. Whereas $h = 1$ for structural right-handedness, $h = -1$ for structural left-handedness. Together with the pitch 2Ω of the helical columns, h is responsible for the phenomenon of circular Bragg reflection: provided that the film thickness is sufficiently large and λ_0 lies within the so-called Bragg wavelength-regime, an axially excited chiral STF exhibits extremely high reflectance if the handedness of the incident light matches its structural handedness, and extremely low reflectance if otherwise [9–11].

The influence of χ has not been systematically evaluated, either theoretically or experimentally. Yet it is of very high importance, as the perusal of optical literature on the related columnar thin films (CTFs) easily demonstrates [12]. Chiral STFs as well as CTFs are typically fabricated by directing a collimated vapor flux onto a substrate. The average direction of vapor flux makes the angle χ_v to the substrate, this angle being carefully controlled in order to engineer the appropriate nanostructural morphology and realize the desired value of χ [13–15].

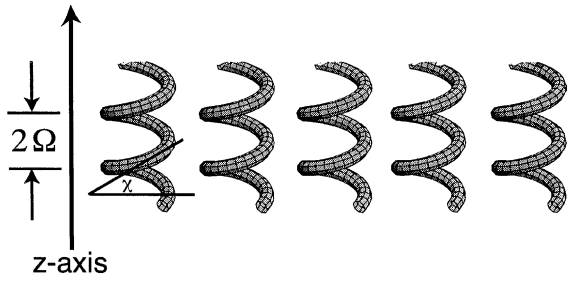

Fig. 1. Schematic of the morphology of a structurally right-handed (i.e., $h = 1$) chiral sculptured thin film, with 2Ω as the structural period and χ as the local inclination angle.

Therefore, the influence of the key structural factor χ on the emissive properties of chiral STFs of finite width but infinite lateral extent was investigated. Sample numerical results from parametric studies as well as from a realistic example are presented here, along with the conclusions drawn therefrom. An $\exp(-i\omega t)$ time-dependence is implicit; vectors are underlined and dyadics are double-underlined, while column 4-vectors as well as 4×4 matrixes are additionally enclosed in square brackets; $r = x\underline{u}_x + y\underline{u}_y + z\underline{u}_z$ is the position vector with $\underline{u}_x$, $\underline{u}_y$ and $\underline{u}_z$ as the cartesian unit vectors; and the z axis is parallel to the thickness direction.

2. Theory in brief

The canonical boundary value problem in the present context is that of a chiral STF which occupies the region $0 \leqslant z \leqslant L$, while the half-spaces $z \leqslant 0$ and $z \geqslant L$ are vacuous. The source is distributed uniformly in any xy plane, but its distribution can be a function of z.

Frequency-domain electromagnetic fields inside the chiral STF must satisfy the Maxwell curl postulates

$$\left.\begin{aligned} \nabla \times \underline{E}(\underline{r}) &= i\omega\mu_0 \underline{H}(\underline{r}), \\ \nabla \times \underline{H}(\underline{r}) &= -i\omega \underline{\underline{\epsilon}}(\underline{r}) \cdot \underline{E}(\underline{r}) + \underline{J}^{so}(\underline{r}), \end{aligned}\right\} \quad 0 \leqslant z \leqslant L, \tag{1}$$

wherein $\mu_0 = 4\pi \times 10^{-7}$ H m^{-1} is the permeability of free space and $\underline{J}^{so}(\underline{r})$ is the source current density phasor. The nonhomogeneous, frequency-dependent permittivity dyadic of the chosen chiral STF is expressed as follows [9]:

$$\begin{aligned} \underline{\underline{\epsilon}}(\underline{r}) = \epsilon_0 &\underline{\underline{S}}_z(z,h) \cdot \underline{\underline{S}}_y(\chi) \\ &\cdot \left[\epsilon_a \underline{u}_z\underline{u}_z + \epsilon_b \underline{u}_x\underline{u}_x + \epsilon_c \underline{u}_y\underline{u}_y\right] \\ &\cdot \underline{\underline{S}}_y^{-1}(\chi) \cdot \underline{\underline{S}}_z^{-1}(z,h). \end{aligned} \tag{2}$$

In this equation, $\epsilon_0 = 8.854 \times 10^{-12}$ F m^{-1} is the free-space permittivity; the inclination dyadic

$$\begin{aligned} \underline{\underline{S}}_y(\chi) = \underline{u}_y\underline{u}_y &+ (\underline{u}_x\underline{u}_x + \underline{u}_z\underline{u}_z)\cos\chi \\ &+ (\underline{u}_z\underline{u}_x - \underline{u}_x\underline{u}_z)\sin\chi \end{aligned} \tag{3}$$

represents the locally columnar microstructure of any chiral STF with $\chi > 0°$; while the rotation dyadic

$$\underline{\underline{S}}_z(z,h) = \underline{u}_z\underline{u}_z + (\underline{u}_x\underline{u}_x + \underline{u}_y\underline{u}_y)\cos\left(\frac{\pi z}{\Omega}\right) + h(\underline{u}_y\underline{u}_x - \underline{u}_x\underline{u}_y)\sin\left(\frac{\pi z}{\Omega}\right). \quad (4)$$

As the lateral extent of the chiral STF is infinite and the source current density phasor is independent of both x and y, the electromagnetic field phasors $\underline{E}(\underline{r}) \equiv \underline{E}(z)$ and $\underline{H}(\underline{r}) \equiv \underline{H}(z)$ for all $z \in (-\infty, \infty)$. Light is emitted into the upper and the lower half-spaces, the electric field phasor being

$$\underline{E}(\underline{z}) = \begin{cases} (b_L\underline{u}_- + b_R\underline{u}_+)\exp(-ik_0 z), & z \leqslant 0, \\ (c_L\underline{u}_+ + c_R\underline{u}_-)\exp[ik_0(z-L)], & z \geqslant L, \end{cases} \quad (5)$$

where $\underline{u}_\pm = (\underline{u}_x \pm i\underline{u}_y)/\sqrt{2}$ and $k_0 = \omega\sqrt{\epsilon_0\mu_0} = 2\pi/\lambda_0$ is the free-space wavenumber. Whereas b_L and c_L are the amplitudes of the left-circularly polarized (LCP) components, b_R and c_R are the amplitudes of the right-circularly polarized (RCP) components, of the emitted plane waves.

The boundary value problem boils down to the 4×4 matrix algebraic relation [8]

$$\begin{bmatrix} c_L + c_R \\ i(c_L - c_R) \\ -i(c_L - c_R)/\eta_0 \\ (c_L + c_R)/\eta_0 \end{bmatrix} = [\underline{\underline{B}}(L,h)]e^{i[\underline{\underline{P}}']L}\left\{ \begin{bmatrix} b_L + b_R \\ -i(b_L - b_R) \\ -i(b_L - b_R)/\eta_0 \\ -(b_L + b_R)/\eta_0 \end{bmatrix} + \sqrt{2}\int_0^L e^{-i[\underline{\underline{P}}']z_s}[\underline{\gamma}'(z_s)]\,dz_s \right\}. \quad (6)$$

Here, $\eta_0 = \sqrt{\mu_0/\epsilon_0}$ is the intrinsic impedance of free space; the matrixes

$$[\underline{\underline{B}}(z,h)] = \begin{bmatrix} \cos(\pi z/\Omega) & -h\sin(\pi z/\Omega) & 0 & 0 \\ h\sin(\pi z/\Omega) & \cos(\pi z/\Omega) & 0 & 0 \\ 0 & 0 & \cos(\pi z/\Omega) & -h\sin(\pi z/\Omega) \\ 0 & 0 & h\sin(\pi z/\Omega) & \cos(\pi z/\Omega) \end{bmatrix} \quad (7)$$

and

$$[\underline{\underline{P}}'] = \begin{bmatrix} 0 & -ih\pi/\omega & 0 & \omega\mu_0 \\ ih\pi/\omega & 0 & -\omega\mu_0 & 0 \\ 0 & -\omega\epsilon_0\epsilon_c & 0 & -ih\pi/\omega \\ \omega\epsilon_0\tilde{\epsilon}_d & 0 & ih\pi/\omega & 0 \end{bmatrix}, \quad (8)$$

the source 4-vector

$$[\underline{\gamma}'(z)] = \begin{bmatrix} 0 \\ 0 \\ J_y^{so}(z)\cos(\pi z/\Omega) - hJ_x^{so}(z)\sin(\pi z/\Omega) \\ -J_x^{so}(z)\cos(\pi z/\Omega) - hJ_y^{so}(z)\sin(\pi z/\Omega) + J_z^{so}(z)\frac{\tilde{\epsilon}_d}{\epsilon_a\epsilon_b}(\epsilon_b - \epsilon_a)\sin\chi\cos\chi \end{bmatrix}, \quad (9)$$

while

$$\tilde{\epsilon}_d = \epsilon_a\epsilon_b/(\epsilon_a\cos^2\chi + \epsilon_b\sin^2\chi). \quad (10)$$

Provided the source current density phasor is known and the relative remote possibility of Voigt wave propagation [16] at the frequency of interest is discounted, (6) can be solved using standard techniques in order to determine the four emission amplitudes $b_{L,R}$ and $c_{L,R}$.

A variety of results can be obtained using the presented formulation. In order to elucidate the effect of χ, which appears critically in the definition of $\tilde{\epsilon}_d$, let the source current density phasor be specified simply but meaningfully as follows: The handedness of the source current density phasor is either the same as that of the chiral STF or the opposite; i.e., the source configuration is either co-wound or contra-wound. The former possibility entertains the case for harmonic generation in the helical columns of the chiral STF, while the latter possibility models the case for bioluminescent emission from macromolecular strands curled around the helical columns. After eliminating normally and binormally directed source current densities from consideration but keeping only the tangentially directed source current densities for simplicity [17], let the entire chiral STF be occupied uniformly by the source such that

$$\underline{J}^{so}(z) = J_{\tau 0}\underline{\underline{S}}_z(z, \pm h)\cdot\underline{\underline{S}}_y(\chi)\cdot\underline{u}_x, \quad 0 \leqslant z \leqslant L. \quad (11)$$

with the upper sign taken for co-wound and the lower sign for contra-wound source configurations. Thus, the emission source dipoles are either stuck to or curled around the helical columns.

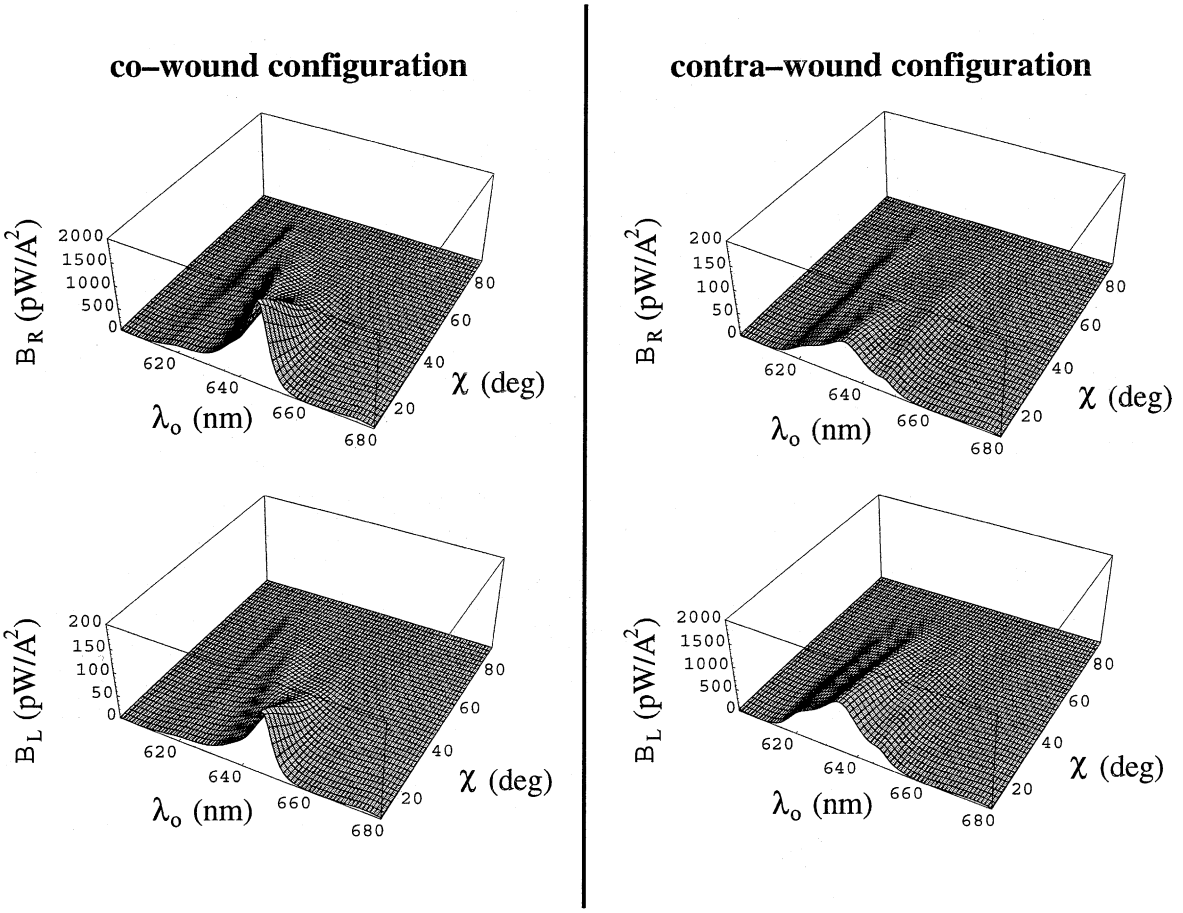

Fig. 2. Emission efficiencies $\mathscr{B}_{\mathrm{R}}$ and $\mathscr{B}_{\mathrm{L}}$ computed as functions of $\chi \in [0°, 90°]$ and λ_0, when $\epsilon_a = 2.7$, $\epsilon_b = 3.0$ and $\epsilon_c = 2.84$ are nondispersive over the $\lambda_0 \in [600, 680]$ nm regime; $h = 1$, $\lambda_0^{\mathrm{Br}} = 633$ nm, $\Omega = \lambda_0^{\mathrm{Br}}/(\epsilon_c^{1/2} + \tilde{\epsilon}_d^{1/2})$ and $L = 48\Omega$.

Incidentally, lasing by fluorescent dyes in cholesteric liquid crystals shows evidence of both types of source configurations [18].

3. Numerical results and discussion

3.1. Parametric investigation

Details of the solution procedure are available in the predecessor paper [8]. Calculations of the emission efficiencies [1]

$$\mathscr{B}_{\mathrm{R,L}} = \frac{1}{2\eta_0}\left|\frac{b_{\mathrm{R,L}}}{J_{\tau 0}}\right|^2, \quad \mathscr{C}_{\mathrm{R,L}} = \frac{1}{2\eta_0}\left|\frac{c_{\mathrm{R,L}}}{J_{\tau 0}}\right|^2 \tag{12}$$

were made for structurally right-handed chiral STFs, in a parametric investigation of the role of χ. As the films are assumed to be occupied uniformly by the source, there is no difference between the upper and the lower half-spaces; hence, all numerical studies correctly yielded $\mathscr{B}_{\mathrm{R}} = \mathscr{C}_{\mathrm{R}}$ and $\mathscr{B}_{\mathrm{L}} = \mathscr{C}_{\mathrm{L}}$. The half-period Ω was selected so that the center-wavelength λ_0^{Br} of the Bragg regime remained invariant, i.e., $\Omega = \lambda_0^{\mathrm{Br}}/(\epsilon_c^{1/2} + \tilde{\epsilon}_d^{1/2})$ [9]. For the sample numerical results presented here, $\lambda_0^{\mathrm{Br}} = 633$ nm, $L = 48\Omega$ and $h = 1$.

Fig. 2 shows the calculated emission efficiencies as functions of χ and λ_0 for the co- and contra-

[1] The following definitions are slightly different from those provided in the predecessor paper [8].

wound source configurations, when $\epsilon_a = 2.7$, $\epsilon_b = 3.0$ and $\epsilon_c = 2.84$ are non-dispersive over the $\lambda_0 \in [600, 680]$ nm regime. These plots confirm the following two earlier findings [8]:

(i) The emission spectrums are highly localized with respect to the wavelength λ_0 either in or in the immediate neighborhood of the Bragg regime.

(ii) The polarization state of the emitted light is virtually circular, and its handedness is identical to the structural handedness of the source configuration.

More significantly, these plots highlight the key role played by the local inclination angle χ. The emission efficiencies are high for low values of χ, and vice versa. This relationship between χ and the emission efficiencies is dramatically illustrated by the spectrums for the co- and contra-wound source configurations, shown in Fig. 3 for three values of χ.

Let $\chi^{\rm pi} \in [0°, 90°]$ be defined as the solution (if one exists) of the equation

$$\epsilon_c = \epsilon_a \epsilon_b / (\epsilon_a \cos^2 \chi^{\rm pi} + \epsilon_b \sin^2 \chi^{\rm pi}), \tag{13}$$

then

$$\epsilon_c \begin{cases} < \tilde{\epsilon}_d \\ = \tilde{\epsilon}_d \\ > \tilde{\epsilon}_d \end{cases} \quad \text{for } \chi \begin{cases} < \chi^{\rm pi}, \\ = \chi^{\rm pi}, \\ > \chi^{\rm pi}, \end{cases} \tag{14}$$

for the values of ϵ_a, ϵ_b and ϵ_c used to generate Figs. 2 and 3. Many other calculations, not reported here, also show that the emission efficiencies are higher for $\epsilon_c < \tilde{\epsilon}_d$ than for $\epsilon_c > \tilde{\epsilon}_d$, with $\epsilon_c = \tilde{\epsilon}_d$ providing a baseline. For the data used to produce Figs. 2 and 3, $\chi^{\rm pi} = 45°$.

The angle $\chi^{\rm pi}$ should be called the pseudo-isotropy angle [19,20]. When a normally incident plane wave axially excites a chiral STF that possesses $\chi = \chi^{\rm pi}$, reflection and transmission occur as if the chiral STF were isotropic and homogeneous (despite being anisotropic and nonhomogeneous), and the phenomenon of circular Bragg reflection vanishes. However, the graphs in Fig. 3 clearly show that emission betrays the anisotropy, nonhomogeneity and handedness of pseudo-isotropic chiral STFs – because the two source configurations emit differently from each other even when $\chi = \chi^{\rm pi}$.

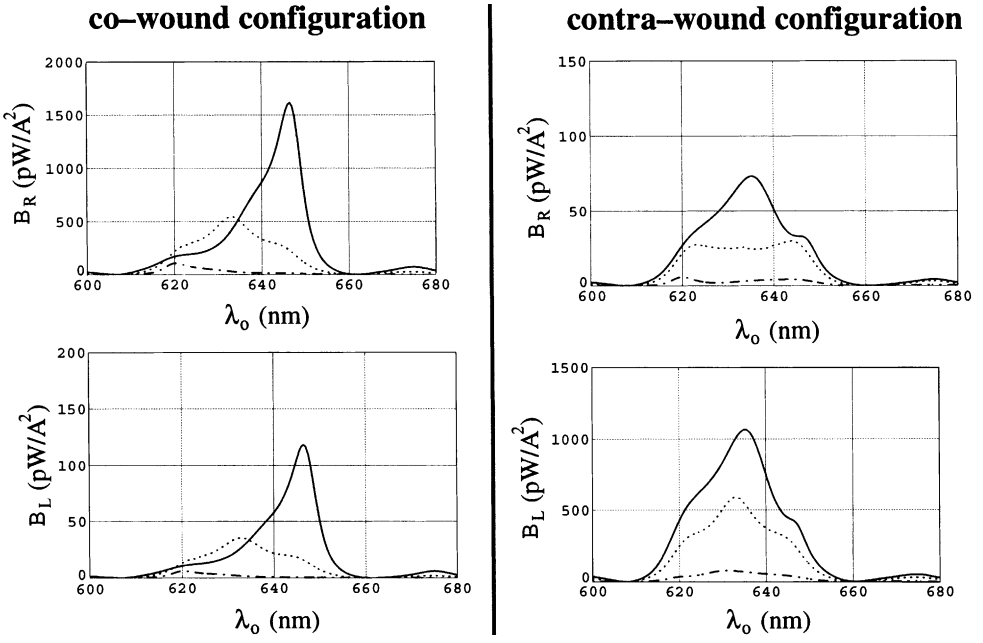

Fig. 3. Spectral sections of the plots of Fig. 2, for $\chi = 15°$ (solid line), 45° (dotted line) and 75° (dashed–dotted line).

The critical nature of $\chi^{\rm pi}$ is brought out in Figs. 2 and 3 in another way also. For $\chi \ll \chi^{\rm pi}$, emission from the co-wound source configuration is strongly peaked at the long-wavelength edge of the Bragg regime; the peak shifts to the short-wavelength edge for $\chi \gg \chi^{\rm pi}$; while the peak is situated inside the Bragg spectrum for χ in the neighborhood of $\chi^{\rm pi}$. On the other hand, the emission spectrum is fairly symmetrically distributed over the entire Bragg regime for the contra-wound source configuration, regardless of the value of χ. Although an explanation for these features is not yet available, the presented observations are consistent with those experimentally observed and numerically simulated for lasing in dye-doped cholesteric crystals (for which $\chi = 0°$ and $\epsilon_a = \epsilon_c$) [18].

3.2. A realistic example

As no data are available on the actual values of ϵ_a, ϵ_b, ϵ_c and χ for any chiral STF, the efficacy of the conclusions drawn from the parametric studies of Section 3.1 cannot be yet reported for actual chiral STFs. In a preliminary move towards realism, data for the related CTFs can however be

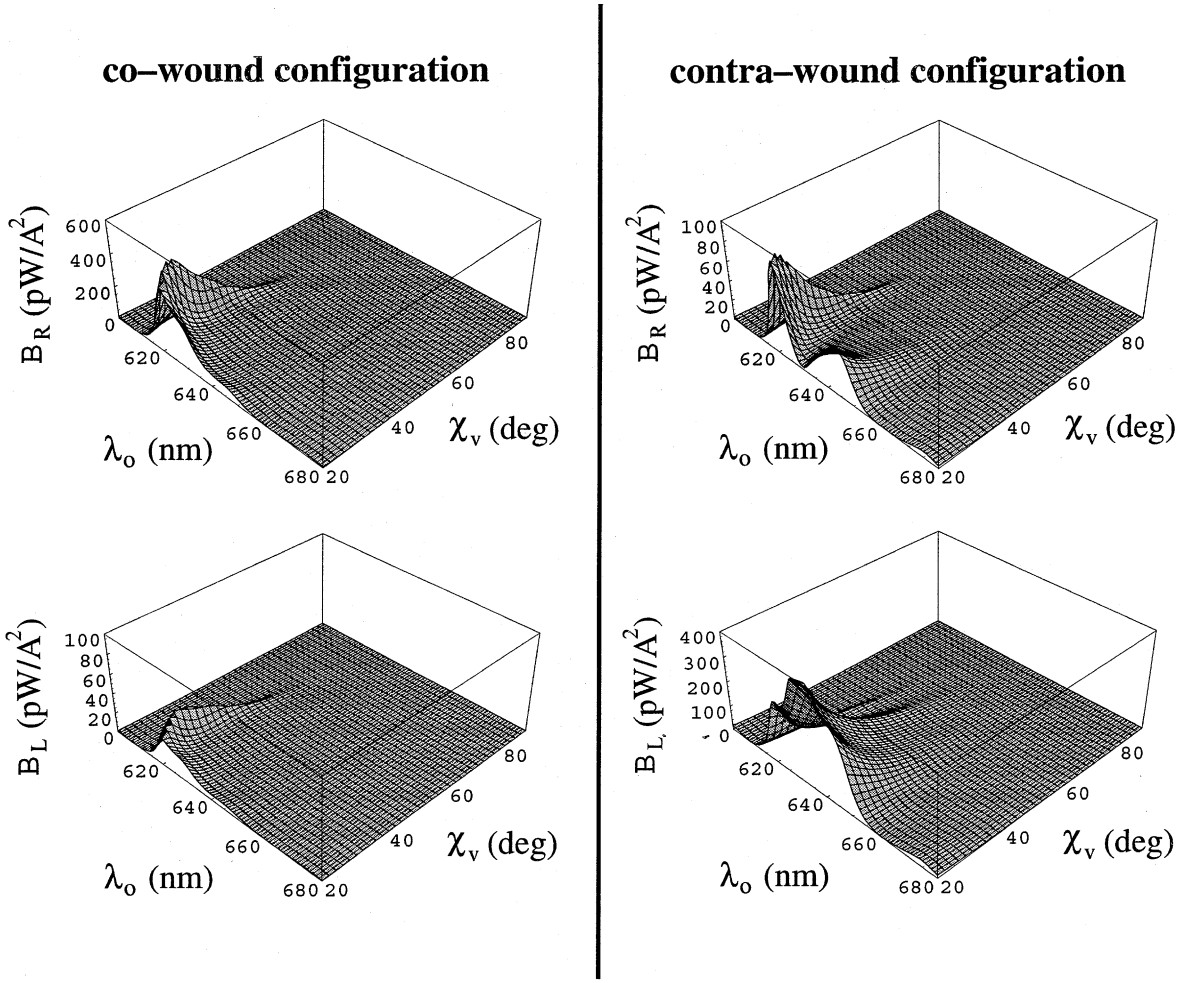

Fig. 4. Emission efficiencies $\mathscr{B}_{\rm R}$ and $\mathscr{B}_{\rm L}$ computed as functions of $\chi_{\rm v} \in [20°, 90°]$ and $\lambda_0 \in [600, 680]$ nm, when ϵ_a, ϵ_b, ϵ_c and χ are given by (15); $h = 1$, $\lambda_0^{\rm Br} = 633$ nm, $\Omega = \lambda_0^{\rm Br}/(\epsilon_c^{1/2} + \tilde{\epsilon}_d^{1/2})$ and $L = 48\Omega$.

used. A CTF simply is a homogeneous STF – obtained in the limit $\Omega \to \infty$ [9]. Data on CTFs too is sparse, but enough is available to enable initial work on chiral STFs.

For CTFs made of titanium oxide, the measurements at $\lambda_0 = 633$ nm reported by Hodgkinson et al. [21] yield the following empirical relations:

$$\left.\begin{array}{l} \epsilon_a = (1.0443 + 2.7394v - 1.3697v^2)^2, \\ \epsilon_b = (1.6765 + 1.5649v - 0.7825v^2)^2, \\ \epsilon_c = (1.3586 + 2.1109v - 1.0554v^2)^2, \\ \tan\chi = 2.8818\tan\chi_{\rm v}, \end{array}\right\}$$
$$20^\circ \leqslant \chi_{\rm v} \leqslant 90^\circ. \qquad (15)$$

In these equations, $v = \chi_{\rm v}/(\pi/2)$, wherein $\chi_{\rm v}$ is the vapor incidence angle in radian.

Eqs. (15) were employed to calculate the emission efficiencies of a structurally right-handed chiral STF made of titanium oxide as functions of $\chi_{\rm v}$ and λ_0. The center-wavelength of the Bragg regime was fixed at $\lambda_0^{\rm Br} = 633$ nm, the half-period $\Omega = \lambda_0^{\rm Br}/(\epsilon_c^{1/2} + \tilde{\epsilon}_d^{1/2})$, and the thickness $L = 48\Omega$. Dispersion was effectively ignored for this initial study, but can certainly be incorporated [8,22] upon the availability of adequate data.

The computed emission efficiencies are shown in Fig. 4 for the co-wound as well as the contra-wound configurations, as functions of $\chi_{\rm v} \in [20^\circ, 90^\circ]$ and $\lambda_0 \in [600, 680]$ nm. Despite the

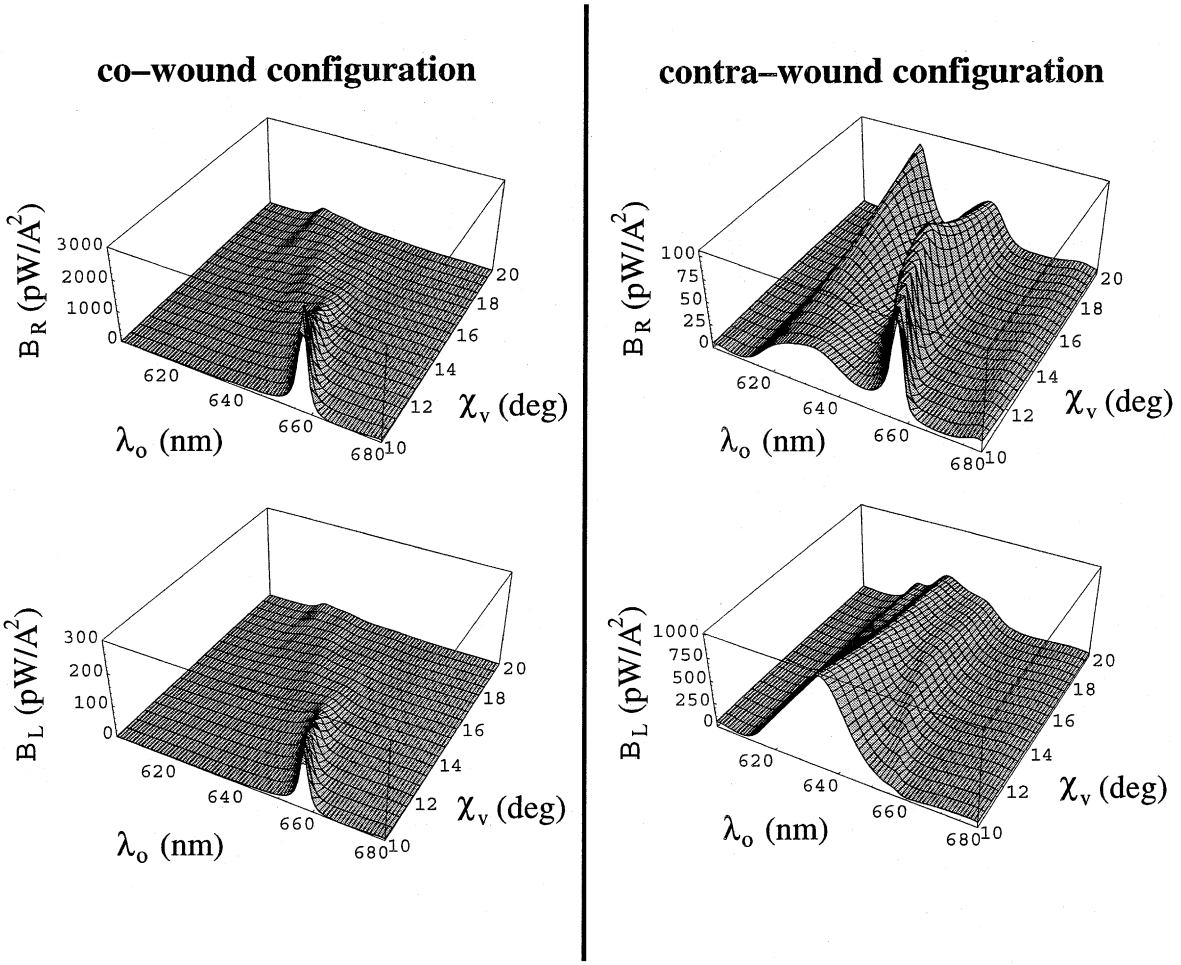

Fig. 5. Same as Fig. 4, but for $\chi_{\rm v} \in [10^\circ, 20^\circ]$.

dependence of $\epsilon_{a,b,c}$ on χ for the titanium oxide chiral STFs, the broad spectral characteristics of emission are the same as in Fig. 2 (for which ϵ_a, ϵ_b and ϵ_c are uncorrelated with χ).

An examination of (15) reveals that $\epsilon_c > \tilde{\epsilon}_d$ in Fig. 4, which implies that χ must be greater than $\chi^{\rm pi}$ for the titanium oxide CTFs of Hodgkinson et al. [21]. The experimental data underlying (15) was collected over $\chi_{\rm v} \in [20°, 90°]$, and is therefore strictly valid in that regime only. However, on extrapolating it to $\chi_{\rm v} < 20°$, the value of $\chi^{\rm pi}$ can be estimated at $\sim 40.7°$ in correspondence with $\chi_{\rm v}^{\rm pi} \simeq 16.6°$.

Shown in Fig. 5 are the computed emission efficiencies for the extrapolation regime $\chi_{\rm v} \in [10°, 20°]$. This regime covers the pseudo-isotropy angle from both sides. The spectral characteristics of the emission efficiencies are quite similar to the sectional plots presented in Fig. 3. The only exception is the double-peak feature in the plots of $\mathscr{B}_{\rm R}$ for the contra-wound configuration in Figs. 4 and 5. Although no explanation was readily forthcoming for this feature, it is not very significant because $\mathscr{B}_{\rm L}$ totally dominates $\mathscr{B}_{\rm R}$ in the Bragg regime. Furthermore, this feature may be a somewhat dubious artifact, as it appears for $\chi_{\rm v}$ at the limit of the fabrication process [21].

4. Conclusions

Several conclusions on the emission characteristics of chiral STFs had been given in the predecessor paper [8]. In addition to the two recounted in Section 3.1, the numerical results obtained here confirm the following:

(iii) The peak emission efficiencies are higher for the co-wound than for the contra-wound configurations.

The predecessor paper did not, however, elucidate the role of the local inclination angle χ. Neither was the watershed constituted by pseudo-isotropy identified therein. These significant roles have been clarified by the parametric investigation and the realistic example considered here. The following three conclusions emerge therefrom:

(iv) The emission spectrum is spread over the entire Bragg regime for the contra-wound source configuration.

(v) In contrast, for the co-wound source configuration, the emission spectrum is spread over the Bragg regime only when χ is in the neighborhood of $\chi^{\rm pi}$. Otherwise, the emission spectrum is highly localized in the short-wavelength (resp. long-wavelength) vicinity of the Bragg regime for $\chi > \chi^{\rm pi}$ (resp. $\chi < \chi^{\rm pi}$).

(vi) Highly efficient emission requires that χ be considerably less than $\chi^{\rm pi}$, regardless of the source configuration.

To end, the realistic example of Section 3.2 clearly indicates that strong emitters made of chiral STFs ought to be easily realizable, because the minimum value of χ realized thus far is $\sim 25°$ [13]. Thus the ample promise of chiral STFs as bioluminescence platforms [8] and sources of circularly polarized light [7] is strongly reaffirmed, and calls out for experimental research. Yet another attractive possibility is to fabricate chiral STF lasers from dye-doped polymers, in the manner suggested elsewhere [23,24].

Acknowledgements

The author humbly dedicates this work to Mr. Yusuf Hamied, under whose chairmanship the Mumbai pharmaceutical firm CIPLA is now distributing an inexpensive cocktail of anti-AIDS drugs in less developed countries. An anonymous reviewer is thanked for several suggestions to improve the presentation.

References

[1] H.C. Chen, Theory of Electromagnetic Waves, TechBooks, Fairfax, VA, USA, 1993.
[2] W.S. Weiglhofer, Electromagnetics 19 (1999) 563.
[3] W.-Y. Yin, L.-W. Li, I. Wolff, Int. J. Numer. Modelling 12 (1999) 209.
[4] W.S. Weiglhofer, A. Lakhtakia, Int. J. Appl. Electromag. Mech. 6 (1995) 221.
[5] A. Lakhtakia, W.S. Weiglhofer, IEE Proc.-Microw. Antennas Propag. 144 (1997) 57.
[6] A. Lakhtakia, V.C. Venugopal, Microw. Opt. Technol. Lett. 13 (1996) 339.

[7] V.C. Venugopal, A. Lakhtakia, Proc. R. Soc. London A 454 (1998) 1535;
Proc. R. Soc. London A 455 (1999) 4383 (E).
[8] A. Lakhtakia, Opt. Commun. 188 (2001) 313 (The numerical results presented in this paper hold for $J_{\tau 0} = 1$.).
[9] V.C. Venugopal, A. Lakhtakia, in: O.N. Singh, A. Lakhtakia (Eds.), Electromagnetic Fields in Unconventional Materials and Structures, Wiley, New York, 2000 (Chapter 5).
[10] Q. Wu, I.J. Hodgkinson, A. Lakhtakia, Opt. Eng. 39 (2000) 1863.
[11] I.J. Hodgkinson, Q.h. Wu, A. Lakhtakia, M.W. McCall, Opt. Commun. 177 (2000) 79.
[12] I.J. Hodgkinson, Q.h. Wu, Birefringent Thin Films and Polarizing Elements, World Scientific, Singapore, 1997.
[13] R. Messier, T. Gehrke, C. Frankel, V.C. Venugopal, W. Otaño, A. Lakhtakia, J. Vac. Sci. Technol. A 15 (1997) 2148.
[14] R. Messier, V.C. Venugopal, P.D. Sunal, J. Vac. Sci. Technol. A 18 (2000) 538.
[15] R. Knepper, R. Messier, Proc. SPIE 4467 (2001) 87.
[16] A. Lakhtakia, Opt. Commun. 157 (1998) 193.
[17] R. Aris, Vectors, Tensors, and the Basic Equations of Fluid Mechanics, Prentice-Hall, Englewood Cliffs, NJ, USA, 1962 (Sec. 3.12).
[18] V.I. Kopp, B. Fan, H.K.M. Vithana, A.Z. Genack, Opt. Lett. 23 (1998) 1707.
[19] I. Abdulhalim, Europhys. Lett. 48 (1999) 177.
[20] A. Lakhtakia, W.S. Weiglhofer, J. Opt. A 2 (2000) 107.
[21] I.J. Hodgkinson, Q.h. Wu, J. Hazel, Appl. Opt. 37 (1998) 2653.
[22] V.C. Venugopal, A. Lakhtakia, Eur. Phys. J. AP 10 (2000) 173.
[23] A. Lakhtakia, R. Messier, M.J. Brett, K. Robbie, Innovat. Mater. Res. 1 (1996) 1965.
[24] E. White, E.C. Shors, Dental Clin. North Amer. 30 (1986) 49.

15 March 2002

ELSEVIER

Optics Communications 203 (2002) 447

OPTICS COMMUNICATIONS

www.elsevier.com/locate/optcom

Corrigendum to "Local inclination angle: a key structural factor in emission from chiral sculptured thin films" [Opt. Commun. 202 (2002) 103–112]☆

Akhlesh Lakhtakia

CATMAS, Department of Engineering Science and Mechanics, Pennsylvania State University, 16802-6812, University Park, PA, USA

Eq. (8) has been printed incorrectly and should read as follows:

$$[\underline{\underline{P'}}] = \begin{bmatrix} 0 & -ih\pi/\Omega & 0 & \omega\mu_0 \\ ih\pi/\Omega & 0 & -\omega\mu_0 & 0 \\ 0 & -\omega\varepsilon_0\varepsilon_c & 0 & -ih\pi/\Omega \\ \omega\varepsilon_0\tilde{\varepsilon}_d & 0 & ih\pi/\Omega & 0 \end{bmatrix}. \tag{8}$$

☆ PII of original article S0030-4018(01)01696-0.

E-mail address: ax14@psu.edu (A. Lakhtakia).

PII: S0030-4018(02)01176-8

ON RADIATION FROM CANONICAL SOURCE CONFIGURATIONS EMBEDDED IN STRUCTURALLY CHIRAL MATERIALS

Akhlesh Lakhtakia
CATMAS—Computational & Theoretical Materials Sciences Group
Department of Engineering Science and Mechanics
Pennsylvania State University
University Park, PA 16802-6812

Received 27 September 2002

ABSTRACT: *Radiation due to six canonical configurations for the source current density embedded in a structurally chiral medium is analyzed theoretically. The radiation spectrum is highly dependent on whether its source is co-chiral or cross-chiral, and is localized either in or on the edges of the Bragg regime. The obtained conclusions hold for both chiral liquid crystals and chiral sculptured thin films doped with fluorescent dyes, etc.* © 2003 Wiley Periodicals, Inc. Microwave Opt Technol Lett 37: 37–40, 2003; Published online in Wiley InterScience (www.interscience.wiley.com). DOI 10.1002/mop.10818

Key words: *Bragg regime; fluorescence; lasing; luminescence; radiation; structurally chiral medium*

1. INTRODUCTION

Not only does radiation carry the signature of its source, but it is also affected by the medium into which it is emitted. That effect is clearly evinced in the dyadic Green functions available in closed-form for several different classes of linear homogeneous mediums [1–3]. If the medium is nonhomogeneous, its effect on the characteristics of the radiation becomes even more significant. Witness to this fact is optical radiation from dye-doped chiral nematic liquid crystals [4–6], which is known to be almost circularly polarized and confined to the so-called Bragg-wavelength regime of these periodically nonhomogeneous materials [7, 8]. Theoretical confirmation by explicit solution of the Maxwell curl postulates has been obtained, with radiation possible at wavelengths inside the Bragg regime as well as at one of its edges [9]. Radiation at the edge of the Bragg regime is also consistent with a density-of-states argument, which emerges from viewing a doped chiral nematic liquid crystal as a photonic crystal [10].

Chiral nematic liquid crystals as well as chiral smectic liquid crystals exemplify structurally chiral materials—which are anisotropic, unidirectionally nonhomogeneous, and helicoidally periodic substances [11, 12]. Their solid-state counterparts are the so-called chiral sculptured thin films [13–15]. In this paper, we focus on the characteristics of radiation from canonical source configurations embedded in a structurally chiral material. The source configurations could be excited either electronically or optically [5], and could represent lasing [6], luminescence [5], or fluorescence [16]. An $\exp(-i\omega t)$ time-dependence is implicit with ω as the angular frequency and t as the time; vectors are underlined and dyadics are double-underlined, while column-4 vectors as well as 4×4 matrixes are additionally enclosed in square brackets; and $\underline{r} = x\underline{u}_x + y\underline{u}_y + z\underline{u}_z$ is the position vector with $\underline{u}_x$, $\underline{u}_y$, and $\underline{u}_z$ as the Cartesian unit vectors.

2. BOUNDARY VALUE PROBLEM

The canonical boundary value problem in the present context is that of a structurally chiral medium which occupies the slab region $0 \le z \le L$, while the half-spaces $z \le 0$ and $z \ge L$ are vacuous. Dielectric response properties are assumed. The source is distributed uniformly in any xy plane, but its distribution can depend on z. The structurally chiral medium is nonhomogeneous along the z axis.

Frequency-domain electromagnetic fields inside the slab region must satisfy the Maxwell curl postulates

$$\left.\begin{aligned} \nabla \times \underline{E}(\underline{r}) &= i\omega\mu_0 \underline{H}(\underline{r}) \\ \nabla \times \underline{H}(\underline{r}) &= -i\omega \underline{\underline{\varepsilon}}(\underline{r}) \cdot \underline{E}(\underline{r}) + \underline{J}^{so}(\underline{r}) \end{aligned}\right\}, \qquad 0 \le z \le L, \quad (1)$$

where $\mu_0 = 4\pi \times 10^{-7}$ H m^{-1} is the permeability of free space and $\underline{J}^{so}(\underline{r})$ is the source current density phasor. The nonhomogeneous, frequency-dependent permittivity dyadic of the chosen medium is expressed as follows [17]:

$$\underline{\underline{\varepsilon}}(\underline{r}) = \varepsilon_0 \underline{\underline{S}}_z(z, h) \cdot \underline{\underline{S}}_y(\chi) \cdot [\varepsilon_a \underline{u}_z\underline{u}_z + \varepsilon_b \underline{u}_x\underline{u}_x + \varepsilon_c \underline{u}_y\underline{u}_y] \times \underline{\underline{S}}_y^{-1}(\chi) \cdot \underline{\underline{S}}_z^{-1}(z, h). \quad (2)$$

In this equation, the relative permittivity scalars $\varepsilon_{a,b,c}$ are functions of ω; $\varepsilon_0 = 8.854 \times 10^{-12}$ F m^{-1} is the free-space permittivity; the tilt dyadic

$$\underline{\underline{S}}_y(\chi) = \underline{u}_y\underline{u}_y + (\underline{u}_x\underline{u}_x + \underline{u}_z\underline{u}_z)\cos\chi + (\underline{u}_z\underline{u}_x - \underline{u}_x\underline{u}_z)\sin\chi \quad (3)$$

involves the angle $\chi \ge 0°$; while the rotation dyadic

$$\underline{\underline{S}}_z(z, h) = \underline{u}_z\underline{u}_z + (\underline{u}_x\underline{u}_x + \underline{u}_y\underline{u}_y)\cos\left(\frac{\pi z}{\Omega}\right) + h(\underline{u}_y\underline{u}_x - \underline{u}_x\underline{u}_y)\sin\left(\frac{\pi z}{\Omega}\right) \quad (4)$$

contains 2Ω as the structural period. The structural handedness parameter h can take one of only two values: $h = 1$ for right-handedness and $h = -1$ for left-handedness. The angle $\chi = 0°$ and $\varepsilon_c = \varepsilon_a$ for chiral nematic liquid crystals [7, 8].

As the lateral extent of the slab region is infinite and the source current density phasor is independent of both x and y, the electromagnetic field phasors $\underline{E}(\underline{r}) \equiv \underline{E}(z)$ and $\underline{H}(\underline{r}) \equiv \underline{H}(z)$ for all $z \in (-\infty, \infty)$. Radiation is emitted into the upper and the lower half-spaces, with the electric field phasor given by

$$\underline{E}(\underline{z}) = \begin{cases} (b_L\underline{u}_- + b_R\underline{u}_+)\exp(-ik_0 z), & z \le 0 \\ (c_L\underline{u}_+ + c_R\underline{u}_-)\exp[ik_0(z - L)], & z \ge L \end{cases} \quad (5)$$

where $\underline{u}_\pm = (\underline{u}_x \pm i\underline{u}_y)/\sqrt{2}$ and $k_0 = \omega\sqrt{\varepsilon_0\mu_0}$ is the free-space wavenumber. The free-space wavelength is denoted by $\lambda_0 = 2\pi/k_0$. Whereas b_L and c_L are the amplitudes of the left circularly polarized (LCP) components, b_R and c_R are the amplitudes of the right circularly polarized (RCP) components of the radiated plane waves.

The boundary value problem amounts to the following algebraic relation [17]:

$$\begin{bmatrix} c_L + c_R \\ i(c_L - c_R) \\ -i(c_L - c_R)/\eta_0 \\ (c_L + c_R)/\eta_0 \end{bmatrix} = [\underline{\underline{B}}(L, h)] e^{i[\underline{\underline{P}}']L} \left\{ \begin{bmatrix} b_L + b_R \\ -i(b_L - b_R) \\ -i(b_L - b_R)/\eta_0 \\ -(b_L + b_R)/\eta_0 \end{bmatrix} + \sqrt{2}[\underline{C}] \right\}. \quad (6)$$

Here and hereafter, $\eta_0 = \sqrt{\mu_0/\varepsilon_0}$ is the intrinsic impedance of free space; the 4×4 matrixes

$$[\underline{\underline{B}}(z,\,h)] = \begin{bmatrix} \cos\left(\frac{\pi z}{\Omega}\right) & -h\sin\left(\frac{\pi z}{\Omega}\right) & 0 & 0 \\ h\sin\left(\frac{\pi z}{\Omega}\right) & \cos\left(\frac{\pi z}{\Omega}\right) & 0 & 0 \\ 0 & 0 & \cos\left(\frac{\pi z}{\Omega}\right) & -h\sin\left(\frac{\pi z}{\Omega}\right) \\ 0 & 0 & h\sin\left(\frac{\pi z}{\Omega}\right) & \cos\left(\frac{\pi z}{\Omega}\right) \end{bmatrix} \tag{7}$$

and

$$[\underline{\underline{P}}'] = \begin{bmatrix} 0 & -ih\pi/\Omega & 0 & \omega\mu_0 \\ ih\pi/\Omega & 0 & -\omega\mu_0 & 0 \\ 0 & -\omega\varepsilon_0\varepsilon_c & 0 & -ih\pi/\Omega \\ \omega\varepsilon_0\tilde{\varepsilon}_d & 0 & ih\pi/\Omega & 0 \end{bmatrix}; \tag{8}$$

while

$$\tilde{\varepsilon}_d = \varepsilon_a\varepsilon_b/(\varepsilon_a\cos^2\chi + \varepsilon_b\sin^2\chi) \tag{9}$$

is a meaningful shorthand notation [20]. The column-4 vector $[\underline{C}]$ involves the source current density as well as the constitutive properties of the slab region $z \in [0,\,L]$. Eq. (6) can be solved using standard techniques in order to determine the four-radiation amplitudes $b_{L,R}$ and $c_{L,R}$.

3. CANONICAL SOURCE CONFIGURATIONS

Because the structurally chiral mediums are helicoidally nonhomogeneous, a helicoidal representation for the source current density is naturally appropriate. The tangential, the normal, and the binormal unit vectors in a helicoidal coordinate system conformal with the chosen medium are denoted by $\underline{\underline{S}}_z(z,\,h)\cdot\underline{u}_{\tau,n,b}$, respectively, where the unit vectors

$$\left.\begin{aligned} \underline{u}_\tau &= \underline{u}_x\cos\chi + \underline{u}_z\sin\chi \\ \underline{u}_n &= -\underline{u}_x\sin\chi + \underline{u}_z\cos\chi \\ \underline{u}_b &= -\underline{u}_y \end{aligned}\right\}. \tag{10}$$

The source current density can be decomposed into a co-chiral and a cross-chiral parts as follows:

$$\begin{aligned} \underline{J}^{so}(z) = {} & \underline{\underline{S}}_z(z,\,h)\cdot[J_n^{co}(z)\underline{u}_n + J_\tau^{co}(z)\underline{u}_\tau + J_b^{co}(z)\underline{u}_b] \\ & + \underline{\underline{S}}_z(z,\,-h)\cdot[J_n^{cr}(z)\underline{u}_n + J_\tau^{cr}(z)\underline{u}_\tau + J_b^{cr}(z)\underline{u}_b], \qquad z\in[0,\,L]. \end{aligned} \tag{11}$$

Thus, $J_{n,\tau,b}^{co,cr}(z)$ represent the six canonical source configurations possible.

For our present purposes, we suppose that $\underline{J}^{so}(z) = \underline{0}$ for $z \in [0,\,z_p]$ and $z \in [z_q,\,L]$, $0 < z_p < z_q < L$, and that

$$\begin{aligned} \underline{J}^{so}(z) = {} & \underline{\underline{S}}_z(z,\,h)\cdot[J_{n0}^{co}\underline{u}_n + J_{\tau 0}^{co}\underline{u}_\tau + J_{b0}^{co}\underline{u}_b] \\ & + \underline{\underline{S}}_z(z,\,-h)\cdot[J_{n0}^{cr}\underline{u}_n + J_{\tau 0}^{cr}\underline{u}_\tau + J_{b0}^{cr}\underline{u}_b], \qquad z\in[z_p,\,z_q]. \end{aligned} \tag{12}$$

Thus the source current density is present inside the layer $z \in [z_p, z_q]$, and absent everywhere else.

Accordingly, following the analysis initiated in [17], we obtain

$$\begin{aligned} [\underline{C}] = {} & [\underline{\underline{\tilde{F}}}_c(0,\,-i[\underline{\underline{P}}'];\,z_p,\,z_q)] \begin{bmatrix} 0 \\ 0 \\ -J_{b0}^{co} \\ \left\{\begin{aligned} &\frac{\tilde{\varepsilon}_d}{\varepsilon_a\varepsilon_b}[(\varepsilon_b J_{n0}^{co}\sin\chi - \varepsilon_a J_{\tau 0}^{co}\cos\chi) \\ &+ (\varepsilon_b - \varepsilon_a)\sin\chi\cos\chi(J_{n0}^{cr}\cos\chi + J_{\tau 0}^{cr}\sin\chi)\end{aligned}\right\} \end{bmatrix} \\ & + \left[\underline{\underline{\tilde{F}}}_c\left(\frac{2\pi}{\Omega},\,-i[\underline{\underline{P}}'];\,z_p,\,z_q\right)\right] \begin{bmatrix} 0 \\ 0 \\ -J_{b0}^{cr} \\ J_{n0}^{cr}\sin\chi - J_{\tau 0}^{cr}\cos\chi \end{bmatrix} \\ & + h\left[\underline{\underline{\tilde{F}}}_s\left(\frac{2\pi}{\Omega},\,-i[\underline{\underline{P}}'];\,z_p,\,z_q\right)\right] \begin{bmatrix} 0 \\ 0 \\ J_{n0}^{cr}\sin\chi - J_{\tau 0}^{cr}\cos\chi \\ J_{b0}^{cr} \end{bmatrix}. \end{aligned} \tag{13}$$

The 4×4 matrixes $[\underline{\underline{\tilde{F}}}_c(q,\,[\underline{\underline{A}}];\,z,\,\zeta)]$ and $[\underline{\underline{\tilde{F}}}_s(q,\,[\underline{\underline{A}}];\,z,\,\zeta)]$ are functions of wavenumber q and matrix $[\underline{\underline{A}}]$, as well as the distances z and ζ. Both are best computed after diagonalizing the matrix $[\underline{\underline{A}}]$; thus, $[\underline{\underline{A}}] = [\underline{\underline{T}}][\underline{\underline{Q}}][\underline{\underline{T}}]^{-1}$, with the diagonal matrix $[\underline{\underline{Q}}]$ containing the eigenvalues of $[\underline{\underline{A}}]$ and the orthogonal matrix $[\underline{\underline{T}}]$ comprising the eigenvectors of $[\underline{\underline{A}}]$ [18]. Then,

$$[\underline{\underline{\tilde{F}}}_{c,s}(q,\,[\underline{\underline{A}}];\,z,\,\zeta)] = [\underline{\underline{F}}_{c,s}(q,\,[\underline{\underline{A}}];\,z)] - [\underline{\underline{F}}_{c,s}(q,\,[\underline{\underline{A}}];\,\zeta)], \tag{14}$$

where the 4×4 matrixes

$$\begin{aligned} [\underline{\underline{F}}_c(q,\,[\underline{\underline{A}}];\,z)] = {} & [\underline{\underline{T}}]\{[\underline{\underline{I}}] \\ & + q^2[\underline{\underline{Q}}]^{-2}\}^{-1}\{[\underline{\underline{I}}]\cos qz + q[\underline{\underline{Q}}]^{-1}\sin qz\}[\underline{\underline{Q}}]^{-1}e^{[\underline{\underline{Q}}]z}[\underline{\underline{T}}]^{-1} \end{aligned} \tag{15}$$

and

$$\begin{aligned} [\underline{\underline{F}}_s(q,\,[\underline{\underline{A}}];\,z)] = {} & [\underline{\underline{T}}]\{[\underline{\underline{I}}] + \\ & q^2[\underline{\underline{Q}}]^{-2}\}^{-1}\{[\underline{\underline{I}}]\sin qz - q[\underline{\underline{Q}}]^{-1}\cos qz\}[\underline{\underline{Q}}]^{-1}e^{[\underline{\underline{Q}}]z}[\underline{\underline{T}}]^{-1} \end{aligned} \tag{16}$$

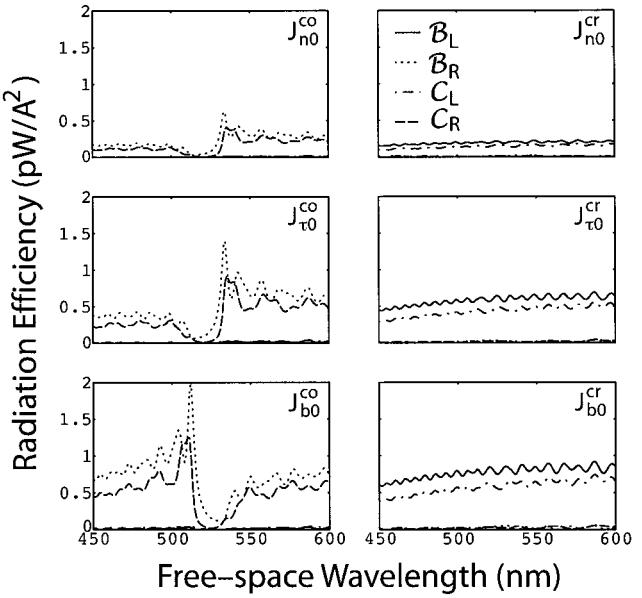

Figure 1 Radiation efficiencies versus wavelength due to canonical source configurations of different types identified in Eq. (12). The structurally chiral medium is characterized by Eq. (18) with $p_a = 1.6$, $p_b = 2.0$, $p_c = 1.7$, $\chi = 30°$, $\Omega = 150$ nm, $L = 60\Omega$, and $h = 1$. The Bragg regime is delineated by $\lambda_0 \in [513.4, 531.8]$ nm. The source current densities are confined to the region $z \in [20\Omega, 22\Omega]$

are functions of q, $[\underline{\underline{A}}]$, and z; while $[\underline{\underline{I}}]$ is the 4×4 identity matrix. In this treatment, we have discounted the relatively remote possibility of Voigt wave propagation [21, 22] in the wavelength regime of interest.

4. NUMERICAL RESULTS AND CONCLUSIONS

Calculations of the radiation efficiencies

$$\mathscr{B}_{R,L} = \frac{1}{2\eta_0}\left(\frac{|b_{R,L}|^2}{|\underline{J}^{so}(z_p)|^2}\right), \qquad \mathscr{C}_{R,L} = \frac{1}{2\eta_0}\left(\frac{|c_{R,L}|^2}{|\underline{J}^{so}(z_p)|^2}\right) \tag{17}$$

were made for structural right-handedness ($h = 1$), with the source current density specified through Eq. (12). The relative permittivity scalars $\varepsilon_{a,b,c}$ were modeled as single-resonance Lorentzian functions of λ_0 as per [17, 23]:

$$\varepsilon_{a,b,c} = 1 + p_{a,b,c}\left[1 + \left(10^{-2} - i\,\frac{180 \times 10^{-9}}{\lambda_0}\right)^2\right]^{-1}, \tag{18}$$

where the oscillator strengths $p_a = 1.6$, $p_b = 2.0$, and $p_c = 1.7$. Accordingly, dissipation is moderate in the $\lambda_0 \in [400, 800]$ nm regime. The chosen values of the tilt angle $\chi = 30°$ and the half-period $\Omega = 150$ nm ensure that the Bragg regime is delineated by $\lambda_0 \in [513.4, 531.8]$ nm. The thickness ratio $L/\Omega = 60$ was selected so that the circular Bragg phenomenon is fully developed.

Eq. (12) contains six canonical configurations of the source-current density, characterized individually by the quantities $J^{co,cr}_{n0,\tau 0,b0}$. For each of these configurations, the radiation efficiencies are plotted in Figure 1 as functions of the wavelength. The relevant sources are confined to the thin layer identified by $z_p = 20\Omega$ and $z_q = 22\Omega$. As noted in [9, 17], for $J^{co,cr}_{\tau 0}$ only, Figure 1 shows that a clear distinction exists between radiation due to co- and cross-chiral source current densities. The edges of the Bragg regime are conspicuously marked by high radiation efficiencies for all three co-chiral source configurations in Figure 1, while the Bragg regime is not discernible at all for the three cross-chiral source configurations. In Figure 2, for which $z_p = 10\Omega$ and $z_q = 40\Omega$, a more substantial portion of the structurally chiral medium is occupied by sources, and the Bragg regime is then identifiable also in the spectrums of radiation from the cross-chiral source configurations.

From both figures, it is clear that the radiation spectrum is far more localized for the co-chiral than for the cross-chiral source configurations. The peak radiation efficiencies are higher for the co-chiral than for the cross-chiral source configurations. The polarization state of the radiation is virtually circular, and its handedness is identical to the structural handedness of the responsible canonical source configuration. These findings had previously held for $J^{co,cr}_{\tau 0}$ only, but now they hold for $J^{co,cr}_{n0}$ and $J^{co,cr}_{b0}$ as well.

In Figures 1 and 2, the radiation is localized on the long-wavelength edge of the Bragg regime for J^{co}_{n0} and $J^{co}_{\tau 0}$, but on the short-wavelength edge for J^{co}_{b0}. With the assumption that dispersion and dissipation in the chosen wavelength regime are small enough, the edges of the Bragg regime are proportional to $\sqrt{|\varepsilon_c|}$ and $\sqrt{|\tilde{\varepsilon}_d|}$ [19]. For the value of χ chosen for Figures 1 and 2, $|\tilde{\varepsilon}_d| > |\varepsilon_c|$. As χ increases, ε_c and $\tilde{\varepsilon}_d$ come closer in magnitude. Simultaneously, the Bragg regime blue-shifts; and it also narrows to a minimum, and could even vanish (at the so-called pseudo-isotropic point, whose existence depends on the constitutive parameter values [9, 20]). The peak of the radiation efficiency spectrum, for any of the three co-chiral source configurations, moves towards the middle of the Bragg regime. A further increase in χ makes $|\varepsilon_c|$ exceed $|\tilde{\varepsilon}_d|$, widening as well as blue-shifting the Bragg regime. At sufficiently high values of χ, the radiation is localized on the short-wavelength edge of the Bragg regime for J^{co}_{n0} and $J^{co}_{\tau 0}$, but on the long-wavelength edge for J^{co}_{b0}. This is depicted in Figure 3, the graphs for which were calculated at $\chi = 75°$.

Mixed source configurations are likely to be present in many situations. Furthermore, the emission bandwidth of the source could cover only a part, or all, or none of the Bragg regime. Therefore, radiation spectrums are going to be more complicated

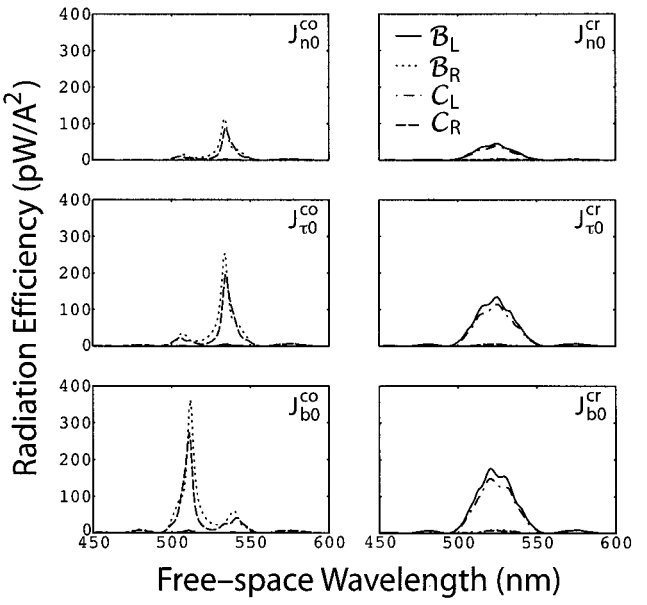

Figure 2 Same as in Fig. 1, except that the source current densities are confined to the region $z \in [10\Omega, 40\Omega]$

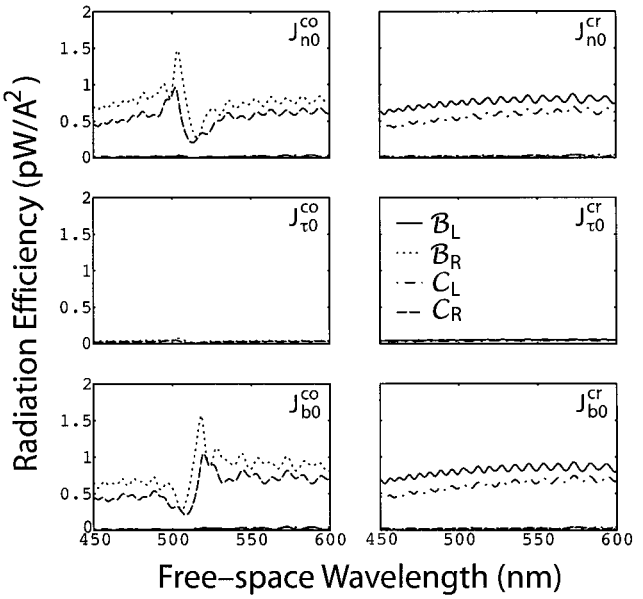

Figure 3 Same as in Fig. 1, except that $\chi = 75°$. The Bragg regime is delineated by $\lambda_0 \in [506.8, 514.5]$ nm

than the ones shown in Figures 1–3. For instance, Chen et al. [5] reported a change in the sign of what amounts to the difference $\mathscr{B}_L - \mathscr{B}_R$ for a dye-doped chiral nematic liquid crystal film—as the wavelength changed from one side of the Bragg regime to the other side. Based on the theoretical results reported here, we can conclude that the luminophores (the dye molecules) in the film must have been arranged in both co- and cross-chiral configurations, and that the emission bandwidth of these luminophores completely covered the Bragg regime.

To conclude, we have considered all six canonical configurations for the source-current density that could cause a structurally chiral medium to fluoresce, lase, or otherwise emit radiation. The radiation spectrum is highly dependent on whether its source is co-chiral or cross-chiral, and is localized either in or on the edges of the Bragg regime. The obtained conclusions hold for both chiral liquid-crystal elastomers and chiral sculptured thin films impregnated with fluorescent dyes, etc.

REFERENCES

1. H.C. Chen, Theory of electromagnetic waves, McGraw-Hill, New York, 1983, chaps. 9–11.
2. W.S. Weiglhofer, Analytic methods and free-space dyadic Green's functions, Radio Sci 28 (1993), 847–857.
3. W.S. Weiglhofer, Frequency-dependent dyadic Green's functions for bianisotropic media, in T.W. Barrett and D.M. Grimes (Eds.), Advanced electromagnetism: Foundations, theory and applications, World Scientific, Singapore, 1995, pp 376–389.
4. I.P. Il'chishin, E.A. Tikhonov, V.G. Tishchenko, and M.T. Shpak, Generation of a tunable radiation by impurity cholesteric liquid crystals, JETP Lett 32 (1980), 24–27.
5. S.H. Chen, D. Katsis, A.W. Schmid, J.C. Mastrangelo, T. Tsutsui, and T.N. Blanton, Circularly polarized light generated by photoexcitation of luminophores in glassy liquid-crystal films, Nature 397 (1999), 506–508.
6. M. Ozaki, M. Kasano, D. Ganzke, W. Haase, and K. Yoshino, Mirrorless lasing in a dye-doped ferroelectric liquid crystal, Adv Mater 14 (2002), 306–309.
7. P.G. de Gennes and J. Prost, The physics of liquid crystals, 2nd ed., Clarendon Press, Oxford, UK, 1993, chap. 6.
8. S. Chandrasekhar, Liquid crystals, 2nd ed., Cambridge University Press, Cambridge, UK, 1992, chap. 4.
9. A. Lakhtakia, Local inclination angle: A key structural factor in emission from chiral sculptured thin films, Opt Commun 202 (2002), 103–111; erratum: 202 (2002), 447.
10. V.I. Kopp, B. Fan, H.K.M. Vithana, and A.Z. Genack, Low-threshold lasing at the edge of a photonic stop band in cholesteric liquid crystals, Opt Lett 23 (1998), 1707–1709.
11. A. Lakhtakia and W.S. Weiglhofer, On light propagation in helicoidal bianisotropic mediums, Proc R Soc Lond A 448 (1995), 419–437; erratum: 454 (1998), 3275.
12. A. Lakhtakia and W.S. Weiglhofer, A comparative study of planewave propagation in helicoidal bianisotropic mediums and isotropic chiral mediums, J Opt A: Pure Appl Opt 2 (2000), 107–111.
13. R. Messier and A. Lakhtakia, Sculptured thin films II: Experiments and applications, Mater Res Innovat 2 (1999), 217–222.
14. R. Messier, V.C. Venugopal, and P.D. Sunal, Origin and evolution of sculptured thin films, J Vac Sci Technol A 18 (2000), 1538–1545.
15. I. Hodgkinson and Q.H. Wu, Inorganic chiral optical materials, Adv Mater 13 (2001), 889–897.
16. M. Voigt, M. Chambers, and M. Grell, On the circular polarization of fluorescence from dyes dissolved in chiral nematic liquid crystals, Chem Phys Lett 347 (2001), 173–177.
17. A. Lakhtakia, On bioluminescent emission from chiral sculptured thin films, Opt Commun 188 (2001), 313–320.
18. H. Hochstadt, Differential equations, Dover Press, New York, 1975, p 56.
19. V.C. Venugopal and A. Lakhtakia, Sculptured thin films: Conception, optical properties, and applications, in O.N. Singh and A. Lakhtakia (Eds.), Electromagnetic fields in unconventional materials and structures, Wiley, New York, 2000, chap. 5.
20. A. Lakhtakia, Pseudo-isotropic and maximum-bandwidth points for axially excited chiral sculptured thin films, Microwave Opt Technol Lett 34 (2002), 367–371.
21. A. Lakhtakia, Anomalous axial propagation in helicoidal bianisotropic media, Opt Commun 157 (1998), 193–201.
22. J. Gerardin and A. Lakhtakia, Conditions for Voigt wave propagation in linear, homogeneous, dielectric mediums, Optik 112 (2001), 493–495.
23. C. Kittel, Introduction to solid state physics, 4th ed., Wiley Eastern, New Delhi, 1974, p 469.

THE GENERALIZED FOSTER THEOREM AND NETWORK-*Q*

Changhong Liang and Tao Su
School of Electronics Engineering
Xidian University
Xi'an 710071, P. R. China

Received 23 September 2002

ABSTRACT: *This paper proves the generalized Foster theorem, which can be applied to any lossy situation, while the original Foster theorem [1] only applied to reactive termination. Furthermore, the formula of* Q *with network parameters is described. One example, the quality factor* Q *of a pass-through resonant cavity, is given here. It is clearly seen that the slope of the reactance function may be negative in a lossy situation.* © 2003 Wiley Periodicals, Inc. Microwave Opt Technol Lett 37: 40–45, 2003; Published online in Wiley InterScience (www.interscience.wiley.com). DOI 10.1002/mop.10819

Key words: *generalized Foster theorem; loss termination; network parameters; network-*Q

Available online at www.sciencedirect.com
SCIENCE DIRECT®
Optics Communications 216 (2003) 139–150
OPTICS COMMUNICATIONS
www.elsevier.com/locate/optcom

Theory of second-harmonic-generated radiation from chiral sculptured thin films for bio-sensing

Erik E. Steltz, Akhlesh Lakhtakia *

CATMAS – Computational and Theoretical Materials Sciences Group, Department of Engineering Science and Mechanics, Pennsylvania State University, 212 EES Building, University Park, PA 16802–6812, USA

Received 20 March 2002; received in revised form 10 June 2002; accepted 26 November 2002

Abstract

The theory of second-harmonic-generated radiation (SHGR) from a chiral sculptured thin film (STF) for bio-sensing is presented. Linear emission (LE) is supposedly due to luminescence-producing bio-reactions occurring in the void regions of the chiral STF platform. The associated linear electromagnetic fields generate a nonlinear source polarization field in the material that the platform is made of, provided the material has significant nonlinear properties in an appropriate wavelength-regime. Information contained in the polarization state of SHGR could either supplement information gleaned from LE or be useful just by itself.

PACS: 77.55.+f; 78.20.−e; 78.20.Bh; 78.60.Ps

Keywords: Bio-sensors; Luminescence; Sculptured thin films; Second-harmonic-generated radiation

1. Introduction

A typical nanoscale bio-sensor employs a porous platform infiltrated by a bio-selective species. When a sample containing the species to be sensed (along with some reaction-enabling chemicals, if necessary) is brought in contact with the platform, a reaction occurs. The reaction products disturb some physical property, the degree of disturbance yielding an indication of the concentration of the species to be sensed [1–3].

Porous silicon has emerged as a desirable platform for *optical* sensing of biological substances [4]. This is in part because of the bio-compatibility [5], and in part due to the room-temperature visible luminescence [6], of porous silicon. However, porous silicon has an isotropic three-dimensional texture – so that the emitted light is not highly polarized, and a potentially important channel of information thus goes

* Corresponding author. Tel: +1-814-863-4319; fax: +1-814-863-7967.
E-mail address: AXL4@psu.edu (A. Lakhtakia).

0030-4018/02/$ - see front matter
doi:10.1016/S0030-4018(02)02284-8

unutilized. Furthermore, the relatively broadband luminescence of porous silcon has to be narrowed by confinement between two distributed Bragg reflectors [4].

Research on the optical response characteristics of chiral sculptured thin films (STFs) has shown that both desirable features – a high degree of polarization and a narrow bandwidth – can be realized by texturing the void regions of a porous platform. Chiral STFs are unidirectionally nonhomogeneous, anisotropic, porous materials that are nano-engineered using physical vapor deposition [7–9]. These materials display the so-called circular Bragg phenomenon because their helicoidal microstructure is both periodic and handed [10,11]. Basically, a structurally right-handed (resp. left-handed) chiral STF only a few periods thick almost completely reflects axially incident, right (resp. left) circularly polarized light with wavelength lying in the so-called Bragg regime; while the reflection of left (resp. right) circularly polarized light in the same wavelength-regime is very little. Borrowing from the language of crystallography, we can say that a chiral STF has a band gap [12, p. 297] for normally incident circularly polarized plane waves of one kind, but not for those of the orthogonal kind. This phenomenon has been experimentally verified and exploited in the design of several types of optical filters [13].

Analyte DNA single-strand fragments, if present in a sample along with an appropriate rare-earth complex, will hybridize with probe DNA fragments containing complementary gene sequences – thereby generating luminescence [14–16]. For genomic analysis, probe DNA fragments must be introduced in the void regions of a chiral STF. The post-reaction, double-strand DNA fragments can either stick to or entwine about the helicoidal microcolumns of the film, leading to the postulation of canonical source configurations comprising exclusively either co-wound or contra-wound filamentary sources of photons, respectively [17]. Initial theoretical investigations have shown that the circular Bragg phenomenon must then be evident in the emission spectrums [17,18]. Thus, in contrast with porous silicon bio-sensors, luminescence would not ensue from the platform but from the bio-reactions taking place in the void regions. Indirect verification is provided by the spectral characteristics of lasing in dye-doped cholesteric liquid crystals [19,20], which are topologically related to chiral STFs.

Although a STF platform is itself not luminescent in the foregoing scenario, it can still radiate light due to any significant nonlinear optical properties it may possess. Electromagnetic fields created by the photon source filaments (present in the void regions) with free-space wavelength λ_0 could trigger harmonic generation in the STF microcolumns [1] at wavelength λ_0/q, $q = 2, 3, \ldots$. The spectrums of both the linear and the harmonic radiations – emanating, respectively, directly and indirectly from the reaction of the rare-earth complex with the probe and the analyte DNA fragments within a STF platform – could be examined to determine the presence of the gene sequence in question and ascertain its concentration. This would reduce errors due to mis-hybridization that occurs in spite of the expected sequence specificity [21].

With this motivation, we present here the theory of second-harmonic-generated radiation (SHGR) – corresponding to $q = 2$ – from chiral STFs for bio-sensing in the modality described in the two previous paragraphs. Section 2 provides an appropriately detailed treatment of the theory as well as of the associated algorithm for its numerical implementation. Briefly, the frequency-domain Maxwell curl postulates are solved for both LE and SHGR. LE is directly due to canonical source current densities present in the void regions of a chiral STF, while SHGR is due to a nonlinear source polarization phasor [22] induced by the linear fields inside the chiral STF. Linear permittivity and nonlinear susceptibility functions are assumed for the locally homogenized material's anisotropic properties [23,24]. Illustrative data on the intensity and polarization states of LE and SHGR, as well as conclusions drawn therefrom, are presented in Section 3.

A note about notation. Vectors are underlined and dyadics are double-underlined. Column vectors as well as matrixes are additionally enclosed in square brackets. The position vector is denoted by

[1] Whereas the sources of linear emission (LE) lie in the void regions, the skeleton of the STF is envisaged here as the site of harmonic generation. Of course, harmonic generation could also occur in the void regions, under favorable conditions.

$\underline{r} = x\underline{u}_x + y\underline{u}_y + z\underline{u}_z$ with $\underline{u}_x$, $\underline{u}_y$ and $\underline{u}_z$ as the Cartesian unit vectors; and the z axis is parallel to the thickness direction. An $\exp(-\mathrm{i}\omega t)$ time dependence is implicit, with ω as the angular frequency and t is the time.

2. Theory

2.1. Preliminaries

Both LE and SHGR from a chiral STF can be handled with the same basic framework [10]; and so the common features are briefly recounted in this subsection.

Let a chiral STF occupy the region $0 \leqslant z \leqslant L$ while the half-spaces $z < 0$ and $z > L$ are vacuous. The radiation source is assumed to be a function of z but not of x and y, i.e., the photon source filaments are uniformly distributed in the transverse plane.

Frequency-domain electromagnetic fields inside the chiral STF must satisfy the Maxwell curl postulates

$$\begin{aligned} \nabla \times \underline{E}(\underline{r},\omega) &= \mathrm{i}\omega\mu_0 \underline{H}(\underline{r},\omega), \\ \nabla \times \underline{H}(\underline{r},\omega) &= -\mathrm{i}\omega \underline{\underline{\epsilon}}(\underline{r},\omega) \cdot \underline{E}(\underline{r},\omega) + \underline{J}^{\mathrm{so}}(\underline{r},\omega), \end{aligned} \qquad 0 < z < L, \tag{1}$$

where $\mu_0 = 4\pi \times 10^{-7}$ H m^{-1} is the permeability of free space (i.e., vacuum) and $\underline{J}^{\mathrm{so}}(\underline{r},\omega)$ is the source current density phasor. The nonhomogeneous, frequency-dependent permittivity dyadic [25] of the chosen chiral STF is expressed as follows [10]:

$$\underline{\underline{\epsilon}}(\underline{r},\omega) = \epsilon_0 \underline{\underline{S}}_z(z) \cdot \underline{\underline{S}}_y(\chi) \cdot \left[\epsilon_a(\omega)\underline{u}_z\underline{u}_z + \epsilon_b(\omega)\underline{u}_x\underline{u}_x + \epsilon_c(\omega)\underline{u}_y\underline{u}_y\right] \cdot \underline{\underline{S}}_y^{\mathrm{T}}(\chi) \cdot \underline{\underline{S}}_z^{\mathrm{T}}(z). \tag{2}$$

In this equation, $\epsilon_0 = 8.854 \times 10^{-12}$ F m^{-1} is the free-space permittivity; $\epsilon_{a,b,c}(\omega)$ are relative permittivity scalars which are dependent on the linear properties of the material that the film is made of as well as of the matter filling the void regions [23]; the tilt dyadic

$$\underline{\underline{S}}_y(\chi) = \underline{u}_y\underline{u}_y + (\underline{u}_x\underline{u}_x + \underline{u}_z\underline{u}_z)\cos\chi + (\underline{u}_z\underline{u}_x - \underline{u}_x\underline{u}_z)\sin\chi \tag{3}$$

represents the locally columnar microstructure of any chiral STF with $\chi > 0°$; the rotation dyadic

$$\underline{\underline{S}}_z(z) = \underline{u}_z\underline{u}_z + \left(\underline{u}_x\underline{u}_x + \underline{u}_y\underline{u}_y\right)\cos\left(\frac{\pi z}{\Omega}\right) + \left(\underline{u}_y\underline{u}_x - \underline{u}_x\underline{u}_y\right)\sin\left(\frac{\pi z}{\Omega}\right) \tag{4}$$

contains 2Ω as the structural period; while the superscript T stands for the transpose. The chosen STF is structurally right-handed.

As the lateral extent of the chiral STF is assumed infinite and the source distribution is supposedly independent of both x and y, the electromagnetic field phasors $\underline{E}(\underline{r},\omega) \equiv \underline{E}(z,\omega)$ and $\underline{H}(\underline{r},\omega) \equiv \underline{H}(z,\omega)$ $\forall z \in (-\infty,\infty)$. As a result of photon production inside the chiral STF, radiation is emitted into the upper and the lower half-spaces. The electric field phasor of the radiation is stated as

$$\underline{E}(\underline{z},\omega) = \begin{cases} \left[b_{\mathrm{L}}(\omega)\underline{u}_- + b_{\mathrm{R}}(\omega)\underline{u}_+\right]\exp(-\mathrm{i}k_0 z), & z \leqslant 0, \\ \left[c_{\mathrm{L}}(\omega)\underline{u}_+ + c_{\mathrm{R}}(\omega)\underline{u}_-\right]\exp[\mathrm{i}k_0(z-L)], & z \geqslant L, \end{cases} \tag{5}$$

where $\underline{u}_\pm = (\underline{u}_x \pm \mathrm{i}\underline{u}_y)/\sqrt{2}$ and $k_0 = \omega\sqrt{\epsilon_0\mu_0} = 2\pi/\lambda_0$ is the free-space wavenumber. The magnetic field phasor of the radiation may be computed by applying the relation $\underline{H}(\underline{z},\omega) = \nabla \times \underline{E}(\underline{z},\omega)/(\mathrm{i}\omega\mu_0)$ to the foregoing expression. Whereas $b_{\mathrm{L}}(\omega)$ and $c_{\mathrm{L}}(\omega)$ are the amplitudes of the left-circularly polarized (LCP) components, $b_{\mathrm{R}}(\omega)$ and $c_{\mathrm{R}}(\omega)$ are the amplitudes of the right-circularly polarized (RCP) components, of the radiated plane waves.

For a specified photon source distribution $\underline{J}^{\mathrm{so}}(z,\omega)$, $0 \leqslant z \leqslant L$, the coefficients $b_{\mathrm{L}}(\omega)$, $b_{\mathrm{R}}(\omega)$, $c_{\mathrm{L}}(\omega)$ and $c_{\mathrm{R}}(\omega)$ can be computed by solving four simultaneous algebraic equations stated in matrix notation as follows [17]:

$$\frac{1}{\sqrt{2}}\begin{bmatrix} c_{\mathrm{L}}(\omega)+c_{\mathrm{R}}(\omega) \\ \mathrm{i}[c_{\mathrm{L}}(\omega)-c_{\mathrm{R}}(\omega)] \\ -\mathrm{i}[c_{\mathrm{L}}(\omega)-c_{\mathrm{R}}(\omega)]/\eta_0 \\ [c_{\mathrm{L}}(\omega)+c_{\mathrm{R}}(\omega)]/\eta_0 \end{bmatrix} = [\underline{\underline{B}}(L)]\mathrm{e}^{\mathrm{i}[\underline{\underline{P}}'(\omega)]L}\left\{ \frac{1}{\sqrt{2}}\begin{bmatrix} b_{\mathrm{L}}(\omega)+b_{\mathrm{R}}(\omega) \\ -\mathrm{i}[b_{\mathrm{L}}(\omega)-b_{\mathrm{R}}(\omega)] \\ -\mathrm{i}[b_{\mathrm{L}}(\omega)-b_{\mathrm{R}}(\omega)]/\eta_0 \\ -[b_{\mathrm{L}}(\omega)+b_{\mathrm{R}}(\omega)]/\eta_0 \end{bmatrix} + \int_0^L \mathrm{e}^{-\mathrm{i}[\underline{\underline{P}}'(\omega)]z_s}[\underline{\gamma}'(z_s,\omega)]\mathrm{d}z_s \right\}. \tag{6}$$

Here and hereafter, $\eta_0 = \sqrt{\mu_0/\epsilon_0}$ is the intrinsic impedance of free space; the 4×4 matrix

$$[\underline{\underline{B}}(z)] = \begin{bmatrix} \cos(\frac{\pi z}{\Omega}) & -\sin(\frac{\pi z}{\Omega}) & 0 & 0 \\ \sin(\frac{\pi z}{\Omega}) & \cos(\frac{\pi z}{\Omega}) & 0 & 0 \\ 0 & 0 & \cos(\frac{\pi z}{\Omega}) & -\sin(\frac{\pi z}{\Omega}) \\ 0 & 0 & \sin(\frac{\pi z}{\Omega}) & \cos(\frac{\pi z}{\Omega}) \end{bmatrix} \tag{7}$$

denotes a rotation about the z-axis; the 4×4 kernel matrix

$$[\underline{\underline{P}}'(\omega)] = \begin{bmatrix} 0 & -\mathrm{i}\pi/\Omega & 0 & \omega\mu_0 \\ \mathrm{i}\pi/\Omega & 0 & -\omega\mu_0 & 0 \\ 0 & -\omega\epsilon_0\epsilon_c(\omega) & 0 & -\mathrm{i}\pi/\Omega \\ \omega\epsilon_0\tilde{\epsilon}_d(\omega) & 0 & \mathrm{i}\pi/\Omega & 0 \end{bmatrix} \tag{8}$$

employs the function

$$\tilde{\epsilon}_d(\omega) = \frac{\epsilon_a(\omega)\epsilon_b(\omega)}{\epsilon_a(\omega)\cos^2\chi + \epsilon_b(\omega)\sin^2\chi}, \tag{9}$$

while the source column vector

$$[\underline{\gamma}'(z,\omega)] = \begin{bmatrix} 0 \\ 0 \\ \left\{ J_y^{\mathrm{so}}(z,\omega)\cos(\frac{\pi z}{\Omega}) - J_x^{\mathrm{so}}(z,\omega)\sin(\frac{\pi z}{\Omega}) \right\} \\ \left\{ -J_x^{\mathrm{so}}(z,\omega)\cos(\frac{\pi z}{\Omega}) - J_y^{\mathrm{so}}(z,\omega)\sin(\frac{\pi z}{\Omega}) + \right. \\ \left. J_z^{\mathrm{so}}(z,\omega)\frac{\tilde{\epsilon}_d(\omega)}{\epsilon_a(\omega)\epsilon_b(\omega)}[\epsilon_b(\omega)-\epsilon_a(\omega)]\sin\chi\cos\chi \right\} \end{bmatrix}. \tag{10}$$

2.2. Tangential source filaments

The morphology of chiral STFs being helicoidal – to which one expects the photon source filaments would conform – a helicoidal representation for the source current density phasor is appropriate [17]. In this paper, we assume that the photon source filaments are aligned tangentially with respect to the film's columnar morphology, fill the entire thin film uniformly, and produce photons at an angular frequency ω_1. If these filaments are co-wound, we set

$$\underline{J}_{\mathrm{co}}^{\mathrm{so}}(z,\omega_1) = J_{\tau 0}\underline{\underline{S}}_z(z)\cdot(\underline{u}_x\cos\chi + \underline{u}_z\sin\chi), \quad 0 \leqslant z \leqslant L, \tag{11}$$

with $J_{\tau 0}$ representing the photon production strength; alternatively,

$$\underline{J}_{\mathrm{contra}}^{\mathrm{so}}(z,\omega_1) = J_{\tau 0}\underline{\underline{S}}_z^{\mathrm{T}}(z)\cdot(\underline{u}_x\cos\chi + \underline{u}_z\sin\chi), \quad 0 \leqslant z \leqslant L, \tag{12}$$

for contra-wound filaments. Combinations of these two canonical configurations can also be handled by the described procedures. The duration of photon production and emission is assumed to be far in excess of $2\pi/\omega_1$, which permits the use of frequency-domain analysis for LE as well as SHGR.

2.2.1. Linear emission

We set $\omega = \omega_1$ in (6) for LE; and either

$$[\underline{\gamma}'(z,\omega_1)]_{\rm co} = J_{\tau 0}\cos\chi \begin{bmatrix} 0 \\ 0 \\ 0 \\ -\frac{\tilde{\epsilon}_d(\omega_1)}{\epsilon_b(\omega_1)} \end{bmatrix} \tag{13}$$

in conformity with (11) for co-wound source filaments, or

$$[\underline{\gamma}'(z,\omega_1)]_{\rm contra} = J_{\tau 0}\cos\chi \begin{bmatrix} 0 \\ 0 \\ -\sin\left(\frac{2\pi z}{\Omega}\right) \\ [\epsilon_b(\omega_1)-\epsilon_a(\omega_1)]\frac{\tilde{\epsilon}_d(\omega_1)}{\epsilon_a(\omega_1)\epsilon_b(\omega_1)}\sin^2\chi - \cos\left(\frac{2\pi z}{\Omega}\right) \end{bmatrix} \tag{14}$$

for contra-wound source filaments in accordance with (12). Thus, the four coefficients $b_{\rm L,R}(\omega_1)$ and $c_{\rm L,R}(\omega_1)$ can be computed by solving (6), following which step the LE efficiencies

$$\mathsf{B}_{\rm L,R}(\omega_1) = \frac{1}{2\eta_0}\left|\frac{b_{\rm L,R}(\omega_1)}{J_{\tau 0}}\right|^2, \quad \mathsf{C}_{\rm L,R}(\omega_1) = \frac{1}{2\eta_0}\left|\frac{c_{\rm L,R}(\omega_1)}{J_{\tau 0}}\right|^2 \tag{15}$$

can be obtained as functions of ω_1.

Although the integration on the right side of (6) can be implemented analytically for LE [17], we chose a numerical technique for eventual ease in handling SHGR. For this purpose, we first set up the column vector

$$[\underline{f}(z)] = \left[E_x(z,\omega_1), \quad E_y(z,\omega_1), \quad H_x(z,\omega_1), \quad H_y(z,\omega_1)\right]^{\rm T}. \tag{16}$$

It satisfies the equation [17]

$$[\underline{f}(z)] = [\underline{\underline{B}}(z,h)]\mathrm{e}^{\mathrm{i}[\underline{\underline{P}}'(\omega_1)]z}\left\{[\underline{f}(0)] + \int_0^z \mathrm{e}^{-\mathrm{i}[\underline{\underline{P}}'(\omega_1)]z_s}[\underline{\gamma}'(z_s,\omega_1)]\mathrm{d}z_s\right\}, \quad 0 \leqslant z \leqslant L, \tag{17}$$

and possesses the boundary values

$$[\underline{f}(0)] = \frac{1}{\sqrt{2}}\begin{bmatrix} b_{\rm L}(\omega_1)+b_{\rm R}(\omega_1) \\ -\mathrm{i}[b_{\rm L}(\omega_1)-b_{\rm R}(\omega_1)] \\ -\mathrm{i}[b_{\rm L}(\omega_1)-b_{\rm R}(\omega_1)]/\eta_0 \\ -[b_{\rm L}(\omega_1)+b_{\rm R}(\omega_1)]/\eta_0 \end{bmatrix}, \quad [\underline{f}(L)] = \frac{1}{\sqrt{2}}\begin{bmatrix} c_{\rm L}(\omega_1)+c_{\rm R}(\omega_1) \\ \mathrm{i}[c_{\rm L}(\omega_1)-c_{\rm R}(\omega_1)] \\ -\mathrm{i}[c_{\rm L}(\omega_1)-c_{\rm R}(\omega_1)]/\eta_0 \\ [c_{\rm L}(\omega_1)+c_{\rm R}(\omega_1)]/\eta_0 \end{bmatrix}. \tag{18}$$

Then, we divided the span $0 \leqslant z \leqslant L$ into N equal segments of thickness $\Delta z = L/N$ each, and defined

$$[\underline{\Delta}_\ell] = \frac{\Delta z}{2}\left\{\mathrm{e}^{-\mathrm{i}[\underline{\underline{P}}'(\omega_1)]z_{\ell-1}}[\underline{\gamma}'(z_{\ell-1},\omega_1)] + \mathrm{e}^{-\mathrm{i}[\underline{\underline{P}}'(\omega_1)]z_\ell}[\underline{\gamma}'(z_\ell,\omega_1)]\right\}, \quad \ell \in [1,N]. \tag{19}$$

Accordingly, (17) was approximated as

$$[\underline{f}(n\Delta z)] \approx [\underline{\underline{B}}(n\Delta z)]\mathrm{e}^{\mathrm{i}[\underline{\underline{P}}'(\omega_1)]n\Delta z}\left\{[\underline{f}(0)] + \sum_{\ell=1}^{n}[\underline{\Delta}_\ell]\right\}, \quad n \in [1,N]. \tag{20}$$

Setting $n = N$ in (20) and making use of the boundary values (18) therein, we computed the coefficients $b_{\rm L,R}(\omega_1)$ and $c_{\rm L,R}(\omega_1)$. Then, $b_{\rm L,R}(\omega_1)$ were used in (20) to compute $[\underline{f}(n\Delta z)]$ $\forall n \in [1, N-1]$.

2.2.2. Second-harmonic-generated radiation

The direct sources of SHGR are not the photon source filaments, but the nonlinear dielectric properties of the chiral STF. The field phasor $\underline{E}(z,\omega_1)$ gives rise to a nonlinear source polarization phasor $\underline{P}^{\rm NLS}(z,\omega_2)$, $0 \leqslant z \leqslant L$, where [26,27]

$$\omega_2 = 2\omega_1. \tag{21}$$

Hence,

$$\underline{J}^{\rm so}(z,\omega_2) = -{\rm i}\omega_2 \underline{P}^{\rm NLS}(z,\omega_2), \quad 0 \leqslant z \leqslant L. \tag{22}$$

The nonlinear source polarization phasor is best expressed in matrix notation as [26]

$$\begin{bmatrix} P_x^{\rm NLS}(z,\omega_2) \\ P_y^{\rm NLS}(z,\omega_2) \\ P_z^{\rm NLS}(z,\omega_2) \end{bmatrix} = 2 \begin{bmatrix} \cos(\frac{\pi z}{\Omega}) & -\sin(\frac{\pi z}{\Omega}) & 0 \\ \sin(\frac{\pi z}{\Omega}) & \cos(\frac{\pi z}{\Omega}) & 0 \\ 0 & 0 & 1 \end{bmatrix} \begin{bmatrix} \cos\chi & 0 & -\sin\chi \\ 0 & 1 & 0 \\ \sin\chi & 0 & \cos\chi \end{bmatrix}$$
$$\times \begin{bmatrix} d_{33}(\omega_1) & d_{32}(\omega_1) & d_{31}(\omega_1) & d_{36}(\omega_1) & d_{35}(\omega_1) & d_{34}(\omega_1) \\ d_{23}(\omega_1) & d_{22}(\omega_1) & d_{21}(\omega_1) & d_{26}(\omega_1) & d_{25}(\omega_1) & d_{24}(\omega_1) \\ d_{13}(\omega_1) & d_{12}(\omega_1) & d_{11}(\omega_1) & d_{16}(\omega_1) & d_{15}(\omega_1) & d_{14}(\omega_1) \end{bmatrix}$$
$$\times \begin{bmatrix} \cos^2\chi & 0 & \sin^2\chi & 0 & -\sin 2\chi & 0 \\ 0 & 1 & 0 & 0 & 0 & 0 \\ \sin^2\chi & 0 & \cos^2\chi & 0 & \sin 2\chi & 0 \\ 0 & 0 & 0 & \cos\chi & 0 & \sin\chi \\ \frac{1}{2}\sin 2\chi & 0 & -\frac{1}{2}\sin 2\chi & 0 & \cos 2\chi & 0 \\ 0 & 0 & 0 & -\sin\chi & 0 & \cos\chi \end{bmatrix}^{\rm T}$$
$$\times \begin{bmatrix} \cos^2(\frac{\pi z}{\Omega}) & \sin^2(\frac{\pi z}{\Omega}) & 0 & 0 & 0 & -\sin\frac{2\pi z}{\Omega} \\ \sin^2(\frac{\pi z}{\Omega}) & \cos^2(\frac{\pi z}{\Omega}) & 0 & 0 & 0 & \sin\frac{2\pi z}{\Omega} \\ 0 & 0 & 1 & 0 & 0 & 0 \\ 0 & 0 & 0 & \cos(\frac{\pi z}{\Omega}) & \sin(\frac{\pi z}{\Omega}) & 0 \\ 0 & 0 & 0 & -\sin(\frac{\pi z}{\Omega}) & \cos(\frac{\pi z}{\Omega}) & 0 \\ \frac{1}{2}\sin\frac{2\pi z}{\Omega} & -\frac{1}{2}\sin\frac{2\pi z}{\Omega} & 0 & 0 & 0 & \cos\frac{2\pi z}{\Omega} \end{bmatrix}^{\rm T} \begin{bmatrix} E_x^2(z,\omega_1) \\ E_y^2(z,\omega_1) \\ E_z^2(z,\omega_1) \\ 2E_y(z,\omega_1)E_z(z,\omega_1) \\ 2E_x(z,\omega_1)E_z(z,\omega_1) \\ 2E_x(z,\omega_1)E_y(z,\omega_1) \end{bmatrix}, \tag{23}$$

where

$$E_z(z,\omega_1) = \frac{\epsilon_b(\omega_1) - \epsilon_a(\omega_1)}{\epsilon_a(\omega_1)\epsilon_b(\omega_1)} \tilde{\epsilon}_d(\omega_1) \cos\chi \sin\chi \left[E_x(z,\omega_1) \cos\left(\frac{\pi z}{\Omega}\right) + E_y(z,\omega_1) \sin\left(\frac{\pi z}{\Omega}\right) \right]. \tag{24}$$

The subscripts on the nonlinear susceptibilities $d_{33}(\omega_1)$, etc., were chosen for ready interpretation in the notation of Fig. 1.5.2. of Boyd's famous book on nonlinear optical materials [27]. The delineation of the nonlinear susceptibilities of the chiral STF must take into account the linear and the nonlinear properties as well as the volume fractions of all the materials in the STF platform [24].

Consistently with (20) then, (6) may be specialized for SHGR as

$$\frac{1}{\sqrt{2}} \begin{bmatrix} c_{\rm L}(\omega_2) + c_{\rm R}(\omega_2) \\ {\rm i}[c_{\rm L}(\omega_2) - c_{\rm R}(\omega_2)] \\ -{\rm i}[c_{\rm L}(\omega_2) - c_{\rm R}(\omega_2)]/\eta_0 \\ [c_{\rm L}(\omega_2) + c_{\rm R}(\omega_2)]/\eta_0 \end{bmatrix} \approx [\underline{\underline{B}}(L)] {\rm e}^{{\rm i}[\underline{\underline{P}}'(\omega_2)]L} \left\{ \frac{1}{\sqrt{2}} \begin{bmatrix} b_{\rm L}(\omega_2) + b_{\rm R}(\omega_2) \\ -{\rm i}[b_{\rm L}(\omega_2) - b_{\rm R}(\omega_2)] \\ -{\rm i}[b_{\rm L}(\omega_2) - b_{\rm R}(\omega_2)]/\eta_0 \\ -[b_{\rm L}(\omega_2) + b_{\rm R}(\omega_2)]/\eta_0 \end{bmatrix} + \sum_{\ell=1}^{n} [\underline{\underline{I}}_\ell] \right\}, \tag{25}$$

where

$$[\underline{\underline{\Gamma}}_\ell] = \frac{\Delta z}{2}\left\{ \mathrm{e}^{-\mathrm{i}[\underline{\underline{P}}'(\omega_2)]z_{\ell-1}}[\underline{\gamma}'(z_{\ell-1},\omega_2)] + \mathrm{e}^{-\mathrm{i}[\underline{\underline{P}}'(\omega_2)]z_\ell}[\underline{\gamma}'(z_\ell,\omega_2)] \right\}, \quad \ell \in [1,N] \tag{26}$$

and

$$[\underline{\gamma}'(z,\omega_2)] = -\mathrm{i}\omega_2 \begin{bmatrix} 0 \\ 0 \\ P_y^{\mathrm{NLS}}(z,\omega_2)\cos(\frac{\pi z}{\Omega}) - P_x^{\mathrm{NLS}}(z,\omega_2)\sin(\frac{\pi z}{\Omega}) \\ \Big\{ -P_x^{\mathrm{NLS}}(z,\omega_2)\cos(\frac{\pi z}{\Omega}) - P_y^{\mathrm{NLS}}(z,\omega_2)\sin(\frac{\pi z}{\Omega}) \\ +P_z^{\mathrm{NLS}}(z,\omega_2)\frac{\tilde{\epsilon}_d(\omega_2)}{\epsilon_a(\omega_2)\epsilon_b(\omega_2)}[\epsilon_b(\omega_2)-\epsilon_a(\omega_2)]\sin\chi\cos\chi \Big\} \end{bmatrix}. \tag{27}$$

Clearly, the calculation of $[\underline{\underline{\Gamma}}_\ell]$ requires knowledge of $[\underline{\underline{f}}(\ell\Delta z - \Delta z)]$ and $[\underline{\underline{f}}(\ell\Delta z)]$ that were computed for LE. After determining the coefficients $b_{\mathrm{L,R}}(\omega_2)$ and $c_{\mathrm{L,R}}(\omega_2)$ from (25), the SHGR efficiencies

$$\mathsf{B}_{\mathrm{L,R}}(\omega_2) = \frac{1}{2\eta_0}\left|\frac{b_{\mathrm{L,R}}(\omega_2)}{J_{\tau 0}}\right|^2, \quad \mathsf{C}_{\mathrm{L,R}}(\omega_2) = \frac{1}{2\eta_0}\left|\frac{c_{\mathrm{L,R}}(\omega_2)}{J_{\tau 0}}\right|^2 \tag{28}$$

were found.

3. Numerical results and discussion

The relative permittivity scalars $\epsilon_{a,b,c}$ were modelled as single-resonance Lorentzian functions of the free-space wavelength $\lambda_0 = 2\pi/(\omega\sqrt{\mu_0\epsilon_0})$ as [12, p. 472]

$$\epsilon_{a,b,c}(\lambda_0) = 1 + p_{a,b,c}\left[1 + \left(N_{a,b,c}^{-1} - \mathrm{i}\lambda_{a,b,c}\lambda_0^{-1}\right)^2\right]^{-1}, \tag{29}$$

where the oscillator strengths are denoted by $p_{a,b,c}$, while the parameters $\lambda_{a,b,c}$ and $N_{a,b,c}$ assist in the delineation of resonances and absorption bands, respectively. The values $p_a = 1.6$, $p_b = 2.0$, $p_c = 1.7$, $\lambda_{a,b,c} = 180$ nm and $N_{a,b,c} = 100$ were selected so that the resonance wavelengths of $\epsilon_{a,b,c}$ lie in the ultraviolet regime [12], while dissipation is weak in the $\lambda_0 \in [200, 800]$ nm regime. More complex wavelength-dependencies can be easily handled as well by our numerical technique. The chosen values of the tilt angle $\chi = 30^\circ$ and $\Omega = 150$ nm ensure that the Bragg regime is delineated by $\lambda_0 \in [513.4, 531.8]$ nm. The thickness ratio $L/\Omega = 60$ was selected so that the circular Bragg phenomenon is fully developed [10]. All calculations were carried out with $\Delta z = 5$ nm, after ascertaining that smaller values of Δz did not change the radiation efficiencies by more than 1%.

Chiral STFs are locally orthorhombic, which issue is incorporated in (2) for the linear properties. Insofar as second harmonic generation is concerned, two orthorhombic sub-classes are possible [28], of which the so-called 222 class has the simpler symmetry [29]. The 222 class was therefore chosen to provide illustrative data. Accordingly, $d_{mn} = 0$ for all m and n in (23), except that d_{14}, d_{25} and d_{36} are non-zero. As the wavelength $\lambda_{0_1} = 2\pi/(\omega_1\sqrt{\mu_0\epsilon_0})$ is considerably larger than the resonance wavelengths of the material, we took the Kleinman symmetry condition [27] to hold.

The radiation efficiency $B_{\mathrm{L}}(\omega_n)$ is the same as $C_{\mathrm{L}}(\omega_n)$, $n = 1, 2$; likewise, $B_{\mathrm{R}}(\omega_n) = C_{\mathrm{R}}(\omega_n)$, $n = 1, 2$. This is because the chiral STF is assumed to be uniformly filled by the source filaments. Hence, spectrums of only $C_{\mathrm{L,R}}(\omega_n)$ are shown here.

3.1. Linear emission

We begin with the LE spectrums shown in Figs. 1 and 2 for the co-wound and the contra-wound source configurations, respectively. A comparison with the LE spectrums presented in the predecessor paper [17]

shows that the calculations with our numerical integration technique are virtually identical to those obtained with the analytical technique for both source configurations, assuming that the source filaments completely impregnate the chiral STF. Luminescence is clearly localized with respect to λ_0, either in or in the immediate neighborhood of the Bragg regime.

The polarization state of a plane wave comprises the shape of its vibration ellipse and its handedness. From Figs. 1 and 2, it is evident that the vibration ellipse of the radiation is virtually circular, with its handedness identical to the handedness of the source configuration. Thus, both desirable objectives – a high degree of polarization and a narrow bandwidth – are evident in the LE spectrums.

3.2. Second-harmonic-generated radiation

As mentioned earlier, for the calculation of the SHGR spectrums, we assumed Kleinman symmetry to hold: $d_{14} = d_{25} = d_{36} = \delta$. These spectrums are presented in Figs. 3 and 4 for the co-wound and the contra-wound photon source filaments, respectively. As in Figs. 1 and 2, SHGR is highly localized with respect to

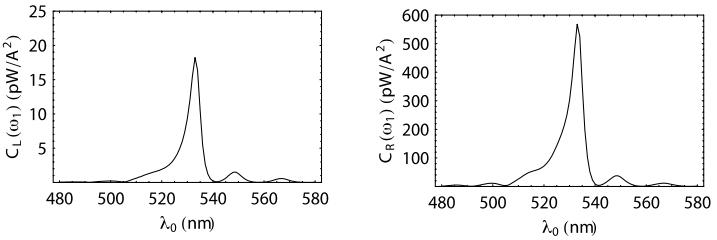

Fig. 1. Computed spectrums of the LE efficiences $C_{L,R}(\omega_1)$ for co-wound source filaments. See Section 3 for the various constitutive and geometric parameters used.

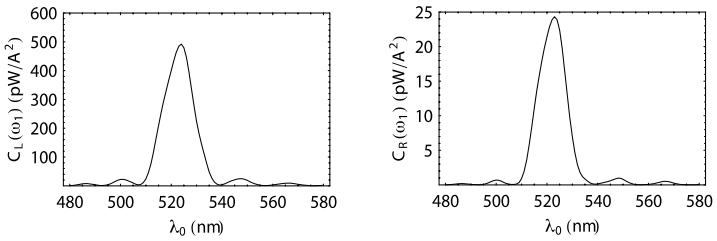

Fig. 2. Same as Fig. 1, except that the photon source filaments are contra-wound.

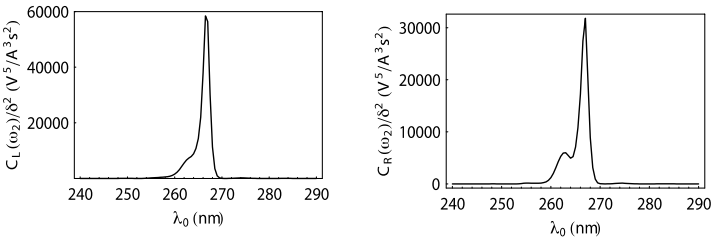

Fig. 3. Computed spectrums of the SHGR efficiencies $C_{L,R}(\omega_2)$ when $d_{36} = d_{25} = d_{14} = \delta$ CV^{-2}, for co-wound source filaments. See Section 3 for the other constitutive and geometric parameters used.

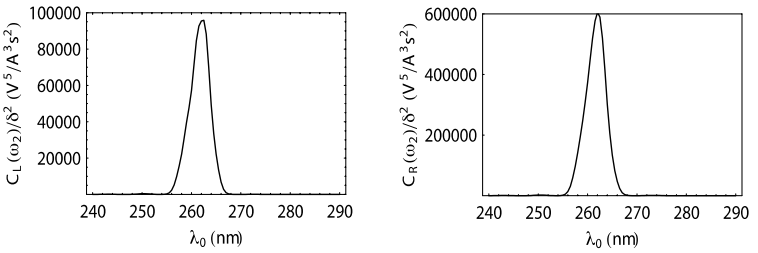

Fig. 4. Same as Fig. 3, except that the photon source filaments are contra-wound.

λ_0. Indeed, the SHGR bandwidth is roughly half of the LE bandwidth. In contrast to Figs. 1 and 2 however, the handedness of SHGR is *opposite* the handedness of the source filaments.

The vibration ellipse of SHGR is neither circular (as in Fig. 1) nor linear, but somewhere in between those two extremes, for co-wound source filaments. On the other hand, according to Fig. 4, the vibration ellipse is virtually circular for the contra-wound source configuration, similarly to Fig. 2. These results underscore the importance of the polarization state of SHGR as an additional source of bio-sensory information.

We also decided to examine the individual roles of the nonlinear susceptibilities d_{36}, d_{25} and d_{14} – by setting two of these to zero while keeping the third equal to δ. The resulting SHGR spectrums are presented in Figs. 5–10.

All six of these figures exhibit localization of SHGR in the same manner as their counterparts (Figs. 1 and 2) for LE. This implies that the localization of SHGR is entirely due to the Bragg phenomenon displayed also by LE: If LE intensity is strong, as it will be at a wavelength either in or in the immediate vicinity of the Bragg regime, strong electromagnetic fields must be generated inside the chiral STF. Hence,

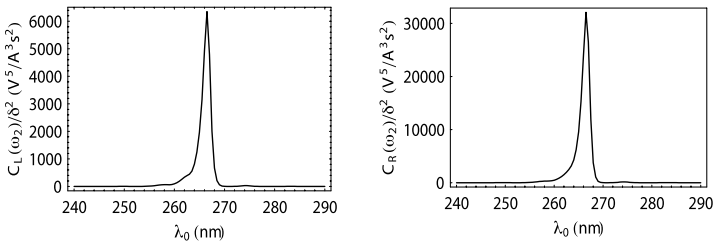

Fig. 5. Computed spectrums of the SHGR efficiencies $C_{L,R}(\omega_2)$ when $d_{36} = \delta\ CV^{-2}$, $d_{25} = 0$, and $d_{14} = 0$ for co-wound source filaments. See Section 3 for the various constitutive and geometric parameters used.

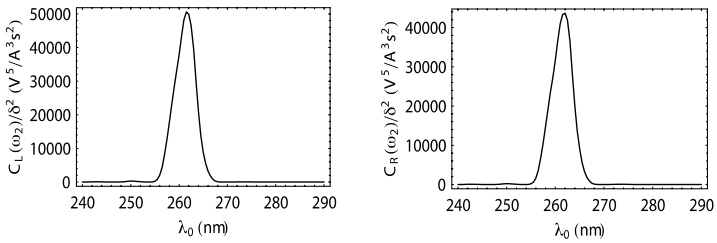

Fig. 6. Same as Fig. 5, except that the photon source filaments are contra-wound.

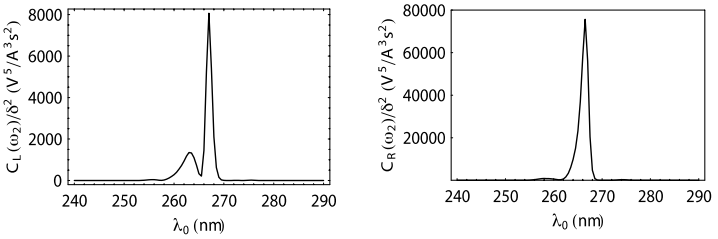

Fig. 7. Same as Fig. 5, except for $d_{14} = 0$, $d_{25} = \delta\ CV^{-2}$, and $d_{36} = 0$.

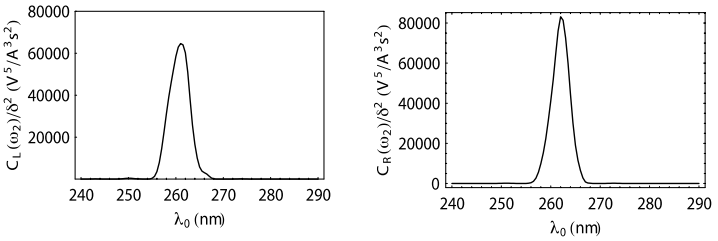

Fig. 8. Same as Fig. 7, except that the photon source filaments are contra-wound.

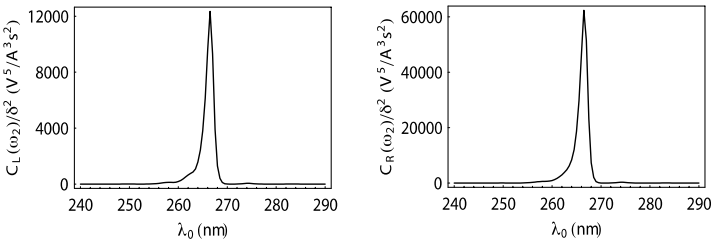

Fig. 9. Same as Fig. 5, except for $d_{36} = 0$, $d_{25} = 0$, and $d_{14} = \delta\ CV^{-2}$.

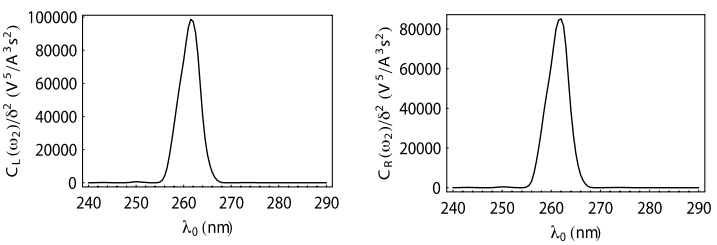

Fig. 10. Same as Fig. 9, except that the photon source filaments are contra-wound.

the nonlinear source polarization phasor at half the particular wavelength would also be of high magnitude, giving rise to strong SHGR. The LE and the SHGR spectrums can therefore be generally expected to be similar in form.

The polarization states of SHGR due to d_{36}, d_{25} and d_{14} individually are all different. They are also different from the ones depicted in Figs. 3 and 4. When the Kleinman symmetry condition holds, fields due to all three nonlinear susceptibilities must interact to produce the spectrums of Figs. 3 and 4. Collectively, the presented spectrums suggest that the nonlinear properties of chiral STFs could be engineered – possibly by evaporating two or more materials simultaneously during physical vapor deposition [7,8] – to take full advantage of the additional bio-sensory information offered by the SHGR characteristics.

The presented numerical results as well as the results of other calculations indicate the significance of the relationship between the SHGR intensity, the linear fields in the chiral STF, and the void fraction. The sources of the linear fields are the filaments occupying the void regions of the film. Clearly, the higher the void fraction, the more photon sources could be formed, and the greater could be the linear field magnitudes (subject to the constraints imposed by the morphology of the film). But second harmonic generation would occur only in the material(s) that the film is made of; and very high void fractions would therefore reduce the SHGR intensity. A compromise between these two trends appears necessary, to be fixed both by experimentation on chiral STFs with different void fractions as well as by careful selection of material(s) to make chiral STFs with.

A related issue is the efficiency of second harmonic generation within a chiral STF platform. Since nonlinear susceptibilities are generally quite small in magnitude, it has been known for long that the phases of linear and second harmonic fields must be carefully managed for efficient harmonic generation [30]. The so-called phase-matching conditions are commonly exploited when the medium of second harmonic generation is homogeneous and in the form of a slab [27]. For nonhomogeneous (and anisotropic) materials, these conditions are not known yet and their discovery constitutes an area of future research. Even in the absence of theoretical guidance, however, optimization of second harmonic emission strengths can be experimentally pursued, perhaps using wedges in lieu of planar slabs.

4. Concluding remarks

Recent trends in bio-sensors [2,21,31] strongly indicate the desirability of the development of new modalities for bio-sensing. In this work, we offer second harmonic emission generated indirectly (in the skeleton) by luminescence-producing bio-reactions (occurring in the void regions) of chiral STFs as a new multi-wavelength modality. Information contained in the polarization state of SHGR could supplement information gleaned from LE (directly attributable to bio-reactions); alternatively, the former could be useful just by itself. In either case, experimental investigations are warranted – particularly, with respect to emitted intensities and sensitivity to reactant amounts and concentrations.

References

[1] D. Ivnitski, I. Abdel–Hamid, P. Atanasov, E. Wilkins, Biosens. Bioelectron. 14 (1999) 599.
[2] T. Vo-Dinh, B. Cullum, Fresenius' J. Anal. Chem. 366 (2000) 540.
[3] J. Kong, M.G. Chapline, H. Dai, Adv. Mater. 13 (2001) 1384.
[4] S. Chan, Y. Li, L.J. Rothberg, B.L. Miller, P.M. Fauchet, Mater. Sci. Eng. C 15 (2001) 277.
[5] V. Chin, B.E. Collins, M.J. Sailor, S.N. Bhatia, Adv. Mater. 13 (2001) 1877.
[6] L. Brus, J. Phys. Chem. 98 (1994) 3575.
[7] R. Messier, V.C. Venugopal, P.D. Sunal, J. Vac. Sci. Technol. A 18 (2000) 1538.
[8] Y. Taga, Mater. Sci. Eng. C 15 (2001) 231.
[9] I. Hodgkinson, Q.h. Wu, Adv. Mater. 13 (2001) 889.
[10] V.C. Venugopal, A. Lakhtakia, in: O.N. Singh, A. Lakhtakia (Eds.), Electromagnetic Fields in Unconventional Materials and Structures, Wiley, New York, 2000 (Chapter 5).
[11] M.W. McCall, Math. Comput. Model. 34 (2001) 1483.

[12] C. Kittel, Introduction to Solid State Physics, fourth ed., Wiley Eastern, New Delhi, 1974.
[13] A. Lakhtakia, Mater. Sci. Eng. C 19 (2002) 427.
[14] X.-H. Xu, A.J. Bard, J. Am. Chem. Soc. 117 (1995) 2627.
[15] A. Islam, N. Ikeda, A. Yoshimura, T. Ohno, Inorg. Chem. 37 (1998) 3093.
[16] E.S. Handy, A.J. Pal, M.F. Rubner, J. Am. Chem. Soc. 121 (1999) 3525.
[17] A. Lakhtakia, Opt. Commun. 188 (~~2000~~) 313. 2001
[18] A. Lakhtakia, Opt. Commun. 202 (2002) 103, erratum: 203 (2002) 447.
[19] V.I. Kopp, B. Fan, H.K.M. Vithana, A.Z. Genack, Opt. Lett. 23 (1998) 1707.
[20] H. Finkelmann, S.T. Kim, A. Muñoz, P. Palffy–Muhoray, B. Taheri, Adv. Mater. 13 (2001) 1069.
[21] F. Naef, D.A. Lim, N. Patil, M. Magnasco, Phys. Rev. E 65 (2002) 040902.
[22] N. Bloembergen, Nonlinear Optics, fourth ed., World Scientific, Singapore, 1995, p. 69.
[23] J.A. Sherwin, A. Lakhtakia, Math. Comput. Model. 34 (2001) 1499, erratums: 35 (2002) 1355.
[24] A. Lakhtakia, W.S. Weiglhofer, Int. J. Electron. 87 (2000) 1401.
[25] H.C. Chen, Theory of Electromagnetic Waves, TechBooks Fairfax, VA, USA, 1993 (Chapter 1).
[26] A. Lakhtakia, V.C. Venugopal, Microw. Opt. Technol. Lett. 13 (1996) 339.
[27] R.W. Boyd, Nonlinear Optics, Academic Press, San Diego, CA, USA, 1992 (Chapter 1).
[28] B.A. Auld, Acoustic Fields and Waves in Solids, vol. I, Wiley, New York, 1973, p. 380.
[29] C. Klein, C.S. Hurlbut Jr., Manual of Mineralogy, 20th ed., Wiley, New York, 1985, p. 71.
[30] J.A. Armstrong, N. Bloembergen, J. Ducuing, P.S. Pershan, Phys. Rev. 127 (1962) 1918.
[31] M. Nagel, P. Haring Bolivar, M. Brucherseifer, H. Kurz, A. Bosserhoff, R. Büttner, Appl. Phys. Lett. 80 (2002) 154.

AN ESSENTIAL DIFFERENCE BETWEEN DIELECTRIC MIRRORS AND CHIRAL MIRRORS

Akhlesh Lakhtakia and Jian Xu
CATMAS—Computational & Theoretical Materials Sciences Group
Department of Engineering Science & Mechanics
212 Earth–Engineering Sciences Building
Pennsylvania State University, University Park, PA 16802-6812

Received 31 March 2005

ABSTRACT: *The boundary conditions on the exposed face of a dielectric mirror are shown to be effectively the same as those for perfect electric conductors, whereas the boundary conditions on the exposed face of a chiral mirror are very different from those for either perfect electric conductors or perfect magnetic conductors. Cavities between two chiral mirrors have a relatively uniform field distribution, which is significant for spectral-hole filters and coherent light generation.* © 2005 Wiley Periodicals, Inc. Microwave Opt Technol Lett 47: 63–64, 2005; Published online in Wiley InterScience (www.interscience.wiley.com). DOI 10.1002/mop.21082

Key words: *boundary conditions; chiral mirror; cholesteric liquid crystal; dielectric mirror; sculptured thin film*

1. INTRODUCTION AND ANALYSIS

Metals in bulk are virtually perfect electric conductors over a large frequency range, and therefore are often employed as mirrors. In some instances, however, as the absorption due to their conductivity can be undesirable, metallic mirrors are replaced by dielectric mirrors. These are stacks of alternating quarter-wave layers of two homogeneous materials of high and low refractive indexes [1, 2]. In a certain frequency band, the periodicity of a dielectric mirror leads to the display of the Bragg phenomenon, which is characterized by very high reflectances and very small absorption.

Another type of nonmetallic mirror is furnished by cholesteric liquid crystals (CLCs) [5]. A CLC is a uniaxial dielectric material whose optical axis uniformly rotates about a fixed axis, which is usually normal to two parallel planes. When a circularly polarized plane wave is normally incident on one of those planes, it is highly reflected provided (i) the structural handedness or chirality of the CLC matches the handedness of the incident plane wave, (ii) the CLC is sufficiently thick, and (iii) the frequency lies in a certain band. If the chirality of the CLC is opposed to the handedness of the incident plane wave, there is very little reflectance. A similar functionality is demonstrated by chiral sculptured thin films [6]. Such mirrors are called chiral mirrors.

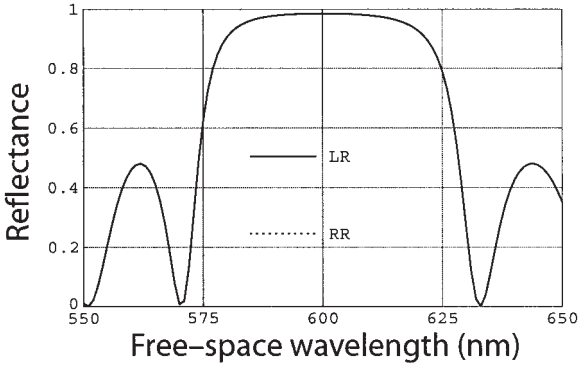

Figure 1 Computed reflectance R_{LR} of a dielectric mirror as a function of the free-space wavelength. The chosen dielectric mirror is made of alternating quarter-wave layers of two materials. The refractive indexes and layer thicknesses are 2.0 and 75 nm for the first material, 1.8 and 83.33 nm for the second material. The mirror comprises 21 layers of the first material and 20 layers of the second material. The design wavelength is 600 nm so that the design frequency is 500 THz. For this mirror, $R_{RR} \equiv 0$

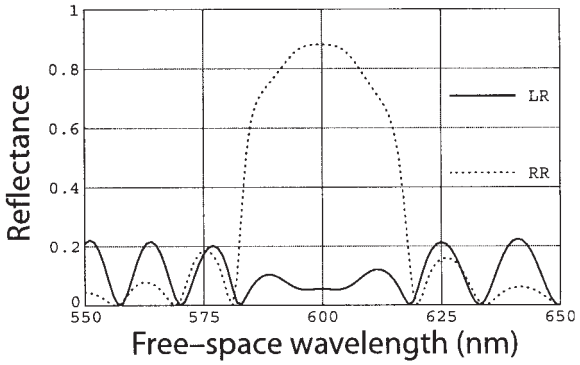

Figure 2 Computed reflectances R_{LR} (solid line) and R_{RR} (dotted line) of a chiral mirror as functions of the free-space wavelength. The chosen chiral mirror is made of a structurally right-handed CLC with ordinary refractive index of 1.65, extraordinary refractive index of 1.72, and structural period of 356.1 nm. The mirror is 20-structural-periods thick, the design wavelength is 600 nm, and the design frequency is 500 THz

The interposition of a layer of some dielectric medium between two dielectric mirrors creates a planar cavity, which functions as a spectral reflection-hole filter. Such filters are widely used in optics and optoelectronics [3, 4]. A similar interposition of an isotropic dielectric layer between two chiral mirrors also creates a planar cavity, as suggested by Adams et al. [7] in 1971 and realized subsequently by several research groups [6, 8]. This communication was engendered by our investigation into the possible interchangeability of dielectric and chiral mirrors when designing planar cavities for circularly polarized light.

For definiteness, let the incident plane wave be right circularly polarized (RCP). The plane wave reflected by a mirror can have RCP and left circularly polarized (LCP) components, in general. Let R_{LR} denote the reflectance of a RCP plane wave as a LCP plane wave, while R_{RR} denotes the reflectance of a RCP plane wave as a RCP plane wave. The spectra of these two reflectances suffice for a comparative study of dielectric mirrors and chiral mirrors.

Figure 1 shows the computed R_{LR} spectrum of a dielectric mirror designed to function best at a free-space wavelength of 600 nm, whereas $R_{RR} \equiv 0$. Were the incident plane wave to be LCP, then R_{RL} would be equal to R_{LR}, and R_{LL} would be null valued. In other words, a dielectric mirror reverses the circular polarization state on reflection.

Figure 2 shows the computed R_{LR} and R_{RR} spectra of a structurally right-handed chiral mirror designed to function best also at a free-space wavelength of 600 nm. Note that R_{RR} is very high, whereas R_{LR} is very low and can be decreased even further by the use of impedance-matching layers [9]. Thus, the circular polarization state is not reversed on reflection by a chiral mirror.[1]

Let us analyze the handedness of the reflected plane wave in relation to that of the incident plane wave. Suppose that the plane $z = 0$ is the exposed face of a mirror, whereas both incidence and reflection take place in the half-space $z \leq 0$. Then, the total electric field phasor in this half-space can be stated in general as

[1] Were the incident plane wave to be LCP, R_{LL} would be small whereas $R_{RL} = R_{LR}$; thus, the device would not serve as a mirror.

$$\mathbf{E}_{tot}(z) = \frac{\hat{\mathbf{x}} - i\hat{\mathbf{y}}}{\sqrt{2}} \exp(ik_0 z) + r_L \frac{\hat{\mathbf{x}} - i\hat{\mathbf{y}}}{\sqrt{2}} \exp(-ik_0 z) + r_R \frac{\hat{\mathbf{x}} + i\hat{\mathbf{y}}}{\sqrt{2}} \exp(-ik_0 z), \quad z \le 0, \quad (1)$$

and the corresponding total magnetic field phasor as

$$\mathbf{H}_{tot}(z) = \frac{i}{\eta_0} \frac{\hat{\mathbf{x}} - i\hat{\mathbf{y}}}{\sqrt{2}} \exp(ik_0 z) - r_L \frac{i}{\eta_0} \frac{\hat{\mathbf{x}} - i\hat{\mathbf{y}}}{\sqrt{2}} \exp(-ik_0 z) + r_R \frac{i}{\eta_0} \frac{\hat{\mathbf{x}} + i\hat{\mathbf{y}}}{\sqrt{2}} \exp(-ik_0 z), \quad z \le 0, \quad (2)$$

where k_0 is the free-space wavenumber and η_0 is the intrinsic impedance of free space; $\hat{\mathbf{x}}$ and $\hat{\mathbf{y}}$ are Cartesian unit vectors; and $R_{LR} = |r_L|^2$ and $R_{RR} = |r_R|^2$.

For the dielectric mirror, it follows from Figure 1 that $|r_L| \approx 1$ and $r_R = 0$; that is, either the tangential electric field phasor or the tangential magnetic field phasor on the face $z = 0$ is vanishingly small. Figure 3 shows spectra of $|\mathbf{E}(0)|$ and $\eta_0|\mathbf{H}(0)|$. At the design frequency, the tangential electric field phasor is null valued, whereas the tangential magnetic field phasor is double that of the incident plane wave. Clearly then, a dielectric mirror is similar to a perfect electric conductor at the design frequency, and reverses the circular polarization state of the reflected plane wave in relation to that of the incident plane wave.

Figure 4 shows the spectra of $|\mathbf{E}(0)|$ and $\eta_0|\mathbf{H}(0)|$ for a chiral mirror in the reflection band centered at the design frequency. Neither the tangential electric-field phasor nor the tangential magnetic-field phasor on the exposed face are of vanishingly small magnitudes; thus, a chiral mirror is similar neither to a perfect electric conductor nor a perfect magnetic conductor at the design frequency.

2. CONCLUSIONS

We conclude from the foregoing analysis that it is impossible to replace a chiral mirror by a dielectric mirror in resonant cavities for employment as reflection-hole filters and for coherent light generation. Furthermore, the field distribution in a cavity between two chiral mirrors is very different from that in a cavity between two dielectric mirrors. In fact, whereas the field between two dielectric mirrors is of the standing-wave type with uniform distribution of nodes and anti-nodes, this distribution is impossible between two chiral mirrors. In the latter cavity, the field is circularly polarized but not of the standing-wave type—which may have certain unique applications because the electric field between two chiral mirrors is relatively uniform. As an example, when designing a resonant-cavity light-emitting device, spatial-gain hole-burning can be effectively suppressed if a polarization-independent gain medium is inserted in the cavity between two chiral mirrors [10, 11].

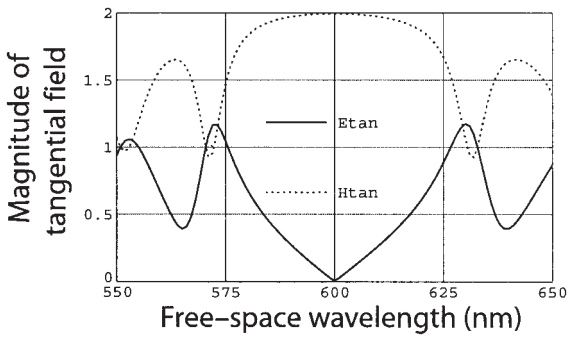

Figure 3 Magnitudes of $\mathbf{E}(0)$ (solid line) and $\eta_0\mathbf{H}(0)$ (dotted line) on the exposed face of a dielectric mirror as functions of the free-space wavelength. The chosen dielectric mirror is the same as that in Fig. 1

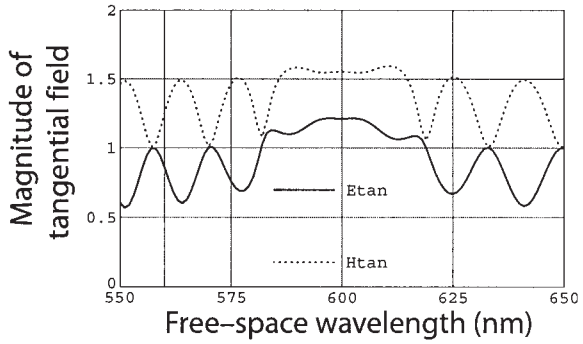

Figure 4 Magnitudes of $\mathbf{E}(0)$ (solid line) and $\eta_0\mathbf{H}(0)$ (dotted line) on the exposed face of a chiral mirror as functions of the free-space wavelength. The chosen chiral mirror is the same as that in Fig. 2

REFERENCES

1. J.D. Rancourt, Optical thin films, Macmillan, New York, 1987.
2. H.A. Macleod, Thin-film optical filters, Institute of Physics, Bristol, United Kingdom, 2001.
3. G.P. Agrawal and N.K. Dutta, Semiconductor lasers, Van Nostrand Reinhold, New York, 1993.
4. N. Kaiser and H.K. Pulker (Eds.), Optical interference coatings, Springer, Berlin, Germany, 2003.
5. J.L. Fergason, Cholesteric structure I: Optical properties, Mol Cryst 1 (1966), 293–307.
6. A. Lakhtakia and R. Messier, Sculptured thin films: Nanoengineered morphology and optics, SPIE Press, Bellingham, WA, 2005.
7. J. Adams, W. Haas, and J. Dailey, Cholesteric films as optical filters, J Appl Phys 42 (1971), 4096–4098.
8. Y.-C. Yang, C.-S. Kim, J.-E. Kim, H.Y. Park, J.-C. Lee, and Y.-J. Jeon, Photonic defect modes of cholesteric liquid crystals, Phys Rev B 60 (1999), 6852–6854.
9. I.J. Hodgkinson, Q.H. Wu, M. Arnold, M.W. McCall, and A. Lakhtakia, Chiral mirror and optical resonator designs for circularly polarized light: Suppression of cross-polarized reflectances and transmittances, Opt Commun 210 (2002), 202–211.
10. J. E. Stockley, G.D. Sharp, and K.M. Johnson, Fabry-Perot etalon with polymer cholesteric liquid-crystal mirrors, Optics Lett 24 (1999), 55–57.
11. Y. Tanaka, H. Takano, and T. Kurokawa, Circular polarization resonator based on cholesteric liquid crystal, Jpn J Phys 43 (2004), 1062–1067.

10.1098/rspa.2000.0694

THE ROYAL SOCIETY

Optical interconnects realizable with thin-film helicoidal bianisotropic mediums

By Elif Ertekin and Akhlesh Lakhtakia

Computational and Theoretical Materials Sciences Group (CATMAS), Department of Engineering Science and Mechanics, 212 Earth–Engineering Sciences Building, Pennsylvania State University, University Park, PA 16802–6812, USA

Received 22 May 2000; revised 21 August 2000; accepted 20 September 2000

Parallel-plate waveguides consisting of a thin-film helicoidal bianisotropic medium (TFHBM) layer bounded by dielectric half-spaces are shown to support guided wave propagation with guide wavenumbers dependent on the direction of signal propagation. Thus, the TFHBM interconnect behaves as a *space-guide*. The modal fields and power transmission distributions, as determined by the time-averaged Poynting vector, are investigated and a scheme classifying each guided wave mode as either *hybrid electric* or *hybrid magnetic* is presented.

Keywords: optical interconnects; anisotropic waveguides; sculptured thin films; space-guides; hybrid modes

1. Introduction

Implementation of optoelectronic devices requires the development of optical interconnects which, in addition to providing effective signal transmission, must be simple to fabricate on integrated circuitry. In this paper, we present a theoretical study which indicates that thin-film helicoidal bianisotropic mediums (TFHBMs) are very suitable for realizing optical interconnects. In fact, the adoption of semiconducting TFHBMs may result in efficient use of the available surface area (often called *real-estate*) in electronic chips.

TFHBMs constitute one of two canonical classes of sculptured thin films (STFs), which are non-homogeneous anisotropic thin films with nano-engineered morphologies consisting of parallel columns shaped as chevrons, S shapes, C shapes, helices, etc. (Lakhtakia *et al*. 1996). Two recent reviews (Messier & Lakhtakia 1999; Venugopal & Lakhtakia 2000*a*), as well as the proceedings of two recent conferences (Lakhtakia & Messier 1999; Lakhtakia *et al*. 2000), are recommended for a survey of most developments in STF research.

An STF behaves as a unidirectionally non-homogeneous continuum when excited by time-harmonic fields at sufficiently low frequencies (i.e. when the principal wavelengths of light are large compared with the columnar diameter). Since the conception of STFs in 1995, several possible applications have been proposed, including laser mirrors, multi-notch filters, optical gas sensors and low-permittivity materials (Venugopal & Lakhtakia 2000*a*). Theoretical work on applications has led the way,

but experimental work is now also gathering steam. Most recently, linear and circular thin-film polarization filters (Hodgkinson *et al.* 1999) and spectral-hole filters (Hodgkinson *et al.* 2000*a*) have been realized, and humidity sensors have also been tested (Wu *et al.* 2000).

TFHBMs microstructurally comprise helical columns so that they are periodically non-homogeneous along, say, the z-axis. Young & Kowal (1959) realized the first TFHBM in 1959, though technological limitations prevented the verification of a chiral columnar structure. The first TFHBM for which the chiral structure was verified was developed in 1995 (Robbie *et al.* 1995). TFHBMs can be fabricated by thermal evaporation at high vacuum levels with various materials (including MgF_2, SiO_x and CaF_2) and with sufficient control of features such as porosity, structural period and columnar angle of rise (Robbie & Brett 1997; Hodgkinson *et al.* 1998; Monteiro *et al.* 1998; Messier *et al.* 2000). A recently developed serial bideposition technique can be used to realize TFHBMs which exhibit high optical activity with typical values for optical rotation of $5^\circ\ \mu\mathrm{m}^{-1}$ (Hodgkinson *et al.* 2000*b*).

Examining guided wave propagation in a TFHBM layer occupying the region between two parallel conducting plates, Lakhtakia (1999) had proposed waveguiding applications for TFHBM layers. For optical interconnects, however, waveguiding TFHBM layers should be interfaced with dielectric materials instead of conductors. Accordingly, in § 2, we formulate the boundary-value problem for waveguiding in a TFHBM layer bounded by isotropic dielectric half-spaces on both sides. The formulated problem allows us to derive the dispersion equation that must be solved to determine allowed guide wavenumbers. The results of our numerical studies are presented in § 3, where we elucidate the *space-guide* concept, which encompasses the efficient use of semiconductor real-estate that the implementation of TFHBM interconnects may offer. The characteristics of the lower-order propagation modes are presented in detail.

2. Theoretical analysis

(*a*) *Constitutive relations*

Suppose a linear dielectric TFHBM completely fills the region $|z| \leqslant \frac{1}{2}D$, while the half-spaces $z \leqslant -\frac{1}{2}D$ and $z \geqslant \frac{1}{2}D$ are filled by an isotropic dielectric medium with a relative permittivity scalar $\epsilon_r(\omega)$. The frequency-domain electromagnetic constitutive relations of the TFHBM are as follows:

$$\boldsymbol{D}(\boldsymbol{r},\omega) = \epsilon_0 \underline{\underline{\epsilon}}(z,\omega) \cdot \boldsymbol{E}(\boldsymbol{r},\omega), \quad \boldsymbol{B}(\boldsymbol{r},\omega) = \mu_0 \boldsymbol{H}(\boldsymbol{r},\omega), \quad |z| \leqslant \tfrac{1}{2}D. \tag{2.1}$$

Here, ω is the angular frequency, ϵ_0 and μ_0 are, respectively, the permittivity and permeability of free space (i.e. vacuum), the relative permittivity dyadic $\underline{\underline{\epsilon}}(z,\omega)$ is given by

$$\underline{\underline{\epsilon}}(z,\omega) = \underline{\underline{S}}_z(z - \tfrac{1}{2}D) \cdot \underline{\underline{S}}_y(\chi) \cdot \underline{\underline{\epsilon}}^{\circ}_{\mathrm{ref}}(\omega) \cdot \underline{\underline{S}}_y^{\mathrm{T}}(\chi) \cdot \underline{\underline{S}}_z^{\mathrm{T}}(z - \tfrac{1}{2}D), \tag{2.2}$$

and the superscript 'T' denotes the transpose. The *reference* relative permittivity dyadic is defined as

$$\underline{\underline{\epsilon}}^{\circ}_{\mathrm{ref}}(\omega) = \epsilon_a(\omega)\boldsymbol{u}_z\boldsymbol{u}_z + \epsilon_b(\omega)\boldsymbol{u}_x\boldsymbol{u}_x + \epsilon_c(\omega)\boldsymbol{u}_y\boldsymbol{u}_y, \tag{2.3}$$

where $\boldsymbol{u}_x$, $\boldsymbol{u}_y$ and $\boldsymbol{u}_z$ are the Cartesian unit vectors, and $\epsilon_a(\omega)$, $\epsilon_b(\omega)$, and $\epsilon_c(\omega)$ are frequency-dependent scalars. We assume the absence of absorption, which is realistic

for optical waveguides (Sodha & Ghatak 1977; Hodgkinson *et al.* 2000*c*). In general, $\underline{\underline{\epsilon}}^{\circ}_{\rm ref}(\omega)$ is a biaxial dyadic, with $\epsilon_b(\omega) > \epsilon_c(\omega) > \epsilon_a(\omega)$, as suggested by evidence from columnar thin films (Hodgkinson & Wu 1997); but we note that the presented formalism does not rely on these assumptions. Furthermore, we set $\epsilon_a(\omega) > \epsilon_r(\omega)$ in our numerical studies in order to ensure the existence of guided wave modes.

The rotational non-homogeneity of the TFHBM is exhibited through the dyadic

$$\underline{\underline{S}}_z(z) = (\boldsymbol{u}_x\boldsymbol{u}_x + \boldsymbol{u}_y\boldsymbol{u}_y)\cos\left(\frac{\pi z}{\Omega}\right) + (\boldsymbol{u}_y\boldsymbol{u}_x - \boldsymbol{u}_x\boldsymbol{u}_y)\sin\left(\frac{\pi z}{\Omega}\right) + \boldsymbol{u}_z\boldsymbol{u}_z, \qquad (2.4)$$

in which 2Ω is the structural period. In the tilt dyadic

$$\underline{\underline{S}}_y(\chi) = (\boldsymbol{u}_x\boldsymbol{u}_x + \boldsymbol{u}_z\boldsymbol{u}_z)\cos\chi + (\boldsymbol{u}_z\boldsymbol{u}_x - \boldsymbol{u}_x\boldsymbol{u}_z)\sin\chi + \boldsymbol{u}_y\boldsymbol{u}_y, \qquad (2.5)$$

χ is the so-called angle of rise above the xy-plane; typically, $\chi \geqslant 20^\circ$ (Messier *et al.* 2000). Equation (2.4) holds for a structurally right-handed TFHBM.

(*b*) *Field representation*

A specific guided wave mode can be delineated with the following equations:

$$\left.\begin{aligned} \boldsymbol{E}(\boldsymbol{r}) &= \exp[\mathrm{i}\kappa(x\cos\psi + y\sin\psi)]\boldsymbol{e}(z,\kappa,\psi), \\ \boldsymbol{H}(\boldsymbol{r}) &= \exp[\mathrm{i}\kappa(x\cos\psi + y\sin\psi)]\boldsymbol{h}(z,\kappa,\psi), \end{aligned}\right\} \quad -\infty < z < \infty. \qquad (2.6)$$

Here, the angle ψ denotes the propagation direction and κ is the modal guide wavenumber whose values have to be determined.

On substituting the constitutive relations (2.1) and the Fourier representations (2.6) into the time-harmonic Maxwell curl equations,

$$\nabla\times\boldsymbol{E}(\boldsymbol{r}) = \mathrm{i}\omega\boldsymbol{B}(\boldsymbol{r}), \qquad \nabla\times\boldsymbol{H}(\boldsymbol{r}) = -\mathrm{i}\omega\boldsymbol{D}(\boldsymbol{r}),$$

the following 4×4 matrix ordinary differential equation emerges:

$$\frac{\mathrm{d}}{\mathrm{d}z}[\underline{f}(z,\kappa,\psi)] = \mathrm{i}[\underline{\underline{P}}(z,\kappa,\psi)][\underline{f}(z,\kappa,\psi)], \quad |z| < \tfrac{1}{2}D. \qquad (2.7)$$

In this expression, the 4×4 matrix $[\underline{\underline{P}}]$ is

$$\begin{bmatrix} 0 & 0 & 0 & \omega\mu_0 \\ 0 & 0 & -\omega\mu_0 & 0 \\ \tfrac{1}{2}\omega\epsilon_0(\epsilon_c - \tilde{\epsilon}_d)\sin\left(\dfrac{2\pi z}{\Omega}\right) & -\omega\epsilon_0\left[\tilde{\epsilon}_d\sin^2\left(\dfrac{\pi z}{\Omega}\right) + \epsilon_c\cos^2\left(\dfrac{\pi z}{\Omega}\right)\right] & 0 & 0 \\ \omega\epsilon_0\left[\tilde{\epsilon}_d\cos^2\left(\dfrac{\pi z}{\Omega}\right) + \epsilon_c\sin^2\left(\dfrac{\pi z}{\Omega}\right)\right] & -\tfrac{1}{2}\omega\epsilon_0(\epsilon_c - \tilde{\epsilon}_d)\sin\left(\dfrac{2\pi z}{\Omega}\right) & 0 & 0 \end{bmatrix}$$

$$
+\kappa\frac{\tilde{\epsilon}_d(\epsilon_a-\epsilon_b)}{2\epsilon_a\epsilon_b}\sin(2\chi)
$$

$$
\times\begin{bmatrix}
\cos\psi\cos\left(\dfrac{\pi z}{\Omega}\right) & \cos\psi\sin\left(\dfrac{\pi z}{\Omega}\right) & 0 & 0\\
\sin\psi\cos\left(\dfrac{\pi z}{\Omega}\right) & \sin\psi\sin\left(\dfrac{\pi z}{\Omega}\right) & 0 & 0\\
0 & 0 & \sin\psi\sin\left(\dfrac{\pi z}{\Omega}\right) & -\cos\psi\sin\left(\dfrac{\pi z}{\Omega}\right)\\
0 & 0 & -\sin\psi\cos\left(\dfrac{\pi z}{\Omega}\right) & \cos\psi\cos\left(\dfrac{\pi z}{\Omega}\right)
\end{bmatrix}
$$

$$
+\omega\frac{\kappa^2}{k_0^2}\begin{bmatrix}
0 & 0 & \dfrac{\tilde{\epsilon}_d}{\epsilon_a\epsilon_b}\mu_0\cos\psi\sin\psi & -\dfrac{\tilde{\epsilon}_d}{\epsilon_a\epsilon_b}\mu_0\cos\psi\cos\psi\\
0 & 0 & \dfrac{\tilde{\epsilon}_d}{\epsilon_a\epsilon_b}\mu_0\sin\psi\sin\psi & -\dfrac{\tilde{\epsilon}_d}{\epsilon_a\epsilon_b}\mu_0\cos\psi\sin\psi\\
-\epsilon_0\sin\psi\cos\psi & \epsilon_0\cos\psi\cos\psi & 0 & 0\\
-\epsilon_0\sin\psi\sin\psi & \epsilon_0\sin\psi\cos\psi & 0 & 0
\end{bmatrix} \tag{2.8}
$$

the column 4-vector

$$
[\underline{f}(z,\kappa,\psi)] = [e_x(z,\kappa,\psi), e_y(z,\kappa,\psi), h_x(z,\kappa,\psi), h_y(z,\kappa,\psi)]^{\mathrm{T}}, \tag{2.9}
$$

while $\tilde{\epsilon}_d = \epsilon_a\epsilon_b/(\epsilon_a\cos^2\chi + \epsilon_b\sin^2\chi)$. In the limit $\Omega\to\infty$, the obtained matrix differential equation tallies with that given by Abdulhalim (1999) for homogeneous biaxial dielectrics.

The solution of (2.7) can be expressed by the relationship

$$
[\underline{f}(\tfrac{1}{2}D,\kappa,\psi)] = [\underline{\underline{T}}(D,\kappa,\psi)][\underline{f}(-\tfrac{1}{2}D,\kappa,\psi)]. \tag{2.10}
$$

The transition matrix $[\underline{\underline{T}}(D,\kappa,\psi)]$ is computed by the piecewise homogeneity approximation method (Venugopal & Lakhtakia 2000*b*), whereby the non-homogeneous TFHBM layer is modelled by N homogeneous sublayers, each of which differs slightly in constitution from the adjacent sublayers.

In the two half-spaces, the leakage fields accompanying a guided wave mode are simply planewave solutions of the time-harmonic Maxwell equations. Thus (Venugopal & Lakhtakia 2000*b*),

$$
\left.\begin{aligned}
\boldsymbol{E}(\boldsymbol{r}) &= (b_s\boldsymbol{s} + b_p\boldsymbol{p}_-)\exp[\mathrm{i}\boldsymbol{k}_-\cdot(\boldsymbol{r}+\tfrac{1}{2}D\boldsymbol{u}_z)],\\
\boldsymbol{H}(\boldsymbol{r}) &= \frac{1}{\eta}(b_s\boldsymbol{p}_- - b_p\boldsymbol{s})\exp[\mathrm{i}\boldsymbol{k}_-\cdot(\boldsymbol{r}+\tfrac{1}{2}D\boldsymbol{u}_z)],
\end{aligned}\right\} \quad z\leqslant-\tfrac{1}{2}D \tag{2.11}
$$

in the lower half-space and

$$
\left.\begin{aligned}
\boldsymbol{E}(\boldsymbol{r}) &= (c_s\boldsymbol{s} + c_p\boldsymbol{p}_+)\exp[\mathrm{i}\boldsymbol{k}_+\cdot(\boldsymbol{r}-\tfrac{1}{2}D\boldsymbol{u}_z)],\\
\boldsymbol{H}(\boldsymbol{r}) &= \frac{1}{\eta}(c_s\boldsymbol{p}_+ - c_p\boldsymbol{s})\exp[\mathrm{i}\boldsymbol{k}_+\cdot(\boldsymbol{r}-\tfrac{1}{2}D\boldsymbol{u}_z)],
\end{aligned}\right\} \quad z\geqslant\tfrac{1}{2}D \tag{2.12}
$$

in the upper half-space. Here, b_s and b_p are the amplitudes of the perpendicular- and the parallel-polarized components of the fields leaking into the half-space $z\leqslant-\frac{1}{2}D$,

and c_s and c_p likewise denote leakage into the half-space $z \geqslant \frac{1}{2}D$. The vectors appearing in (2.11) and (2.12) are given by

$$\left.\begin{aligned} \boldsymbol{s} &= -\boldsymbol{u}_x \sin\psi + \boldsymbol{u}_y \cos\psi, \\ \boldsymbol{p}_\pm &= \mp(\boldsymbol{u}_x \cos\psi + \boldsymbol{u}_y \sin\psi)[1-(\kappa/k)^2]^{1/2} + \boldsymbol{u}_z(\kappa/k), \\ \boldsymbol{k}_\pm &= k[(\boldsymbol{u}_x \cos\psi + \boldsymbol{u}_y \sin\psi)\kappa/k \pm \boldsymbol{u}_z[1-(\kappa/k)^2]^{1/2}], \end{aligned}\right\} \tag{2.13}$$

where $k = k_0\sqrt{\epsilon_r}$, $\eta = \eta_0/\sqrt{\epsilon_r}$, $k_0 = \omega\sqrt{\epsilon_0\mu_0}$ is the free-space wavenumber, and $\eta_0 = \sqrt{\mu_0/\epsilon_0}$ is the intrinsic impedance of free space. Guided wave propagation is possible only if $\kappa > k$; otherwise, energy launched into the TFHBM layer must leak into the two half-spaces. For later reference, we delineate (i) the unit vectors $\boldsymbol{u}_\ell = \boldsymbol{u}_x \cos\psi + \boldsymbol{u}_y \sin\psi$ and $\boldsymbol{u}_\perp = \boldsymbol{s}$ in the xy-plane and (ii) the free-space wavelength $\lambda_0 = 2\pi/k_0$.

(*c*) *Dispersion equation*

Since the tangential components of $\boldsymbol{E}(\boldsymbol{r})$ and $\boldsymbol{H}(\boldsymbol{r})$ must be continuous across the bimaterial interfaces $z = -\frac{1}{2}D$ and $z = \frac{1}{2}D$, the boundary values of $[\underline{f}(z,\kappa,\psi)]$ are expressed as (Venugopal & Lakhtakia 2000*b*)

$$\left.\begin{aligned} [\underline{f}(-\tfrac{1}{2}D,\kappa,\psi)] &= [\underline{\underline{K}}(\kappa,\psi)][0,0,b_s,b_p]^{\mathrm{T}}, \\ [\underline{f}(\tfrac{1}{2}D,\kappa,\psi)] &= [\underline{\underline{K}}(\kappa,\psi)][c_s,c_p,0,0]^{\mathrm{T}}, \end{aligned}\right\} \tag{2.14}$$

where the matrix function $[\underline{\underline{K}}(\kappa,\psi)]$ is

$$\left[\begin{array}{cc} -\sin\psi & -\cos\psi\left[1-\left(\dfrac{\kappa}{k}\right)^2\right]^{1/2} \\ \cos\psi & -\sin\psi\left[1-\left(\dfrac{\kappa}{k}\right)^2\right]^{1/2} \\ -\eta^{-1}\cos\psi\left[1-\left(\dfrac{\kappa}{k}\right)^2\right]^{1/2} & \eta^{-1}\sin\psi \\ -\eta^{-1}\sin\psi\left[1-\left(\dfrac{\kappa}{k}\right)^2\right]^{1/2} & -\eta^{-1}\cos\psi \end{array}\right.$$

$$\left.\begin{array}{cc} -\sin\psi & \cos\psi\left[1-\left(\dfrac{\kappa}{k}\right)^2\right]^{1/2} \\ \cos\psi & \sin\psi\left[1-\left(\dfrac{\kappa}{k}\right)^2\right]^{1/2} \\ \eta^{-1}\cos\psi\left[1-\left(\dfrac{\kappa}{k}\right)^2\right]^{1/2} & \eta^{-1}\sin\psi \\ \eta^{-1}\sin\psi\left[1-\left(\dfrac{\kappa}{k}\right)^2\right]^{1/2} & -\eta^{-1}\cos\psi \end{array}\right]. \tag{2.15}$$

Upon combining (2.14) with (2.10), we get the linear system

$$\begin{bmatrix} c_s \\ c_p \\ 0 \\ 0 \end{bmatrix} = \{[\underline{\underline{K}}(\kappa,\psi)]^{-1}[\underline{\underline{T}}(D,\kappa,\psi)][\underline{\underline{K}}(\kappa,\psi)]\} \begin{bmatrix} 0 \\ 0 \\ b_s \\ b_p \end{bmatrix} \equiv [\underline{\underline{\hat{T}}}] \begin{bmatrix} 0 \\ 0 \\ b_s \\ b_p \end{bmatrix}, \tag{2.16}$$

which we rearrange to obtain

$$\begin{bmatrix} \hat{T}_{33} & \hat{T}_{34} & 0 & 0 \\ \hat{T}_{43} & \hat{T}_{44} & 0 & 0 \\ \hat{T}_{23} & \hat{T}_{24} & 0 & -1 \\ \hat{T}_{13} & \hat{T}_{14} & -1 & 0 \end{bmatrix} \begin{bmatrix} b_s \\ b_p \\ c_s \\ c_p \end{bmatrix} \equiv [\underline{\underline{A}}] \begin{bmatrix} b_s \\ b_p \\ c_s \\ c_p \end{bmatrix} = \begin{bmatrix} 0 \\ 0 \\ 0 \\ 0 \end{bmatrix}, \tag{2.17}$$

where $\hat{T}_{mn}$ represents the mnth element of the 4×4 matrix $[\underline{\underline{\hat{T}}}]$. Only eight of the 16 elements of $[\underline{\underline{\hat{T}}}]$ enter (2.17), because no plane waves are incident on the TFHBM layer from the two half-spaces.

Our interest lies in determining pairs of (κ, ψ) such that not all of the coefficients b_s, b_p, c_s and c_p are null-valued. Thus emerges the dispersion equation

$$\det[\underline{\underline{A}}] = \hat{T}_{34}\hat{T}_{43} - \hat{T}_{33}\hat{T}_{44} = 0. \tag{2.18}$$

It involves only four elements of $[\underline{\underline{\hat{T}}}]$, while the remaining four elements of $[\underline{\underline{\hat{T}}}]$ in (2.17) help in determining the relative values of the leakage field coefficients. For guided wave propagation in a given direction $\boldsymbol{u}_\ell$, values of κ denoted by $\kappa_\psi^{(r)}$ $(r = 1, 2, 3, \dots)$ that satisfy the dispersion equation have to be numerically determined, where the roots are indexed by the integer r in descending order of their magnitudes.

3. Numerical results and discussion

We implemented the aforementioned procedure using the C programming language and the IMSL C numerical library subroutines for complex linear algebra. Determining the guide wavenumbers $\kappa_\psi^{(r)}$ for given propagation directions $\boldsymbol{u}_\ell$, we looked at the guided wave mode shapes and power transmission profiles for the TFHBM waveguide. We satisfactorily tested our computer program for the straightforward case of an isotropic homogeneous dielectric slab waveguide (Sodha & Ghatak 1977). We also validated our program against known results for homogeneous anisotropic waveguides that emerge from our formulation on setting $1/\Omega = 0$ (Marcuse 1978; Marcuse & Kaminow 1979; Seshadri 1998). Finally, we successfully checked our calculation of $[\underline{\underline{\hat{T}}}]$ against those of Venugopal & Lakhtakia (2000*b*), who had used a rotating Cartesian basis to solve a differential equation that differs from (but is equivalent to) equation (2.7), in contrast to our use of a fixed Cartesian basis.

Only representative numerical results are provided here, the reader being referred to Ertekin (2000) for numerous other relevant results. For waveguiding by a TFHBM layer, we set $\epsilon_a = 3.0$, $\epsilon_b = 4.6$, $\epsilon_c = 3.8$ and $\chi = 30^\circ$, in accordance with measured data reported by Hodgkinson & Wu (1997) for columnar thin films of titanium oxide deposited at a vapour flux angle of 60° with respect to the substrate normal. We also fixed our attention at $\lambda_0 = 600\,\mathrm{nm}$, while the propagation direction $\boldsymbol{u}_\ell$, the waveguide thickness D and the half-period Ω were varied.

By successively decreasing the sublayer thickness D/N, we established the convergence characteristics of the numerical scheme to determine the transition matrix $[\underline{\underline{T}}]$ using the piecewise homogeneity approximation method (Venugopal & Lakhtakia 2000*b*). In all instances, we found that all elements of $[\underline{\underline{T}}]$ converged within $\pm 0.1\%$ error in magnitude when $D/N = 2.5$ nm.

Values of $\det[\underline{\underline{A}}]$ were initially sampled within the domain $1.0 < (\kappa/k_0) \leqslant 2.2$ at 1200 equal intervals. A sign change in both the real and imaginary parts of $\det[\underline{\underline{A}}]$ within an interval indicates that a root $\kappa_\psi^{(r)}$ may lie within. The location of the roots thus guessed were refined with a simple bracketing bisection algorithm (Schilling & Harris 2000), with the twin conditions that (i) $\det[\underline{\underline{A}}(D, \kappa, \psi)]$ undergoes a sign change in a small interval given by $|(\kappa_\psi^{(r)} - \kappa)/k_0| < 10^{-10}$, and (ii) that $|\det[\underline{\underline{A}}]| \leqslant 10^{-10}$ in that interval.

(*a*) *Guide wavenumbers*

Let us first note some general characteristics of the proposed TFHBM interconnect. The relation $\det[\underline{\underline{A}}(D, \kappa, \psi)] = \det[\underline{\underline{A}}(D, \kappa, \psi + \pi)]^*$ holds independently of all parameters, the asterisk denoting the complex conjugate. Therefore, the guide wavenumbers $\kappa_\psi^{(r)}$ for propagation directions $\boldsymbol{u}_\ell$ and $-\boldsymbol{u}_\ell$ are the same. In the special case that the layer consists of an integral number of periods (i.e. the ratio D/Ω is an even integer), the additional relation $\det[\underline{\underline{A}}(D, \kappa, \psi)] = \det[\underline{\underline{A}}(D, \kappa, \pi - \psi)]$ holds. This arises because all three principal axes of the permittivity dyadic $\underline{\underline{\epsilon}}(z, \omega)$ rotate, as per equation (2.2), about the z-axis, through an integral number of turns between the planes $z = -\frac{1}{2}D$ and $z = \frac{1}{2}D$, thereby imposing a symmetry constraint.

The normalized roots $\kappa_\psi^{(r)}/k_0$ calculated for $D = 8\Omega$, $\Omega = 200$ nm and $\psi = 0$, 15, 30, 45, 60, 75 and 90° are shown in figure 1*a*. A complete understanding for waveguiding in all directions given by $\psi \in [0°, 360°]$ is established by examining $\kappa_\psi^{(r)}$ for $\psi \in [0°, 90°]$ because both symmetry relations described in the previous paragraph are valid for this case. The figure clearly shows that the guide wavenumbers depend on ψ. Therefore, a TFHBM layer is a *space-guide* through which different signals can be transported in different directions with different phase velocities $\omega/\kappa_\psi^{(r)}$.

The variability of $\kappa_\psi^{(r)}$ with ψ is most pronounced around the lower values of $\kappa_\psi^{(r)}$ (where the solutions of the dispersion equation are widely spaced) and less evident for values of $\kappa_\psi^{(r)}$ near the upper bound for roots (where the solutions are closely spaced). Additionally, the directional dependence of $\kappa_\psi^{(r)}$ appears to persist even for smaller values of the ratio D/Ω, which is evident from parts (*b*) and (*c*) of figure 1 (for which $D/\Omega = 1$).

The number density of guided wave modes is less when D is small. This conclusion emerges from a comparison of parts (*a*) ($D = 8\Omega = 1600$ nm), (*b*) ($D = \Omega = 200$ nm) and (*c*) ($D = \Omega = 1600$ nm) of figure 1. In contrast, the mode number density appears to be largely unaffected by the half-period Ω. For instance, anywhere between 17 and 20 modes can be found in the domain $1.0 \leqslant \kappa/k_0 \leqslant 2.2$ for any ψ in parts (*a*) and (*b*) of figure 1, where $D = 1600$ nm; but only three modes exist in figure 1*c* ($D = 200$ nm) for all ψ. Thus the availability of guided wave modes can be tailored by properly choosing the layer thickness D.

We also studied the directional dependence of the guide wavenumbers for the more specific case of a uniaxial TFHBM layer. While we do not present our computed results here, $\kappa_\psi^{(r)}$ still exhibits a dependence on ψ. The same dependence on ψ has

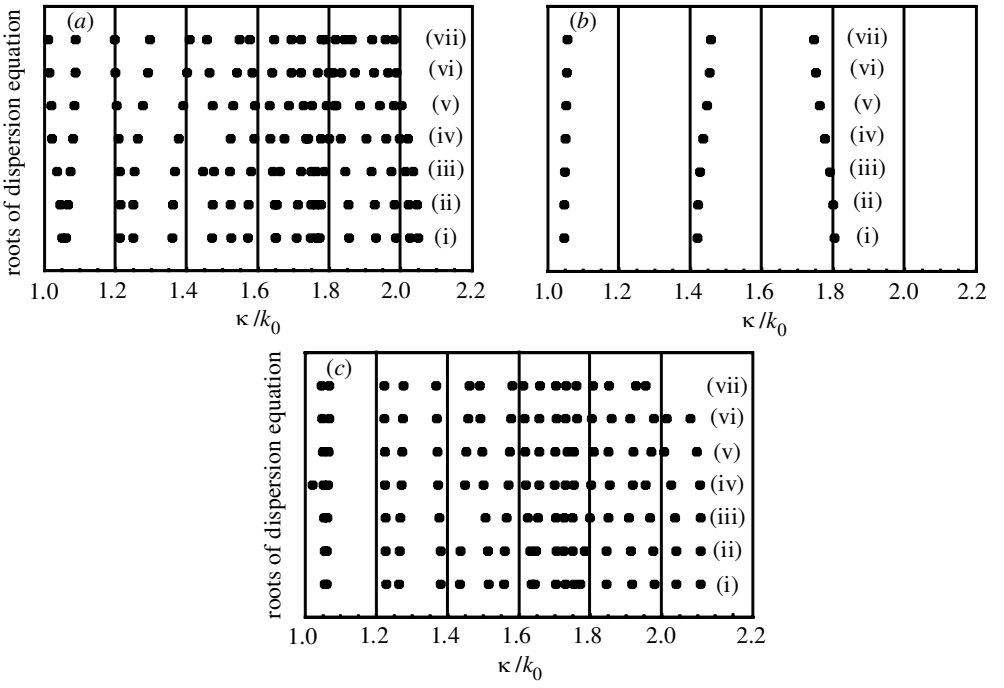

Figure 1. Roots of dispersion equation for varying angles of propagation ψ; $\lambda_0 = 600$ nm, $\epsilon_a = 3.0$, $\epsilon_b = 4.6$, $\epsilon_c = 3.8$, $\chi = 30^\circ$, $\Omega = 200$ nm. ψ (deg): (i) 0; (ii) 15; (iii) 30; (iv) 45; (v) 60; (vi) 75; (vii) 90. (*a*) $D = 8\Omega = 1600$ nm; (*b*) $D = \Omega = 200$ nm; (*c*) $D = \Omega = 1600$ nm.

been noted (and explained) for the axial excitation of uniaxial TFHBM layers by plane waves (Venugopal & Lakhtakia 1998).

A noticeable feature of figure 1*a*, *b* is that $\kappa_\psi^{(r)}$ has an upper bound which varies with ψ. For instance, in figure 1*a*, we see that $\kappa_\psi^{(r)} < 2.049 k_0$ for $\psi = 0^\circ$, whereas $\kappa_\psi^{(r)} < 1.981 k_0$ for $\psi = 90^\circ$. The upper bound decreases monotonically as ψ increases from 0° to 90°. From extensive numerical testing, we found that the upper bound on $\kappa_\psi^{(r)}$ varies with χ, ψ, D and Ω for given ϵ_a, ϵ_b and ϵ_c. Furthermore, the bound $k_0\sqrt{\epsilon_a} \leqslant \kappa_\psi^{(r)} \leqslant k_0\sqrt{\epsilon_b}$ emerged for all combinations of parameters tested. This bound is reasonable because (i) ϵ_a and ϵ_b are the smallest and largest principal components, respectively, of $\underline{\underline{\epsilon}}(z,\omega)$, and (ii) $\epsilon_a > \epsilon_r$.

(*b*) *Guided wave mode shapes and power transmission profiles*

The modal fields and power transmission associated with each of the guided wave modes identified in figure 1*a* were studied next. To obtain the mode shapes, we first calculated the value of $[\underline{f}(z,\kappa,\psi)] = [e_x, e_y, h_x, h_y]^{\mathrm{T}}$ for all $z \in [-\frac{1}{2}D, \frac{1}{2}D]$ by solving (2.10) at the $N = 640$ evenly spaced intervals, and then determined

$$\left.\begin{aligned} e_z &= \frac{-\{\kappa(h_y\cos\psi - h_x\sin\psi) \\ &\qquad -\tfrac{1}{2}\omega\epsilon_o(\epsilon_a-\epsilon_b)\sin(2\chi)[e_x\cos(\pi z/\Omega) + e_y\sin(\pi z/\Omega)]\}\tilde{\epsilon}_d}{\omega\epsilon_o\epsilon_a\epsilon_b}, \\ h_z &= \frac{-\kappa(e_x\sin\psi - e_y\cos\psi)}{\omega\mu_o}, \end{aligned}\right\} \tag{3.1}$$

for $|z| \leqslant \frac{1}{2}D$. As the evaluation of $[\underline{f}(z,\kappa,\psi)]$ requires knowledge of the leakage field components given in (2.14), the coefficients b_s, b_p, c_s and c_p have to be ascertained. Satisfaction of the criterion for guided wave propagation, $\det[\underline{\underline{A}}] = 0$, ensures that by specifying the (numerical) value of any one of the leakage amplitudes (i.e. b_s, b_p, c_s and c_p), we can solve for the remaining three.

The time-averaged power flow in the propagation direction is given by

$$P_\ell(z) = \tfrac{1}{2}\boldsymbol{u}_\ell \cdot \mathrm{Re}[\boldsymbol{e}(z,\kappa,\psi) \times \boldsymbol{h}^*(z,\kappa,\psi)].$$

For any guided wave mode with wavenumber $\kappa_\psi^{(r)}$, $P_\ell(z)$ provides the power transmission distribution throughout the region $|z| \leqslant \frac{1}{2}D$. All the presented results are normalized so that

$$\frac{1}{D}\int_{-\frac{1}{2}D}^{\frac{1}{2}D} P_\ell(z)\,\mathrm{d}z = 1\ \mathrm{W\ m^{-2}}$$

for all guided wave modes.

For simplicity, we denote the electric and magnetic fields along $\boldsymbol{u}_\ell$ as the longitudinal field components $e_\ell = \boldsymbol{e}\cdot\boldsymbol{u}_\ell$ and $h_\ell = \boldsymbol{h}\cdot\boldsymbol{u}_\ell$, and the fields in the direction $\boldsymbol{u}_\perp$ as $e_\perp = \boldsymbol{e}\cdot\boldsymbol{u}_\perp$ and $h_\perp = \boldsymbol{h}\cdot\boldsymbol{u}_\perp$. We first present the field plots and the power transmission distribution associated with modes propagating in the direction $\boldsymbol{u}_\ell = \boldsymbol{u}_x$ (i.e. $\psi = 0^\circ$), and then for $\psi = 75^\circ$. The relationships and patterns that appear in these results are applicable to other propagation directions as well.

As a basis for comparison with the modes of propagation in the proposed TFHBM interconnect, we considered an isotropic planar waveguide of thickness $D = 1600$ nm. Numerical results for this comparison waveguide were obtained by our program by setting $\epsilon_a = \epsilon_b = \epsilon_c = \epsilon_{\mathrm{iso}} = 3.8$ and $1/\Omega = 0$. The modal guide wavenumbers are denoted by $\kappa_{\mathrm{iso}}^{(r)}$, which is not a function of ψ. Odd values of r correspond to transverse electric (TE) modes and even r correspond to transverse magnetic (TM) modes. For all TE modes (Sodha & Ghatak 1977),

$$e_\perp^{\mathrm{iso}} \propto \begin{cases} \cos\left[\sqrt{k_0^2\epsilon_{\mathrm{iso}} - (\kappa_{\mathrm{iso}}^{(r)})^2}\,z\right], & r = 1,5,9,\ldots, \\ \sin\left[\sqrt{k_0^2\epsilon_{\mathrm{iso}} - (\kappa_{\mathrm{iso}}^{(r)})^2}\,z\right], & r = 3,7,11,\ldots, \end{cases} \tag{3.2}$$

and likewise, for all TM modes,

$$h_\perp^{\mathrm{iso}} \propto \begin{cases} \cos\left[\sqrt{k_0^2\epsilon_{\mathrm{iso}} - (\kappa_{\mathrm{iso}}^{(r)})^2}\,z\right], & r = 2,6,10,\ldots, \\ \sin\left[\sqrt{k_0^2\epsilon_{\mathrm{iso}} - (\kappa_{\mathrm{iso}}^{(r)})^2}\,z\right], & r = 4,8,12,\ldots, \end{cases} \tag{3.3}$$

where $|z| \leqslant \frac{1}{2}D$ in all cases. We note here that the selection of the relative permittivity $\epsilon_{\mathrm{iso}} = 3.8$ is arbitrary and does not correspond in any way to the proposed TFHBM interconnect with reference relative permittivities $\epsilon_a = 3.0$, $\epsilon_b = 4.6$ and $\epsilon_c = 3.8$.

In figure 2, the mode shapes associated with the wavenumber $\kappa_{\psi=0^\circ}^{(1)} \approx 2.049k_0$ (see figure 1*a*) in the TFHBM interconnect are presented. The magnitudes of $e_\perp$, e_z, e_ℓ, $h_\perp$, h_z and h_ℓ are plotted between the lower bimaterial interface $z = -\frac{1}{2}D$ and the upper bimaterial interface $z = \frac{1}{2}D$. Outside of this domain, the fields decay exponentially, as delineated by (2.11) and (2.12). Components of both $\boldsymbol{E}$ and $\boldsymbol{H}$

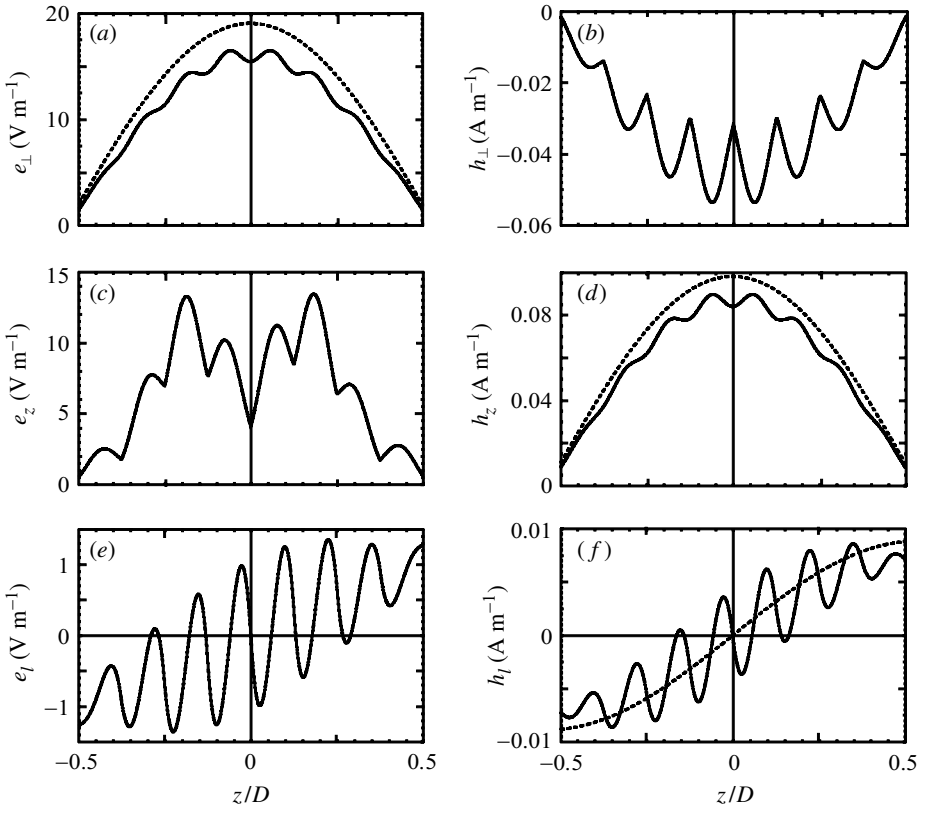

Figure 2. Field magnitudes associated with the HE_1 mode with guide wavenumber $\kappa^{(1)}_{\psi=0^\circ} = 2.049k_0$, in the proposed TFHBM interconnect; see figure 1*a* for parameter values. The dotted lines indicate the fields in the TE_1 mode of the comparison waveguide (isotropic planar waveguide with $D = 1600$ nm and $\epsilon_{\rm iso} = 3.8$).

in the directions $\boldsymbol{u}_\perp$, $\boldsymbol{u}_\ell$ and $\boldsymbol{u}_z$ are all present, which exemplifies the differences between the proposed dielectric TFHBM interconnects and the comparison waveguides. Whereas $e_\ell = e_z = 0$ for TE modes and $h_\ell = h_z = 0$ for TM modes in an isotropic planar waveguide, the modes in a TFHBM interconnect are instead *hybrid* modes with fields present in all three coordinate directions. Yet there are similarities as well.

The electric field component $e_\perp^{\rm iso}$ associated with the TE_1 mode in an isotropic planar waveguide is symmetric with respect to z, as shown also in figure 2. The variation of $e_\perp$ with z for the mode in the TFHBM layer associated with $\kappa^{(1)}_{\psi=0^\circ} \approx 2.049k_0$ is quite similar, except for certain small ripples. For instance, there are eight half-turns in the TFHBM layer and there are eight ripples in every field plot in figure 2. These ripples can be attributed to the periodicity of the TFHBM along the z-axis (Nagle & Lakhtakia 1996), and are characteristic of periodic systems by virtue of the Floquet–Lyapunov theorem (Hochstadt 1975). Preliminarily based on the similarity of the modal field $e_\perp$ in the TFHBM interconnect to that of $e_\perp^{\rm iso}$ for a TE_1 mode in the comparison waveguide, let us classify this mode as a *hybrid electric* mode, namely HE_1.

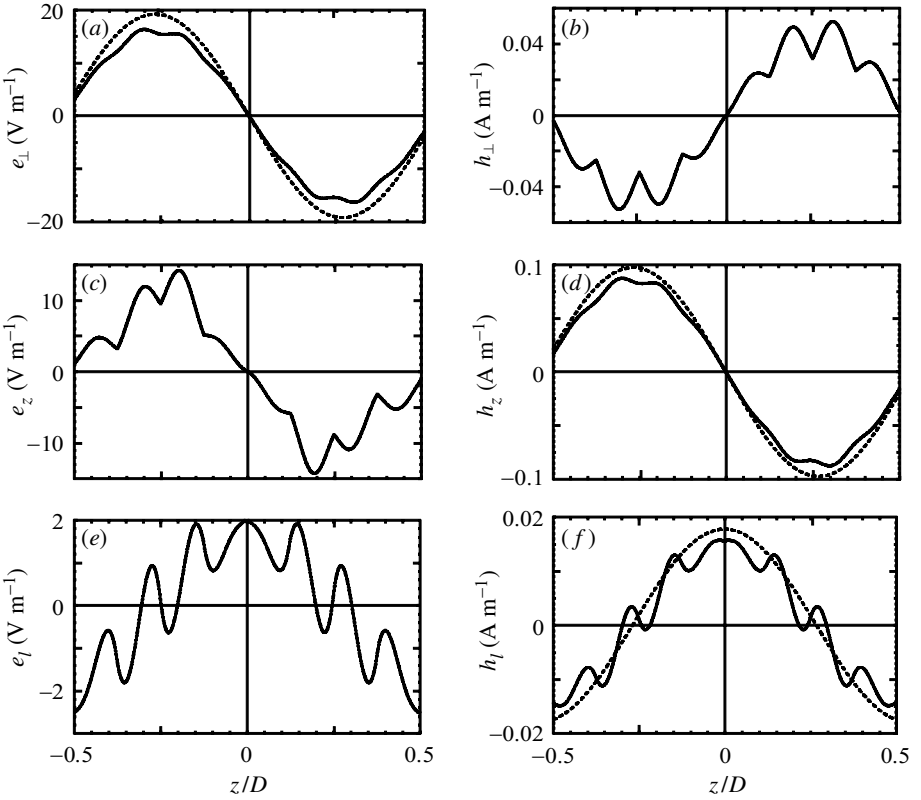

Figure 3. Same as figure 2, but for the HE_2 mode with guide wavenumber $\kappa^{(2)}_{\psi=0^\circ} = 2.026k_0$. The dotted lines indicate the fields in the TE_2 mode of the comparison waveguide.

The next guided wave mode in the proposed TFHBM interconnect is associated with $\kappa^{(2)}_{\psi=0^\circ} \approx 2.026k_0$ in figure 1*a*. The mode shape is delineated by the field plots shown in figure 3. Again, all three components of $\boldsymbol{e}$ and $\boldsymbol{h}$ are present: the mode is a hybrid one. Most importantly, the electric field $e_\perp$ appears to be virtually odd with respect to z, in contrast to the HE_1 mode depicted in figure 2. Furthermore, $e_\perp$ quite resembles $e^{\mathrm{iso}}_\perp$ for the TE_2 mode (with guide wavenumber $\kappa^{(3)}_{\mathrm{iso}}$) in the comparison waveguide, also shown in figure 3. Based on this similarity, the TFHBM mode is classified as the second hybrid electric mode, HE_2.

Additionally, the TFHBM waveguide supports modes of propagation which should be classified as hybrid magnetic (HM) modes. In the propagation direction $\boldsymbol{u}_\ell = \boldsymbol{u}_x$, the first of these, HM_1, occurs at the wavenumber $\kappa^{(6)}_{\psi=0^\circ} \approx 1.772k_0$. The modal $\boldsymbol{E}$ and $\boldsymbol{H}$ fields are plotted in figure 4. As with the HE modes, all field components are present and the mode is again hybrid. This time, the modal field $h_\perp$ resembles $h^{\mathrm{iso}}_\perp$ for the TM_1 mode (with wavenumber $\kappa^{(2)}_{\mathrm{iso}}$) in the comparison waveguide, as shown also in figure 4. The next HM mode occurs with wavenumber $\kappa^{(8)}_{\psi=0^\circ} \approx 1.747k_0$. Once again, comparison with $h^{\mathrm{iso}}_\perp$ for the TM_2 mode in the isotropic planar waveguide suggests that the mode associated with $\kappa^{(8)}_{\psi=0^\circ} \approx 1.747k_0$ in the TFHBM interconnect should be classified as HM_2. Let us note the eight ripples in the $h_\perp$ versus z plots of figures 4 and 5, similar to the ripples in the $e_\perp$ versus z plots of figures 2 and 3.

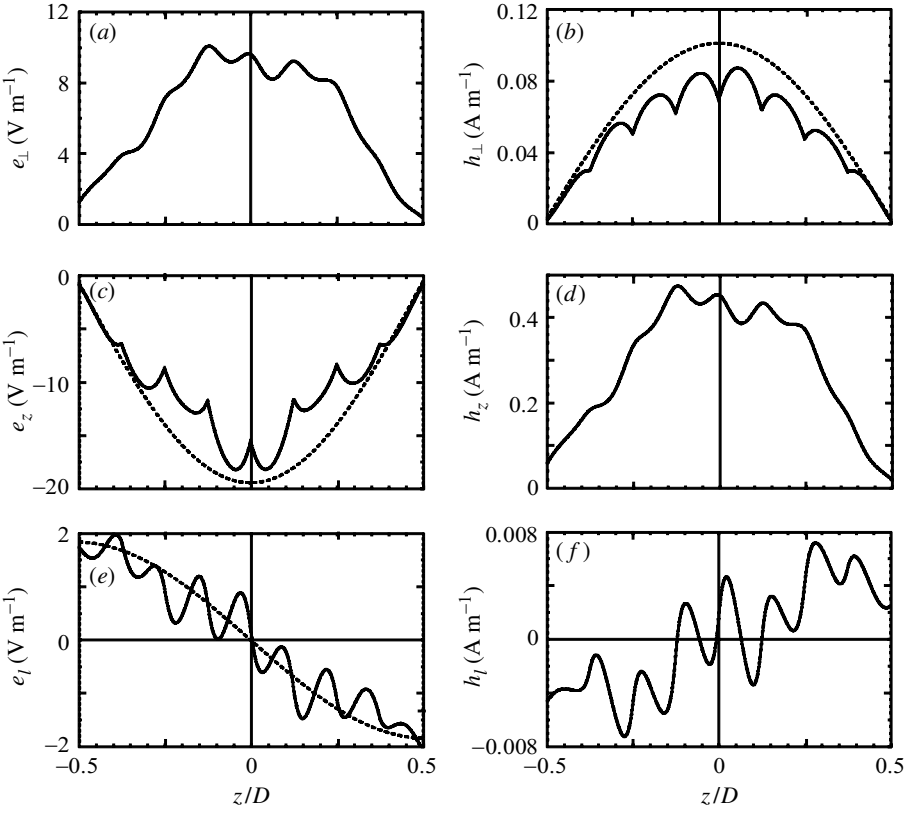

Figure 4. Same as figure 2, but for the HM_1 mode with guide wavenumber $\kappa^{(6)}_{\psi=0^\circ} = 1.772k_0$. The dotted lines indicate the fields in the TM_1 mode of the comparison waveguide.

The power transmission profiles for the guided wave modes HE_1, HE_2, HM_1 and HM_2 propagating along the x-axis are shown in figure 6. The dashed lines represent the power transmission profiles for the TE_1, TE_2, TM_1 and TM_2 modes in the comparison waveguide. Clearly, the power transmission profiles for the HE and HM modes do resemble those of the corresponding TE and TM modes in the comparison waveguide, though the former again demonstrate rippling. For instance, the HE_1 mode (with wavenumber $\kappa^{(1)}_{\psi=0} \approx 2.049k_0$) transports most of the power through the core region of the interconnect, and its power distribution resembles that of the TE_1 mode. The same is true of the HM_1 mode (occurring at $\kappa^{(6)}_{\psi=0^\circ} \approx 1.772k_0$) for which the power distribution resembles that of the TM_1 mode. The HE_2 and HM_2 modes do not transmit most of their power centrally. Within the domain $|z| \leqslant \frac{1}{2}D$, the power transmission profiles for the HE_2 and HM_2 mode are both similar to the TE_2 and TM_2 mode, respectively. Thus the HE_1, HE_2, HM_1 and HM_2 modes in the TFHBM interconnect along $\boldsymbol{u}_x$ are, respectively, comparable with the TE_1, TE_2, TM_1 and TM_2 modes in the isotropic planar waveguide.

While we do not present the obtained results in their entirety here (see Ertekin 2000), the classification of HE and HM modes is best achieved by considering the power transmission profiles rather than the modal field plots for $e_\perp$ and $h_\perp$. Comparison of the modal field plots for $E_\perp$ and $H_\perp$ with those of TE and TM modes

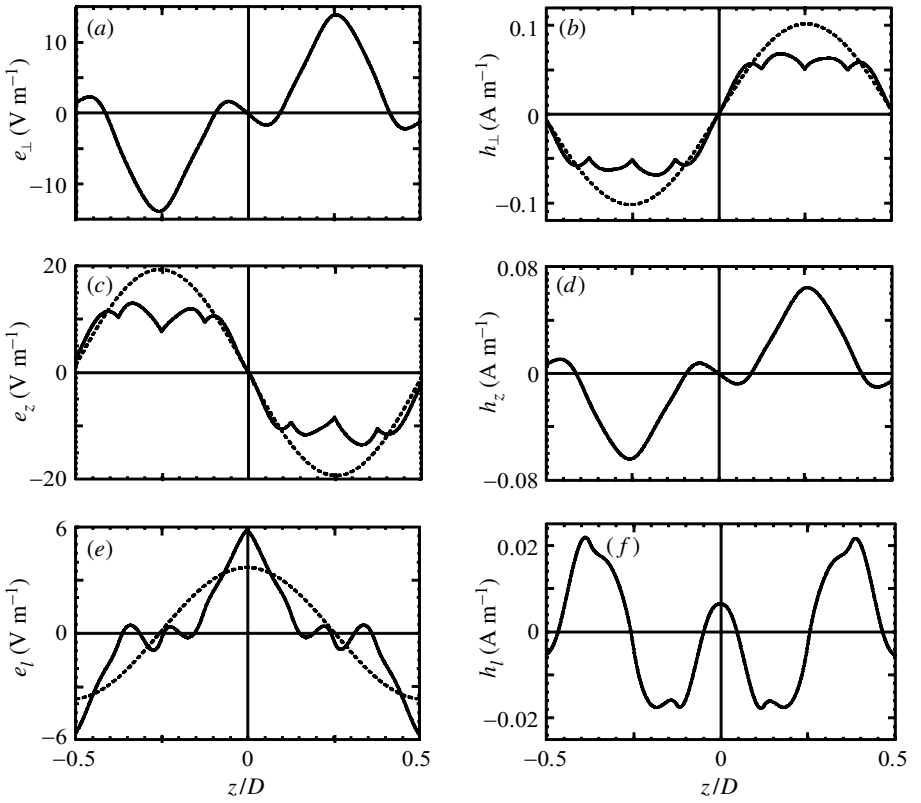

Figure 5. Same as figure 2, but for the HM_2 mode with guide wavenumber $\kappa^{(8)}_{\psi=0^\circ} = 1.747k_0$. The dotted lines indicate the fields in the TM_2 mode of the comparison waveguide.

does not appear to be a valid mechanism for discriminating between HE and HM modes. This is illustrated in figures 7 and 8 for modes propagating in the direction given by $\psi = 75^\circ$. The $e_\perp$ versus z plots for the first four HE modes (with wavenumbers $\kappa^{(r)}_{\psi=75^\circ}$ $(r = 1, 2, 3, 4)$) are shown in figure 7. As with the modal fields for $\psi = 0^\circ$, these fields are strikingly similar to $e_\perp$ in TE_1, TE_2, TE_3 and TE_4 modes in the comparison waveguide. The similarity of $e_\perp$ between the HE_n and TE_n modes persists in any propagation direction $\boldsymbol{u}_\ell$. Further, for each successive HE mode, $e_\perp$ is alternately even and odd with respect to z. However, while the correspondence of $e_\perp$ in HE and TE modes is exhibited for all HE modes studied, the same relationship is not preserved for the so-called HM modes.

In figure 8 are given $h_\perp$ versus z plots for the first four HM modes for the propagation direction delineated by $\psi = 75^\circ$. These modes correspond to the guide wavenumbers $\kappa^{(r)}_{\psi=75^\circ}$ $(r = 5, 6, 8, 9)$. The relationship between $h_\perp$ for HM_n modes in the TFHBM interconnect and TM_n modes in the comparison waveguide exhibited for $\boldsymbol{u}_\ell = \boldsymbol{u}_x$ now breaks down. In general, $h_\perp$ in the HM_n mode does not resemble $h^{\mathrm{iso}}_\perp$ for the corresponding TM_n mode. In fact, $h_\perp$ for none of the HM modes depicted is either an even or odd function of z. For the propagation direction $\boldsymbol{u}_\ell = \boldsymbol{u}_x$, the similarities exhibited between the $h_\perp$ versus z plots for HM_n and TM_n modes thus appear to be exceptional. The relationship does not hold in general; in particular, it does not hold for the other extreme case $\boldsymbol{u}_\ell = \boldsymbol{u}_y$ (i.e. $\psi = 90^\circ$).

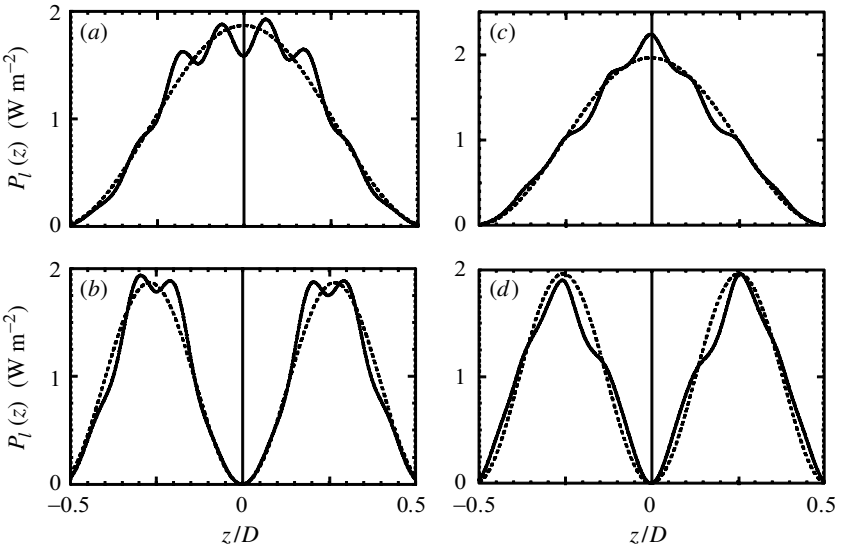

Figure 6. $P_\ell(z)$ for (a) HE_1 ($\kappa^{(1)}_{\psi=0^\circ} = 2.049k_0$), ($b$) HE_2 ($\kappa^{(2)}_{\psi=0^\circ} = 2.026k_0$), ($c$) HM_1 ($\kappa^{(6)}_{\psi=0^\circ} = 1.772k_0$) and ($d$) HM_2 ($\kappa^{(8)}_{\psi=0^\circ} = 1.747k_0$) modes for $\psi = 0^\circ$. Same parameter values as figure 1a. The dotted lines show $P^{\mathrm{iso}}_\ell(z)$ for the TE_1, TE_2, TM_1 and TM_2 modes in the comparison waveguide.

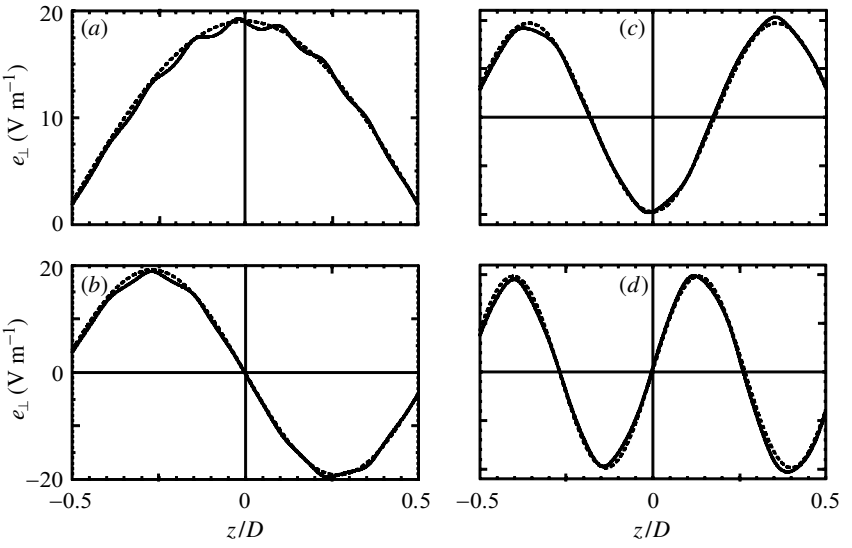

Figure 7. Magnitude of $e_\perp$ versus z for the first four HE propagation modes for $\psi = 75^\circ$: (a) HE_1, $\kappa^{(1)}_{\psi=75^\circ} = 1.988k_0$; ($b$) HE_2, $\kappa^{(2)}_{\psi=75^\circ} = 1.965k_0$; ($c$) HE_3, $\kappa^{(3)}_{\psi=75^\circ} = 1.926k_0$; ($d$) HE_4, $\kappa^{(4)}_{\psi=75^\circ} = 1.870k_0$. Same parameter values as for figure 1a. The dotted lines show $e^{\mathrm{iso}}_\perp$ for the first four TE modes in the comparison waveguide.

The modal field characteristics exhibited in general by the HE modes, and not exhibited in general by the HM modes, relate to the specific constitutive properties of the chosen TFHBM layer. Whereas its dielectric properties are anisotropic and rotationally non-homogeneous, its magnetic properties are isotropic and homo-

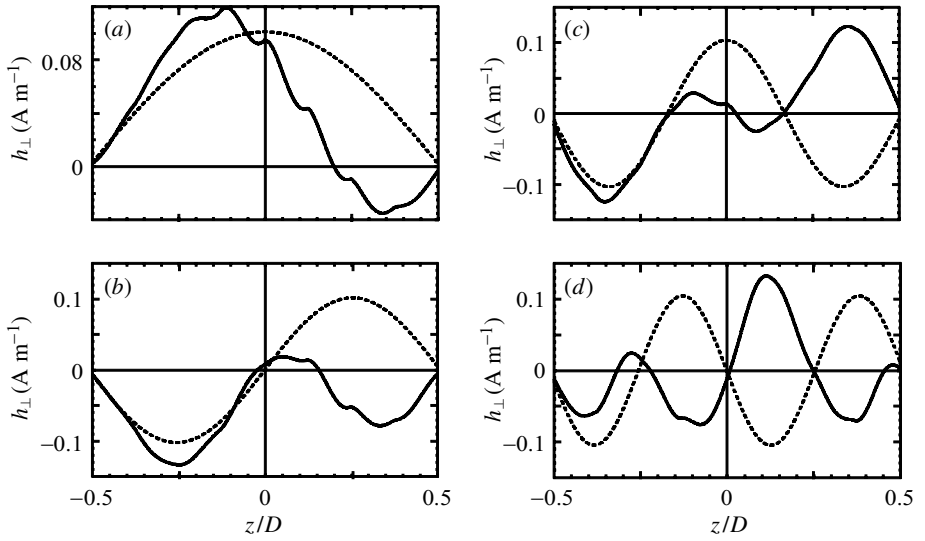

Figure 8. Magnitude of $h_\perp$ versus z in the first four HM propagation modes (normalized) for $\psi = 75°$: (*a*) HM_1, $\kappa^{(5)}_{\psi=75°} = 1.834k_0$; (*b*) HM_2, $\kappa^{(6)}_{\psi=75°} = 1.810k_0$; (*c*) HM_3, $\kappa^{(8)}_{\psi=75°} = 1.767k_0$; (*d*) HM_4, $\kappa^{(9)}_{\psi=75°} = 1.720k_0$. Same parameter values as for figure 1*a*. The dotted lines show $h^{\mathrm{iso}}_\perp$ for the first four TM modes in the comparison waveguide.

geneous. On the other hand, the comparison waveguide has isotropic dielectric and magnetic properties. We know that even in a homogeneous uniaxial crystal, the two types of characteristic planewaves (ordinary and extraordinary (Chen 1993)) cannot be transformed into one another. In contrast, in an isotropic dielectric material, that transformation can be affected very easily by virtue of duality. Still, power transmission profiles provide the means of classification of modes in the proposed TFHBM interconnects.

In figure 9, we show the power transmission profiles $P_\ell(z)$ for the HE_1, HE_2, HE_3 and HE_4 modes with wavenumbers $\kappa^{(r)}_{\psi=75°}$ $(r = 1, 2, 3, 4)$. In figure 10, $P_\ell(z)$ curves are provided for the HM_1, HM_2, HM_3 and HM_4 modes with wavenumbers $\kappa^{(r)}_{\psi=75°}$ $(r = 5, 6, 8, 9)$. In both figures, the dashed lines correspond to the power distributions for the corresponding TE and TM modes in the comparison waveguide. Figure 9 illustrates that power transmission profiles for the HE_n mode and the TE_n mode are similar. Likewise, power distributions for HM_n modes and TM_n modes are comparable. These relationships exist for all modes in any propagation direction $\boldsymbol{u}_\ell$. The power transmission profiles thus establish a consistent robust mechanism for modal classification of all propagation modes supported by the TFHBM interconnects.

Our numerical studies uncovered other general characteristics of the modal fields in TFHBM interconnects as well. For any given mode except for those with very smallest guide wavenumbers $\kappa^{(r)}_\psi$ (e.g. $r > 10$, plots for which are not depicted here), the inequalities $\{e_\ell \ll e_\perp, e_z\}$ and $\{h_\ell \ll h_\perp, h_z\}$ hold. For $r > 10$, all field components are comparable in magnitude. A notable difference between a TFHBM interconnect and an isotropic planar waveguide is that the modes $\kappa^{(1)}_{\mathrm{iso}}, \kappa^{(2)}_{\mathrm{iso}}, \kappa^{(3)}_{\mathrm{iso}}, \ldots,$ are alternately TE and TM in the latter, but this pattern does not hold in the former. Indeed, there appears to be no discernible relationship in the ordering of HE and HM modes in TFHBM interconnects. For instance, in the $\psi = 0°$ direction, the modes

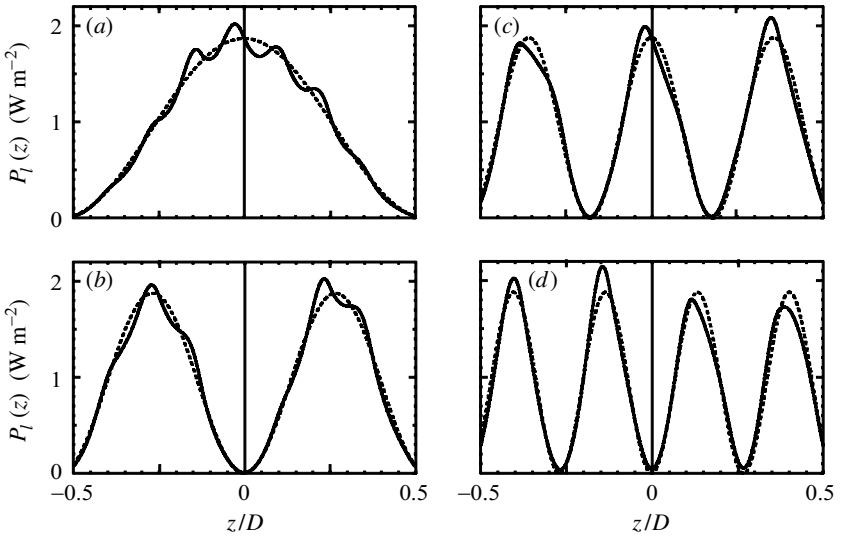

Figure 9. $P_\ell(z)$ for(*a*) HE_1, $\kappa^{(1)}_{\psi=75^\circ} = 1.988k_0$, (*b*) HE_2, $\kappa^{(2)}_{\psi=75^\circ} = 1.965k_0$, (*c*) HE_3, $\kappa^{(3)}_{\psi=75^\circ} = 1.926k_0$, (*d*) HE_4, $\kappa^{(4)}_{\psi=75^\circ} = 1.870k_0$ modes for $\psi = 75^\circ$. Same parameter values as for figure 1*a*. The dotted lines show $P^{\mathrm{iso}}_\ell(z)$ for the TE_1, TE_2, TE_3 and TE_4 modes in the comparison waveguide.

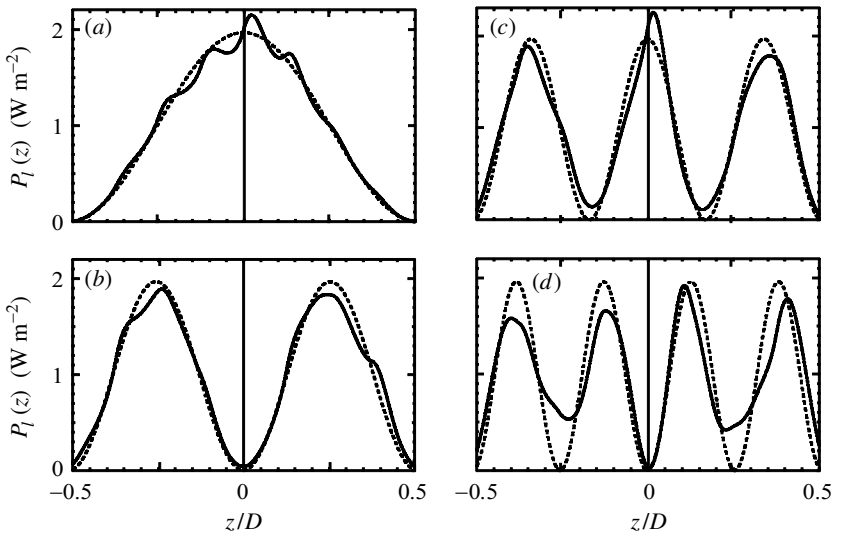

Figure 10. $P_\ell(z)$ for (*a*) HM_1, $\kappa^{(5)}_{\psi=75^\circ} = 1.834k_0$, (*b*) HM_2, $\kappa^{(6)}_{\psi=75^\circ} = 1.810k_0$, (*c*) HM_3, $\kappa^{(8)}_{\psi=75^\circ} = 1.767k_0$, (*d*) HM_4, $\kappa^{(9)}_{\psi=75^\circ} = 1.720k_0$ modes for $\psi = 75^\circ$. Same parameter values as for figure 1*a*. The dotted lines show $P^{\mathrm{iso}}_\ell(z)$ for the TM_1, TM_2, TM_3 and TM_4 modes in the comparison waveguide.

for $\kappa^{(r)}_{\psi=0^\circ}$ $(r = 1, \ldots, 5, 7)$ are HE and those for $\kappa^{(r)}_{\psi=0^\circ}$ $(r = 6, 8, 9, 10)$ are HM. On the other hand, in the $\psi = 75^\circ$ direction, the HE modes are associated with $\kappa^{(r)}_{\psi=75^\circ}$ $(r = 1, \ldots, 4, 7)$ and the HM modes with $\kappa^{(r)}_{\psi=75^\circ}$ $(r = 5, 6, 8, 9)$.

A general lack of symmetry about the central plane $z = 0$ is obvious in figures 2–10,

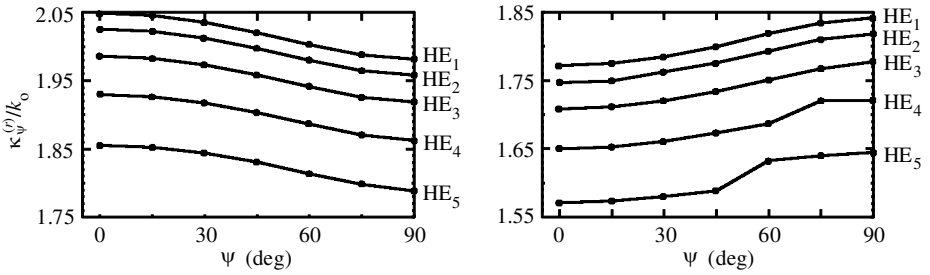

Figure 11. Guide wavenumbers $\kappa_\psi^{(r)}$ as a function of ψ for (a) the first five HE modes and (b) the first five HM modes, in a TFHBM interconnect. Same parameter values as for figure 1a.

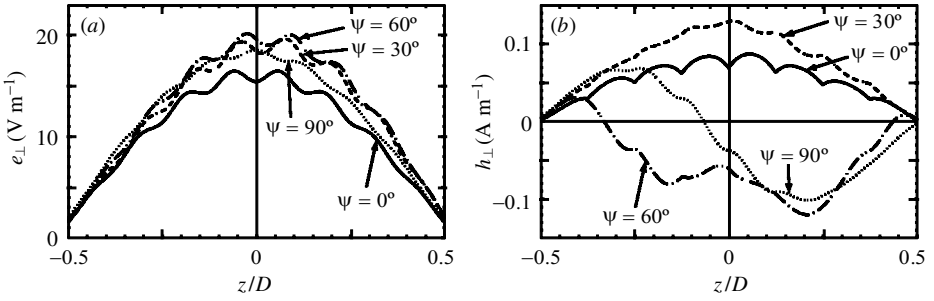

Figure 12. Magnitudes of (a) $e_\perp$ versus z for HE_1 modes and (b) $h_\perp$ versus z for HM_1 modes, in a TFHBM interconnect. Same parameter values as for figure 1a.

being more pronounced in some plots than in others. This is because

$$\underline{\underline{\epsilon}}(z,\omega) \neq \underline{\underline{\epsilon}}(-z,\omega) \quad \forall z \in [-\tfrac{1}{2}D, \tfrac{1}{2}D],$$

which inequality follows from (2.2). In the limit $\Omega \to \infty$, the inequality changes to an equality (i.e. $\underline{\underline{\epsilon}}(z,\omega) \to \underline{\underline{\epsilon}}(-z,\omega)\ \forall z \in [-\frac{1}{2}D, \frac{1}{2}D]$), which is the reason for the occurrence of the even and the odd symmetries of the modal fields with respect to z in the comparison waveguide.

(c) *Space-guide*

Thus far, we have only hinted at the *space-guide* concept: the capacity of the proposed TFHBM interconnect to simultaneously support propagation modes with different phase velocities $\omega/\kappa_\psi^{(r)}$ in different directions. This feature, which can make the proposed TFHBM interconnect an efficient transport mechanism for signals, is now established in detail.

The variation of κ_ψ^r with ψ for a given mode of order $n \leqslant 5$ (i.e. HE_n or HM_n) is displayed in figure 11 for a particular interconnect. The $\kappa_\psi^{(r)}$ values for any HE_n or HM_n mode are strongly dependent on ψ. Let us take the HE_1 mode, for instance. The guide wavenumber decreases monotonically from $2.049k_0$ for $\psi = 0°$ to $1.982k_0$ for $\psi = 90°$. In contrast, the guide wavenumber increases from $1.772k_0$ for $\psi = 0°$ to $1.842k_0$ for $\psi = 90°$ for the HM_1 mode. These variations hold for all the other modes in figure 11 and reflect the apparent randomness in the ordering of HE and HM modes with the index r in any fixed propagation direction $\boldsymbol{u}_\ell$.

In figure 12 are provided the $e_\perp$ versus z plots for the HE_1 modes and the $h_\perp$ versus z plots for the HM_1 modes, for propagation directions specified by $\psi = 0$, 30,

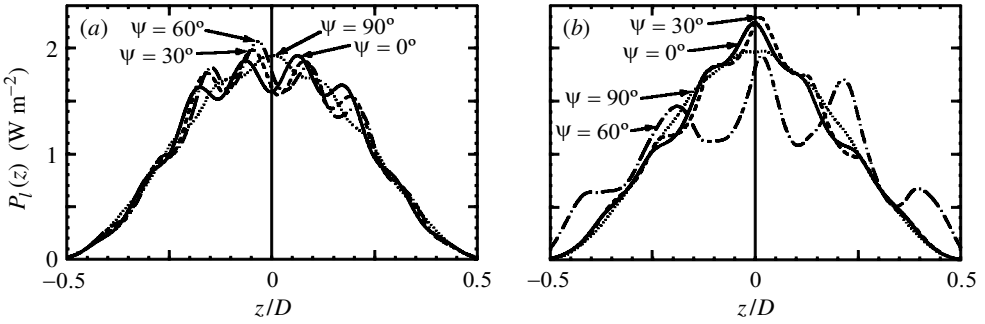

Figure 13. $P_\ell(z)$ versus z for (a) HE_1 and (b) HM_1 modes, in a TFHBM interconnect. Same parameter values as for figure 1a.

60 and 90°. While there are some differences which arise from the anisotropy and the non-homogeneity of the TFHBM, the variation of $e_\perp$ with respect to z is comparable in all directions. Thus it appears that all HE_1 modes propagating in any direction $\boldsymbol{u}_\ell$ in the transverse plane of the space-guide will have similar modal characteristics. However, for the HM_1 modes, the $h_\perp$ versus z plots for the various propagation directions are distinctly dissimilar in figure 12; and the dielectric anisotropy and non-homogeneity of the space-guide impart more significant directional dependence to the mode shape.

The power transmission profiles of the HE_1 and HM_1 modes are illustrated in figure 13 for $\psi = 0$, 30, 60 and 90°. These plots are quite similar to each other for the HE_1 mode, as also are the plots for the HM_1 mode. Thus we can expect the power transmission profile for a given mode (HE_n or HM_n) to be relatively invariant with respect to the propagation direction $\boldsymbol{u}_\ell$ in the space-guide.

Clearly, the HE_n mode launched in one direction will not interfere with the HE_n mode launched in some other direction, and the same holds true for any HM_n mode, at least for small values of n. Indeed, several HE and HM modes of low order can be launched in different directions, while taking care that their guide wavenumbers are all different. Obviously, hardware requirements will put a limit on the number of channels a TFHBM space-guide can realistically support in actual circuitry.

Columnar thin films (CTFs) are obtained in the limit $\Omega \to \infty$. Being anisotropic continuums, CTFs can also serve as space-guides. However, in that context two characteristics of TFHBMs set them apart from CTFs. The first is that a finite value of Ω serves as an additional design parameter for choosing appropriately distinct modes for communication. The second characteristic is mechanical. The stress in a CTF is anisotropic in the substrate plane, being more along the x-axis than along the y-axis (Knepper & Messier 2000). This can result in vertical cleavage and fracture, particularly, for $\chi > 45°$. But the helicoidal microstructure of TFHBMs ought to resist vertical cleavage and fracture, which expectation is borne out by microindentation experiments (Seto *et al.* 1999).

4. Conclusion

We have demonstrated the potential feasibility of dielectric TFHBM layers as planar interconnects in integrated optoelectronic circuitry. We have shown that a TFHBM layer bounded by dielectric half-spaces supports guided wave propagation, with guide

wavenumbers showing a strong dependence on the propagation direction delineated by the angle ψ. Thus, due to its anisotropic non-homogeneous nature, the TFHBM interconnect behaves as a *space-guide* which can transport different signals in different directions, thereby offering efficient use of semi-conductor real-estate.

We have suggested a classification scheme for the guided modes in the TFHBM interconnect which, based primarily on the power transmission characteristics, groups the modes into two distinct classes: hybrid electric (HE) and hybrid magnetic (HM). The mode shapes and the power density profiles of these modes have been investigated. While the modal field distributions for only the HE modes appear comparable with those in isotropic planar waveguides, the power transmission profiles for both HE and HM modes are qualitatively similar to those in isotropic planar waveguides.

We thank two anonymous reviewers for several constructive comments. This work was supported in part by a US National Science Foundation Graduate Fellowship to E.E.

References

Abdulhalim, I. 1999 Analytic propagation matrix method for linear optics of arbitrary biaxial layered media. *J. Opt.* A **1**, 646–653.

Chen, H. 1993 *Theory of electromagnetic waves*. Fairfax, VA: TechBooks.

Ertekin, E. 2000 Space-guides: efficient optical interconnects made from a thin-film helicoidal bianisotropic medium. MS thesis, Pennsylvania State University, University Park, PA, USA.

Hochstadt, H. 1975 *Differential equations: a modern approach*, ch. 5. New York: Dover.

Hodgkinson, I. J. & Wu, Q. H. 1997 *Birefringent thin films and polarizing elements*. Singapore: World Scientific.

Hodgkinson, I. J., Wu, Q. H. & McPhun, A. J. 1998 Incremental-growth model for the deposition of spatially modulated thin film nanostructures. *J. Vac. Sci. Technol.* B **16**, 2811–2816.

Hodgkinson, I. J., Wu, Q. H., Lakhtakia, A. & Messier, R. 1999 Linear and circular polarization filters using sculptured thin films. *OSA Opt. Photon. News* (December issue) **10**, 30–31.

Hodgkinson, I. J., Wu, Q. H., Lakhtakia, A. & McCall, M. W. 2000*a* Spectral-hole filter fabricated using sculptured thin-film technology. *Opt. Commun.* **177**, 79–84.

Hodgkinson, I. J., Wu, Q. H., Knight, B., Lakhtakia, A. & Robbie, K. 2000*b* Vacuum deposition of chiral sculptured thin films with high optical activity. *Appl. Opt.* **39**, 642–648.

Hodgkinson, I. J., Wu, Q., Thorn, K. E. & Arnold, M. D. 2000*c* Vacuum-deposited thin film polarizing elements for use with linearly and circularly polarized light at visible and infra-red wavelengths. *Proc. SPIE* **4097**, 266–279.

Knepper, R. & Messier, R. 2000 Morphology and mechanical properties of oblique angle columnar thin films. *Proc. SPIE* **4097**, 291–298.

Lakhtakia, A. 1999 Towards sculptured thin films (STFs) as optical interconnects. *Optik* **110**, 289–293.

Lakhtakia, A. & Messier, R. F. (eds) 1999 *Engineered nanostructural films and materials*. Bellingham, WA: SPIE Optical Engineering Press.

Lakhtakia, A., Messier, R., Brett, M. J. & Robbie, K. 1996 Sculptured thin films (STFs) for optical, chemical and biological applications. *Innov. Mat. Res.* **1**, 165–176.

Lakhtakia, A., Weiglhofer, W. S. & Messier, R. F. (eds) 2000 *Complex mediums*. Bellingham, WA: SPIE Optical Engineering Press.

Marcuse, D. 1978 Modes of a symmetric slab optical waveguide in birefringent media. Part I. Optical axis not in plane of slab. *IEEE J. Quant. Electron.* **14**, 736–741.

Marcuse, D. & Kaminow, I. P. 1979 Modes of a symmetric slab optical waveguide in birefringent media. Part II. Slab with coplanar optical axis. *IEEE J. Quant. Electron.* **15**, 92–101.

Messier, R. & Lakhtakia, A. 1999 Sculptured thin films. II. Experiments and applications. *Mater. Res. Innov.* **2**, 217–222.

Messier, R., Venugopal, V. C. & Sunal, P. D. 2000 Origin and evolution of sculptured thin films. *J. Vac. Sci. Technol.* A **18**, 1538–1545.

Monteiro, O. R., Vizir, A. & Brown, I. G. 1998 Multilayer thin-films with chevron-like microstructure. *J. Phys.* D **31**, 3188–3196.

Nagle, S. F. & Lakhtakia, A. 1996 Shear axial modes in a PCTSCM. Part II. Towards transduction applications. *Sensors Actuators* A **55**, 139–147.

Robbie, K. & Brett, M. J. 1997 Sculptured thin films and glancing angle deposition: growth mechanics and applications. *J. Vac. Sci. Technol.* A **15**, 1460–1465.

Robbie, K., Brett, M. J. & Lakhtakia, A. 1995 First thin film realization of a helicoidal bianisotropic medium. *J. Vac. Sci. Technol.* A **13**, 2991–2993.

Schilling, R. J. & Harris, S. L. 2000 *Applied numerical methods for engineers using MATLAB and C*. Pacific Grove, CA: Brooks/Cole.

Seshadri, S. R. 1998 Ray model for a planar anisotropic waveguide. *J. Opt. Soc. Am.* A **15**, 972–977.

Seto, M. W., Robbie, K., Vick, D., Brett, M. J. & Kuhn, L. 1999 Mechanical response of thin films with helical microstructures. *J. Vac. Sci. Technol.* B **17**, 2172–2177.

Sodha, M. S. & Ghatak, A. K. 1977 *Inhomogeneous optical waveguides*. New York: Plenum.

Venugopal, V. C. & Lakhtakia, A. 1998 On optical rotation and ellipticity transformation by axially excited slabs of dielectric thin-film helicoidal bianisotropic mediums (TFHBMs). *Int. J. Appl. Electromagn. Mech.* **9**, 201–210.

Venugopal, V. C. & Lakhtakia, A. 2000*a* Sculptured thin films: conception, optical properties and applications. In *Electromagnetic fields in unconventional materials and structures* (ed. O. N. Singh & A. Lakhtakia). Wiley.

Venugopal, V. C. & Lakhtakia, A. 2000*b* Electromagnetic plane-wave response characteristics of non-axially excited slabs of dielectric thin-film helicoidal bianisotropic mediums. *Proc. R. Soc. Lond.* A **456**, 125–161.

Wu, A. T., Seto, M. & Brett, M. J. 2000 Capacitive SiO humidity sensors with novel microstructures. *Sensors Materials* **11**, 493–505.

Young, N. O. & Kowal, J. 1959 Optically active flourite films. *Nature* **183**, 104–105.

Structurally perturbed chiral Bragg reflectors for elliptically polarized light

Ian Hodgkinson, Qi Hong Wu, Lakshman De Silva, and Matthew Arnold

Department of Physics, University of Otago, P.O. Box 56, Dunedin, New Zealand

Akhlesh Lakhtakia and Martin McCall

Department of Physics, Imperial College, Prince Consort Road, London SW7 2BZ, UK

Received April 26, 2005; revised manuscript received June 17, 2005; accepted June 20, 2005

The structure of an inorganic chiral medium represented as a stack of identical form-birefringent layers that twist steadily with increasing thickness is perturbed by realigning a fraction of each layer to a fixed direction. Experimental results show that the resulting chiral–birefringent composite medium exhibits Bragg resonance with elliptically polarized light, and simulations indicate that Bragg reflectors can be designed for any polarization including linear. © 2005 Optical Society of America

OCIS codes: 160.1190, 260.1440, 310.1620, 310.1860.

A resurgence of interest in inorganic structurally chiral media[1,2] is in turn leading to refinement of deposition techniques. A current focus is the development of complex substrate motion algorithms for maintaining the integrity of spiral nanostructures as they grow in vacuum[3] or for the direct synthesis of new handed materials. In this Letter we report the deposition of a chiral–birefringent composite material that exhibits Bragg resonance with light of elliptical polarization (EP). We show, via simulations, that the Bragg resonance can be nanoengineered for any elliptical polarization, including the special cases of circular polarization (CP) and linear polarization (LP). Chiral–birefringent structures are common in nature,[4,5] and the work that we report here was inspired by our observations of overlapping chiral structures in the New Zealand native manuka beetle.

In Fig. 1(a) one dielectric period of a standard chiral material for CP light is shown schematically as a stack of identical birefringent layers that twist steadily with increasing thickness.[2] Each layer has physical thickness d, and the dielectric period, which is the repeat distance for the dielectric properties, has physical thickness Ω. The in-plane principal refractive indices of the layer are n_2 and n_3. The fast axis, which is parallel to axis 2, is marked on the individual layers of the chiral stack. The Bragg resonant wavelength for CP light is $\lambda_{\mathrm{Br}}=2\,n_{\mathrm{av}}\Omega$, where $n_{\mathrm{av}}=(n_2+n_3)/2$ is the average of the in-plane refractive indices. In Fig. 1(b) the standard structure has been perturbed by a realignment of part of each layer to a fixed direction. In the new structure the sublayer thicknesses are $d_A=f_A d$ and $d_B=f_B d$, where f_A is the fraction of the chiral medium A and $f_B=1-f_A$ is the fraction of the birefringent material B. The new structure (b) has the same average refractive index and the same dielectric period as structure (a), and hence the same Bragg wavelength. However, whereas the layer axes of structure (a) are uniformly twisted as is appropriate for resonance with CP light, medium B imposes a pair of fixed axes upon structure (b). The intended optical effect is Bragg resonance for EP light rather than CP light.

The apparatus that we used for computer-controlled serial bideposition[2] of test layers of inorganic chiral–birefringent composite material in vacuum is shown schematically in Fig. 2. A form-birefringent sublayer of material A, for example, is grown by depositing thickness $d_A/2$ at fixed vapor angle θ_v and azimuthal angle ξ followed by the same thickness at azimuthal angle $\xi+\pi$. Such a sublayer has principal axis 1 perpendicular to the substrate, axis 2 (the fast axis) in the deposition plane and parallel to the substrate, and axis 3 (the slow axis) perpendicular to the deposition plane. Composite chiral–birefringent materials emulating the structure that is illustrated in Fig. 1(b) were fabricated by engaging the angular sequence for ξ,

$$0,\pi;0,\pi;\Delta\xi,\Delta\xi+\pi;0,\pi;2\Delta\xi,2\Delta\xi+\pi;0,\pi;\ldots,$$

and depositing the appropriate thicknesses.

Figure 3 illustrates the fiber-optic reflectometer that we used for measuring the copolarized reflectance of chiral–birefringent composite coatings. The fixed Fresnel rhomb provides a phase retardation of

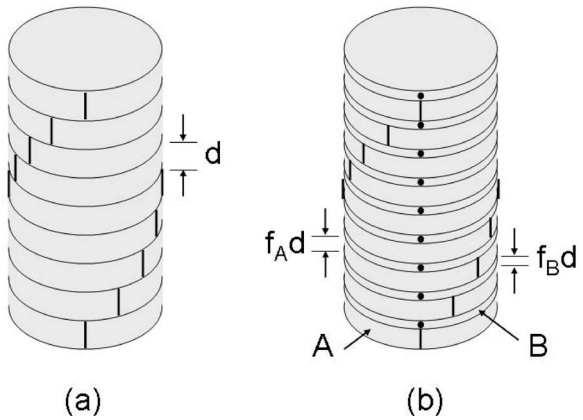

Fig. 1. One dielectric period of (a) a standard chiral structure represented as a twisted stack of birefringent layers and (b) a chiral–birefringent composite material with the same Bragg wavelength. The bars and dots mark the fast axes of the layers and sublayers, respectively.

0146-9592/05/192629-3/$15.00

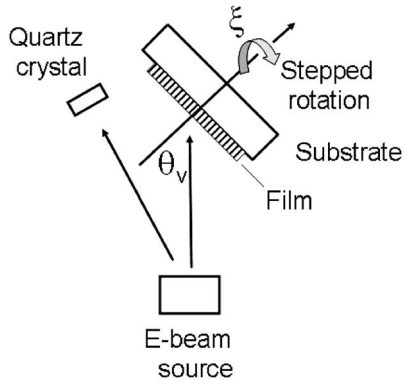

Fig. 2. Apparatus for depositing chiral–birefringent composite materials.

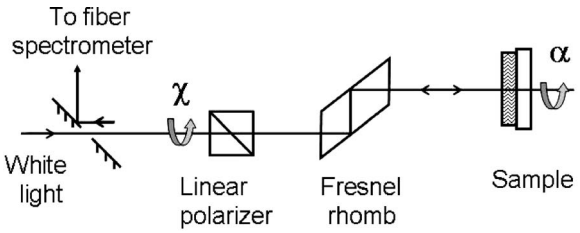

Fig. 3. Apparatus for recording the copolarized reflectance of chiral–birefringent composite coatings.

$\pi/2$, independent of visible wavelength,[6] between the horizontal and vertical components of the incident light transmitted by the linear polarizer. It follows that the combination of the linear polarizer and the Fresnel rhomb acts as an elliptical polarizer for the incident light and as an analyzer set to the same elliptical state for the reflected light. By adjusting the angle of the polarizer within the range $-\pi/4 \leqslant \chi \leqslant \pi/4$ of auxiliary angle χ, and the angle of the sample within the range $-\pi/2 \leqslant \alpha \leqslant \pi/2$ of azimuthal angle α, we can determine the copolarized reflectance experimentally for all independent polarizations.[6] Note that (i) $\chi = \pm \tan^{-1}(b/a)$, where a and b are the major and minor axes of the polarization ellipse, respectively, $\chi = -\pi/4$ corresponds to left-handed CP, $-\pi/4 < \chi < 0$ to left-handed EP, $\chi = 0$ to LP, $0 < \chi < \pi/4$ to right-handed EP, $\chi = \pi/4$ corresponds to the right-handed CP state, and (ii) α specifies the orientation of the polarization ellipse with respect to the sample.

To illustrate the concept of a Bragg medium optimized for elliptically polarized light we consider a right-handed chiral–birefringent composite film that we fabricated from titania using the following parameters: deposition rate 1 nm/s, substrate temperature 300°C, background pressure of oxygen 1.5×10^{-4} Torr, $\theta_v = 63°$, $\Delta\xi = 14.4°$, $f_B = 0.3$, sublayer thicknesses chosen to yield a visible Bragg resonance, $N = 12$ dielectric periods, cover refractive index $n_C = 1$, and substrate refractive index $n_S = 1.52$. Copolarized spectra reflected from the sample, and observed in real time as the polarizer and the sample were rotated manually, revealed strong dependence on λ, χ, and α. At resonance the Bragg peak appeared as a single peak with sidebands as shown in Fig. 4, and the Bragg wavelength was estimated as $\lambda_{Br} = (577 \pm 3)$ nm, and the peak reflectance was estimated as ≈ 0.3. Following these preliminary observations maps of copolarized reflectance covering all independent polarization states were recorded at the Bragg wavelength (Fig. 5). From a set of eight equivalent maps, recorded during a $2\pi \times 2\pi$ scan of the polarizer and the sample, we determined the polarization parameters of the EP Bragg resonance as $\chi_{Br} = (16 \pm 3)°$ and $\alpha_{Br} = (1 \pm 3)°$.

Further values relating to the structure were estimated as follows. A stylus instrument was used to measure the total thickness of the 12-period coating with the result 1975 nm, and hence $\Omega \approx 165$ nm, $d_A \approx 9.2$ nm, and $d_B \approx 4.0$ nm. Using the equation $\lambda_{Br} = 2n_{av}\Omega$, we obtained $n_{av} \approx 1.75$, and a simulation of the optical properties, using Berreman 4×4 matrix algebra,[7] required $n_3 - n_2 \approx 0.07$ to yield the experimental value of the peak reflectance at the Bragg resonance. A plot of normalized copolarized reflectance versus χ for wavelength λ_{Br} and with the azimuthal angle of the sample set at α_{Br} is shown for the composite coating in Fig. 6(a). Such a characteristic reflectance profile shows that the EP Bragg resonance is twice as large as the corresponding reflectance with CP light.

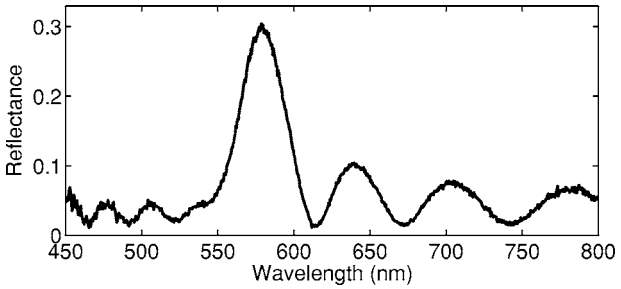

Fig. 4. Copolarized reflectance spectrum recorded for a right-handed birefringent–chiral composite coating with fabrication parameters $\theta_v = 63°$, $\Delta\xi = 14.4°$, $f_B = 0.3$, $N = 12$, $n_C = 1$, and $n_S = 1.52$.

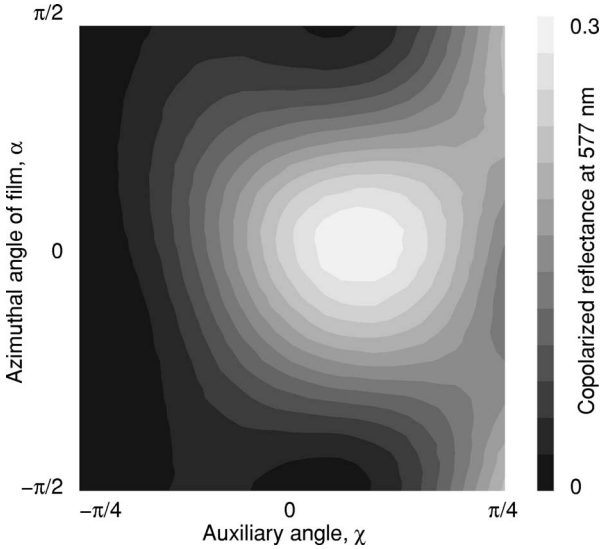

Fig. 5. Copolarized reflectance map recorded for a right-handed chiral–birefringent composite coating with fabrication parameters $\theta_v = 63°$, $f_B = 0.3$, $N = 12$, and $n_C = 1$, $n_S = 1.52$.

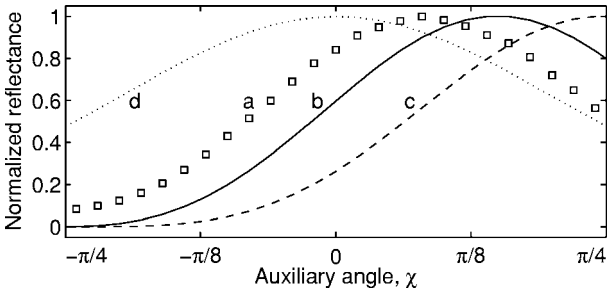

Fig. 6. Normalized copolarized reflectance profiles recorded at λ_{Br}, α_{Br} for (a) the chiral–birefringent composite coating fabricated with $f_B=0.3$, $N=12$, air and glass bounding media; (b) a simulation of a similar coating with $f_B=0$, $N=12$; (c) an index-matched simulation with $f_B=0$, $N=50$ that positions the Bragg resonance at $\chi=\pi/4$ (right-handed CP); and (d) an index-matched simulation with $f_B=0.5$, $N=50$ that positions the Bragg resonance at $\chi=0$ (LP).

Simulations show that the polarization and strength of the Bragg resonance (from either structure in Fig. 1) may be influenced by spurious reflections associated with mismatch of the refractive indices of the cover, film, and substrate. Relevant to our discussion here a simulation [Fig. 6(b)] with $f_B=0$, $n_{av}=1.75$, $n_3-n_2=0.07$, $n_C=1$, $n_S=1.52$, $N=12$ yields $\chi_{Br}=27°$, a value that is significantly larger than the experimental value with $f_B=0.3$. The perturbed structure in Fig. 1(b), in which the axes of the sublayers of A and B are parallel at the start of the dielectric period, is optimized for maximum peak reflectance and minimum $|\chi_{Br}|$ for a given f_B. In principle spurious reflections can be reduced to negligible levels by index matching or with phase- and amplitude-matched antireflection coatings.[2,8] In a range of simulations of right-handed composite structures with $n_3-n_2=0.07$, $N=50$, and with spurious reflections eliminated by index matching ($n_C=n_{av}=n_S=1.52$) we were able to position the Bragg resonance anywhere within the range $0\leqslant\chi_{Br}\leqslant\pi/4$ by choosing f_B from the range $0\leqslant f_B\leqslant 0.5$. Characteristic reflectance profiles simulated for the CP and LP cases are shown in Figs. 6(c) and 6(d).

Additional insight into the perturbed chiral structure can be obtained by expressing it as a sequence of twisted birefringent sublayers A_j and aligned birefringent sublayers B, … $BA_{j-1}BA_jBA_{j+1}B$ …, and then rearranging as a sequence of symmetric Herpin periods with general structure $(B/2)A_j(B/2)$. Each Herpin period can be replaced by an equivalent sublayer C_j, with effective principal axes and effective principal refractive indices.[7] Application of the method to the chiral–birefringent coating that we have discussed in this Letter shows that the equivalent medium C is basically right-handed but with out-of-phase oscillations of approximate amplitude 0.01 on the in-plane effective refractive index values and with an oscillation of approximate amplitude 15° on the azimuthal angle of the effective fast axis.

In conclusion, we have described a structural perturbation that changes the polarization of Bragg resonance of a chiral reflector from circular to elliptical. In principle any desired polarization, circular, elliptical, or linear, can be nanoengineered for the resonance. The new materials may expand the scope of existing and developing areas where handed materials are employed, such as chiral fiber Bragg gratings[9] and chiral photonic defect-mode lasers.[10]

Financial support for this project was received from the New Zealand New Economy Research Fund (contract CO8814) and from the MacDiarmid Institute for Advanced Materials and Nanotechnology. Ian Hodgkinson's e-mail address is ijh@physics.otago.ac.nz.

References

1. A. Lakhtakia and R. Messier, *Sculptured Thin Films: Nanoengineered Morphology and Optics*, Press Monograph PM143 (SPIE, 2005).
2. Q. H. Wu, I. J. Hodgkinson, and A. Lakhtakia, Opt. Eng. (Bellingham) **39**, 1863 (2000).
3. S. R. Kennedy and M. J. Brett, J. Vac. Sci. Technol. B **22**, 1184 (2004).
4. A. C. Neville, *Biology of Fibrous Composites: Development Beyond the Cell Membrane* (Cambridge U. Press, 1993).
5. M. Srinivasarao, Chem. Rev. (Washington, D.C.) **99**, 1935 (1999).
6. M. Born and E. Wolf, *Principles of Optics* (Pergamon, 1980).
7. I. J. Hodgkinson and Q. H. Wu, *Birefringent Thin Films and Polarizing Elements* (World Scientific, 1998).
8. I. J. Hodgkinson, Q. H. Wu, M. Arnold, M. W. McCall, and A. Lakhtakia, Opt. Commun. **210**, 201 (2002).
9. A. Z. Genack, V. I. Kopp, V. M. Churikov, J. Singer, N. Chao, and D. Neugroshl, Proc. SPIE **5508**, 57 (2004).
10. J. Schmidtke, W. Stille, and H. Finkelmann, Phys. Rev. Lett. **90**, 083902 (2003).

Available online at www.sciencedirect.com
SCIENCE DIRECT®
Optics Communications 251 (2005) 10–22
OPTICS COMMUNICATIONS
www.elsevier.com/locate/optcom

Sculptured nematic thin films with periodically modulated tilt angle as rugate filters

John A. Polo Jr. [a,*], Akhlesh Lakhtakia [b,1]

[a] Department of Physics and Technology, Edinboro University of Pennsylvania, Edinboro, PA 16444, USA
[b] CATMAS — Computational and Theoretical Materials Sciences Group, Department of Engineering Science and Mechanics, Pennsylvania State University, University Park, PA 16802, USA

Received 9 October 2004; accepted 25 February 2005

Abstract

The reflectances and transmittances of linearly polarized light are calculated using the piecewise homogeneity approximation for a sculptured nematic thin film (SNTF) with a sinusoidally varying (local) columnar tilt angle. Empirical data on TiO_2, available in the literature, are used to realistically model the variation of the permittivity dyadic with the tilt angle. Wave propagation is taken to occur in the morphologically significant plane of the SNTF. Several Bragg peaks occur, with the fundamental peak making a tilt-modulated SNTF suitable for exploitation similarly to a rugate filter. Additionally, the appearance of a spectral hole in the fundamental Bragg peak is demonstrated with the inclusion of a central defect layer.

PACS: 77.55.+f; 78.20.Ek; 78.20.Fm; 78.66.−w

Keywords: Nanowire assemblies; Nematic morphology; Rugate filter; Spectral hole; Sculptured thin film

1. Introduction

The optical properties of sculptured thin films (STFs) have been studied now for some time. Many potential uses have been proposed and some of them have been realized, as becomes clear from three review chapters [1–3]. Most of the research effort, however, has concentrated on *chiral* STFs, which are assemblies of helical nanowires, and exhibit the circular Bragg phenomenon [4,5]. In contrast, little theoretical work has been done on sculptured *nematic* thin films (SNTFs) which are assemblies of nanowires whose morphology

* Corresponding author. Tel.: +1 814 7322655; fax: +1 814 7322455.
E-mail addresses: polo@edinboro.edu (J.A. Polo Jr.), axl4@psu.edu (A. Lakhtakia).
[1] Tel.: +1 814 863 4319; fax: +1 814 865 9974.

0030-4018/$ - see front matter © 2005 Elsevier B.V. All rights reserved.
doi:10.1016/j.optcom.2005.02.075

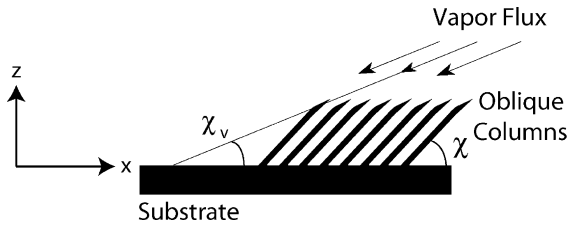

Fig. 1. Tilt angle χ and vapor incidence angle χ_v for a columnar thin film.

evolves during fabrication essentially in just two dimensions, although such films have been grown for more than a decade [6,7].

The nanowires of a STF grow when a highly collimated vapor is directed at a substrate at suitable temperature and pressure [2]. As shown in Fig. 1, when the substrate is stationary and the average directionality of the vapor flux is fixed, the nanowires grow at an angle with respect to the substrate plane [8–10]. A thin film comprising parallel straight nanowires is called a columnar thin film (CTF). The tilt angle χ of the straight nanowires, in general, is larger than the vapor incidence angle χ_v. By changing χ_v during deposition, the nanowires can be shaped to a wide variety of two-dimensional curves in order to produce SNTFs [7].[2]

Some of the SNTF morphologies already produced include chevrons and S-shaped nanowires [6,7,11]. If the dielectric properties in a SNTF vary periodically along the z-axis (i.e., normal to the substrate plane), then this film should exhibit the linear Bragg phenomenon when interrogated by a normally incident plane wave [10,12]. In particular, SNTFs are natural candidates for making rugate filters [13,14] using thin-film technology, as has been shown theoretically for *canonical* SNTFs [15,16] and experimentally for other types of SNTFs [11,17,18]. Generally, the variation of a pertinent refractive index with respect to z is sinusoidal in rugate filters [11,13,14].

To our knowledge, most theoretical analyses either modeled the SNTFs as being isotropic with only a periodically changing refractive index [17,18] or ignored the complications arising in the anisotropic permittivity tensor owing to continuous changes in χ_v [15,16]. The sole exception is a short communication from McPhun et al. [11], wherein a reasonable attempt was made to accommodate the structural and dielectric properties of real SNTFs. However, the treatments in all foregoing references were confined to normally incident plane waves.

Attention is focused in this paper on the responses of SNTFs to linearly polarized plane waves propagating in the morphologically significant plane (i.e., the xz plane). The chosen STFs are supposed to be fabricated by varying the vapor incidence angle sinusoidally as a function of film thickness during deposition, i.e., χ_v is a sinusoidal function of z. We use an experimentally deduced relationship between χ_v and the permittivity dyadic of the SNTF to capture the optical consequences of the resultant morphology of the nanowires [19], and we determine the reflectances and transmittances of the film using the piecewise homogeneity approximation technique [1,4]. Although our calculations were carried out for TiO_2 SNTFs, using empirical relations for TiO_2 CTFs developed by Hodgkinson et al. [19], qualitatively similar conclusions should hold for similar SNTFs made of other materials.

After establishing the planewave response characteristics of the sinusoidally tilt-modulated SNTFs, we turn our attention to the effects of introducing a defect in the middle of the film. As has been demonstrated with isotropic periodic thin films [20,21], cholesteric liquid crystals [22], chiral STFs [23,24], and slanted chiral STFs [25], suitable defects can produce narrow spectral reflection holes in Bragg regimes. We explore the characteristics of the spectral hole in terms of various deposition and geometric parameters.

The remainder of this paper is organized as follows: in Section 2, the matrix differential equation for wave propagation in the morphologically significant plane (the xz plane) of a SNTF is developed. The details of the tilt-modulation are presented in Section 3 along with the related variations in the permittivity dyadic of the SNTF. Calculated spectrums of the reflectances are presented in Section 4 for a range of parameters. Section 5

[2] Chiral STFs require a rotation of the substrate about an axis perpendicular to the substrate.

contains an explication of the effects of introducing a defect layer in the middle of the SNTF and characterizes its effect for various situations. Concluding remarks are made in Section 6.

2. Matrix ordinary differential equation

With varying χ_v and the assumption of purely linear and dielectric response properties, the constitutive relations of a SNTF are

$$\underline{D}(\underline{r}) = \underline{\underline{\epsilon}}(z) \cdot \underline{E}(\underline{r}) = \epsilon_0 \underline{\underline{S}}_y \cdot \underline{\underline{\epsilon}}^0_{\text{ref}} \cdot \underline{\underline{S}}_y^{-1} \cdot \underline{E}(\underline{r}), \tag{1}$$

$$\underline{B}(\underline{r}) = \mu_0 \underline{H}(\underline{r}), \tag{2}$$

where ϵ_0 and μ_0 are the permittivity and permeability of free space. The unitary dyadic $\underline{\underline{S}}_y$ describing the nanowire tilt as a function of z is written as

$$\underline{\underline{S}}_y = (\underline{u}_x\underline{u}_x + \underline{u}_z\underline{u}_z)\cos\chi + (\underline{u}_z\underline{u}_x - \underline{u}_x\underline{u}_z)\sin\chi + \underline{u}_y\underline{u}_y, \tag{3}$$

where $\chi \equiv \chi(z)$, and $\underline{u}_x$, $\underline{u}_y$ and $\underline{u}_z$ are the Cartesian unit vectors. The permittivity dyadic of any STF is locally orthorhombic [1]; hence,

$$\underline{\underline{\epsilon}}^0_{\text{ref}} = \epsilon_a \underline{u}_z\underline{u}_z + \epsilon_b \underline{u}_x\underline{u}_x + \epsilon_c \underline{u}_y\underline{u}_y. \tag{4}$$

As $\underline{\underline{\epsilon}}^0_{\text{ref}}$ is a function of χ_v [7,19], it is also a function of z. Furthermore, $\underline{\underline{\epsilon}}^0_{\text{ref}}$ depends on the angular frequency ω of the incident electromagnetic field.

In order to determine the planewave response of a SNTF of thickness L, the constitutive relations (1) and (2) are substituted into the frequency-domain Maxwell curl postulates

$$\left.\begin{aligned} \nabla \times \underline{E}(\underline{r}) &= \mathrm{i}\omega\mu_0 \underline{H}(\underline{r}) \\ \nabla \times \underline{H}(\underline{r}) &= -\mathrm{i}\omega \underline{\underline{\epsilon}}(z) \cdot \underline{E}(\underline{r}) \end{aligned}\right\}, \quad 0 < z < L, \tag{5}$$

where an $\exp(-\mathrm{i}\omega t)$ time-dependence is implicit. Consistently with the assumption of the incident planewave propagating in the xz plane, the fields inside the SNTF are expressed in terms of their Fourier amplitudes, relative to variation in the x direction, as

$$\underline{E}(\underline{r}) = [e_x(z,k)\underline{u}_x + e_y(z,k)\underline{u}_y + e_z(z,k)\underline{u}_z]\exp(\mathrm{i}kx), \tag{6}$$

$$\underline{H}'(\underline{r}) = [h_x(z,k)\underline{u}_x + h_y(z,k)\underline{u}_y + h_z(z,k)\underline{u}_z]\exp(\mathrm{i}kx), \tag{7}$$

where k is the transverse wavenumber determined by the incidence conditions.

Eqs. (5) then separate into two algebraic equations and four ordinary differential equations (ODEs). The two algebraic equations are

$$\begin{aligned} e_z(z) &= \tfrac{(\epsilon_a-\epsilon_b)}{2\epsilon_a\tau}\sin 2\chi\, e_x(z) - \tfrac{k}{\omega\epsilon_0\epsilon_a\tau} h_y(z), \\ h_z(z) &= \tfrac{k}{\omega\mu_0} e_y(z), \end{aligned} \tag{8}$$

where

$$\tau = \cos^2\chi + \frac{\epsilon_b}{\epsilon_a}\sin^2\chi. \tag{9}$$

The four coupled ODEs can be represented compactly as the matrix ODE [15,16,26,27]

$$\frac{\mathrm{d}}{\mathrm{d}\zeta}\left[\underline{f}(\zeta)\right] = \frac{\mathrm{i}\Omega}{\pi}\left[\underline{\underline{P}}(\zeta)\right] \cdot \left[\underline{f}(\zeta)\right]. \tag{10}$$

In anticipation of the periodicity to be imposed in Section 3, the matrix ODE (10) has been written in terms of the normalized coordinate

$$\zeta = \pi z/\Omega, \tag{11}$$

where Ω is the half-period of the sinusoidal variation of $\chi_v(z)$. The x- and y-directed components of the electromagnetic field phasors are arranged in the column vector

$$\left[\underline{f}(\zeta)\right] = \begin{bmatrix} e_x(\zeta) \\ e_y(\zeta) \\ h_x(\zeta) \\ h_y(\zeta) \end{bmatrix}. \tag{12}$$

The 4×4 kernel matrix on the right side of (10) is

$$\left[\underline{\underline{P}}(\zeta)\right] = \begin{bmatrix} -\tilde{A}\sin 2\chi & 0 & 0 & \omega\mu_0 - \tilde{B} \\ 0 & 0 & -\omega\mu_0 & 0 \\ 0 & \tilde{C} - \tilde{F}_3 & 0 & 0 \\ \tilde{F}_2 - \tilde{F}_1\sin^2 2\chi & 0 & 0 & -\tilde{A}\sin 2\chi \end{bmatrix},$$

where

$$\tilde{A} = \frac{k(\epsilon_b - \epsilon_a)}{2\epsilon_a \tau}, \quad \tilde{B} = \frac{k^2}{\omega \epsilon_0 \epsilon_a \tau},$$
$$\tilde{C} = \frac{k^2}{\omega \mu_0}, \quad \tilde{F}_1 = \frac{\omega \epsilon_0 (\epsilon_b - \epsilon_a)^2}{4\epsilon_a \tau},$$
$$\tilde{F}_2 = \omega \epsilon_0 \epsilon_b \tilde{\tau}, \quad \tilde{F}_3 = \omega \epsilon_0 \epsilon_c, \quad \tilde{\tau} = \cos^2\chi + \frac{\epsilon_a}{\epsilon_b}\sin^2\chi. \tag{13}$$

In order to solve the boundary value problem necessary to determine the reflectances and the transmittances, it is convenient to recast the formulation in terms of a 4×4 matrix $[\underline{\underline{M}}(\zeta)]$ (called the matrizant), such that [4,28]

$$\left[\underline{f}(\zeta)\right] = \left[\underline{\underline{M}}(\zeta)\right] \cdot \left[\underline{f}(0)\right]. \tag{14}$$

It then follows that:

$$\frac{\mathrm{d}}{\mathrm{d}\zeta}\left[\underline{\underline{M}}(\zeta)\right] = \frac{\mathrm{i}\Omega}{\pi}\left[\underline{\underline{P}}(\zeta)\right] \cdot \left[\underline{\underline{M}}(\zeta)\right], \tag{15}$$

subject to the boundary condition

$$\left[\underline{\underline{M}}(0)\right] = \left[\underline{\underline{I}}\right], \tag{16}$$

where $[\underline{\underline{I}}]$ is the identity matrix. Eqs. (15) and (16) constitute an initial value problem. The matrizant can be calculated by exploiting the piecewise homogeneity approximation technique [1,4], following which the reflectances and the transmittances for s- and p-polarized planewaves can be calculated for incident planewaves using standard techniques.

3. Modeling of tilt variation

Sinusoidal variation in χ_v with respect to z can be described by

$$\chi_\mathrm{v}(z) = \tilde{\chi}_\mathrm{v} + \delta_\mathrm{v}\sin(\pi z/\Omega), \tag{17}$$

where $\tilde{\chi}_\mathrm{v}$ represents the average vapor incidence angle, whereas δ_v is the amplitude and $2\,\Omega$ is the period of oscillation. When $\delta_\mathrm{v} = 0$, the SNTF is macroscopically homogeneous and Bragg phenomenons cannot occur.

In order to investigate wave propagation through a SNTF, χ_v must be related to two resultant properties of the film: the tilt angle χ and the local permittivity dyadic $\underline{\underline{\epsilon}}^0_{\mathrm{ref}}$. Empirical relationships have been determined for TiO_2 CTFs by Hodgkinson et al. [19] as follows:

$$\epsilon_a = \left[1.0443 + 2.7394\left(\frac{\chi_\mathrm{v}}{\pi/2}\right) - 1.3697\left(\frac{\chi_\mathrm{v}}{\pi/2}\right)^2\right]^2, \tag{18}$$

$$\epsilon_b = \left[1.6765 + 1.5649\left(\frac{\chi_\mathrm{v}}{\pi/2}\right) - 0.7825\left(\frac{\chi_\mathrm{v}}{\pi/2}\right)^2\right]^2, \tag{19}$$

$$\epsilon_c = \left[1.3586 + 2.1109\left(\frac{\chi_\mathrm{v}}{\pi/2}\right) - 1.0554\left(\frac{\chi_\mathrm{v}}{\pi/2}\right)^2\right]^2, \tag{20}$$

$$\tan\chi = 2.8818\tan\chi_\mathrm{v}, \tag{21}$$

where χ_v and χ are in radian. From the experimental data underlying the foregoing equations, non-polynomial expressions describing the permittivity can also be obtained [29], but the quadratic expressions sufficed for our present purpose. As stated in the introductory section, in the absence of actual data for SNTFs, we decided to apply the foregoing relations for CTFs for SNTFs as well.

Two comments must be made at this stage:

(i) When growing a columnar thin film, it is commonplace to consider the vapor as being directed from the first quadrant of the xz plane, as shown in Fig. 1; then, $\chi_\mathrm{v} \in (0, \pi/2]$ and $\chi \in (0, \pi/2]$ such that $\chi \geqslant \chi_\mathrm{v}$. However, (17) clearly accommodates $\chi_\mathrm{v} \in [\pi/2, \pi)$, which should be interpreted as the vapor being directed from the second quadrant of the xz plane. Since, (18)–(21) are symmetric about $\chi_\mathrm{v} = \pi/2$ they remain valid in the second quadrant, correctly yielding $\chi \in [\pi/2, \pi)$ such that $\chi \leqslant \chi_\mathrm{v}$; furthermore, $\epsilon_{a,b,c}$ remain invariant when $\chi_\mathrm{v} = (\pi/2) - \vartheta_\mathrm{v}$ is replaced by $\chi_\mathrm{v} = (\pi/2) + \vartheta_\mathrm{v}$ such that $\vartheta_\mathrm{v} \in [0, \pi/2)$. In summary, (18)–(21) are adequate for $\chi_\mathrm{v} \in (0, \pi)$.

(ii) The scalars $\epsilon_{a,b,c}$ are held to be independent of χ_v for canonical SNTFs [1,2]. The fabrication of a canonical SNTF requires

manipulation not only of the substrate orientation but also of the vapor flux and the deposition rate, in order to modulate the incremental porosity and density of the growing thin film. Only then can $\epsilon_{a,b,c}$ be kept invariant with respect to the changing vapor incidence angle. Canonical SNTFs are not the focus of this paper.

4. Planewave response of tilt-modulated SNTF

For all calculations presented in this section, we chose $\Omega = 75$ nm. This choice places one of the dominant features of the remittance spectrums near the free-space wavelength $\lambda_0 = 630$ nm, the same wavelength at which Hodgkinson et al. [19] performed their experiments to arrive at (18)–(21). Dispersion and dissipation are neglected here, as the required data is unavailable, but that should not seriously impair the qualitative conclusions arrived at by us. Furthermore, we set $L = 60\,\Omega$, unless otherwise noted, so that the Bragg phenomenon is well-developed.

Closed-form solutions of (15) are not known to exist under the conditions being studied here. Numerical solutions of that equation were obtained using the piecewise homogeneity approximation technique [1,4]. In this technique, the STF is partitioned into a multitude of optically thin slices parallel to the plane $z = 0$. Each slice is treated as if it has a uniform permittivity dyadic which is the same as that of the STF at the midpoint of the slice. The efficient application of this method to chiral STFs has been described elsewhere [28], and was applied by us for the chosen SNTFs. The accuracy depends on the slice thickness; based on experience, we set the slice thickness at 0.1 nm.

Using an algorithm to determine $[\underline{\underline{M}}(\zeta)]$ subject to the constraint (16), we were able to solve the boundary value problem for determining the planewave remittances (reflectances and transmittances) [30]. The eight remittances are as follows: R_{ss}, R_{sp}, R_{ps}, R_{pp}, T_{ss}, T_{sp}, T_{ps} and T_{pp}. Here, for instance, R_{ps} is the fraction of the incident power density reflected as a p-polarized planewave when the incident planewave is s-polarized. We note that $\underline{u}_y \cdot \underline{E} = 0$ (resp. $\underline{u}_y \cdot \underline{H} = 0$) for p-polarized (resp. s-polarized) planewaves in free space. The symmetries of $[\underline{\underline{P}}(\zeta)]$ enjoin that cross-polarized remittances ($R_{sp,ps}$ and $T_{sp,ps}$) are identically zero [15,16].

4.1. Normal incidence

Let the angle θ denote the angle of planewave incidence with respect to the z-axis; then

$$k = (2\pi/\lambda_0)\sin\theta, \tag{22}$$

where λ_0 is the free-space wavelength. We commence our discussion of reflectance spectrums when the normal-incidence conditions prevail, i.e., $\theta = 0$.

4.1.1. $\tilde{\chi}_v = 30°$

Calculated reflectances as functions of λ_0 are shown in Fig. 2 for both s- and p-polarizations when $\tilde{\chi}_v = 30°$ and $\delta_v = 10°$. The corresponding transmittances are not shown because $T_{pp} = 1 - R_{pp}$ and $T_{ss} = 1 - R_{ss}$ due to dissipation having been ignored in (18)–(21). Dispersion having been ignored as well, we confined ourselves to wavelengths not very far from $\lambda_0 = 630$ nm, the wavelength for which (18)–(21) are strictly valid.

The spectrums of the reflectances for both polarizations look very similar. Both exhibit prominent Bragg peaks near $\lambda_0 = 570$ nm with maximum reflectances close to unity. The Bragg regimes differ by approximately 11 nm with the peaks at roughly $\lambda_0 = 563$ nm and $\lambda_0 = 582$ nm for R_{pp} and R_{ss}, respectively. A shorter and much narrower 2nd harmonic peak at half the wavelength of the large peak can be seen in the spectrum of R_{ss} at $\lambda_0 = 289$ nm; and a 2nd harmonic peak is also visible in the R_{pp}-spectrum at $\lambda_0 = 279$ nm, although it is much weaker and barely visible above the background oscillations. We caution that the spectral location of harmonics shall be affected by dispersion, which is ignored here.

Outside the fundamental Bragg regimes (near 570-nm wavelength), both reflectance spectrums exhibit oscillations with roughly constant

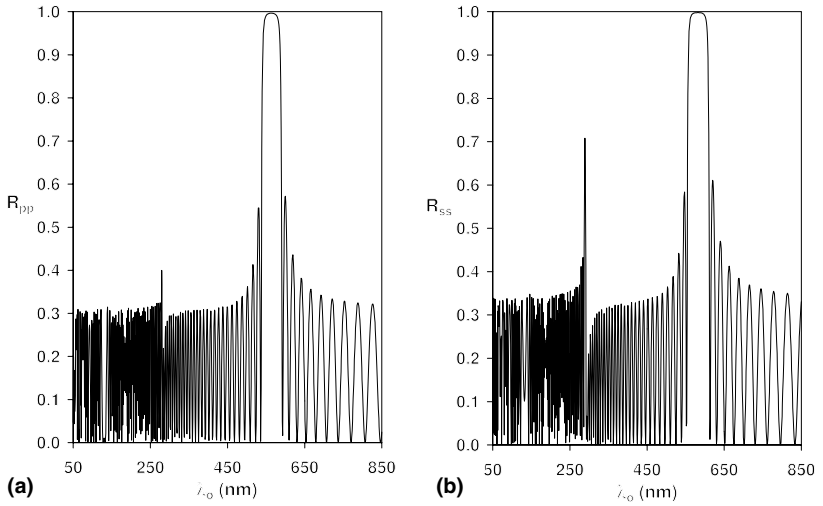

Fig. 2. Reflectance spectrums of a tilt-modulated SNTF made of TiO_2 with $\tilde{\chi}_v = 30°$, $\delta_v = 10°$, $\Omega = 75$ nm and $L = 60\,\Omega$. The incident planewave is normally directed, i.e., $\theta = 0$: (a) R_{pp}; (b) R_{ss}.

amplitude over the entire range of wavelengths displayed. One exception occurs in the wavelength-regime just above the 2nd harmonic Bragg peaks. Here, the amplitude of oscillation in the spectrum goes to zero.

Fig. 3 shows the effects of increasing the tilt-modulation amplitude to $\delta_v = 20°$. Several changes can be noted. The fundamental Bragg regimes for both polarizations broaden significantly. The reflectances saturate to a value of unity over a wavelength-regime with sharp roll-offs, the Bragg regimes thus having "top-hat" profiles. The fundamental Bragg regime for R_{pp} extends from roughly 541 to 598 nm, while that for R_{ss} from 538 to 618 nm.

The 2nd harmonic peak in the spectrum of R_{ss} also strengthens to the maximum possible, and broadens as well, in comparison with Fig. 2, but

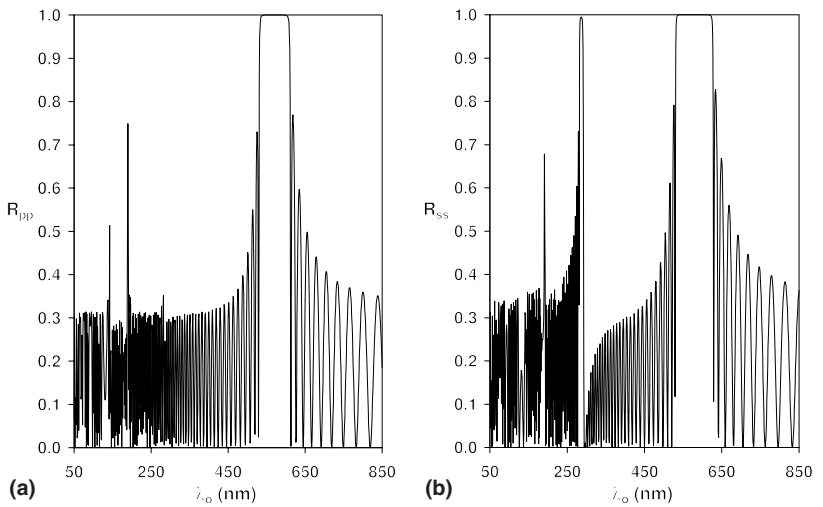

Fig. 3. Same as Fig. 2, except that $\delta_v = 20°$.

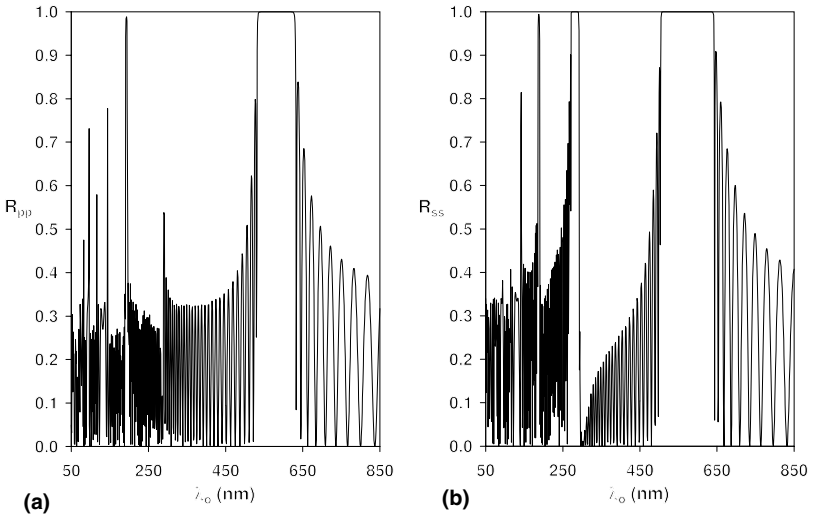

Fig. 4. Same as Fig. 2, except that $\delta_v = 30°$.

the 2nd harmonic peak in the R_{pp}-spectrum diminishes in contrast. However, extremely narrow 3rd and 4th harmonic peaks appear in the R_{pp}-spectrum at $\lambda_0 = 190$ nm and $\lambda_0 = 142$ nm, respectively. A 3rd harmonic peak is visible in the R_{ss}-spectrum, as well, at $\lambda_0 = 191$ nm. Oscillations outside the Bragg regimes also change with the increase in modulation amplitude.

The results for maximum possible modulation (i.e., $\delta_v = 30°$) are shown in Fig. 4. With the exception of the growth of the 2nd harmonic Bragg peak in the spectrum of R_{pp}, all of the trends noted when δ_v was increased from 10° to 20° continue with the further increase of δ_v to 30°.

A careful examination of results for all three levels of modulation show that the width of the fundamental Bragg regime in the R_{pp}-spectrum grows primarily on the long-wavelength side as the modulation amplitude is increased. The fundamental peak width in the R_{ss} spectrum, however, grows more symmetrically with the short-wavelength side growing slightly more than the long-wavelength side. Thus there is a slight red-shift in the fundamental Bragg regime of the R_{pp}-spectrum, and a blue-shift in the same regime of the R_{ss}-spectrum. Similar results hold for all $\chi_v \in (0, \pi/2)$; and we therefore conclude that tilt modulation provides an attractive route for increasing the bandwidth of SNTF rugate filters.

4.1.2. $\tilde{\chi}_v = 90°$

When $\tilde{\chi}_v = 90°$, we have a special case. Because the elements of the matrix $[\underline{\underline{P}}]$ are symmetric with variation of χ_v about 90°, the period of $[\underline{\underline{P}}]$ is halved. Hence, the fundamental Bragg regime must appear at about $\lambda_0 = 285$ nm. Indeed that is true, as exemplified by Fig. 5. Other numerical results, not presented here, confirm that an increase of the ratio $\delta_v/\tilde{\chi}_v$ increases the bandwidth of the fundamental Bragg regime even for $\tilde{\chi}_v = 90°$.

4.1.3. *Full modulation* ($\delta_v = \tilde{\chi}_v$)

At full modulation the film becomes highly reflective. Fig. 6(a) shows the spectrum of R_{pp}[3] for $L = 20\ \Omega$ and $\tilde{\chi}_v = \delta_v = 90°$. Even at this small thickness ($L = 20\ \Omega$), the fundamental Bragg peak is not only well-defined, but has saturated over a substantial wavelength range with rapid roll-off at both edges. The 2nd and 3rd harmonic peaks are also quite strong with heights greater than 0.95. Although not shown, even for 10 Ω-thickness the fundamental Bragg peak very nearly reaches unit height.

Full modulation at other values of $\tilde{\chi}_v$ show similarly strong fundamental Bragg peaks, although not to the degree exhibited when $\tilde{\chi}_v = 90°$. For

[3] The spectrum of R_{ss} can be used equivalently, to the same effect.

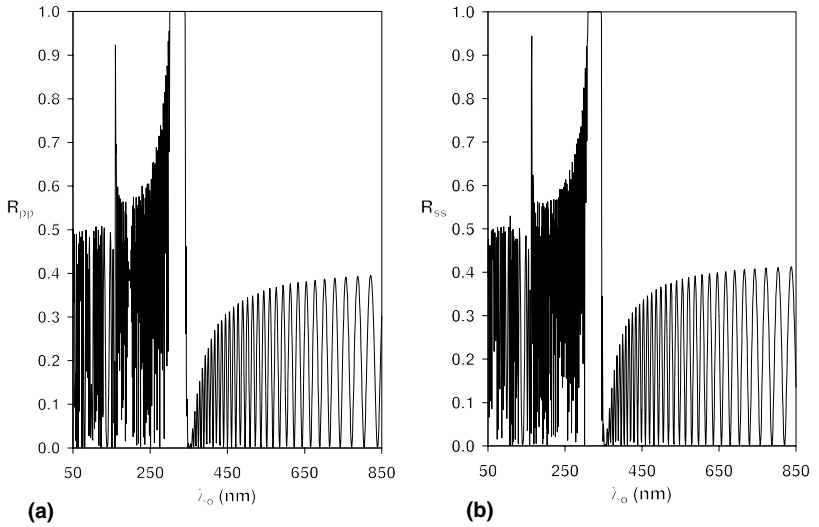

Fig. 5. Same as Fig. 2, except that $\tilde{\chi}_v = 90°$ and $\delta_v = 60°$.

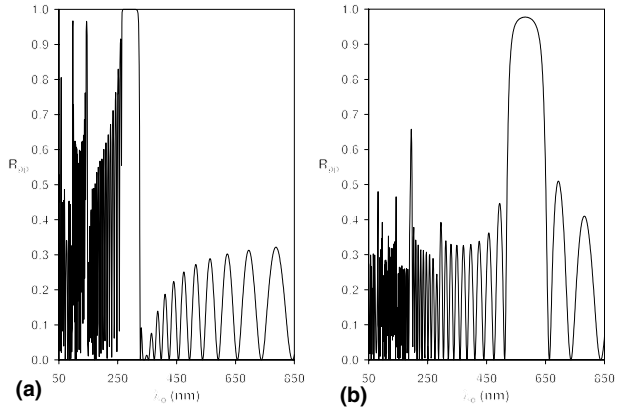

Fig. 6. R_{pp}-spectrums of a tilt-modulated SNTF made of TiO_2 with $\Omega = 75$ nm and $L = 20\,\Omega$: (a) $\tilde{\chi}_v = \delta_v = 90°$; (b) $\tilde{\chi}_v = \delta_v = 30°$.

comparison, Fig. 6(b) shows the results for $\tilde{\chi}_v = 30°$. The peak does not quite reach a height of unity, but is still very strong for such a thin film. Unlike the spectrum for $\tilde{\chi}_v = 90°$, harmonic peaks are relatively weak.

4.2. Oblique incidence

Planewave remittances were also calculated at several different angles of incidence for various sets of SNTF parameters. Figs. 7 and 8 show the results for $\theta = 60°$ and $\theta = 80°$, respectively, when $\tilde{\chi}_v = \delta_v = 30°$ and $L = 60\,\Omega$. Several trends become apparent on comparing Figs. 4, 7, and 8.

As with chiral STFs [31], the Bragg regimes blue-shift as the angle of incidence is increased. The central wavelengths λ_{mid} of the peaks were estimated for several other angles of incidence. It was found that λ_{mid} is linearly related to $\cos^2\theta$, as illustrated in Fig. 9 with a plot of λ_{mid} vs. $\cos^2\theta$ when $\tilde{\chi}_v = \delta_v = 30°$, for the fundamental R_{pp} peak. All harmonic peaks for both polarizations behave similarly.

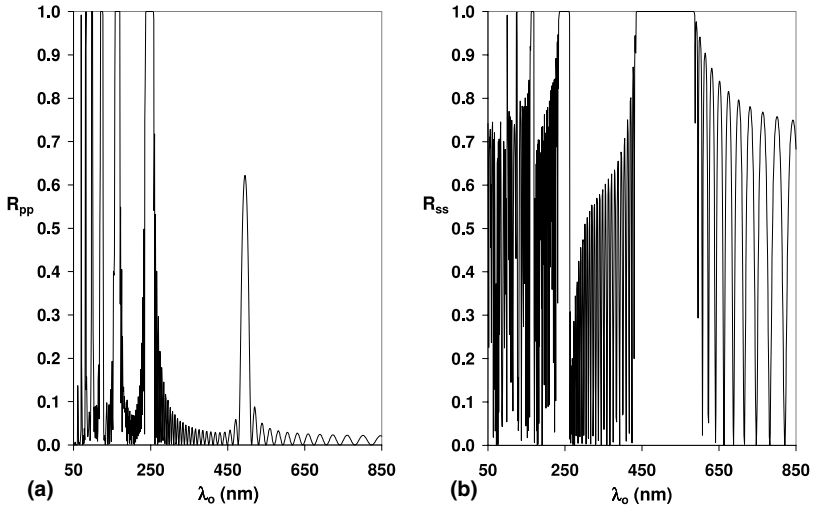

Fig. 7. Reflectance spectrums for $\theta = 60°$ of a tilt-modulated SNTF made of TiO_2 with $\tilde{\chi}_v = \delta_v = 30°$, $\Omega = 75$ nm and $L = 60\,\Omega$: (a) R_{pp}; (b) R_{ss}.

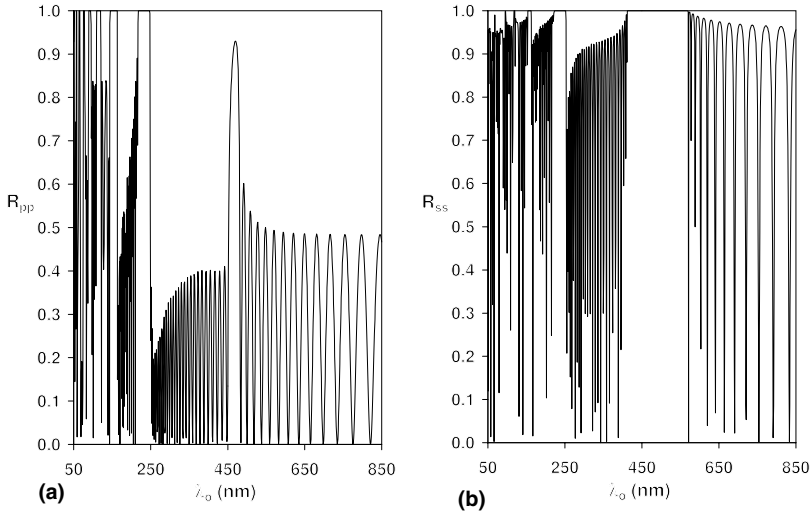

Fig. 8. Same as Fig. 7, except that $\theta = 80°$: (a) R_{pp}; (b) R_{ss}.

The most obvious polarization-dependent effect involves the oscillations in the reflectance spectrums. The R_{pp}-spectrums show a reduction of the oscillations at $\theta = 60°$ and then a return to strong oscillations at $\theta = 80°$. On the other hand, calculations at both angles show a monotonic increase in oscillations in the R_{ss}-spectrums as θ is increased. Additional calculations not shown indicate that a minimum oscillation amplitude for R_{pp} occurs near $\theta = 67°$: the oscillations monotonically decrease in amplitude as θ is increased until about $\theta = 67°$, and thereafter monotonically increase in amplitude as θ is increased.

The radically different behavior for the two linear polarizations with a minimum for the p-polarization is reminiscent of the Brewster effect [32, Section. 1.5.3]. If the values of three individual components of the permittivity dyadic at the

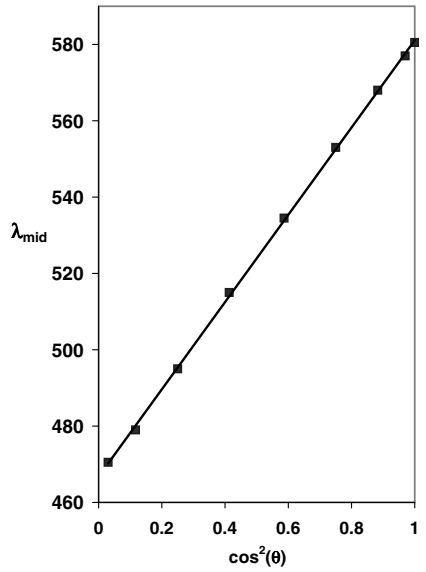

Fig. 9. λ_{mid} vs. $\cos^2\theta$ for the fundamental Bragg peak in the spectrum of R_{pp} when $\tilde{\chi}_{\text{v}} = \delta_{\text{v}} = 30^\circ$ and $L = 60\,\Omega$. The straight line is a least-squared-error fit to the discrete data points.

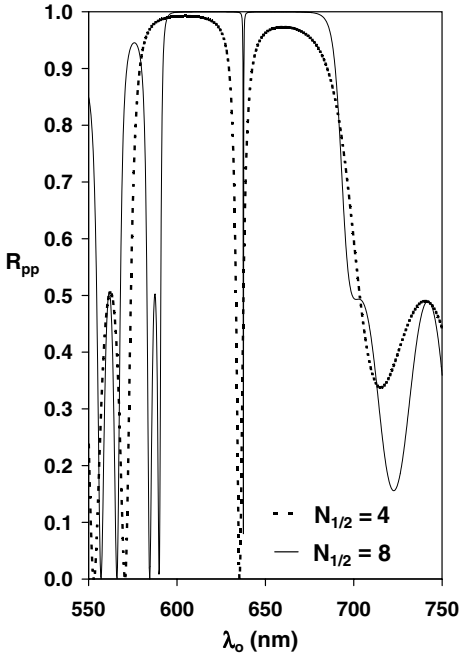

Fig. 10. R_{pp}-spectrums for $\theta = 0^\circ$ of a tilt-modulated SNTF with a central defect layer, as described in Section 5.

surface of the film are used to calculate the Brewster angle for an isotropic, homogeneous dielectric material, the angle ranges between 67° and 68°. Thus, outside the Bragg regimes, the polarization-sensitivity of the SNTF appears to be similar to an isotropic material's.

The other polarization-dependent phenomenon is the change in spectral profiles of the Bragg regimes. In the R_{pp}-spectrum, the fundamental Bragg regime becomes narrower and shorter as θ approaches 67°. All of the other regimes (at shorter wavelengths) do the opposite: they become broader and taller. In contrast, all of the Bragg regimes in the R_{ss}-spectrum broaden as θ increases.

Although the results shown here are only for $\chi_{\text{v}} = 30^\circ$ and $\delta_{\text{v}} = 30^\circ$, calculations using other values of both angles yield similar conclusions for oblique incidence. In some cases, however, the harmonic peaks in the R_{pp}-spectrum may also become shorter and narrower as the Brewster angle is approached rather than taller and wider as noted earlier in this section for $\chi_{\text{v}} = \delta_{\text{v}} = 30^\circ$.

5. Tilt-modulated SNTF with a central defect

It is well known that introducing a defect in the middle of a periodic system can produce a spectral hole in the Bragg regime [20,21]. The spectral hole is a dip in the Bragg regime over a very narrow range of the spectrum where the reflectance goes to zero. We attempted to create the same phenomenon in the tilt-modulated SNTF by including a thin, homogeneous layer in the middle of the film as the defect.

The effect of the defect was investigated for a TiO_2 SNTF with $\tilde{\chi}_{\text{v}} = 90^\circ$, $\delta_{\text{v}} = 60^\circ$ and $\Omega = 150$ nm. The value of Ω was chosen so as to shift the fundamental Bragg peak closer to $\lambda_0 = 630$ nm, the wavelength at which the permittivity parameters were measured. The thickness of the SNTF sections above and below the defect layer was set at $N_{1/2}2\Omega$, where $N_{1/2} > 0$ is an integer.

The defect layer was chosen to be 65-nm thick with $\tilde{\chi}_{\text{v}} = 90^\circ$ and $\delta_{\text{v}} = 0^\circ$. Then, $\underline{u}_x \cdot \underline{\underline{\epsilon}} \cdot \underline{u}_x = \underline{u}_y \cdot \underline{\underline{\epsilon}} \cdot \underline{u}_y = 5.8274\epsilon_0$, and the wavelength for an electromagnetic wave without x- and y-dependences is 261 nm in the defect layer when

$\lambda_0 = 630$ nm. The central defect layer is thus a quarter-wavelength thick.

The normal-incidence spectrums of R_{pp} in the vicinity of the fundamental Bragg peak are shown in Fig. 10 for $N_{1/2} = 4$ and $N_{1/2} = 8$. As the SNTF sections become thicker, this figures indicates that the spectral hole narrows and red-shifts. Parenthetically, the spectrums of R_{pp} were chosen to illustrate the point, but the R_{ss}-spectrums could equally well have been used; indeed, except for slightly wider holes and different positions, the spectrums of R_{ss} look very similar to those of R_{pp}.

The red-shift of the spectral hole, as the thickness of the SNTF sections is increased, slows with increasing thickness. The wavelength of the hole minimum, denoted by λ_{hole}, appears to approach an asymptotic value. Fig. 11 shows λ_{hole} as a

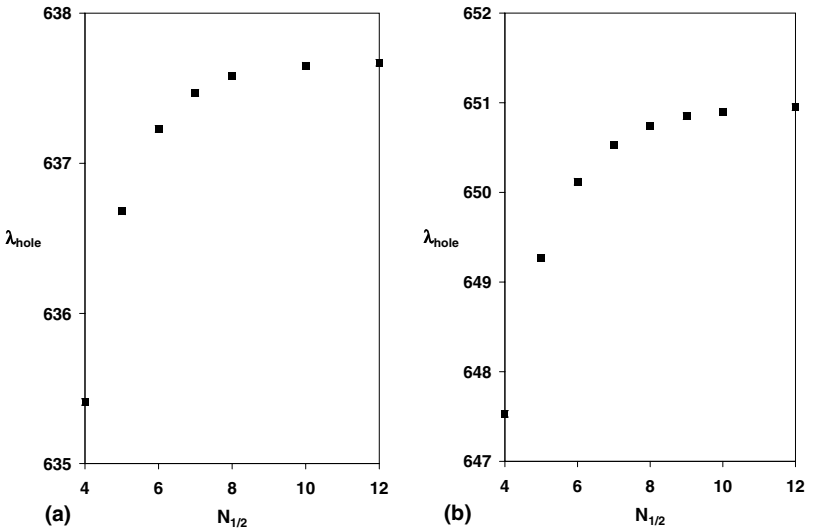

Fig. 11. λ_{hole} vs. $N_{1/2}$ when $\theta = 0°$, $\tilde{\chi}_v = 90°$, $\delta_v = 60°$ and $\Omega = 150$ nm. See Section 5 for other details: (a) p-polarization; (b) s-polarization.

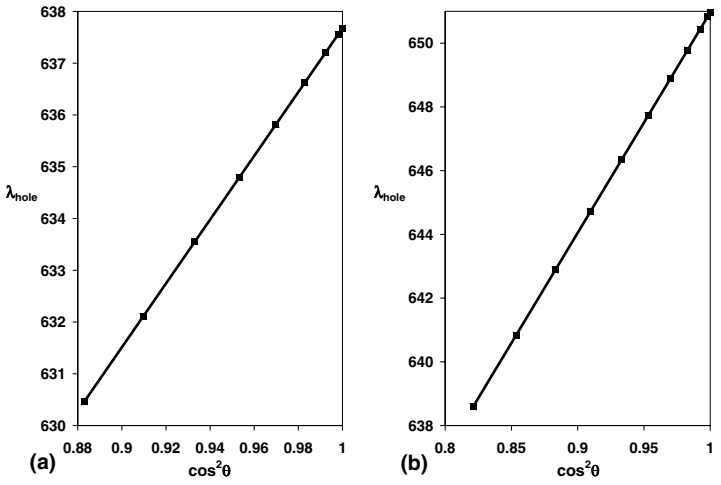

Fig. 12. λ_{hole} vs. $\cos^2\theta$ for $\tilde{\chi}_v = 90°$, $\delta_v = 60°$, $\Omega = 150$ nm and $N_{1/2} = 15$. See Section 5 for other details. The straight lines are least-squared-error fits to the discrete data points: (a) p-polarization; (b) s-polarization.

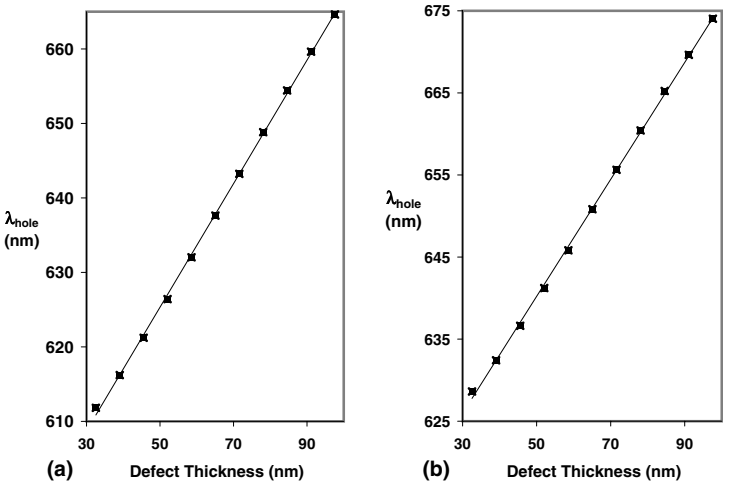

Fig. 13. λ_{hole} vs. defect thickness for $\tilde{\chi}_v = 90°$, $\delta_v = 60°$, $\Omega = 150$ nm and $N_{1/2} = 8$. See Section 5 for other details. The straight lines are least-squared-error fits to the discrete data points: (a) p-polarization; (b) s-polarization.

function of $N_{1/2}$ for both linear polarizations. Although the values of λ_{hole} for the two polarizations are different, they exhibit very similar spectral shifts as functions of film thickness. As $N_{1/2}$ is increased from 4 to 12, λ_{hole} changes by approximately 2 and 3 nm for R_{pp} and R_{ss}, respectively.

The effect of the angle of incidence θ on λ_{hole} was also investigated. As was the case for λ_{mid} describing the position of the Bragg peaks, λ_{hole} appears to be linearly related to $\cos^2\theta$. Fig. 12 shows plots of λ_{hole} vs. $\cos^2\theta$ for both polarizations, when $\tilde{\chi}_v = 90°$, $\delta_v = 60°$ and $N_{1/2} = 15$. The calculations were performed every 2.5° in the range $0° \leqslant \theta \leqslant 20°$. As can be seen in the figure, a linear fit is extremely good. Although the most likely applications of the SNTFs would be for normal-incidence conditions, the calculations were extended to $\theta = 80°$ and indicate that the relation is valid over a much wider range. Although not illustrated here, we observed that the hole width is also affect by the angle of incidence, and decreases as θ increases.

Finally, λ_{hole} was calculated as a function of the defect layer thickness at normal incidence, for both s- and p-polarizations. Results are shown in Fig. 13 for a range of change in defect thickness of ±50% of the quarter-wavelength value when $\tilde{\chi}_v = 90°$, $\delta_v = 60°$ and $N_{1/2} = 8$. The relationship between λ_{hole} and defect thickness is very nearly linear.

6. Conclusion

A realistic model of a tilt-modulated SNTF has been developed using available empirical data for columnar thin films. It has been demonstrated that such films are functionally similar to rugate filters for linearly polarized light. Reflection and transmission spectrums show Bragg peaks, depending on the average tilt angle $\tilde{\chi}_v$ of the nanowires and the amplitude δ_v of the modulation. The locations of the Bragg peaks for p-polarization are in general different from the locations of the Bragg peaks for s-polarization. The bandwidths of the Bragg peaks depend on the level of modulation, with higher modulation leading to broader peaks. The peaks blue-shift as the angle of incidence is increased with a linear relationship between the central wavelength and $\cos^2\theta$.

Outside of the Bragg regimes the spectrums exhibit significant oscillation. The oscillations in the spectrums for p-polarization decease in amplitude to near zero as the angle of incidence is increased toward the Brewster angle for a comparable isotropic material. The oscillations in the spectrums for s-polarization, on the other hand, grow in amplitude monotonically as the angle of incidence is increased.

A spectral hole can be introduced in the fundamental Bragg peak with the inclusion of a defect in

the middle of the film, consisting of a layer close to a quarter-wavelength thick with constant tilt angle. The width of the hole becomes narrower as thickness of the film is increased. There is also a slight dependance of the spectral position of the hole on the modulated film thickness. However, the position of the hole changes very little for total thickness beyond 30 cycles of modulation. The position of the spectral hole varies linearly with $\cos^2\theta$. To a good approximation, the spectral position of the hole depends linearly on the thickness of the defect layer.

The tilt-modulated SNTF offers many design possibilities for optical filters to be used with linearly polarized light. Fundamental Bragg peaks can be exploited as broadband filters. For narrowband filters, a central defect layer can be included, the bandwidth depending on the thicknesses of the SNTF sections as well as of the defect layer. Fine tuning can be conveniently achieved by varying the angle of incidence. The tilt-modulated SNTF thus offers yet another option in the growing number of useful structures made with STF technology [33,34]. As with chiral STFs [1–3], both passive optical devices as well as sensor devices based on tilt-modulated SNTFs can be envisioned.

References

[1] V.C. Venugopal, A. Lakhtakia, in: O.N. Singh, A. Lakhtakia (Eds.), Electromagnetic Fields in Unconventional Materials and Structures, Wiley, New York, 2000, p. 151.
[2] A. Lakhtakia, R. Messier, in: W.S. Weiglhofer, A. Lakhtakia (Eds.), Introduction to Complex Mediums for Optics and Electromagnetics, SPIE, Bellingham, WA, 2003, p. 447.
[3] M.W. McCall, in: W.S. Weiglhofer, A. Lakhtakia (Eds.), Introduction to Complex Mediums for Optics and Electromagnetics, SPIE, Bellingham, WA, 2003, p. 479.
[4] V.C. Venugopal, A. Lakhtakia, Proc. R. Soc. Lond. A 456 (2000) 125.
[5] J.B. Geddes III, A. Lakhtakia, Opt. Commun. 225 (2003) 141.
[6] T. Motohiro, Y. Taga, Appl. Opt. 28 (1989) 2466.
[7] R. Messier, T. Gehrke, C. Frankel, V.C. Venugopal, W. Otaño, A. Lakhtakia, J. Vac. Sci. Technol. A 15 (1997) 2148.
[8] H.A. Macleod, Thin-film Optical Filters, Institute of Physics, Bristol, UK, 2001.
[9] D.M. Mattox, The Foundations of Vacuum Coating Technology, Noyes Publications, Norwich, New York, 2003.
[10] I.J. Hodgkinson, Q.h. Wu, Birefringent Thin Films and Polarizing Elements, World Scientific, Singapore, 1997.
[11] A.J. McPhun, Q.H. Wu, I.J. Hodgkinson, Electron. Lett. 34 (1998) 360.
[12] N. Kaiser, H.K. Pulker (Eds.), Optical Interference Coatings, Springer, Berlin, 2003.
[13] W.H. Southwell, J. Opt. Soc. Am. A 5 (1988) 1558.
[14] R. Overend, D.R. Gibson, R. Marshall, Vacuum 43 (1992) 51.
[15] V.C. Venugopal, A. Lakhtakia, Opt. Commun. 149 (1998) 217.
[16] A. Lakhtakia, V.C. Venugopal, R. Messier, Microw. Opt. Technol. Lett. 18 (1998) 147.
[17] K. Robbie, A.J.P. Hnatiw, M.J. Brett, R.I. MacDonald, J.N. McMullin, Electron. Lett. 33 (1997) 1213.
[18] K. Kaminska, M. Suzuki, K. Kimura, Y. Taga, K. Robbie, J. Appl. Phys. 95 (2004) 3055.
[19] I.J. Hodgkinson, Q.h. Wu, J. Hazel, Appl. Opt. 37 (1998) 2653.
[20] H.A. Haus, C.V. Shank, IEEE J. Quantum Electron. 12 (1976) 532.
[21] G.P. Agrawal, S. Radic, IEEE Photon. Technol. Lett. 6 (1994) 995.
[22] Y.-C. Yang, C.-S. Lee, J.-E. Kim, H.Y. Park, Phys. Rev. E 60 (1999) 6852.
[23] A. Lakhtakia, M. McCall, Opt. Commun. 168 (1999) 457.
[24] I.J. Hodgkinson, Q.h. Wu, A. Lakhtakia, M.W. McCall, Opt. Commun. 177 (2000) 79.
[25] F. Wang, A. Lakhtakia, Opt. Commun. 215 (2003) 79.
[26] D.W. Berreman, J. Opt. Soc. Am. 62 (1972) 502.
[27] I. Abdulhalim, L. Benguigui, R. Weil, J. Phys. (Paris) 46 (1985) 815.
[28] J.A. Polo Jr., A. Lakhtakia, Opt. Commun. 230 (2004) 369.
[29] F. Chiadini, A. Lakhtakia, Opt. Commun. 231 (2004) 257.
[30] A. Lakhtakia, AEÜ Int. J. Electron. Commun. 56 (2002) 169, corrections; 57 (2003) 79.
[31] V.C. Venugopal, A. Lakhtakia, Eur. Phys. J. Appl. Phys. 10 (2000) 173.
[32] M. Born, E. Wolf, Principles of Optics, sixth ed., Pergamon Press, London, 1980.
[33] M.W. Horn, M.D. Pickett, R. Messier, A. Lakhtakia, Nanotechnology 15 (2003) 303.
[34] I.J. Hodgkinson, A. Lakhtakia, Q.h. Wu, L. De Silva, M.W. McCall, Opt. Commun. 239 (2004) 353.

Available online at www.sciencedirect.com
SCIENCE DIRECT®
Optics Communications 242 (2004) 13–21
OPTICS COMMUNICATIONS
www.elsevier.com/locate/optcom

Tilt-modulated chiral sculptured thin films: an alternative to quarter-wave stacks

John A. Polo Jr. [a,*], Akhlesh Lakhtakia [b,1]

[a] Department of Physics and Technology, Edinboro University of Pennsylvania, Meadville Street, Edinboro, PA 16444, USA
[b] CATMAS – Computational and Theoretical Materials Sciences Group, Department of Engineering Science and Mechanics, Pennsylvania State University, University Park, PA 16802, USA

Received 2 April 2004; received in revised form 15 July 2004; accepted 28 July 2004

Abstract

The reflectances and transmittances of light incident normally on a chiral sculptured thin film with a periodically modulated tilt angle are calculated using the piecewise homogeneity approximation method. The necessary concurrent modulation of the local permittivity dyadic are accounted for by using empirically determined parameters. For modulation lengths equal to half the unmodulated structural period of the film, the circular Bragg phenomenon displayed by unmodulated chiral STFs is destroyed. It is demonstrated that the chosen nanomaterial then acts as a conventional dielectric mirror.

PACS: 77.55.+f; 78.20.Ek; 78.20.Fm; 78.66.−w
Keywords: Dielectric mirror; Physical vapor deposition; Quarter-wave stack; Sculptured thin film; Structural chirality

1. Introduction

Light incident normally on a stack of dielectric layers of alternating high and low permittivity is strongly reflected, when the free-space wavelength lies within the so-called Bragg regime. If the stack is designed so that each layer thickness is a quarter of the light wavelength within the layer, the reflectance is maximized. With enough layers, the quarter-wave stack acts as a dielectric mirror. The bandwidth of the Bragg regime is determined by the difference in the relative permittivities of the two materials. The layers being made of isotropic materials, the polarization state of the incident light does not matter [1]. If, however, the layers are constructed of orthorhombic materials (whose

* Corresponding author. Tel.: +1 814 732 2655; fax: +1 814 732 2455.
E-mail addresses: polo@edinboro.edu (J.A. Polo), akhlesh@psu.edu (A. Lakhtakia).
[1] Tel.: +1 814 863 4319; fax: +1 814 865 9974.

0030-4018/$ - see front matter
doi:10.1016/j.optcom.2004.07.059

dielectric response properties are described by a relative permittivity dyadic rather than a relative permittivity scalar), the Bragg regime depends on the polarization state of the incident light [2].

Chiral sculptured thin films (STFs) consist of helical nanowires oriented perpendicular to the surface of the film. The nanowires have noncircular cross-sections resulting in the chiral STF possessing a locally anisotropic permittivity dyadic which varies helicoidally in a direction normal to the substrate. Within the Bragg regime, circularly polarized light of handedness matching the structural handedness of the chiral STF is strongly reflected, while light of the opposite handedness is not. This effect is known as the circular Bragg phenomenon (CBP). Unlike reflection from an isotropic dielectric mirror (for which the circular polarization state is reversed upon reflection), reflection (if it occurs) by a sufficiently thick chiral STF does not reverse the circular polarization state [3,4]. Thus, a single chiral STF cannot function as a conventional dielectric mirror.

One way to realize a circular-polarization-independent mirror with chiral STFs is to make a cascade of two chiral STFs which are identical except that their structural handednesses are opposite [5]. However, that way doubles the device thickness in exchange for independence of the circular polarization state of the incident light. More disturbingly, dissipation inside the chiral STFs can vitiate the desired independence quite seriously [6]. We report here an alternative that does not suffer from the two foregoing problems.

The tilt angle (i.e., the angle of rise) of the helicoidal nanowires can be easily modulated during the physical vapor deposition of a chiral STF by changing the vapor incidence angle. Experience with columnar thin films [7] indicates that the local permittivity dyadic of a chiral STF must also be modulated by continuously changing the tilt angle [8]. We studied the optical responses of tilt-modulated chiral STFs to normally incident plane waves, using the data collected by Hodgkinson et al. on TiO_2 columnar thin films [7]. The piecewise homogeneity approximation method [9] was applied in order to determine the remittances of tilt-modulated chiral STFs. We determined that when the vapor incidence angle is sinusoidally modulated with a period equal to half of the helicoidal pitch, the CBP displayed by a unmodulated chiral STF is replaced by Bragg reflection similar to that from a quarter-wave stack. Thus, STF technology can be used for realizing conventional dielectric mirrors.

The outline of this paper is as follows. The matrix ordinary differential equation describing propagation in chiral STFs is presented in Section 2. Section 3 contains a description of the tilt-modulation. Calculated optical remittances for both circularly and linearly polarized light are presented in Section 4. The effect of changing the amplitude of the modulation of the vapor incidence angle is explored and the crucial role of the changing local permittivity dyadic is elucidated.

2. Matrix ordinary differential equation

The frequency-domain constitutive relations of an unmodulated chiral STF can be written as [3]

$$\begin{aligned}\underline{D}(\underline{r}) &= \epsilon_0 \underline{\underline{S}}_z(z)\cdot\underline{\underline{S}}_y(\chi)\cdot\underline{\underline{\epsilon}}^0_{\rm ref}\cdot\underline{\underline{S}}_y^{-1}(\chi)\cdot\underline{\underline{S}}_z^{-1}(z)\cdot\underline{E}(\underline{r})\\ &= \underline{\underline{\epsilon}}(z)\cdot\underline{E}(\underline{r}),\end{aligned} \tag{1}$$

$$\underline{B}(\underline{r}) = \mu_0 \underline{H}(\underline{r}), \tag{2}$$

where $\underline{E}$ and $\underline{B}$ represent the primitive electric and magnetic fields, respectively; $\underline{D}$ and $\underline{H}$ represent the induction electric and magnetic fields, respectively; and ϵ_0 and μ_0 are the permittivity and the permeability, respectively, of free space. As chiral STFs are locally biaxial, the *reference* relative permittivity dyadic is given by

$$\underline{\underline{\epsilon}}^0_{\rm ref} = \epsilon_a \underline{u}_z\underline{u}_z + \epsilon_b \underline{u}_x\underline{u}_x + \epsilon_c \underline{u}_y\underline{u}_y, \tag{3}$$

where $\underline{u}_x$, $\underline{u}_y$ and $\underline{u}_z$ are the Cartesian unit vectors. The locally aciculate morphology of chiral STF is described by the dyadic

$$\begin{aligned}\underline{\underline{S}}_y(\chi) &= (\underline{u}_x\underline{u}_x + \underline{u}_z\underline{u}_z)\cos\chi\\ &\quad + (\underline{u}_z\underline{u}_x - \underline{u}_x\underline{u}_z)\sin\chi + \underline{u}_y\underline{u}_y,\end{aligned} \tag{4}$$

where $\chi \in (0, \pi/2]$ is the tilt angle relative to the xy plane. The dyadic function

$$\begin{aligned}\underline{\underline{S}}_z(z) &= (\underline{u}_x\underline{u}_x + \underline{u}_y\underline{u}_y)\cos(\pi z/\Omega)\\ &\quad + (\underline{u}_y\underline{u}_x - \underline{u}_x\underline{u}_y)\sin(\pi z/\Omega) + \underline{u}_z\underline{u}_z\end{aligned} \tag{5}$$

describes the helicoidal rotation of the permittivity dyadic $\underline{\underline{\epsilon}}(z)$, with 2Ω as the structural period along the z-axis. As stated, Eq. (1) describes a structurally right-handed chiral STF.

Tilt-modulation means that χ is not constant but varies as a function of depth into the film (along the z-axis). In addition, $\underline{\underline{\epsilon}}^{0}_{\text{ref}}$ also becomes a function of z. The variation of χ with z prevents the exploitation of the Oseen transformation which has been used to great advantage for unmodulated chiral STFs [3,10]. As we are interested in normally incident light, all electromagnetic fields are independent of x and y; therefore, $\underline{E}(\underline{r}) \equiv \underline{E}(z)$ and $\underline{H}(\underline{r}) \equiv \underline{H}(z)$. The frequency-domain Maxwell curl postulates

$$\left.\begin{aligned} \nabla \times \underline{E}(\underline{r}) &= \mathrm{i}\omega\mu_0 \underline{H}(\underline{r}) \\ \nabla \times \underline{H}(\underline{r}) &= -\mathrm{i}\omega \underline{\underline{\epsilon}}(z) \cdot \underline{E}(\underline{r}) \end{aligned}\right\}, \tag{6}$$

where ω is the angular frequency, then separate into two algebraic equations and four ordinary differential equations (ODEs). The two algebraic equations are

$$\left.\begin{aligned} E_z(\zeta) &= -\tfrac{\epsilon_{zx}}{\epsilon_{zz}} E_x(\zeta) - \tfrac{\epsilon_{zy}}{\epsilon_{zz}} E_y(\zeta) \\ H_z(\zeta) &= 0 \end{aligned}\right\}, \tag{7}$$

where

$$\left.\begin{aligned} \zeta &= \tfrac{\pi z}{\Omega} \\ \epsilon_{zx} &= \tfrac{\epsilon_0}{2}(\epsilon_b - \epsilon_a)\sin(2\chi)\cos\zeta \\ \epsilon_{zy} &= \tfrac{\epsilon_0}{2}(\epsilon_b - \epsilon_a)\sin(2\chi)\sin\zeta \\ \epsilon_{zz} &= \epsilon_0 \epsilon_a \tau \\ \tau &= \cos^2\chi + \tfrac{\epsilon_b}{\epsilon_a}\sin^2\chi \end{aligned}\right\}. \tag{8}$$

The four coupled ODEs can be represented compactly as the matrix ODE [11,12]

$$\frac{\mathrm{d}}{\mathrm{d}\zeta}[\underline{f}(\zeta)] = \frac{\mathrm{i}\Omega}{\pi}[\underline{\underline{P}}(\zeta)] \cdot [\underline{f}(\zeta)], \tag{9}$$

where the x- and y-directed components of the electromagnetic field phasors are arranged in the column vector

$$[\underline{f}(\zeta)] = \begin{bmatrix} E_x(\zeta) \\ E_y(\zeta) \\ H_x(\zeta) \\ H_y(\zeta) \end{bmatrix}. \tag{10}$$

The 4×4 kernel matrix in (9) is

$$[\underline{\underline{P}}(\zeta)] = \begin{bmatrix} 0 & 0 & 0 & \omega\mu_0 \\ 0 & 0 & -\omega\mu_0 & 0 \\ \frac{1}{2}\left(F_1\sin^2 2\chi - F_2 + F_3\right)\sin 2\zeta & \left(F_1\sin^2 2\chi - F_2\right)\sin^2\zeta - F_3\cos^2\zeta & 0 & 0 \\ \left(-F_1\sin^2 2\chi + F_2\right)\cos^2\zeta + F_3\sin^2\zeta & \frac{1}{2}\left(-F_1\sin^2 2\chi + F_2 - F_3\right)\sin 2\zeta & 0 & 0 \end{bmatrix}, \tag{11}$$

where

$$F_1 = \frac{\omega\epsilon_0(\epsilon_b - \epsilon_a)^2}{4\epsilon_a\tau}, \quad F_2 = \omega\epsilon_0\epsilon_b\tau', \quad F_3 = \omega\epsilon_0\epsilon_c, \quad \tau' = \cos^2\chi + \frac{\epsilon_a}{\epsilon_b}\sin^2\chi.$$

In order to solve the boundary value problem necessary to determine the reflectances and the transmittances, it is convenient to recast the formulation in terms of a 4×4 matrix $[\underline{\underline{M}}(\zeta)]$ (called the matrizant), such that [9,13]

$$[\underline{f}(\zeta)] = [\underline{\underline{M}}(\zeta)][\underline{f}(0)]. \tag{12}$$

It then follows that

$$\frac{\mathrm{d}}{\mathrm{d}\zeta}[\underline{\underline{M}}(\zeta)] = \frac{\mathrm{i}\Omega}{\pi}[\underline{\underline{P}}(\zeta)] \cdot [\underline{\underline{M}}(\zeta)], \quad [\underline{\underline{M}}(0)] = [\underline{\underline{I}}], \tag{13}$$

where $[\underline{\underline{I}}]$ is the identity matrix. The matrizant can be calculated after exploiting the piecewise homogeneity approximation [9], following which the reflectances and the transmittances can be calculated for normally incident plane waves.

3. Tilt-modulated chiral STF

Suppose that the tilt angle χ is modulated about a constant value with an integer number of cycles

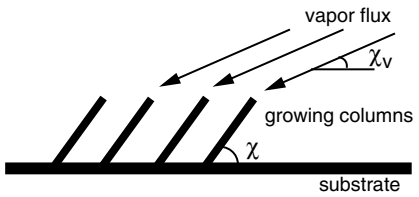

Fig. 1. Tilt angle χ and vapor incidence angle χ_v for a columnar thin film.

over a distance of one structural period. In order to accomplish this, the vapor incidence angle χ_v must be modulated during physical vapor deposition of the film. The relationship between χ and χ_v for a columnar thin film is depicted in Fig. 1. For TiO_2 columnar thin films, Hodgkinson et al. [7] obtained the relationships

$$\epsilon_a = \left[1.0443 + 2.7394\left(\frac{\chi_v}{\pi/2}\right) - 1.3697\left(\frac{\chi_v}{\pi/2}\right)^2\right]^2, \tag{14}$$

$$\epsilon_b = \left[1.6765 + 1.5649\left(\frac{\chi_v}{\pi/2}\right) - 0.7825\left(\frac{\chi_v}{\pi/2}\right)^2\right]^2, \tag{15}$$

$$\epsilon_c = \left[1.3586 + 2.1109\left(\frac{\chi_v}{\pi/2}\right) - 1.0554\left(\frac{\chi_v}{\pi/2}\right)^2\right]^2, \tag{16}$$

and

$$\tan\chi = 2.8818\tan\chi_v, \tag{17}$$

where χ_v is in radian. From the experimental data underlying the foregoing equations, non-polynomial expressions can also be obtained [14], but the quadratic expressions sufficed for our present purpose.

The sinusoidal modulation of the vapor incidence angle may be expressed as

$$\chi_v = \tilde{\chi}_v + \delta_v \sin(2N_{\mathrm{mod}}\zeta), \tag{18}$$

where $\tilde{\chi}_v$ is the average value of χ_v, δ_v is the modulation amplitude, and N_{mod} is the number of oscillations over a structural half-period of the STF, which may be either integer or half-integer. For all calculations presented here, we chose $\Omega = 200$ nm and $\tilde{\chi}_v = 35^\circ$, while the thickness of the chiral STF is $L = 60\Omega$.

4. Optical response of χ modulated chiral STF

With the dielectric properties of the chosen STF defined, (13) can be solved numerically using the piecewise homogeneity approximation. In this approximation, the material is divided into a series of slices perpendicular to the helical axis. Each slice is then treated as if it has a uniform permittivity dyadic, with the value taken to be that of the STF at the center of the slice. The efficient application of this method to unmodulated chiral STFs has been described elsewhere [13]. The precision of the approximation depends on the slice thickness. Based on previous calculations, the slice thickness was chosen to be 0.1 nm. Once the matrizant $[\underline{\underline{M}}(L)]$ has been determined, the optical remittances of the film can be determined by solving a boundary value problem. It is known that the values of the remittances saturate as L is increased. For this reason, the remittances were calculated for a film thickness of 60Ω.

In the following subsections, linear reflectances and transmittances are denoted by R_{ss}, R_{sp}, R_{ps}, R_{pp}, T_{ss}, T_{sp}, T_{ps} and T_{pp}. Here, for instance R_{ps} is the fraction of the incident power density reflected as a p-polarized plane wave when the incident plane wave is s-polarized. Circular reflectances and transmittances are denoted by R_{RR}, R_{RL}, R_{LR}, R_{LL}, T_{RR}, T_{RL}, T_{LR} and T_{LL}, where R_{LR} is the fraction of the incident power density reflected as a left circularly polarized (LCP) plane wave when the incident plane wave is right circularly polarized (RCP).

4.1. Unmodulated chiral STF

The circular remittances of an unmodulated chiral STF are shown in Fig. 2 as functions of the free-space wavelength λ_0. As can be seen in Fig. 2(a), a RCP plane wave is strongly reflected for a range of wavelengths 780 nm $\lesssim \lambda_0 \lesssim$ 810 nm, which is the Bragg regime for normal incidence, while an incident LCP plane wave is largely

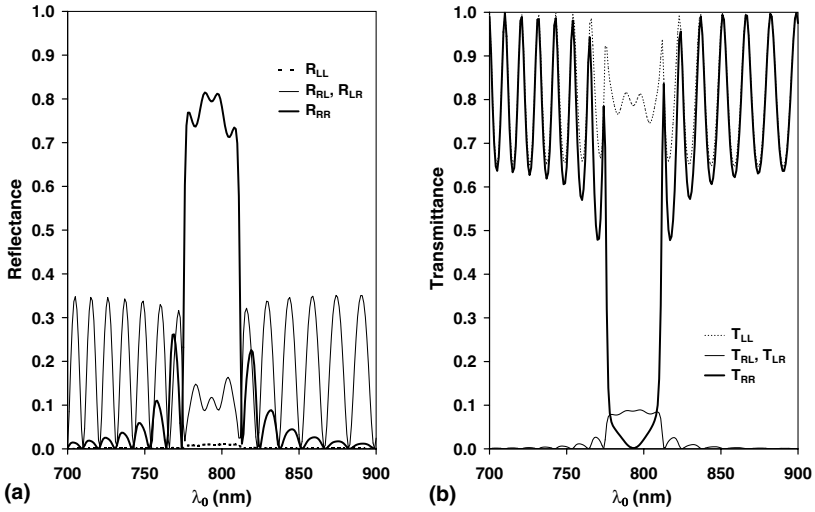

Fig. 2. Circular remittance spectrums of a chiral STF made of titanium dioxide with $\delta_v = 0$, $\tilde{\chi}_v = 35°$, $\Omega = 200$ nm and $L = 60\Omega$.

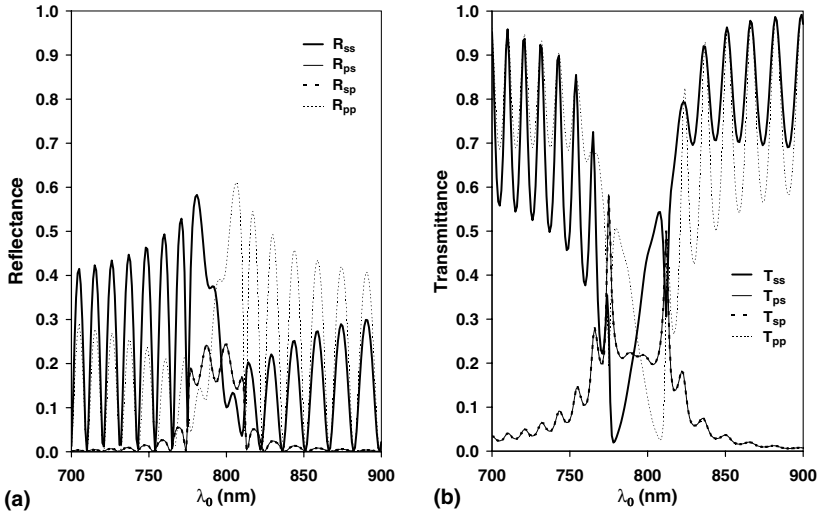

Fig. 3. Same as Fig. 2, except that linear remittance spectrums are shown.

transmitted in the same regime. The large values of R_{RR} within the Bragg regime indicate that RCP light is nearly completely reflected and maintains its circular polarization state upon reflection.

Fig. 3 shows the spectrums of the linear remittances of the chosen thin film. Unlike the circular polarization case, the large cross-polarized remittances show that the linear polarization state is *not* conserved on Bragg reflection due to an unmodulated chiral STF.

4.2. Tilt-modulated chiral STF

The high value of R_{RR} is the hallmark of the CBP. Fig. 4 shows the calculated values R_{RR} vs. λ_0 for various values of the tilt-modulation amplitude δ_v, when the modulation period is equal to Ω (i.e., $N_{mod} = 1$). This figure clearly shows a suppression of the CBP as δ_v is increased. As δ_v increases to $\sim 10°$, all indications of the circular Bragg phenomenon steadily diminish to the

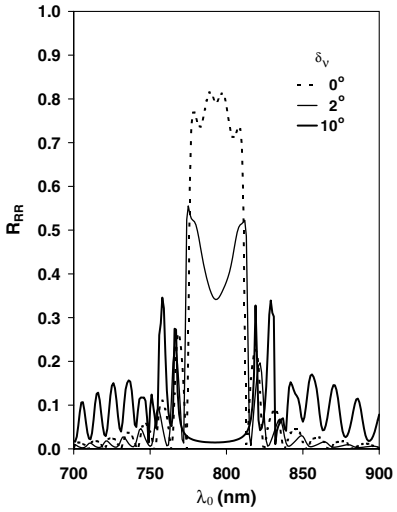

Fig. 4. Spectrum of R_{RR} for $N_{mod} = 1$ and various values of δ_v. Other parameters are the same as for Fig. 2.

vanishing point. *The effect of interest in this paper occurs with the annihilation of the CBP.*

A complete picture of the effect of tilt-modulation is provided by Fig. 5 which contains spectrums of all eight circular remittances when $\delta_v = 10°$ and $N_{mod} = 1$. Fig. 5(a) shows that, over a range of wavelengths which is slightly bigger than the Bragg regime of the unmodulated chiral STF, the cross-polarized circular reflectances are virtually unity. Furthermore, Fig. 5(b) shows that all transmittances are virtually null-valued over the same range of wavelengths. This behavior is suggestive of reflection from a conventional dielectric mirror which reverses the handedness of circular polarization. In order to verify that the chosen STF is acting as a conventional dielectric mirror over this new regime, the linear remittances were also calculated. Fig. 6 shows the results. The mirror-like behavior of the tilt-modulated chiral STF is clearly demonstrated with nearly unity co-polarized linear reflectances; the spectrums of R_{ss} and R_{pp} appear as one curve over the mirror regime.

Transition to conventional mirror reflection was not observed for any other period of the modulation, although various modulation periods, for which there are an integer number in a distance 2Ω, were tried.

Fig. 7 illustrates, with a plot of R_{LR} vs. λ_0 for various values of δ_v, the effect of varying δ_v to values larger than required to obtain the conventional mirror effect. Although the spectrums of R_{LR} are shown in this figure, the spectrums of R_{RL},R_{ss}, and R_{pp} could have been shown just as well, all

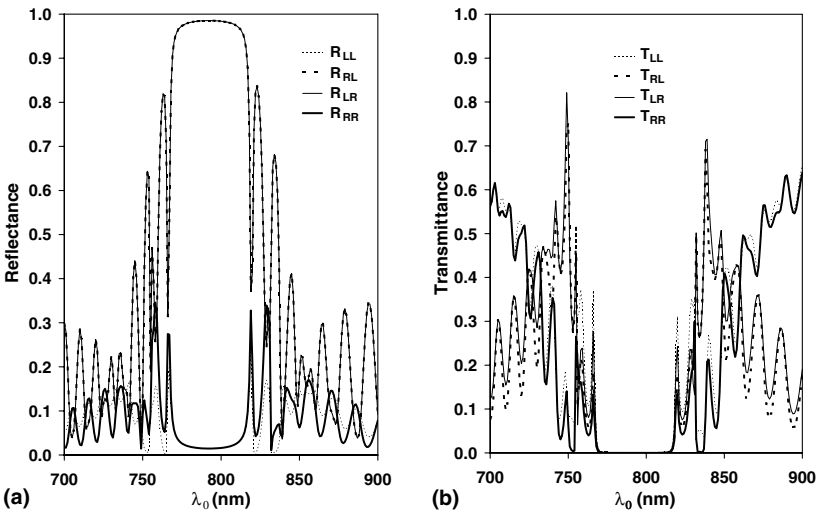

Fig. 5. Circular remittance spectrums of a tilt-modulated chiral STF made of titanium dioxide with $N_{mod} = 1$, $\delta_v = 10°$, $\tilde{\chi}_v = 35°$, $\Omega = 200$ nm and $L = 60\Omega$.

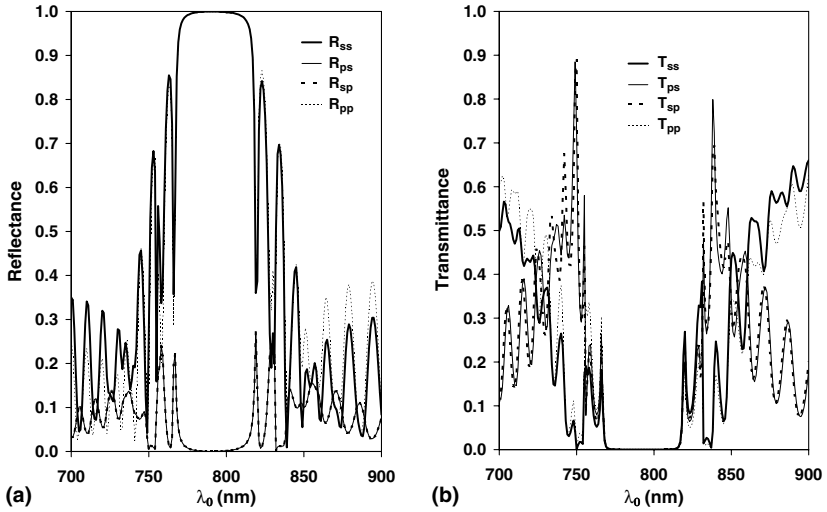

Fig. 6. Same as Fig. 5, except that linear remittance spectrums are shown.

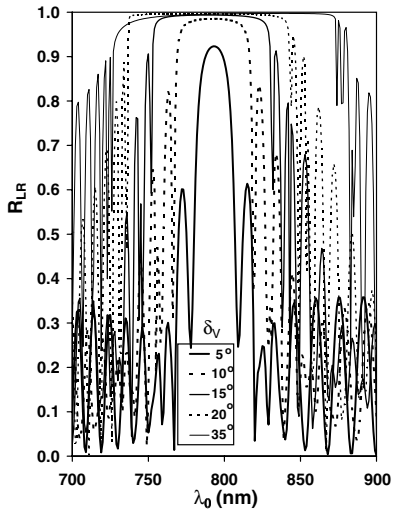

Fig. 7. Spectrum of R_{LR} of a chiral STF made of titanium dioxide with $N_{mod} = 1$, $\tilde{\chi}_v = 35°$, $\Omega = 200$ nm and $L = 60\Omega$ for various values of δ_v.

leading to the same conclusions. The width of the reflection regime increases with increasing amplitudes of modulation. The change in regime width is nearly linearly dependent on the modulation amplitude until $\delta_v = 25°$, at which point the spectrums begins to level off. We must note here that the maximum value of δ_v cannot exceed $\tilde{\chi}_v$.

4.3. Source of the mirror effect

Modulation of the vapor incidence angle χ_v not only modulates the tilt angle χ, but the components of the reference relative permittivity dyadic (i.e., ϵ_a, ϵ_b and ϵ_c) as well. To determine which modulations are responsible for the mirror effect,

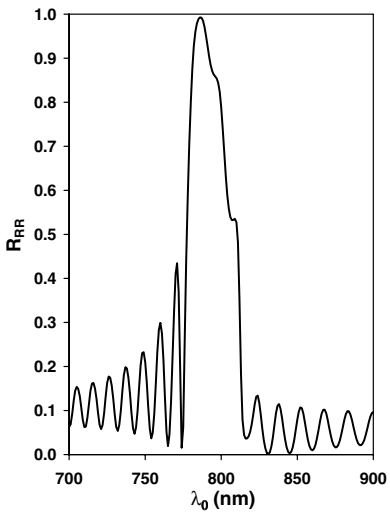

Fig. 8. Spectrum of R_{RR} of a chiral STF made of titanium dioxide with $N_{mod} = 1$, $\delta_v = 10°$, $\tilde{\chi}_v = 35°$, $\Omega = 200$ nm and $L = 60\Omega$, but with modulation of the reference relative permittivity dyadic suppressed.

each factor was modulated separately. Fig. 8 shows the spectrum of R_{RR} when the variation of $\underline{\underline{\epsilon}}^0_{ref}$ is suppressed. This leaves only a modulation in χ and the resultant modulation of the permittivity dyadic of the STF due solely to the helicoidal structure. Comparison with Fig. 4 shows that the CBP is still present although perturbed somewhat. At the lower edge of the regime, the peak height has grown in Fig. 8 from a value close to 0.8 to nearly 1.0. At the upper edge of the regime, the peak is sloped rather than flat.

For computing the spectrum shown in Fig. 9, $\underline{\underline{\epsilon}}^0_{ref}$ was modulated as χ_v was modulated, but the tilt angle χ describing the conformation of the hel-

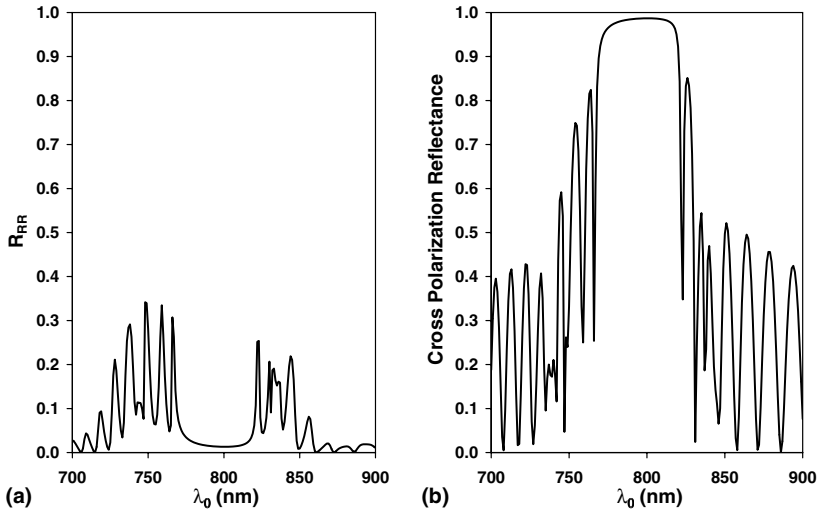

Fig. 9. Circular reflectance spectrums when $N_{mod} = 1$, $\delta_v = 0°$, $\tilde{\chi}_v = 35°$, $\Omega = 200$ nm and $L = 60\Omega$, but permittivity modulated as if $\delta_v = 10°$. (a) R_{RR}, (b) R_{RL} or R_{LR}.

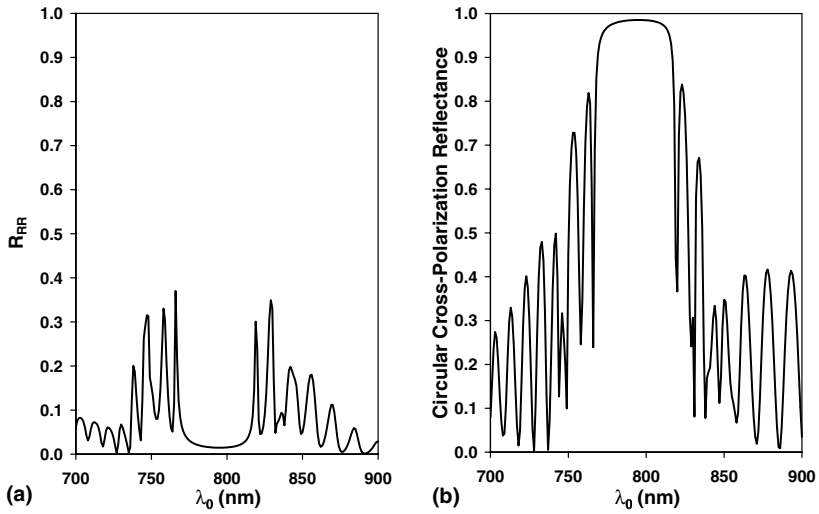

Fig. 10. Circular reflectance spectrums when $N_{mod} = 1$, $\delta_v = 0°$, $\tilde{\chi}_v = 35°$, $\Omega = 200$ nm and $L = 60\Omega$, but ϵ_a and ϵ_c modulated as if $\delta_v = 10°$. (a) R_{RR}, (b) R_{RL} or R_{LR}.

ical nanowires was held fixed. It can be seen that the CBP has been destroyed and replaced by the conventional mirror effect. To further isolate the cause of the conventional mirror effect, each of the three components of $\underline{\underline{\epsilon}}^{0}_{\text{ref}}$ was modulated separately while the other two were held fixed at the unmodulated values. Only a simultaneous modulation of ϵ_a and ϵ_b was found to produce the conventional mirror response. The results are shown in Fig. 10. Within the mirror regime, the results are nearly identical to those obtained for full modulation of all components of $\underline{\underline{\epsilon}}^{0}_{\text{ref}}$ and χ, as comparison with Fig. 5(a) shows.

5. Concluding remarks

We have thus demonstrated that, by modulating the vapor incidence angle appropriately, chiral STFs can be grown to function as conventional dielectric mirrors over a range of wavelengths for normally incident plane waves – instead of as circular polarization mirrors that (unmodulated) chiral STFs are known well for. Although our calculations made use of data available for columnar thin films of TiO_2, we suspect that our conclusions are generally robust.

As a conventional dielectric mirror, a tilt-modulated chiral STF has at least two advantages over the quarter-wave stack. First, the latter requires the deposition of two different materials in order to create a permittivity contrast between adjacent layers, but the former requires only a single material. Second, the range of wavelengths over which the quarter-wave stack acts as a reflector is governed by the difference in the permittivity of the two materials, and a change in the bandwidth of the reflective regime will entail changing layer thicknesses and/or the selection of different materials. With tilt-modulated chiral STFs, however, the bandwidth of the mirror regime can be altered simply by adjusting the amplitude of tilt-modulation.

The mirror effect of the tilt-modulated chiral STF will extend the already large number of proposed and actual applications [3,4] of STFs, and offers the convenience of creating a wide variety of devices with a single manufacturing process. As with the unmodulated chiral STFs which display the CBP, the tilt-modulated chiral STF—because of its porosity – may prove useful as a sensor as well as a passive optical element.

References

[1] J.D. Rancourt, Optical Thin Films, Macmillan, New York, USA, 1987.
[2] I.J. Hodgkinson, Q.h. Wu, Birefringent Thin Films and Polarizing Elements, World Scientific, Singapore, 1997.
[3] V.C. Venugopal, A. Lakhtakia, in: O.N. Singh, A. Lakhtakia (Eds.), Electromagnetic Fields in Unconventional Materials and Structures, Wiley, New York, 2000, p. 151.
[4] A. Lakhtakia, R. Messier, in: W.S. Weiglhofer, A. Lakhtakia (Eds.), Introduction to Complex Mediums for Optics and Electromagnetics, SPIE Press, Bellingham, WA, USA, 2003, p. 447.
[5] A. Lakhtakia, V.C. Venugopal, Microw. Opt. Technol. Lett. 17 (1998) 135.
[6] A. Lakhtakia, I.J. Hodgkinson, Opt. Commun. 167 (1999) 191.
[7] I.J. Hodgkinson, Q.h. Wu, J. Hazel, Appl. Opt. 37 (1998) 2653.
[8] A. Lakhtakia, Microw. Opt. Technol. Lett. 34 (2002) 103.
[9] V.C. Venugopal, A. Lakhtakia, Proc. R. Soc. Lond. A 456 (2000) 125.
[10] A. Lakhtakia, W.S. Weiglhofer, Liq. Cryst. 15 (1993) 659.
[11] D.W. Berreman, J. Opt. Soc. Am. 62 (1972) 502.
[12] I. Abdulhalim, L. Benguigui, R. Weil, J. Phys. (Paris) 46 (1985) 815.
[13] J.A. Polo Jr., A. Lakhtakia, Opt. Commun. 230 (2004) 369.
[14] F. Chiadini, A. Lakhtakia, Opt. Commun. 231 (2004) 257.

Eur. Phys. J. AP **20**, 91–103 (2002)
DOI: 10.1051/epjap:2002079

THE EUROPEAN PHYSICAL JOURNAL
APPLIED PHYSICS

Coupling of Rayleigh-Wood anomalies and the circular Bragg phenomenon in slanted chiral sculptured thin films

F. Wang[a], A. Lakhtakia[b], and R. Messier[c]

CATMAS – Computational and Theoretical Materials Sciences Group, Department of Engineering Science and Mechanics, Pennsylvania State University, University Park, PA 16802-6812, USA

Received: 2 May 2002 / Received in final form and accepted: 9 August 2002
Published online: 25 October 2002 –

Abstract. Slanted chiral sculptured thin films (STFs) are introduced as nano-engineered materials that are effectively periodic in two orthogonal directions. Their periodicities normal and parallel to the substrate plane are related by a slant angle. A coupled wave theory is formulated and implemented for the planewave response of a slanted chiral STF of finite thickness. Numerical results show that the nonspecular remittances and the Rayleigh-Wood anomalies due to periodicity parallel to the substrate plane are tightly coupled to the specular nature of the circular Bragg phenomenon displayed due to periodicity normal to the substrate plane. In the Bragg regime, the left- and the right-circularly polarized components of the incident plane wave are redirected in non-trivially different directions. The potential of slanted chiral STFs as narrowband circular polarization beamsplitters is established.

PACS. 42.25.Fx Diffraction and scattering – 42.40.Eq Holographic optical elements; holographic gratings – 42.79.Dj Gratings

1 Introduction

Periodic structures of two kinds are commonplace in optics [1–3]. The first are diffraction gratings [4], most of which are periodically corrugated surfaces, though periodic arrays of identical scatterers and imprinted frequency-selective surfaces are also pressed into service. When a plane wave is incident on a diffraction grating, it may be reflected/transmitted into a multitude of discrete directions in addition to the specular directions. By virtue of the Floquet-Bloch theorem [5,6], the reflected/transmitted field is a discrete angular spectrum of propagating as well as evanescent planewaves. As the frequency or the angle of incidence is altered, an evanescent plane wave may turn into a propagating one or vice versa, the phenomenon being termed the Rayleigh-Wood anomaly [7,8].

The second kind of periodic structures are volume gratings. A volume grating is formed by the periodic variation of the constitutive properties normal to a set of parallel planar surfaces. These gratings have been employed for over a century in optical filters [9,10], and are also found in many biological structures [2]. Both reflection and transmission are purely specular. The distinctive characteristic of *reflection* volume gratings is the Bragg phenomenon [11], which is virtually total reflection in a certain frequency band – of great significance for optical fiber communication [12]. Reflection volume gratings made of either chiral liquid crystals [13] or chiral sculptured thin films [14] display total reflection only for plane waves of one circular polarization, but not for the other.

Thus, one type of periodic structures are distinguished by nonspecular reflection/transmission and the Rayleigh-Wood anomalies, while the other type of periodic structures reflect/transmit only in the specular direction but display the Bragg phenomenon. The coupling of these two types of periodic structures is likely to be rich in physical phenomenons and application, in particular when the volume grating is sensitive to circular polarization.

The first attempt towards that coupling involved the stacking of a surface-relief diffraction grating and a chiral volume grating [15,16]. This coupling involves two distinct interactions: (i) of linear polarization and circular polarization, and (ii) of nonspecular propagation with the specular Bragg phenomenon. Numerical studies showed that the circular Bragg phenomenon is virtually immune to the presence of the surface-relief grating, indicating that chiral volume gratings can be diffraction-coupled efficiently to other optical elements.

In this paper, we present a new – and a more intimate – coupling between the two types of periodic structures, achievable using sculptured thin film (STF) technology. Several physical vapor deposition techniques

[a] e-mail: fuw101@psu.edu
[b] e-mail: axl4@psu.edu
[c] e-mail: mes17@psu.edu

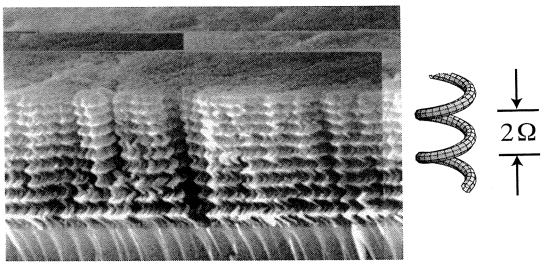

Fig. 1. Scanning electron micrograph of a chiral sculptured thin film. Shown alongside is a schematic of its helical morphology with structural period 2Ω along the normal to the substrate plane.

have emerged for manufacturing STFs [17–22], and much theoretical and experimental progress on the optics of chiral STFs has been reported in the preceding few years [14]. The nanostructure of a STF comprises clusters of 3–5 nm diameter that form parallel columns (which are clusters of the basic clusters) and are bent in some fanciful forms with column and feature sizes 30 nm or larger. Accordingly, a STF is a unidirectionally nonhomogeneous continuum with direction-dependent properties at visible and infrared wavelengths. These properties can be delineated sectionwise along a direction normal (say, the z-axis) to the substrate plane (the xy plane). Chiral STFs evince the circular Bragg phenomenon for normally as well as obliquely incident plane waves [23,24].

Normally, the substrate is rotated at a constant angular velocity about the z-axis when a chiral STF is grown [17–22]. The helical columns of a chiral STF grow upright; see Figure 1. For our present purposes, however, we need the columns to be slanted at an angle α to the z-axis. One way of achieving this morphology may be by rotating the substrate with a variable angular velocity, as discussed elsewhere [21,25].

A slanted chiral STF will thus be helicoidally nonhomogeneous about an axis inclined at an angle α to the z-axis, and shall therefore be periodic in the substrate plane as well as normal to the substrate plane. Periodicity in the substrate plane will give rise to nonspecular reflection/transmission and the associated Rayleigh-Wood anomalies, while periodicity normal to the substrate plane will be responsible for the circular Bragg phenomenon (which does not involve change in the direction of propagation). The coupling between the two types of periodicities will be mediated entirely by a single parameter: the slant angle α.

The plan of this paper is as follows. Section 2 provides a detailed description of the theoretical treatment of the planewave response of a slanted chiral STF. First, the geometry of the boundary value problem, the constitutive relations of the slanted chiral STF, and the field representations above and below the thin film are presented. Then, the coupled wave theory [26,27] is used to formulate a matrix ordinary differential equation [24] for the fields excited in the thin film. Finally, the numerical solution procedure adopted for the boundary value problem

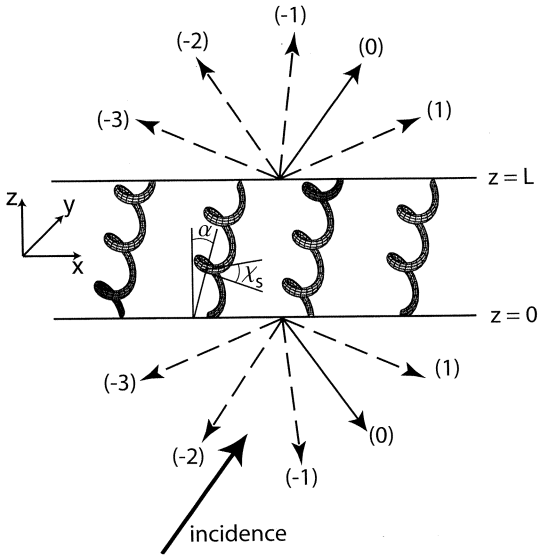

Fig. 2. Schematic of the boundary value problem involving a slanted chiral sculptured thin film. Specular reflection and transmission carry the label ($n = 0$) and are identified by solid arrows, while nonspecular reflection and transmission carry the labels ($n \neq 0$) and are identified by dashed arrows. As $\alpha \to 0^\circ$, all nonspecular reflections/transmissions fold into the specular reflection/transmission.

is described. Section 3 is devoted to the presentation and discussion of the numerical results obtained for normal incidence. An $\exp(-i\omega t)$ time-dependence is implicit, with ω as the angular frequency of the incident plane wave, and t as the time.

2 Theoretical analysis

Let the region $0 \leq z \leq L$ be occupied by a slanted chiral STF, as shown in Figure 2, while the half-spaces $z \leq 0$ and $z \geq L$ are vacuous. A plane wave is incident from the lower half-space $z \leq 0$ on to the plane $z = 0$. As a result, reflection and transmission into the two half-spaces occurs.

2.1 Constitutive relations of the slanted chiral STF

The relative permittivity dyadic $\underline{\underline{\epsilon}}(\mathbf{r})$ of the slanted chiral STF is factorable as

$$\underline{\underline{\epsilon}}(\mathbf{r}) = \underline{\underline{S}}_y(-\alpha) \cdot \underline{\underline{S}}_z(\mathbf{r}) \cdot \underline{\underline{S}}_y(\chi_s) \cdot \underline{\underline{\epsilon}}_{\text{ref}}(\lambda_0) \cdot \underline{\underline{S}}_y^T(\chi_s) \cdot \underline{\underline{S}}_z^T(\mathbf{r}) \cdot \underline{\underline{S}}_y^T(-\alpha), \quad (1)$$

where the position vector $\mathbf{r} = x\mathbf{u}_x + y\mathbf{u}_y + z\mathbf{u}_z$, and the superscript T denotes the transpose. Current experimental evidence indicates that most STFs are locally biaxial in general [20,30], which is mirrored in the reference relative

permittivity dyadic [23]

$$\underline{\underline{\epsilon}}_{\rm ref}(\lambda_0) = \epsilon_a(\lambda_0)\,\mathbf{u}_z\mathbf{u}_z + \epsilon_b(\lambda_0)\,\mathbf{u}_x\mathbf{u}_x + \epsilon_c(\lambda_0)\,\mathbf{u}_y\mathbf{u}_y\,, \tag{2}$$

with λ_0 denoting the wavelength in free space (*i.e.*, vacuum). The wavelength-dependences of the scalars $\epsilon_{a,b,c}$ are assumed to emerge from a single–resonance Lorentzian model [28,29] as

$$\epsilon_{a,b,c}(\lambda_0) = 1 + \frac{p_{a,b,c}}{\left[1 + \left(N_{a,b,c}^{-1} - \mathrm{i}\,\lambda_{a,b,c}\,\lambda_0^{-1}\right)^2\right]}\,, \tag{3}$$

where $p_{a,b,c}$ are the oscillator strengths. The parameters $\lambda_{a,b,c}$ and $N_{a,b,c}$ determine the resonance wavelengths and absorption linewidths. Based on the local columnarity of the STFs, we surmise that $|\epsilon_b(\lambda_0)| \geq |\epsilon_c(\lambda_0)| \geq |\epsilon_a(\lambda_0)|$ away from the resonance wavelengths of the bulk material [23,31].

The rotational nonhomogeneity of the slanted chiral STF is captured by the dyadic

$$\underline{\underline{S}}_z(\mathbf{r}) = (\mathbf{u}_x\mathbf{u}_x + \mathbf{u}_y\mathbf{u}_y)\,\cos\left[\frac{\pi}{\Omega}\,(\mathbf{r}\cdot\mathbf{u}_\ell)\right] + h\,(\mathbf{u}_y\mathbf{u}_x - \mathbf{u}_x\mathbf{u}_y)\,\sin\left[\frac{\pi}{\Omega}\,(\mathbf{r}\cdot\mathbf{u}_\ell)\right] + \mathbf{u}_z\mathbf{u}_z\,, \tag{4}$$

the axis of rotational nonhomogeneity (*i.e.*, the helical axis) being parallel to the unit vector $\mathbf{u}_\ell = \sin\alpha\,\mathbf{u}_x + \cos\alpha\,\mathbf{u}_z$. The half-pitch of the helical columns is denoted by Ω. The parameter $h = 1$ for structural right-handedness, while $h = -1$ for structural left-handedness.

The dyadic

$$\underline{\underline{S}}_y(\gamma) = (\mathbf{u}_x\mathbf{u}_x + \mathbf{u}_z\mathbf{u}_z)\,\cos\gamma + (\mathbf{u}_z\mathbf{u}_x - \mathbf{u}_x\mathbf{u}_z)\,\sin\gamma + \mathbf{u}_y\mathbf{u}_y \tag{5}$$

serves two different roles. Whereas $\underline{\underline{S}}_y(\chi_s)$ delineates the role of the growth process with $90^\circ - \chi_s$ being the angle of declination from the helical axis, $\underline{\underline{S}}_y(-\alpha)$ represents the slanted orientation of the helical axis. Since STFs are generally fabricated using physical vapor deposition [18–22], the growing columns of a STF must be oriented at some angle to the substrate plane such that the so-called angle of rise $\chi = \chi_s - \alpha$. Hence, $\chi \in (0^\circ, 90^\circ]$ for the ideal helical columns of a slanted chiral STF to always grow upwards in relation to the substrate plane, while $0^\circ < \chi_s < 90^\circ$ is mandated by the equation of a helix. When $\alpha = 0^\circ$, the slant is absent and the usual chiral STFs are represented by $\underline{\underline{\epsilon}}(\mathbf{r}) \equiv \underline{\underline{\epsilon}}(z)$.

2.2 Field representation

Clearly, $\underline{\underline{\epsilon}}(\mathbf{r}) \equiv \underline{\underline{\epsilon}}(x,z)$ is periodic in directions parallel to the x and the z axes, but is independent of y. Therefore, the field representation in the two half-spaces must be periodic with respect to x and comprise both specular and nonspecular planewave components in accordance with the Floquet-Bloch theorem [5,6,26].

Let the incident plane wave propagate at an angle $\theta_{\rm inc}$ to the $+z$-axis and at an angle $\psi_{\rm inc}$ to the $+x$-axis (in the xy plane). Hence, the incident, the reflected and the transmitted electromagnetic field phasors are best expressed in a set of Floquet harmonics [27] respectively, as follows:

$$\mathbf{E}_{\rm i} = \sum_{n=0,\,\pm1,\,\pm2,\,\ldots} \left[\frac{(\mathrm{i}\,\mathbf{s}_n - \mathbf{p}_n^+)}{\sqrt{2}}\,a_L^{(n)} - \frac{(\mathrm{i}\,\mathbf{s}_n + \mathbf{p}_n^+)}{\sqrt{2}}\,a_R^{(n)}\right] \times \exp\left[\mathrm{i}\,(k_{xn}\,x + k_{y0}\,y + k_{zn}\,z)\right]\,, \quad z \leq 0\,, \tag{6}$$

$$\mathbf{H}_{\rm i} = \sum_{n=0,\,\pm1,\,\pm2,\,\ldots} \frac{-\mathrm{i}}{\eta_0}\left[\frac{(\mathrm{i}\,\mathbf{s}_n - \mathbf{p}_n^+)}{\sqrt{2}}\,a_L^{(n)} + \frac{(\mathrm{i}\,\mathbf{s}_n + \mathbf{p}_n^+)}{\sqrt{2}}\,a_R^{(n)}\right] \times \exp\left[\mathrm{i}\,(k_{xn}\,x + k_{y0}\,y + k_{zn}\,z)\right]\,, \quad z \leq 0\,. \tag{7}$$

$$\mathbf{E}_{\rm r} = \sum_{n=0,\,\pm1,\,\pm2,\,\ldots} \left[-\frac{(\mathrm{i}\,\mathbf{s}_n - \mathbf{p}_n^-)}{\sqrt{2}}\,r_L^{(n)} + \frac{(\mathrm{i}\,\mathbf{s}_n + \mathbf{p}_n^-)}{\sqrt{2}}\,r_R^{(n)}\right] \times \exp\left[\mathrm{i}\,(k_{xn}\,x + k_{y0}\,y - k_{zn}\,z)\right]\,, \quad z \leq 0\,, \tag{8}$$

$$\mathbf{H}_{\rm r} = \sum_{n=0,\,\pm1,\,\pm2,\,\ldots} \frac{-\mathrm{i}}{\eta_0}\left[-\frac{(\mathrm{i}\,\mathbf{s}_n - \mathbf{p}_n^-)}{\sqrt{2}}\,r_L^{(n)} - \frac{(\mathrm{i}\,\mathbf{s}_n + \mathbf{p}_n^-)}{\sqrt{2}}\,r_R^{(n)}\right] \times \exp\left[\mathrm{i}\,(k_{xn}\,x + k_{y0}\,y - k_{zn}\,z)\right]\,, \quad z \leq 0\,. \tag{9}$$

$$\mathbf{E}_{\rm t} = \sum_{n=0,\,\pm1,\,\pm2,\,\ldots} \left[\frac{(\mathrm{i}\,\mathbf{s}_n - \mathbf{p}_n^+)}{\sqrt{2}}\,t_L^{(n)} - \frac{(\mathrm{i}\,\mathbf{s}_n + \mathbf{p}_n^+)}{\sqrt{2}}\,t_R^{(n)}\right] \times \exp\left\{\mathrm{i}\,[k_{xn}\,x + k_{y0}\,y + k_{zn}\,(z-L)]\right\}\,, \quad z \geq L\,, \tag{10}$$

$$\mathbf{H}_{\rm t} = \sum_{n=0,\,\pm1,\,\pm2,\,\ldots} \frac{-\mathrm{i}}{\eta_0}\left[\frac{(\mathrm{i}\,\mathbf{s}_n - \mathbf{p}_n^+)}{\sqrt{2}}\,t_L^{(n)} + \frac{(\mathrm{i}\,\mathbf{s}_n + \mathbf{p}_n^+)}{\sqrt{2}}\,t_R^{(n)}\right] \times \exp\left\{\mathrm{i}\,[k_{xn}\,x + k_{y0}\,y + k_{zn}\,(z-L)]\right\}\,, \quad z \geq L\,. \tag{11}$$

In (6–11) and thereafter, $\eta_0 = \sqrt{\mu_0/\epsilon_0}$ is the intrinsic impedance of free space. The horizontal wavenumbers

$$\left.\begin{aligned} k_{xn} &= k_0\sin\theta_{\rm inc}\cos\psi_{\rm inc} + n\,\kappa_x\,, \quad n = 0,\,\pm1,\,\pm2,\,\ldots \\ k_{y0} &= k_0\sin\theta_{\rm inc}\sin\psi_{\rm inc} \end{aligned}\right\}\,, \tag{12}$$

where $k_0 = \omega\sqrt{\mu_0\,\epsilon_0} = 2\pi/\lambda_0$ is the free-space wavenumber, and

$$\kappa_x = (\pi/\Omega)\,|\sin\alpha| \tag{13}$$

is in accord with the x-periodicity of the slanted chiral STF with period $L_x = 2\Omega/|\sin\alpha|$.

The vertical wavenumbers

$$k_{zn} = \begin{cases} +\left(k_0^2 - k_{xn}^2 - k_{y0}^2\right)^{1/2}\,; & \text{if } k_0^2 \geq k_{xn}^2 + k_{y0}^2 \\ +i\,\left(k_{xn}^2 + k_{y0}^2 - k_0^2\right)^{1/2}\,; & \text{otherwise} \end{cases} \tag{14}$$

are either real-valued (for propagating harmonics) or imaginary (for evanescent harmonics).

The nth-order Floquet harmonic in any of the fields (6–11) involves *L*eft and *R*ight circularly polarized (LCP and RCP) components with amplitudes $a_L^{(n)}$ and $a_R^{(n)}$ for the incident plane wave, $r_L^{(n)}$ and $r_R^{(n)}$ for the reflected field, and $t_L^{(n)}$ and $t_R^{(n)}$ for the transmitted field. As the incident plane wave is a Floquet harmonic of order 0, the coefficients $a_L^{(n)} = a_R^{(n)} = 0 \, \forall n \neq 0$. The vectors

$$\left.\begin{array}{l} \mathbf{s}_n = \frac{-k_{y0}\,\mathbf{u}_x + k_{xn}\,\mathbf{u}_y}{k_{xyn}} \\ \mathbf{p}_n^{\pm} = \mp \left(\frac{k_{xn}\,\mathbf{u}_x + k_{y0}\,\mathbf{u}_y}{k_{xyn}} \right) \frac{k_{zn}}{k_0} + \frac{k_{xyn}}{k_0}\,\mathbf{u}_z \end{array}\right\} \quad \forall n \,, \quad (15)$$

individually denote linear polarization of the perpendicular and the parallel types in electromagnetics literature [32], respectively, with respect to the direction vectors $\mathbf{d}_n^{\pm} = (k_{xn}\,\mathbf{u}_x + k_{y0}\,\mathbf{u}_y \pm k_{zn}\,\mathbf{u}_z)/k_0$; whilst

$$k_{xyn} = +\sqrt{k_{xn}^2 + k_{y0}^2} \quad (16)$$

is defined for convenience. The unit vectors $\mathbf{s}_n$, $\mathbf{p}_n^{\pm}$ and $\mathbf{d}_n^{\pm}$ form a right-handed triad; and we define possibly complex-valued angles θ_n and ψ_n *via* the relationship $\mathbf{d}_n^{\pm} = (\mathbf{u}_x \cos\psi_n + \mathbf{u}_y \sin\psi_n)\sin\theta_n \pm \mathbf{u}_z \cos\theta_n$. If the nth-order reflected/transmitted Floquet harmonic is of the propagating (*i.e.*, non-evanescent) kind, the angles θ_n and ψ_n are real-valued.

Since $\left\{a_L^{(n)}\right\}$ and $\left\{a_R^{(n)}\right\}$ are supposedly known, the amplitude sets $\left\{r_L^{(n)}\right\}$, $\left\{r_R^{(n)}\right\}$, $\left\{t_L^{(n)}\right\}$ and $\left\{t_R^{(n)}\right\}$, $(n = 0, \pm1, \pm2, ...)$, have to be determined by solving a boundary value problem.

2.3 Matrix ordinary differential equation

Each of the nine components $\epsilon_{pq}(x,z)$, $(p,q = x,y,z)$, of the relative permittivity dyadic $\underline{\underline{\epsilon}}(\mathbf{r})$ of (1) is represented as

$$\epsilon_{pq}(x,z) = \sum_{n=0,\,\pm1,\,\pm2} \epsilon_{pq}^{(n)}(z)\,\exp\left(\mathrm{i}n\kappa_x x\right) \,, \quad p,q = x,y,z \quad (17)$$

where $\epsilon_{pq}^{(n)}(z)$ are the Fourier amplitudes. The Floquet-Bloch theorem entails the decompositions

$$\mathbf{E}(\mathbf{r}) = \sum_{n=0,\,\pm1,\,\pm2,\,...} \left[E_x^{(n)}(z)\,\mathbf{u}_x + E_y^{(n)}(z)\,\mathbf{u}_y + E_z^{(n)}(z)\,\mathbf{u}_z \right] \times \exp\left[\mathrm{i}\left(k_{xn}\,x + k_{y0}y\right)\right] \,, \quad 0 \le z \le L \,, \quad (18)$$

$$\mathbf{H}(\mathbf{r}) = \sum_{n=0,\,\pm1,\,\pm2,\,...} \left[H_x^{(n)}(z)\,\mathbf{u}_x + H_y^{(n)}(z)\,\mathbf{u}_y + H_z^{(n)}(z)\,\mathbf{u}_z \right] \times \exp\left[\mathrm{i}\left(k_{xn}\,x + k_{y0}y\right)\right] \,, \quad 0 \le z \le L \,, \quad (19)$$

for the electromagnetic field phasors. Parenthetically, we note that Rokushima and Yamakita [33] also used the Floquet-Bloch theorem for locally uniaxial chiral liquid crystals, but their representation is periodic not with respect to the x-axis but with respect to the helical axis (which is parallel to the unit vector $\underline{\underline{S}}_y(-\alpha)\cdot\mathbf{u}_z$).

On substituting (17–19) in the frequency-domain Maxwell curl postulates

$$\left.\begin{array}{l} \nabla\times\mathbf{E}(\mathbf{r}) = \mathrm{i}\omega\mu_0\,\mathbf{H}(\mathbf{r}) \\ \nabla\times\mathbf{H}(\mathbf{r}) = -\mathrm{i}\omega\epsilon_0\,\underline{\underline{\epsilon}}(\mathbf{r})\cdot\mathbf{E}(\mathbf{r}) \end{array}\right\} \,, \quad 0 < z < L \,, \quad (20)$$

and exploiting the orthogonalities of the functions $\exp[\mathrm{i}(k_{xn}x + k_{y0}y)]$ across any plane z = constant, we derive the following set of coupled wave equations:

$$\frac{\mathrm{d}}{\mathrm{d}z}E_x^{(n)}(z) - \mathrm{i}k_{xn}\,E_z^{(n)}(z) = \mathrm{i}k_0\eta_0\,H_y^{(n)}(z) \,, \quad (21)$$

$$\frac{\mathrm{d}}{\mathrm{d}z}E_y^{(n)}(z) - \mathrm{i}k_{y0}\,E_z^{(n)}(z) = -\mathrm{i}k_0\eta_0\,H_x^{(n)}(z) \,, \quad (22)$$

$$k_{y0}\,E_x^{(n)}(z) - k_{xn}\,E_y^{(n)}(z) = -\,k_0\eta_0\,H_z^{(n)}(z) \,, \quad (23)$$

$$\frac{\mathrm{d}}{\mathrm{d}z}H_x^{(n)}(z) - \mathrm{i}k_{xn}\,H_z^{(n)}(z) = -\frac{\mathrm{i}k_0}{\eta_0}\sum_{\tilde{n}=0,\,\pm1,\,\pm2,\,...} \left[\epsilon_{yx}^{(n-\tilde{n})}(z)\,E_x^{(\tilde{n})}(z) + \epsilon_{yy}^{(n-\tilde{n})}(z)\,E_y^{(\tilde{n})}(z) + \epsilon_{yz}^{(n-\tilde{n})}(z)\,E_z^{(\tilde{n})}(z) \right] \,, \quad (24)$$

$$\frac{\mathrm{d}}{\mathrm{d}z}H_y^{(n)}(z) - \mathrm{i}k_{y0}\,H_z^{(n)}(z) = \frac{\mathrm{i}k_0}{\eta_0} \times \sum_{\tilde{n}=0,\,\pm1,\,\pm2,\,...} \left[\epsilon_{xx}^{(n-\tilde{n})}(z)\,E_x^{(\tilde{n})}(z) + \epsilon_{xy}^{(n-\tilde{n})}(z)\,E_y^{(\tilde{n})}(z) + \epsilon_{xz}^{(n-\tilde{n})}(z)\,E_z^{(\tilde{n})}(z) \right] \,, \quad (25)$$

$$k_{y0}\,H_x^{(n)}(z) - k_{xn}\,H_y^{(n)}(z) = \frac{k_0}{\eta_0} \times \sum_{\tilde{n}=0,\,\pm1,\,\pm2,\,...} \left[\epsilon_{zx}^{(n-\tilde{n})}(z)\,E_x^{(\tilde{n})}(z) + \epsilon_{zy}^{(n-\tilde{n})}(z)\,E_y^{(\tilde{n})}(z) + \epsilon_{zz}^{(n-\tilde{n})}(z)\,E_z^{(\tilde{n})}(z) \right] \,. \quad (26)$$

These six equations hold for all $n = 0, \pm1, \pm2, ...$

Clearly, an infinite number of terms cannot be added on a computer. Therefore, we restrict the summations to $|n| \le N_T$, and then define the $(2N_T + 1) \times 1$ column matrixes $[\underline{E}_p(z)]$ and $[\underline{H}_p(z)]$, $(p = x,y,z)$, as follows:

$$\left.\begin{array}{l} [\underline{E}_p(z)] = \left[E_p^{(n)}(z)\right] \\ [\underline{H}_p(z)] = \left[H_p^{(n)}(z)\right] \end{array}\right\} \,, \; n = 0, \pm1, ..., \pm N_T \,, \; p = x,y,z \,. \quad (27)$$

Likewise, we define the $(2N_T+1)\times(2N_T+1)$ matrixes

$$\left.\begin{aligned}\left[\underline{\underline{K}}_x\right] &= \left[k_{xn}\,\delta_{n,\tilde{n}}\right]\\ \left[\underline{\underline{K}}_y\right] &= k_{y0}\left[\delta_{n,\tilde{n}}\right]\end{aligned}\right\}, \quad n,\tilde{n}=0,\pm1,...,\pm N_T \tag{28}$$

and

$$\left[\underline{\underline{\epsilon}}_{pq}(z)\right] = \left[\epsilon_{pq}^{(n-\tilde{n})}(z)\right], \quad n,\tilde{n}=0,\pm1,...,\pm N_T, \quad p,q=x,y,z, \tag{29}$$

where $\delta_{n,\tilde{n}}$ is the Kronecker delta. Equations (21–26) can now be expressed in matrix form as follows:

$$\frac{\mathrm{d}}{\mathrm{d}z}\left[\underline{E}_x(z)\right] - \mathrm{i}\left[\underline{\underline{K}}_x\right]\cdot\left[\underline{E}_z(z)\right] = \mathrm{i}k_0\eta_0\left[\underline{H}_y(z)\right], \tag{30}$$

$$\frac{\mathrm{d}}{\mathrm{d}z}\left[\underline{E}_y(z)\right] - \mathrm{i}\left[\underline{\underline{K}}_y\right]\cdot\left[\underline{E}_z(z)\right] = -\mathrm{i}k_0\eta_0\left[\underline{H}_x(z)\right], \tag{31}$$

$$\left[\underline{\underline{K}}_y\right]\cdot\left[\underline{E}_x(z)\right] - \left[\underline{\underline{K}}_x\right]\cdot\left[\underline{E}_y(z)\right] = -k_0\,\eta_0\left[\underline{H}_z(z)\right], \tag{32}$$

$$\frac{\mathrm{d}}{\mathrm{d}z}\left[\underline{H}_x(z)\right] - \mathrm{i}\left[\underline{\underline{K}}_x\right]\cdot\left[\underline{H}_z(z)\right] = -\frac{\mathrm{i}k_0}{\eta_0}\left(\left[\underline{\underline{\epsilon}}_{yx}(z)\right]\cdot\left[\underline{E}_x(z)\right] + \left[\underline{\underline{\epsilon}}_{yy}(z)\right]\cdot\left[\underline{E}_y(z)\right] + \left[\underline{\underline{\epsilon}}_{yz}(z)\right]\cdot\left[\underline{E}_z(z)\right]\right), \tag{33}$$

$$\frac{\mathrm{d}}{\mathrm{d}z}\left[\underline{H}_y(z)\right] - \mathrm{i}\left[\underline{\underline{K}}_y\right]\cdot\left[\underline{H}_z(z)\right] = \frac{\mathrm{i}k_0}{\eta_0}\left(\left[\underline{\underline{\epsilon}}_{xx}(z)\right]\cdot\left[\underline{E}_x(z)\right] + \left[\underline{\underline{\epsilon}}_{xy}(z)\right]\cdot\left[\underline{E}_y(z)\right] + \left[\underline{\underline{\epsilon}}_{xz}(z)\right]\cdot\left[\underline{E}_z(z)\right]\right), \tag{34}$$

$$\left[\underline{\underline{K}}_y\right]\cdot\left[\underline{H}_x(z)\right] - \left[\underline{\underline{K}}_x\right]\cdot\left[\underline{H}_y(z)\right] = \frac{k_0}{\eta_0}\left(\left[\underline{\underline{\epsilon}}_{zx}(z)\right]\cdot\left[\underline{E}_x(z)\right] + \left[\underline{\underline{\epsilon}}_{zy}(z)\right]\cdot\left[\underline{E}_y(z)\right] + \left[\underline{\underline{\epsilon}}_{zz}(z)\right]\cdot\left[\underline{E}_z(z)\right]\right). \tag{35}$$

Equations (32, 35) help us eliminate $[\underline{E}_z(z)]$ and $[\underline{H}_z(z)]$ in favor of $[\underline{E}_x(z)]$, $[\underline{E}_y(z)]$, $[\underline{H}_x(z)]$ and $[\underline{H}_y(z)]$, by yielding

$$\left[\underline{E}_z(z)\right] = -\left[\underline{\underline{\epsilon}}_{zz}(z)\right]^{-1}\cdot\left[\underline{\underline{\epsilon}}_{zx}(z)\right]\cdot\left[\underline{E}_x(z)\right] - \left[\underline{\underline{\epsilon}}_{zz}(z)\right]^{-1}\cdot\left[\underline{\underline{\epsilon}}_{zy}(z)\right]\cdot\left[\underline{E}_y(z)\right] + \frac{\eta_0}{k_0}\left[\underline{\underline{\epsilon}}_{zz}(z)\right]^{-1}\cdot\left[\underline{\underline{K}}_y\right]\cdot\left[\underline{H}_x(z)\right] - \frac{\eta_0}{k_0}\left[\underline{\underline{\epsilon}}_{zz}(z)\right]^{-1}\cdot\left[\underline{\underline{K}}_x\right]\cdot\left[\underline{H}_y(z)\right], \tag{36}$$

and

$$\left[\underline{H}_z(z)\right] = \frac{1}{k_0\,\eta_0}\left(\left[\underline{\underline{K}}_x\right]\cdot\left[\underline{E}_y(z)\right] - \left[\underline{\underline{K}}_y\right]\cdot\left[\underline{E}_x(z)\right]\right). \tag{37}$$

Substituting $[\underline{E}_z(z)]$ and $[\underline{H}_z(z)]$ into (30, 31, 33, 34), and performing some algebraic manipulations, we derive the following $4(2N_T+1)\times4(2N_T+1)$ matrix ordinary differential equation:

$$\frac{\mathrm{d}}{\mathrm{d}z}\left[\underline{\mathbf{f}}(z)\right] = \mathrm{i}\left[\underline{\underline{\mathbf{P}}}(z)\right]\cdot\left[\underline{\mathbf{f}}(z)\right], \quad 0<z<L. \tag{38}$$

The column vector

$$\left[\underline{\mathbf{f}}(z)\right] = \begin{bmatrix}\left[\underline{E}_x(z)\right]\\ \left[\underline{E}_y(z)\right]\\ \eta_0\left[\underline{H}_x(z)\right]\\ \eta_0\left[\underline{H}_y(z)\right]\end{bmatrix} \tag{39}$$

contains $4(2N_T+1)$ components, while the $4(2N_T+1)\times4(2N_T+1)$ kernel matrix $\left[\underline{\underline{\mathbf{P}}}(z)\right]$ is given in Appendix.

2.4 Boundary value problem

Equation (38) substantially defines the boundary value problem to be solved. The solution of (38) is of the form

$$\left[\underline{\mathbf{f}}(L)\right] = \left[\underline{\underline{\mathbf{M}}}(L)\right]\cdot\left[\underline{\mathbf{f}}(0)\right], \tag{40}$$

where the matrizant $\left[\underline{\underline{\mathbf{M}}}(z)\right]$ satisfies the matrix equation

$$\frac{\mathrm{d}}{\mathrm{d}z}\left[\underline{\underline{\mathbf{M}}}(z)\right] = \mathrm{i}\left[\underline{\underline{\mathbf{P}}}(z)\right]\cdot\left[\underline{\underline{\mathbf{M}}}(z)\right], \quad 0<z<L, \tag{41}$$

with the initial value

$$\left[\underline{\underline{\mathbf{M}}}(0)\right] = \left[\underline{\underline{I}}\right], \tag{42}$$

where $[\underline{\underline{I}}]$ is the identity matrix of size $(4N_T+2)\times(4N_T+2)$.

Continuity of the tangential components of the electric and magnetic field phasors across the planes $z=0$ and $z=L$ must be enforced with respect to the Floquet harmonic of any order n for all z. According to (6–11), we have

$$\left[\underline{\mathbf{f}}(0)\right] = \begin{bmatrix}\left[\underline{\underline{Y}}_e\right]\\ \left[\underline{\underline{Y}}_h\right]\end{bmatrix}\cdot\begin{bmatrix}\left[\underline{a}_L\right]\\ \left[\underline{a}_R\right]\end{bmatrix} + \begin{bmatrix}\left[\underline{\underline{Y}}_e\right]^*\\ -\left[\underline{\underline{Y}}_h\right]^*\end{bmatrix}\cdot\begin{bmatrix}\left[\underline{r}_L\right]\\ \left[\underline{r}_R\right]\end{bmatrix} \tag{43}$$

and

$$\left[\underline{\mathbf{f}}(L)\right] = \begin{bmatrix}\left[\underline{\underline{Y}}_e\right]\\ \left[\underline{\underline{Y}}_h\right]\end{bmatrix}\cdot\begin{bmatrix}\left[\underline{t}_L\right]\\ \left[\underline{t}_R\right]\end{bmatrix}, \tag{44}$$

where the asterisk denotes the conjugate transpose. The column vectors

$$\left.\begin{aligned}\left[\underline{a}_L\right] &= \left[a_L^{(n)}\right], & \left[\underline{a}_R\right] &= \left[a_R^{(n)}\right]\\ \left[\underline{r}_L\right] &= \left[r_L^{(n)}\right], & \left[\underline{r}_R\right] &= \left[r_R^{(n)}\right]\\ \left[\underline{t}_L\right] &= \left[t_L^{(n)}\right], & \left[\underline{t}_R\right] &= \left[t_R^{(n)}\right]\end{aligned}\right\} \tag{45}$$

are of size $2N_T+1$, while the matrixes

$$\left[\underline{\underline{Y}}_e\right] = \begin{bmatrix}\left[\underline{\underline{Y}}_{xL}\right] & \left[\underline{\underline{Y}}_{xR}\right]\\ \left[\underline{\underline{Y}}_{yL}\right] & \left[\underline{\underline{Y}}_{yR}\right]\end{bmatrix}, \quad \left[\underline{\underline{Y}}_h\right] = \mathrm{i}\begin{bmatrix}-\left[\underline{\underline{Y}}_{xL}\right] & \left[\underline{\underline{Y}}_{xR}\right]\\ -\left[\underline{\underline{Y}}_{yL}\right] & \left[\underline{\underline{Y}}_{yR}\right]\end{bmatrix} \tag{46}$$

are of size $(4N_T+2)\times(4N_T+2)$. The square matrixes

$$\left.\begin{aligned}\left[\underline{\underline{Y}}_{xL}\right] &= \left[\xi_n\,\delta_{n,\tilde{n}}\right]\,, \qquad \left[\underline{\underline{Y}}_{yR}\right] = \left[\zeta_n\,\delta_{n,\tilde{n}}\right]\\ \left[\underline{\underline{Y}}_{xR}\right] &= \left[\xi_n^*\,\delta_{n,\tilde{n}}\right]\,, \qquad \left[\underline{\underline{Y}}_{yL}\right] = \left[\zeta_n^*\,\delta_{n,\tilde{n}}\right]\end{aligned}\right\} \tag{47}$$

employ the complex numbers

$$\left.\begin{aligned}\xi_n &= \tfrac{1}{\sqrt{2}}\left(\tfrac{k_{xn}\,k_{zn}}{k_0\,k_{xyn}} - \mathrm{i}\,\tfrac{k_{y0}}{k_{xyn}}\right)\\ \zeta_n &= \tfrac{1}{\sqrt{2}}\left(\tfrac{k_{y0}\,k_{zn}}{k_0\,k_{xyn}} - \mathrm{i}\,\tfrac{k_{xn}}{k_{xyn}}\right)\end{aligned}\right\}\,, \quad n=0,\,\pm1,\,...,\,\pm N_T\,. \tag{48}$$

Substitution of (43–44) into (40) leads to the algebraic matrix equation

$$\begin{bmatrix}\left[\underline{\underline{Y}}_e\right]\\ \left[\underline{\underline{Y}}_h\right]\end{bmatrix}\cdot\begin{bmatrix}\left[\underline{t}_L\right]\\ \left[\underline{t}_R\right]\end{bmatrix} - \left[\underline{\underline{\mathbf{M}}}\,(L)\right]\cdot\begin{bmatrix}\left[\underline{\underline{Y}}_e\right]^*\\ -\left[\underline{\underline{Y}}_h\right]^*\end{bmatrix}\cdot\begin{bmatrix}\left[\underline{r}_L\right]\\ \left[\underline{r}_R\right]\end{bmatrix} = \left[\underline{\underline{\mathbf{M}}}\,(L)\right]\cdot\begin{bmatrix}\left[\underline{\underline{Y}}_e\right]\\ \left[\underline{\underline{Y}}_h\right]\end{bmatrix}\cdot\begin{bmatrix}\left[\underline{a}_L\right]\\ \left[\underline{a}_R\right]\end{bmatrix}\,, \tag{49}$$

which has to be solved by standard numerical techniques for simultaneous linear algebraic equations [34].

2.5 Piecewise homogeneity approximation method

The matrix $\left[\underline{\underline{\mathbf{M}}}\,(L)\right]$ of (41) was computed using the piecewise homogeneity approximation method [24]. In this method, the slanted chiral STF is modelled to consist of electrically thin sublayers normal to z-axis. The dielectric properties of the film are considered to be homogeneous within each sublayer, but varying from sublayer to sublayer.

The region $0 \le z \le L$ is divided into N_ℓ sublayers, each of thickness $\Delta z = L/N_\ell$. Let $z_j = j\Delta z$, $(j=0,\,1,\,...,\,N_\ell-1)$, and we approximate $\underline{\underline{\epsilon}}(\mathbf{r})$ in the jth sublayer as

$$\underline{\underline{\epsilon}}(\mathbf{r}) \approx \frac{\underline{\underline{\epsilon}}\,(x,z_j)+\underline{\underline{\epsilon}}\,(x,z_{j+1})}{2}\,, \qquad z_j<z<z_{j+1}\,,\quad j=[0,\,N_\ell-1]\,. \tag{50}$$

Taking the spatial Fourier transforms of the two sides of (50) with respect to x, and by virtue of (29), we obtain the approximate value of $\left[\underline{\underline{\epsilon}}_{pq}\,(z)\right]$, $(p,q=x,y,z)$, in the jth sublayer as

$$\left[\underline{\underline{\epsilon}}_{pq}\right]_j \approx \frac{\left[\underline{\underline{\epsilon}}_{pq}\,(z_j)\right]+\left[\underline{\underline{\epsilon}}_{pq}\,(z_{j+1})\right]}{2}\,, \qquad p,q=x,y,z\,,\quad j\in[0,\,N_\ell-1]\,. \tag{51}$$

By propagating the tangential components of the electromagnetic fields across each sublayer, we obtain

$$\left[\underline{\mathbf{f}}\,(z_{j+1})\right] = \left[\underline{\underline{\mathbf{M}}}_j\right]\cdot\left[\underline{\mathbf{f}}\,(z_j)\right]\,, \quad j\in[0,\,N_\ell-1]\,, \tag{52}$$

where

$$\begin{aligned}\left[\underline{\underline{\mathbf{M}}}_j\right] &= \exp\left\{\mathrm{i}\,\left[\underline{\underline{\mathbf{P}}}_j\right]\Delta z\right\}\\ &= \left[\underline{\underline{I}}\right] + \lim_{r\to\infty}\sum_{m=1}^{r}\frac{(\mathrm{i}\,\Delta z)^m\left[\underline{\underline{\mathbf{P}}}_j\right]^m}{m!}\,,\end{aligned} \tag{53}$$

and $\left[\underline{\underline{\mathbf{P}}}_j\right] = \left[\underline{\underline{\mathbf{P}}}(\frac{z_j+z_{j+1}}{2})\right]$ is to be computed using (50). The number of the terms r in the actual calculation of the sum in (53) was determined by satisfaction of the following two convergence criterions for $1\le u\le 4(2N_T+1)$, $1\le v\le 4(2N_T+1)$:

$$-10^{-12} \le \frac{\mathrm{Re}\left\{\left[\frac{(\mathrm{i}\,\Delta z)^{r+1}}{(r+1)!}\left[\underline{\underline{\mathbf{P}}}_j\right]^{r+1}\right]_{uv}\right\}}{\mathrm{Re}\left\{\left[\left[\underline{\underline{I}}\right]+\sum_{m=1}^{r}\frac{(\mathrm{i}\,\Delta z)^m}{m!}\left[\underline{\underline{\mathbf{P}}}_j\right]^m\right]_{uv}\right\}} \le 10^{-12}, \tag{54}$$

$$-10^{-12} \le \frac{\mathrm{Im}\left\{\left[\frac{(\mathrm{i}\,\Delta z)^{r+1}}{(r+1)!}\left[\underline{\underline{\mathbf{P}}}_j\right]^{r+1}\right]_{uv}\right\}}{\mathrm{Im}\left\{\left[\left[\underline{\underline{I}}\right]+\sum_{m=1}^{r}\frac{(\mathrm{i}\,\Delta z)^m}{m!}\left[\underline{\underline{\mathbf{P}}}_j\right]^m\right]_{uv}\right\}} \le 10^{-12}. \tag{55}$$

The matrix $\left[\underline{\underline{\mathbf{M}}}\,(L)\right]$ was then estimated as

$$\left[\underline{\underline{\mathbf{M}}}\,(L)\right] \approx \left[\underline{\underline{\mathbf{M}}}_{N_\ell-1}\right]\cdot\left[\underline{\underline{\mathbf{M}}}_{N_\ell-2}\right]\cdots\left[\underline{\underline{\mathbf{M}}}_1\right]\cdot\left[\underline{\underline{\mathbf{M}}}_0\right]\,, \tag{56}$$

with adequately large N_ℓ.

Once $\left[\underline{\underline{\mathbf{M}}}\,(L)\right]$ was determined, using the piecewise homogeneity approximation method, the planewave response of the slanted chiral STF was obtained by solving (49) for the four sets of the unknown amplitudes $\left\{r_L^{(n)}\right\}$, $\left\{r_R^{(n)}\right\}$, $\left\{t_L^{(n)}\right\}$ and $\left\{t_R^{(n)}\right\}$, $(n=0,\,\pm1,\,...,\,\pm N_T)$.

2.6 Reflectances and transmittances

The time-averaged power incident over the periodic cell ΔS: $\{0<x<L_x\,, 0<y<1\}$ at the $z=0$ plane is given by

$$\begin{aligned}P_{\mathrm{i}} &= \frac{1}{2}\mathrm{Re}\left\{\iint_{\Delta S}\left(\mathbf{E}_{\mathrm{i}}\times\mathbf{H}_{\mathrm{i}}^*\right)\cdot\mathbf{u}_z\,\mathrm{d}x\,\mathrm{d}y\right\}\\ &= -\frac{L_x}{\eta_0}\,\mathrm{Im}\left[\xi_0\,\zeta_0\right]\left(|a_L^{(0)}|^2+|a_R^{(0)}|^2\right)\,,\end{aligned} \tag{57}$$

since $a_L^{(n)}$ and $a_R^{(n)}$ are all null-valued for $n\ne0$. Similarly, the power density reflected at the $z=0$ plane into the lower half-space $z\le0$, as well as the power transmitted across the slanted chiral STF into the upper half-space $z\ge L$, over the same periodic cell are given by

$$P_{\mathrm{r}} = -\frac{L_x}{\eta_0}\sum_{n=0,\,\pm1,\,...,\,\pm N_T}\mathrm{Im}\left[\xi_n\,\zeta_n\right]\left(|r_L^{(n)}|^2+|r_R^{(n)}|^2\right) \tag{58}$$

and

$$P_{\rm t} = -\frac{L_x}{\eta_0} \sum_{n=0,\,\pm1,\,\ldots,\,\pm N_T} \mathrm{Im}\left[\xi_n\,\zeta_n\right] \left(|t_L^{(n)}|^2 + |t_R^{(n)}|^2\right) . \tag{59}$$

On account of (58–59), we define the reflectances ($R_{LL}^{(n)}$, etc.) and the transmittances ($T_{LL}^{(n)}$, etc.) as follows:

$$\begin{bmatrix} R_{LL}^{(n)} & R_{LR}^{(n)} \\ R_{RL}^{(n)} & R_{RR}^{(n)} \end{bmatrix} = \frac{\mathrm{Im}(\xi_n\,\zeta_n)}{\mathrm{Im}(\xi_0\,\zeta_0)} \begin{bmatrix} \frac{|r_L^{(n)}|^2}{|a_L^{(0)}|^2} & \frac{|r_L^{(n)}|^2}{|a_R^{(0)}|^2} \\ \frac{|r_R^{(n)}|^2}{|a_L^{(0)}|^2} & \frac{|r_R^{(n)}|^2}{|a_R^{(0)}|^2} \end{bmatrix} ,$$

$$\begin{bmatrix} T_{LL}^{(n)} & T_{LR}^{(n)} \\ T_{RL}^{(n)} & T_{RR}^{(n)} \end{bmatrix} = \frac{\mathrm{Im}(\xi_n\,\zeta_n)}{\mathrm{Im}(\xi_0\,\zeta_0)} \begin{bmatrix} \frac{|t_L^{(n)}|^2}{|a_L^{(0)}|^2} & \frac{|t_L^{(n)}|^2}{|a_R^{(0)}|^2} \\ \frac{|t_R^{(n)}|^2}{|a_L^{(0)}|^2} & \frac{|t_R^{(n)}|^2}{|a_R^{(0)}|^2} \end{bmatrix} . \tag{60}$$

The principle of conservation of energy mandates the inequalities

$$\sum_{n=0,\,\pm1,\,\ldots,\,\pm N_T} \left(R_{LL}^{(n)} + R_{RL}^{(n)} + T_{LL}^{(n)} + T_{RL}^{(n)}\right) \le 1 , \tag{61}$$

$$\sum_{n=0,\,\pm1,\,\ldots,\,\pm N_T} \left(R_{LR}^{(n)} + R_{RR}^{(n)} + T_{LR}^{(n)} + T_{RR}^{(n)}\right) \le 1 . \tag{62}$$

The inequalities reduce to equalities for non-dissipative materials.

3 Results and discussion

3.1 Preliminaries

The algorithm described in the preceding section was implemented using double-precision arithmetic in Fortran 90 on a Solaris computer. A structurally right-handed slanted chiral STF was chosen with the following constitutive and other parameters: $p_a = 2.0$, $p_b = 2.6$ and $p_c = 2.1$; $\lambda_a = \lambda_c = 140$ nm and $\lambda_b = 150$ nm; $N_a = N_b = N_c = 100$; $L = 8100$ nm; $\Omega = 300$ nm; $\chi_s = 30°$. The chosen constitutive parameters are potentially realizable using silicon dioxide, and are thus likely to be compatible with semiconductor and optical technologies. For compatibility with the commonplace planar structures in electronics and optics, we examined only the normal-incidence case (*i.e.*, $\theta_{\rm inc} = 0°$) with $\psi_{\rm inc} = 0°$; hence, $\sin\psi_n = 0\ \forall n$. From numerous computational tests, we confirmed that the sublayer thickness $\Delta z = 6$ nm sufficed for the convergence of $\left[\underline{\underline{\mathbf{M}}}\,(L)\right]$ for $\lambda_0 \in [900, 1200]$ nm.

The maximum order parameter for the Floquet harmonics was fixed at $N_T = 3$ for the chosen wavelength-regime, after ensuring that every reflectance and transmittance greater than 0.001 converges to 1% accuracy. All propagating harmonics and some evanescent harmonics were thereby covered. Moreover, we ensured that the left sides of both (61) and (62) converged, and that neither condition was violated by more than 1 ppm.

3.2 Unslanted chiral STF

Let us begin with an unslanted chiral STF, *i.e.*, $\alpha = 0°$. The response of this film to normally incident plane waves has been extensively studied, theoretically [11,23,29] as well as experimentally [17,20].

The hallmark of an axially excited chiral STF is the circular Bragg phenomenon. Provided the film thickness is sufficiently large and λ_0 lies within a certain wavelength-regime, the reflectance is much higher if the handedness of the incident plane wave matches the structural handedness of the film than if otherwise. The center-wavelength of this regime is estimated as

$$\lambda_0^{\rm Br} \approx \Omega \left[\sqrt{\epsilon_c\left(\lambda_0^{\rm Br}\right)} + \sqrt{\tilde{\epsilon}_d\left(\lambda_0^{\rm Br}\right)}\right] , \tag{63}$$

where

$$\tilde{\epsilon}_d\left(\lambda_0\right) = \frac{\epsilon_a\left(\lambda_0\right)\,\epsilon_b\left(\lambda_0\right)}{\epsilon_a\left(\lambda_0\right)\cos^2\chi_s + \epsilon_b\left(\lambda_0\right)\sin^2\chi_s} . \tag{64}$$

Grating theory provides an explanation for the polarization-sensitive Bragg phenomenon – a plane wave of matching handedness effectively encounters a Bragg grating, while that of the other handedness does not [35].

Figure 3 shows a comparison of the reflectances and transmittances computed using the algorithm of Section 2 against those computed using the semi–analytical method available for this special case ($\alpha = \theta_{\rm inc} = 0°$) available elsewhere [29,36]. All reflectances and transmittances must be specular when $\alpha = 0°$, regardless of theirs order n, in view of the definitions (12, 13). The Bragg regime, as predicted by (63), is obvious in the plots: $\sum_n R_{RR}^{(n)} >> \sum_n R_{LL}^{(n)}$ and $\sum_n T_{RR}^{(n)} << \sum_n T_{LL}^{(n)}$ while $\sum_n R_{RL}^{(n)} \approx \sum_n R_{LR}^{(n)}$ and $\sum_n T_{RL}^{(n)} \approx \sum_n T_{LR}^{(n)}$ are very small in the Bragg regime. The coincidence of the two sets of results presented in Figure 3, as well as of other results for $\alpha = 0°$ [23,33,37], provided us the necessary confidence to move to $\alpha \neq 0°$.

3.3 Slanted chiral STF

Only for $\alpha \neq 0°$ does a distinction between Floquet harmonics of order $n = 0$ and $n \neq 0$ appears, the former being classified as *specular* and the latter as *nonspecular* in the literature on diffraction gratings [4]. With only normal incidence (*i.e.*, $\theta_{\rm inc} = \psi_{\rm inc} = 0°$) considered in this section, non-negligible remittances (*i.e.*, reflectances and transmittances) were found to be only of orders $n = \pm 2$ (nonspecular if $\alpha \neq 0°$) and $n = 0$ (specular for all α), regardless of the value of α. The remittances of other orders turned out to be negligible (<0.01) in the wavelength-regime focused on. Plots of only the non-negligible remittances are presented in this paper. All presented results apply for negative values of α, provided all remittances of order n are considered as the remittances of order $-n$.

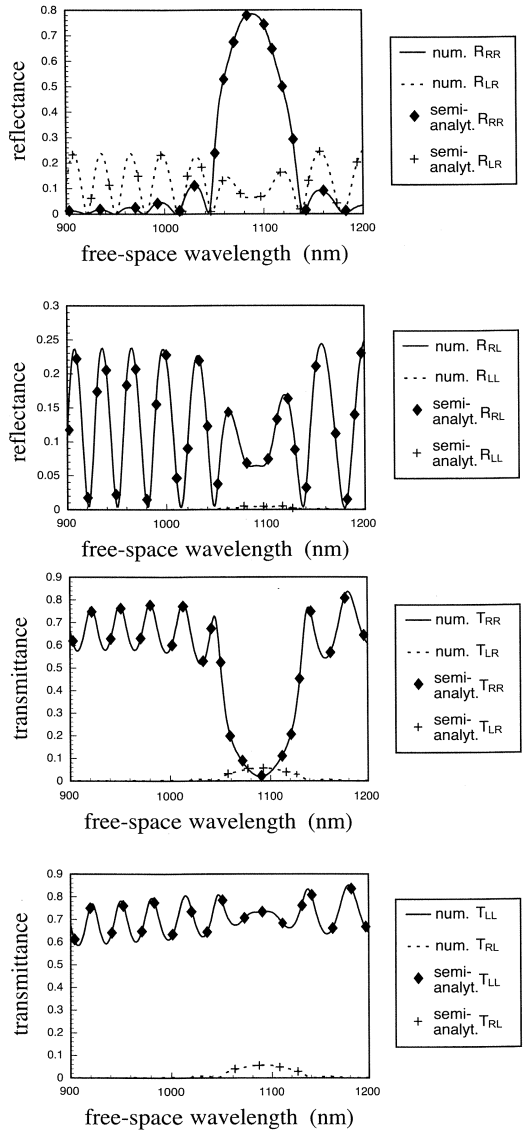

Fig. 3. Reflectances $R_{RR} = \sum_n R_{RR}^{(n)}$, etc., and transmittances $T_{RR} = \sum_n T_{RR}^{(n)}$, etc., computed using the algorithm of Section 2 are compared against the results from the semi-analytical method available elsewhere [29,36]. The various parameters used are as follows: $\alpha = 0°$, $\chi_s = 30°$, $p_a = 2.0$, $p_b = 2.6$, $p_c = 2.1$, $\lambda_a = \lambda_c = 140\,\text{nm}$, $\lambda_b = 150\,\text{nm}$, $N_a = N_b = N_c = 100$, $\Omega = 300\,\text{nm}$, $h = 1$, $L = 8100\,\text{nm}$, $\theta_{\text{inc}} = \psi_{\text{inc}} = 0°$.

Figures 4 and 5 comprise plots of the reflectances and the transmittances of order $n = 0$ and -2 as functions of λ_0 when $\alpha = 10°$ and $15°$, respectively. The characteristic signature of the circular Bragg phenomenon is found as a broad crest in the plot of $R_{RR}^{(-2)}$ and a trough in the plot of $T_{RR}^{(0)}$, positioned between 1000 nm and 1100 nm. Thus, a normally incident RCP plane wave is mostly reflected obliquely: at an angle $90° + \sin^{-1}\left[(\lambda_0/\Omega)\sin\alpha\right]$ to the $+x$-axis. Since $\lambda_0/\Omega \sim 3.3$, a slight increase in α results in more oblique reflection.

When the incident plane wave is LCP, however, $T_{LL}^{(0)}$ dominates all the other remittances in the same regime. Hence, the LCP plane wave is mostly transmitted without change of direction – in a fashion similar to that for $\alpha = 0°$. Clearly, the Bragg phenomenon is *partially* nonspecular for slanted chiral STFs, which can be exploited as circular polarization splitters and polarization-sensitive direction couplers.

The center-wavelength of the Bragg regime shifts to smaller values with increasing α. This blue-shift is captured by the modification of (63) to

$$\lambda_0^{\text{Br}} \approx (\Omega\cos\alpha)\left[\sqrt{\epsilon_c\left(\lambda_0^{\text{Br}}\right)} + \sqrt{\tilde{\epsilon}_d\left(\lambda_0^{\text{Br}}\right)}\right]. \qquad (65)$$

In other words, the period of the slanted chiral STF along the z-axis is effectively reduced from 2Ω to $2\Omega\cos\alpha$, for the production of the circular Bragg phenomenon. The $\cos\alpha$ dependence is in accord with the orange color of multi-domain cholesteric liquid crystals that were fabricated to reflect the red color [38].

We determined the center-wavelength λ_0^{Br} as a function of α, from the computed spectrums of $R_{RR}^{(-2)}$. The results are compared with the prediction from (65) in Figure 6(a), and the excellent correspondence for $\alpha \in [0°, 15°]$ lends credibility to (65).

Figure 6(b) contains a plot of the full-width-at-half-maximum (FWHM) bandwidth $\Delta\lambda_0^{\text{Br}}$ as a function of α. This plot clearly shows the thinning of the Bragg regime with increase in α. Indeed, the circular Bragg phenomenon vanishes for $\alpha > 17.1°$. The reason for the disappearance of that phenomenon is best explained *via* the so-called Rayleigh-Wood anomalies as follows.

Just as for the commonplace surface-relief gratings [4], nonspecular Floquet harmonics exist in the two half-spaces. A Floquet harmonic of order n propagates energy away from the slanted chiral STF provided k_{zn} is real-valued, *i.e.*, for wavelengths $\lambda_0 < \lambda_{0_n}^{\text{RW}}$, where

$$\lambda_{0_n}^{\text{RW}} = \frac{2\Omega}{|n|\,|\sin\alpha|} \qquad (66)$$

follows from (12–14). At the higher wavelengths $\lambda_0 > \lambda_{0_n}^{\text{RW}}$, the nth-order harmonic is evanescent along the z-axis, and does not participate in the statements (61) and (62) of the principle of conservation of energy. The conversion of the nth-order Floquet harmonic from propagating to evanescent, or *vice versa*, as λ_0 either increases or decreases across $\lambda_{0_n}^{\text{RW}}$ is a Rayleigh-Wood anomaly. Table 1 shows computed values of $\lambda_{0_n}^{\text{RW}}$, $(n = \pm1, \pm2, \pm3)$, for several different values of $\alpha \in [0°, 18°]$.

Specifically, as α increases from $0°$, $\lambda_{0_{-2}}^{\text{RW}}$ decreases from "infinity" and begins to approach the center-wavelength λ_0^{Br} of the Bragg regime predicted by (65). Table 1 records the blue-shifts of both $\lambda_{0_{-2}}^{\text{RW}}$ and λ_0^{Br} as α increases, but the decrease in $\lambda_{0_{-2}}^{\text{RW}}$ is more rapid than the decrease in λ_0^{Br}.

When $\alpha = 15°$, $\lambda_{0_{-2}}^{\text{RW}}$ is about 100 nm larger than λ_0^{Br}. Still, the spectrums of $R_{RR}^{(-2)}$ and $T_{RR}^{(0)}$ in Figure 4 are clearly affected, the signature features of the circular Bragg phenomenon being quite irregular in comparison to those in Figure 2 for $\alpha = 0°$. The same features in Figure 3

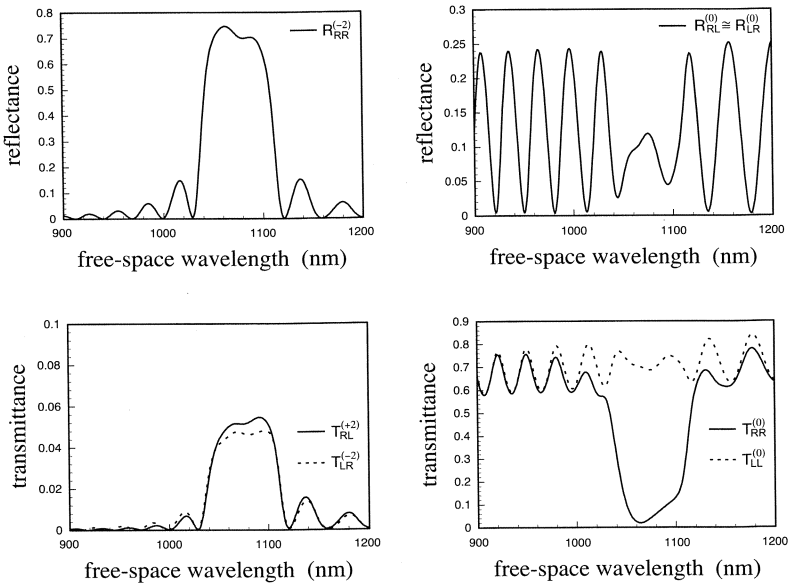

Fig. 4. Remittances of order n, computed for the following parameters: $\alpha = 10°$, $\chi_s = 30°$, $p_a = 2.0$, $p_b = 2.6$, $p_c = 2.1$, $\lambda_a = \lambda_c = 140\,\text{nm}$, $\lambda_b = 150\,\text{nm}$, $N_a = N_b = N_c = 100$, $\Omega = 300\,\text{nm}$, $h = 1$, $L = 8100\,\text{nm}$, $\theta_{\text{inc}} = \psi_{\text{inc}} = 0°$. Remittances of maximum magnitudes less than 0.01 are not shown.

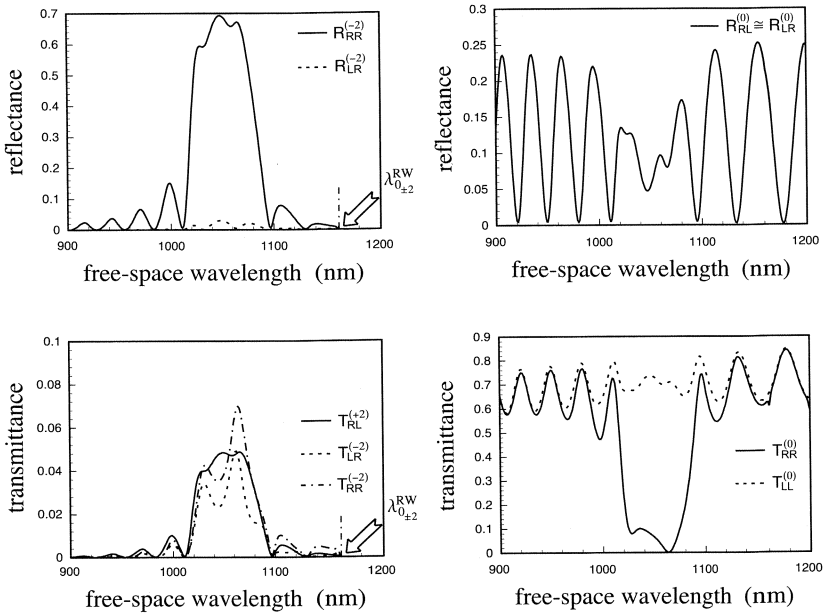

Fig. 5. Same as Figure 4, but for $\alpha = 15°$.

are mildly irregular for $\alpha = 10°$ when $\lambda_{0_{-2}}^{\text{RW}}$ is about 700 nm larger than λ_0^{Br}. Moreover, as $\lambda_{0_{-2}}^{\text{RW}}$ approaches λ_0^{Br}, non-specular transmission in the Bragg regime becomes significant – thus, $T_{RR}^{(-2)}$ is not negligible for $\alpha = 15°$ in Figure 5, in contrast to its values for $\alpha = 10°$ in Figure 4.

A further increase in α makes $\lambda_{0_{-2}}^{\text{RW}}$ come even closer to λ_0^{Br} as predicted by (65). For example, the two wavelengths are virtually equal in Table 1 when $\alpha = 16.7°$. The actual Bragg regime in Figure 7 for this value of α is blue-shifted relative to the prediction from (65); the peak value of $R_{RR}^{(-2)}$ is noticeably smaller than in Figures 3–5; and the Bragg regime is also narrower. Subversion of the circular Bragg phenomenon is also indicated by the non-negligible values of $R_{LR}^{(-2)}$ in Figure 7, in striking contrast to the cases of lower values of $\alpha = 10°$.

Table 1. Center-wavelengths λ_0^{Br} of the Bragg regime predicted by (65), and the wavelength $\lambda_{0_n}^{\mathrm{RW}}$ of the Rayleigh-Wood anomaly of order n.

α	0°	10°	15°	16.7°	17.1°	17.6°	18°
λ_0^{Br} (nm)	1090	1073	1053	1044	1042	1039	1036
$\lambda_{0_{+1}}^{\mathrm{RW}}$ (nm)	†	3456	2318	2088	2040	1984	1942
$\lambda_{0_{+2}}^{\mathrm{RW}}$ (nm)	†	1728	1159	1044	1020	992	971
$\lambda_{0_{+3}}^{\mathrm{RW}}$ (nm)	†	1152	773	696	680	661	647

† not applicable

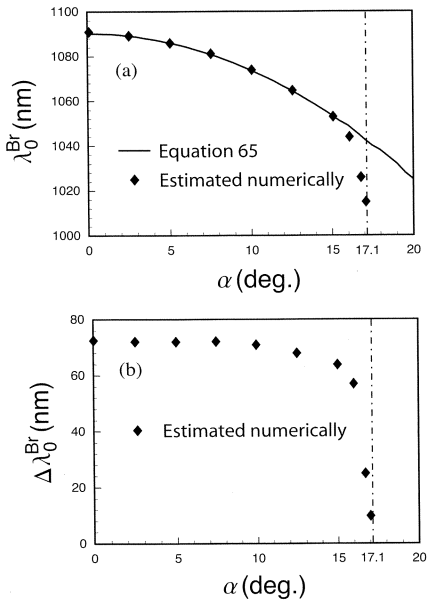

Fig. 6. (a) Center-wavelength λ_0^{Br} as a function of the slant angle α, estimated using equation (65) (solid line) and the algorithm of Section 2 (squares). (b) The FWHM bandwidth $\Delta\lambda_0^{\mathrm{Br}}$ of the Bragg regime calculated using the same algorithms. The various parameters used are as follows: $\chi_s = 30^\circ$, $p_a = 2.0$, $p_b = 2.6$, $p_c = 2.1$, $\lambda_a = \lambda_c = 140\,\mathrm{nm}$, $\lambda_b = 150\,\mathrm{nm}$, $N_a = N_b = N_c = 100$, $\Omega = 300\,\mathrm{nm}$, $h = 1$, $L = 8100$ nm, $\theta_{\mathrm{inc}} = \psi_{\mathrm{inc}} = 0^\circ$. The circular Bragg phenomenon vanishes for $\alpha > 17.1^\circ$.

The circular Bragg phenomenon virtually disappears when $\alpha = 17.1^\circ$, with the peak value of $R_{RR}^{(-2)}$ dropping to one-half of its value for $\alpha = 0^\circ$. Figure 8 shows the non-negligible remittances calculated for $\alpha = 17.6^\circ$. Clearly, the rapid blue-shift of $\lambda_{0_{-2}}^{\mathrm{RW}}$ has highly subverted the circular Bragg phenomenon, leaving some minor peaks of reflectances (*i.e.*, of $R_{RR}^{(-2)}$) and transmittances (*i.e.*, of $T_{LR}^{(-2)}$ and $T_{RR}^{(-2)}$) which become even less prominent with further increase of α.

Finally, we should mention that the spectrums of the specular reflectances $R_{RL}^{(0)} \approx R_{LR}^{(0)}$ are virtually unaffected by α outside of the Bragg regime – as is evident from Figures 5, 7 and 8. However, for $\alpha > 15^\circ$, some very narrow features do exist in the long-wavelength portions of the spectrums of the specular reflectances and specular transmittances. Some of these narrow features result from overflow problems [27,33] in that the matrix $[\underline{\underline{\mathbf{M}}}(L)]$ is somewhat ill-conditioned by the presence of evanescent Floquet harmonics of higher orders, for higher values of α.[1] This conclusion was affirmed by reducing the thickness L, when many of the features vanished. Their presence in the plots, however, does not affect the conclusions drawn.

A technological consequence of the results presented in the previous figures is the possibility of using slanted chiral STFs as narrowband circular-polarization beamsplitters. With constitutive properties chosen such that $\lambda_{0_{-2}}^{\mathrm{RW}}$ is greater than the value of λ_0^{Br} predicted by (65), a slanted chiral STF of structural right/left-handedness would redirect the right/left circularly polarized component of an incident beam, but allow the left/right circularly polarized component of the beam to pass through without change of direction – in a narrow wavelength-regime. The reflected beam would propagate obliquely with respect to the $-z$-axis, with reflection being more oblique for greater α. For $\lambda_{0_{-2}}^{\mathrm{RW}}$ only slightly greater than the value of λ_0^{Br} predicted by (65), the reflected beam would be virtually orthogonal to the incident beam. This technological consequence of the coupling of the circular Bragg phenomenon and the Rayleigh-Wood anomalies in a slanted chiral STF appears very promising.

3.4 Slanted chiral STF on a perfect reflector

The circular-polarization-sensitive beamsplitting abilities of a slanted chiral STF can be exploited purely in the reflection mode, provided the plane $z = L$ is made highly reflecting. Suppose this plane is a perfect electric conductor, which means that no transmission can occur. Equations (40–48) still hold, except that the upper boundary condition (44) must be modified to

$$[\underline{\mathbf{f}}(L)] = \begin{bmatrix} [0] \\ [0] \\ \eta_0 [H_{xL}] \\ \eta_0 [H_{yL}] \end{bmatrix}, \tag{67}$$

where $[0]$ is a null vector of size $2N_T + 1$, while the column vectors $[H_{xL}]$ and $[H_{yL}]$ of the same size contain the unknown boundary values of the magnetic field phasor components at $z = L_-$. Equation (49) thereby alters

[1] In the presented method, $N_T \geq 2$ is necessary in view of (17), even though all non-specular remittances are null-valued. This could lead to overflow problems when computing the matrizant $\underline{\underline{\mathbf{M}}}(L)$.

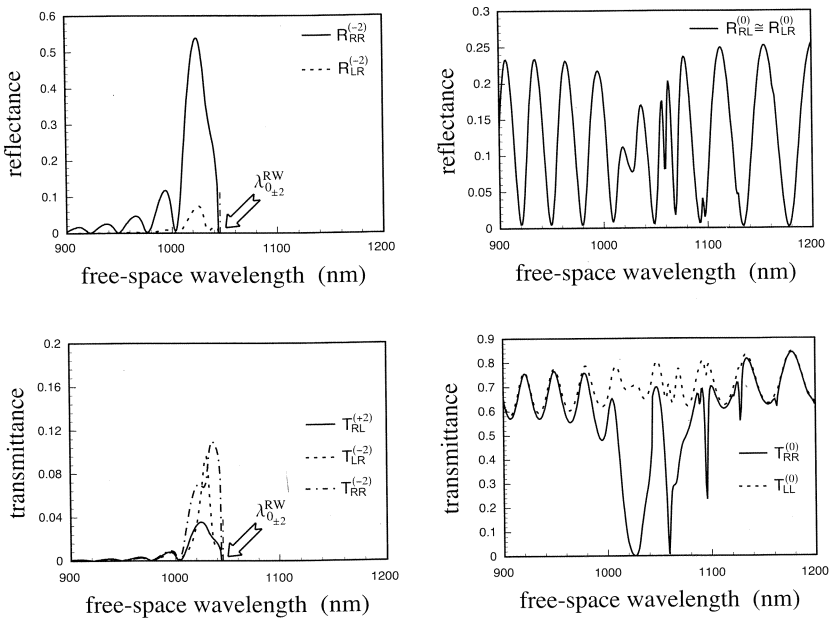

Fig. 7. Same as Figure 4, but for $\alpha = 16.7^\circ$.

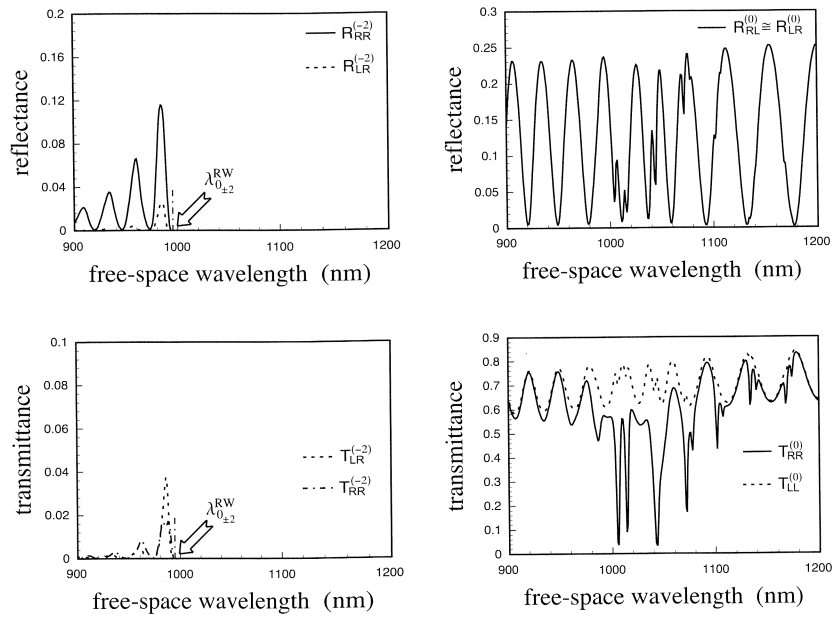

Fig. 8. Same as Figure 4, but for $\alpha = 17.6^\circ$.

as follows:

$$\begin{bmatrix} [0] \\ [0] \\ \eta_0\,[H_{xL}] \\ \eta_0\,[H_{yL}] \end{bmatrix} - \left[\underline{\underline{\mathbf{M}}}\,(L)\right] \cdot \begin{bmatrix} \left[\underline{\underline{Y}}_e\right]^* \\ -\left[\underline{\underline{Y}}_h\right]^* \end{bmatrix} \cdot \begin{bmatrix} [\underline{r}_L] \\ [\underline{r}_R] \end{bmatrix} = \left[\underline{\underline{\mathbf{M}}}\,(L)\right] \cdot \begin{bmatrix} \left[\underline{\underline{Y}}_e\right] \\ \left[\underline{\underline{Y}}_h\right] \end{bmatrix} \cdot \begin{bmatrix} [\underline{a}_L] \\ [\underline{a}_R] \end{bmatrix} . \quad (68)$$

This equation has to be solved for $[\underline{r}_L]$, $[\underline{r}_R]$, $[H_{xL}]$ and $[H_{yL}]$.

The calculations for Figure 5 were repeated, but for the plane $z = 0$ as a perfect reflector. Spectrums of the computed reflectances (for $\alpha = 15^\circ$) are presented in Figure 9. The Bragg regime is clearly evident as a craggy mesa in the spectrum of $R_{RR}^{(-2)}$ in Figure 9; furthermore, transmission being impossible, the Bragg regime is also evident in the spectrum of $R_{LL}^{(+2)}$. Thus, operating in the reflection mode, a slanted chiral STF will redirect normally incident LCP and RCP plane waves in totally different directions on either side of the $-z$-axis, and without change of polarization – provided the wavelength lies in the Bragg regime.

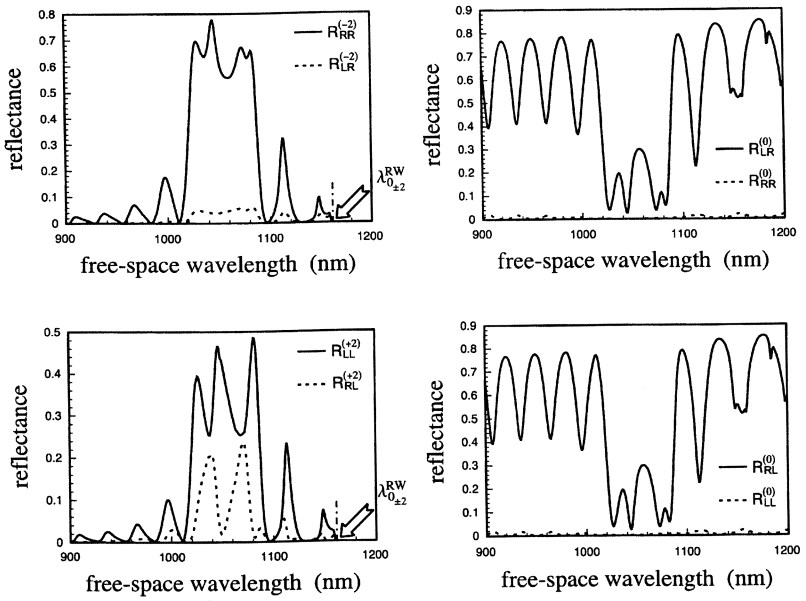

Fig. 9. Reflectances of order n when the plane $z = L$ is a perfect electric conductor, computed for the following parameters: $\alpha = 15^\circ$, $\chi_s = 30^\circ$, $p_a = 2.0$, $p_b = 2.6$, $p_c = 2.1$, $\lambda_a = \lambda_c = 140\,\text{nm}$, $\lambda_b = 150\,\text{nm}$, $N_a = N_b = N_c = 100$, $\Omega = 300\,\text{nm}$, $h = 1$, $L = 8100$ nm, $\theta_{\text{inc}} = \psi_{\text{inc}} = 0^\circ$. Reflectances of maximum magnitudes less than 0.01 are not shown.

4 Concluding remarks

In this paper, we have introduced slanted chiral sculptured thin films as straightforward extensions of (unslanted) chiral STFs. Whereas the latter are periodically nonhomogeneous only in a direction normal to the substrate plane, the former are periodically nonhomogeneous in that direction as well as in the substrate plane as well. The two periodicities are intimately coupled by the slant angle α.

A coupled wave theory is formulated for the planewave response of a slanted chiral STF of finite thickness. The theory was numerically implemented for normally incident plane waves. Results show that the nonspecular remittances and the Rayleigh-Wood anomalies due to periodicity in the substrate plane are tightly coupled to the specular nature of the circular Bragg phenomenon displayed due to periodicity normal to the substrate plane. In the Bragg regime, the left- and the right-circularly polarized components of the incident plane wave are redirected in non-trivially different directions.

As the angle α increases from zero, the Bragg regime as well as the Rayleigh-Wood anomalies shift towards shorter wavelengths. The blue-shift of the Rayleigh-Wood anomalies is faster than that of the Bragg regime. The latter's bandwidth decreases so much so that eventually the circular Bragg phenomenon disappears. The potential of slanted chiral STFs as narrowband circular polarization beamsplitters is thus established.

We emphasize in conclusion that slanted chiral STFs with imperfectly helical columns have already been realized [21], but the relationship between α and χ_s has yet not been ascertained. Once the morphological geometry has been quantitatively established, the presented methodology can be used to calculate the planewave responses of these STFs as well. The nature of interaction between the two orthogonal periodicities being the same as discussed in Section (3.3), the conclusions made in this paper for slanted STFs with ideal helical columns would also apply when the columns are imperfectly helical.

The first author is grateful for financial support during the 2001–2002 academic year from the Weiss Graduate Scholars Program at the Pennsylvania State University.

Appendix

The $4(2N_T + 1) \times 4(2N_T + 1)$ kernel matrix $\left[\underline{\underline{\mathbf{P}}}(z)\right]$ is given as

$$\left[\underline{\underline{\mathbf{P}}}(z)\right] = \begin{bmatrix} \left[\underline{\underline{P}}_{11}(z)\right] & \left[\underline{\underline{P}}_{12}(z)\right] & \left[\underline{\underline{P}}_{13}(z)\right] & \left[\underline{\underline{P}}_{14}(z)\right] \\ \left[\underline{\underline{P}}_{21}(z)\right] & \left[\underline{\underline{P}}_{22}(z)\right] & \left[\underline{\underline{P}}_{23}(z)\right] & \left[\underline{\underline{P}}_{24}(z)\right] \\ \left[\underline{\underline{P}}_{31}(z)\right] & \left[\underline{\underline{P}}_{32}(z)\right] & \left[\underline{\underline{P}}_{33}(z)\right] & \left[\underline{\underline{P}}_{34}(z)\right] \\ \left[\underline{\underline{P}}_{41}(z)\right] & \left[\underline{\underline{P}}_{42}(z)\right] & \left[\underline{\underline{P}}_{43}(z)\right] & \left[\underline{\underline{P}}_{44}(z)\right] \end{bmatrix}, \tag{69}$$

where $\left[\underline{\underline{P}}_{ij}\right]$ $(i, j = 1, 2, 3, 4)$ are $(2N_T + 1) \times (2N_T + 1)$ square matrices and calculated in the specific form as

$$\begin{aligned} \left[\underline{\underline{P}}_{11}(z)\right] &= -\left[\underline{\underline{K}}_x\right] \cdot \left[\underline{\underline{\epsilon}}_{zz}(z)\right]^{-1} \cdot \left[\underline{\underline{\epsilon}}_{zx}(z)\right] \\ \left[\underline{\underline{P}}_{12}(z)\right] &= -\left[\underline{\underline{K}}_x\right] \cdot \left[\underline{\underline{\epsilon}}_{zz}(z)\right]^{-1} \cdot \left[\underline{\underline{\epsilon}}_{zy}(z)\right] \\ \left[\underline{\underline{P}}_{13}(z)\right] &= \frac{1}{k_0}\left[\underline{\underline{K}}_x\right] \cdot \left[\underline{\underline{\epsilon}}_{zz}(z)\right]^{-1} \cdot \left[\underline{\underline{K}}_y\right] \\ \left[\underline{\underline{P}}_{14}(z)\right] &= k_0\left[\underline{\underline{I}}\right] - \frac{1}{k_0}\left[\underline{\underline{K}}_x\right] \cdot \left[\underline{\underline{\epsilon}}_{zz}(z)\right]^{-1} \cdot \left[\underline{\underline{K}}_x\right] \end{aligned} \tag{70}$$

$$
\begin{aligned}
\left[\underline{\underline{P}}_{21}(z)\right] &= -\left[\underline{\underline{K}}_y\right]\cdot\left[\underline{\underline{\epsilon}}_{zz}(z)\right]^{-1}\cdot\left[\underline{\underline{\epsilon}}_{zx}(z)\right]\\
\left[\underline{\underline{P}}_{22}(z)\right] &= -\left[\underline{\underline{K}}_y\right]\cdot\left[\underline{\underline{\epsilon}}_{zz}(z)\right]^{-1}\cdot\left[\underline{\underline{\epsilon}}_{zy}(z)\right]\\
\left[\underline{\underline{P}}_{23}(z)\right] &= -k_0\left[\underline{\underline{I}}\right]+\frac{1}{k_0}\left[\underline{\underline{K}}_y\right]\cdot\left[\underline{\underline{\epsilon}}_{zz}(z)\right]^{-1}\cdot\left[\underline{\underline{K}}_y\right]\\
\left[\underline{\underline{P}}_{24}(z)\right] &= -\frac{1}{k_0}\left[\underline{\underline{K}}_y\right]\cdot\left[\underline{\underline{\epsilon}}_{zz}(z)\right]^{-1}\cdot\left[\underline{\underline{K}}_x\right] \qquad (71)
\end{aligned}
$$

$$
\begin{aligned}
\left[\underline{\underline{P}}_{31}(z)\right] &= k_0\Big(\left[\underline{\underline{\epsilon}}_{yz}(z)\right]\cdot\left[\underline{\underline{\epsilon}}_{zz}(z)\right]^{-1}\cdot\left[\underline{\underline{\epsilon}}_{zx}(z)\right]\\
&\quad -\left[\underline{\underline{\epsilon}}_{yx}(z)\right]-\frac{1}{k_0^2}\left[\underline{\underline{K}}_x\right]\cdot\left[\underline{\underline{K}}_y\right]\Big)\\
\left[\underline{\underline{P}}_{32}(z)\right] &= k_0\Big(\left[\underline{\underline{\epsilon}}_{yz}(z)\right]\cdot\left[\underline{\underline{\epsilon}}_{zz}(z)\right]^{-1}\cdot\left[\underline{\underline{\epsilon}}_{zy}(z)\right]\\
&\quad -\left[\underline{\underline{\epsilon}}_{yy}(z)\right]+\frac{1}{k_0^2}\left[\underline{\underline{K}}_x\right]\cdot\left[\underline{\underline{K}}_x\right]\Big)\\
\left[\underline{\underline{P}}_{33}(z)\right] &= -\left[\underline{\underline{\epsilon}}_{yz}(z)\right]\cdot\left[\underline{\underline{\epsilon}}_{zz}(z)\right]^{-1}\cdot\left[\underline{\underline{K}}_y\right]\\
\left[\underline{\underline{P}}_{34}(z)\right] &= \left[\underline{\underline{\epsilon}}_{yz}(z)\right]\cdot\left[\underline{\underline{\epsilon}}_{zz}(z)\right]^{-1}\cdot\left[\underline{\underline{K}}_x\right] \qquad (72)
\end{aligned}
$$

$$
\begin{aligned}
\left[\underline{\underline{P}}_{41}(z)\right] &= -k_0\Big(\left[\underline{\underline{\epsilon}}_{xz}(z)\right]\cdot\left[\underline{\underline{\epsilon}}_{zz}(z)\right]^{-1}\cdot\left[\underline{\underline{\epsilon}}_{zx}(z)\right]\\
&\quad -\left[\underline{\underline{\epsilon}}_{xx}(z)\right]+\frac{1}{k_0^2}\left[\underline{\underline{K}}_y\right]\cdot\left[\underline{\underline{K}}_y\right]\Big)\\
\left[\underline{\underline{P}}_{42}(z)\right] &= -k_0\Big(\left[\underline{\underline{\epsilon}}_{xz}(z)\right]\cdot\left[\underline{\underline{\epsilon}}_{zz}(z)\right]^{-1}\cdot\left[\underline{\underline{\epsilon}}_{zy}(z)\right]\\
&\quad -\left[\underline{\underline{\epsilon}}_{xy}(z)\right]-\frac{1}{k_0^2}\left[\underline{\underline{K}}_y\right]\cdot\left[\underline{\underline{K}}_x\right]\Big)\\
\left[\underline{\underline{P}}_{43}(z)\right] &= \left[\underline{\underline{\epsilon}}_{xz}(z)\right]\cdot\left[\underline{\underline{\epsilon}}_{zz}(z)\right]^{-1}\cdot\left[\underline{\underline{K}}_y\right]\\
\left[\underline{\underline{P}}_{44}(z)\right] &= -\left[\underline{\underline{\epsilon}}_{xz}(z)\right]\cdot\left[\underline{\underline{\epsilon}}_{zz}(z)\right]^{-1}\cdot\left[\underline{\underline{K}}_x\right]. \qquad (73)
\end{aligned}
$$

References

1. M. Gale, Phys. World **2**, 24 (October 1989)
2. A.R. Parker, Am. Sci. **87**, 248 (1999)
3. A.R. Parker, J. Opt. A: Pure Appl. Opt. **2**, R15 (2000)
4. *Selected Papers on Diffraction Gratings*, edited by D. Maystre (SPIE Optical Engineering Press, Bellingham, WA, 1993)
5. T.K. Gaylord, M.G. Moharam, Proc. IEEE **73**, 894 (1985)
6. A. Lakhtakia, V.K. Varadan, V.V. Varadan, J. Opt. Soc. Am. A **6**, 1675 (1989); **7**, 951 (1990)
7. C.H. Palmer Jr., J. Opt. Soc. Am. **42**, 269 (1952)
8. A. Hessel, A.A. Oliner, Appl. Opt. **4**, 1275 (1965)
9. *Selected Papers on Linear Optical Composite Materials*, edited by A. Lakhtakia (SPIE Optical Engineering Press, Bellingham, WA, 1996)
10. H.A. Macleod, *Thin-Film Optical Filters* (Institute of Physics Publishing, Bristol, UK, 2001)
11. J.B. Geddes III, A. Lakhtakia, Eur. Phys. J. AP **17**, 21 (2002)
12. A. Othonos, Rev. Sci. Instrum. **68**, 4309 (1997)
13. P.G. de Gennes, J. Prost, *The Physics of Liquid Crystals*, 2nd edn. (Clarendon Press, Oxford, UK, 1993), Chap. 6
14. A. Lakhtakia, Mater. Sci. Eng. C **19**, 427 (2002)
15. M.W. McCall, A. Lakhtakia, Electromagnetics **23**, in press
16. M.W. McCall, A. Lakhtakia, Proc. SPIE **4806**, 129 (2002)
17. I. Hodgkinson, Q.h. Wu, Adv. Mater. **13**, 889 (2001)
18. K. Robbie, M.J. Brett, A. Lakhtakia, J. Vac. Sci. Technol. A **12**, 2991 (1995)
19. F. Liu, M.T. Umlor, L. Shen, J. Weston, W. Eads, J.A. Barnard, G.J. Mankey, J. Appl. Phys. **85**, 5486 (1999)
20. I.J. Hodgkinson, Q.h. Wu, B. Knight, A. Lakhtakia, K. Robbie, Appl. Opt. **39**, 642 (2000)
21. R. Messier, V.C. Venugopal, P.D. Sunal, J. Vac. Sci. Technol. B **18**, 1538 (2000)
22. M. Suzuki, Y. Taga, Jpn. J. Appl. Phys. Pt. 2 **40**, L358 (2001)
23. V.C. Venugopal, A. Lakhtakia, in *Electromagnetic Fields in Unconventional Materials and Structures*, edited by O.N. Singh, A. Lakhtakia (Wiley, New York, NY, 2000), pp. 151–216
24. V.C. Venugopal, A. Lakhtakia, Proc. R. Soc. London A **456**, 125 (2000)
25. R. Messier, A. Lakhtakia, V.C. Venugopal, P.D. Sunal, Vac. Technol. Coating **2**, 40 (October 2001)
26. K. Rokushima, J. Yamakita, J. Opt. Soc. Am. **73**, 901 (1983)
27. J.M. Jarem, P.P. Banerjee, *Computational Methods for Electromagnetic and Optical Systems* (Marcel Dekker, New York, NY, 2000), Chap. 3
28. C. Kittel, *Introduction to Solid State Physics* (Wiley Eastern, New Delhi, India, 1974), Chap. 13
29. A. Lakhtakia, Eur. Phys. J. AP **8**, 129 (1999)
30. I. Hodgkinson, Q.h. Wu, Appl. Opt. **38**, 3621 (1999)
31. I. Hodgkinson, Q.h. Wu, *Birefingent Thin Films and Polarizing Elements* (World Scientific, Singapore, 1997), Chap. 16
32. J.D. Jackson, *Classical Electrodynamics*, 3rd edn. (Wiley, New York, NY, 1999), Sect. 7.3
33. K. Rokushima, J. Yamakita, J. Opt. Soc. Am. A **4**, 27 (1987)
34. G. Strang, *Introduction to Applied Mathematics* (Wellesley-Cambridge Press, Wellesley, MA, 1986), Chap. 1
35. M.W. McCall, Math. Comput. Model. **34**, 1483 (2001)
36. V.C. Venugopal, A. Lakhtakia, Eur. Phys. J. AP **10**, 173 (2000)
37. I. Abdulhalim, L. Benguigui, R. Weil, J. Phys. (Paris) **46**, 815 (1985)
38. P. Kipfer, R. Klappert, H.P. Herzig, J. Grupp, R. Dändliker, Opt. Eng. **41**, 638 (2002)

$$
\begin{aligned}
\left[\underline{\underline{P}}_{21}(z)\right] &= -\left[\underline{\underline{K}}_y\right]\cdot\left[\underline{\underline{\epsilon}}_{zz}(z)\right]^{-1}\cdot\left[\underline{\underline{\epsilon}}_{zx}(z)\right]\\
\left[\underline{\underline{P}}_{22}(z)\right] &= -\left[\underline{\underline{K}}_y\right]\cdot\left[\underline{\underline{\epsilon}}_{zz}(z)\right]^{-1}\cdot\left[\underline{\underline{\epsilon}}_{zy}(z)\right]\\
\left[\underline{\underline{P}}_{23}(z)\right] &= -k_0\left[\underline{\underline{I}}\right]+\frac{1}{k_0}\left[\underline{\underline{K}}_y\right]\cdot\left[\underline{\underline{\epsilon}}_{zz}(z)\right]^{-1}\cdot\left[\underline{\underline{K}}_y\right]\\
\left[\underline{\underline{P}}_{24}(z)\right] &= -\frac{1}{k_0}\left[\underline{\underline{K}}_y\right]\cdot\left[\underline{\underline{\epsilon}}_{zz}(z)\right]^{-1}\cdot\left[\underline{\underline{K}}_x\right] \qquad (71)
\end{aligned}
$$

$$
\begin{aligned}
\left[\underline{\underline{P}}_{31}(z)\right] &= k_0\Big(\left[\underline{\underline{\epsilon}}_{yz}(z)\right]\cdot\left[\underline{\underline{\epsilon}}_{zz}(z)\right]^{-1}\cdot\left[\underline{\underline{\epsilon}}_{zx}(z)\right]\\
&\quad -\left[\underline{\underline{\epsilon}}_{yx}(z)\right]-\frac{1}{k_0^2}\left[\underline{\underline{K}}_x\right]\cdot\left[\underline{\underline{K}}_y\right]\Big)\\
\left[\underline{\underline{P}}_{32}(z)\right] &= k_0\Big(\left[\underline{\underline{\epsilon}}_{yz}(z)\right]\cdot\left[\underline{\underline{\epsilon}}_{zz}(z)\right]^{-1}\cdot\left[\underline{\underline{\epsilon}}_{zy}(z)\right]\\
&\quad -\left[\underline{\underline{\epsilon}}_{yy}(z)\right]+\frac{1}{k_0^2}\left[\underline{\underline{K}}_x\right]\cdot\left[\underline{\underline{K}}_x\right]\Big)\\
\left[\underline{\underline{P}}_{33}(z)\right] &= -\left[\underline{\underline{\epsilon}}_{yz}(z)\right]\cdot\left[\underline{\underline{\epsilon}}_{zz}(z)\right]^{-1}\cdot\left[\underline{\underline{K}}_y\right]\\
\left[\underline{\underline{P}}_{34}(z)\right] &= \left[\underline{\underline{\epsilon}}_{yz}(z)\right]\cdot\left[\underline{\underline{\epsilon}}_{zz}(z)\right]^{-1}\cdot\left[\underline{\underline{K}}_x\right] \qquad (72)
\end{aligned}
$$

$$
\begin{aligned}
\left[\underline{\underline{P}}_{41}(z)\right] &= -k_0\Big(\left[\underline{\underline{\epsilon}}_{xz}(z)\right]\cdot\left[\underline{\underline{\epsilon}}_{zz}(z)\right]^{-1}\cdot\left[\underline{\underline{\epsilon}}_{zx}(z)\right]\\
&\quad -\left[\underline{\underline{\epsilon}}_{xx}(z)\right]+\frac{1}{k_0^2}\left[\underline{\underline{K}}_y\right]\cdot\left[\underline{\underline{K}}_y\right]\Big)\\
\left[\underline{\underline{P}}_{42}(z)\right] &= -k_0\Big(\left[\underline{\underline{\epsilon}}_{xz}(z)\right]\cdot\left[\underline{\underline{\epsilon}}_{zz}(z)\right]^{-1}\cdot\left[\underline{\underline{\epsilon}}_{zy}(z)\right]\\
&\quad -\left[\underline{\underline{\epsilon}}_{xy}(z)\right]-\frac{1}{k_0^2}\left[\underline{\underline{K}}_y\right]\cdot\left[\underline{\underline{K}}_x\right]\Big)\\
\left[\underline{\underline{P}}_{43}(z)\right] &= \left[\underline{\underline{\epsilon}}_{xz}(z)\right]\cdot\left[\underline{\underline{\epsilon}}_{zz}(z)\right]^{-1}\cdot\left[\underline{\underline{K}}_y\right]\\
\left[\underline{\underline{P}}_{44}(z)\right] &= -\left[\underline{\underline{\epsilon}}_{xz}(z)\right]\cdot\left[\underline{\underline{\epsilon}}_{zz}(z)\right]^{-1}\cdot\left[\underline{\underline{K}}_x\right]. \qquad (73)
\end{aligned}
$$

References

1. M. Gale, Phys. World **2**, 24 (October 1989)
2. A.R. Parker, Am. Sci. **87**, 248 (1999)
3. A.R. Parker, J. Opt. A: Pure Appl. Opt. **2**, R15 (2000)
4. *Selected Papers on Diffraction Gratings*, edited by D. Maystre (SPIE Optical Engineering Press, Bellingham, WA, 1993)
5. T.K. Gaylord, M.G. Moharam, Proc. IEEE **73**, 894 (1985)
6. A. Lakhtakia, V.K. Varadan, V.V. Varadan, J. Opt. Soc. Am. A **6**, 1675 (1989); **7**, 951 (1990)
7. C.H. Palmer Jr., J. Opt. Soc. Am. **42**, 269 (1952)
8. A. Hessel, A.A. Oliner, Appl. Opt. **4**, 1275 (1965)
9. *Selected Papers on Linear Optical Composite Materials*, edited by A. Lakhtakia (SPIE Optical Engineering Press, Bellingham, WA, 1996)
10. H.A. Macleod, *Thin–Film Optical Filters* (Institute of Physics Publishing, Bristol, UK, 2001)
11. J.B. Geddes III, A. Lakhtakia, Eur. Phys. J. AP **17**, 21 (2002)
12. A. Othonos, Rev. Sci. Instrum. **68**, 4309 (1997)
13. P.G. de Gennes, J. Prost, *The Physics of Liquid Crystals,* 2nd edn. (Clarendon Press, Oxford, UK, 1993), Chap. 6
14. A. Lakhtakia, Mater. Sci. Eng. C **19**, 427 (2002)
15. M.W. McCall, A. Lakhtakia, Electromagnetics **23**, in press
16. M.W. McCall, A. Lakhtakia, Proc. SPIE **4806**, 129 (2002)
17. I. Hodgkinson, Q.h. Wu, Adv. Mater. **13**, 889 (2001)
18. K. Robbie, M.J. Brett, A. Lakhtakia, J. Vac. Sci. Technol. A **12**, 2991 (1995)
19. F. Liu, M.T. Umlor, L. Shen, J. Weston, W. Eads, J.A. Barnard, G.J. Mankey, J. Appl. Phys. **85**, 5486 (1999)
20. I.J. Hodgkinson, Q.h. Wu, B. Knight, A. Lakhtakia, K. Robbie, Appl. Opt. **39**, 642 (2000)
21. R. Messier, V.C. Venugopal, P.D. Sunal, J. Vac. Sci. Technol. B **18**, 1538 (2000)
22. M. Suzuki, Y. Taga, Jpn. J. Appl. Phys. Pt. 2 **40**, L358 (2001)
23. V.C. Venugopal, A. Lakhtakia, in *Electromagnetic Fields in Unconventional Materials and Structures*, edited by O.N. Singh, A. Lakhtakia (Wiley, New York, NY, 2000), pp. 151–216
24. V.C. Venugopal, A. Lakhtakia, Proc. R. Soc. London A **456**, 125 (2000)
25. R. Messier, A. Lakhtakia, V.C. Venugopal, P.D. Sunal, Vac. Technol. Coating **2**, 40 (October 2001)
26. K. Rokushima, J. Yamakita, J. Opt. Soc. Am. **73**, 901 (1983)
27. J.M. Jarem, P.P. Banerjee, *Computational Methods for Electromagnetic and Optical Systems* (Marcel Dekker, New York, NY, 2000), Chap. 3
28. C. Kittel, *Introduction to Solid State Physics* (Wiley Eastern, New Delhi, India, 1974), Chap. 13
29. A. Lakhtakia, Eur. Phys. J. AP **8**, 129 (1999)
30. I. Hodgkinson, Q.h. Wu, Appl. Opt. **38**, 3621 (1999)
31. I. Hodgkinson, Q.h. Wu, *Birefingent Thin Films and Polarizing Elements* (World Scientific, Singapore, 1997), Chap. 16
32. J.D. Jackson, *Classical Electrodynamics,* 3rd edn. (Wiley, New York, NY, 1999), Sect. 7.3
33. K. Rokushima, J. Yamakita, J. Opt. Soc. Am. A **4**, 27 (1987)
34. G. Strang, *Introduction to Applied Mathematics* (Wellesley-Cambridge Press, Wellesley, MA, 1986), Chap. 1
35. M.W. McCall, Math. Comput. Model. **34**, 1483 (2001)
36. V.C. Venugopal, A. Lakhtakia, Eur. Phys. J. AP **10**, 173 (2000)
37. I. Abdulhalim, L. Benguigui, R. Weil, J. Phys. (Paris) **46**, 815 (1985)
38. P. Kipfer, R. Klappert, H.P. Herzig, J. Grupp, R. Dändliker, Opt. Eng. **41**, 638 (2002)

Eur. Phys. J. Appl. Phys. **24**, 91 (2003)
DOI: 10.1051/epjap:2003069

THE EUROPEAN PHYSICAL JOURNAL APPLIED PHYSICS

Erratum

Coupling of Rayleigh-Wood anomalies and the circular Bragg phenomenon in slanted chiral sculptured thin films

F. Wang[a], A. Lakhtakia[b], and R. Messier[c]

CATMAS – Computational and Theoretical Materials Sciences Group, Department of Engineering Science and Mechanics, Pennsylvania State University, University Park, PA 16802-6812, USA

Received: 22 July 2003 / Accepted: 1 August 2003
Published online: 29 September 2003 –

Eur. Phys. J. AP **20**, 91 (2002)

The square matrixes $\left[\underline{\underline{\mathrm{Y}}}_{\mathrm{e}}\right]^{*}$ and $\left[\underline{\underline{\mathrm{Y}}}_{\mathrm{h}}\right]^{*}$ in equation (43) of the subject paper [1] should correctly read as

$$\left[\underline{\underline{\mathrm{Y}}}_{\mathrm{e}}\right]^{*} = \begin{bmatrix} \mathrm{diag}[\xi_n^*] & \mathrm{diag}[\xi_n] \\ \mathrm{diag}[\zeta_n] & \mathrm{diag}[\zeta_n^*] \end{bmatrix}, \quad \left[\underline{\underline{\mathrm{Y}}}_{\mathrm{h}}\right]^{*} = i \begin{bmatrix} \mathrm{diag}[\xi_n] & -\mathrm{diag}[\xi_n^*] \\ \mathrm{diag}[\zeta_n^*] & -\mathrm{diag}[\zeta_n] \end{bmatrix}, \tag{1}$$

where $\mathrm{diag}[\xi_n]$ is a diagonal matrix containing ξ_n, etc., and

$$\xi_n^* = \frac{1}{\sqrt{2}} \left(\frac{k_{xn} k_{zn}}{k_0 k_{xyn}} + i \frac{k_{y0}}{k_{xyn}} \right), \tag{2}$$

$$\zeta_n^* = \frac{1}{\sqrt{2}} \left(\frac{k_{y0} k_{zn}}{k_0 k_{xyn}} + i \frac{k_{xn}}{k_{xyn}} \right). \tag{3}$$

The presented numerical results are not affected. Any inconvenience is regretted.

[a] e-mail: fuw101@psu.edu
[b] e-mail: axl4@psu.edu
[c] e-mail: mes17@psu.edu

Available online at www.sciencedirect.com
SCIENCE DIRECT®
Optics Communications 235 (2004) 107–132
OPTICS COMMUNICATIONS
www.elsevier.com/locate/optcom

Lateral shifts of optical beams on reflection by slanted chiral sculptured thin films

Fei Wang [1], Akhlesh Lakhtakia *

CATMAS – Computational and Theoretical Materials Sciences Group, Department of Engineering Science and Mechanics, Pennsylvania State University, 212 EES Building, University Park, PA 16802-6812, USA

Received 18 December 2003; received in revised form 18 December 2003; accepted 18 February 2004

Abstract

A theoretical investigation of lateral shifts of circularly polarized beams on reflection by a slanted chiral sculptured thin film (STF) is presented. First, the response of the slanted chiral STF to an obliquely incident plane wave is obtained by rigorous coupled-wave analysis; then, the angular-spectrum representation of beams is exploited for beam diffraction. Two types of lateral shifts of Gaussian beams are studied in detail. One is the lateral shift of a 2D co-handed beam that is mostly reflected due to the circular Bragg phenomenon. This lateral shift can be either forward or backward, depending on the angle of incidence. The other type of lateral shift is the Goos–Hänchen shift that occurs when a beam is totally reflected. The Goos–Hänchen shift comprises components both in and normal to the plane of incidence, when the incident beam is 3D Gaussian. The Goos–Hänchen shift is affected by both the structural handedness and the slantedness of the slanted chiral STF in nanotechnologically significant ways.

PACS: 42.70.-a; 78.20.-e; 78.66.-w; 78.67,-n; 81.07.-b

Keywords: Beam shift; Gaussian beam; Goos–Hänchen shift; Nanomaterials; Sculptured thin film; Structural handedness

1. Introduction

Lateral shifts suffered by optical beams on refraction at planar bimedium interfaces are fairly easy to envision, but not always the shifts suffered on reflection. Yet shifts on reflection do happen [1], with the Goos–Hänchen shifts being known quite well [2]. Typically, such shifts are no more than a small fraction of the free-space wavelength, and are often ignored unless a multiplicity of reflection events (as in waveguides) intensifies the effect [1]. The advent of nanomaterials, however, makes even small shifts significant because the morphological scales of these materials are also small fractions of the free-space wavelength [3].

* Corresponding author. Tel.: +1-814-863-4319; fax: +1-814-865-9974.
E-mail addresses: FUW101@psu.edu (F. Wang), AXL4@psu.edu (A. Lakhtakia).
[1] Fax: +1-814-863-7967.

0030-4018/$ - see front matter
doi:10.1016/j.optcom.2004.02.050

The magnitude of a reflection shift is highly influenced by the morphology of the refracting nanomaterial [3], which strongly indicates that beam shifts facilitated by emerging classes of materials be investigated. Sculptured thin films (STFs) are a class of nanomaterials grown by physical vapor deposition [4,5]. Microscopically, STFs are porous assemblies of nanowires of 10–300 nm diameter. The interstitial voids among the nanowires can be controlled to exhibit specific shapes and sizes [5,6]. Macroscopically, STFs are unidirectionally nonhomogeneous, anisotropic continuums.

The constituent nanowires of a chiral STF are shaped like helixes [7]. From the macroscopic point of view, these chiral STFs are classified as a subset of helicoidal bianisotropic mediums (HBMs) – which are rotationally nonhomogeneous continuums [8]. Indeed, the hallmark of the optical responses of HBMs on excitation by plane waves is the circular Bragg phenomenon, which has been intensively investigated in both frequency- and time-domains and has been exploited for several types of optical devices [5,9–12]. Briefly, a circularly polarized plane wave of the same handedness as the helical nanowires of a chiral STF is substantially reflected in a wavelength regime called the Bragg regime, while that of the other handedness is not.

The helical nanowires of a chiral STF grow upright on a substrate. Recently, *slanted* chiral STFs were introduced as straightforward extensions thereof [14]. The helical nanowires of a slanted chiral STF are supposed to grow at an angle $\alpha \neq 0$ with respect to the normal to the substrate [4,13]. Macroscopically, a slanted chiral STF is therefore helicoidally nonhomogeneous about an axis that is not perpendicular to the substrate plane. In view of the effective periodicity of the constitutive parameters both parallel and normal to the substrate plane, a slanted chiral STF couples the circular Bragg phenomenon which is purely specular to nonspecular diffraction (and Rayleigh–Wood anomalies [15]) associated with diffraction gratings [16]. The slant angle α totally controls the interaction of these two optical phenomenons [14,17].

Due to the interaction between specular and nonspecular phenomenons, practical applications of slanted chiral STFs are likely to involve optical beams which are either continuous-wave or pulsed. Therefore, it seems necessary to understand the diffraction of optical beams by these nanomaterials. Our focus here is on the lateral shifts of beams due to reflection by slanted chiral STFs.

The plan of this paper is as follows. Section 2 is devoted to theoretical analysis. It provides the frequency-domain constitutive relations of a slanted chiral STF as well as its planewave response, in order to formulate the angular-spectrum representation of 2D and 3D optical beams on diffraction. The thin film is assumed to lie between two identical, homogeneous, nondissipative, dielectric half-spaces, in order to study two different types of problems. A rigorous coupled-wave analysis (RCWA) is stably implemented for the accurate computation of planewave diffraction [18–20]. The optical beams, which are reflected and transmitted in discrete harmonic orders, are then formulated by recombining the whole contribution of the angular-spectrum of plane waves on diffraction. Section 3 is devoted to numerical results. First, the planewave response of a slanted chiral STF is briefly presented for oblique incidence, focusing on the circular Bragg phenomenon as well as total reflection. Then, the lateral shifts, including the Goos–Hänchen shifts, of both 2D and 3D circularly polarized beams are presented for varying angles of incidence. An $\exp(-i\omega t)$ time-dependent is implicit, with ω as the angular frequency and t as time. A Cartesian coordinate system (x, y, z) is used, with the substrate normal being parallel to the z axis.

2. Theoretical analysis

2.1. Constitutive relations

Let the region $0 < z < d$ be occupied by a slanted chiral STF, as shown in Fig. 1. The half-spaces $z \leqslant 0$ and $z \geqslant d$ are filled with a homogeneous, isotropic, dielectric medium of refractive index n_{hs}.

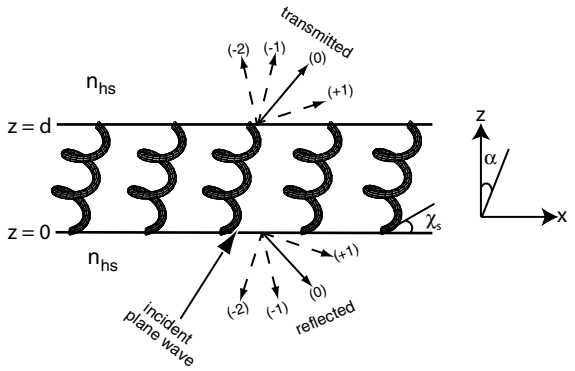

Fig. 1. Schematic of the boundary value problem involving a slanted chiral STF of thickness d illuminated by an obliquely incident plane wave. The lower and the upper half-spaces are filled by a homogeneous, nondissipative, dielectric medium of refractive index $n_{\rm hs}$. Both specular ($n = 0$) and nonspecular ($n \neq 0$) reflections and transmissions occur when $\alpha \neq 0$, but all nonspecular reflections/transmissions fold into the specular reflection/transmission when $\alpha = 0$.

The relative permittivity dyadic of the slanted chiral STF is factorable as

$$\underline{\underline{\epsilon}}(\mathbf{r},\lambda_0) = \underline{\underline{S}}_y(-\alpha)\cdot\underline{\underline{S}}_z(\mathbf{r})\cdot\underline{\underline{S}}_y(\chi_s)\cdot\underline{\underline{\epsilon}}_{\rm ref}(\lambda_0)\cdot\underline{\underline{S}}_y^{\rm T}(\chi_s)\cdot\underline{\underline{S}}_z^{\rm T}(\mathbf{r})\cdot\underline{\underline{S}}_y^{\rm T}(-\alpha),\quad 0<z<d, \tag{1}$$

where the position vector $\mathbf{r} = x\mathbf{u}_x + y\mathbf{u}_y + z\mathbf{u}_z$, λ_0 is the free-space wavelength, and the superscript T denotes the transpose. As most STFs are locally orthorhombic [21,22], the reference relative permittivity dyadic is given by [7]

$$\underline{\underline{\epsilon}}_{\rm ref}(\lambda_0) = \epsilon_a(\lambda_0)\mathbf{u}_z\mathbf{u}_z + \epsilon_b(\lambda_0)\mathbf{u}_x\mathbf{u}_x + \epsilon_c(\lambda_0)\mathbf{u}_y\mathbf{u}_y. \tag{2}$$

The wavelength-dependences of the scalars $\epsilon_{a,b,c}$ are assumed in Section 3 to emerge from a single-resonance Lorentzian model [23,24] as

$$\epsilon_{a,b,c}(\lambda_0) = 1 + \frac{p_{a,b,c}}{\left[1 + (N_{a,b,c}^{-1} - i\lambda_{a,b,c}\lambda_0^{-1})^2\right]}, \tag{3}$$

where $p_{a,b,c}$ are the oscillator strengths. The parameters $\lambda_{a,b,c}$ and $N_{a,b,c}$ determine the resonance wavelengths and absorption linewidths.

The rotational nonhomogeneity of the chosen thin film is captured by the rotation dyadic

$$\underline{\underline{S}}_z(\mathbf{r}) = \left(\mathbf{u}_x\mathbf{u}_x + \mathbf{u}_y\mathbf{u}_y\right)\cos\left[\frac{\pi}{\Omega}(\mathbf{r}\cdot\mathbf{u}_\ell)\right] + h\left(\mathbf{u}_y\mathbf{u}_x - \mathbf{u}_x\mathbf{u}_y\right)\sin\left[\frac{\pi}{\Omega}(\mathbf{r}\cdot\mathbf{u}_\ell)\right] + \mathbf{u}_z\mathbf{u}_z, \tag{4}$$

the helical axis being parallel to the unit vector $\mathbf{u}_\ell = \mathbf{u}_x\sin\alpha + \mathbf{u}_z\cos\alpha$. The structural period along the helical axis is denoted by 2Ω. The parameter $h = 1$ for structural right-handedness, while $h = -1$ for structural left-handedness. The dyadic

$$\underline{\underline{S}}_y(\sigma) = (\mathbf{u}_x\mathbf{u}_x + \mathbf{u}_z\mathbf{u}_z)\cos\sigma + (\mathbf{u}_x\mathbf{u}_z - \mathbf{u}_z\mathbf{u}_x)\sin\sigma + \mathbf{u}_y\mathbf{u}_y \tag{5}$$

serves two different roles: whereas $\underline{\underline{S}}_y(\chi_s)$ delineates the role of the growth process with $(\pi/2) - \chi_s$ being the angle of declination from the helical axis, $\underline{\underline{S}}_y(-\alpha)$ represents the slanted orientation of that axis. The slant angle α is restricted to the range $(-\chi_s, \chi_s)$ due to the fact that the helical nanowires of a slanted chiral STF must be pointed upwards in relation to the substrate plane [14]. When $\alpha = 0$, the slant is absent and the

usual chiral STFs are represented by $\underline{\underline{\epsilon}}(\mathbf{r},\lambda_0) \equiv \underline{\underline{\epsilon}}(z,\lambda_0)$. From here onwards, the dependences of various quantities on λ_0 are implicit.

2.2. Rigorous coupled-wave analysis for planewave incidence

The next step is to formulate the response of a slanted chiral STF to an obliquely incident plane wave. Let the incident plane wave propagate with the wavevector $\mathbf{k}_+^{(0)} = k_x^{(0)}\mathbf{u}_x + k_y^{(0)}\mathbf{u}_y + k_z^{(0)}\mathbf{u}_z$ from the lower half-space $z \leqslant 0$. The incident, the reflected and transmitted electromagnetic field phasors are expressed in a set of Floquet harmonics, respectively, as follows:

$$\mathbf{E}_{\mathrm{i}} = \sum_{n\in\mathbb{Z}} \left(\mathbf{L}_+^{(n)} a_{\mathrm{L}}^{(n)} + \mathbf{R}_+^{(n)} a_{\mathrm{R}}^{(n)} \right) \exp\left(\mathrm{i}\mathbf{k}_+^{(n)} \cdot \mathbf{r} \right), \quad z \leqslant 0, \tag{6}$$

$$\mathbf{H}_{\mathrm{i}} = \frac{-\mathrm{i}n_{\mathrm{hs}}}{\eta_0} \sum_{n\in\mathbb{Z}} \left(\mathbf{L}_+^{(n)} a_{\mathrm{L}}^{(n)} - \mathbf{R}_+^{(n)} a_{\mathrm{R}}^{(n)} \right) \exp\left(\mathrm{i}\mathbf{k}_+^{(n)} \cdot \mathbf{r} \right), \quad z \leqslant 0, \tag{7}$$

$$\mathbf{E}_{\mathrm{r}} = \sum_{n\in\mathbb{Z}} \left(\mathbf{L}_-^{(n)} r_{\mathrm{L}}^{(n)} + \mathbf{R}_-^{(n)} r_{\mathrm{R}}^{(n)} \right) \exp\left(\mathrm{i}\mathbf{k}_-^{(n)} \cdot \mathbf{r} \right), \quad z \leqslant 0, \tag{8}$$

$$\mathbf{H}_{\mathrm{r}} = \frac{-\mathrm{i}n_{\mathrm{hs}}}{\eta_0} \sum_{n\in\mathbb{Z}} \left(\mathbf{L}_-^{(n)} r_{\mathrm{L}}^{(n)} - \mathbf{R}_-^{(n)} r_{\mathrm{R}}^{(n)} \right) \exp\left(\mathrm{i}\mathbf{k}_-^{(n)} \cdot \mathbf{r} \right), \quad z \leqslant 0, \tag{9}$$

$$\mathbf{E}_{\mathrm{t}} = \sum_{n\in\mathbb{Z}} \left(\mathbf{L}_+^{(n)} t_{\mathrm{L}}^{(n)} + \mathbf{R}_+^{(n)} t_{\mathrm{R}}^{(n)} \right) \exp\left(\mathrm{i}\mathbf{k}_+^{(n)} \cdot \tilde{\mathbf{r}} \right), \quad z \geqslant d, \tag{10}$$

$$\mathbf{H}_{\mathrm{t}} = \frac{-\mathrm{i}n_{\mathrm{hs}}}{\eta_0} \sum_{n\in\mathbb{Z}} \left(\mathbf{L}_+^{(n)} t_{\mathrm{L}}^{(n)} - \mathbf{R}_+^{(n)} t_{\mathrm{R}}^{(n)} \right) \exp\left(\mathrm{i}\mathbf{k}_+^{(n)} \cdot \tilde{\mathbf{r}} \right), \quad z \geqslant d. \tag{11}$$

In (6)–(11) and hereafter, $\eta_0 = \sqrt{\mu_0/\epsilon_0}$ is the intrinsic impedance of free space; while $\{a_{\mathrm{L}}^{(n)}, a_{\mathrm{R}}^{(n)}\}$, $\{r_{\mathrm{L}}^{(n)}, r_{\mathrm{R}}^{(n)}\}$ and $\{t_{\mathrm{L}}^{(n)}, t_{\mathrm{R}}^{(n)}\}$, respectively, are complex-valued amplitudes of the left- and right-circularly polarized (LCP and RCP) components of the nth-order harmonic constituent of the incident, reflected and transmitted fields. The symbol $\mathbb{Z}$ represents the set $\{0, \pm1, \pm2, \ldots\}$ of all integers, and $\tilde{\mathbf{r}} = \mathbf{r} - d\mathbf{u}_z$.

The wavevectors $\mathbf{k}_\pm^{(n)}$ as well as the circular polarization vectors $\mathbf{L}_\pm^{(n)}$ and $\mathbf{R}_\pm^{(n)}$ of the nth-order harmonics are compatible with the phase-matching and the Floquet conditions; thus,

$$\mathbf{k}_\pm^{(n)} = k_x^{(n)}\mathbf{u}_x + k_y^{(0)}\mathbf{u}_y \pm k_z^{(n)}\mathbf{u}_z, \tag{12}$$

$$\mathbf{L}_\pm^{(n)} = \pm\left(i\mathbf{s}^{(n)} - \mathbf{p}_\pm^{(n)} \right)/\sqrt{2}, \tag{13}$$

$$\mathbf{R}_\pm^{(n)} = \mp\left(i\mathbf{s}^{(n)} + \mathbf{p}_\pm^{(n)} \right)/\sqrt{2}. \tag{14}$$

In these expressions, the vectors

$$\left.\begin{aligned} \mathbf{s}^{(n)} &= \tfrac{-k_y^{(0)}}{k_{xy}^{(n)}}\mathbf{u}_x + \tfrac{k_x^{(n)}}{k_{xy}^{(n)}}\mathbf{u}_y \\ \mathbf{p}_\pm^{(n)} &= \mp\tfrac{k_z^{(n)}}{k_0 n_{\mathrm{hs}}}\left(\tfrac{k_x^{(n)}}{k_{xy}^{(n)}}\mathbf{u}_x + \tfrac{k_y^{(0)}}{k_{xy}^{(n)}}\mathbf{u}_y \right) + \tfrac{k_{xy}^{(n)}}{k_0 n_{\mathrm{hs}}}\mathbf{u}_z \end{aligned}\right\} \tag{15}$$

help denote linearly polarized planar fields of s- and p-types, in electromagnetics literature [16,25], with respect to the wavevector $\mathbf{k}_\pm^{(n)}$. The scalars

$$\left.\begin{aligned}
\kappa_x &= (\pi/\Omega)|\sin\alpha| \\
k_x^{(n)} &= k_x^{(0)} + n\kappa_x \\
k_z^{(n)} &= +\sqrt{k_0^2 n_{\mathrm{hs}}^2 - (k_{xy}^{(n)})^2} \\
k_{xy}^{(n)} &= +\sqrt{(k_x^{(n)})^2 + (k_y^{(0)})^2}
\end{aligned}\right\} \tag{16}$$

depend on the out-of-plane period $\Lambda_x = 2\Omega/|\sin\alpha|$ of the slanted chiral STF along the x axis. The free-space wavenumber is denoted by $k_0 = \omega\sqrt{\mu_0\epsilon_0} = 2\pi/\lambda_0$.

The incident plane wave is the Floquet harmonic of order 0; hence, $a_{\mathrm{L}}^{(n)} = a_{\mathrm{R}}^{(n)} = 0\ \forall n \neq 0$. Since $\{a_{\mathrm{L}}^{(n)}, a_{\mathrm{R}}^{(n)}\}$ are supposed to be known, the amplitude pairs $\{r_{\mathrm{L}}^{(n)}, r_{\mathrm{R}}^{(n)}\}$ and $\{t_{\mathrm{L}}^{(n)}, t_{\mathrm{R}}^{(n)}\}$ need to be determined for all n. The RCWA, which is widely used for 1D and 2D grating diffraction problems, permits us to delineate the spectral characteristics of planewave diffraction by a slanted chiral STF.

The spatially periodic variation of $\underline{\underline{\epsilon}}(\mathbf{r})$ of (1) is represented by the Fourier series expansion

$$\underline{\underline{\epsilon}}(\mathbf{r}) = \sum_{n\in\mathbb{Z}} \underline{\underline{\epsilon}}^{(n)} \exp\left[\mathrm{i}n(\kappa_x x + \kappa_z z)\right], \quad 0 < z < d, \tag{17}$$

where

$$\underline{\underline{\epsilon}}^{(n)} = \sum_{\sigma,\sigma'} \epsilon_{\sigma\sigma'}^{(n)} \mathbf{u}_\sigma \mathbf{u}_{\sigma'}, \quad \sigma, \sigma' = x, y, z, \tag{18}$$

are constant-value dyadics; and $\kappa_z = (\pi/\Omega)\cos\alpha$ is in accord with the period $\Lambda_z = 2\Omega/\cos\alpha$ of the slanted chiral STF normal to the substrate plane (i.e., along the z axis). Wave propagation occurs inside the thin-film material such that the electromagnetic field phasors therein can be decomposed as

$$\mathbf{E}(\mathbf{r}) = \sum_{n\in\mathbb{Z}} \left[E_x^{(n)}(z)\mathbf{u}_x + E_y^{(n)}(z)\mathbf{u}_y + E_z^{(n)}(z)\mathbf{u}_z\right] \exp\left[\mathrm{i}\left(k_x^{(n)} x + k_y^{(0)} y\right)\right] \tag{19}$$

and

$$\mathbf{H}(\mathbf{r}) = \sum_{n\in\mathbb{Z}} \left[H_x^{(n)}(z)\mathbf{u}_x + H_y^{(n)}(z)\mathbf{u}_y + H_z^{(n)}(z)\mathbf{u}_z\right] \exp\left[\mathrm{i}\left(k_x^{(n)} x + k_y^{(0)} y\right)\right], \tag{20}$$

where $E_{x,y,z}^{(n)}$ and $H_{x,y,z}^{(n)}$ are unknown functions of $z \in (0, d)$. Following Chateau and Hugonin [20], we also define

$$\left.\begin{aligned}
\tilde{E}_\sigma^{(n)}(z) &= E_\sigma^{(n)}(z)\exp(-\mathrm{i}n\kappa_z z) \\
\tilde{H}_\sigma^{(n)}(z) &= H_\sigma^{(n)}(z)\exp(-\mathrm{i}n\kappa_z z)
\end{aligned}\right\}, \quad \sigma = x, y, z. \tag{21}$$

On substituting (17)–(21) in the the frequency-domain Maxwell curl postulates

$$\left.\begin{aligned}
\nabla\times\mathbf{E}(\mathbf{r}) &= \mathrm{i}\omega\mu_0\mathbf{H}(\mathbf{r}) \\
\nabla\times\mathbf{H}(\mathbf{r}) &= -\mathrm{i}\omega\epsilon_0\underline{\underline{\epsilon}}(\mathbf{r})\cdot\mathbf{E}(\mathbf{r})
\end{aligned}\right\}, \quad 0 < z < d, \tag{22}$$

and exploiting the orthogonalities of the functions $\exp(\mathrm{i}\mathbf{k}_\pm^{(n)}\cdot\mathbf{r})$ across any plane $z =$ constant, we derive the following set of coupled-wave equations for $z \in (0, d)$:

$$\frac{\mathrm{d}}{\mathrm{d}z}\tilde{E}_x^{(n)}(z) + \mathrm{i}n\kappa_z\tilde{E}_x^{(n)}(z) - \mathrm{i}k_x^{(n)}\tilde{E}_z^{(n)}(z) = \mathrm{i}k_0\eta_0\tilde{H}_y^{(n)}(z), \tag{23}$$

$$\frac{\mathrm{d}}{\mathrm{d}z}\tilde{E}_y^{(n)}(z) + \mathrm{i}n\kappa_z\tilde{E}_y^{(n)}(z) - \mathrm{i}k_y^{(0)}\tilde{E}_z^{(n)}(z) = -\mathrm{i}k_0\eta_0\tilde{H}_x^{(n)}(z), \tag{24}$$

$$k_y^{(0)}\tilde{E}_x^{(n)}(z) - k_x^{(n)}\tilde{E}_y^{(n)}(z) = -k_0\eta_0\tilde{H}_z^{(n)}(z), \tag{25}$$

$$\frac{\mathrm{d}}{\mathrm{d}z}\tilde{H}_x^{(n)}(z)+\mathrm{i}n\kappa_z\tilde{H}_x^{(n)}(z)-\mathrm{i}k_x^{(n)}\tilde{H}_z^{(n)}(z)=-\frac{\mathrm{i}k_0}{\eta_0}\sum_{n'\in\mathbb{Z}}\left[\epsilon_{yx}^{(n-n')}\tilde{E}_x^{(n')}(z)+\epsilon_{yy}^{(n-n')}\tilde{E}_y^{(n')}(z)+\epsilon_{yz}^{(n-n')}\tilde{E}_z^{(n')}(z)\right], \tag{26}$$

$$\frac{\mathrm{d}}{\mathrm{d}z}\tilde{H}_y^{(n)}(z)+\mathrm{i}n\kappa_z\tilde{H}_y^{(n)}(z)-\mathrm{i}k_y^{(0)}\tilde{H}_z^{(n)}(z)=\frac{\mathrm{i}k_0}{\eta_0}\sum_{n'\in\mathbb{Z}}\left[\epsilon_{xx}^{(n-n')}\tilde{E}_x^{(n')}(z)+\epsilon_{xy}^{(n-n')}\tilde{E}_y^{(n')}(z)+\epsilon_{xz}^{(n-n')}\tilde{E}_z^{(n')}(z)\right], \tag{27}$$

$$k_y^{(0)}\tilde{H}_x^{(n)}(z)-k_x^{(n)}\tilde{H}_y^{(n)}(z)=\frac{k_0}{\eta_0}\sum_{n'\in\mathbb{Z}}\left[\epsilon_{zx}^{(n-n')}\tilde{E}_x^{(n')}(z)+\epsilon_{zy}^{(n-n')}\tilde{E}_y^{(n')}(z)+\epsilon_{zz}^{(n-n')}\tilde{E}_z^{(n')}(z)\right]. \tag{28}$$

Eqs. (23)–(28) hold for all $n\in\mathbb{Z}$, and are thus an infinite system of first-order ordinary differential equations (ODEs). For numerical solution, we first restrict the summations on their right sides to $|n|\leqslant N_\mathrm{t}$, and then define the four column vectors

$$\left.\begin{array}{ll}\left[\underline{\tilde{E}}_\sigma(z)\right]=\left[\tilde{E}_\sigma^{(n)}(z)\right], & \left[\underline{E}_\sigma(z)\right]=\left[E_\sigma^{(n)}(z)\right]\\ \left[\underline{\tilde{H}}_\sigma(z)\right]=\left[\tilde{H}_\sigma^{(n)}(z)\right], & \left[\underline{H}_\sigma(z)\right]=\left[H_\sigma^{(n)}(z)\right]\end{array}\right\},\quad \sigma=x,y,z;\ n\in[-N_\mathrm{t},N_\mathrm{t}] \tag{29}$$

of size $(2N_\mathrm{t}+1)$. Likewise, we define the diagonal $(2N_\mathrm{t}+1)\times(2N_\mathrm{t}+1)$ matrixes

$$\left.\begin{array}{l}\left[\underline{\underline{K}}_x\right]=\left[k_x^{(n)}\delta_{n,n'}\right]\\ \left[\underline{\underline{\kappa}}_z\right]=\kappa_z\left[n\delta_{n,n'}\right]\end{array}\right\},\quad n,n'\in[-N_\mathrm{t},N_\mathrm{t}], \tag{30}$$

where $\delta_{n,n'}$ is the Kronecker delta, and the Toeplitz matrixes

$$\left[\underline{\underline{\epsilon}}_{\sigma\sigma'}\right]=\left[\epsilon_{\sigma\sigma'}^{(n-n')}\right],\quad \sigma=x,y,z;\ n,n'\in[-N_\mathrm{t},N_\mathrm{t}]. \tag{31}$$

Substituting (25) and (28) into (23), (24), (26) and (27) thereafter, in order to eliminate the normal electromagnetic fields components (i.e., $\tilde{E}_z^{(n)}$ and $\tilde{H}_z^{(n)}$), and performing some algebraic manipulations, we derive the shift-invariant matrix ODE

$$\frac{\mathrm{d}}{\mathrm{d}z}\left[\underline{\tilde{\mathbf{f}}}(z)\right]=\mathrm{i}\left[\underline{\underline{\tilde{\mathbf{P}}}}\right]\left[\underline{\tilde{\mathbf{f}}}(z)\right],\quad 0<z<d. \tag{32}$$

The column vector

$$\left[\underline{\tilde{\mathbf{f}}}(z)\right]=\left[\left[\underline{\tilde{E}}_x(z)\right]^\mathrm{T},\quad \left[\underline{\tilde{E}}_y(z)\right]^\mathrm{T},\quad \eta_0\left[\underline{\tilde{H}}_x(z)\right]^\mathrm{T},\quad \eta_0\left[\underline{\tilde{H}}_y(z)\right]^\mathrm{T}\right]^\mathrm{T} \tag{33}$$

contains $4(2N_\mathrm{t}+1)$ components, and the z-independent matrix $[\underline{\underline{\tilde{\mathbf{P}}}}]$ is given in the Appendix.

The matrix ODE (32) has the solution [26]

$$\left[\underline{\tilde{\mathbf{f}}}(z_2)\right]=\left[\underline{\underline{\tilde{\mathbf{G}}}}\right]\exp\left\{\mathrm{i}(z_2-z_1)[\underline{\underline{\tilde{\mathbf{D}}}}]\right\}\left[\underline{\underline{\tilde{\mathbf{G}}}}\right]^{-1}\left[\underline{\tilde{\mathbf{f}}}(z_1)\right], \tag{34}$$

where the columns of the square matrix $[\underline{\underline{\tilde{\mathbf{G}}}}]$ are the successive eigenvectors of $[\underline{\underline{\tilde{\mathbf{P}}}}]$, and the diagonal matrix $[\underline{\underline{\tilde{\mathbf{D}}}}]$ contains the corresponding eigenvalues of $[\underline{\underline{\tilde{\mathbf{P}}}}]$. The assumption here is that $[\underline{\underline{\tilde{\mathbf{P}}}}]$ is diagonalizable, i.e., it has $4(2N_\mathrm{t}+1)$ linearly independent eigenvectors.

In order to solve the boundary value problem, we have to determine the column vector

$$\left[\underline{\mathbf{f}}(z)\right]=\left[\left[\underline{E}_x(z)\right]^\mathrm{T},\quad \left[\underline{E}_y(z)\right]^\mathrm{T},\quad \eta_0\left[\underline{H}_x(z)\right]^\mathrm{T},\quad \eta_0\left[\underline{H}_y(z)\right]^\mathrm{T}\right]^\mathrm{T} \tag{35}$$

instead of $[\underline{\tilde{\mathbf{f}}}(z)]$. The two column vectors are simply related to each other as

$$[\underline{\mathbf{f}}(z)] = [\underline{\underline{\mathbf{C}}}(z)]\left[\tilde{\underline{\mathbf{f}}}(z)\right], \tag{36}$$

where the diagonal matrix

$$[\underline{\underline{\mathbf{C}}}(z)] = [\exp(\mathrm{i}\tilde{n}\kappa_z z)\delta_{n,n'}], \quad n, n' \in [1, 4(2N_\mathrm{t}+1)]; \tag{37}$$

$\tilde{n} = \mathrm{Mod}[n-1, 2N_\mathrm{t}+1] - N_\mathrm{t}$; and $\mathrm{Mod}[n, n']$ denotes the remainder when n is divided by n', with n and n' being positive integers. According to (34) and (36), we obtain the relation

$$[\underline{\mathbf{f}}(z_2)] = [\underline{\underline{\mathbf{G}}}(z_2)]\exp\left\{\mathrm{i}(z_2 - z_1)[\tilde{\underline{\underline{\mathbf{D}}}}]\right\}[\underline{\underline{\mathbf{G}}}(z_1)]^{-1}[\underline{\mathbf{f}}(z_1)], \tag{38}$$

where the matrix

$$[\underline{\underline{\mathbf{G}}}(z)] = [\underline{\underline{\mathbf{C}}}(z)][\tilde{\underline{\underline{\mathbf{G}}}}] \tag{39}$$

is a periodic function of z; hence,

$$[\underline{\mathbf{f}}(d)] = [\underline{\underline{\mathbf{G}}}(d)]\exp\left\{\mathrm{i}d\left[\tilde{\underline{\underline{\mathbf{D}}}}\right]\right\}[\underline{\underline{\mathbf{G}}}(0)]^{-1}[\underline{\mathbf{f}}(0)]. \tag{40}$$

The continuity of the tangential components of the electric and magnetic field phasors across the two boundaries $z = 0$ and $z = d$ must be enforced with respect to the Floquet harmonic of any order n. Therefore, we get

$$\left[\underline{\mathbf{f}}(0)\right] = \begin{bmatrix} \left[\underline{\underline{Y}}_\mathrm{e}^{+}\right] & \left[\underline{\underline{Y}}_\mathrm{e}^{-}\right] \\ \left[\underline{\underline{Y}}_\mathrm{h}^{+}\right] & \left[\underline{\underline{Y}}_\mathrm{h}^{-}\right] \end{bmatrix} \begin{bmatrix} [\underline{\mathbf{A}}] \\ [\underline{\mathbf{R}}] \end{bmatrix}, \quad \left[\underline{\mathbf{f}}(d)\right] = \begin{bmatrix} \left[\underline{\underline{Y}}_\mathrm{e}^{+}\right] & [\underline{0}] \\ \left[\underline{\underline{Y}}_\mathrm{h}^{+}\right] & [\underline{0}] \end{bmatrix} \begin{bmatrix} [\underline{\mathbf{T}}] \\ [\underline{0}] \end{bmatrix}, \tag{41}$$

where the column vectors

$$[\underline{\mathbf{A}}] = \begin{bmatrix} a_\mathrm{L}^{(n)} \\ a_\mathrm{R}^{(n)} \end{bmatrix}, \quad [\underline{\mathbf{R}}] = \begin{bmatrix} r_\mathrm{L}^{(n)} \\ r_\mathrm{R}^{(n)} \end{bmatrix}, \quad [\underline{\mathbf{T}}] = \begin{bmatrix} t_\mathrm{L}^{(n)} \\ t_\mathrm{R}^{(n)} \end{bmatrix} \tag{42}$$

are of size $4N_\mathrm{t}+2$. The square matrixes $[\underline{\underline{Y}}_\mathrm{e}^{\pm}]$ and $[\underline{\underline{Y}}_\mathrm{h}^{\pm}]$ of size $(4N_\mathrm{t}+2)\times(4N_\mathrm{t}+2)$ are quite sparse; and their nonzero entries are calculated as follows:

$$\left.\begin{aligned} \left[\underline{\underline{Y}}_\mathrm{e}^{\pm}\right]_{nn'} &= (-\mathrm{i}/n_\mathrm{hs})\left[\underline{\underline{Y}}_\mathrm{h}^{\pm}\right]_{nn'} = \mathbf{L}_{\pm}^{(n)}\cdot\mathbf{u}_x \quad \text{if } n = n' \in [1, (2N_\mathrm{t}+1)] \\ \left[\underline{\underline{Y}}_\mathrm{e}^{\pm}\right]_{nn'} &= (-\mathrm{i}/n_\mathrm{hs})\left[\underline{\underline{Y}}_\mathrm{h}^{\pm}\right]_{nn'} = \mathbf{L}_{\pm}^{(n)}\cdot\mathbf{u}_y \quad \text{if } n = n' + 2N_\mathrm{t} + 1 \\ \left[\underline{\underline{Y}}_\mathrm{e}^{\pm}\right]_{nn'} &= (i/n_\mathrm{hs})\left[\underline{\underline{Y}}_\mathrm{h}^{\pm}\right]_{nn'} = \mathbf{R}_{\pm}^{(n)}\cdot\mathbf{u}_x \quad \text{if } n = n' - 2N_\mathrm{t} - 1 \\ \left[\underline{\underline{Y}}_\mathrm{e}^{\pm}\right]_{nn'} &= (i/n_\mathrm{hs})\left[\underline{\underline{Y}}_\mathrm{h}^{\pm}\right]_{nn'} = \mathbf{R}_{\pm}^{(n)}\cdot\mathbf{u}_y \quad \text{if } n = n' \in [(2N_\mathrm{t}+2), (4N_\mathrm{t}+2)] \end{aligned}\right\}. \tag{43}$$

Finally, substituting (41) into (40), we get

$$\begin{bmatrix} \left[\underline{\underline{U}}_\mathrm{T}\right] \\ \left[\underline{\underline{V}}_\mathrm{T}\right] \end{bmatrix}[\underline{\mathbf{T}}] + \begin{bmatrix} \mathrm{e}^{\mathrm{i}d\left[\tilde{\underline{\underline{D}}}_1\right]} & [\underline{0}] \\ [\underline{0}] & \mathrm{e}^{\mathrm{i}d\left[\tilde{\underline{\underline{D}}}_2\right]} \end{bmatrix} \begin{bmatrix} \left[\underline{\underline{U}}_\mathrm{R}\right] \\ \left[\underline{\underline{V}}_\mathrm{R}\right] \end{bmatrix}[\underline{\mathbf{R}}] = \begin{bmatrix} \mathrm{e}^{\mathrm{i}d\left[\tilde{\underline{\underline{D}}}_1\right]} & [\underline{0}] \\ [\underline{0}] & \mathrm{e}^{\mathrm{i}d\left[\tilde{\underline{\underline{D}}}_2\right]} \end{bmatrix} \begin{bmatrix} \left[\underline{\underline{U}}_\mathrm{A}\right] \\ \left[\underline{\underline{V}}_\mathrm{A}\right] \end{bmatrix}[\underline{\mathbf{A}}], \tag{44}$$

where $[\tilde{\underline{\underline{D}}}_1]$ and $[\tilde{\underline{\underline{D}}}_2]$ are the upper and lower diagonal submatrixes of $[\tilde{\underline{\underline{\mathbf{D}}}}]$, respectively, and the following three rectangular matrixes have been used for notational brevity:

$$\begin{bmatrix} \begin{bmatrix} \underline{\underline{U}}_{\mathrm{T}} \end{bmatrix} \\ \begin{bmatrix} \underline{\underline{V}}_{\mathrm{T}} \end{bmatrix} \end{bmatrix} = \left[\underline{\underline{\mathbf{G}}}(d)\right]^{-1} \begin{bmatrix} \begin{bmatrix} \underline{\underline{Y}}_{\mathrm{e}}^{+} \end{bmatrix} \\ \begin{bmatrix} \underline{\underline{Y}}_{\mathrm{h}}^{+} \end{bmatrix} \end{bmatrix}, \tag{45}$$

$$\begin{bmatrix} \begin{bmatrix} \underline{\underline{U}}_{\mathrm{R}} \end{bmatrix} \\ \begin{bmatrix} \underline{\underline{V}}_{\mathrm{R}} \end{bmatrix} \end{bmatrix} = -\left[\underline{\underline{\mathbf{G}}}(0)\right]^{-1} \begin{bmatrix} \begin{bmatrix} \underline{\underline{Y}}_{\mathrm{e}}^{-} \end{bmatrix} \\ \begin{bmatrix} \underline{\underline{Y}}_{\mathrm{h}}^{-} \end{bmatrix} \end{bmatrix}, \tag{46}$$

$$\begin{bmatrix} \begin{bmatrix} \underline{\underline{U}}_{\mathrm{A}} \end{bmatrix} \\ \begin{bmatrix} \underline{\underline{V}}_{\mathrm{A}} \end{bmatrix} \end{bmatrix} = \left[\underline{\underline{\mathbf{G}}}(0)\right]^{-1} \begin{bmatrix} \begin{bmatrix} \underline{\underline{Y}}_{\mathrm{e}}^{+} \end{bmatrix} \\ \begin{bmatrix} \underline{\underline{Y}}_{\mathrm{h}}^{+} \end{bmatrix} \end{bmatrix}. \tag{47}$$

For calculating the unknown $[\underline{\mathbf{R}}]$ and $[\underline{\mathbf{T}}]$, the R-matrix propagating algorithm [20,27] – which is based on the rearrangement of the positions of the eigenvalues of $[\underline{\underline{\tilde{\mathbf{P}}}}]$ in the diagonal matrix $[\underline{\underline{\tilde{\mathbf{D}}}}]$ – should be utilized in order to avoid numerical instabilities, especially when N_{t} is large [18,19]. Therefore, the entries on the diagonal of $[\underline{\underline{\tilde{\mathbf{D}}}}]$ (thus $[\underline{\underline{\tilde{D}}}_1]$ and $[\underline{\underline{\tilde{D}}}_2]$ also) are rearranged in increasing order of the imaginary part, and the columns of $[\underline{\underline{\tilde{\mathbf{G}}}}]$ are rearranged accordingly [28]. The final algebraic equation

$$\begin{bmatrix} \mathrm{e}^{-\mathrm{i}d\left[\underline{\underline{\tilde{D}}}_1\right]} \begin{bmatrix} \underline{\underline{U}}_{\mathrm{T}} \end{bmatrix} & \begin{bmatrix} \underline{\underline{U}}_{\mathrm{R}} \end{bmatrix} \\ \begin{bmatrix} \underline{\underline{V}}_{\mathrm{T}} \end{bmatrix} & \mathrm{e}^{\mathrm{i}d\left[\underline{\underline{\tilde{D}}}_2\right]} \begin{bmatrix} \underline{\underline{V}}_{\mathrm{R}} \end{bmatrix} \end{bmatrix} \begin{bmatrix} [\underline{\mathbf{T}}] \\ [\underline{\mathbf{R}}] \end{bmatrix} = \begin{bmatrix} \begin{bmatrix} \underline{\underline{U}}_{\mathrm{A}} \end{bmatrix} \\ \mathrm{e}^{\mathrm{i}d\left[\underline{\underline{\tilde{D}}}_2\right]} \begin{bmatrix} \underline{\underline{V}}_{\mathrm{A}} \end{bmatrix} \end{bmatrix} [\underline{\mathbf{A}}], \tag{48}$$

yielded by (44) for the determination of $[\underline{\mathbf{R}}]$ and $[\underline{\mathbf{T}}]$ is algorithmically stable due to the fact that the exponential terms $\mathrm{e}^{\mathrm{i}d[\underline{\underline{\tilde{D}}}_1]}$ and $\mathrm{e}^{\mathrm{i}d[\underline{\underline{\tilde{D}}}_2]}$ will never become overwhelming in magnitude because of the rearrangement of the eigenvalues. The matrix inverse operation required to solve (48) for $[\underline{\mathbf{R}}]$ and $[\underline{\mathbf{T}}]$ is then easily accomplished, using standard techniques [29], for arbitrary d and N_{t}.

Once $\{r_{\mathrm{L}}^{(n)}, r_{\mathrm{R}}^{(n)}\}$ and $\{t_{\mathrm{L}}^{(n)}, t_{\mathrm{R}}^{(n)}\}$ for all n have been determined using the RCWA, the nth-order reflection and transmission coefficients

$$\mathrm{r}_{IJ}^{(n)} = \frac{r_I^{(n)}}{a_J^{(0)}}, \quad \mathrm{t}_{IJ}^{(n)} = \frac{t_I^{(n)}}{a_J^{(0)}}, \quad I,J = \mathrm{L},\mathrm{R} \tag{49}$$

can be computed as functions of the wavevector $\mathbf{k}_{+}^{(0)}$ of the incident plane wave. Reflectances ($\mathrm{R}_{\mathrm{LL}}^{(n)}$, etc.) and transmittances ($\mathrm{T}_{\mathrm{LL}}^{(n)}$, etc.) of order n can be additionally calculated as

$$\mathrm{R}_{IJ}^{(n)} = \frac{\mathrm{Re}[k_z^{(n)}]}{\mathrm{Re}[k_z^{(0)}]} |\mathrm{r}_{IJ}^{(n)}|^2, \quad \mathrm{T}_{IJ}^{(n)} = \frac{\mathrm{Re}[k_z^{(n)}]}{\mathrm{Re}[k_z^{(0)}]} |\mathrm{t}_{IJ}^{(n)}|^2, \quad I,J = \mathrm{L},\mathrm{R}. \tag{50}$$

Co-polarized reflection/transmission coefficients and remittances – i.e., reflectances and transmission coefficients – subscripted RR (LL) are labeled as co-handed and those subscripted LL (RR) are labeled as cross-handed, when the chiral STF is structurally right(left)-handed.

Parenthetically, we note the special case when $\alpha = 0$. Then, all nonspecular reflection and transmission coefficients fold into the specular coefficients

$$\mathrm{r}_{IJ}^{(0)} \Leftarrow \sum_{|n| \leqslant N_{\mathrm{t}}} \mathrm{r}_{IJ}^{(n)}, \quad \mathrm{t}_{IJ}^{(0)} \Leftarrow \sum_{|n| \leqslant N_{\mathrm{t}}} \mathrm{t}_{IJ}^{(n)}, \quad I,J = \mathrm{L},\mathrm{R}. \tag{51}$$

Accordingly, the reflectances and transmittances for $\alpha = 0$ can only be specular; hence,

$$\mathrm{R}_{IJ}^{(0)} = |\mathrm{r}_{IJ}^{(0)}|^2, \quad \mathrm{T}_{IJ}^{(0)} = |\mathrm{t}_{IJ}^{(0)}|^2, \quad I,J = \mathrm{L},\mathrm{R}. \tag{52}$$

2.3. Angular-spectrum representation of 3D optical beams

Having formulated the diffraction of a plane wave by a slanted chiral STF, we move on the diffraction of a 3D optical beam. Let $\theta_{\rm i} \in (-\pi/2, \pi/2)$ and $\psi_{\rm i} \in (-\pi, \pi]$, respectively, be the mean angles of beam incidence with respect to the z axis and the x axis in the xy plane. We introduce the coordinate system $(\bar{x}, \bar{y}, \bar{z})$, where

$$\left.\begin{aligned} \bar{x} &= x\cos\theta_{\rm i}\cos\psi_{\rm i} + y\cos\theta_{\rm i}\sin\psi_{\rm i} - z\sin\theta_{\rm i} \\ \bar{y} &= -x\sin\psi_{\rm i} + y\cos\psi_{\rm i} \\ \bar{z} &= x\sin\theta_{\rm i}\cos\psi_{\rm i} + y\sin\theta_{\rm i}\sin\psi_{\rm i} + z\cos\theta_{\rm i} - h_0/\cos\theta_{\rm i} \end{aligned}\right\}, \tag{53}$$

as shown in Fig. 2, with $\mathbf{u}_{\bar{x}}$, $\mathbf{u}_{\bar{y}}$ and $\mathbf{u}_{\bar{z}}$ being the basis vectors. The $z\bar{z}$ plane is the plane of incidence; while the $\bar{x}$ and $\bar{y}$ axes are parallel and perpendicular to the plane of incidence, respectively. The z coordinate of the origin of the $(\bar{x}, \bar{y}, \bar{z})$ coordinate system is h_0 in the (x, y, z) coordinate system.

The incident beam can be decomposed into an angular spectrum of plane waves [30]. The planewave angular spectrum can then be multiplied by the reflection or transmission coefficients and recombined to produce the reflected or the transmitted beams [31,32].

In the half-space $z \leqslant 0$, the electromagnetic field phasors of the 3D incident beam are written in the $(\bar{x}, \bar{y}, \bar{z})$ coordinate system as

$$\mathbf{E}_{\rm i}(\bar{x}, \bar{y}, \bar{z}) = \int_{-\infty}^{\infty}\int_{-\infty}^{\infty} \Psi(\vartheta_x, \vartheta_y)\mathbf{e}_{\rm i}(\vartheta_x, \vartheta_y) \times \exp[{\rm i}k_0 n_{\rm hs}(\vartheta_x\bar{x} + \vartheta_y\bar{y} + \vartheta_z\bar{z})]\,{\rm d}\vartheta_x\,{\rm d}\vartheta_y \tag{54}$$

and

$$\mathbf{H}_{\rm i}(\bar{x}, \bar{y}, \bar{z}) = \int_{-\infty}^{\infty}\int_{-\infty}^{\infty} \Psi(\vartheta_x, \vartheta_y)\mathbf{h}_{\rm i}(\vartheta_x, \vartheta_y) \times \exp[{\rm i}k_0 n_{\rm hs}(\vartheta_x\bar{x} + \vartheta_y\bar{y} + \vartheta_z\bar{z})]\,{\rm d}\vartheta_x\,{\rm d}\vartheta_y. \tag{55}$$

In (54) and (55), the real-valued ϑ_x and ϑ_y together define the angular spectrum of plane waves, while $\vartheta_z = +\sqrt{1 - \vartheta_x^2 - \vartheta_y^2}$ is either real-valued or complex-valued. The unit vectors $\mathbf{e}_{\rm i}(\vartheta_x, \vartheta_y)$ and $\mathbf{h}_{\rm i}(\vartheta_x, \vartheta_y)$,

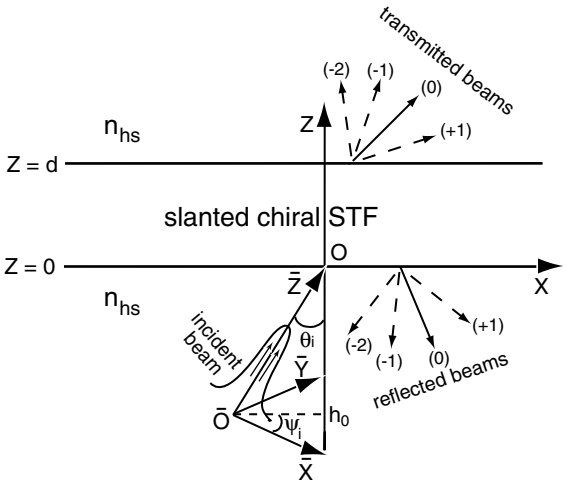

Fig. 2. Coordinate system $(\bar{x}, \bar{y}, \bar{z})$ for a 3D optical beam incident on a slanted chiral STF. The diffracted optical beams are associated with both specular ($n = 0$) and nonspecular ($n \neq 0$) modes of reflection and transmission when $\alpha \neq 0$, but all nonspecular beams fold into the specular ones when $\alpha = 0$.

respectively, represent the electric and magnetic fields of a plane wave specified by $(\vartheta_x, \vartheta_y)$; while the angular-spectrum function $\Psi(\vartheta_x, \vartheta_y)$ defines the profile of the incident beam.

Substituting (53) into (54) and (55), we obtain the more useful representation

$$\left.\begin{aligned}\mathbf{E}_{\mathrm{i}}(x,y,z) &= \int_{-\infty}^{\infty}\int_{-\infty}^{\infty}\Psi(\vartheta_x,\vartheta_y)\mathbf{e}_{\mathrm{i}}(\vartheta_x,\vartheta_y)\exp[\mathrm{i}(\mathbf{k}_+^{(0)}\cdot\mathbf{r}+\varphi_0)]\,\mathrm{d}\vartheta_x\,\mathrm{d}\vartheta_y\\ \mathbf{H}_{\mathrm{i}}(x,y,z) &= \int_{-\infty}^{\infty}\int_{-\infty}^{\infty}\Psi(\vartheta_x,\vartheta_y)\mathbf{h}_{\mathrm{i}}(\vartheta_x,\vartheta_y)\exp[\mathrm{i}(\mathbf{k}_+^{(0)}\cdot\mathbf{r}+\varphi_0)]\,\mathrm{d}\vartheta_x\,\mathrm{d}\vartheta_y\end{aligned}\right\},\quad z<0, \tag{56}$$

where $\varphi_0 = -\vartheta_z h_0/\cos\theta_{\mathrm{i}}$. The quantity $\mathbf{k}_+^{(0)} \equiv \mathbf{k}_+^{(0)}(\vartheta_x, \vartheta_y)$ in these two equations symbolizes the wavevector of each planewave contributor of the incident beam; thus,

$$\mathbf{k}_+^{(0)} = k_x^{(0)}\mathbf{u}_x + k_y^{(0)}\mathbf{u}_y + k_z^{(0)}\mathbf{u}_z, \tag{57}$$

where

$$k_x^{(0)} = k_0 n_{\mathrm{hs}}(\vartheta_x\cos\theta_{\mathrm{i}}\cos\psi_{\mathrm{i}} - \vartheta_y\sin\psi_{\mathrm{i}} + \vartheta_z\sin\theta_{\mathrm{i}}\cos\psi_{\mathrm{i}}), \tag{58}$$

$$k_y^{(0)} = k_0 n_{\mathrm{hs}}(\vartheta_x\cos\theta_{\mathrm{i}}\sin\psi_{\mathrm{i}} + \vartheta_y\cos\psi_{\mathrm{i}} + \vartheta_z\sin\theta_{\mathrm{i}}\sin\psi_{\mathrm{i}}), \tag{59}$$

and

$$k_z^{(0)} = k_0 n_{\mathrm{hs}}(-\vartheta_x\sin\theta_{\mathrm{i}} + \vartheta_z\cos\theta_{\mathrm{i}}). \tag{60}$$

In order to evaluate $\mathbf{e}_{\mathrm{i}}(\vartheta_x, \vartheta_y)$ and $\mathbf{h}_{\mathrm{i}}(\vartheta_x, \vartheta_y)$, it is assumed that each of the contributing plane waves of the incident beam locally has an identical polarization state that is characterized by a constant-valued pair $\{a_{\mathrm{L}}^{(0)}, a_{\mathrm{R}}^{(0)}\}$. As a matter of fact, the incident beam's local planewave polarization state can be defined in a variety of ways [31,33]. However, the polarization states of finite-extent beams are not the same as the local polarization states of their planewave components [34]. Following [33] as well, we think it is reasonable to consider beams whose polarization states are approximately circular.

Hence, approximately LCP beams are simulated by setting $a_{\mathrm{R}}^{(0)} = 0$, and approximately RCP beams by $a_{\mathrm{L}}^{(0)} = 0$. In analogy with (6) and (7), $\mathbf{e}_{\mathrm{i}}$ and $\mathbf{h}_{\mathrm{i}}$ for each planewave component $(\vartheta_x, \vartheta_y)$ are written in terms of $\{a_{\mathrm{L}}^{(0)}, a_{\mathrm{R}}^{(0)}\}$ as

$$\mathbf{e}_{\mathrm{i}} = \mathbf{L}_+^{(0)}a_{\mathrm{L}}^{(0)} + \mathbf{R}_+^{(0)}a_{\mathrm{R}}^{(0)},\quad \mathbf{h}_{\mathrm{i}} = \frac{-\mathrm{i}n_{\mathrm{hs}}}{\eta_0}\left[\mathbf{L}_+^{(0)}a_{\mathrm{L}}^{(0)} - \mathbf{R}_+^{(0)}a_{\mathrm{R}}^{(0)}\right], \tag{61}$$

where $\mathbf{L}_+^{(0)}$ and $\mathbf{R}_+^{(0)}$ are defined in (13) and (14), respectively, to vary with $\mathbf{k}_+^{(0)}$ (and thus with ϑ_x and ϑ_y).

The reflected and the transmitted optical beams are to be calculated by combining the contributions of every incident planewave component. Therefore, the electromagnetic field phasors of the nth-order reflected and transmitted beams are written as follows:

$$\mathbf{E}_{\mathrm{r}}^{(n)}(x,y,z) = \int_{-\infty}^{\infty}\int_{-\infty}^{\infty}\Psi(\vartheta_x,\vartheta_y)\mathbf{e}_{\mathrm{r}}^{(n)}(\vartheta_x,\vartheta_y)\times\exp[\mathrm{i}(\mathbf{k}_-^{(n)}\cdot\mathbf{r}+\varphi_0)]\,\mathrm{d}\vartheta_x\,\mathrm{d}\vartheta_y,\quad z<0, \tag{62}$$

$$\mathbf{H}_{\mathrm{r}}^{(n)}(x,y,z) = \int_{-\infty}^{\infty}\int_{-\infty}^{\infty}\Psi(\vartheta_x,\vartheta_y)\mathbf{h}_{\mathrm{r}}^{(n)}(\vartheta_x,\vartheta_y)\times\exp[\mathrm{i}(\mathbf{k}_-^{(n)}\cdot\mathbf{r}+\varphi_0)]\,\mathrm{d}\vartheta_x\,\mathrm{d}\vartheta_y,\quad z<0, \tag{63}$$

$$\mathbf{E}_{\mathrm{t}}^{(n)}(x,y,z) = \int_{-\infty}^{\infty}\int_{-\infty}^{\infty}\Psi(\vartheta_x,\vartheta_y)\mathbf{e}_{\mathrm{t}}^{(n)}(\vartheta_x,\vartheta_y)\times\exp[\mathrm{i}(\mathbf{k}_+^{(n)}\cdot\tilde{\mathbf{r}}+\varphi_0)]\,\mathrm{d}\vartheta_x\,\mathrm{d}\vartheta_y,\quad z>d, \tag{64}$$

$$\mathbf{H}_{\mathrm{t}}^{(n)}(x,y,z) = \int_{-\infty}^{\infty}\int_{-\infty}^{\infty}\Psi(\vartheta_x,\vartheta_y)\mathbf{e}_{\mathrm{t}}^{(n)}(\vartheta_x,\vartheta_y)\times\exp[\mathrm{i}(\mathbf{k}_+^{(n)}\cdot\tilde{\mathbf{r}}+\varphi_0)]\,\mathrm{d}\vartheta_x\,\mathrm{d}\vartheta_y,\quad z>d. \tag{65}$$

In these expressions, the electric and magnetic fields vectors $\mathbf{e}_{\mathrm{r}}^{(n)}$, $\mathbf{h}_{\mathrm{r}}^{(n)}$, $\mathbf{e}_{\mathrm{t}}^{(n)}$ and $\mathbf{h}_{\mathrm{t}}^{(n)}$ are calculated in the similar way as $\mathbf{e}_{\mathrm{i}}$ and $\mathbf{h}_{\mathrm{i}}$ of (61), thus,

$$\mathbf{e}_{\mathrm{r}}^{(n)} = \mathbf{L}_{-}^{(n)} r_{\mathrm{L}}^{(n)} + \mathbf{R}_{-}^{(n)} r_{\mathrm{R}}^{(n)}, \quad \mathbf{h}_{\mathrm{r}}^{(n)} = \frac{-\mathrm{i}n_{\mathrm{hs}}}{\eta_0}\left[\mathbf{L}_{-}^{(n)} r_{\mathrm{L}}^{(n)} - \mathbf{R}_{-}^{(n)} r_{\mathrm{R}}^{(n)}\right], \tag{66}$$

and

$$\mathbf{e}_{\mathrm{t}}^{(n)} = \mathbf{L}_{+}^{(n)} t_{\mathrm{L}}^{(n)} + \mathbf{R}_{+}^{(n)} t_{\mathrm{R}}^{(n)}, \quad \mathbf{h}_{\mathrm{t}}^{(n)} = \frac{-\mathrm{i}n_{\mathrm{hs}}}{\eta_0}\left[\mathbf{L}_{+}^{(n)} t_{\mathrm{L}}^{(n)} - \mathbf{R}_{+}^{(n)} t_{\mathrm{R}}^{(n)}\right]. \tag{67}$$

For (66) and (67), $\mathbf{L}_{\pm}^{(n)}$ and $\mathbf{R}_{\pm}^{(n)}$ are defined in (13) and (14), respectively; while the amplitude pairs $\{r_{\mathrm{L}}^{(n)}, r_{\mathrm{R}}^{(n)}\}$ and $\{t_{\mathrm{L}}^{(n)}, t_{\mathrm{R}}^{(n)}\}$, which are functions of ϑ_x and ϑ_y, need to be determined by means of the RCWA formulated in Section 2.2 for each of the planewave component of the incident beam. The electromagnetic fields of the reflected and transmitted beams are thereafter obtained from (62) to (65).

Additionally, similar definitions as (51) are needed for the electromagnetic field phasors of diffracted beams when $\alpha = 0$; i.e.,

$$\mathbf{E}_{\mathrm{r}}^{(0)}(x,y,z) \Leftarrow \sum_{|n|\leqslant N_{\mathrm{t}}} \mathbf{E}_{\mathrm{r}}^{(n)}(x,y,z), \quad \mathbf{H}_{\mathrm{r}}^{(0)}(x,y,z) \Leftarrow \sum_{|n|\leqslant N_{\mathrm{t}}} \mathbf{H}_{\mathrm{r}}^{(n)}(x,y,z) \tag{68}$$

and

$$\mathbf{E}_{\mathrm{t}}^{(0)}(x,y,z) \Leftarrow \sum_{|n|\leqslant N_{\mathrm{t}}} \mathbf{E}_{\mathrm{t}}^{(n)}(x,y,z), \quad \mathbf{H}_{\mathrm{t}}^{(0)}(x,y,z) \Leftarrow \sum_{|n|\leqslant N_{\mathrm{t}}} \mathbf{H}_{\mathrm{t}}^{(n)}(x,y,z), \tag{69}$$

because all nonspecular field phasors fold into the specular ones [32].

2.4. Lateral shifts on reflection

The foregoing theoretical formulation is suitable for the computation of lateral shifts of reflected optical beams in the following two problems:

- *Problem A:* The half-spaces of reflection and transmission are vacuous (i.e., $n_{\mathrm{hs}} = 1$).
- *Problem B:* The half-spaces of reflection and transmission are occupied by a mediums that is optically denser than the slanted chiral STF.

Our focus in Problem A lay on the circular Bragg phenomenon [14], but on the total reflection phenomenon in Problem B [2,36].

Both 2D and 3D Gaussian optical beams were considered, with the former being a special case of, but simpler than, the latter. The angular-spectrum function of the 3D incident beam is [31,37]

$$\Psi(\vartheta_x, \vartheta_y) = \frac{\rho_0^2}{2\pi} \exp\left[-\frac{1}{2}\rho_0^2\left(\vartheta_x^2 + \vartheta_y^2\right)\right], \tag{70}$$

where $\rho_0 = k_0 n_{\mathrm{hs}} w_0$ and w_0 is the width of the beam waist. The incident 2D Gaussian beam is represented through the angular-spectrum function

$$\Psi(\vartheta_x, \vartheta_y) = \frac{\rho_0}{\sqrt{2\pi}} \exp\left(-\frac{1}{2}\rho_0^2\vartheta_x^2\right)\delta(\vartheta_y), \tag{71}$$

where $\delta(\cdot)$ is the Dirac delta function.

The reflected beam of order n shifts by $\mathbf{d}^{(n)}$ in the xy plane relative to the incident beam. This shift is represented by the relative difference between the first moments of the energy densities of the electric fields $\mathbf{E}_{\mathrm{i}}(\mathbf{r})$ and $\mathbf{E}_{\mathrm{r}}^{(n)}(\mathbf{r})$, respectively, evaluated on the interface plane $z = 0$. Thus,

$$\mathbf{d}^{(n)} = \mathbf{\Delta}_{\mathrm{r}}^{(n)} - \mathbf{\Delta}_{\mathrm{i}}, \tag{72}$$

where

$$\mathbf{\Delta}_{\mathrm{i}} = \left(\int_{-\infty}^{\infty} \int_{-\infty}^{\infty} (x\mathbf{u}_x + y\mathbf{u}_y) |\mathbf{E}_{\mathrm{i}}|^2 \mathrm{d}x\, \mathrm{d}y \right) \left(\int_{-\infty}^{\infty} \int_{-\infty}^{\infty} |\mathbf{E}_{\mathrm{i}}|^2 \, \mathrm{d}x\, \mathrm{d}y \right)^{-1} \tag{73}$$

and

$$\mathbf{\Delta}_{\mathrm{r}}^{(n)} = \left(\int_{-\infty}^{\infty} \int_{-\infty}^{\infty} (x\mathbf{u}_x + y\mathbf{u}_y) |\mathbf{E}_{\mathrm{r}}^{(n)}|^2 \, \mathrm{d}x\, \mathrm{d}y \right) \left(\int_{-\infty}^{\infty} \int_{-\infty}^{\infty} |\mathbf{E}_{\mathrm{r}}^{(n)}|^2 \, \mathrm{d}x\, \mathrm{d}y \right)^{-1}. \tag{74}$$

A lateral shift is always in the plane of incidence (i.e., the $\bar{z}z$ plane) for incident 2D beams, but may comprise components both in and normal to the $\bar{z}z$ plane for incident 3D beams.

Let $\mathbf{d}_{\mathrm{L}}^{(n)}$ and $\mathbf{d}_{\mathrm{R}}^{(n)}$ denote the nth-order lateral shifts by LCP and RCP incident beams, respectively. It is convenient to represent $\mathbf{d}_{\mathrm{L}}^{(n)}$ and $\mathbf{d}_{\mathrm{R}}^{(n)}$ in the form

$$\left.\begin{aligned} \mathbf{d}_{\mathrm{L}}^{(n)} &= d_{\mathrm{L}}^{(n)\parallel} \mathbf{u}_{\parallel} + d_{\mathrm{L}}^{(n)\perp} \mathbf{u}_{\perp} \\ \mathbf{d}_{\mathrm{R}}^{(n)} &= d_{\mathrm{R}}^{(n)\parallel} \mathbf{u}_{\parallel} + d_{\mathrm{R}}^{(n)\perp} \mathbf{u}_{\perp} \end{aligned}\right\}, \tag{75}$$

where the unit vectors $\mathbf{u}_{\parallel} = \mathbf{u}_{\bar{y}} \times \mathbf{u}_z$ and $\mathbf{u}_{\perp} = \mathbf{u}_{\bar{y}}$ are parallel and perpendicular to the $\bar{z}z$ plane, respectively. Clearly, $d_{\mathrm{L}}^{(n)\parallel}$ and $d_{\mathrm{R}}^{(n)\parallel}$ represent the in-plane shifts; while $d_{\mathrm{L}}^{(n)\perp}$ and $d_{\mathrm{R}}^{(n)\perp}$ represent the out-of-plane shifts [33].

3. Numerical results and discussion

3.1. Preliminaries

Calculations were made with the following constitutive and geometric parameters for the slanted chiral STF: $p_a = 2.0$, $p_b = 2.6$, $p_c = 2.1$; $\lambda_a = \lambda_c = 140$ nm, $\lambda_c = 150$ nm; $N_a = N_b = N_c = 1000$; $\Omega = 200$ nm; $d = 60\ \Omega$; $\chi_s = 30°$; and $h = 1$. The chosen value of the ratio d/Ω is large enough for the circular Bragg phenomenon to be fully developed [7,14]. For simplicity, we set $h_0 = 0$. Several appropriate values of α were used.

When a plane wave is incident on a slanted chiral STF, the center-wavelength λ_0^{Br} of the Bragg regime is to be estimated by solving the equation [14,35,36]

$$\lambda_0^{\mathrm{Br}} - \Omega \cos\alpha \cos^{1/2}\tilde{\theta}_{\mathrm{i}} \left[\sqrt{\epsilon_c(\lambda_0^{\mathrm{Br}})} + \sqrt{\tilde{\epsilon}_d(\lambda_0^{\mathrm{Br}})} \right] = 0, \tag{76}$$

where $\tilde{\theta}_{\mathrm{i}}$ is the angle of incidence with respect to the z axis and

$$\tilde{\epsilon}_d(\lambda_0) = \frac{\epsilon_a(\lambda_0)\epsilon_b(\lambda_0)}{\epsilon_a(\lambda_0)\cos^2\chi_s + \epsilon_b(\lambda_0)\sin^2\chi_s}. \tag{77}$$

Numerical investigation shows that the estimate of λ_0^{Br} afforded by (76) is reliable when $\cos\tilde{\theta}_{\mathrm{i}} \in [\frac{\sqrt{3}}{2}, 1]$. For the chosen thin-film properties, we estimate that $\lambda_0^{\mathrm{Br}} = 727$ nm when $\tilde{\theta}_{\mathrm{i}} = \alpha = 0$.

For Problem A, $n_{\mathrm{hs}} = 1$ and we confined our investigations to the wavelength $\lambda_0 = \lambda_0^{\mathrm{Br}}|_{\tilde{\theta}_{\mathrm{i}}=0}$, i.e., in the center of the Bragg wavelength-regime for normal incidence. Total reflection of an incident beam is impossible under these conditions.

For Problem B, we set $n_{\mathrm{hs}} = 4$ so that the chosen thin film is optically rarer than the ambient medium at $\lambda_0 = 727$ nm. Total reflection of the incident beam must occur when $|\theta_{\mathrm{i}}|$ exceeds a critical value θ_{ic}. The circular Bragg phenomenon still exists at sub-critical angles of incidence, but in a highly telescoped fashion [36]; and we mostly investigated Goos–Hänchen shifts [2,36,40].

The 3D Gaussian beam profile was uniformly discretized to a 80×80 mesh in the spectral domain $\{(\vartheta_x, \vartheta_y) | \sqrt{\vartheta_x^2 + \vartheta_y^2} \leq 4/\rho_0\}$, which was sufficient to calculate the approximate value of $|\mathbf{E}_\mathrm{i}|^2$ of (54) with less than 0.01% inaccuracy. Accordingly, $80 \times 80 = 6400$ plane waves corresponding to different values of the pair $(\vartheta_x, \vartheta_y)$ were generated to span the entire angular spectrum of the diffracted beams. The maximum order of the Floquet harmonics was fixed at $N_\mathrm{t} = 9$ for the chosen wavelength-regime, after ensuring that every planewave reflectance and transmittance greater than 10^{-4} in magnitude converged to 0.1% accuracy. All propagating harmonics and some evanescent harmonics were thereby covered. Computed values of $\mathbf{d}_\mathrm{L}^{(n)}$ and $\mathbf{d}_\mathrm{R}^{(n)}$ for varying $\sin\theta_\mathrm{i}$ and $\psi_\mathrm{i} \in (-\pi, \pi]$ are presented in Figs. 5,7,10–12, 15 and 16; while the remaining figures are reserved for the discussion of planewave responses.

3.2. Problem A: slanted chiral STF in vacuum

3.2.1. Planewave incidence

Let us commence by considering the response of a slanted chiral STF to a plane wave whose wavevector makes the angles (i) $\tilde{\theta}_\mathrm{i}$ to the z axis and (ii) $\tilde{\psi}_\mathrm{i}$ to the x axis in the xy plane. Parenthetically, the plane wave response has been studied elsewhere for normal incidence [14].

The most prominent feature of the planewave responses of both unslanted and slanted chiral STFs is due to the circular Bragg phenomenon, which is circular-polarization-selective reflection in the Bragg regime [7,14]. The circular Bragg phenomenon is indicated by a high co-handed reflectance in the Bragg regime. Although this reflectance is purely specular for $\alpha = 0$, it is nonspecular for $\alpha \neq 0$ as it then occurs in the $n = -2\mathrm{sign}(\alpha)$ harmonic component of the reflected field, regardless of the structural handedness of the film.

Figs. 3 and 4 present key planewave remittances for arbitrary incidence in either the xz plane (i.e., $\tilde{\psi}_\mathrm{i} = 0°$) or the yz plane (i.e., $\tilde{\psi}_\mathrm{i} = 90°$) for both $\alpha = 0°$ and $\alpha = 10°$, when $n_\mathrm{hs} = 1$ and $\lambda_0 = \lambda_0^\mathrm{Br}|_{\tilde{\theta}_\mathrm{i}=0}$. The circular Bragg phenomenon is clearly identifiable as a broad ridge in the plots of $\mathrm{R}_\mathrm{RR}^{(-2)}$ (for $\alpha = 10°$) and $\mathrm{R}_\mathrm{RR}^{(0)}$ (for $\alpha = 0°$) in Fig. 4, as well as in the plots of $\mathrm{T}_\mathrm{LL}^{(0)}$ in Fig. 3, because the chosen STF is structurally right-handed. The angular spread of the Bragg regime – quantitated as the $\tilde{\theta}_\mathrm{i}$-span of the broad ridge in a co-handed reflectance plot at a fixed wavelength – becomes asymmetric and sensitive to $\tilde{\psi}_\mathrm{i}$ when $\alpha \neq 0$ (Figs. 4(c) and (d)), presenting a striking contrast to the almost symmetric pattern of the Bragg regime for $\alpha = 0$ (Figs. 4(a) and (b)). In fact, because of the effect of the Rayleigh–Wood anomalies of order $n = \mp 2$ which occur at

$$\lambda_{0_{\mp 2}}^\mathrm{RW} = \frac{n_\mathrm{hs}\Omega}{|\sin\alpha|}\left(\sqrt{1 - \left(\sin\tilde{\theta}_\mathrm{i}\sin\tilde{\psi}_\mathrm{i}\right)^2} \pm \sin\tilde{\theta}_\mathrm{i}\cos\tilde{\psi}_\mathrm{i}\mathrm{sign}(\alpha)\right), \tag{78}$$

the circular Bragg phenomenon for $\alpha \neq 0$ is forced to shift its angular position, and is even subverted either in part or totally when $|\alpha|$ is large [14].

3.2.2. Lateral shift of Gaussian beam on Bragg reflection

In general, lateral shifts on reflection are expected because every planewave component of an incident beam experiences different phase and magnitude changes on reflection. A co-handed incident beam would be mostly reflected, and thus shifted with little distortion in profile, when its angular spectrum lies totally within the angular spread of the Bragg regime (if possible at that wavelength). Fig. 5 shows the in-plane shift of a 2D RCP Gaussian beam, with parameters chosen such that it is mostly reflected by either an unslanted chiral STF ($\alpha = 0°$) or a slanted chiral STF ($\alpha = 10°$), when $n_\mathrm{hs} = 1$. The in-plane shift presented in this figure was calculated as

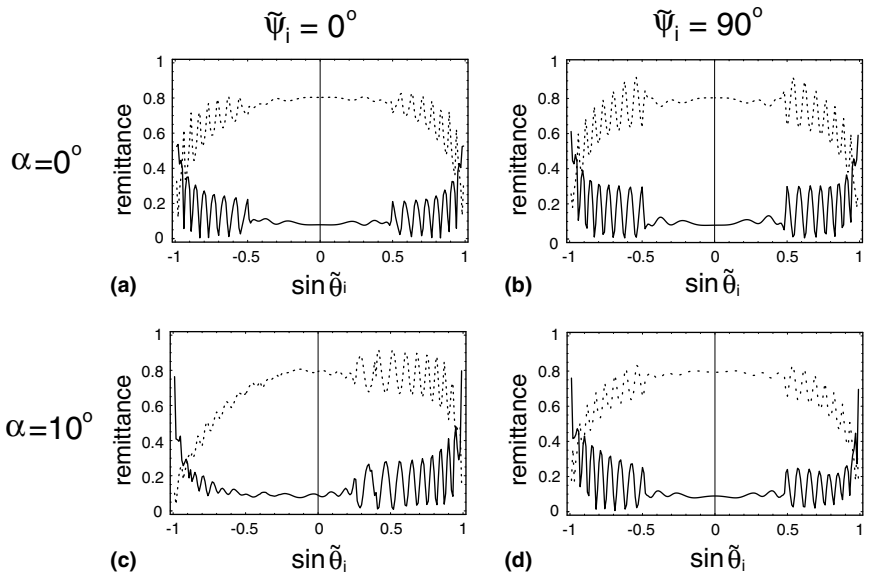

Fig. 3. Spectrums of planewave remittances (a, b) $R^{(0)}_{LL} + R^{(0)}_{RL}$ (solid lines) and $T^{(0)}_{LL}$ (dotted lines), calculated for an *unslanted* chiral STF of $\alpha = 0°$; and (c, d) $\sum_{|n| \leqslant N_t} (R^{(n)}_{LL} + R^{(n)}_{RL})$ (solid lines) and $T^{(0)}_{LL}$ (dotted lines), calculated for a *slanted* chiral STF of $\alpha = 10°$. The following parameters were used for calculations: $p_a = 2.0$, $p_b = 2.6$, $p_c = 2.1$; $\lambda_a = \lambda_c = 140$ nm, $\lambda_c = 150$ nm; $N_a = N_b = N_c = 1000$; $\Omega = 200$ nm, $d = 60\ \Omega$, $\chi_s = 30°$, and $n_{hs} = 1$. The chosen wavelength $\lambda_0 = \lambda_0^{Br}|_{\tilde{\theta}_i = 0}$ so that (a, b) $\lambda_0 = 727$ nm and (c, d) $\lambda_0 = 716$ nm.

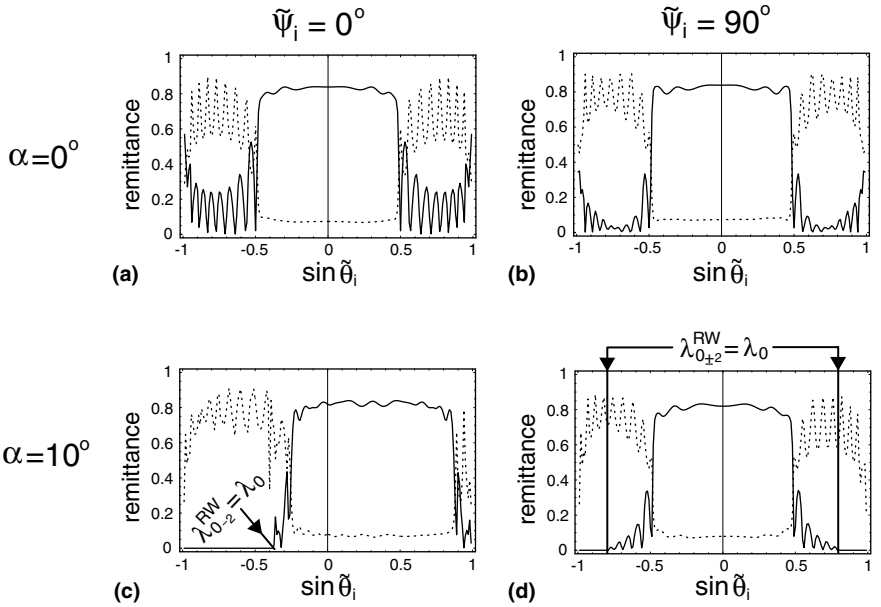

Fig. 4. Same as Fig. 3, except the remittances plotted are (a, b) $R^{(0)}_{RR}$ (solid lines) and $T^{(0)}_{LR} + T^{(0)}_{RR}$ (dotted lines) for $\alpha = 0°$; and (c, d) $R^{(-2)}_{RR}$ (solid lines) and $\sum_{|n| \leqslant N_t} (T^{(n)}_{LR} + T^{(n)}_{RR})$ (dotted lines) for $\alpha = 10°$.

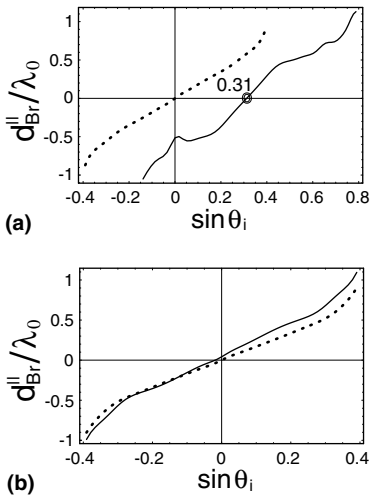

Fig. 5. Normalized in-plane shift $d_{\mathrm{Br}}^{\parallel}/\lambda_0$ as a function of $\sin\theta_{\mathrm{i}}$, when $\alpha = 0°$ (dotted lines) and $\alpha = 10°$ (solid lines). The incident beam is 2D RCP Gaussian, $\lambda_0 = \lambda_0^{\mathrm{Br}}|_{\tilde{\theta}_{\mathrm{i}}=0}$, $w_0 = 4\lambda_0$, and $h_0 = 0$. (a) $\psi_{\mathrm{i}} = 0°$, and (b) $\psi_{\mathrm{i}} = 90°$. The values of θ_{i} chosen lie squarely within the angular spread of the Bragg regime, so that the co-handed beam is mostly reflected. Other parameters are the same as for Fig. 3.

$$d_{\mathrm{Br}}^{\parallel} = \begin{cases} d_{\mathrm{R}}^{(0)\parallel}, & \alpha = 0, \\ d_{\mathrm{R}}^{(\mp 2)\parallel}, & \alpha \gtrless 0, \end{cases} \tag{79}$$

with the out-of-plane shift $d_{\mathrm{Br}}^{\perp} \equiv 0$. Clearly, the in-plane shift is always *forward* (i.e., $d_{\mathrm{Br}}^{\parallel}\sin\theta_{\mathrm{i}} \geqslant 0$) and almost symmetric with respect to θ_{i} when $\alpha = 0$. However, when $\alpha \neq 0$, the in-plane shift could be either forward or *backward* (i.e., $d_{\mathrm{Br}}^{\parallel}\sin\theta_{\mathrm{i}} \leqslant 0$), depending on θ_{i}. For example, Fig. 5(a) shows negative $d_{\mathrm{Br}}^{\parallel}$ for $\sin\theta_{\mathrm{i}} \in (0, 0.31)$ when $\psi_{\mathrm{i}} = 0°$ and $\alpha = 10°$. The reason for occurrence of a backward shift is simply because reflection occurs mostly in the order $n = -2\mathrm{sign}(\alpha)$. Incidentally, negative shifts do not violate causality [38,39].

Analogously to the Goos–Hänchen shift [2,40], the in-plane shift of a co-handed beam on Bragg reflection can be estimated by

$$d_{\mathrm{Br}}^{\parallel} \approx \begin{cases} -\frac{\partial\varphi\left(\mathrm{r}_{\mathrm{RR}}^{(0)}\right)}{\partial\tilde{\kappa}}\left[1 + \mathcal{O}\left(\mathrm{R}_{\mathrm{LR}}^{(0)}/\mathrm{R}_{\mathrm{RR}}^{(0)}\right)\right], & \alpha = 0, \\ -\frac{\partial\varphi\left(\mathrm{r}_{\mathrm{RR}}^{(\mp 2)}\right)}{\partial\tilde{\kappa}}\left[1 + \mathcal{O}\left(\mathrm{R}_{\mathrm{LR}}^{(\mp 2)}/\mathrm{R}_{\mathrm{RR}}^{(\mp 2)}\right)\right], & \alpha \gtrless 0, \end{cases} \tag{80}$$

where $\varphi(\sigma)$ is the phase φ of the planewave reflection coefficient σ computed by setting $\tilde{\theta}_{\mathrm{i}} = \theta_{\mathrm{i}}$, and $\tilde{\kappa} = k_0 n_{\mathrm{hs}}\sin\tilde{\theta}_{\mathrm{i}}$. This simple formula is adequate because the reflection coefficient does not change significantly in magnitude when $\tilde{\theta}_{\mathrm{i}}$ lies squarely within the angular spread of the Bragg regime and the thin film is sufficiently thick; see Figs. 3 and 4. In addition, because $\mathrm{R}_{\mathrm{LR}}^{(0)} << \mathrm{R}_{\mathrm{RR}}^{(0)}$ (for $\alpha = 0$) and $\mathrm{R}_{\mathrm{LR}}^{(\mp 2)} << \mathrm{R}_{\mathrm{RR}}^{(\mp 2)}$ (for $\alpha \gtrless 0$) in the Bragg regime, the minute items $\mathcal{O}(\mathrm{R}_{\mathrm{LR}}^{(0)}/\mathrm{R}_{\mathrm{RR}}^{(0)})$ and $\mathcal{O}(\mathrm{R}_{\mathrm{LR}}^{(\mp 2)}/\mathrm{R}_{\mathrm{RR}}^{(\mp 2)})$ on the right side of (80) can be omitted.

The phases of the reflection coefficients $\mathrm{r}_{\mathrm{RR}}^{(0)}$ (for $\alpha = 0°$) and $\mathrm{r}_{\mathrm{RR}}^{(-2)}$ (for $\alpha = 10°$) are presented in Fig. 6 as functions of $\tilde{\theta}_{\mathrm{i}}$ and $\tilde{\psi}_{\mathrm{i}}$. In fact, the phases in Fig. 6 appear to be approximately second-order polynomials of $\sin\tilde{\theta}_{\mathrm{i}}$ that are defined piecewise. Correspondingly, $d_{\mathrm{Br}}^{\parallel}$ should be approximately linearly proportional to $\sin\theta_{\mathrm{i}}$, which is predicted by (80) and basically confirmed by the plots of Fig. 5. In addition, the plot of

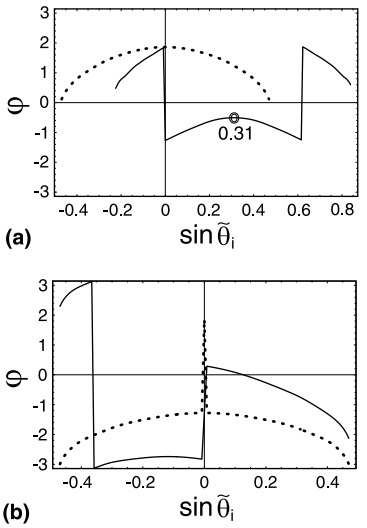

Fig. 6. Phases of the planewave reflection coefficients $r_{RR}^{(0)}$ (dotted lines) for $\alpha = 0°$, and $r_{RR}^{(-2)}$ (solid lines) for $\alpha = 10°$. (a) $\tilde{\psi}_i = 0°$, and (b) $\tilde{\psi}_i = 90°$. Other parameters are the same as for Fig. 3.

$\varphi(r_{RR}^{(-2)})$ in Fig. 6(a) is symmetric about $\sin\tilde{\theta}_i = 0.31$, but not about $\sin\tilde{\theta}_i = 0$, which explains the backward shifts in Fig. 5(a) for the slanted chiral STF.

3.2.3. Secondary lateral shift on Bragg reflection

When $\alpha \neq 0$, the reflected field comprises beams of different orders n. The evanescent planewave components of different reflected beams would die away from the interface $z = 0$, but the propagating components would not. Thus, lateral shifts of different orders are possible, as indicated by (75).

Our focus in this section lies on the circular Bragg phenomenon for $\alpha \neq 0$. The dominant Bragg reflection of a co-handed incident beam, which occurs in the order $n = -2\text{sign}(\alpha)$, is always accompanied by a weak reflection in the order $n = 0$ (i.e., $0.01 < |\mathbf{E}_r^{(0)}|^2/|\mathbf{E}_i|^2 < 0.1$). Certainly, the reflected beam of order $n = 0$ will laterally shift away from the incident beam. Fig. 7 shows the in-plane shift $d_R^{(0)\|}$ of a 2D RCP Gaussian beam, when $\lambda_0 = \lambda_0^{Br}|_{\tilde{\theta}_i=0}$ and $\alpha = 10°$. The shift $d_R^{(0)\|}$ oscillates with θ_i about the zero value, indicating that the specularly reflected beam can shift in the forward as well as the backward directions.

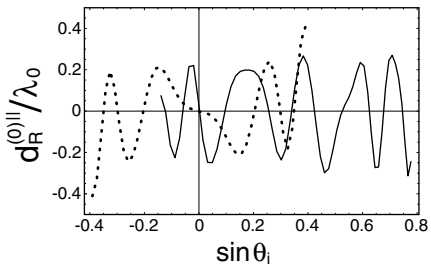

Fig. 7. Normalized in-plane shift $d_R^{(0)\|}/\lambda_0$ as a function of $\sin\theta_i$, calculated for $\psi_i = 0°$ (solid line) and $\psi_i = 90°$ (dotted line), when $\alpha = 10°$. The incident beam is 2D RCP Gaussian, and the values of θ_i chosen lie squarely within the angular spread of the Bragg regime. A shift is shown only if $|\mathbf{E}_r^{(0)}|^2/|\mathbf{E}_i|^2 > 0.01$. Other parameters are the same as for Fig. 5.

A comparison of Figs. 5 and 7 indicates a distinction between $d_{\mathrm{R}}^{(0)\parallel}$ and $d_{\mathrm{Br}}^{\parallel}$ when $\alpha \neq 0$, implying the fact that the lateral shifts of different orders are different. The circular Bragg phenomenon being the chief attractive feature of chiral STFs, secondary lateral shifts are of incidental importance.

3.3. Problem B: slanted chiral STF in an optically denser medium

3.3.1. Planewave incidence

Experience with unslanted chiral STFs indicates that the circular Bragg phenomenon must be affected by the value of n_{hs} [36]. Typically, when the half-spaces $z \leqslant 0$ and $z \geqslant d$ are not vacuous, but filled with a homogeneous medium that is optically denser than the slanted chiral STF, the angular spread of the Bragg regime is restricted by the occurrence of total reflection. Figs. 8 and 9 present the planewave reflectances for arbitrary incidences when $n_{\mathrm{hs}} = 4$ and $\lambda_0 = 727$ nm. The circular Bragg phenomenon still exists but its angular spread is highly restrained, as seen from comparing Figs. 4 and 9 even for $\alpha = 0$. Instead, total reflection into the half-space of incidence occurs when $|\tilde{\theta}_{\mathrm{i}}|$ reaches the critical value $\tilde{\theta}_{\mathrm{ic}} \approx \sin^{-1} 0.47$ for both LCP and RCP plane waves, as may be concluded from the plots of $\mathrm{R}_{\mathrm{LL}}^{(0)} + \mathrm{R}_{\mathrm{RL}}^{(0)}$ (Fig. 8) and the plots of $\mathrm{R}_{\mathrm{LR}}^{(0)} + \mathrm{R}_{\mathrm{RR}}^{(0)}$ (Fig. 9).

Total reflection is purely specular whether $\alpha = 0$ or not, in contrast to the circular Bragg phenomenon which is not specular when $\alpha \neq 0$. Indeed, the reflectance plots in Figs. 8 and 9 look independent of α in the total-reflection regime $|\sin\tilde{\theta}_{\mathrm{i}}| \in [0.47, 1)$, thereby implying the insensitivity of the total-reflection phenomenon to either the structural handedness or the slantedness of the chosen thin film.

3.3.2. Total reflection of a Gaussian beam

As an incident plane wave is totally reflected in the $n = 0$ order, so does an optical beam. The lateral shift of the reflected beam under the total-reflection condition is called the Goos–Hänchen shift [2]

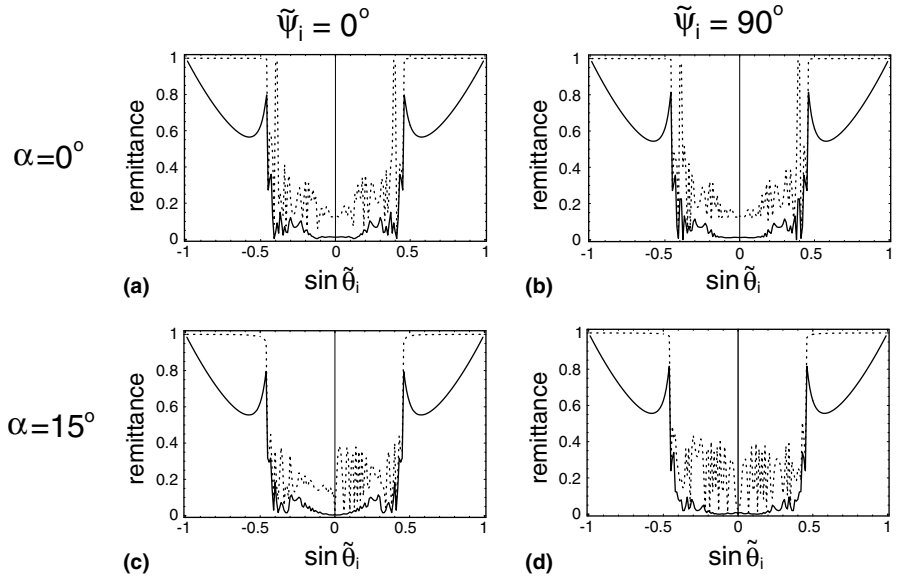

Fig. 8. Spectrums of planewave reflectances $\mathrm{R}_{\mathrm{LL}}^{(0)}$ (solid lines) and $\mathrm{R}_{\mathrm{LL}}^{(0)} + \mathrm{R}_{\mathrm{RL}}^{(0)}$ (dotted lines), calculated for (a, b) $\alpha = 0^{\circ}$ and (c, d) $\alpha = 15^{\circ}$. Same parameters as for Fig. 3, except $n_{\mathrm{hs}} = 4$ and $\lambda_0 = 727$ nm.

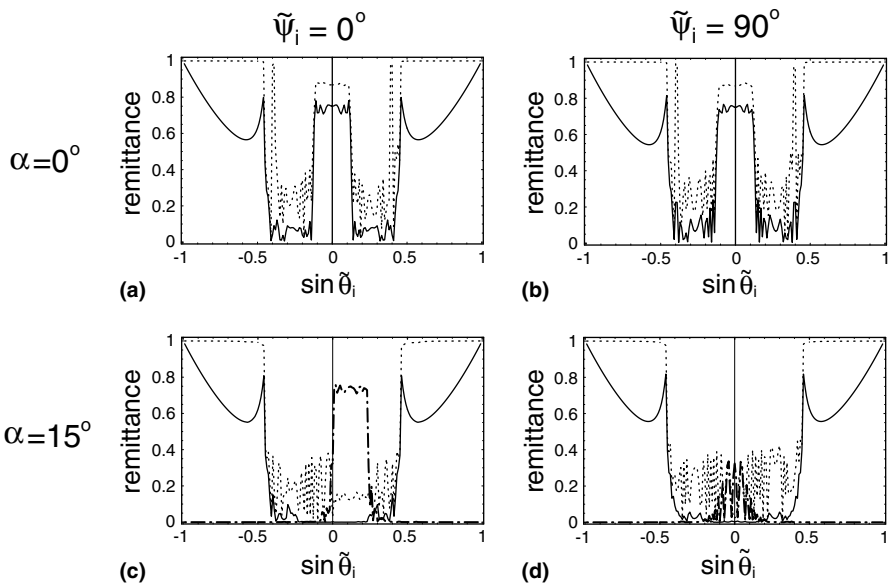

Fig. 9. Same as Fig. 8, except the reflectances plotted are $R_{RR}^{(0)}$ (solid lines), $R_{LR}^{(0)} + R_{RR}^{(0)}$ (dotted lines) and $R_{RR}^{(-2)}$ (dashed-dotted lines). The plots of $R_{RR}^{(-2)}$ are only for $\alpha = 15^\circ$.

Table 1
Values of θ_{ic} for various w_0 as estimated by (82) and from actual computation

w_0	Estimated from (82)	Computed for 2D beam	Computed for 3D beam
$2\lambda_{hs}$	37.2°	39.3°	39.9°
$3\lambda_{hs}$	34.1°	35.1°	35.6°
$4\lambda_{hs}$	32.6°	32.9°	32.9°
$6\lambda_{hs}$	31.1°	31.3°	31.3°

$$\mathbf{d}^{GH} = \mathbf{d}^{(0)} \tag{81}$$

for arbitrary α. Two different Goos–Hänchen shifts are possible, one for LCP beams and the other for RCP beams [36]. The shifts are denoted by $\mathbf{d}_L^{GH}$ and $\mathbf{d}_R^{GH}$, respectively.

Since a beam is an angular continuum of plane waves, the critical angle θ_{ic} for a beam is certainly different from its planewave counterpart $\tilde{\theta}_{ic}$. Table 1 shows the approximate values of θ_{ic} obtained from actual computation as well as from a simple estimation procedure. The value of θ_{ic} was actually computed by ascertaining that $|\mathbf{E}_r^{(0)}|^2$ rises to $0.995|\mathbf{E}_i|^2$ as $|\theta_i|$ increases to θ_{ic}. The simple estimate

$$\theta_{ic} \approx \tilde{\theta}_{ic} + \sin^{-1}(2/\rho_0) \tag{82}$$

is based on the assumption that all planewave components in the domain $\{(\vartheta_x, \vartheta_y) | \sqrt{\vartheta_x^2 + \vartheta_y^2} \leqslant 2/\rho_0\}$ of an incident beam should be totally reflected. As is clear from Table 1, (82) is a good predictor of θ_{ic}, especially when $w_0 \geqslant 3\lambda_{hs}$, where $\lambda_{hs} = \lambda_0/n_{hs}$ is the wavelength in the medium filling the half-space of incidence and reflection. Numerous computational results showed that θ_{ic} is largely unaffected by ψ_i. The computed values of θ_{ic} are employed for all the plots presented in Figs. 10, 12 and 15.

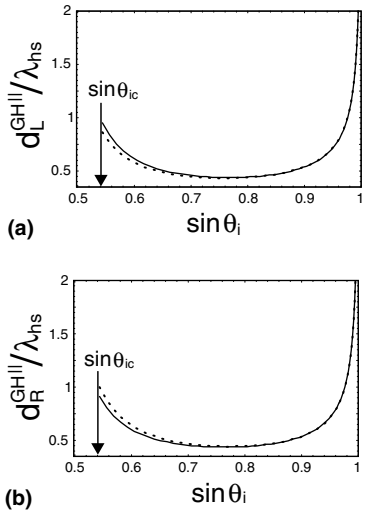

Fig. 10. Normalized Goos–Hänchen shifts (a) $d_L^{GH\parallel}/\lambda_{hs}$ and (b) $d_R^{GH\parallel}/\lambda_{hs}$ as functions of $\sin\theta_i \in [\sin\theta_{ic}, 1)$, calculated for $\alpha = 0°$ (dotted lines) and $\alpha = 15°$ (solid lines), when $\psi_i = 120°$, $n_{hs} = 4$, $\lambda_0 = 727$ nm, and $w_0 = 4\lambda_{hs}$. Other parameters are the same as for Fig. 5.

3.3.3. Goos–Hänchen shifts of 2D Gaussian beams

Fig. 10 shows the Goos–Hänchen shifts$d_L^{GH\parallel}$ and $d_R^{GH\parallel}$ as functions of $\sin\theta_i \in [\sin\theta_{ic}, 1)$ when the incident beam is 2D. Similarly, Fig. 11 presents $d_L^{GH\parallel}$ and $d_R^{GH\parallel}$ plotted against $\psi_i \in (-180°, 180°]$ when $\theta_i = 37.5° > \theta_{ic}$. It is clear from Fig. 10 that α affects the Goos–Hänchen shift at low angles of incidence for total reflection.

A distinction between $d_L^{GH\parallel}$ and $d_R^{GH\parallel}$ is unambiguously evident at low values of $|\theta_i| > \theta_{ic}$ when $\alpha = 0$ (Fig. 11). However, that distinction diminishes for all post-critical θ_i when $\alpha \neq 0$, as illustrated by the plots

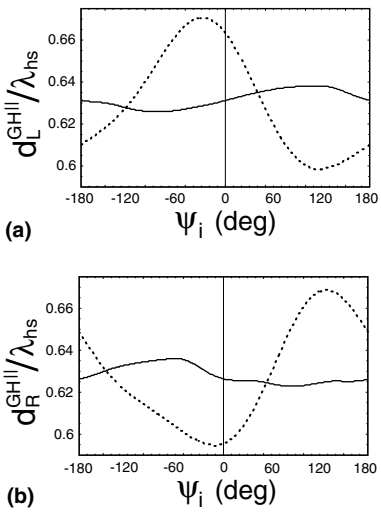

Fig. 11. Same as Fig. 10, except $d_L^{GH\parallel}/\lambda_{hs}$ and $d_R^{GH\parallel}/\lambda_{hs}$ are plotted against $\psi_i \in (-180°, 180°]$, for a fixed post-critical $\theta_i = 37.5°$.

in Fig. 11 for $\alpha = 15°$. Similarly, the variations of $d_{\mathrm{L}}^{\mathrm{GH}\parallel}$ and $d_{\mathrm{R}}^{\mathrm{GH}\parallel}$ with ψ_{i} are less pronounced for $\alpha \neq 0$ than for $\alpha = 0$.

Although the foregoing effects of α may be considered small in conventional optics practice, as they amount to small fractions of the wavelength, their nanotechnological significance cannot be denied [3]. That becomes evident on noting that quantum dots are 1–2 nm in diameter, globular proteins are of 6 nm diameter, while gate oxide films have been shrunk to about 2 nm in thickness [41]. In comparison, 1% of the typical λ_0 in the visible regime is between 4 and 7 nm.

Fig. 12 shows the effect of the beam waist width w_0 on the Goos–Hänchen shift when $\alpha = 15°$. Enhancement of the beam waist decreases the critical angle θ_{ic}, as shown by Table 1 also. Furthermore, both $d_{\mathrm{L}}^{\mathrm{GH}\parallel}$ and $d_{\mathrm{R}}^{\mathrm{GH}\parallel}$ decrease (increase) with increasing beam waist when the post-critical $|\theta_{\mathrm{i}}|$ is low (high).

The Goos–Hänchen shift of a 2D Gaussian beam can be estimated by

$$\left.\begin{aligned} d_{\mathrm{L}}^{\mathrm{GH}\parallel} &\approx -\mathrm{R}_{\mathrm{LL}}^{(0)} \frac{\partial\varphi\left(\mathrm{r}_{\mathrm{LL}}^{(0)}\right)}{\partial\tilde{\kappa}} - \mathrm{R}_{\mathrm{RL}}^{(0)} \frac{\partial\varphi\left(\mathrm{r}_{\mathrm{RL}}^{(0)}\right)}{\partial\tilde{\kappa}} \\ d_{\mathrm{R}}^{\mathrm{GH}\parallel} &\approx -\mathrm{R}_{\mathrm{LR}}^{(0)} \frac{\partial\varphi\left(\mathrm{r}_{\mathrm{LR}}^{(0)}\right)}{\partial\tilde{\kappa}} - \mathrm{R}_{\mathrm{RR}}^{(0)} \frac{\partial\varphi\left(\mathrm{r}_{\mathrm{RR}}^{(0)}\right)}{\partial\tilde{\kappa}} \end{aligned}\right\}, \tag{83}$$

in analogy with (80). Figs. 13 and 14 contain the plots of φ of different reflection coefficients, for both $\alpha = 0°$ and $\alpha = 15°$. Although $\varphi(\mathrm{r}_{\mathrm{LL}}^{(0)})$ and $\varphi(\mathrm{r}_{\mathrm{RR}}^{(0)})$ are little affected by α (Fig. 13(b)), $\varphi(\mathrm{r}_{\mathrm{RL}}^{(0)})$ and $\varphi(\mathrm{r}_{\mathrm{LR}}^{(0)})$ are absolutely under its influence at low values of $|\theta_{\mathrm{i}}| \geqslant \tilde{\theta}_{\mathrm{ic}}$ (Fig. 13(a)). According to (83), the Goos–Hänchen shift $d_{\mathrm{L}}^{\mathrm{GH}\parallel}$ and $d_{\mathrm{R}}^{\mathrm{GH}\parallel}$ should be affected by α at low values of $|\theta_{\mathrm{i}}| \geqslant \theta_{\mathrm{ic}}$, by noting the fact that $\mathrm{R}_{\mathrm{RL}}^{(0)}/\mathrm{R}_{\mathrm{LL}}^{(0)}$ and $\mathrm{R}_{\mathrm{LR}}^{(0)}/\mathrm{R}_{\mathrm{RR}}^{(0)}$ are not trivial at low values of $|\tilde{\theta}_{\mathrm{i}}| \geqslant \tilde{\theta}_{\mathrm{ic}}$ (Figs. 8 and 9). Similarly, because $\varphi(\mathrm{r}_{\mathrm{LL}}^{(0)}) \approx \varphi(\mathrm{r}_{\mathrm{RR}}^{(0)})$ and $\varphi(\mathrm{r}_{\mathrm{RL}}^{(0)}) \neq \varphi(\mathrm{r}_{\mathrm{LR}}^{(0)})$ for $\alpha = 0$ (Fig. 14(a)), a distinction between $d_{\mathrm{L}}^{\mathrm{GH}\parallel}$ and $d_{\mathrm{R}}^{\mathrm{GH}\parallel}$ is undoubtedly evident when $\alpha = 0$ (Fig. 11). However, that distinction reduces when $\alpha \neq 0$, because $\varphi(\mathrm{r}_{\mathrm{LL}}^{(0)}) \approx \varphi(\mathrm{r}_{\mathrm{RR}}^{(0)})$ and the difference between $\varphi(\mathrm{r}_{\mathrm{LR}}^{(0)})$ and $\varphi(\mathrm{r}_{\mathrm{RL}}^{(0)})$ is minute then (Fig. 14(b)).

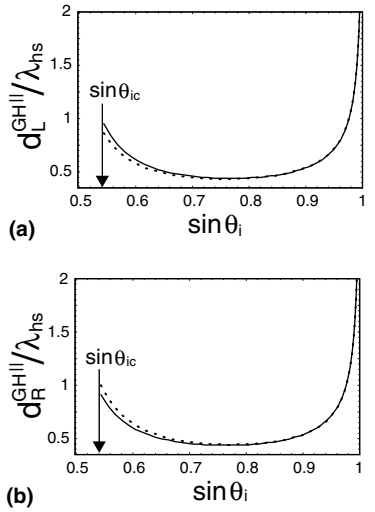

Fig. 12. Normalized Goos–Hänchen shifts (a) $d_{\mathrm{L}}^{\mathrm{GH}\parallel}/\lambda_{\mathrm{hs}}$ and (b) $d_{\mathrm{R}}^{\mathrm{GH}\parallel}/\lambda_{\mathrm{hs}}$ as functions of $\sin\theta_{\mathrm{i}} \in [\sin\theta_{\mathrm{ic}}, 1)$, calculated for $w_0 = 2\lambda_{\mathrm{hs}}$ (dotted lines) and $w_0 = 4\lambda_{\mathrm{hs}}$ (solid lines), when $\alpha = 15°$. Other parameters are the same as for Fig. 10.

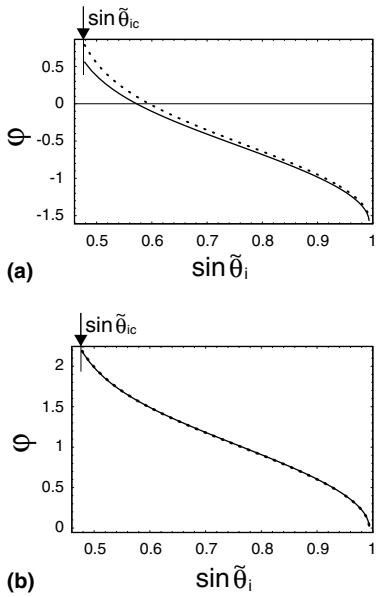

Fig. 13. Phases of the planewave reflection coefficients (a) $r_{LR}^{(0)}$ and (b) $r_{RR}^{(0)}$ as functions of $\sin\tilde{\theta}_i \in [\sin\tilde{\theta}_{ic}, 1)$, calculated for $\alpha = 0°$ (dotted lines) and $\alpha = 15°$ (solid lines), when $\tilde{\psi}_i = 120°$. Other parameters are the same as for Fig. 8.

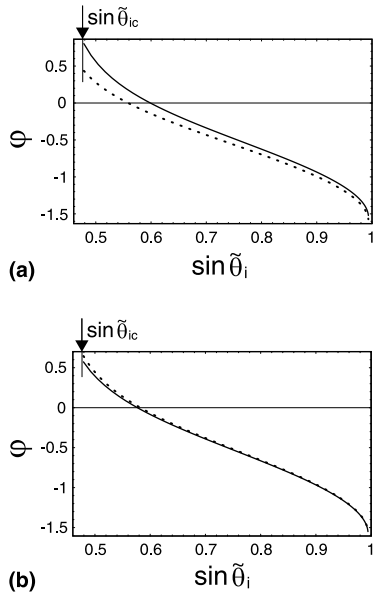

Fig. 14. Phases of the planewave reflection coefficients $r_{LR}^{(0)}$ (solid lines) and $r_{RL}^{(0)}$ (dotted lines) as functions of $\sin\tilde{\theta}_i \in [\sin\tilde{\theta}_{ic}, 1)$, calculated for (a) $\alpha = 0°$ and (b) $\alpha = 15°$, when $\tilde{\psi}_i = 120°$. Other parameters are the same as for Fig. 8.

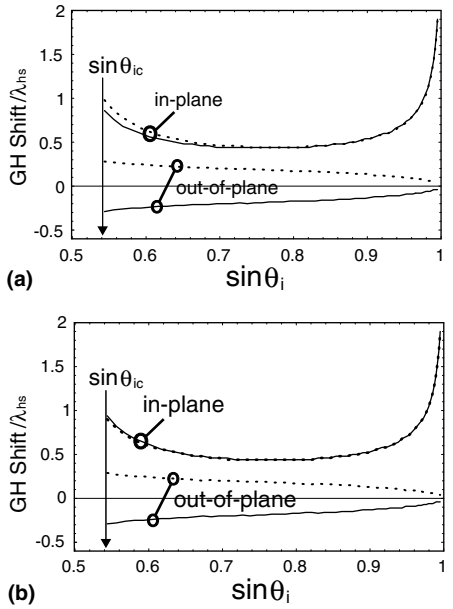

Fig. 15. Normalized in-plane Goos–Hänchen shifts $d_{\mathrm{L}}^{\mathrm{GH}\parallel}/\lambda_{\mathrm{hs}}$ (solid lines) and $d_{\mathrm{R}}^{\mathrm{GH}\parallel}/\lambda_{\mathrm{hs}}$ (dotted lines), and normalized out-of-plane Goos–Hänchen shifts $d_{\mathrm{L}}^{\mathrm{GH}\perp}/\lambda_{\mathrm{hs}}$ (solid lines) and $d_{\mathrm{R}}^{\mathrm{GH}\perp}/\lambda_{\mathrm{hs}}$ (dotted lines) as functions of $\sin\theta_{\mathrm{i}} \in [\sin\theta_{\mathrm{ic}}, 1)$, calculated for (a) $\alpha = 0°$ and (b) $\alpha = 15°$. The incident beam is 3D and Gaussian. Other parameters are the same as for Fig. 10.

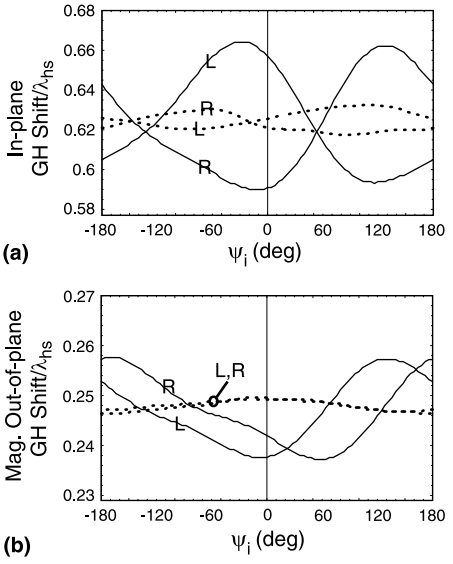

Fig. 16. (a) Normalized in-plane Goos–Hänchen shifts $d_{\mathrm{L}}^{\mathrm{GH}\parallel}/\lambda_{\mathrm{hs}}$ and $d_{\mathrm{R}}^{\mathrm{GH}\parallel}/\lambda_{\mathrm{hs}}$, and (b) magnitudes of normalized out-of-plane Goos–Hänchen shifts $-d_{\mathrm{L}}^{\mathrm{GH}\perp}/\lambda_{\mathrm{hs}}$ and $d_{\mathrm{R}}^{\mathrm{GH}\perp}/\lambda_{\mathrm{hs}}$ as functions of $\psi_{\mathrm{i}} \in (-180°, 180°]$, calculated for $\alpha = 0°$ (solid lines) and $\alpha = 15°$ (dotted lines), when $\theta_{\mathrm{i}} = 37.5° > \theta_{\mathrm{ic}}$. Other parameters are the same as for Fig. 15.

3.3.4. Goos–Hänchen shifts of 3D Gaussian beams

Fig. 15 presents the plots of $\mathbf{d}_{\mathrm{L}}^{\mathrm{GH}}$ and $\mathbf{d}_{\mathrm{R}}^{\mathrm{GH}}$ against $\sin\theta_{\mathrm{i}} \in [\sin\theta_{\mathrm{ic}}, 1)$ for $\alpha = 0°$ and $\alpha = 15°$, when the beam is 3D. The most prominent feature of the Goos–Hänchen phenomenon for 3D circularly polarized beams is that both in-plane ($\mathrm{d}_{\mathrm{L}}^{\mathrm{GH}\parallel}$ and $\mathrm{d}_{\mathrm{R}}^{\mathrm{GH}\parallel}$) and out-of-plane ($\mathrm{d}_{\mathrm{L}}^{\mathrm{GH}\perp}$ and $\mathrm{d}_{\mathrm{R}}^{\mathrm{GH}\perp}$) shifts are not zero. In fact, the out-of-plane Goos–Hänchen shift increases in amplitude as the post-critical $|\theta_{\mathrm{i}}|$ decreases.

Furthermore, because $d_{\mathrm{L}}^{\mathrm{GH}\perp} < 0$ and $d_{\mathrm{R}}^{\mathrm{GH}\perp} > 0$ for any $|\theta_{\mathrm{i}}| \geqslant \theta_{\mathrm{ic}}$, the direction of the out-of-plane Goos–Hänchen shift depends on the handedness of the incident beam in relation to the structural handedness of the thin film. In contrast, the in-plane Goos–Hänchen shift is always directed forward and exhibits characteristics similar to that of a 2D beam. Specifically, $d_{\mathrm{L}}^{\mathrm{GH}\parallel} \neq d_{\mathrm{R}}^{\mathrm{GH}\parallel}$ at low values of $|\theta_{\mathrm{i}}| \geqslant \theta_{\mathrm{ic}}$ when $\alpha = 0$ (Fig. 15(a)), but that distinction diminishes for all post-critical θ_{i} when $\alpha \neq 0$ (Fig. 15(b)).

The effect of ψ_{i} on the Goos–Hänchen shift of a 3D beam is illustrated in Fig. 16, wherein $\theta_{\mathrm{i}} = 37.5° > \theta_{\mathrm{ic}}$. Both in-plane and out-of-plane Goos–Hänchen shifts are less affected by ψ_{i} for $\alpha \neq 0$ than for $\alpha = 0$. In addition, it is clear from Fig. 16(b) that $|d_{\mathrm{L}}^{\mathrm{GH}\perp}| \approx |d_{\mathrm{R}}^{\mathrm{GH}\perp}|$ for $\alpha \neq 0$, but not for $\alpha = 0$, thereby implying that the magnitude of out-of-plane Goos–Hänchen shift is not affected by the structural handedness of the slanted chiral STF with $\alpha \neq 0$.

Finally, it needs to be mentioned that the occurrence of out-of-plane Goos–Hänchen shift depends on the ellipticity of the polarization state of the 3D incident beam. For example, when the incident 3D beam is approximately linearly polarized (i.e., either s- or p-polarized), no out-of-plane shift would occur on total reflection.

4. Concluding remarks

In this paper, we considered lateral shifts of circularly polarized beams on reflection by slanted chiral sculptured thin films. Slanted chiral STFs constitute a class of thin-film materials with great promise for many optoelectronic applications. In general, these thin films are anisotropic and rotationally nonhomogeneous along an axis that is slanted at an angle α to the normal of the substrate plane.

The frequency-domain electromagnetic responses of a slanted chiral STF to both plane waves and 3D optical beams were formulated for arbitrary incidence. A rigorous coupled-wave analysis was implemented with a stable algorithm to describe the planewave response of the slanted chiral STF, and the angular-spectrum representation of beams was exploited for beam diffraction. Both 2D and 3D Gaussian beams of approximately circular polarization states were considered.

Two types of lateral shifts of beams were calculated and discussed. One is the lateral shift of a co-handed optical beam that is mostly reflected due to the circular Bragg phenomenon. The other is the Goos–Hänchen shift that occurs when the beam is incident on the thin film from an optically denser medium and then totally reflected. Although the circular Bragg phenomenon is not precisely specular when $\alpha \neq 0$, the total-reflection phenomenon is purely specular for any α.

Several important results were obtained concerning the two types of lateral shifts of beams. They are listed as follows:

- The lateral shift of a co-handed beam on Bragg reflection could be either forward or backward when $\alpha \neq 0$, depending on the angle of incidence.
- The Goos–Hänchen shift is affected by α at low angles of incidence for total reflection. This effect is nanotechnologically significant.
- The in-plane Goos–Hänchen shift is affected by the structural handedness of the slanted chiral STF, especially for $\alpha = 0$, when the post-critical angle of incidence is low.

- When the incident beam is 3D, both in-plane and out-of-plane Goos–Hänchen shifts occur on total reflection. In particular, the out-of-plane Goos–Hänchen shift increases in amplitude as the angle of incidence decreases, and it can be either forward or backward.

The shifts at low-ultraviolet and longer wavelengths are large enough in magnitude to be significant for nanotechnology.

Acknowledgements

The authors thank Abdul H. Aziz of the Penn State Institute for High Performance Computing Applications for computing assistance. F.W. thanks the Penn State Weiss Graduate Program for a Dissertation Fellowship.

Appendix A

The $4(2N_t+1)\times 4(2N_t+1)$ kernel matrix $[\underline{\underline{\tilde{\mathbf{P}}}}]$ is given as

$$\left[\underline{\underline{\tilde{\mathbf{P}}}}\right]=\begin{bmatrix}\left[\underline{\underline{\tilde{P}}}_{11}\right] & \left[\underline{\underline{\tilde{P}}}_{12}\right] & \left[\underline{\underline{\tilde{P}}}_{13}\right] & \left[\underline{\underline{\tilde{P}}}_{14}\right]\\ \left[\underline{\underline{\tilde{P}}}_{21}\right] & \left[\underline{\underline{\tilde{P}}}_{22}\right] & [P_{23}] & \left[\underline{\underline{\tilde{P}}}_{24}\right]\\ \left[\underline{\underline{\tilde{P}}}_{31}\right] & \left[\underline{\underline{\tilde{P}}}_{32}\right] & \left[\underline{\underline{\tilde{P}}}_{33}\right] & \left[\underline{\underline{\tilde{P}}}_{34}\right]\\ \left[\underline{\underline{\tilde{P}}}_{41}\right] & \left[\underline{\underline{\tilde{P}}}_{42}\right] & \left[\underline{\underline{\tilde{P}}}_{43}\right] & \left[\underline{\underline{\tilde{P}}}_{44}\right]\end{bmatrix}, \tag{A.1}$$

wherein the sixteen $(2N_t+1)\times(2N_t+1)$ submatrixes are defined as follows:

$$\begin{aligned}
\left[\underline{\underline{\tilde{P}}}_{11}\right] &= -[\underline{\underline{\kappa}}_z]-[\underline{\underline{K}}_x][\underline{\underline{\epsilon}}_{zz}]^{-1}[\underline{\underline{\epsilon}}_{zx}],\\
\left[\underline{\underline{\tilde{P}}}_{12}\right] &= -[\underline{\underline{K}}_x][\underline{\underline{\epsilon}}_{zz}]^{-1}[\underline{\underline{\epsilon}}_{zy}],\\
\left[\underline{\underline{\tilde{P}}}_{13}\right] &= \frac{k_y^{(0)}}{k_0}[\underline{\underline{K}}_x][\underline{\underline{\epsilon}}_{zz}]^{-1},\\
\left[\underline{\underline{\tilde{P}}}_{14}\right] &= k_0\left[\underline{\underline{I}}\right]-\frac{1}{k_0}[\underline{\underline{K}}_x][\underline{\underline{\epsilon}}_{zz}]^{-1}[\underline{\underline{K}}_x],
\end{aligned} \tag{A.2}$$

$$\begin{aligned}
\left[\underline{\underline{\tilde{P}}}_{21}\right] &= -k_y^{(0)}[\underline{\underline{\epsilon}}_{zz}]^{-1}[\underline{\underline{\epsilon}}_{zx}],\\
\left[\underline{\underline{\tilde{P}}}_{22}\right] &= -[\underline{\underline{\kappa}}_z]-k_y^{(0)}[\underline{\underline{\epsilon}}_{zz}]^{-1}[\underline{\underline{\epsilon}}_{zy}],\\
\left[\underline{\underline{\tilde{P}}}_{23}\right] &= -k_0[\underline{\underline{I}}]+\frac{\left(k_y^{(0)}\right)^2}{k_0}\left[\underline{\underline{\epsilon}}_{zz}\right]^{-1},\\
\left[\underline{\underline{\tilde{P}}}_{24}\right] &= -\frac{k_y^{(0)}}{k_0}[\underline{\underline{\epsilon}}_{zz}]^{-1}[\underline{\underline{K}}_x],
\end{aligned} \tag{A.3}$$

$$\begin{aligned}
\left[\underline{\underline{\tilde{P}}}_{31}\right] &= -\frac{k_y^{(0)}}{k_0}[\underline{\underline{K}}_x]+k_0\left([\underline{\underline{\epsilon}}_{yz}][\underline{\underline{\epsilon}}_{zz}]^{-1}[\underline{\underline{\epsilon}}_{zx}]-[\underline{\underline{\epsilon}}_{yx}]\right),\\
\left[\underline{\underline{\tilde{P}}}_{32}\right] &= \frac{1}{k_0}[\underline{\underline{K}}_x][\underline{\underline{K}}_x]+k_0\left([\underline{\underline{\epsilon}}_{yz}][\underline{\underline{\epsilon}}_{zz}]^{-1}[\underline{\underline{\epsilon}}_{zy}]-[\underline{\underline{\epsilon}}_{yy}]\right),\\
\left[\underline{\underline{\tilde{P}}}_{33}\right] &= -[\underline{\underline{\kappa}}_z]-k_y^{(0)}[\underline{\underline{\epsilon}}_{yz}][\underline{\underline{\epsilon}}_{zz}]^{-1},\\
\left[\underline{\underline{\tilde{P}}}_{34}\right] &= [\underline{\underline{\epsilon}}_{yz}][\underline{\underline{\epsilon}}_{zz}]^{-1}[\underline{\underline{K}}_x],
\end{aligned} \tag{A.4}$$

$$
\begin{aligned}
\left[\underline{\underline{\tilde{P}}}_{41}\right] &= -\frac{\left(k_y^{(0)}\right)^2}{k_0}\left[\underline{\underline{I}}\right] - k_0\left(\left[\underline{\underline{\epsilon}}_{xz}\right]\left[\underline{\underline{\epsilon}}_{zz}\right]^{-1}\left[\underline{\underline{\epsilon}}_{zx}\right] - \left[\underline{\underline{\epsilon}}_{xx}\right]\right),\\
\left[\underline{\underline{\tilde{P}}}_{42}\right] &= \frac{k_y^{(0)}}{k_0}\left[\underline{\underline{K}}_x\right] - k_0\left(\left[\underline{\underline{\epsilon}}_{xz}\right]\left[\underline{\underline{\epsilon}}_{zz}\right]^{-1}\left[\underline{\underline{\epsilon}}_{zy}\right] - \left[\underline{\underline{\epsilon}}_{xy}\right]\right),\\
\left[\underline{\underline{\tilde{P}}}_{43}\right] &= k_y^{(0)}\left[\underline{\underline{\epsilon}}_{xz}\right]\left[\underline{\underline{\epsilon}}_{zz}\right]^{-1},\\
\left[\underline{\underline{\tilde{P}}}_{44}\right] &= -\left[\underline{\underline{\kappa}}_z\right] - \left[\underline{\underline{\epsilon}}_{xz}\right]\left[\underline{\underline{\epsilon}}_{zz}\right]^{-1}\left[\underline{\underline{K}}_x\right].
\end{aligned}
\tag{A.5}
$$

The $(2N_t + 1) \times (2N_t + 1)$ identity matrix is denoted by $[\underline{I}]$.

References

[1] F. de Fornel, Evanescent Waves: From Newtonian Optics to Atomic Optics, Springer, Heidelberg, Germany, 2000.
[2] H.K.V. Lotsch, Optik 32 (1970) 189.
[3] A. Lakhtakia, Proc. SPIE 5218 (2003) 29.
[4] R. Messier, V.C. Venugopal, P.D. Sunal, J. Vac. Sci. Technol. B 18 (2000) 1538.
[5] I.J. Hodgkinson, Q.h. Wu, Adv. Mater. 13 (2001) 889.
[6] R. Messier, A. Lakhtakia, Mater. Res. Innovat. 2 (1999) 217.
[7] V.C. Venugopal, A. Lakhtakia, in: O.N. Singh, A. Lakhtakia (Eds.), Electromagnetic Fields in Unconventional Materials and Structures, Wiley, New York, NY, USA, 2000 (Chapter 5).
[8] A. Lakhtakia, W.S. Weiglhofer, Proc. R. Soc. Lond. A 448 (1995) 419, corrections: 454 (1998) 3275.
[9] V.C. Venugopal, A. Lakhtakia, Proc. R. Soc. Lond. A 456 (2000) 125.
[10] J. Wang, A. Lakhtakia, J.B. Geddes III, Optik 113 (2002) 213.
[11] A. Lakhtakia, R. Messier, in: W.S. Weiglhofer, A. Lakhtakia (Eds.), Introduction to Complex Mediums for Optics and Electromagnetics, SPIE Press, Bellingham, WA, USA, 2003, pp. 447–478.
[12] M.W. McCall, in: W.S. Weiglhofer, A. Lakhtakia (Eds.), Introduction to Complex Mediums for Optics and Electromagnetics, SPIE Press, Bellingham, WA, USA, 2003, pp. 479–506.
[13] R. Messier, A. Lakhtakia, V.C. Venugopal, P.D. Sunal, Vac. Technol. Coating 2 (10) (2001) 40.
[14] F. Wang, A. Lakhtakia, R. Messier, Eur. Phys. J. Appl. Phys. 20 (2002) 91, corrections: 24 (2003) 91.
[15] W.C. Meecham, J. Appl. Phys. 27 (1956) 361.
[16] D. Maystre (Ed.), Selected Papers on Diffraction Gratings, SPIE Press, Bellingham, WA, 1993.
[17] F. Wang, A. Lakhtakia, Opt. Commun. 215 (2003) 79.
[18] M.G. Moharam, E.B. Grann, D.A. Pommet, T.K. Gaylord, J. Opt. Soc. Am. A 12 (1995) 1068.
[19] M.G. Moharam, D.A. Pommet, E.B. Grann, T.K. Gaylord, J. Opt. Soc. Am. A 12 (1995) 1077.
[20] N. Chateau, J. Hugonin, J. Opt. Soc. Am. A 11 (1994) 1321.
[21] I.J. Hodgkinson, Q.h. Wu, B. Knight, A. Lakhtakia, K. Robbie, Appl. Opt. 39 (2000) 642.
[22] I. Hodgkinson, Q.h. Wu, Appl. Opt. 38 (1999) 3621.
[23] C. Kittel, Introduction to Solid State Physics, fourth ed., Wiley Eastern, New Delhi, India, 1974 (Chapter 13).
[24] C.F. Bohren, D.R. Huffman, Absorption and Scattering of Light by Small Particles, Wiley, New York, NY USA, 1983, 247-251.
[25] J.A. Kong, Electromagnetic Wave Theory, Wiley, New York, NY, USA, 1986.
[26] H. Hochstadt, Differential Equations: A Modern Approach, Dover Press, New York, NY, USA, 1975.
[27] L. Li, J. Opt. Soc. Am. A 10 (1993) 2581.
[28] F. Wang, M.W. Horn, A. Lakhtakia, Microelectron. Eng. 71 (2004) 34.
[29] Y. Jaluria, Computer Methods for Engineering, Taylor & Francis, Washington, DC, USA, 1996.
[30] P.C. Clemmow, The Plane Wave Spectrum Representation of Electromagnetic Fields, Pergamon Press, New York, NY, USA, 1956.
[31] S. Peng, G.M. Morris, J. Opt. Soc. Am. A 13 (1996) 993.
[32] A. Lakhtakia, M.W. McCall, Arch. Elektr. Übertr. 57 (2003) 23.
[33] F.I. Baida, D. Van Labeke, J.M. Vigoureux, J. Opt. Soc. Am. A 17 (2000) 858.
[34] J. Lekner, J. Opt. A: Pure Appl. Opt. 5 (2003) 6.
[35] V.C. Venugopal, A. Lakhtakia, Eur. Phys. J. Appl. Phys. 10 (2000) 173.
[36] A. Lakhtakia, Arch. Elektr. Übertr. 56 (2002) 169, corrections: 57 (2003) 79.
[37] H.A. Haus, Waves and Fields in Optoelectronics, Prentice-Hall, Englewood Cliffs, NJ, USA, 1984 (Chapter 5).

[38] W.J. Wild, C.L. Giles, Phys. Rev. A 25 (1982) 2099.
[39] A. Lakhtakia, Electromagnetics 23 (2003) 71.
[40] A. Haibel, G. Nimtz, A.A. Stahlhofen, Phys. Rev. E 63 (2001) 047601.
[41] A.M. Stoneham, Mater. Sci. Eng. C 23 (2003) 235.

AEÜ International Journal of Electronics and Communications

Response of Chiral Sculptured Thin Films to Dipolar Sources

Akhlesh Lakhtakia and Martin W. McCall

Abstract: Dyadic Green functions (DGFs) are formulated, for a chiral sculptured thin film (STF) sandwiched between two vacuous half-spaces, as angular spectrums of propagating and evanescent plane waves. Asymptotic evaluation of the DGFs is carried out to obtain simple far-field expressions. The radiation patterns of dipolar sources held close to the chiral STF are computed and discussed, in relation to the circular Bragg phenomenon that the chosen nanomaterials are known to display on illumination by circularly polarized plane waves.

Keywords: Circular Bragg phenomenon, Dipolar sources, Dyadic Green functions, Near field, Sculptured thin films

1. Introduction

Sculptured thin films (STFs) are a new class of nanomaterials [1, 2] that emerged during the 1990s from the widely used columnar thin films (CTFs) [3, 4]. The microstructure of CTFs consists of almost identical, straight and parallel columns with elliptical cross-sections. The columns in a STF are not straight, but have been engineered to grow as curves that veer away from the substrate. The column diameters range from 10 to 300 nm, and a wide variety of two- and three-dimensional as well as sectionwise cascaded morphologies can be nano engineered [5, 6]. STFs are therefore porous materials, the shapes and volume fractions of whose void regions can also be produced for specific optical and other applications [2].

Chiral STFs comprise parallel helical columns. These films can be regarded as unidirectionally and rotationally nonhomogeneous, dielectric continuums in the optical regime [1]. Special interest has been garnered in optics by chiral STFs – which exemplify the so-called helicoidal bianisotropic mediums [7] – as the circular Bragg phenomenon [8–10] exhibited by them upon plane wave excitation parallel to their axis of nonhomogeneity can be harnessed for a variety of optical filtering and fluid sensing applications [11]. When the wavelength of normally incident radiation is approximately equal to the *optical period* of the nonhomogeneity the helicoidal morphology acts as a mirror for circularly polarized plane waves of one handedness, but not for the other handedness. Discrimination of circularly polarized plane waves, based on handedness, is also evinced for oblique incidence conditions [12–14].

Although plane wave excitation is the norm in optics, recent developments in near-field microscopy [15] necessitate consideration of other types of excitation – e.g., with evanescent waves [16] and point dipoles [17]. Evanescent waves are essential constituents of beams, which are known to experience shifts on reflection. Therefore, recently Goos-Hänchen shifts displayable by chiral STFs were theoretically analyzed [18]. Dipolar sources are useful in modeling nanoprobes (and even single-molecule probes) commonly employed in scanning near-field microscopy [15], for examining surfaces as well as for lithography in the optoelectronics area [19, 20]. As discussed elsewhere [11, 21, 22], STFs hold considerable promise for optoelectronic applications. Furthermore, chiral STFs could be useful in patterning the surfaces of biosubstrates for enhanced absorption of desirable enantiomers of biochemicals [23, 24]. Also, STFs could roughen surfaces for enhancing Raman scattering, which is the basis of a commonly used spectroscopic technique [25]. These possibilities motivated the research communicated here.

Accordingly, in Section 2, we present the frequency-domain constitutive relations of a chiral STF as well as its planewave response in order to formulate dyadic Green functions (DGFs) for a chiral STF sandwiched between two vacuous half-spaces. The DGFs are formulated as angular spectrums of propagating and evanescent plane waves. Asymptotic evaluation of the DGFs to obtain simple far-field expressions is then accomplished. Section 3 is devoted to the illustration of far-field radiation patterns of dipolar sources held close to a chiral STF.

The notation used is as follows: Vectors are in boldface, while dyadics are double-underlined. The position vector is denoted by $\mathbf{r} = x\mathbf{u}_x + y\mathbf{u}_y + z\mathbf{u}_z$, where $\mathbf{u}_x$, $\mathbf{u}_y$ and $\mathbf{u}_z$ are the cartesian unit vectors. An $\exp(-i\omega t)$ time-dependence is implicit, with ω as the angular frequency and t as time.

2. Theory

2.1 Constitutive relations

Suppose the slab region $0 < z < L$ is occupied by a chiral STF, while the lower half-space $z < 0$ and the upper half-

Received May 24, 2002. Revised August 30, 2002.

A. Lakhtakia, CATMAS-Computational & Theoretical Materials Science Group, Department of Engineering Science and Mechanics, Pennsylvania State University, University Park, PA 16802-6812, USA. E-mail: AXL4@psu.edu
Martin W. McCall, Department of Physics, The Blackett Laboratory, Imperial College London, Prince Consort Road, London SW7 2BW, UK.
Correspondence to A. Lakhtakia.

space $z > L$ are vacuous. The constitutive relations of free space or vacuum are written as

$$\left.\begin{aligned} \mathbf{D}(\mathbf{r}) &= \epsilon_0\,\mathbf{E}(\mathbf{r}) \\ \mathbf{B}(\mathbf{r}) &= \mu_0\,\mathbf{H}(\mathbf{r}) \end{aligned}\right\}, \qquad z<0 \quad \text{or} \quad z>L\,, \tag{1}$$

where $\epsilon_0 = 8.854 \times 10^{-12}$ F/m and $\mu_0 = 4\pi \times 10^{-7}$ H/m.

The chiral STF is periodically nonhomogeneous along the z axis, and its frequency-domain constitutive relations are best stated as [12]

$$\left.\begin{aligned} \mathbf{D}(\mathbf{r}) &= \epsilon_0\, \underline{\underline{S}}_z(z) \bullet \underline{\underline{S}}_y(\chi) \bullet \Big[\epsilon_a\,\mathbf{u}_z\mathbf{u}_z + \epsilon_b\,\mathbf{u}_x\mathbf{u}_x \\ &\quad + \epsilon_c\,\mathbf{u}_y\mathbf{u}_y\Big] \bullet \underline{\underline{S}}_y^{-1}(\chi) \bullet \underline{\underline{S}}_z^{-1}(z) \bullet \mathbf{E}(\mathbf{r}) \\ \mathbf{B}(\mathbf{r}) &= \mu_0 \mathbf{H}(\mathbf{r}) \end{aligned}\right\}, \quad 0<z<L\,. \tag{2}$$

Here, ϵ_a, ϵ_b and ϵ_c are three frequency-dependent scalars; the tilt dyadic

$$\underline{\underline{S}}_y(\chi) = \mathbf{u}_y\mathbf{u}_y + (\mathbf{u}_x\mathbf{u}_x + \mathbf{u}_z\mathbf{u}_z)\,\cos\chi + (\mathbf{u}_z\mathbf{u}_x - \mathbf{u}_x\mathbf{u}_z)\,\sin\chi \tag{3}$$

is a function of the angle $\chi \in (0^\circ,\, 90^\circ]$; and the rotation dyadic

$$\underline{\underline{S}}_z(z) = \mathbf{u}_z\mathbf{u}_z + \left(\mathbf{u}_x\mathbf{u}_x + \mathbf{u}_y\mathbf{u}_y\right)\cos\left(\frac{\pi z}{\Omega}\right) + h\,\left(\mathbf{u}_y\mathbf{u}_x - \mathbf{u}_x\mathbf{u}_y\right)\sin\left(\frac{\pi z}{\Omega}\right) \tag{4}$$

involves $2\,\Omega$ as the structural period. The parameter $h = +1$ for structural right-handedness, and $h = -1$ for structural left-handedness.

2.2 Planewave response

An essential ingredient of our formulation is the computation of the reflection and transmission coefficients of a chiral STF excited by an obliquely incident plane wave.

Suppose that a plane wave is obliquely incident on the chiral STF from the lower half-space, with [12]

$$\mathbf{E}_{inc}(\mathbf{r}) = \left[a_L\,\mathbf{L}_+(\kappa_x,\kappa_y) + a_R\,\mathbf{R}_+(\kappa_x,\kappa_y)\right] \times \exp(i\mathbf{k}_+ \bullet \mathbf{r})\,, \quad z \le 0\,, \tag{5}$$

as the associated electric field phasor. Here and hereafter, a_L and a_R are known complex-valued amplitudes; $k_0 = \omega(\epsilon_0\mu_0)^{1/2}$ is the free space wavenumber and $\lambda_0 = 2\pi/k_0$ is the free space wavelength; κ_x and κ_y are the transverse wavenumbers defined by the direction of the incident radiation, but identical for all subsequently generated beams through the satisfaction of phase-matching conditions across the planes $z = 0$ and $z = L$; while

$$\left.\begin{aligned} \mathbf{L}_\pm(\kappa_x,\kappa_y) &= \pm(i\mathbf{s} - \mathbf{p}_\pm)/\sqrt{2} \\ \mathbf{R}_\pm(\kappa_x,\kappa_y) &= \mp(i\mathbf{s} + \mathbf{p}_\pm)/\sqrt{2} \\ \mathbf{s}(\kappa_x,\kappa_y) &= -(1/\kappa)\left(\kappa_y\mathbf{u}_x - \kappa_x\mathbf{u}_y\right) \\ \mathbf{p}_\pm(\kappa_x,\kappa_y) &= \mp(\alpha/\kappa k_0)\left(\kappa_x\mathbf{u}_x + \kappa_y\mathbf{u}_y\right) \\ &\quad + (\kappa/k_0)\mathbf{u}_z \\ \mathbf{k}_\pm(\kappa_x,\kappa_y) &= \kappa_x\mathbf{u}_x + \kappa_y\mathbf{u}_y \pm \alpha\mathbf{u}_z = k_0\,\mathbf{s}\times\mathbf{p}_\pm \\ \kappa(\kappa_x,\kappa_y) &= +\left(\kappa_x^2 + \kappa_y^2\right)^{1/2} \\ \alpha(\kappa_x,\kappa_y) &= +\left(k_0^2 - \kappa^2\right)^{1/2} \end{aligned}\right\}. \tag{6}$$

The resultant geometry is schematically depicted in Figure 1.

The vector functions $\mathbf{L}_\pm$ and $\mathbf{R}_\pm$ assist in representing left- and right-circularly polarized (LCP and RCP) plane waves. A plane wave is classified as *evanescent* if α is purely imaginary, and as *propagating* if α is real-valued.

The electric field phasors associated with the reflected and the transmitted plane waves are stated as

$$\mathbf{E}_{ref}(\mathbf{r}) = \left[r_L\,\mathbf{L}_-(\kappa_x,\kappa_y) + r_R\,\mathbf{R}_-(\kappa_x,\kappa_y)\right] \times \exp(i\mathbf{k}_- \bullet \mathbf{r})\,, \quad z \le 0\,, \tag{7}$$

and

$$\mathbf{E}_{tr}(\mathbf{r}) = \left[t_L\,\mathbf{L}_+(\kappa_x,\kappa_y) + t_R\,\mathbf{R}_+(\kappa_x,\kappa_y)\right] \times \exp\left[i\,(\mathbf{k}_+ \bullet \mathbf{r} - \alpha L)\right]\,, \quad z \ge L\,, \tag{8}$$

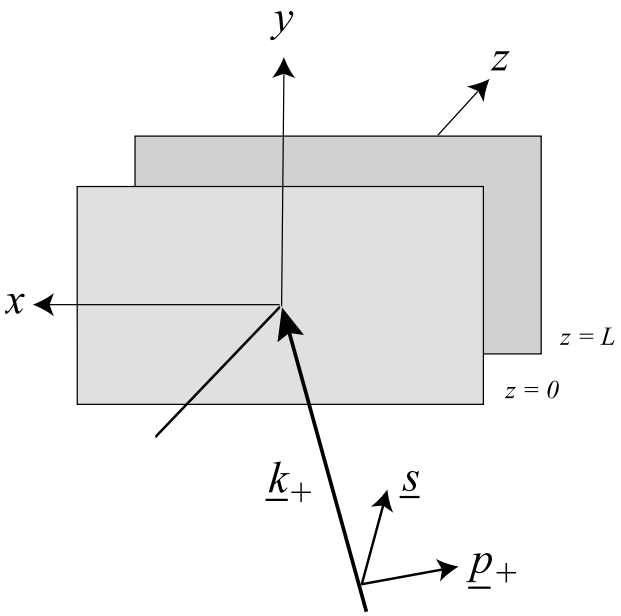

Fig. 1. Schematic for the excitation of a chiral STF by the plane wave described by (5). The chiral STF occupies the space between the planes $z = 0$ and $z = L$. Note that the vector $\mathbf{s}$ lies in the xy plane; and that the three vectors $\mathbf{k}_+$, $\mathbf{s}$ and $\mathbf{p}_+$ are mutually orthogonal.

respectively, with $r_{L,R}$ and $t_{L,R}$ as unknown complex-valued amplitudes. Their determination can be easily computed following the piecewise constant approximation described elsewhere [14]. More recently, the numerical implementation of a matrix polynomial expansion technique [26] has also been reported [27, 28]. For our present purposes, it suffices to state that the doubly subscripted reflection and transmission coefficients appearing in the relations

$$\begin{bmatrix} r_L \\ r_R \end{bmatrix} = \begin{bmatrix} r_{LL} & r_{LR} \\ r_{RL} & r_{RR} \end{bmatrix} \begin{bmatrix} a_L \\ a_R \end{bmatrix} \tag{9}$$

and

$$\begin{bmatrix} t_L \\ t_R \end{bmatrix} = \begin{bmatrix} t_{LL} & t_{LR} \\ t_{RL} & t_{RR} \end{bmatrix} \begin{bmatrix} a_L \\ a_R \end{bmatrix} \tag{10}$$

can be easily computed as functions of κ_x and κ_y [14, 27].

2.3 Dyadic Green functions

Let us now obtain expressions for dyadic Green functions for a chiral STF sandwiched between two vacuous half-spaces. Suppose, initially, that the chiral STF is absent and all space is vacuous. Then, the electric field phasor everywhere can be derived as follows [29, 30]:

$$\mathbf{E}(\mathbf{r}) = i\omega\mu_0 \iiint \left[\underline{\underline{G}}_0(\mathbf{r};\mathbf{r}') \bullet \mathbf{J}(\mathbf{r}') \right] d^3\mathbf{r}' - \nabla \times \iiint \left[\underline{\underline{G}}_0(\mathbf{r};\mathbf{r}') \bullet \mathbf{K}(\mathbf{r}') \right] d^3\mathbf{r}' . \tag{11}$$

Here, $\mathbf{r}$ is the field point, $\mathbf{r}'$ is the source point, $\mathbf{J}(\mathbf{r}')$ and $\mathbf{K}(\mathbf{r}')$ are the source electric and magnetic current densities, respectively; while

$$\underline{\underline{G}}_0(\mathbf{r};\mathbf{r}') = \left(\underline{\underline{I}} + \nabla\nabla/k_0^2 \right) \left[\exp(ik_0 R)/4\pi R \right] \tag{12}$$

is the infinite-medium DGF for free space, with $\underline{\underline{I}}$ as the identity dyadic, $\mathbf{R} = \mathbf{r} - \mathbf{r}'$ and $R = |\mathbf{R}|$.

For our present purposes, sources of circularly polarized plane waves are preferred. Therefore, we define two Beltrami source densities, being appropriate linear combinations of electric and magnetic currents, as follows [31]:

$$\left. \begin{aligned} \mathbf{W}_L &= \mathbf{J} - (k_0/i\omega\mu_0)\,\mathbf{K} \\ \mathbf{W}_R &= \mathbf{J} + (k_0/i\omega\mu_0)\,\mathbf{K} \end{aligned} \right\} . \tag{13}$$

These canonical sources of circularly polarized radiation can be conceived of as co-located pairs of electric and magnetic dipoles that are either parallel or anti-parallel. Accordingly, (11) is rewritten as

$$\mathbf{E}(\mathbf{r}) = \frac{i\omega\mu_0}{2} \iiint \left[\underline{\underline{G}}_{L0}(\mathbf{r};\mathbf{r}') \bullet \mathbf{W}_L(\mathbf{r}') + \underline{\underline{G}}_{R0}(\mathbf{r};\mathbf{r}') \bullet \mathbf{W}_R(\mathbf{r}') \right] d^3\mathbf{r}' , \tag{14}$$

where

$$\underline{\underline{G}}_{L0}(\mathbf{r};\mathbf{r}') = \left[\underline{\underline{I}} + (1/k_0)\nabla \times \underline{\underline{I}} \right] \bullet \underline{\underline{G}}_0(\mathbf{r};\mathbf{r}') \tag{15}$$

and

$$\underline{\underline{G}}_{R0}(\mathbf{r};\mathbf{r}') = \left[\underline{\underline{I}} - (1/k_0)\nabla \times \underline{\underline{I}} \right] \bullet \underline{\underline{G}}_0(\mathbf{r};\mathbf{r}') . \tag{16}$$

Next, let the chiral STF be present and – in consonance with Section 2.2 – let the sources lie exclusively in the lower half-space. Then the electric field in either of the two half-spaces must be given by

$$\mathbf{E}(\mathbf{r}) = \frac{i\omega\mu_0}{2} \iiint \left[\underline{\underline{G}}_L(\mathbf{r};\mathbf{r}') \bullet \mathbf{W}_L(\mathbf{r}') + \underline{\underline{G}}_R(\mathbf{r};\mathbf{r}') \bullet \mathbf{W}_R(\mathbf{r}') \right] d^3\mathbf{r}' , \quad z' < 0, \quad z < 0 \quad \text{or} \quad z > L , \tag{17}$$

where the DGFs $\underline{\underline{G}}_L(\mathbf{r};\mathbf{r}')$ and $\underline{\underline{G}}_R(\mathbf{r};\mathbf{r}')$ take the presence of the chiral STF into account. Synthesis of these two DGFs is accomplished through the decompositions

$$\underline{\underline{G}}_L(\mathbf{r};\mathbf{r}') = \begin{cases} \underline{\underline{G}}_{L0}(\mathbf{r};\mathbf{r}') + \underline{\underline{G}}_{L\rho}(\mathbf{r};\mathbf{r}') , & z < 0 , \; z' < 0 \\ \underline{\underline{G}}_{L\tau}(\mathbf{r};\mathbf{r}') , & z > L , \; z' < 0 \end{cases} \tag{18}$$

and

$$\underline{\underline{G}}_R(\mathbf{r};\mathbf{r}') = \begin{cases} \underline{\underline{G}}_{R0}(\mathbf{r};\mathbf{r}') + \underline{\underline{G}}_{R\rho}(\mathbf{r};\mathbf{r}') , & z < 0 , \; z' < 0 \\ \underline{\underline{G}}_{R\tau}(\mathbf{r};\mathbf{r}') , & z > L , \; z' < 0 \end{cases} . \tag{19}$$

As the planewave response of a chiral STF can be calculated, the remaining four dyadic functions on the right sides of (18) and (19) may be derived therefrom. For this purpose, we begin with a spectral representation of $\underline{\underline{G}}_0(\mathbf{r};\mathbf{r}')$ as [32, 33]

$$\underline{\underline{G}}_0(\mathbf{r};\mathbf{r}') = -\mathbf{u}_z\mathbf{u}_z k_0^{-2}\,\delta(\mathbf{R}) + \int_{-\infty}^{\infty}\int_{-\infty}^{\infty} \frac{i}{4\pi^2\alpha} \times (\mathbf{ss} + \mathbf{p}_\pm\mathbf{p}_\pm) \exp(i\mathbf{k}_\pm \bullet \mathbf{R})\, d\kappa_x\, d\kappa_y , \quad \begin{cases} z > z' \\ z < z' \end{cases} , \tag{20}$$

where $\delta(\mathbf{R})$ is the Dirac delta function. Clearly, $\underline{\underline{G}}_0(\mathbf{r};\mathbf{r}')$ is an angular spectrum of both propagating and evanescent plane waves. Therefore, all other DGFs possess analogous structures. In (20), the upper signs apply for $z > z'$, and the lower signs for $z < z'$.

From (15), (16) and (20), we obtain the representations

$$\underline{\underline{G}}_{L0}(\mathbf{r};\mathbf{r}') = -\mathbf{u}_z\mathbf{u}_z k_0^{-2}\,\delta(\mathbf{R}) + \int_{-\infty}^{\infty}\int_{-\infty}^{\infty} \frac{i}{4\pi^2\alpha} \times \mathbf{L}_\pm\mathbf{R}_\pm \exp\left(i\mathbf{k}_\pm \bullet \mathbf{R}\right)\, d\kappa_x\, d\kappa_y\,, \quad \begin{cases} z > z' \\ z < z' \end{cases}, \tag{21}$$

and

$$\underline{\underline{G}}_{R0}(\mathbf{r};\mathbf{r}') = -\mathbf{u}_z\mathbf{u}_z k_0^{-2}\,\delta(\mathbf{R}) + \int_{-\infty}^{\infty}\int_{-\infty}^{\infty} \frac{i}{4\pi^2\alpha} \times \mathbf{R}_\pm\mathbf{L}_\pm \exp\left(i\mathbf{k}_\pm \bullet \mathbf{R}\right)\, d\kappa_x\, d\kappa_y\,, \quad \begin{cases} z > z' \\ z < z' \end{cases}. \tag{22}$$

Then, in strict analogy with the reflected and transmitted plane waves in Section 2.2, we are able to devise the expressions

$$\underline{\underline{G}}_{L\rho}(\mathbf{r};\mathbf{r}') = \int_{-\infty}^{\infty}\int_{-\infty}^{\infty} \frac{i}{4\pi^2\alpha}\, \underline{\underline{\rho}}_L(\kappa_x,\kappa_y) \times \exp\left[i\left(\mathbf{k}_-\bullet\mathbf{r} - \mathbf{k}_+\bullet\mathbf{r}'\right)\right] d\kappa_x\, d\kappa_y\,, \quad z<0\,,\quad z'<0\,, \tag{23}$$

$$\underline{\underline{G}}_{R\rho}(\mathbf{r};\mathbf{r}') = \int_{-\infty}^{\infty}\int_{-\infty}^{\infty} \frac{i}{4\pi^2\alpha}\, \underline{\underline{\rho}}_R(\kappa_x,\kappa_y) \times \exp\left[i\left(\mathbf{k}_-\bullet\mathbf{r} - \mathbf{k}_+\bullet\mathbf{r}'\right)\right] d\kappa_x\, d\kappa_y\,, \quad z<0\,,\quad z'<0\,, \tag{24}$$

$$\underline{\underline{G}}_{L\tau}(\mathbf{r};\mathbf{r}') = \int_{-\infty}^{\infty}\int_{-\infty}^{\infty} \frac{i}{4\pi^2\alpha}\, \underline{\underline{\tau}}_L(\kappa_x,\kappa_y) \times \exp\left[i\left(\mathbf{k}_+\bullet\mathbf{r} - \alpha L - \mathbf{k}_+\bullet\mathbf{r}'\right)\right] d\kappa_x\, d\kappa_y\,, \quad z>L\,,\quad z'<0\,, \tag{25}$$

and

$$\underline{\underline{G}}_{R\tau}(\mathbf{r};\mathbf{r}') = \int_{-\infty}^{\infty}\int_{-\infty}^{\infty} \frac{i}{4\pi^2\alpha}\, \underline{\underline{\tau}}_R(\kappa_x,\kappa_y) \times \exp\left[i\left(\mathbf{k}_+\bullet\mathbf{r} - \alpha L - \mathbf{k}_+\bullet\mathbf{r}'\right)\right] d\kappa_x\, d\kappa_y\,, \quad z>L\,,\quad z'<0 \tag{26}$$

for the remaining dyadic functions on the right sides of (18) and (19). The reflection and the transmission dyadics entering the four previous expressions are specified as follows:

$$\left.\begin{aligned} \underline{\underline{\rho}}_L(\kappa_x,\kappa_y) &= r_{LL}\,\mathbf{L}_-\mathbf{R}_+ + r_{RL}\,\mathbf{R}_-\mathbf{R}_+ \\ \underline{\underline{\rho}}_R(\kappa_x,\kappa_y) &= r_{LR}\,\mathbf{L}_-\mathbf{L}_+ + r_{RR}\,\mathbf{R}_-\mathbf{L}_+ \\ \underline{\underline{\tau}}_L(\kappa_x,\kappa_y) &= t_{LL}\,\mathbf{L}_+\mathbf{R}_+ + t_{RL}\,\mathbf{R}_+\mathbf{R}_+ \\ \underline{\underline{\tau}}_R(\kappa_x,\kappa_y) &= t_{LR}\,\mathbf{L}_+\mathbf{L}_+ + t_{RR}\,\mathbf{R}_+\mathbf{L}_+ \end{aligned}\right\}. \tag{27}$$

2.4 Asymptotic evaluation

Even if exact analytical expressions for r_{LL}, etc., were somehow miraculously found, the integrations on the right sides of (23)–(26) would have to be performed numerically. However, in many applications, only the asymptotic expressions in the limit $k_0 R \to \infty$ are needed.

The method of stationary phase is applied for this purpose [34, 35]. Correct to order $(1/k_0R)$, in the limit $k_0R \to \infty$, we get

$$\underline{\underline{G}}_{L\rho,R\rho}(\mathbf{r};\mathbf{r}') \to 2\underline{\underline{\rho}}_{L,R}\left(\frac{k_0(x-x')}{d_\rho}, \frac{k_0(y-y')}{d_\rho}\right) \times \frac{\exp(ik_0d_\rho)}{4\pi d_\rho}\,, \quad z \ll 0\,, \quad z' < 0\,, \tag{28}$$

and

$$\underline{\underline{G}}_{L\tau,R\tau}(\mathbf{r};\mathbf{r}') \to 2\underline{\underline{\tau}}_{L,R}\left(\frac{k_0(x-x')}{d_\tau}, \frac{k_0(y-y')}{d_\tau}\right) \times \frac{\exp(ik_0d_\tau)}{4\pi d_\tau}\,, \quad z \gg L\,, \quad z' < 0\,, \tag{29}$$

where the distances

$$\left.\begin{aligned} d_\rho &= +\left[(x-x')^2 + (y-y')^2 + (z+z')^2\right]^{1/2} \\ d_\tau &= +\left[(x-x')^2 + (y-y')^2 + (z-L-z')^2\right]^{1/2} \end{aligned}\right\}. \tag{30}$$

3. Numerical results and discussion

3.1 Dipolar sources

We investigated the response of a chiral STF to sources comprising electric and magnetic dipoles. As any chiral STF discriminates between LCP and RCP plane waves

strongly in the Bragg regimes, we chose two different Beltrami source configurations:

(a) $\mathbf{J}(\mathbf{r}) = -i\omega(p/2)\,\mathbf{u}_s\,\delta(\mathbf{r} - d\mathbf{u}_z)$ and
$\mathbf{K}(\mathbf{r}) = -(i\omega\mu_0/k_0)\,\mathbf{J}(\mathbf{r})$,

and

(b) $\mathbf{J}(\mathbf{r}) = -i\omega(p/2)\,\mathbf{u}_s\,\delta(\mathbf{r} - d\mathbf{u}_z)$ and
$\mathbf{K}(\mathbf{r}) = (i\omega\mu_0/k_0)\,\mathbf{J}(\mathbf{r})$.

Both canonical source configurations nominally comprise a pair of oscillating parallel electric and magnetic dipoles co-located at $\mathbf{r} = d\mathbf{u}_z$, $(d < 0)$, with $\mathrm{Re}\left[pe^{-i\omega t}\right]$ being the oscillating electric dipole moment. Obviously, an electric or a magnetic dipolar source is simply a linear combination of the two canonical source configurations.

The two Beltrami source configurations are of the left-handed and the right-handed types, respectively, and radiate left-handed and right-handed electromagnetic fields which have been decomposed in the previous section as angular spectrums of LCP and RCP plane waves. In the far zone, the radiation emitted by the two sources in the broadside directions is either a LCP or a RCP plane wave (when all space is matter-free); therefore, as $k_0|d| \to \infty$, the radiation intercepted by the chiral STF is virtually a circularly polarized plane wave.

The unit vector $\mathbf{u}_s = (\mathbf{u}_x \cos\phi_s + \mathbf{u}_y \sin\phi_s)\sin\theta_s + \mathbf{u}_z \cos\theta_s$ represents the orientation of the dipolar sources as shown in Figure 2.

When $\theta_s = 0$ and $|k_0 d|$ is sufficiently large, the radiation intercepted by the chiral STF is likely to be of low significance [36]. On the other hand, the radiation incident on the chiral STF must be substantially in the form of a normally incident beam for $\theta_s = \pi/2$ and sufficiently large $|k_0 d|$.

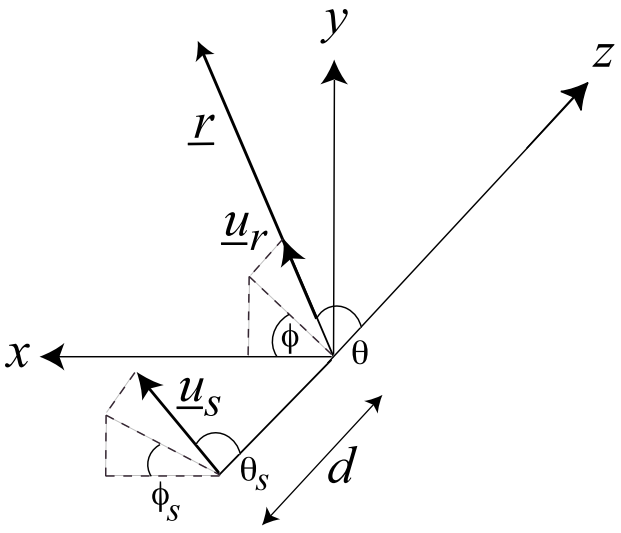

Fig. 2. Geometry for the far-field calculations relating to (28)–(31). The chiral STF (not shown) resides between the planes $z = 0$ and $z = L$ as in Figure 1.

For either of the two configurations of dipolar sources, an expression for the electric field applicable at locations far away from the sources as well as the chiral STF can be obtained from (17) as

$$\mathbf{E}(r, \theta, \phi) \to \left[\omega^2 \mu_0 p \frac{\exp(ik_0 r)}{4\pi r}\right] \mathbf{e}(\theta, \phi)\,. \qquad (31)$$

Here, $\mathbf{u}_r(\theta, \phi) \bullet \mathbf{e}(\theta, \phi) = 0$, $\mathbf{u}_r(\theta, \phi) = (\mathbf{u}_x \cos\phi + \mathbf{u}_y \sin\phi)\sin\theta + \mathbf{u}_z \cos\theta$ is the unit radial vector in the spherical coordinate system, and $r = |\mathbf{r}|$.

3.2 Selected parameters

Calculations of $\mathbf{e}(\theta, \phi)$ were made for the following constitutive and geometric parameters: $h = 1$, $\epsilon_a = 2.7$, $\epsilon_b = 3.0$, $\epsilon_c = 2.72$, $\chi = 30^\circ$, $L = 60\,\Omega$, $\Omega = 200\,\mathrm{nm}$, $d = -10\lambda_0$, and $r = 10^5\lambda_0$. Dissipation and dispersion in the chosen chiral STFs were ignored for these illustrative calculations in the $\lambda_0 \in [550, 750]\,\mathrm{nm}$ regime, which is supposed to lie far away from the absorption resonances of $\epsilon_{a,b,c}$. The ratio L/Ω is large enough so that circular Bragg phenomenon is fully developed [8, 14]. The appearance of the Bragg regime in the electromagnetic spectrum depends on $\epsilon_{a,b,c}$, χ and Ω; if any of these constitutive parameters is changed (or if the angle of planewave incidence is altered), the center-wavelength and the bandwidth of the Bragg regime change in a largely predictable fashion [8, 12, 14].

The Bragg regime is roughly $\lambda_0 \in [659,\ 684]\,\mathrm{nm}$ for normally incident plane waves [10, 37], while a gradual blue-shift of the Bragg regime occurs for increasingly oblique incidence [12], for the chosen parameters. All graphs reproduced in this communication were drawn for $\lambda_0 = 600, 672$, or $744\,\mathrm{nm}$. Before continuing, we must caution the reader that plots of $|\mathbf{e}|^2$ are expected to function as the radiation patterns only at distances far from the chiral STF and the dipolar source; in particular, values of $|\mathbf{e}(\theta, \phi)|^2$ in the vicinity of $\theta = \pi/2$ do not possess physical significance because the asymptotic evaluation is invalid close to the chiral STF.

Computed values of $|\mathbf{e}(\theta, \phi)|^2$ in the xz and the yz planes, for various types of dipolar sources, are shown in Figures 3–9. The source configuration is left-handed for the top plots, and right-handed for the bottom plots, in each figure. These plots yield the radiation patterns only at locations far away from the chiral STF (if present) and the source. The dashed circles of indicated radius provide the scale.

3.3 Vertically directed dipolar sources

Let us begin with vertically directed dipolar sources, for which $\mathbf{u}_s = \mathbf{u}_z$. Figure 3 shows plots of $|\mathbf{e}(\theta, \phi)|^2$ computed in the xz and the yz planes after setting $\epsilon_a = \epsilon_b = \epsilon_c = 1$ in the foregoing equations. In the absence of any

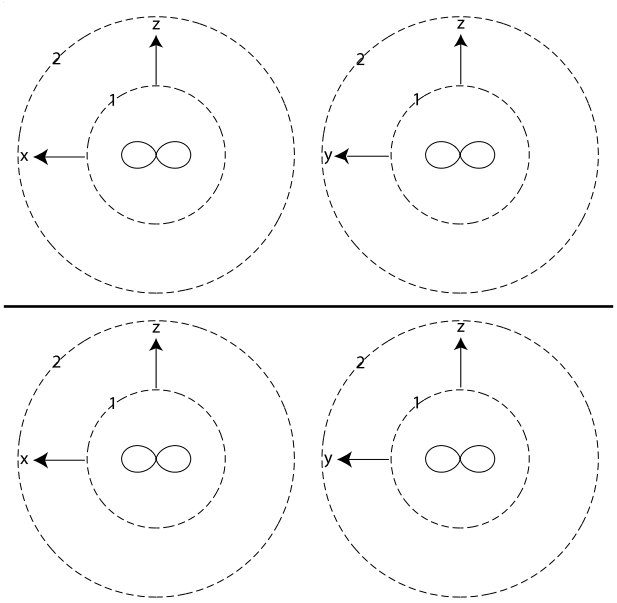

Fig. 3. Computed values of $|\mathbf{e}(\theta, \phi)|^2$ in the *xz* and the *yz* planes, for *z*-directed Beltrami dipolar sources radiating at $\lambda_0 = 600$, 672 or 744 nm. The source configuration is left-handed for the top plots, and right-handed for the bottom plots. The chiral STF is absent (i.e., $\epsilon_a = \epsilon_b = \epsilon_c = 1$). See Section (3.2) for all other parameters. The dashed circles of indicated radius provide the scale.

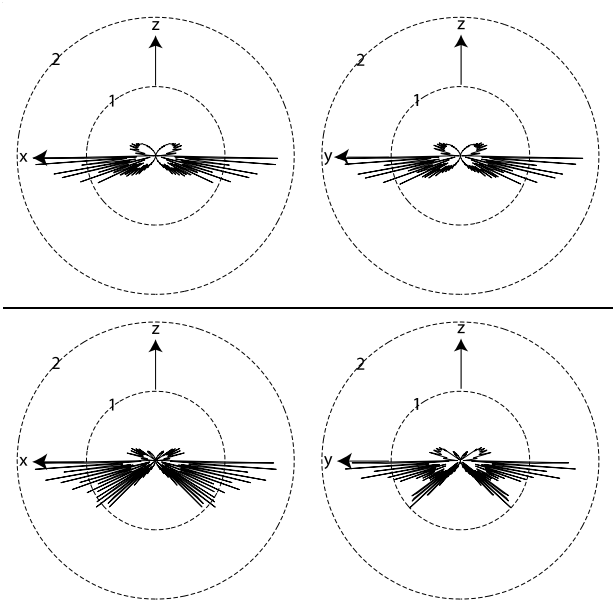

Fig. 4. Computed values of $|\mathbf{e}(\theta, \phi)|^2$ in the *xz* and the *yz* planes, for *z*-directed Beltrami dipolar sources radiating at $\lambda_0 = 600$ nm. The source configuration is left-handed for the top plots, and right-handed for the bottom plots. The following parameters were used for calculations: $h = 1$, $\epsilon_a = 2.7$, $\epsilon_b = 3.0$, $\epsilon_c = 2.72$, $\chi = 30°$, $L = 60\,\Omega$, $\Omega = 200$ nm, $d = -10\lambda_0$, and $r = 10^5\lambda_0$.

matter, the radiation patterns must possess circular symmetry in the horizontal (i.e., *xy*) plane and appear as figures-of-eight in any vertical plane [38], to which the plots in Figure 3 attest. Clearly, $|\mathbf{e}|^2$ is independent of the handedness of the Beltrami source configurations, as it must.

The effects of the presence of the chosen right-handed STF are evident in the plots presented in Figures 4–6. These plots contain several Fabry-Perot rings in the lower (i.e., reflection) half-space which arise due to thickness resonances inside the film. Fabry-Perot rings (see e.g. [34] Fig. 7.60) are also present in the upper, or the transmission, half-space, but are considerably muted.

All three figures demonstrate a slight disturbance of the circular symmetry in the horizontal plane by the chiral STF. As witness thereof, the plots of $|\mathbf{e}|^2$ in the *xz* and the *yz* planes are somewhat different, in contrast with Figure 3. This asymmetric feature can be attributed to the fact that the helicoidal symmetry of a chiral STF is not circular: whereas the former is expressed in three-dimensional space, the latter requires only a two-dimensional space. In the context of the planewave response of a chiral STF, a similar dependence of reflection and transmission on the projection $\mathbf{E}_{inc}(\mathbf{r}) \bullet \underline{\underline{S}}_z(z) \bullet \underline{\underline{S}}_y(\chi) \bullet \mathbf{u}_x$ on the illuminated side of the chiral STF has already been noted [39]. The same dependence must underlie the radiation patterns presented here, because the DGFs of Section 2.3 are constructed from continuous angular spectrums of plane waves.

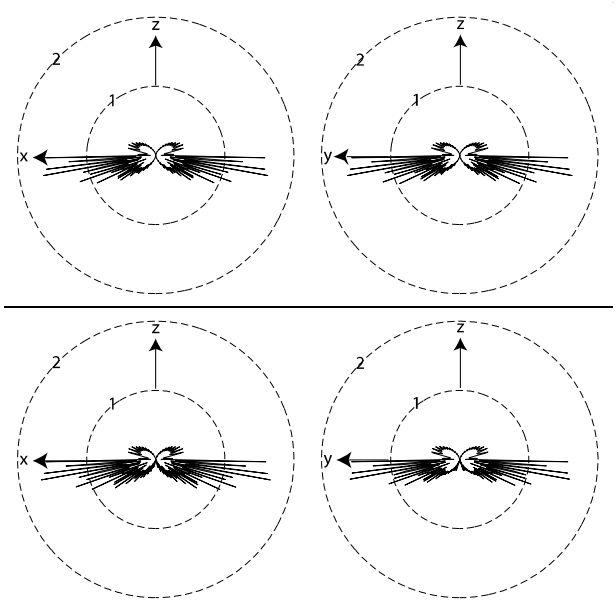

Fig. 5. Same as Figure 4, but for $\lambda_0 = 672$ nm.

Evidence of the circular Bragg phenomenon is provided by a comparison of Figures 4 and 5 with Figure 6. The radiation patterns in the first two figures clearly depend on the handedness of the source configuration, but

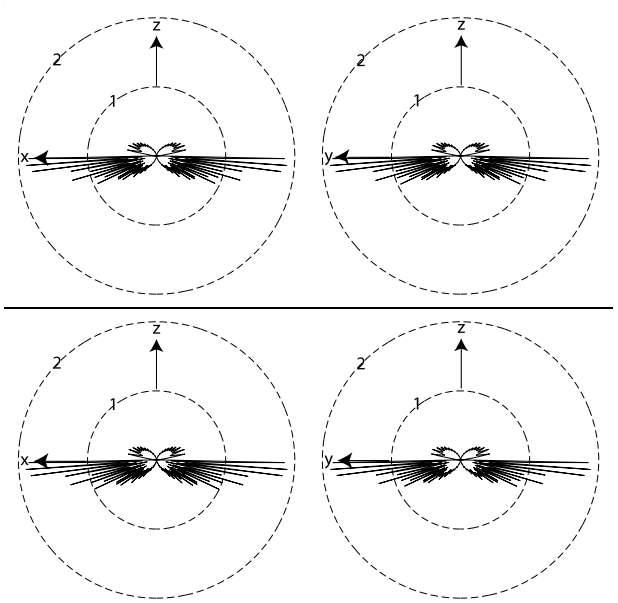

Fig. 6. Same as Figure 4, but for $\lambda_0 = 744\,\text{nm}$.

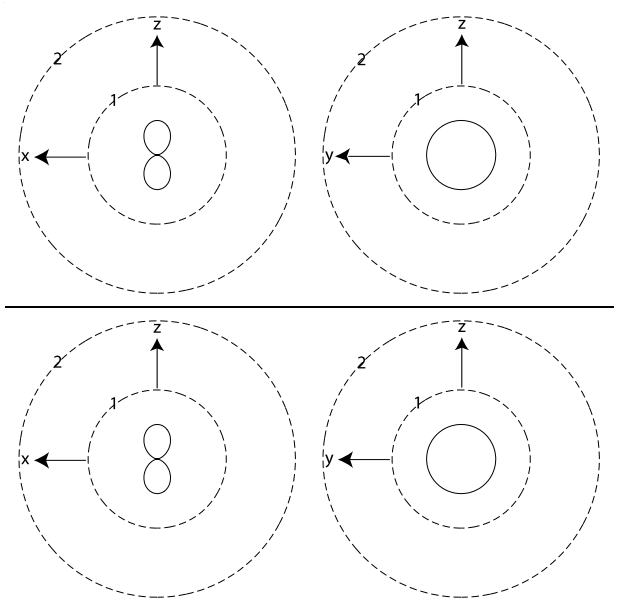

Fig. 7. Computed values of $|\mathbf{e}(\theta, \phi)|^2$ in the xz and the yz planes, for x-directed Beltrami dipolar sources radiating at $\lambda_0 = 600$, 672 or 744 nm. The source configuration is left-handed for the top plots, and right-handed for the bottom plots. The chiral STF is absent (i.e., $\epsilon_a = \epsilon_b = \epsilon_c = 1$). See Section (3.2) for all other parameters.

not (at least, perceptibly) in the third figure. This dependence can be attributed to the circular Bragg phenomenon excited by obliquely incident plane waves [12, 14]. For normally incident plane waves, the center-wavelength of the Bragg regime is 672 nm, and it blue-shifts for oblique incidence. That is the reason for the radiation patterns to be different for the two different Beltrami source configurations radiating at $\lambda = 600$ and 672 nm, but not when $\lambda_0 = 744\,\text{nm}$.

Far-field radiation from the z-directed dipolar sources is virtually absent for θ in the vicinity of 0 and π, in Figures 4–6. This is not surprising, because either the electric field or the magnetic field is null-valued along the dipole axis [36, 38]. As dipole radiation is broadside, not endfire – which is evident from Figure 3 – the chiral STF is not axially excited; therefore, it does not reradiate in directions close to the z axis.

3.4 Horizontally directed dipolar sources

The situation changes dramatically when $\theta_s = \pi/2$, so that the dipolar sources are directed in the xy plane. For definiteness, we chose $\mathbf{u}_s = \mathbf{u}_x$. Figure 7 shows plots of $|\mathbf{e}(\theta, \phi)|^2$ computed in the xz and the yz planes, when the chiral STF is not present. As the main lobes of the radiation lie along the z axis in the absence of matter, the chiral STF is definitely excited along its axis of nonhomogeneity.

Figures 8, 9 and 10, respectively, show the radiation patterns in the presence of the chosen chiral STF, when $\lambda_0 = 600$, 672 and 744 nm. In all three figures, circular symmetry in the horizontal plane is conspicuously absent. On the one hand, this merely follows the radiation patterns of horizontally directed dipolar sources in the absence of matter, as depicted in Figure 7. On the other hand, some lack of circular symmetry in the xy plane is also due to the noncircular (but helicoidal) symmetry of chiral STFs.

Just as for the vertically directed sources of Section 3.4, the radiation patterns in Figures 8–10 contain very prominent Fabry-Perot rings in the reflection half-space. However, unlike the plots in Figures 4–6, the Fabry-Perot rings in the transmission half-space are not insubstantial.

But the most prominent features of the radiation patterns in Figures 8–10 are due to the circular Bragg phenomenon. For normally incident plane waves, the center-wavelength of the Bragg regime is 672 nm, and it blue-shifts for oblique incidence [14]. This is clearly indicated in Figure 9 by the presence of the wedge located at $\theta = 0$ – in the transmission half-space – for the right-handed Beltrami source configuration. The wavelength for Figure 8 is lower than for Figure 9, so that the wedge in the transmission half-space lies around $\theta = \pi/4$ for the right-handed Beltrami source configuration. The wedge is absent in Figures 8 and 9 for the left-handed Beltrami source configuration, but a double-fang feature appears in the reflection half-space located at $\theta = \pi$, such that $|\mathbf{e}(0, \phi)|^2 \sim |\mathbf{e}(\pi, \phi)|^2$. The diversity with respect to the handedness of the source configuration is virtually absent in Figure 10, as the circular Bragg phenomenon is not excited at $\lambda_0 = 744\,\text{nm}$.

The wedge and the double-fang feature for the right-handed source configuration in Figures 8 and 9 are the cumulative expressions of the circular Bragg phenomenon known for normally and obliquely incident plane waves. As the fields radiated by a source configuration can be

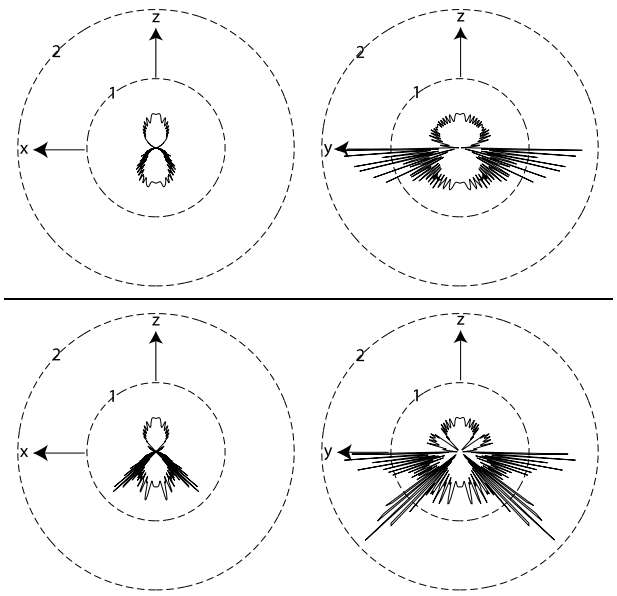

Fig. 8. Computed values of $|\mathbf{e}(\theta, \phi)|^2$ in the xz and the yz planes, for x-directed Beltrami dipolar sources radiating at $\lambda_0 = 600\,\text{nm}$. The source configuration is left-handed for the top plots, and right-handed for the bottom plots. The following parameters were used for calculations: $h = 1$, $\epsilon_a = 2.7$, $\epsilon_b = 3.0$, $\epsilon_c = 2.72$, $\chi = 30°$, $L = 60\,\Omega$, $\Omega = 200\,\text{nm}$, $d = -10\lambda_0$, and $r = 10^5\lambda_0$.

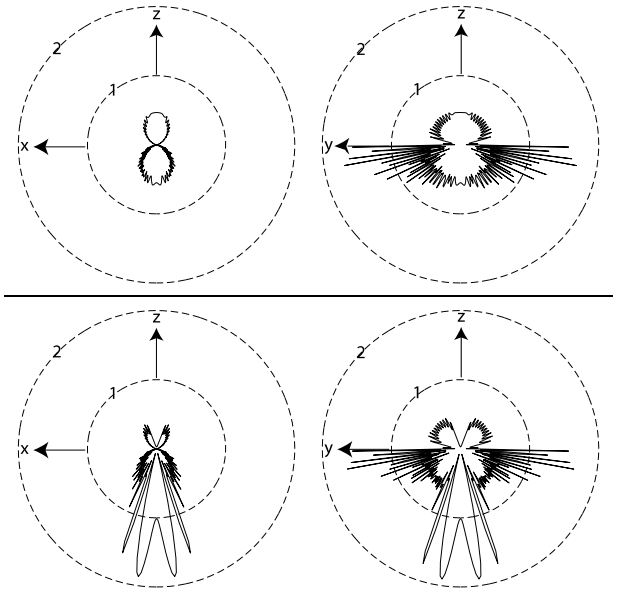

Fig. 9. Same as Figure 8, but for $\lambda_0 = 672\,\text{nm}$.

decomposed into an angular continuum of circularly polarized plane waves, the characteristic features of the Bragg phenomenon – if displayed by a segment of that continuum – coalesce to create either the wedge or the double-fang feature in the radiation pattern.

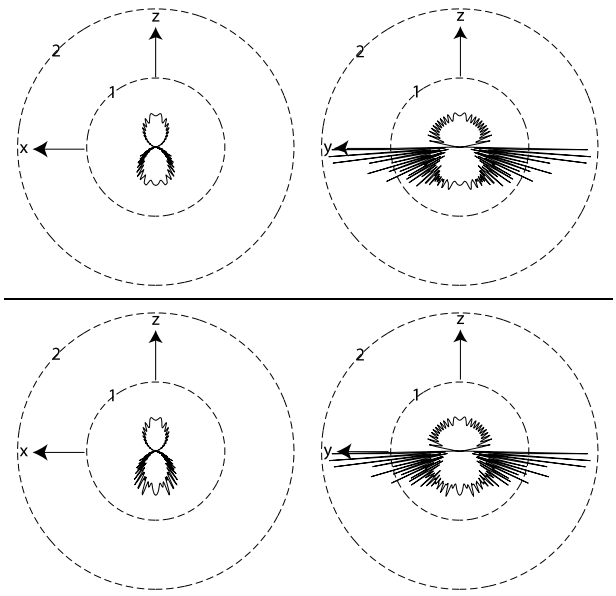

Fig. 10. Same as Figure 8, but for $\lambda_0 = 744\,\text{nm}$.

3.5 Dependence on source location

The final issue worth mentioning here is the virtual independence of the radiation pattern in the transmission half-space on the location of the dipolar sources. This can be explained as follows: The electric field illuminating the face of the chiral STF, proportional to the sum of $\underline{\underline{G}}_{L0}(x, y, 0; 0, 0, d) \cdot \mathbf{W}_L(0, 0, d)$ and $\underline{\underline{G}}_{R0}(x, y, 0; 0, 0, d) \cdot \mathbf{W}_R(0, 0, d)$, contains both propagating and evanescent plane waves. The evanescent components do not contribute to far-zone transmitted intensity. The propagating components affect the phases but not the amplitudes of $\underline{\underline{G}}_{L\tau}(x, y, z; 0, 0, d) \cdot \mathbf{W}_L(0, 0, d)$ and $\underline{\underline{G}}_{R\tau}(x, y, z; 0, 0, d) \cdot \mathbf{W}_R(0, 0, d)$ in the far zone.

On the other hand, far away from the chiral STF in the reflection half-space, the total field comprises two parts: (i) the direct radiation from the source configuration, and (ii) the field reflected by the chiral STF. The two parts must interfere, with their relative phase depending on d; hence the radiation pattern in the reflection half-space must depend on the source location.

Confirmation of the foregoing conclusions is provided by comparison of Figure 9 ($d = -10\lambda_0$) with Figures 11 ($d = -\lambda_0$) and 12 ($d = -100\lambda_0$). All other parameters for these three figures are identical.

4. Concluding remarks

In the previous sections, we presented dyadic Green functions for reflection and transmission by a chiral sculptured thin film. As the DGFs were synthesized in the form of angular spectrums of left- and right-circularly polar-

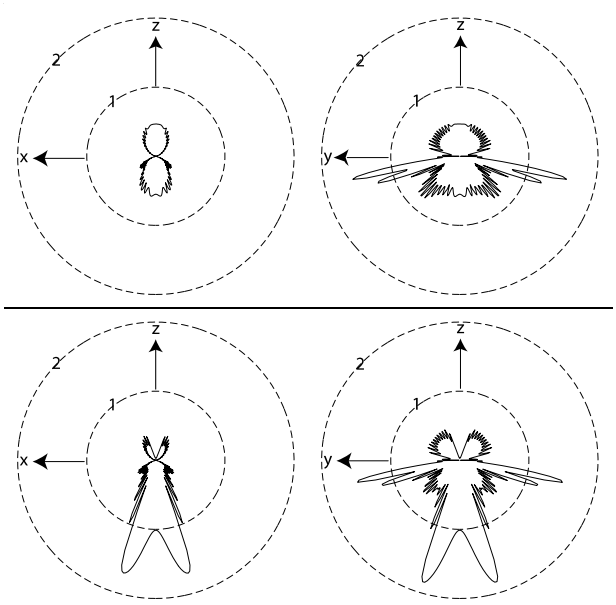

Fig. 11. Same as Figure 9, but for $d = -\lambda_0$.

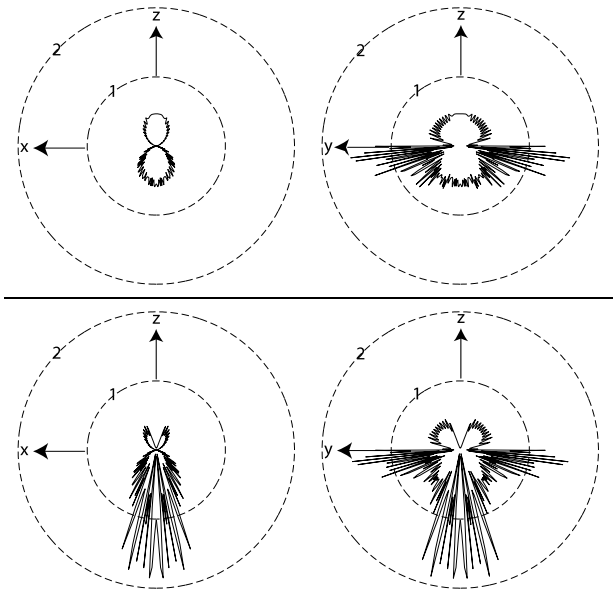

Fig. 12. Same as Figure 9, but for $d = -100\lambda_0$.

ized plane waves, the DGFs were naturally formulated in order to take advantage of the Beltrami representation of source current densities. The circular Bragg phenomenon displayed by chiral STFs on planewave excitation was shown to underlie the discriminatory treatment of left- and right-handed source configurations. We expect the understanding gleaned from this work to be useful in near-field microscopy of sculptured thin films, other nanostructured materials, and nanotextured surfaces.

Acknowledgement. A. L. thanks the Weiss Graduate Fellowship Program at the Pennsylvania State University for partial financial support. M.W.M. acknowledges the support of the *Engineering and Physical Sciences Research Council* of Great Britain (EPSRC grant no. GR/R55078/01).

References

[1] Lakhtakia, A.: Director-based theory for the optics of sculptured thin films. Optik **107** (1997), 57–61.
[2] Messier, R.; Lakhtakia, A.: Sculptured thin films-II. Experiments and applications. Mater. Res. Innovat. **2** (1999), 217–222.
[3] Macleod, H.A.: Thin-film Optical Filters. Bristol, UK: Institute of Physics, 2001.
[4] Taga, Y.: Recent progress of nanotechnologies of thin films for industrial applications. Mater. Sci. Engg. C **15** (2001), 231–235.
[5] Messier, R.; Venugopal, V.C.; Sunal, P.D.: Origin and evolution of sculptured thin films. J. Vac. Sci. Technol. A **18** (2000), 1538–1545.
[6] Suzuki, M.; Taga, Y.: Integrated sculptured thin films. Jpn. J. Appl. Phys. Pt. 2 **40** (2001), L358–L359.
[7] Lakhtakia, A.; Weiglhofer, W.S.: Axial propagation in general helicoidal bianisotropic media. Microw. Opt. Technol. Lett. **6** (1993), 804–806.
[8] Lakhtakia, A.; Venugopal, V.C.: On Bragg reflection by helicoidal bianisotropic mediums. Arch. Elektr. Übertr. **53** (1999), 287–290.
[9] Wu, Q.; Hodgkinson, I.J.; Lakhtakia, A.: Circular polarization filters made of chiral sculptured thin films: experimental and simulation results. Opt. Engg. **39** (2000), 1863–1868.
[10] McCall, M.W.: Axial electromagnetic wave propagation in inhomogeneous dielectrics. Math. Comput. Model. **34** (2001), 1483–1498.
[11] Lakhtakia, A.: Sculptured thin films: accomplishments and emerging uses. Mater. Sci. Engg. C **19** (2002), 427–434.
[12] Venugopal, V.C.; Lakhtakia, A.: On absorption by non-axially excited slabs of dielectric thin-film helicoidal bianisotripic mediums. Eur. Phys. J. Appl. Phys. **10** (2000), 173–184.
[13] Hodgkinson, I.J.; Wu, Q.H.; Thorn, K.E.; Lakhtakia, A.; McCall, M.W.: Spacerless circular-polarization spectral-hole filters using chiral sculptured thin films: theory and experiment. Opt. Commun. **184** (2000), 57–66.
[14] Venugopal, V.C.; Lakhtakia, A.: Electromagnetic plane-wave response characteristics of non-axially excited slabs of dielectric thin-film helicoidal bianisotropic mediums. Proc. R. Soc. Lond. A **456** (2000), 125–161.
[15] Paesler, M.A.; Moyer, P.J.: Near-Field Optics: Theory, Instrumentation, and Applications. New York: Wiley, 1996.
[16] de Fornel, F.: Evanescent Waves from Newtonian Optics to Atomic Optics. Heidelberg: Springer, 2000.
[17] Jackson, J.D.: Classical Electrodynamics. New York: Wiley, 1999.
[18] Lakhtakia, A.: Truncation of angular spread of Bragg zones by total reflection, and Goos-Hänchen shifts exhibited by chiral sculptured thin films. Arch. Elektr. Übertr. **56** (2002), 169–176. Erratum to [18]: Arch. Elektr. Übertr. **57** (2003), 79.
[19] Naber, A.; Kock, H.; Fuchs, H.: High-resolution lithography with near-field optical microscopy. Scanning **18** (1996), 567–571.

[20] Kühn, S.; Hettich, C.; Schmitt, C.; Poizat, J.-P.; Sandoghdar, V.: Diamond colour centres as a nanoscopic light source for scanning near-field optical microscopy. J. Microscopy **202** (2001), 2–6.
[21] McCall, M.W.: Sculptured thin film optoelectronics. Proc. SPIE **4467** (2001), 110–120.
[22] McCall, M.W.; Lakhtakia, A.: Integrated optical polarization filtration *via* sculptured-thin-film technology. J. Mod. Opt. **48** (2001), 2179–2184.
[23] Riedel, M.; Müller, B.; Wintermantel, E.: Protein adsorption and monocyte activation of germanium nanopyramids. Biomaterials **22** (2001), 2307–2316.
[24] Müller, B.: Natural formation of nanostructures: From fundamentals in metal heteroepitaxy to applications in optics and biomaterials science. Surf. Rev. Lett. **8** (2001), 169–228.
[25] Campion, A.; Kambhampati, P.: Surface-enhanced Raman scattering. Chem. Soc. Rev. **27** (1998), 241–250.
[26] Lakhtakia, A.; Weiglhofer, W.S.: Further results on light propagation in helicoidal bianisotropic mediums: oblique incidence. Proc. R. Soc. Lond. A **453** (1997), 93–105; erratum **456** (2000), 3275.
[27] Schubert, M.; Herzinger, C.M.: Ellipsometry on anisotropic materials: Bragg conditions and phonons in dielectric helical thin films. Phys. Stat. Sol. (a) **188** (2001), 1563–1575.
[28] Polo, Jr., J.A.; Lakhtakia, A.: Numerical implementation of exact analytical solution for oblique propagation in a cholesteric liquid crystal. Microw. Opt. Technol. Lett. **35** (2002), 397–400.
[29] Jones, D.S.: Low frequency electromagnetic radiation. J. Inst. Math. Applics. **23** (1979), 421–447.
[30] Lakhtakia, A.: Polarizability dyadics of small bianisotropic spheres. J. Phys. France **51** (1990), 2235–2242.
[31] Lakhtakia, A.: Beltrami Fields in Chiral Media. Singapore: World Scientific, 1994.
[32] Cho, S.K.: Electromagnetic Scattering. New York: Springer, 1987, chap. 6.
[33] Chew, W.C.: Waves and Fields in Inhomogeneous Media. New York: IEEE Press, 1995, p. 384.
[34] Born, M.; Wolf, E.: Principles of Optics. Oxford, UK: Pergamon, 1987, pp. 753–754.
[35] Lakhtakia, A.: Time-harmonic dyadic Green's functions for reflection and transmission by a chiral slab. Arch. Elektr. Übertr. **47** (1993), 1–5.
[36] Lakhtakia, A.; Iskander, M.F.; Durney, C.H.; Massoudi, H.: Irradiation of prolate spheroidal models of humans and animals in the near field of a small loop antenna. Radio Sci. **17** (1982), 77S–84S.
[37] Lakhtakia, A.; McCall, M.W.: Sculptured thin films as ultranarrow-bandpass circular-polarization filters. Opt. Commun. **168** (1999), 457–465.
[38] Magid, L.M.: Electromagnetic Fields, Energy and Waves. New York: Wiley, 1972.
[39] Venugopal, V.C.; Lakhtakia, A.: On optical rotation and ellipticity transformation by axially excited slabs of dielectric thin-film helicoidal bianisotropic mediums (TFHBMs). Int. J. Appl. Electromag. Mech. **9** (1998), 201–210.

Akhlesh Lakhtakia was born in Lucknow, India, in 1957. After studies at the Institute of Technology, Banaras Hindu University, Varanasi, India and the University of Utah, Salt Lake City, USA, he joined the Pennsylania State University, where he is now a Professor of Engineering Science and Mechanics. He has either authored or co-authored about 600 journal papers and conference publications, and has lectured on waves and complex materials in many countries. His current research interests lie in the electromagnetics and elastodynamics of complex mediums, sculptured thin films, and nanotechnology. For more information on his activities, please visit his website: www.esm.psu.edu/HTMLs/Faculty/Lakhtakia/ALakhtakia.html

Martin W. McCall was born in London, UK, in 1962. He is currently a Reader in Physics at Imperial College, London. Throughout his career he has worked at various times on nonlinear optics, nonlinear dynamics and electromagnetics of complex mediums. He is author or co-author of about 90 papers, and an undergraduate text on classical mechanics.

Available online at www.sciencedirect.com
SCIENCE DIRECT®
Optics Communications 235 (2004) 133–151
OPTICS COMMUNICATIONS
www.elsevier.com/locate/optcom

Response of slanted chiral sculptured thin films to dipolar sources

Fei Wang [1], Akhlesh Lakhtakia *

CATMAS – Computational and Theoretical Materials Sciences Group, Department of Engineering Science and Mechanics, Pennsylvania State University, University Park, PA 16802-6812, USA

Received 30 December 2003; accepted 5 March 2004

Abstract

A theoretical investigation of the electromagnetic response of a slanted chiral sculptured thin film (STF) to dipolar sources is presented. Dyadic Green functions (DGFs) for a slanted chiral STF sandwiched between two vacuous half-spaces are formulated as planewave angular spectrums. First, the response of the slanted chiral STF to obliquely incident plane waves is obtained by rigorous coupled-wave analysis implemented with a stable algorithm; then, asymptotic evaluation of the DGFs is carried in the far-field limit. The radiation patterns of Beltrami source configurations close to a slanted chiral STF are computed and discussed. In particular, certain characteristic features – which are closely related to the circular Bragg phenomenon – in the radiation patterns are found to be spatially asymmetric, because of the effective transverse periodicity of the chosen thin film.

PACS: 77.55.+f; 78.67.−n; 42.70.−a; 42.79.Dj

Keywords: Nanomaterials; Sculptured thin film; Structural handedness; Point dipoles; Beltrami sources; Green functions

1. Introduction

Sculptured thin films (STFs) are a class of nanomaterials that emerged during the 1990s from the widely used columnar thin films [1,2], and are grown by physical vapor deposition [3,4]. The nanostructure of a STF comprises clusters of 3–5 nm diameter that form parallel nanowires and are bent in some fanciful forms. The nanowire diameters range from 10 to 300 nm, and a wide variety of two- and three-dimensional as well as sectionwise cascaded morphologies can be engineered [3,5]. STFs are therefore porous materials, the shapes and volume fractions of whose void regions can also be tailored for specific optical and other applications [2,4].

The nanowires of a chiral STF are helixes. These films can be regarded as unidirectionally and rotationally nonhomogeneous continuums

* Corresponding author. Tel.: +1-814-863-4319; fax: +1-814-865-9974.
E-mail addresses: FUW101@psu.edu (F. Wang), axl4@psu.edu (A. Lakhtakia).
[1] Fax: +1-814-863-7967.

0030-4018/$ - see front matter
doi:10.1016/j.optcom.2004.03.016

with direction-dependent properties at visible and infrared wavelengths. Specific interest has been garnered in optics by their display of the circular Bragg phenomenon [6]: a circularly polarized plane wave of the same handedness as the helical nanowires of a chiral STF is substantially reflected in a certain wavelength regime, while that of the other handedness is not. Grating theory provides an explanation – the co-handed circularly polarized plane wave effectively encounters a Bragg grating, while the cross-handed plane wave merely propagates across a homogeneous slab [7].

Normally, the helical nanowires of a chiral STF grow upright by rotating the substrate at a constant angular velocity during physical vapor deposition. However, the nanowires may be slanted at an angle α to the normal to the substrate plane. One way of achieving this morphology is by rotating the substrate with a variable angular velocity [3,9]. Ideally, a slanted chiral STF thus is helicoidally nonhomogeneous about an axis that is neither tangential nor perpendicular to the substrate plane. In view of the equivalent periodicity both parallel and normal to the substrate plane, the slanted chiral STF couples the circular Bragg phenomenon (which is purely specular) to non-specular diffraction (and Rayleigh–Wood anomalies) associated with diffraction gratings [8]. The angle α totally controls the coupling of these two optical phenomenons [10,11].

In addition to the traditional planewave excitation, recent developments in near-field microscopy necessitate the consideration of other types of excitations – e.g., by evanescent waves and point dipoles [12,13]. Evanescent waves are essential constituents of beams, which are known to experience lateral shifts on reflection [14]. Dipolar sources are useful in modeling nanoprobes in the technique of scanning near-field microscopy for examining surfaces as well as for lithography [15,16]. Chiral STFs are promising candidates for these optoelectronic applications as well as bio-nanotechnological ones [17,18]. In order to further the foregoing and other applications, it is our objective here to characterize the optical responses of slanted chiral STFs to excitation by dipolar sources.

The plan of this paper is as follows. Section 2 is devoted to theoretical analysis. It provides the frequency-domain constitutive relations of a slanted chiral STF as well as its planewave response, in order to formulate the dyadic Green functions (DGFs) of a slanted chiral STF sandwiched between two vacuous half-spaces. A rigorous coupled-wave analysis (RCWA) [19–21] is stably implemented for the accurate computation of planewave diffraction. The DGFs are formulated in terms of angular spectrums of propagating and evanescent plane waves. Asymptotic evaluation of these DGFs to obtain simple expressions in the far-field limit is then performed. Section 3 is devoted to numerical results. First, the planewave response of a slanted chiral STF is studied for oblique incidence for the first time, focusing on the circular Bragg phenomenon as affected by the angle of incidence. Then, the far-field radiation patterns of dipolar sources held close to a slanted chiral STF are presented. An $\exp(-i\omega t)$ time-dependent is implicit, with ω as the angular frequency and t as time.

2. Theoretical analysis

2.1. Constitutive relations

Let the region $0 < z < d$ be occupied by a slanted chiral STF, as shown in Fig. 1, where α is the slant angle of its axis of nonhomogeneity (i.e., the helical axis) with respect to the z axis. The half-spaces $z \leqslant 0$ and $z \geqslant d$ are vacuous. The relative permittivity dyadic of the slanted chiral STF is factorable as

$$\underline{\underline{\epsilon}}(\mathbf{r},\lambda_0) = \underline{\underline{S}}_y(-\alpha)\cdot\underline{\underline{S}}_z(\mathbf{r})\cdot\underline{\underline{S}}_y(\chi_s)\cdot\underline{\underline{\epsilon}}_{\mathrm{ref}}(\lambda_0)\cdot\underline{\underline{S}}_z^{\mathrm{T}}(\chi_s)\cdot\underline{\underline{S}}_z^{\mathrm{T}}(\mathbf{r})\cdot\underline{\underline{S}}_y^{\mathrm{T}}(-\alpha),\quad 0<z<d, \tag{1}$$

where the position vector $\mathbf{r} = x\mathbf{u}_x + y\mathbf{u}_y + z\mathbf{u}_z$, λ_0 is the free-space wavelength, and the superscript T denotes the transpose. As most STFs are locally orthorhombic [22,23], the reference relative permittivity dyadic is given by [6]

$$\underline{\underline{\epsilon}}_{\mathrm{ref}}(\lambda_0) = \epsilon_a(\lambda_0)\mathbf{u}_z\mathbf{u}_z + \epsilon_b(\lambda_0)\mathbf{u}_x\mathbf{u}_x + \epsilon_c(\lambda_0)\mathbf{u}_y\mathbf{u}_y. \tag{2}$$

The wavelength-dependences of the scalars $\epsilon_{a,b,c}$ are assumed in Section 3 to emerge from a single-resonance Lorentzian model [24,25] as

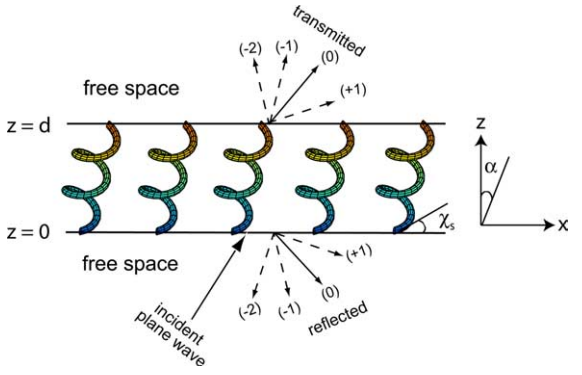

Fig. 1. Schematic of the boundary value problem involving a slanted chiral STF of thickness d illuminated by an obliquely incident plane wave. Both specular ($n = 0$) and nonspecular ($n \neq 0$) reflections and transmissions occur when $\alpha > 0$, but all nonspecular reflections/transmissions fold into the specular reflection/transmission when $\alpha = 0$.

$$\epsilon_{a,b,c}(\lambda_0) = 1 + \frac{p_{a,b,c}}{\left[1 + \left(N_{a,b,c}^{-1} - \mathrm{i}\lambda_{a,b,c}\lambda_0^{-1}\right)^2\right]}, \qquad (3)$$

where $p_{a,b,c}$ are the oscillator strengths. The parameters $\lambda_{a,b,c}$ and $N_{a,b,c}$ determine the resonance wavelengths and absorption linewidths.

The rotational nonhomogeneity of the chosen thin film is captured by the rotation dyadic

$$\underline{\underline{S}}_z(\mathbf{r}) = \left(\mathbf{u}_x\mathbf{u}_x + \mathbf{u}_y\mathbf{u}_y\right)\cos\left[\frac{\pi}{\Omega}(\mathbf{r}\cdot\mathbf{u}_\ell)\right] + h\left(\mathbf{u}_y\mathbf{u}_x - \mathbf{u}_x\mathbf{u}_y\right) \times \sin\left[\frac{\pi}{\Omega}(\mathbf{r}\cdot\mathbf{u}_\ell)\right] + \mathbf{u}_z\mathbf{u}_z, \qquad (4)$$

the helical axis being parallel to the unit vector $\mathbf{u}_\ell = \mathbf{u}_x\sin\alpha + \mathbf{u}_z\cos\alpha$. The structural period along the helical axis is denoted by 2Ω. The parameter $h = 1$ for structural right-handedness, while $h = -1$ for structural left-handedness. The dyadic

$$\underline{\underline{S}}_y(\sigma) = \left(\mathbf{u}_x\mathbf{u}_x + \mathbf{u}_z\mathbf{u}_z\right)\cos\sigma + \left(\mathbf{u}_x\mathbf{u}_z - \mathbf{u}_z\mathbf{u}_x\right)\sin\sigma + \mathbf{u}_y\mathbf{u}_y \qquad (5)$$

serves two different roles: whereas $\underline{\underline{S}}_y(\chi_s)$ delineates the role of the growth process with $(\pi/2) - \chi_s$ being the angle of declination from the helical axis, $\underline{\underline{S}}_y(-\alpha)$ represents the slanted orientation of that axis. The slant angle α is restricted to the range $(-\chi_s, \chi_s)$ due to the fact that the helical nanowires of a slanted chiral STF must be pointed upwards in relation to the substrate plane [10]. When $\alpha = 0$, the slant is absent and the usual chiral STFs are represented by $\underline{\underline{\epsilon}}(\mathbf{r}, \lambda_0) \equiv \underline{\underline{\epsilon}}(z, \lambda_0)$. From here onwards, the dependences of various quantities on λ_0 are implicit.

2.2. Rigorous coupled-wave theory for planewave incidence

The next step is to formulate the response of a slanted chiral STF to an obliquely incident plane wave. Let the incident plane wave propagate with the wavevector $\mathbf{k}_\mathrm{i} = k_x^{(0)}\mathbf{u}_x + k_y^{(0)}\mathbf{u}_y + k_z^{(0)}\mathbf{u}_z$ from the lower half-space $z \leqslant 0$, as shown also in Fig. 1. The incident, the reflected and transmitted electromagnetic field phasors are expressed in a set of Floquet harmonics, respectively, as follows [10]:

$$\mathbf{E}_\mathrm{i} = \sum_{n\in\mathbb{Z}}\left(\mathbf{L}_+^{(n)}a_\mathrm{L}^{(n)} + \mathbf{R}_+^{(n)}a_\mathrm{R}^{(n)}\right)\exp\left(\mathrm{i}\mathbf{k}_+^{(n)}\cdot\mathbf{r}\right), \quad z \leqslant 0, \qquad (6)$$

$$\mathbf{H}_\mathrm{i} = \frac{-\mathrm{i}}{\eta_0}\sum_{n\in\mathbb{Z}}\left(\mathbf{L}_+^{(n)}a_\mathrm{L}^{(n)} - \mathbf{R}_+^{(n)}a_\mathrm{R}^{(n)}\right)\exp\left(\mathrm{i}\mathbf{k}_+^{(n)}\cdot\mathbf{r}\right), \quad z \leqslant 0, \qquad (7)$$

$$\mathbf{E}_\mathrm{r} = \sum_{n\in\mathbb{Z}}\left(\mathbf{L}_-^{(n)}r_\mathrm{L}^{(n)} + \mathbf{R}_-^{(n)}r_\mathrm{R}^{(n)}\right)\exp\left(\mathrm{i}\mathbf{k}_-^{(n)}\cdot\mathbf{r}\right), \quad z \leqslant 0, \qquad (8)$$

$$\mathbf{H}_\mathrm{r} = \frac{-\mathrm{i}}{\eta_0}\sum_{n\in\mathbb{Z}}\left(\mathbf{L}_-^{(n)}r_\mathrm{L}^{(n)} - \mathbf{R}_-^{(n)}r_\mathrm{R}^{(n)}\right)\exp\left(\mathrm{i}\mathbf{k}_-^{(n)}\cdot\mathbf{r}\right), \quad z \leqslant 0, \qquad (9)$$

$$\mathbf{E}_\mathrm{t} = \sum_{n\in\mathbb{Z}}\left(\mathbf{L}_+^{(n)}t_\mathrm{L}^{(n)} + \mathbf{R}_+^{(n)}t_\mathrm{R}^{(n)}\right)\exp\left[\mathrm{i}\mathbf{k}_+^{(n)}\cdot(\mathbf{r} - d\mathbf{u}_z)\right], \quad z \geqslant d, \qquad (10)$$

$$\mathbf{H}_\mathrm{t} = \frac{-\mathrm{i}}{\eta_0}\sum_{n\in\mathbb{Z}}\left(\mathbf{L}_+^{(n)}t_\mathrm{L}^{(n)} - \mathbf{R}_+^{(n)}t_\mathrm{R}^{(n)}\right)\exp\left[\mathrm{i}\mathbf{k}_+^{(n)}\cdot(\mathbf{r} - d\mathbf{u}_z)\right], \quad z \geqslant d. \qquad (11)$$

In (6)–(11) and hereafter, $k_0 = \omega\sqrt{\mu_0\epsilon_0} = 2\pi/\lambda_0$ is the free-space wavenumber and $\eta_0 = \sqrt{\mu_0/\epsilon_0}$ is the intrinsic impedance of free space; while $\{a_\mathrm{L}^{(n)}, a_\mathrm{R}^{(n)}\}$, $\{r_\mathrm{L}^{(n)}, r_\mathrm{R}^{(n)}\}$ and $\{t_\mathrm{L}^{(n)}, t_\mathrm{R}^{(n)}\}$, respectively, are complex-valued amplitudes of the left- and right-circularly polarized (LCP and RCP) components of the nth-order harmonic constituent of the incident, reflected and transmitted fields. The symbol $\mathbb{Z}$ represents the set $\{0, \pm1, \pm2, \ldots\}$ of all integers.

The wavevectors $\mathbf{k}_{\pm}^{(n)}$ as well as the circular polarization vectors $\mathbf{L}_{\pm}^{(n)}$ and $\mathbf{R}_{\pm}^{(n)}$ of the nth-order harmonics are compatible with the phase-matching and the Floquet conditions; thus,

$$\mathbf{k}_{\pm}^{(n)} = k_x^{(n)}\mathbf{u}_x + k_y^{(0)}\mathbf{u}_y \pm k_z^{(n)}\mathbf{u}_z, \tag{12}$$

$$\mathbf{L}_{\pm}^{(n)} = \pm\left(\mathrm{i}\mathbf{s}^{(n)} - \mathbf{p}_{\pm}^{(n)}\right)\Big/\sqrt{2}, \tag{13}$$

$$\mathbf{R}_{\pm}^{(n)} = \mp\left(\mathrm{i}\mathbf{s}^{(n)} + \mathbf{p}_{\pm}^{(n)}\right)\Big/\sqrt{2}. \tag{14}$$

In these expressions, the vectors

$$\mathbf{s}^{(n)} = \frac{-k_y^{(0)}}{k_{xy}^{(n)}}\mathbf{u}_x + \frac{k_x^{(n)}}{k_{xy}^{(n)}}\mathbf{u}_y, \tag{15}$$

$$\mathbf{p}_{\pm}^{(n)} = \mp\frac{k_z^{(n)}}{k_0}\left(\frac{k_x^{(n)}}{k_{xy}^{(n)}}\mathbf{u}_x + \frac{k_y^{(0)}}{k_{xy}^{(n)}}\mathbf{u}_y\right) + \frac{k_{xy}^{(n)}}{k_0}\mathbf{u}_z \tag{16}$$

help denote linearly polarized planar fields of s- and p-types, in electromagnetics literature [8,26], with respect to the wavevector $\mathbf{k}_{\pm}^{(n)}$. The scalars

$$k_x^{(n)} = k_x^{(0)} + n\kappa_x, \tag{17}$$

$$k_z^{(n)} = +\sqrt{k_0^2 - \left(k_{xy}^{(n)}\right)^2}, \tag{18}$$

$$k_{xy}^{(n)} = \sqrt{\left(k_x^{(n)}\right)^2 + \left(k_y^{(0)}\right)^2}, \tag{19}$$

$$\kappa_x = (\pi/\Omega)|\sin\alpha| \tag{20}$$

depend on the transverse period $\Lambda_x = 2\Omega/|\sin\alpha|$ of the slanted chiral STF along the x axis.

The incident plane wave is the Floquet harmonic of order 0; hence, $a_{\mathrm{L}}^{(n)} = a_{\mathrm{R}}^{(n)} = 0\ \forall n \neq 0$. Since $\{a_{\mathrm{L}}^{(n)}, a_{\mathrm{R}}^{(n)}\}$ are supposed to be known, the amplitude sets $\{r_{\mathrm{L}}^{(n)}, r_{\mathrm{R}}^{(n)}\}$ and $\{t_{\mathrm{L}}^{(n)}, t_{\mathrm{R}}^{(n)}\}$ need to be determined. The RCWA, which is widely used for 1D and 2D grating diffraction problems, permits us to delineate the spectral characteristics of planewave diffraction by a slanted chiral STF as follows.

The spatially periodic variation of $\underline{\underline{\epsilon}}(\mathbf{r})$ of (1) is represented by the Fourier expansion

$$\underline{\underline{\epsilon}}(\mathbf{r}) = \sum_{n\in\mathbb{Z}} \underline{\underline{\epsilon}}^{(n)} \exp\left[\mathrm{i}n(\kappa_x x + \kappa_z z)\right], \quad 0 < z < d, \tag{21}$$

where

$$\underline{\underline{\epsilon}}^{(n)} = \sum_{\sigma,\sigma'} \epsilon_{\sigma\sigma'}^{(n)} \mathbf{u}_\sigma \mathbf{u}_{\sigma'}, \quad \sigma, \sigma' = x, y, z \tag{22}$$

are constant-value dyadics; and $\kappa_z = (\pi/\Omega)\cos\alpha$ is in accord with the period $\Lambda_z = 2\Omega/\cos\alpha$ of the slanted chiral STF normal to the substrate plane (i.e., along the z axis). Wave propagation occurs inside the chosen thin film such that the electromagnetic field phasors therein can be decomposed as

$$\mathbf{E}(\mathbf{r}) = \sum_{n\in\mathbb{Z}} \left[E_x^{(n)}(z)\mathbf{u}_x + E_y^{(n)}(z)\mathbf{u}_y + E_z^{(n)}(z)\mathbf{u}_z\right] \times \exp\left[\mathrm{i}\left(k_x^{(n)}x + k_y^{(0)}y\right)\right], \tag{23}$$

$$\mathbf{H}(\mathbf{r}) = \sum_{n\in\mathbb{Z}} \left[H_x^{(n)}(z)\mathbf{u}_x + H_y^{(n)}(z)\mathbf{u}_y + H_z^{(n)}(z)\mathbf{u}_z\right] \times \exp\left[\mathrm{i}\left(k_x^{(n)}x + k_y^{(0)}y\right)\right], \tag{24}$$

where $E_{x,y,z}^{(n)}$ and $H_{x,y,z}^{(n)}$ are unknown functions of $z \in (0, d)$. Following Chateau and Hugonin [21], we also define

$$\left.\begin{aligned} \tilde{E}_\sigma^{(n)}(z) &= E_\sigma^{(n)}(z)\exp(-\mathrm{i}n\kappa_z z) \\ \tilde{H}_\sigma^{(n)}(z) &= H_\sigma^{(n)}(z)\exp(-\mathrm{i}n\kappa_z z) \end{aligned}\right\}, \quad \sigma = x, y, z. \tag{25}$$

On substituting (21)–(25) in the the frequency-domain Maxwell curl postulates

$$\left.\begin{aligned} \nabla\times\mathbf{E}(\mathbf{r}) &= \mathrm{i}\omega\mu_0\mathbf{H}(\mathbf{r}) \\ \nabla\times\mathbf{H}(\mathbf{r}) &= -\mathrm{i}\omega\epsilon_0\underline{\underline{\epsilon}}(\mathbf{r})\cdot\mathbf{E}(\mathbf{r}) \end{aligned}\right\}, \quad 0 < z < d, \tag{26}$$

and exploiting the orthogonalities of the functions $\exp(\mathrm{i}\mathbf{k}_{\pm}^{(n)}\cdot\mathbf{r})$ across any plane $z =$ constant, we derive the following set of coupled-wave equations:

$$\frac{\mathrm{d}}{\mathrm{d}z}\tilde{E}_x^{(n)}(z) + \mathrm{i}n\kappa_z\tilde{E}_x^{(n)}(z) - \mathrm{i}k_x^{(n)}\tilde{E}_z^{(n)}(z) = ik_0\eta_0\tilde{H}_y^{(n)}(z), \tag{27}$$

$$\frac{\mathrm{d}}{\mathrm{d}z}\tilde{E}_y^{(n)}(z) + \mathrm{i}n\kappa_z\tilde{E}_y^{(n)}(z) - \mathrm{i}k_y^{(0)}\tilde{E}_z^{(n)}(z) = -\mathrm{i}k_0\eta_0\tilde{H}_x^{(n)}(z), \tag{28}$$

$$k_y^{(0)}\tilde{E}_x^{(n)}(z) - k_x^{(n)}\tilde{E}_y^{(n)}(z) = -k_0\eta_0\tilde{H}_z^{(n)}(z), \tag{29}$$

$$\frac{\mathrm{d}}{\mathrm{d}z}\tilde{H}_x^{(n)}(z) + \mathrm{i}n\kappa_z\tilde{H}_x^{(n)}(z) - ik_x^{(n)}\tilde{H}_z^{(n)}(z) = -\frac{\mathrm{i}k_0}{\eta_0}\sum_{n'\in\mathbb{Z}}\left[\epsilon_{yx}^{(n-n')}\tilde{E}_x^{(n')}(z) + \epsilon_{yy}^{(n-n')}\tilde{E}_y^{(n')}(z) + \epsilon_{yz}^{(n-n')}\tilde{E}_z^{(n')}(z)\right], \tag{30}$$

$$\frac{\mathrm{d}}{\mathrm{d}z}\tilde{H}_y^{(n)}(z) + \mathrm{i}n\kappa_z\tilde{H}_y^{(n)}(z) - ik_y^{(0)}\tilde{H}_z^{(n)}(z) = \frac{\mathrm{i}k_0}{\eta_0}\sum_{n'\in\mathbb{Z}}\left[\epsilon_{xx}^{(n-n')}\tilde{E}_x^{(n')}(z) + \epsilon_{xy}^{(n-n')}\tilde{E}_y^{(n')}(z) + \epsilon_{xz}^{(n-n')}\tilde{E}_z^{(n')}(z)\right], \tag{31}$$

$$k_y^{(0)}\tilde{H}_x^{(n)}(z) - k_x^{(n)}\tilde{H}_y^{(n)}(z) = \frac{k_0}{\eta_0}\sum_{n'\in\mathbb{Z}}\left[\epsilon_{zx}^{(n-n')}\tilde{E}_x^{(n')}(z) + \epsilon_{zy}^{(n-n')}\tilde{E}_y^{(n')}(z) + \epsilon_{zz}^{(n-n')}\tilde{E}_z^{(n')}(z)\right]. \tag{32}$$

Eqs. (27)–(32) hold for all $n \in \mathbb{Z}$, and are thus an infinite system of first-order ordinary differential equations (ODEs). For numerical solution, we first restrict the summations on their right sides to $|n| \leqslant N_\mathrm{t}$, and then define the four column vectors

$$\left.\begin{aligned}\left[\underline{\tilde{E}}_\sigma(z)\right] &= \left[\tilde{E}_\sigma^{(n)}(z)\right], \quad [\underline{E}_\sigma(z)] = \left[E_\sigma^{(n)}(z)\right]\\ \left[\underline{\tilde{H}}_\sigma(z)\right] &= \left[\tilde{H}_\sigma^{(n)}(z)\right], \quad [\underline{H}_\sigma(z)] = \left[H_\sigma^{(n)}(z)\right]\end{aligned}\right\}, \quad \sigma = x,y,z;\ n \in [-N_\mathrm{t}, N_\mathrm{t}] \tag{33}$$

of size $(2N_\mathrm{t}+1)$. Likewise, we define the diagonal $(2N_\mathrm{t}+1)\times(2N_\mathrm{t}+1)$ matrixes

$$\left.\begin{aligned}\left[\underline{\underline{K}}_x\right] &= \left[k_x^{(n)}\delta_{n,n'}\right]\\ \left[\underline{\underline{\kappa}}_z\right] &= \kappa_z\left[n\delta_{n,n'}\right]\end{aligned}\right\}, \quad n,n' \in [-N_\mathrm{t}, N_\mathrm{t}], \tag{34}$$

where $\delta_{n,n'}$ is the Kronecker delta, and the Toeplitz matrixes

$$\left[\underline{\underline{\epsilon}}_{\sigma\sigma'}\right] = \left[\epsilon_{\sigma\sigma'}^{(n-n')}\right], \quad \sigma = x,y,z;\ n,n' \in [-N_\mathrm{t}, N_\mathrm{t}]. \tag{35}$$

Substituting (29) and (32) into (27), (28), (30) and (31) thereafter, in order to eliminate the normal electromagnetic fields components (i.e., $\tilde{E}_z^{(n)}$ and $\tilde{H}_z^{(n)}$), and performing some algebraic manipulations, we derive the shift-invariant matrix ODE [27]

$$\frac{\mathrm{d}}{\mathrm{d}z}\left[\underline{\tilde{\mathbf{f}}}(z)\right] = \mathrm{i}\left[\underline{\underline{\tilde{\mathbf{P}}}}\right]\left[\underline{\tilde{\mathbf{f}}}(z)\right], \quad 0 < z < d. \tag{36}$$

The column vector

$$\left[\underline{\tilde{\mathbf{f}}}(z)\right] = \left[\left[\underline{\tilde{E}}_x(z)\right]^\mathrm{T}, \left[\underline{\tilde{E}}_y(z)\right]^\mathrm{T}, \eta_0\left[\underline{\tilde{H}}_x(z)\right]^\mathrm{T}, \eta_0\left[\underline{\tilde{H}}_y(z)\right]^\mathrm{T}\right]^\mathrm{T} \tag{37}$$

contains $4(2N_\mathrm{t}+1)$ components, and the z-independent matrix $[\underline{\underline{\tilde{\mathbf{P}}}}]$ is given in Appendix A.

The matrix ODE (36) has the solution [28]

$$\left[\underline{\tilde{\mathbf{f}}}(z_2)\right] = \left[\underline{\underline{\tilde{\mathbf{G}}}}\right]\exp\left\{\mathrm{i}(z_2-z_1)\left[\underline{\underline{\tilde{\mathbf{D}}}}\right]\right\}\left[\underline{\underline{\tilde{\mathbf{G}}}}\right]^{-1}\left[\underline{\tilde{\mathbf{f}}}(z_1)\right], \tag{38}$$

where the columns of the square matrix $[\underline{\underline{\tilde{\mathbf{G}}}}]$ are the successive eigenvectors of $[\underline{\underline{\tilde{\mathbf{P}}}}]$, and the diagonal matrix $[\underline{\underline{\tilde{\mathbf{D}}}}]$ contains the corresponding eigenvalues of $[\underline{\underline{\tilde{\mathbf{P}}}}]$. The assumption here is that $[\underline{\underline{\tilde{\mathbf{P}}}}]$ is diagonalizable, i.e., it has $4(2N_\mathrm{t}+1)$ linearly independent eigenvectors.

In order to solve the boundary value problem, we have to determine the column vector

$$\left[\underline{\mathbf{f}}(z)\right] = \left[[\underline{E}_x(z)]^\mathrm{T}, [\underline{E}_y(z)]^\mathrm{T}, \eta_0[\underline{H}_x(z)]^\mathrm{T}, \eta_0[\underline{H}_y(z)]^\mathrm{T}\right]^\mathrm{T} \tag{39}$$

instead of $[\underline{\tilde{\mathbf{f}}}(z)]$. The two column vectors are simply related to each other as

$$\left[\underline{\mathbf{f}}(z)\right] = \left[\underline{\underline{\mathbf{C}}}(z)\right]\left[\underline{\tilde{\mathbf{f}}}(z)\right], \tag{40}$$

where the diagonal matrix

$$\left[\underline{\underline{\mathbf{C}}}(z)\right] = \left[\exp(\mathrm{i}\tilde{n}\kappa_z z)\delta_{n,n'}\right], \quad n,n' \in [1, 4(2N_\mathrm{t}+1)]; \tag{41}$$

$\tilde{n} = \mathrm{Mod}[n-1, 2N_\mathrm{t}+1] - N_\mathrm{t}$ and $\mathrm{Mod}[m,m']$ denotes the remainder when m is divided by m', with m and m' being positive integers. According to (38) and (40), we obtain the relation

$$\left[\underline{\mathbf{f}}(z_2)\right] = \left[\underline{\underline{\mathbf{G}}}(z_2)\right]\exp\left\{\mathrm{i}(z_2-z_1)\left[\underline{\underline{\tilde{\mathbf{D}}}}\right]\right\} \times \left[\underline{\underline{\mathbf{G}}}(z_1)\right]^{-1}\left[\underline{\mathbf{f}}(z_1)\right], \tag{42}$$

where the matrix

$$\left[\underline{\underline{\mathbf{G}}}(z)\right] = \left[\underline{\underline{\mathbf{C}}}(z)\right]\left[\underline{\underline{\tilde{\mathbf{G}}}}\right] \tag{43}$$

is a periodic function of z; hence,

$$\left[\underline{\mathbf{f}}(d)\right] = \left[\underline{\underline{\mathbf{G}}}(d)\right]\exp\left\{\mathrm{i}d\left[\underline{\underline{\tilde{\mathbf{D}}}}\right]\right\}\left[\underline{\underline{\mathbf{G}}}(0)\right]^{-1}\left[\underline{\mathbf{f}}(0)\right]. \tag{44}$$

The continuity of the tangential components of the electric and magnetic field phasors across the two boundaries $z = 0$ and $z = d$ must be enforced with respect to the Floquet harmonic of any order n. Therefore, we get

$$\begin{aligned}\left[\underline{\mathbf{f}}(0)\right] &= \begin{bmatrix}\left[\underline{\underline{Y}}_{\mathrm{e}}^{+}\right] & \left[\underline{\underline{Y}}_{\mathrm{e}}^{-}\right]\\ \left[\underline{\underline{Y}}_{\mathrm{h}}^{+}\right] & \left[\underline{\underline{Y}}_{\mathrm{h}}^{-}\right]\end{bmatrix}\begin{bmatrix}[\underline{\mathbf{A}}]\\ [\underline{\mathbf{R}}]\end{bmatrix},\\ \left[\underline{\mathbf{f}}(d)\right] &= \begin{bmatrix}\left[\underline{\underline{Y}}_{\mathrm{e}}^{+}\right] & [\underline{0}]\\ \left[\underline{\underline{Y}}_{\mathrm{h}}^{+}\right] & [\underline{0}]\end{bmatrix}\begin{bmatrix}[\underline{\mathbf{T}}]\\ [\underline{0}]\end{bmatrix},\end{aligned} \tag{45}$$

where the column vectors

$$[\underline{\mathbf{A}}] = \begin{bmatrix}a_{\mathrm{L}}^{(n)}\\ a_{\mathrm{R}}^{(n)}\end{bmatrix},\quad [\underline{\mathbf{R}}] = \begin{bmatrix}r_{\mathrm{L}}^{(n)}\\ r_{\mathrm{R}}^{(n)}\end{bmatrix},\quad [\underline{\mathbf{T}}] = \begin{bmatrix}t_{\mathrm{L}}^{(n)}\\ t_{\mathrm{R}}^{(n)}\end{bmatrix} \tag{46}$$

are of size $4N_{\mathrm{t}} + 2$. The square matrixes $[\underline{\underline{Y}}_{\mathrm{e}}^{\pm}]$ and $[\underline{\underline{Y}}_{\mathrm{h}}^{\pm}]$ of size $(4N_{\mathrm{t}} + 2) \times (4N_{\mathrm{t}} + 2)$ are quite sparse; and their nonzero entries are calculated as follows:

$$\begin{aligned}&\left[\underline{\underline{Y}}_{\mathrm{e}}^{\pm}\right]_{nn'} = -\mathrm{i}\left[\underline{\underline{Y}}_{\mathrm{h}}^{\pm}\right]_{nn'} = \mathbf{L}_{\pm}^{(n)}\cdot\mathbf{u}_x\\ &\quad \text{if } n = n' \in [1, (2N_{\mathrm{t}}+1)],\\ &\left[\underline{\underline{Y}}_{\mathrm{e}}^{\pm}\right]_{nn'} = -\mathrm{i}\left[\underline{\underline{Y}}_{\mathrm{h}}^{\pm}\right]_{nn'} = \mathbf{L}_{\pm}^{(n)}\cdot\mathbf{u}_y\\ &\quad \text{if } n = n' + 2N_{\mathrm{t}} + 1,\\ &\left[\underline{\underline{Y}}_{\mathrm{e}}^{\pm}\right]_{nn'} = \mathrm{i}\left[\underline{\underline{Y}}_{\mathrm{h}}^{\pm}\right]_{nn'} = \mathbf{R}_{\pm}^{(n)}\cdot\mathbf{u}_x\\ &\quad \text{if } n = n' - 2N_{\mathrm{t}} - 1,\\ &\left[\underline{\underline{Y}}_{\mathrm{e}}^{\pm}\right]_{nn'} = \mathrm{i}\left[\underline{\underline{Y}}_{\mathrm{h}}^{\pm}\right]_{nn'} = \mathbf{R}_{\pm}^{(n)}\cdot\mathbf{u}_y\\ &\quad \text{if } n = n' \in [(2N_{\mathrm{t}}+2), (4N_{\mathrm{t}}+2)].\end{aligned} \tag{47}$$

Finally, substituting (45) into (44), we get

$$\begin{aligned}&\begin{bmatrix}\left[\underline{\underline{U}}_{\mathrm{T}}\right]\\ \left[\underline{\underline{V}}_{\mathrm{T}}\right]\end{bmatrix}[\underline{\mathbf{T}}] + \begin{bmatrix}\mathrm{e}^{\mathrm{i}d\left[\underline{\underline{\tilde{D}}}_1\right]} & [\underline{0}]\\ [\underline{0}] & \mathrm{e}^{\mathrm{i}d\left[\underline{\underline{\tilde{D}}}_2\right]}\end{bmatrix}\begin{bmatrix}\left[\underline{\underline{U}}_{R}\right]\\ \left[\underline{\underline{V}}_{R}\right]\end{bmatrix}[\underline{\mathbf{R}}]\\ &\quad = \begin{bmatrix}\mathrm{e}^{\mathrm{i}d\left[\underline{\underline{\tilde{D}}}_1\right]} & [\underline{0}]\\ [\underline{0}] & \mathrm{e}^{\mathrm{i}d\left[\underline{\underline{\tilde{D}}}_2\right]}\end{bmatrix}\begin{bmatrix}\left[\underline{\underline{U}}_{A}\right]\\ \left[\underline{\underline{V}}_{A}\right]\end{bmatrix}[\underline{\mathbf{A}}],\end{aligned} \tag{48}$$

where $[\underline{\underline{\tilde{D}}}_1]$ and $[\underline{\underline{\tilde{D}}}_2]$ are the upper and lower diagonal submatrixes of $[\underline{\underline{\tilde{\mathbf{D}}}}]$, respectively, and the rectangular matrixes

$$\begin{bmatrix}\left[\underline{\underline{U}}_{T}\right]\\ \left[\underline{\underline{V}}_{T}\right]\end{bmatrix} = \left[\underline{\underline{\mathbf{G}}}(d)\right]^{-1}\begin{bmatrix}\left[\underline{\underline{Y}}_{\mathrm{e}}^{+}\right]\\ \left[\underline{\underline{Y}}_{\mathrm{h}}^{+}\right]\end{bmatrix} \tag{49}$$

$$\begin{bmatrix}\left[\underline{\underline{U}}_{R}\right]\\ \left[\underline{\underline{V}}_{R}\right]\end{bmatrix} = -\left[\underline{\underline{\mathbf{G}}}(0)\right]^{-1}\begin{bmatrix}\left[\underline{\underline{Y}}_{\mathrm{e}}^{-}\right]\\ \left[\underline{\underline{Y}}_{\mathrm{h}}^{-}\right]\end{bmatrix}, \tag{50}$$

$$\begin{bmatrix}\left[\underline{\underline{U}}_{A}\right]\\ \left[\underline{\underline{V}}_{A}\right]\end{bmatrix} = \left[\underline{\underline{\mathbf{G}}}(0)\right]^{-1}\begin{bmatrix}\left[\underline{\underline{Y}}_{\mathrm{e}}^{+}\right]\\ \left[\underline{\underline{Y}}_{\mathrm{h}}^{+}\right]\end{bmatrix}, \tag{51}$$

are defined for the notational brevity.

For calculating the unknown $[\underline{\mathbf{R}}]$ and $[\underline{\mathbf{T}}]$, the R-matrix propagating algorithm [21,29] – which is based on the rearrangement of the positions of the eigenvalues of $[\underline{\underline{\tilde{\mathbf{P}}}}]$ in the diagonal matrix $[\underline{\underline{\tilde{\mathbf{D}}}}]$ – should be utilized in order to avoid numerical instabilities, especially when N_{t} is large [19,20]. Therefore, the entries on the diagonal of $[\underline{\underline{\tilde{\mathbf{D}}}}]$ (thus $[\underline{\underline{\tilde{D}}}_1]$ and $[\underline{\underline{\tilde{D}}}_2]$ also) are rearranged in increasing order of the imaginary part, and the columns of $[\underline{\underline{\tilde{\mathbf{G}}}}]$ are rearranged accordingly. The final algebraic equation

$$\begin{aligned}&\begin{bmatrix}\mathrm{e}^{-\mathrm{i}d\left[\underline{\underline{\tilde{D}}}_1\right]}\left[\underline{\underline{U}}_{T}\right] & \left[\underline{\underline{U}}_{R}\right]\\ \left[\underline{\underline{V}}_{T}\right] & \mathrm{e}^{\mathrm{i}d\left[\underline{\underline{\tilde{D}}}_2\right]}\left[\underline{\underline{V}}_{R}\right]\end{bmatrix}\begin{bmatrix}[\underline{\mathbf{T}}]\\ [\underline{\mathbf{R}}]\end{bmatrix}\\ &\quad = \begin{bmatrix}\left[\underline{\underline{U}}_{A}\right]\\ \mathrm{e}^{\mathrm{i}d\left[\underline{\underline{\tilde{D}}}_2\right]}\left[\underline{\underline{V}}_{A}\right]\end{bmatrix}[\underline{\mathbf{A}}],\end{aligned} \tag{52}$$

yielded by (48) for the determination of $[\underline{\mathbf{R}}]$ and $[\underline{\mathbf{T}}]$ is algorithmically stable due to the fact that the

exponential terms $e^{id[\tilde{\underline{D}}_1]}$ and $e^{id[\tilde{\underline{D}}_2]}$ will never become overwhelming in magnitude because of the rearrangement of the eigenvalues. The matrix inverse operation required to solve (52) for $[\underline{\mathbf{R}}]$ and $[\underline{\mathbf{T}}]$ is then easily accomplished, using standard techniques [30], for arbitrary d and N_t.

Once $[\underline{\mathbf{R}}]$ and $[\underline{\mathbf{T}}]$ have been determined, the nth-order reflection and transmission coefficients

$$r_{IJ}^{(n)} = \frac{r_I^{(n)}}{a_J^{(0)}}, \quad t_{IJ}^{(n)} = \frac{t_I^{(n)}}{a_J^{(0)}}, \quad I,J = \mathrm{L},\mathrm{R} \tag{53}$$

can be computed as functions of the wavevector $\mathbf{k}_i = \mathbf{k}_+^{(0)}$ of the incident plane wave. Reflectances ($R_{\mathrm{LL}}^{(n)}$, etc.) and transmittances ($T_{\mathrm{LL}}^{(n)}$, etc.) of order n can be additionally calculated as

$$\begin{aligned} R_{IJ}^{(n)} &= \frac{\mathrm{Re}[k_z^{(n)}]}{\mathrm{Re}[k_z^{(0)}]} |r_{IJ}^{(n)}|^2, \\ T_{IJ}^{(n)} &= \frac{\mathrm{Re}[k_z^{(n)}]}{\mathrm{Re}[k_z^{(0)}]} |t_{IJ}^{(n)}|^2, \quad I,J = \mathrm{L},\mathrm{R}. \end{aligned} \tag{54}$$

2.3. Dyadic Green functions

Let us now synthesize the DGFs of a slanted chiral STF bounded by two vacuous half-spaces.

Suppose initially that the slanted chiral STF is absent; then the electric field phasors *everywhere* can be derived as [31]

$$\begin{aligned} \mathbf{E}(\mathbf{r}) = {} & \mathrm{i}\omega\mu_0 \int\int\int_{\mathbb{R}^3} \underline{\underline{\mathbf{G}}}_0(\mathbf{r},\mathbf{r}') \cdot \mathbf{J}(\mathbf{r}')\, \mathrm{d}^3\mathbf{r}' \\ & - \nabla \times \int\int\int_{\mathbb{R}^3} \underline{\underline{\mathbf{G}}}_0(\mathbf{r},\mathbf{r}') \cdot \mathbf{K}(\mathbf{r}')\, \mathrm{d}^3\mathbf{r}', \end{aligned} \tag{55}$$

where $\mathbf{J}(\mathbf{r}')$ and $\mathbf{K}(\mathbf{r}')$ are the externally impressed electric and magnetic current densities, respectively, at the source position $\mathbf{r}'$; while

$$\underline{\underline{\mathbf{G}}}_0(\mathbf{r},\mathbf{r}') = \left(\underline{\underline{\mathbf{I}}} + k_0^{-2}\nabla\nabla\right)[\exp(\mathrm{i}k_0|\mathbf{R}|)/4\pi|\mathbf{R}|] \tag{56}$$

is the infinite-medium DGF for free space. Here and hereafter, $\mathbf{R} = \mathbf{r} - \mathbf{r}'$ and $\underline{\underline{\mathbf{I}}}$ is the identity dyadic.

In consonance with the distinguished role of structural handedness, sources of circularly polarized plane waves are preferred. Hence, we define two Beltrami source densities [32]

$$\mathbf{W}_{\mathrm{L}} = \mathbf{J} + \mathrm{i}\omega\epsilon_0\mathbf{K}, \tag{57}$$

$$\mathbf{W}_{\mathrm{R}} = \mathbf{J} - \mathrm{i}\omega\epsilon_0\mathbf{K} \tag{58}$$

of the left- and right-handed types, respectively. These can be synthesized as co-located pairs of electric and magnetic dipoles that are either parallel or anti-parallel. After substituting (57) and (58) into (55), the electric field can be rewritten as

$$\begin{aligned} \mathbf{E}(\mathbf{r}) = \frac{\mathrm{i}\omega\mu_0}{2} \int\int\int_{\mathbb{R}^3} \Big[& \underline{\underline{\mathbf{G}}}_{\mathrm{L}0}(\mathbf{r},\mathbf{r}') \cdot \mathbf{W}_{\mathrm{L}}(\mathbf{r}') \\ & + \underline{\underline{\mathbf{G}}}_{\mathrm{R}0}(\mathbf{r},\mathbf{r}') \cdot \mathbf{W}_{\mathrm{R}}(\mathbf{r}') \Big]\, \mathrm{d}^3\mathbf{r}', \end{aligned} \tag{59}$$

where

$$\underline{\underline{\mathbf{G}}}_{\mathrm{L}0}(\mathbf{r},\mathbf{r}') = \left(\underline{\underline{\mathbf{I}}} + k_0^{-1}\nabla\times\underline{\underline{\mathbf{I}}}\right)\underline{\underline{\mathbf{G}}}_0(\mathbf{r},\mathbf{r}'), \tag{60}$$

$$\underline{\underline{\mathbf{G}}}_{\mathrm{R}0}(\mathbf{r},\mathbf{r}') = \left(\underline{\underline{\mathbf{I}}} - k_0^{-1}\nabla\times\underline{\underline{\mathbf{I}}}\right)\underline{\underline{\mathbf{G}}}_0(\mathbf{r},\mathbf{r}'). \tag{61}$$

Next, let the slanted chiral STF occupy the region $0 < z < d$. The sources lie exclusively in the lower half-space (i.e., $z' < 0$ hereinafter) without losing generality. Then the electric field in the either of the two half-spaces bordering the thin film must be of the form

$$\begin{aligned} \mathbf{E}(\mathbf{r}) = \frac{\mathrm{i}\omega\mu_0}{2} \int\int\int_{\mathbb{R}^3} \Big[& \underline{\underline{\mathbf{G}}}_{\mathrm{L}}(\mathbf{r},\mathbf{r}') \cdot \mathbf{W}_{\mathrm{L}}(\mathbf{r}') \\ & + \underline{\underline{\mathbf{G}}}_{\mathrm{R}}(\mathbf{r},\mathbf{r}') \cdot \mathbf{W}_{\mathrm{R}}(\mathbf{r}') \Big]\, \mathrm{d}^3\mathbf{r}', \quad z \notin [0,d], \end{aligned} \tag{62}$$

where $\underline{\underline{\mathbf{G}}}_{\mathrm{L}}(\mathbf{r},\mathbf{r}')$ and $\underline{\underline{\mathbf{G}}}_{\mathrm{R}}(\mathbf{r},\mathbf{r}')$ are DGFs that take the presence of the slanted chiral STF into account. Synthesis of these two DGFs is accomplished through the decomposition

$$\underline{\underline{\mathbf{G}}}_J(\mathbf{r},\mathbf{r}') = \begin{cases} \underline{\underline{\mathbf{G}}}_{J0}(\mathbf{r},\mathbf{r}') + \underline{\underline{\mathbf{G}}}_{J\mathrm{r}}(\mathbf{r},\mathbf{r}'), & z < 0, \\ \underline{\underline{\mathbf{G}}}_{J\mathrm{t}}(\mathbf{r},\mathbf{r}'), & z > d, \end{cases} \quad J = \mathrm{L},\mathrm{R}. \tag{63}$$

As the planewave response of a slanted chiral STF can be obtained using the RCWA, $\underline{\underline{\mathbf{G}}}_{J\mathrm{r}}(\mathbf{r},\mathbf{r}')$ and $\underline{\underline{\mathbf{G}}}_{J\mathrm{t}}(\mathbf{r},\mathbf{r}')$ can be derived therefrom. Accordingly, we begin with a spectral representation of $\underline{\underline{\mathbf{G}}}_0(\mathbf{r},\mathbf{r}')$ as [33]

$$\begin{aligned} \underline{\underline{\mathbf{G}}}_0(\mathbf{r},\mathbf{r}') = {} & -k_0^{-2}\delta(\mathbf{R})\mathbf{u}_z\mathbf{u}_z + \frac{\mathrm{i}}{4\pi^2} \int_{-\infty}^{\infty}\int_{-\infty}^{\infty} \left(k_z^{(0)}\right)^{-1} \\ & \times \exp\left(\mathrm{i}\mathbf{k}_\pm^{(0)}\cdot\mathbf{R}\right)\left(\mathbf{s}^{(0)}\mathbf{s}^{(0)} + \mathbf{p}_\pm^{(0)}\mathbf{p}_\pm^{(0)}\right) \mathrm{d}k_x^{(0)}\, \mathrm{d}k_y^{(0)}, \end{aligned} \tag{64}$$

where the upper signs apply for $z > z'$ and the lower signs for $z < z'$, while $\delta(\mathbf{R})$ is the Dirac delta function. It is clear that the second part of $\underline{\underline{\mathbf{G}}}_0(\mathbf{r},\mathbf{r}')$ in (64) is an angular spectrum of both propagating and evanescent plane waves. From (60), (61) and (64), we obtain the similar expressions

$$\underline{\underline{\mathbf{G}}}_{\mathrm{L}0}(\mathbf{r},\mathbf{r}') = -k_0^{-2}\delta(\mathbf{R})\mathbf{u}_z\mathbf{u}_z + \frac{\mathrm{i}}{4\pi^2}\int_{-\infty}^{\infty}\int_{-\infty}^{\infty}\left(k_z^{(0)}\right)^{-1} \times \exp\left(\mathrm{i}\mathbf{k}_{\pm}^{(0)}\cdot\mathbf{R}\right)\mathbf{L}_{\pm}^{(0)}\mathbf{R}_{\pm}^{(0)}\,\mathrm{d}k_x^{(0)}\,\mathrm{d}k_y^{(0)}, \tag{65}$$

$$\underline{\underline{\mathbf{G}}}_{\mathrm{R}0}(\mathbf{r},\mathbf{r}') = -k_0^{-2}\delta(\mathbf{R})\mathbf{u}_z\mathbf{u}_z + \frac{\mathrm{i}}{4\pi^2}\int_{-\infty}^{\infty}\int_{-\infty}^{\infty}\left(k_z^{(0)}\right)^{-1} \times \exp\left(\mathrm{i}\mathbf{k}_{\pm}^{(0)}\cdot\mathbf{R}\right)\mathbf{R}_{\pm}^{(0)}\mathbf{L}_{\pm}^{(0)}\,\mathrm{d}k_x^{(0)}\,\mathrm{d}k_y^{(0)}, \tag{66}$$

with the upper and lower signs applied in the same way as in (64).

By strict analogy with the reflected and transmitted plane waves in Section 2.2, we synthesize the spectral representations of the remaining DGFs in (63) as

$$\underline{\underline{\mathbf{G}}}_{\mathrm{Lr}}(\mathbf{r},\mathbf{r}') = \frac{\mathrm{i}}{4\pi^2}\sum_{n\in\mathbb{Z}}\int_{-\infty}^{\infty}\int_{-\infty}^{\infty}\left(k_z^{(n)}\right)^{-1} \times \exp\left[\mathrm{i}\left(\mathbf{k}_{-}^{(n)}\cdot\mathbf{r} - \mathbf{k}_{+}^{(0)}\cdot\mathbf{r}'\right)\right]\underline{\underline{\mathscr{R}}}_{\mathrm{L}}^{(n)}\,\mathrm{d}k_x^{(0)}\,\mathrm{d}k_y^{(0)}, \quad z < 0, \tag{67}$$

$$\underline{\underline{\mathbf{G}}}_{\mathrm{Rr}}(\mathbf{r},\mathbf{r}') = \frac{\mathrm{i}}{4\pi^2}\sum_{n\in\mathbb{Z}}\int_{-\infty}^{\infty}\int_{-\infty}^{\infty}\left(k_z^{(n)}\right)^{-1} \times \exp\left[\mathrm{i}\left(\mathbf{k}_{-}^{(n)}\cdot\mathbf{r} - \mathbf{k}_{+}^{(0)}\cdot\mathbf{r}'\right)\right]\underline{\underline{\mathscr{R}}}_{\mathrm{R}}^{(n)}\,\mathrm{d}k_x^{(0)}\,\mathrm{d}k_y^{(0)}, \quad z < 0, \tag{68}$$

$$\underline{\underline{\mathbf{G}}}_{\mathrm{Lt}}(\mathbf{r},\mathbf{r}') = \frac{\mathrm{i}}{4\pi^2}\sum_{n\in\mathbb{Z}}\int_{-\infty}^{\infty}\int_{-\infty}^{\infty}\left(k_z^{(n)}\right)^{-1} \times \exp\left[\mathrm{i}\left(\mathbf{k}_{+}^{(n)}\cdot\tilde{\mathbf{r}} - \mathbf{k}_{+}^{(0)}\cdot\mathbf{r}'\right)\right]\underline{\underline{\mathscr{T}}}_{\mathrm{L}}^{(n)}\,\mathrm{d}k_x^{(0)}\,\mathrm{d}k_y^{(0)}, \quad z > d, \tag{69}$$

$$\underline{\underline{\mathbf{G}}}_{\mathrm{Rt}}(\mathbf{r},\mathbf{r}') = \frac{\mathrm{i}}{4\pi^2}\sum_{n\in\mathbb{Z}}\int_{-\infty}^{\infty}\int_{-\infty}^{\infty}\left(k_z^{(n)}\right)^{-1} \times \exp\left[\mathrm{i}\left(\mathbf{k}_{+}^{(n)}\cdot\tilde{\mathbf{r}} - \mathbf{k}_{+}^{(0)}\cdot\mathbf{r}'\right)\right]\underline{\underline{\mathscr{T}}}_{\mathrm{R}}^{(n)}\,\mathrm{d}k_x^{(0)}\,\mathrm{d}k_y^{(0)}, \quad z > d, \tag{70}$$

where $\tilde{\mathbf{r}} = \mathbf{r} - d\mathbf{u}_z$. The reflection and transmission dyadics entering the four previous equations are specified as follows:

$$\underline{\underline{\mathscr{R}}}_{\mathrm{L}}^{(n)}\left(k_x^{(0)},k_y^{(0)}\right) = r_{\mathrm{LL}}^{(n)}\mathbf{L}_{-}^{(n)}\mathbf{R}_{+}^{(0)} + r_{\mathrm{RL}}^{(n)}\mathbf{R}_{-}^{(n)}\mathbf{R}_{+}^{(0)}, \tag{71}$$

$$\underline{\underline{\mathscr{R}}}_{\mathrm{R}}^{(n)}\left(k_x^{(0)},k_y^{(0)}\right) = r_{\mathrm{LR}}^{(n)}\mathbf{L}_{-}^{(n)}\mathbf{L}_{+}^{(0)} + r_{\mathrm{RR}}^{(n)}\mathbf{R}_{-}^{(n)}\mathbf{L}_{+}^{(0)}, \tag{72}$$

$$\underline{\underline{\mathscr{T}}}_{\mathrm{L}}^{(n)}\left(k_x^{(0)},k_y^{(0)}\right) = t_{\mathrm{LL}}^{(n)}\mathbf{L}_{+}^{(n)}\mathbf{R}_{+}^{(0)} + t_{\mathrm{RL}}^{(n)}\mathbf{R}_{+}^{(n)}\mathbf{R}_{+}^{(0)}, \tag{73}$$

$$\underline{\underline{\mathscr{T}}}_{\mathrm{R}}^{(n)}\left(k_x^{(0)},k_y^{(0)}\right) = t_{\mathrm{LR}}^{(n)}\mathbf{L}_{+}^{(n)}\mathbf{L}_{+}^{(0)} + t_{\mathrm{RR}}^{(n)}\mathbf{R}_{+}^{(n)}\mathbf{L}_{+}^{(0)}. \tag{74}$$

As these four dyadics are related to the nth-order Floquet harmonics in the reflected and transmitted fields, all four are dependent on the wavevector $\mathbf{k}_{+}^{(0)}$. Noting that the integrands on the right sides of (67)–(70) are 2D Lebesgue-integrable if the reflection and transmission dyadics in (71)–(74) are bounded, we can carry out the integrations in (67)–(70) numerically.

2.4. Asymptotic evaluation

In many applications related with far-field radiation, only the asymptotic evaluation of the double integrals (67)–(70) in the limit $k_0|\mathbf{r}| \to \infty$ needs to be carried out. The methods of stationary phase and steepest descent path (SDP) are generally used for that purpose [34–36].

As for the double integrals, the contours of integration can be deformed to confine the integration on a local domain defined by two local SDPs [37,38]. The saddle points (or first-order critical points) along each SDP can be employed to establish the truncated Taylor expansion of the integrand, provided that the integrand term is differentiable on the mapped complex domain [38]. Following this approach, the double integrals in (67)–(70) can be asymptotically evaluated without any trouble up to the lowest order $\frac{1}{k_0|\mathbf{r}|}$, provided the observation point $\mathbf{r}$ is not close to the boundaries $z = 0$ and $z = d$, i.e., $-\frac{z}{|\mathbf{r}|} > 10\sqrt{\frac{1}{k_0|\mathbf{r}|}}$ for $z < 0$ and $\frac{(z-d)}{|\tilde{\mathbf{r}}|} > 10\sqrt{\frac{1}{k_0|\tilde{\mathbf{r}}|}}$ for $z > d$.

With the source point $\mathbf{r}'$ set equal to $d'\mathbf{u}_z$, $d' < 0$, the lowest-order approximations of the DGFs in (67)–(70), in the limit $k_0|\mathbf{r}| \to \infty$, turn out to be

$$\underline{\underline{\mathbf{G}}}_{\mathrm{Lr}}(\mathbf{r},\mathbf{r}') \simeq \frac{1}{2\pi|\mathbf{r}|}\sum_{n\in\mathbb{Z}} \underline{\underline{\mathscr{R}}}_{\mathrm{L}}^{(n)}(\alpha_n,\beta_0) \times \exp\left[\mathrm{i}(k_0|\mathbf{r}| - \gamma_n d')\right], \quad z<0, \tag{75}$$

$$\underline{\underline{\mathbf{G}}}_{\mathrm{Rr}}(\mathbf{r},\mathbf{r}') \simeq \frac{1}{2\pi|\mathbf{r}|}\sum_{n\in\mathbb{Z}} \underline{\underline{\mathscr{R}}}_{\mathrm{R}}^{(n)}(\alpha_n,\beta_0) \times \exp\left[\mathrm{i}(k_0|\mathbf{r}| - \gamma_n d')\right], \quad z<0, \tag{76}$$

$$\underline{\underline{\mathbf{G}}}_{\mathrm{Lt}}(\mathbf{r},\mathbf{r}') \simeq \frac{1}{2\pi|\tilde{\mathbf{r}}|}\sum_{n\in\mathbb{Z}} \underline{\underline{\mathscr{T}}}_{\mathrm{L}}^{(n)}(\tilde{\alpha}_n,\tilde{\beta}_0) \times \exp\left[\mathrm{i}(k_0|\tilde{\mathbf{r}}| - \tilde{\gamma}_n d')\right], \quad z>d, \tag{77}$$

$$\underline{\underline{\mathbf{G}}}_{\mathrm{Rt}}(\mathbf{r},\mathbf{r}') \simeq \frac{1}{2\pi|\tilde{\mathbf{r}}|}\sum_{n\in\mathbb{Z}} \underline{\underline{\mathscr{T}}}_{\mathrm{R}}^{(n)}(\tilde{\alpha}_n,\tilde{\beta}_0) \times \exp\left[\mathrm{i}(k_0|\tilde{\mathbf{r}}| - \tilde{\gamma}_n d')\right], \quad z>d, \tag{78}$$

subject to the restrictions stated in the previous paragraph. In (75)–(78) $\alpha_n = k_0\frac{x}{|\mathbf{r}|} - n\Lambda_x$ and $\tilde{\alpha}_n = k_0\frac{x}{|\tilde{\mathbf{r}}|} - n\Lambda_x$ are the saddle points along the SDPs of $k_x^{(0)}$ with respect to the nth-order Floquet harmonics in the reflected and transmitted fields, respectively; while $\beta_0 = k_0\frac{y}{|\mathbf{r}|}$ and $\tilde{\beta}_0 = k_0\frac{y}{|\tilde{\mathbf{r}}|}$ are correspondingly the saddle points along the SDPs of $k_y^{(0)}$. The quantities γ_n and $\tilde{\gamma}_n$ are defined on the top Riemann sheet such that

$$\gamma_n = \sqrt{k_0^2 - \alpha_n^2 - \beta_0^2}, \quad \mathrm{Im}(\gamma) \geqslant 0,$$

$$\tilde{\gamma}_n = \sqrt{k_0^2 - \tilde{\alpha}_n^2 - \tilde{\beta}_0^2}, \quad \mathrm{Im}(\tilde{\gamma}) \geqslant 0.$$

3. Results and discussion

3.1. Preliminaries

We investigated the response of a slanted chiral STF to sources comprising electric and magnetic dipoles. As any chiral STF discriminates between LCP and RCP plane waves strongly in the Bragg regime, we chose two different Beltrami source configurations [39]:

$$\text{(a)} \qquad \mathbf{W}_{\mathrm{L}} = \frac{\mathrm{i}\omega p}{2}\mathbf{u}_s\delta(\mathbf{r}' - d'\mathbf{u}_z), \quad \mathbf{W}_{\mathrm{R}} = \mathbf{0}, \tag{79}$$

$$\text{(b)} \qquad \mathbf{W}_{\mathrm{L}} = \mathbf{0}, \quad \mathbf{W}_{\mathrm{R}} = \frac{\mathrm{i}\omega p}{2}\mathbf{u}_s\delta(\mathbf{r}' - d'\mathbf{u}_z). \tag{80}$$

These configurations are of the left- and right-handed types, respectively. Nominally, either configuration is a pair of parallel electric and magnetic dipoles co-located at $\mathbf{r}' = d'\mathbf{u}_z$, $(d' < 0)$, with $\mathrm{Re}[p\mathrm{e}^{-\mathrm{i}\omega t}]$ being the electric dipole moment; see Fig. 2. The unit vector $\mathbf{u}_s$ represents the orientation of the dipolar sources. For either configuration, the electric field at observation points far from both the sources and the slanted chiral STF is derived from (59) in a normalized form as

$$\mathbf{e}(\mathbf{r}) = \frac{4\pi|\mathbf{r}|\mathbf{E}(\mathbf{r})}{\mu_0 p\omega^2}\exp\left(-\mathrm{i}k_0|\mathbf{r}|\right). \tag{81}$$

Calculations of $\mathbf{e}(\mathbf{r})$ were made with the following constitutive and geometric parameters: $p_a = 2.0$, $p_b = 2.6$, and $p_c = 2.1$; $\lambda_a = \lambda_c = 140$ nm and $\lambda_b = 150$ nm; $N_a = N_b = N_c = 500$; $\Omega = 200$ nm, $d = 60\ \Omega$, $\chi_s = 30°$, and $h = 1$. The chosen constitutive parameters are potentially realizable using silicon dioxide, and are thus likely to be compatible with semiconductor and optical technologies. The ratio d/Ω is large enough so that the circular Bragg phenomenon is fully developed for low values of α [10,11]. The slant angle α was chosen in the range $0° \leqslant \alpha \leqslant 15°$. The dipolar sources were located at $d' = -10\lambda_0$, and the far-field response was calculated at a fixed radial distance $|\mathbf{r}| = 10^5\lambda_0$. The maximum order of the Floquet harmonics was fixed at $N_t = 20$ for the chosen wavelength-regime, after ensuring that every reflectance and transmittance greater than 10^{-4} in magnitude converged to 0.1% accuracy. All propagating harmonics and some evanescent harmonics were thereby covered. Computed values of

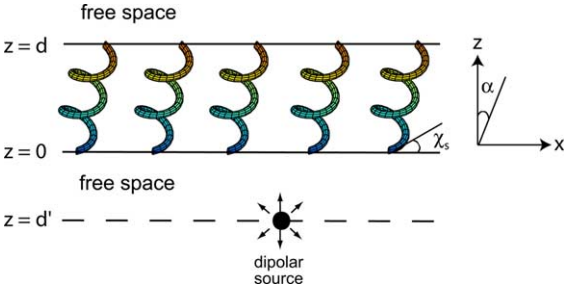

Fig. 2. Schematic of the irradiation of a slanted chiral STF of thickness d by a dipolar source located at $\mathbf{r} = d'\mathbf{u}_z$, $d' < 0$.

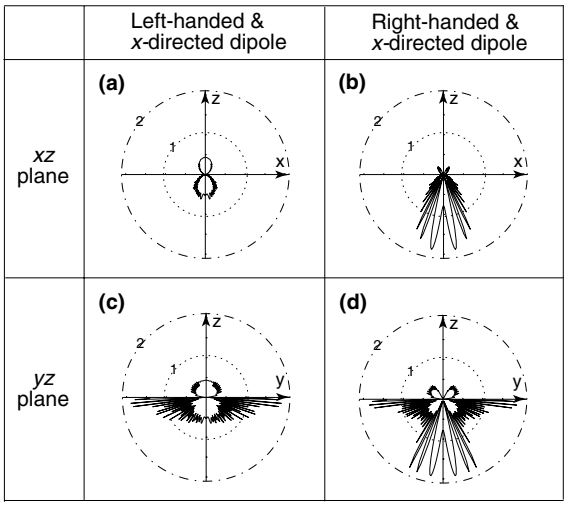

Fig. 3. Computed values of $|\mathbf{e}(\mathbf{r})|^2$ in the xz and yz planes, for x-directed Beltrami dipolar sources radiating at $\lambda_0 = 727$ nm in the presence of an *unslanted* chiral STF. The source configuration is left-handed for the left plots (a, c), and right-handed for the right plots (b, d). The following parameters were used for calculations: $p_a = 2.0$, $p_b = 2.6$, $p_c = 2.1$, $\lambda_a = \lambda_c = 140$ nm , $\lambda_b = 150$ nm, $N_a = N_b = N_c = 500$, $\Omega = 200$ nm, $d = 60$ Ω, $\chi_s = 30°$, $h = 1$, $\alpha = 0°$, $d' = -10\lambda_0$, and $|\mathbf{r}| = 10^5\lambda_0$.

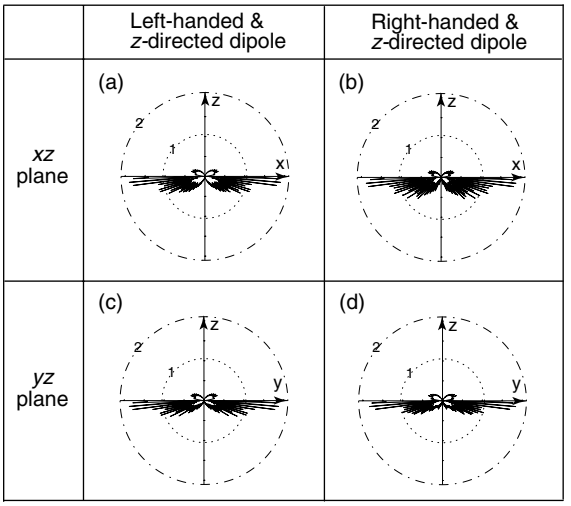

Fig. 4. Same as Fig. 3, but for z-directed Beltrami dipolar sources.

$|\mathbf{e}(\mathbf{r})|^2$ in the xz and yz planes, for various types of dipolar sources are shown in the Figs. 3, 4, and, 9–12.

3.2. Unslanted chiral STF

Let us begin with an unslanted chiral STF, i.e., $\alpha = 0°$. The responses of such films to incident plane waves [6,40] as well as Betrami source configurations [39] have been studied. The most prominent features of the planewave and dipolar responses are due to the circular Bragg phenomenon. With the chosen parameters, the Bragg regime is given by $\lambda_0 \in [702, 752]$ nm for normally incident plane waves; furthermore, the Bragg regime blue-shifts for oblique incidence [41].

Figs. 3 and 4 show plots of $|\mathbf{e}(\mathbf{r})|^2$ in the xz and yz planes for dipolar sources that are oriented parallel (i.e., $\mathbf{u}_s = \mathbf{u}_x$) and perpendicular (i.e., $\mathbf{u}_s = \mathbf{u}_z$), respectively, to the xy plane. The plots for y-directed dipolar sources do not differ qualitatively from those for x-directed sources. The wavelength $\lambda_0 = 727$ nm lies in the middle of the Bragg regime for normal planewave incidence. Evidently, the radiation patterns in Figs. 3 and 4 contain substantial Fabry–Perot rings in the lower (i.e., reflection) half-space which arise due to thickness resonances inside the film. Fabry–Perot rings are also present in the upper (i.e., transmission) half-space, but are considerably muted [39].

One of the two most interesting features of the radiation patterns in Fig. 3 is the presence of a wedge along the z axis in the transmission half-space (Figs. 3(b) and (d)) for the right-handed Beltrami source configuration. That wedge is conspicuously absent for the left-handed Beltrami source configuration, but a double-fang feature – the second of the two interesting features – appears in the reflection half-space (Figs. 3(a) and (c)). The diversity with respect to the handedness of the source configuration is the cumulative expression of the circular Bragg phenomenon observed with normally [6] and obliquely [40] incident plane waves. As the fields radiated by a source configuration can be decomposed into an angular spectrum of circularly polarized plane waves, the characteristic features of the circular Bragg phenomenon – which is displayed by a segment of that angular spectrum when the wavelength belongs to the Bragg regime [40] – coalesce to create the

wedge and/or the double-fang feature in the radiation pattern.

Although the chiral STF is definitely excited along its helical axis (i.e, the z axis) by x- and y-directed sources, it is not axially excited when the dipolar sources are z-directed. In the latter case, the dipolar radiation is broadside, not endfire [42]. Therefore, the radiation patterns in Fig. 4 do not contain evidence of the circular Bragg phenomenon in the form of substantially diverse responses of the chiral STF to the two Beltrami source configurations.

3.3. Slanted chiral STF

3.3.1. Response to planewave incidence

The interaction of the circular Bragg phenomenon and the Rayleigh–Wood anomalies for the special case of plane waves normally incident on a slanted chiral STF has been examined recently [10]. The high transmittance (if absorption is low) for an incident cross-handed plane wave in the Bragg regime remains specular even for $\alpha \neq 0$, being clearly evident in the $n = 0$ harmonic component of the transmitted field. However, the high reflectance of a co-handed plane wave in the same regime becomes nonspecular for $\alpha \neq 0$, as it occurs in the $n = \pm 2$ harmonic component [2] of the reflected field. Furthermore, the Bragg regime blue-shifts as the slant angle increases, and the center-wavelength of the Bragg regime can be estimated by solving the equation [10]

$$\lambda_0^{\mathrm{Br}} - \Omega \cos\alpha \left[\sqrt{\epsilon_c(\lambda_0^{\mathrm{Br}})} + \sqrt{\tilde{\epsilon}_d(\lambda_0^{\mathrm{Br}})} \right] = 0, \tag{82}$$

where

$$\tilde{\epsilon}_d(\lambda_0) = \frac{\epsilon_a(\lambda_0)\epsilon_b(\lambda_0)}{\epsilon_a(\lambda_0)\cos^2\chi_s + \epsilon_b(\lambda_0)\sin^2\chi_s}. \tag{83}$$

Rayleigh–Wood anomalies – the conversion of a Floquet harmonic of order n from either propagating to evanescent or vice versa – for different orders occur at $k_z^{(n)} = 0$, i.e., at wavelengths

$$\lambda_{0_n}^{\mathrm{RW}} = \frac{2\Omega}{|n \sin\alpha|}. \tag{84}$$

As $|\alpha|$ increases, $\lambda_{0_{\pm 2}}^{\mathrm{RW}}$ decreases far more rapidly than λ_0^{Br}, leading to a shrinkage of the Bragg regime; and eventually the circular Bragg phenomenon is completely subverted by the Rayleigh–Wood anomaly for order $n = \mp 2$ for $\alpha \gtrless 0$. For normal incidence and the chosen constitutive parameters, the circular Bragg phenomenon vanishes as $|\alpha|$ increases beyond 17.1°.

Eqs. (82) and (84) must undergo changes for oblique incidence. One the one hand, the Bragg regime is blue-shifted by oblique incidence. The actual functional dependence of λ_0^{Br} on the incident wavevector $\mathbf{k}_{\mathrm{i}} = \mathbf{k}_+^{(0)}$ is very complicated. However, our numerical calculations have suggested that the solution of the equation

$$\lambda_0^{\mathrm{Br}} - \Omega \cos\alpha \sqrt{\frac{k_z^{(0)}}{k_0}} \left[\sqrt{\epsilon_c(\lambda_0^{\mathrm{Br}})} + \sqrt{\tilde{\epsilon}_d(\lambda_0^{\mathrm{Br}})} \right] = 0 \tag{85}$$

provides a good quantitative estimate of λ_0^{Br} when $k_z^{(0)}/k_0 \in [\frac{\sqrt{3}}{2}, 1]$; and this estimate also holds for unslanted chiral STFs [41]. On the other hand, Rayleigh–Wood anomalies for different orders occur at

$$\lambda_{0_n}^{\mathrm{RW}} = \begin{cases} \frac{2\Omega}{|n\sin\alpha|} \left(\sqrt{1 - \left(\frac{k_y^{(0)}}{k_0}\right)^2} \mp \frac{k_x^{(0)}}{k_0} \right), & n > 0, \\ \frac{2\Omega}{|n\sin\alpha|} \left(\sqrt{1 - \left(\frac{k_y^{(0)}}{k_0}\right)^2} \pm \frac{k_x^{(0)}}{k_0} \right), & n < 0, \end{cases} \tag{86}$$

wherein the upper signs apply for $\alpha > 0$ and the lower signs for $\alpha < 0$. Clearly, $\lambda_{0_n}^{\mathrm{RW}} \neq \lambda_{0_{-n}}^{\mathrm{RW}}$ when $k_x^{(0)} \neq 0$, and the value of $\lambda_{0_n}^{\mathrm{RW}}$ is affected by both $k_x^{(0)}/k_0$ and $k_y^{(0)}/k_0$, though in different ways: Whereas an increase of $|k_y^{(0)}/k_0|$ blue-shifts the Rayleigh–Wood anomalies for all orders, an increase of $|k_x^{(0)}/k_0|$ either blue-shifts or red-shifts the Rayleigh–Wood anomaly for order n, depending on the signs of $k_x^{(0)}/k_0$ and n.

The influence of Rayleigh–Wood anomalies on the circular Bragg phenomenon is very explicit in

[2] Specifically, the high-reflectance feature appears in the $n = -2$ harmonic for $\alpha > 0$, and $n = +2$ harmonic for $\alpha < 0$, regardless of the structural handedness of the thin film and the angle of planewave incidence.

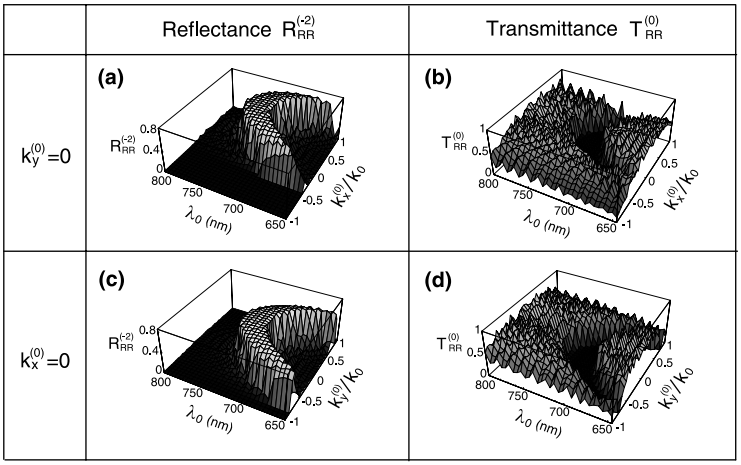

Fig. 5. Spectrums of planewave reflectance $R_{RR}^{(-2)}$ and transmittance $T_{RR}^{(0)}$, calculated for a *slanted* chiral STF with the same properties as for Fig. 3, except that $\alpha = 10°$. The incident plane wave is RCP, and the chiral STF is structurally right-handed. (a, b) Incidence in the *xz* plane; (c, d) incidence in the *yz* plane.

the plots of the reflectances and transmittances for obliquely incident plane waves. Fig. 5 shows the spectrums of $R_{RR}^{(-2)}$ and $T_{RR}^{(0)}$ when $\alpha = 10°$. The spectrums are plotted for

- incidence in the *xz* plane (i.e., $k_y^{(0)} = 0$), and
- incidence in the *yz* plane (i.e., $k_x^{(0)} = 0$).

The circular Bragg phenomenon is clearly identifiable as a ridge in plots of $R_{RR}^{(-2)}$ and as a trough in the plots of $T_{RR}^{(0)}$, both features being absent in the remittance plots (not shown) for incident LCP plane waves because the chosen film is structurally right-handed. For either incidence plane, Fig. 5 indicates that the Bragg regime blue-shifts more for more obliquely incident plane waves, as predicted.

More importantly, as the incidence wavevector $\mathbf{k}_i$ tilts away from the *z* axis, both $\lambda_{0_{\mp 2}}^{RW}$ (for $\alpha \gtrless 0$) and λ_0^{Br} change noticeably. If $\lambda_{0_{\mp 2}}^{RW}$ becomes smaller than λ_0^{Br}, the signature of the circular Bragg phenomenon for incident RCP plane waves disappears. The wavelength-neighborhood of the disappearance depends strongly on the orientation of the plane of incidence with respect to the plane containing the helical axis (i.e., *xz* plane); hence, the circular Bragg phenomenon is far from displaying circular symmetry with respect to the angle $\tan^{-1} k_y^{(0)}/k_x^{(0)}$ when $\alpha \neq 0$.

The dependence of $\lambda_{0_{\mp 2}}^{RW}$ (for $\alpha \gtrless 0$) on $k_x^{(0)}/k_0$ is different from that on $k_y^{(0)}/k_0$. When $k_y^{(0)}/k_0$ is constant, $\lambda_{0_{\mp 2}}^{RW}$ changes linearly with $k_x^{(0)}/k_0$; and the Bragg regime is susceptible to subversion by the Rayleigh–Wood anomaly for order $n = \mp 2$ if $k_x^{(0)}/k_0 \lessgtr 0$. That is the reason for the absence of the Bragg regime in Figs. 5(a) and (b) ($\alpha = 10°$), for $k_x^{(0)}/k_0 \in (-1, -0.37)$. In contrast, $\lambda_{0_{\mp 2}}^{RW}$ is a monotonically decreasing function of $|k_y^{(0)}/k_0|$ for constant $k_x^{(0)}/k_0$. Therefore, in Figs. 5(c) and (d) ($\alpha = 10°$), the Bragg regime is completely subverted by the Rayleigh–Wood anomaly for order $n = -2$ in the angular regime $|k_y^{(0)}/k_0| \in (0.83, 1)$.

The influence of the slant angle $\alpha \gtrless 0$ on the subversion of the circular Bragg phenomenon by the Rayleigh–Wood anomaly for order $n = \mp 2$ had been shown in a predecessor paper, but only for normal incidence. Figs. 6 and 7 present key remittances for arbitrary incidence in either the *xz* plane (i.e., $k_y^{(0)} = 0$) or the *yz* plane (i.e., $k_x^{(0)} = 0$), for $\alpha = 0°, 5°, 10°$, and 15°. For these plots, the wavelength λ_0 was fixed equal to $\tilde{\lambda}_0^{Br}$, which is defined as the solution of Eq. (82) and is therefore the center-wavelength of the Bragg regime for normal incidence. Both figures clearly show that the angular spread of the Bragg regime is asymmetric with respect to $k_x^{(0)}$ but symmetric with respect to $k_y^{(0)}$. The effect of $\alpha \neq 0$ is fairly trivial when the incident plane wave is cross-handed (Fig. 6), but not when the incident plane wave is

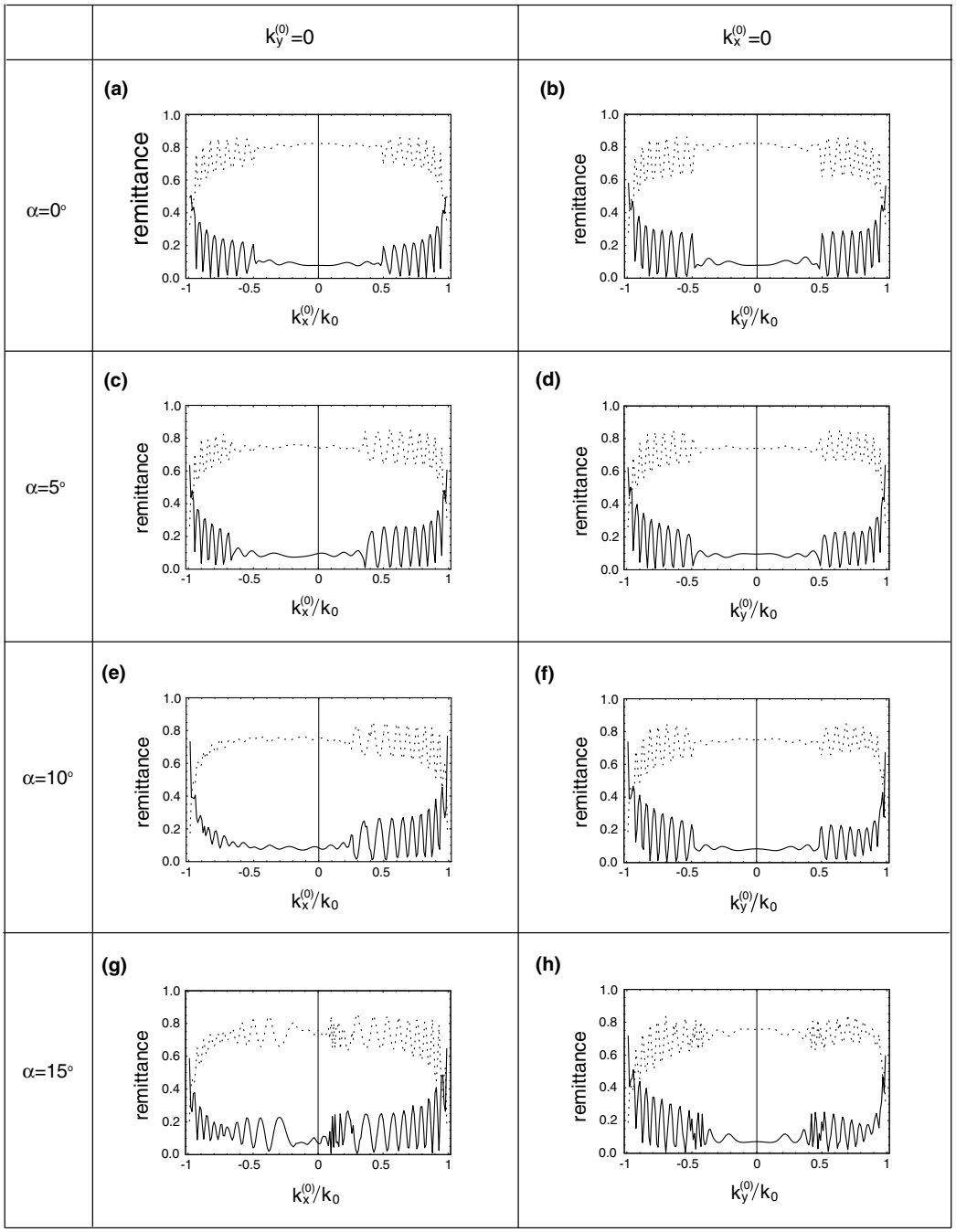

Fig. 6. Dependences of the remittances $R_{\mathrm{RL}}^{(0)} + R_{\mathrm{LL}}^{(0)}$ (solid lines) and $T_{\mathrm{RL}}^{(0)} + T_{\mathrm{LL}}^{(0)}$ (dashed lines) on the obliqueness of planewave incidence: (a, c, e, g) $k_y^{(0)} = 0$; (b, d, f, h) $k_x^{(0)} = 0$. The slanted chiral STF has the same parameters as the unslanted one in Fig. 3, but for the value of α: (a, b) $\alpha = 0°$; (c, d) $\alpha = 5°$; (e, f) $\alpha = 10°$; (g, h) $\alpha = 15°$. The wavelength $\lambda_0 = \lambda_0^{\mathrm{Br}}$, which is defined as the solution of Eq. (82) and is therefore the center-wavelength of the Bragg regime for normal incidence. In (a) and (b), $R_{\mathrm{RL}}^{(0)} + R_{\mathrm{LL}}^{(0)}$ and $T_{\mathrm{RL}}^{(0)} + T_{\mathrm{LL}}^{(0)}$ are replaced by $\sum_{|n| \leqslant N_{\mathrm{t}}} \left[R_{\mathrm{RL}}^{(n)} + R_{\mathrm{LL}}^{(n)} \right]$ and $\sum_{|n| \leqslant N_{\mathrm{t}}} [T_{\mathrm{RL}}^{(n)} + T_{\mathrm{LL}}^{(n)}]$, respectively, because all nonspecular remittances fold into the specular remittances for $\alpha = 0°$.

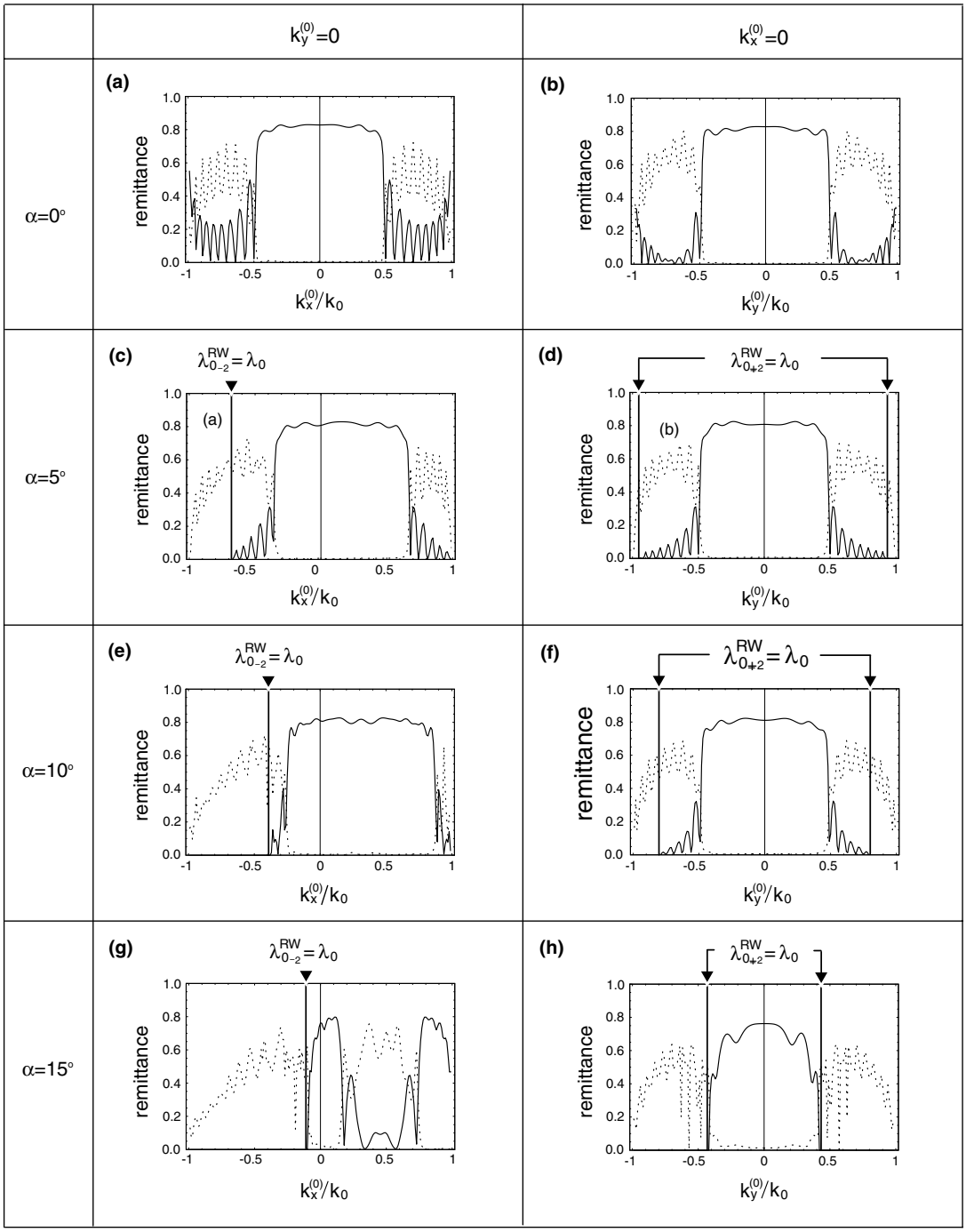

Fig. 7. Same as Fig. 6, except the remittances plotted are $R_{RR}^{(-2)}$ (solid lines) and $T_{RR}^{(0)}$ (dashed lines). In (a) and (b), $R_{RR}^{(-2)}$ and $T_{RR}^{(0)}$ are replaced by $\sum_{|n|\leqslant N_t} R_{RR}^{(n)}$ and $\sum_{|n|\leqslant N_t} T_{RR}^{(n)}$, respectively, because all nonspecular remittances fold into the specular remittances for $\alpha = 0°$.

co-handed (Fig. 7). The asymmetric shift of the Bragg regime due to α is clearly demonstrated in Figs. 7(a), (c), (e) and (g) by the $k_x^{(0)}$-variations of $R_{\mathrm{RR}}^{(-2)}$ and $T_{\mathrm{RR}}^{(0)}$ for co-handed incidence in the xz plane. When α rises to 15°, new features appear in the plots of $R_{\mathrm{RR}}^{(-2)}$ and $T_{\mathrm{RR}}^{(0)}$, as shown in Figs. 7(g) and (h). While partially subverted by a Rayleigh–Wood anomaly, the crest feature in $R_{\mathrm{RR}}^{(-2)}$ splits into two narrower and disconnected portions in Fig. 7(g); and the split is correspondingly present in the plot of $T_{\mathrm{RR}}^{(0)}$ also. The major qualitative difference between Figs. 7(g) and (h) lets us conclude that the circular Bragg phenomenon, whether or not subverted by a Rayleigh–Wood anomaly, becomes strongly sensitive to the plane of incidence when $|\alpha|$ crosses a threshold value.

3.3.2. Parallel dipolar sources

Figs. 8 and 9, respectively, show the radiation patterns of Beltrami dipolar sources in the presence of the slanted chiral STF with $\alpha = 5°$, when $\mathbf{u}_s = \mathbf{u}_x$ and $\mathbf{u}_s = \mathbf{u}_y$. The wavelength was chosen $\lambda_0 = \tilde{\lambda}_0^{\mathrm{Br}} = 724$ nm, i.e., in the middle of the Bragg regime for normal incidence. The characteristic features of these radiation patterns are tailored by the circular Bragg phenomenon discussed in Section 3.3.1. Noticeably, both (i) the wedge in the transmission half-space for the right-handed dipolar sources and (ii) the double-fang feature in the reflection half-space for the left-handed dipolar sources are located asymmetrically in the xz plane about the z axis. In contrast, the radiation patterns are symmetric in the yz plane about the z axis, just as for unslanted chiral STFs. The reason seems clear by virtue of the fact that the circular Bragg phenomenon is significantly circularly asymmetric about the z axis and sensitive to the plane of planewave incidence when $\alpha \neq 0$. No wonder, there is a vast difference between the radiation pattern in the xz plane for $\mathbf{u}_s = \mathbf{u}_x$ (Fig. 8(b)) and that in the yz plane using $\mathbf{u}_s = \mathbf{u}_y$ (Fig. 9(d)).

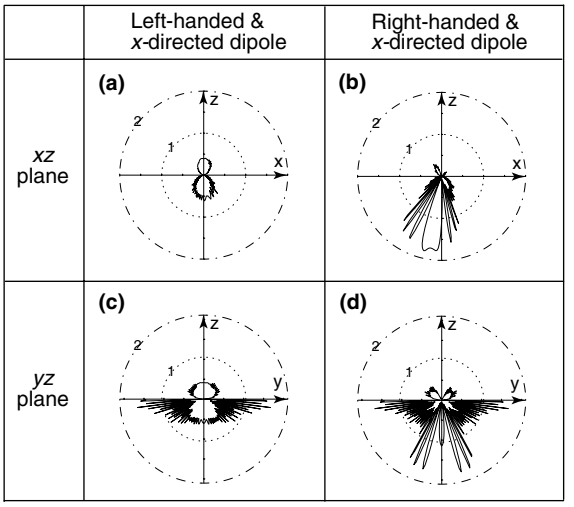

Fig. 8. Same as Fig. 3, but for $\alpha = 5°$ and $\lambda_0 = \tilde{\lambda}_0^{\mathrm{Br}} = 724$ nm.

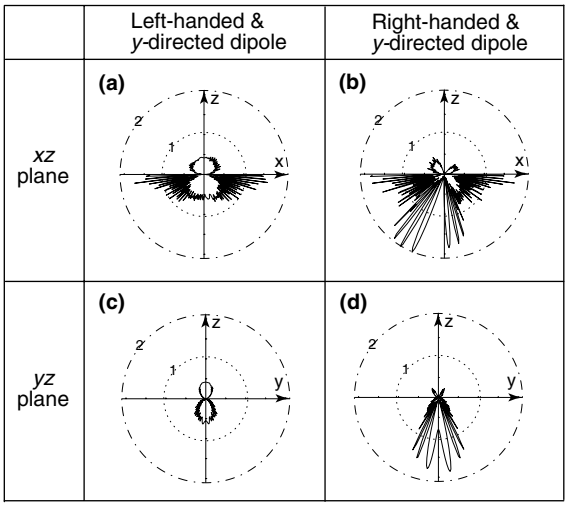

Fig. 9. Same as Fig. 8, but for y-directed Beltrami dipolar sources.

In order to interpret the radiation patterns further, let us define $\varphi(\mathbf{r}) \in (-\pi, \pi]$ as the angle determined by

$$\frac{\mathbf{r}}{|\mathbf{r}|} = \begin{cases} \mathbf{u}_x \cos\varphi(\mathbf{r}) + \mathbf{u}_z \sin\varphi(\mathbf{r}), & \mathbf{r}\cdot\mathbf{u}_y = 0, \\ \mathbf{u}_y \cos\varphi(\mathbf{r}) + \mathbf{u}_z \sin\varphi(\mathbf{r}), & \mathbf{r}\cdot\mathbf{u}_x = 0. \end{cases} \tag{87}$$

In Figs. 8(b) and 9(b), the wedge is centered at $\varphi(\mathbf{r}) < \pi/2$; but it is centered at $\varphi(\mathbf{r}) = \pi/2$ in Figs. 8(d) and 9(d). The reason is that, although the circular Bragg phenomenon shifts in the $+k_x^{(0)}$ direction in the left plots of Fig. 7 as α increases, it does not shift at all along the $k_y^{(0)}$ axis in the right plots of the same figure.

Even though the dominant remittances for cross-handed incident plane waves are always specular (i.e.,

of order $n = 0$) – as exemplified by Fig. 6 – the double-fang features in Figs. 8(a) and 9(a) have rotated counterclockwise with respect to that in Fig. 3(a). These three figures contain the radiation patterns in the *xz* plane; while the corresponding radiation patterns in the *yz* plane (in Figs. 3(c), 8(c) and 9(c)) are symmetric with respect to the *z* axis, regardless of the value of α. The attributes of the circular Bragg phenomenon *versus* α in Fig. 7 also explain the foregoing features of the radiation patterns.

The slant angle α can affect the wedge and the double-fang feature even more drastically than in Figs. 8 and 9, for which $\alpha = 5°$. When α is increased to 10°, Fig. 10 shows that the wedge expands and rotates clockwise so much that there is no transmission for $\varphi(\mathbf{r}) \in (0, \pi/2)$ in the *xz* plane – when $\lambda_0 = \tilde{\lambda}_0^{\mathrm{Br}} = 716$ nm, the Beltrami dipolar source is right-handed, and $\mathbf{u}_s = \mathbf{u}_x$.

The circular Bragg phenomenon being frequency-selective, the wavelength of radiation in relation to the Bragg regime also affects the radiation pattern. Clearly, because of the blue-shift of the Bragg regime for oblique incidence, the wedge and/or the double-fang feature tend to be obliquely oriented when λ_0 is lower than $\tilde{\lambda}_0^{\mathrm{Br}}$. This is exemplified by the radiation patterns in Fig. 11, for

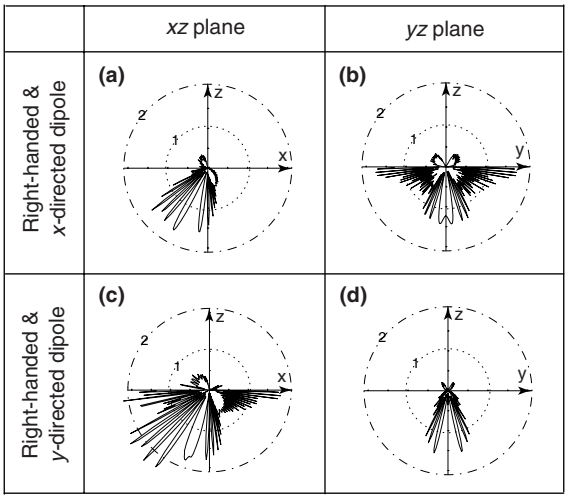

Fig. 10. Computed values of $|\mathbf{e}(\mathbf{r})|^2$ in the *xz* and *yz* planes, for right-handed Beltrami dipolar sources radiating at $\lambda_0 = \tilde{\lambda}_0^{\mathrm{Br}} = 716$ nm. The dipolar source is (a, b) *x*-directed, and (c, d) *y*-directed. The slanted chiral STF has the same parameters as the one for Fig. 8, except that $\alpha = 10°$.

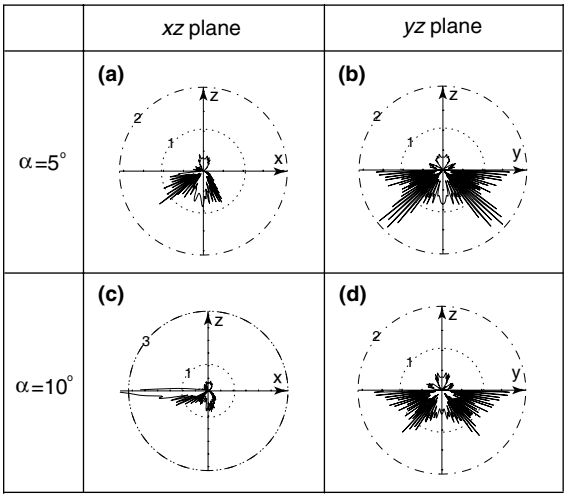

Fig. 11. Computed values of $|\mathbf{e}(\mathbf{r})|^2$ in the *xz* and *yz* planes, for a *x*-directed, right-handed, Beltrami dipolar source radiating at $\lambda_0 = 670$ nm. The slanted chiral STF has the same parameters as the one for Fig. 8, except that (a, b) $\alpha = 5°$ and (c, d) $\alpha = 10°$.

which $\lambda_0 = 670$ nm, the Beltrami dipolar source is right-handed, and $\mathbf{u}_s = \mathbf{u}_x$. The wedge feature is located in the *yz* plane in the $\varphi(\mathbf{r})$-neighborhoods of both $\pi/4$ and $3\pi/4$ for $\alpha = 5°$ (Fig. 11(b)) and $\alpha = 10°$ (Fig. 11(d)) as well.

Incidentally, in Fig. 11(c), enhanced radiation is evident in the *xz* plane, near the surface of the slanted chiral STF for $\alpha = 10°$. Unfortunately, the computation does not seem to be accurate because the asymptotic evaluation procedure is invalid in the vicinity of the slanted chiral STF.

3.3.3. Perpendicular dipolar sources

Because the fields emitted by a perpendicular dipolar source (i.e., $\mathbf{u}_s = \mathbf{u}_z$) are of the end-fire type with respect to the slanted chiral STF, the radiation patterns may not evince any trace of the circular Bragg phenomenon when $|\alpha|$ is small – as suggested by the limiting case of $\alpha = 0°$ in Fig. 4. However, for larger $|\alpha|$, a significant broadside aspect to the interaction between the dipolar source and the thin film is possible. Fig. 12 presents the radiation patterns for $\alpha = 15°$ and *z*-directed dipolar sources radiating at $\lambda_0 = \tilde{\lambda}_0^{\mathrm{Br}} = 702$ nm. Although the plots labeled *a*, *c* and *d* in

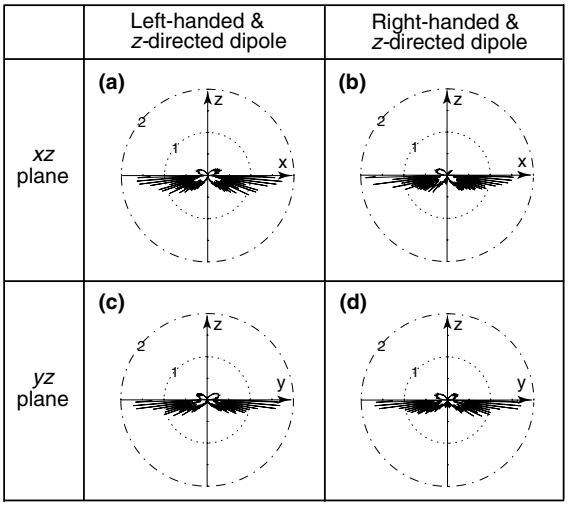

Fig. 12. Same as Fig. 4, but for $\alpha = 15^\circ$ and $\lambda_0 = \tilde{\lambda}_0^{\mathrm{Br}} = 702$ nm.

Fig. 12 look very similar to their counterparts in Fig. 4, a contrast between Fig. 4(b) ($\alpha = 0^\circ$) and 12(b) ($\alpha = 15^\circ$) is evident. A wedge is located in the regime $\varphi(\mathbf{r}) \in (0, \pi/4)$ in Fig. 12(b), but not in Fig. 4(b). Thus, even for perpendicular dipolar sources, the circular Bragg phenomenon can come into play when $\alpha \neq 0$.

4. Concluding remarks

In this paper, we formulated the electromagnetic response characteristics of chiral sculptured thin films, which are anisotropic and periodically nonhomogeneous along an axis slanted at an angle α with respect to the normal of the substrate plane. First, the planewave response of a slanted chiral STF was formulated for arbitrary incidence conditions. A rigorous coupled-wave analysis was implemented with a stable algorithm to describe the planewave response of the slanted chiral STF. Then the dyadic Green functions were set up as angular planewave spectrums. Asymptotic techniques were employed to evaluate the DGFs in the far-field limit. Due to the structural chirality of the chosen thin film, Beltrami source configurations were chosen.

The circular Bragg phenomenon displayed by the slanted chiral STF on planewave excitation was shown to underlie the discriminatory treatment of left- and right-handed Beltrami sources. The appearance of a wedge and/or a double-fang feature in radiation patterns is the cumulative expression of the circular Bragg phenomenon displayed differently by the differently propagating plane waves in the planewave spectrum of the fields emitted by the sources. Because of the transverse periodicity induced by $\alpha \neq 0^\circ$, the slanted chiral STF exhibits a circular Bragg phenomenon that is partially nonspecular; furthermore, it is strongly sensitive to the angle of incidence because of the effect of a Rayleigh–Wood anomaly. As a result, the angular placements of the wedge and the double-fang feature in the radiation pattern can be tailored asymmetrically with respect to the normal of the substrate plane. Furthermore, the radiation pattern would be affected by the value of α especially for right-handed Beltrami source configurations.

Acknowledgements

The authors thank Abdul H. Aziz of the Penn State Institute for High Performance Computing Applications for computing assistance. F.W. thanks the Penn State Weiss Graduate Program for a Dissertation Fellowship. A.L. thanks the Trustees of the Pennsylvania State University for a sabbatical leave-of-absence.

Appendix A

The $4(2N_t + 1) \times 4(2N_t + 1)$ kernel matrix $[\underline{\underline{\tilde{\mathbf{P}}}}]$ is given as

$$\left[\underline{\underline{\tilde{\mathbf{P}}}}\right] = \begin{bmatrix} \left[\underline{\underline{\tilde{P}}}_{11}\right] & \left[\underline{\underline{\tilde{P}}}_{12}\right] & \left[\underline{\underline{\tilde{P}}}_{13}\right] & \left[\underline{\underline{\tilde{P}}}_{14}\right] \\ \left[\underline{\underline{\tilde{P}}}_{21}\right] & \left[\underline{\underline{\tilde{P}}}_{22}\right] & \left[\underline{\underline{\tilde{P}}}_{23}\right] & \left[\underline{\underline{\tilde{P}}}_{24}\right] \\ \left[\underline{\underline{\tilde{P}}}_{31}\right] & \left[\underline{\underline{\tilde{P}}}_{32}\right] & \left[\underline{\underline{\tilde{P}}}_{33}\right] & \left[\underline{\underline{\tilde{P}}}_{34}\right] \\ \left[\underline{\underline{\tilde{P}}}_{41}\right] & \left[\underline{\underline{\tilde{P}}}_{42}\right] & \left[\underline{\underline{\tilde{P}}}_{43}\right] & \left[\underline{\underline{\tilde{P}}}_{44}\right] \end{bmatrix}, \qquad \text{(A.1)}$$

wherein the sixteen $(2N_t+1)\times(2N_t+1)$ submatrixes are defined as follows:

$$\begin{aligned}
\left[\underline{\underline{\tilde{P}}}_{11}\right] &= -\left[\underline{\underline{\kappa}}_{z}\right] - \left[\underline{\underline{K}}_{x}\right]\left[\underline{\underline{\epsilon}}_{zz}\right]^{-1}\left[\underline{\underline{\epsilon}}_{zx}\right],\\
\left[\underline{\underline{\tilde{P}}}_{12}\right] &= -\left[\underline{\underline{K}}_{x}\right]\left[\underline{\underline{\epsilon}}_{zz}\right]^{-1}\left[\underline{\underline{\epsilon}}_{zy}\right],\\
\left[\underline{\underline{\tilde{P}}}_{13}\right] &= \frac{k_y^{(0)}}{k_0}\left[\underline{\underline{K}}_{x}\right]\left[\underline{\underline{\epsilon}}_{zz}\right]^{-1},\\
\left[\underline{\underline{\tilde{P}}}_{14}\right] &= k_0\left[\underline{\underline{I}}\right] - \frac{1}{k_0}\left[\underline{\underline{K}}_{x}\right]\left[\underline{\underline{\epsilon}}_{zz}\right]^{-1}\left[\underline{\underline{K}}_{x}\right],\\
\left[\underline{\underline{\tilde{P}}}_{21}\right] &= -k_y^{(0)}\left[\underline{\underline{\epsilon}}_{zz}\right]^{-1}\left[\underline{\underline{\epsilon}}_{zx}\right],\\
\left[\underline{\underline{\tilde{P}}}_{22}\right] &= -\left[\underline{\underline{\kappa}}_{z}\right] - k_y^{(0)}\left[\underline{\underline{\epsilon}}_{zz}\right]^{-1}\left[\underline{\underline{\epsilon}}_{zy}\right],
\end{aligned} \tag{A.2}$$

$$\begin{aligned}
\left[\underline{\underline{\tilde{P}}}_{23}\right] &= -k_0\left[\underline{\underline{I}}\right] + \frac{\left(k_y^{(0)}\right)^2}{k_0}\left[\underline{\underline{\epsilon}}_{zz}\right]^{-1},\\
\left[\underline{\underline{\tilde{P}}}_{24}\right] &= -\frac{k_y^{(0)}}{k_0}\left[\underline{\underline{\epsilon}}_{zz}\right]^{-1}\left[\underline{\underline{K}}_{x}\right],\\
\left[\underline{\underline{\tilde{P}}}_{31}\right] &= -\frac{k_y^{(0)}}{k_0}\left[\underline{\underline{K}}_{x}\right] + k_0\left(\left[\underline{\underline{\epsilon}}_{yz}\right]\left[\underline{\underline{\epsilon}}_{zz}\right]^{-1}\left[\underline{\underline{\epsilon}}_{zx}\right] - \left[\underline{\underline{\epsilon}}_{yx}\right]\right),\\
\left[\underline{\underline{\tilde{P}}}_{32}\right] &= \frac{1}{k_0}\left[\underline{\underline{K}}_{x}\right]\left[\underline{\underline{K}}_{x}\right]\\
&\quad + k_0\left(\left[\underline{\underline{\epsilon}}_{yz}\right]\left[\underline{\underline{\epsilon}}_{zz}\right]^{-1}\left[\underline{\underline{\epsilon}}_{zy}\right] - \left[\underline{\underline{\epsilon}}_{yy}\right]\left[\underline{\underline{\epsilon}}_{yy}\right]\right),\\
\left[\underline{\underline{\tilde{P}}}_{33}\right] &= -\left[\underline{\underline{\kappa}}_{z}\right] - k_y^{(0)}\left[\underline{\underline{\epsilon}}_{yz}\right]\left[\underline{\underline{\epsilon}}_{zz}\right]^{-1},\\
\left[\underline{\underline{\tilde{P}}}_{34}\right] &= \left[\underline{\underline{\epsilon}}_{yz}\right]\left[\underline{\underline{\epsilon}}_{zz}\right]^{-1}\left[\underline{\underline{K}}_{x}\right],
\end{aligned} \tag{A.3}$$

$$\begin{aligned}
\left[\underline{\underline{\tilde{P}}}_{41}\right] &= -\frac{\left(k_y^{(0)}\right)^2}{k_0}\left[\underline{\underline{I}}\right] - k_0\left(\left[\underline{\underline{\epsilon}}_{xz}\right]\left[\underline{\underline{\epsilon}}_{zz}\right]^{-1}\left[\underline{\underline{\epsilon}}_{zx}\right] - \left[\underline{\underline{\epsilon}}_{xx}\right]\right),\\
\left[\underline{\underline{\tilde{P}}}_{42}\right] &= \frac{k_y^{(0)}}{k_0}\left[\underline{\underline{K}}_{x}\right] - k_0\left(\left[\underline{\underline{\epsilon}}_{xz}\right]\left[\underline{\underline{\epsilon}}_{zz}\right]^{-1}\left[\underline{\underline{\epsilon}}_{zy}\right] - \left[\underline{\underline{\epsilon}}_{xy}\right]\right),\\
\left[\underline{\underline{\tilde{P}}}_{43}\right] &= k_y^{(0)}\left[\underline{\underline{\epsilon}}_{xz}\right]\left[\underline{\underline{\epsilon}}_{zz}\right]^{-1},\\
\left[\underline{\underline{\tilde{P}}}_{44}\right] &= -\left[\underline{\underline{\kappa}}_{z}\right] - \left[\underline{\underline{\epsilon}}_{xz}\right]\left[\underline{\underline{\epsilon}}_{zz}\right]^{-1}\left[\underline{\underline{K}}_{x}\right].
\end{aligned} \tag{A.4}$$

$$\tag{A.5}$$

The $(2N_t+1)\times(2N_t+1)$ identity matrix is denoted by $[\underline{I}]$.

References

[1] A. Lakhtakia, R. Messier, OSA Opt. Photon. News 12 (9) (2001) 26.
[2] R. Messier, A. Lakhtakia, Mater. Res. Innovat. 2 (1999) 217.
[3] R. Messier, V.C. Venugopal, P.D. Sunal, J. Vac. Sci. Technol. B 18 (2000) 1538.
[4] I.J. Hodgkinson, Q.h. Wu, Adv. Mater. 13 (2001) 889.
[5] M. Suzuki, Y. Taga, Jpn. J. Appl. Phys. 2 40 (2001) L358.
[6] V.C. Venugopal, A. Lakhtakia, in: O.N. Singh, A. Lakhtakia (Eds.), Electromagnetic Fields in Unconventional Materials and Structures, Wiley, New York, 2000, p. 151.
[7] M.W. McCall, Math. Comput. Model. 34 (2001) 1483.
[8] D. Maystre (Ed.), Selected Papers on Diffraction Gratings, SPIE Press, Bellingham, WA, USA, 1993.
[9] R. Messier, A. Lakhtakia, V.C. Venugopal, P.D. Sunal, Vac. Technol. Coating 2 (10) (2001) 40.
[10] F. Wang, A. Lakhtakia, R. Messier, Eur. Phys. J. Appl. Phys. 20 (2002) 91.
[11] F. Wang, A. Lakhtakia, Opt. Commun. 215 (2003) 79.
[12] F. de Fornel, Evanescent Waves: From Newtonian Optics to Atomic Optics, Springer, Heidelberg, Germany, 2000.
[13] M.A. Paesler, P.J. Moyer, Near-Field Optics: Theory, Instrumentation, and Application, Wiley, New York, NY, USA, 1996.
[14] A. Lakhtakia, Arch. Elektr. Übertr. 56 (2002) 169, corrections: 57 (2003) 79.
[15] A. Naber, H. Kock, H. Fuchs, Scanning 18 (1996) 567.
[16] S. Kühn, C. Hettich, C. Schmitt, J.P. Poizat, V. Sandoghdar, J. Microscopy 202 (2001) 2.
[17] B. Müller, Surf. Rev. Lett. 8 (2001) 169.
[18] M. Riedel, B. Müller, E. Wintermantel, Biomaterials 22 (2001) 2307.
[19] M.G. Moharam, E.B. Grann, D.A. Pommet, T.K. Gaylord, J. Opt. Soc. Am. A 12 (1995) 1068.
[20] M.G. Moharam, D.A. Pommet, E.B. Grann, T.K. Gaylord, J. Opt. Soc. Am. A 12 (1995) 1077.
[21] N. Chateau, J. Hugonin, J. Opt. Soc. Am. A 11 (1994) 1321.
[22] I.J. Hodgkinson, Q.h. Wu, B. Knight, A. Lakhtakia, K. Robbie, Appl. Opt. 39 (2000) 642.
[23] I.J. Hodgkinson, Q.h. Wu, Appl. Opt. 38 (1999) 3621.
[24] C. Kittel, Introduction to Solid State Physics, fourth ed., Wiley Eastern, New Delhi, India, 1974.
[25] A. Lakhtakia, Eur. Phys. J. Appl. Phys. 8 (1999) 129.
[26] J.A. Kong, Electromagnetic Wave Theory, Wiley, New York, NY, USA, 1986.
[27] In a predecessor paper [10], we had obtained the matrix ODE $\frac{d}{dz}[\mathbf{f}(z)] = i[\underline{\underline{\mathbf{P}}}(z)][\mathbf{f}(z)]$ in lieu of (36), where the matrix

$[\underline{\underline{\mathbf{P}}}(z)]$ is a function of z and the column vector $[\underline{\mathbf{f}}(z)]$ is given in (39).

[28] H. Hochstadt, Differential Equations: A Modern Approach, Dover Press, New York, NY, USA, 1975.
[29] L. Li, J. Opt. Soc. Am. A 10 (1993) 2581.
[30] Y. Jaluria, Computer Methods for Engineering, Taylor & Francis, Washington, DC, USA, 1996.
[31] C.-T. Tai, Dyadic Green Functions in Electromagnetic Theory, second ed., IEEE Press, New York, NY, USA, 1994.
[32] A. Lakhtakia, Beltrami Fields in Chiral Media, World Scientific, Singapore, 1994.
[33] W.C. Chew, Waves and Fields in Inhomogeneous Media, IEEE Press, New York, NY, USA, 1995.
[34] A.K. Jordan, R.H. Lang, Radio Sci. 14 (1979) 1077.
[35] M. Born, E. Wolf, Principles of Optics, 6th ed., Pergamon Press, Oxford, UK, 1987.
[36] D. Bouche, F. Molinet, R. Mittra, Asymptotic Methods in Electromagnetics, Springer, Heidelberg, Germany, 1994.
[37] F. Capolino, S. Maci, L.B. Felsen, Radio Sci. 35 (2000) 579.
[38] F. Wang. Available from <math-ph/0307049>.
[39] A. Lakhtakia, M.W. McCall, Arch. Elektr. Übertr. 57 (2003) 23.
[40] V.C. Venugopal, A. Lakhtakia, Proc. R. Soc. Lond. A 456 (2000) 125.
[41] V.C. Venugopal, A. Lakhtakia, Eur. Phys. J. Appl. Phys. 10 (2000) 173.
[42] A. Lakhtakia, M.F. Iskander, C.H. Durney, H. Massoudi, Radio Sci. 17 (1982) 77S.

Eur. Phys. J. AP **13**, 3–14 (2001)

THE EUROPEAN PHYSICAL JOURNAL APPLIED PHYSICS

Reflection and transmission of optical narrow–extent pulses by axially excited chiral sculptured thin films

J.B. Geddes III[a] and A. Lakhtakia[b]

CATMAS – Computational and Theoretical Materials Sciences Group, Department of Engineering Science and Mechanics, 212 Earth-Engineering Sciences Building, Pennsylvania State University, University Park, PA 16802-6812, USA

Received: 7 June 2000 / Accepted: 18 October 2000

Abstract. Chiral sculptured thin films (STFs) have unidirectionally periodic electromagnetic constitutive properties and therefore exhibit the circular Bragg phenomenon. The time-domain Maxwell equations are solved using finite difference calculus in order to establish the spatiotemporal anatomy of the action of axially excited, chiral STF slabs on optical narrow-extent pulses (NEPs) modulating circularly polarized carrier waves. A Lorentzian model was adopted for the permittivity dyadics of the chiral STFs.
The time-domain manifestation of the circular Bragg phenomenon is focussed on. First, on examining the refraction of NEPs by a chiral STF half-space, a light pipe and the pulse bleeding phenomenon are shown to occur – when the handednesses of the carrier wave and the chiral STF coincide and the carrier wavelength is in the vicinity of the center-wavelength of the Bragg regime. Next, pulse bleeding inside a chiral STF slab is shown to be responsible for the long wakes of reflected pulses and low energy contents of transmitted pulses, when the incident wave spectrums significantly overlap with the Bragg regime and the carrier waves have the same handedness as the chiral STF slab. Thus, a chiral STF slab can drastically affect the shapes, amplitudes, and spectral components of femtosecond pulses.

PACS. 77.55.+f Dielectric thin films – 78.20.Bh Theory, models, and numerical simulation – 42.70.-a Optical materials

1 Introduction

Chiral liquid crystals [1] are now widely used in optics [2]. The fabrication of their solid analogs became possible during the past few years with the development of the sculptured thin-film (STF) technology [3]. Initial research on the planewave response of chiral STFs [4,5] suggested many specialized applications of them [6], some of which would take advantage of their porous nature – such as gas and humidity sensors [7,8]. Other applications could make use of their solid nature, for instance, in solid optics and optoelectronics. The first optical applications are now emerging [9–11] as a result of improved fabrication technology [12,13]; and experimental research on their optical characterization is also advancing [13–15].

All of the optical applications cited exploit the circular Bragg phenomenon that all helicoidal bianisotropic mediums (HBMs) – exemplified by chiral STFs as well as chiral liquid crystals – must display in consequence of their periodically and unidirectionally nonhomogeneous constitution [18]. Let the direction of nonhomogeneity of a chiral STF be parallel to the z axis, while the film completely occupies the region $z_\ell \leq z \leq z_r$. When circularly polarized, monochromatic light falls normally on this film of sufficient thickness, then it is

- almost perfectly reflected if the handedness of incident light coincides with the structural handedness of the film, but
- almost perfectly transmitted if otherwise,

provided absorption within the film is negligible and the free-space wavelength λ_0 of the incident light lies within the Bragg regime. This regime is sufficiently identified by a center-wavelength λ_0^{Br} and its bandwidth is quite narrow [5,13,16]. When absorption cannot be ignored, the foregoing bulleted statements on polarization-sensitive reflection and transmission have to be modified to take absorption into account [17], but the relationship between the handedness of incident light and the structural handedness of the chiral STF remains delicate.

Planewave response characteristics are not sufficient to understand the optics of chiral STFs. This has become clear from analytical examinations of modal energy flows in these materials [19]. The shortcoming must be overcome because femtosecond optical pulses are routinely generated these days [20], and widespread industrial exploitation of such narrow-extent pulses (NEPs) is imminent. The bandwidth of a carrier wave that is amplitude-modulated by a NEP is very wide, and is likely to

[a] e-mail: JBG136@psu.edu
[b] e-mail: AXL4@psu.edu

completely encompass the Bragg wavelength-regime of a chiral STF encountered by it. That possibility will have repercussions on the design of STF-based optical devices. But the time-domain manifestation of the circular Bragg phenomenon is yet not known.

This paper aims to remedy that situation. In broad terms, we had two aims to undertake the work reported here:

A. to establish the nature and the site of the interaction between the handedness of incident light and the structural handedness of an axially excited chiral STF, and
B. to examine the reflection and the transmission of NEPs by an axially excited chiral STF.

As conventional frequency-domain research [4,5,13] relies on solving the Maxwell equations for monochromatic fields, which does not allow for the separation of the effects due to the two interfaces of any slab with free space (*i.e.*, vacuum), a time-domain investigation is necessary. Such an investigation must take several features of chiral STFs into account: (i) unidirectional nonhomogeneity, (ii) anisotropy, (iii) temporal dispersion, and (iv) absorption. Explicit consideration of the last two features is mandated by the wide bandwidths of carrier waves that are amplitude-modulated by NEPs.

In Section 2, we present the constitutive relations of a chiral STF as well as the relevant electromagnetic derivations, and establish a finite–difference algorithm. Numerical results and conclusions are presented in Section 3. Vectors are underlined once and dyadics twice; t denotes time; while $\underline{r} = x\underline{u}_x + y\underline{u}_y + z\underline{u}_z$ is the position vector in a Cartesian coordinate system with $\underline{u}_x$, $\underline{u}_y$ and $\underline{u}_z$ as the unit vectors.

2 Theoretical analysis

As mentioned earlier, the slab region $z_\ell \leq z \leq z_r$, $(z_\ell > 0)$, is occupied by a chiral STF, while the half-spaces $z \leq z_\ell$ and $z \geq z_r$ are vacuous. A carrier wave modulated by a pulse is launched from the plane $z = 0$ at time $t = 0$ in the $+z$ direction. It excites the chiral STF, and eventually metamorphoses into a reflected pulse and a transmitted pulse.

2.1 Constitutive relations

The time-domain constitutive relations of a linear dielectric medium may be expressed as

$$\underline{D}(\underline{r},t) = \epsilon_0 \left(\underline{\underline{\epsilon}} * \underline{E}\right)(\underline{r},t)\,, \tag{1}$$

$$\underline{B}(\underline{r},t) = \mu_0\, \underline{H}(\underline{r},t). \tag{2}$$

Here, $\epsilon_0 = 8.854 \times 10^{-12}$ F/m and $\mu_0 = 4\pi \times 10^{-7}$ H/m are the permittivity and permeability of free space, respectively, while the operation

$$\left(\underline{\underline{\epsilon}} * \underline{E}\right)(\underline{r},t) = \int_0^\infty \underline{\underline{\epsilon}}\,(\underline{r}\ \bullet \underline{u}_z, \tau)\ \bullet \underline{E}\,(\underline{r}, t-\tau)\,\mathrm{d}\tau \tag{3}$$

denotes convolution with respect to time.

The relative permittivity dyadic everywhere is specified by

$$\underline{\underline{\epsilon}}(\underline{r},t) = \begin{cases} \underline{\underline{I}}\,\delta(t)\,, & z \notin [z_\ell,\, z_r] \\ \underline{\underline{S}}_z(z-z_\ell)\ \bullet \underline{\underline{S}}_y(\chi)\ \bullet \underline{\underline{\epsilon}}^{\,o}_{\mathrm{ref}}(t)\ \bullet & \\ \qquad \underline{\underline{S}}_y^{-1}(\chi)\ \bullet \underline{\underline{S}}_z^{-1}(z-z_\ell)\,, & z \in [z_\ell,\, z_r] \end{cases}, \tag{4}$$

where $\underline{\underline{I}}$ is the identity dyadic and $\delta(t)$ is the Dirac delta function. The rotation dyadic

$$\underline{\underline{S}}_z(z) = \underline{u}_z\underline{u}_z + (\underline{u}_x\underline{u}_x + \underline{u}_y\underline{u}_y)\cos\frac{\pi z}{\Omega} + (\underline{u}_y\underline{u}_x - \underline{u}_x\underline{u}_y)\sin\frac{\pi z}{\Omega} \tag{5}$$

captures the anisotropy as well as the rotational nonhomogeneity of a chiral STF, with 2Ω being the structural period. Equation (5) holds for a structurally right-handed (RH) STF; alter the sign of the third term on its right side for a structurally left-handed (LH) STF. Finally, the tilt dyadic

$$\underline{\underline{S}}_y(\chi) = \underline{u}_y\underline{u}_y + (\underline{u}_x\underline{u}_x + \underline{u}_z\underline{u}_z)\cos\chi + (\underline{u}_z\underline{u}_x - \underline{u}_x\underline{u}_z)\sin\chi\,, \tag{6}$$

where $\chi > 0^\circ$ is the so-called angle of rise [6].

Single-resonance Lorentzian characteristics [21] are assumed for the three components of $\underline{\underline{\epsilon}}^{\,o}_{\mathrm{ref}}(t)$; thus [17],

$$\underline{\underline{\epsilon}}^{\,o}_{\mathrm{ref}}(t) = \epsilon_a(t)\,\underline{u}_z\underline{u}_z + \epsilon_b(t)\,\underline{u}_x\underline{u}_x + \epsilon_c(t)\,\underline{u}_y\underline{u}_y\,. \tag{7}$$

In this equation,

$$\epsilon_{a,b,c}(t) = \delta(t) + p_{a,b,c}\left(\frac{2\pi c_0}{\lambda_0^{a,b,c}}\right)\sin\left(\frac{2\pi c_0}{\lambda_0^{a,b,c}}t\right) \times \exp\left(-\frac{c_0 t}{N_{a,b,c}\lambda_0^{a,b,c}}\right)\mathcal{U}(t)\,, \tag{8}$$

where $\mathcal{U}(t)$ is the unit step function and $c_0 = (\epsilon_0\mu_0)^{-1/2}$. The oscillator strengths are denoted by $p_{a,b,c}$; $\lambda_0^{a,b,c}(1 + N_{a,b,c}^{-2})^{-1/2}$ are the resonance wavelengths; while large values of $N_{a,b,c}$ imply narrow absorption bands located around the resonance wavelengths.

2.2 Partial differential equations for axial propagation

Denoting partial differentiation with respect to a variable v as ∂_v, we substitute the constitutive relations (1) and (4) in the source-free Maxwell curl equations $\nabla \times \underline{E}(\underline{r},t) = -\partial_t\,\underline{B}(\underline{r},t)$ and $\nabla \times \underline{H}(\underline{r},t) = \partial_t\,\underline{D}(\underline{r},t)$. For axial propagation, $\partial_x \equiv \partial_y \equiv 0$ and $\nabla \equiv \underline{u}_z\,\partial_z$. Accordingly, we

obtain the following six differential equations:

$$\partial_z E_x(z,t) = -\mu_0 \partial_t H_y(z,t)\,, \tag{9}$$
$$\partial_z E_y(z,t) = \mu_0 \partial_t H_x(z,t)\,, \tag{10}$$
$$\partial_z H_x(z,t) = \epsilon_0 \partial_t \left[\underline{u}_y \bullet \left(\underline{\underline{\epsilon}} * \underline{E} \right)(z,t) \right]\,, \tag{11}$$
$$\partial_z H_y(z,t) = -\epsilon_0 \partial_t \left[\underline{u}_x \bullet \left(\underline{\underline{\epsilon}} * \underline{E} \right)(z,t) \right]\,, \tag{12}$$
$$0 = \partial_t \left[\underline{u}_z \bullet \left(\underline{\underline{\epsilon}} * \underline{E} \right)(z,t) \right]\,, \tag{13}$$
$$0 = \partial_t H_z(z,t)\,. \tag{14}$$

Equation (14) simply means that $H_z(z,t) \equiv H_z(z)$; furthermore $H_z(z,t) = 0$ in view of the initial conditions imposed later. The remaining five equations must be handled together. That is best done using a 5×5 matrix formulation. Let the column 5-vector

$$[\underline{F}(z,t)] = [E_x(z,t),\, E_y(z,t),\, H_x(z,t),\, H_y(z,t),\, E_z(z,t)]^{\mathrm{T}} \tag{15}$$

contain the five remaining components of the electromagnetic field, the superscript $^{\mathrm{T}}$ indicating the transpose. Then, (9)–(13) may be written compactly as

$$\left[\underline{\underline{J}}\right] \partial_z \left[\underline{F}(z,t)\right] = \left[\underline{\underline{Q}}\right] \partial_t \left[\underline{F}(z,t)\right] + \epsilon_0 \partial_t \left\{ \left(\left[\underline{\underline{A}}\right] * \left[\underline{F}\right] \right)(z,t) \right\}\,. \tag{16}$$

In (16), the constitutive properties are contained in the matrix $\left[\underline{\underline{A}}\right](z,t)$ which is identically null-valued for $z \notin [z_\ell,\, z_r]$, while

$$\left[\underline{\underline{A}}\right](z,t) = \left[\begin{array}{cccc} 0 & 0 & 0\,0 & 0 \\ 0 & 0 & 0\,0 & 0 \\ A_{31}(z,t) & A_{32}(z,t) & 0\,0 & A_{35}(z,t) \\ -A_{41}(z,t) & -A_{31}(z,t) & 0\,0 & -A_{45}(z,t) \\ A_{45}(z,t) & A_{35}(z,t) & 0\,0 & A_{55}(z,t) \end{array} \right]\,, \quad z \in [z_\ell,\, z_r]\,, \tag{17}$$

with

$$A_{31} = \left(\epsilon_a \sin^2\chi + \epsilon_b \cos^2\chi - \epsilon_c\right) \times \sin\frac{\pi(z-z_\ell)}{\Omega} \cos\frac{\pi(z-z_\ell)}{\Omega}\,, \tag{18}$$
$$A_{32} = \left(\epsilon_a \sin^2\chi + \epsilon_b \cos^2\chi\right) \times \sin^2\frac{\pi(z-z_\ell)}{\Omega} + \epsilon_c \cos^2\frac{\pi(z-z_\ell)}{\Omega} - 1\,, \tag{19}$$
$$A_{35} = (\epsilon_b - \epsilon_a) \sin\chi\, \cos\chi\, \sin\frac{\pi(z-z_\ell)}{\Omega}\,, \tag{20}$$
$$A_{41} = \left(\epsilon_a \sin^2\chi + \epsilon_b \cos^2\chi\right) \times \cos^2\frac{\pi(z-z_\ell)}{\Omega} + \epsilon_c \sin^2\frac{\pi(z-z_\ell)}{\Omega} - 1\,, \tag{21}$$
$$A_{45} = (\epsilon_b - \epsilon_a) \sin\chi\, \cos\chi\, \cos\frac{\pi(z-z_\ell)}{\Omega}\,, \tag{22}$$
$$A_{55} = \epsilon_a \cos^2\chi + \epsilon_b \sin^2\chi - 1\,. \tag{23}$$

The other two 5×5 matrixes appearing in (16) are as follows:

$$\left[\underline{\underline{J}}\right] = \mathrm{diag}\,[1,\, 1,\, 1,\, 1,\, 0]\,, \tag{24}$$
$$\left[\underline{\underline{Q}}\right] = \left[\begin{array}{ccccc} 0 & 0 & 0 & -\mu_0 & 0 \\ 0 & 0 & \mu_0 & 0 & 0 \\ 0 & \epsilon_0 & 0 & 0 & 0 \\ -\epsilon_0 & 0 & 0 & 0 & 0 \\ 0 & 0 & 0 & 0 & \epsilon_0 \end{array} \right]\,. \tag{25}$$

2.3 Finite difference equations for axial propagation

Analytical solution of (16) is not known and, therefore, we resort to a simple numerical technique. Both space and time are discretized as

$$\left. \begin{array}{l} z_i = i\Delta z\,, \quad i = 0,\, 1,\, 2,\, 3,\, ... \\ t_n = n\Delta t\,, \quad n = 0,\, 1,\, 2,\, 3,\, ... \end{array} \right\}\,, \tag{26}$$

derivatives are replaced by central differences, and the leapfrog method is used [22]. Accordingly, (16) transforms to the difference equation

$$\left[\underline{\underline{J}}\right] \left(\frac{[\underline{F}]_{i+1}^n - [\underline{F}]_{i-1}^n}{2\Delta z} \right) = \left[\underline{\underline{Q}}\right] \bullet \left(\frac{[\underline{F}]_i^{n+1} - [\underline{F}]_i^{n-1}}{2\Delta t} \right) + \epsilon_0 \sum_{m=1}^{n-1} \left[\underline{\underline{A}}\right]_i^m \bullet \left(\frac{[\underline{F}]_i^{n-m+1} - [\underline{F}]_i^{n-m-1}}{2} \right) + \frac{\epsilon_0}{2} \left[\underline{\underline{A}}\right]_i^n \bullet \left([\underline{F}]_i^1 - [\underline{F}]_i^0 \right)\,, \tag{27}$$

wherein the shorthand notation

$$[\underline{F}]_i^n = [\underline{F}(z_i,\, t_n)]\,, \quad \left[\underline{\underline{A}}\right]_i^n = \left[\underline{\underline{A}}(z_i,\, t_n)\right] \tag{28}$$

has been used. Let us note in passing that $\left[\underline{\underline{A}}\right]_i^0$ is null-valued as per (8).

Solving (27) for $[\underline{F}]_i^{n+1}$, we obtain

$$[\underline{F}]_i^{n+1} = [\underline{F}]_i^{n-1} + \beta \left[\underline{\underline{V}}\right] \bullet \left([\underline{F}]_{i+1}^n - [\underline{F}]_{i-1}^n \right) - \sum_{m=1}^{n-1} \left[\underline{\underline{W}}\right]_i^m \bullet \left([\underline{F}]_i^{n-m+1} - [\underline{F}]_i^{n-m-1} \right) \Delta t - \left[\underline{\underline{W}}\right]_i^n \bullet \left([\underline{F}]_i^1 - [\underline{F}]_i^0 \right) \Delta t\,, \tag{29}$$

with

$$\left[\underline{\underline{V}}\right] = c_0^{-1} \left[\underline{\underline{Q}}\right]^{-1} \left[\underline{\underline{J}}\right]\,, \quad \left[\underline{\underline{W}}\right]_i^m = \epsilon_0 \left[\underline{\underline{Q}}\right]^{-1} \left[\underline{\underline{A}}\right]_i^m\,. \tag{30}$$

Here, we have defined the real number $\beta = c_0 \Delta t / \Delta z$. The condition $\beta < 1$ ensures the numerical stability of the algorithm [22].

Equation (29) requires initial as well as boundary conditions. Setting

$$[\underline{F}]_i^0 = [0, 0, 0, 0, 0]^{\mathrm{T}} \; \forall\, i\,, \tag{31}$$

we assert the absence of the electromagnetic field anywhere at time $t = 0$. The boundary condition

$$[\underline{F}]_0^n = g(t_n)[\underline{\varphi}(t_n)] \tag{32}$$

contains a carrier wave represented by the column vector $[\underline{\varphi}(t)]$ that is amplitude-modulated by the pulse function $g(t)$. Equation (29) can now be solved iteratively.

3 Numerical results and discussion

For numerical simulation, the oscillator strengths were set as $p_a = 0.40$, $p_b = 0.52$ and $p_c = 0.42$; while $\lambda_0^a = \lambda_0^c = 280$ nm and $\lambda_0^b = 290$ nm were chosen to lie in the ultraviolet regime. The parameters $N_a = N_b = N_c = 100$ ensured that absorption is moderate in the visible regime. The structural half-period $\Omega = 200$ nm and the tilt angle $\chi = 20^\circ$ were also set. For these parameters, the center-wavelength of the Bragg regime is estimated as $\lambda_0^{\mathrm{Br}} = 516$ nm and the full-width half-maximum (FWHM) bandwidth of the Bragg regime is estimated to be 27 nm [17].

For all numerical results reported here, the boundary condition (32) was defined through

$$[\underline{\varphi}_{\pm}(t)] = \left[\cos(\frac{2\pi c_0}{\lambda_0^{\mathrm{car}}}t), \pm\sin(\frac{2\pi c_0}{\lambda_0^{\mathrm{car}}}t), \right. \\ \left. \mp\eta_0^{-1}\,\sin(\frac{2\pi c_0}{\lambda_0^{\mathrm{car}}}t), \eta_0^{-1}\,\cos(\frac{2\pi c_0}{\lambda_0^{\mathrm{car}}}t), 0\right]^{\mathrm{T}}, \tag{33}$$

$$g(t) = \frac{c_0 t}{2\lambda_0^{\mathrm{car}}}\exp(\frac{-c_0 t}{\lambda_0^{\mathrm{car}}})\,. \tag{34}$$

Whereas $[\underline{\varphi}_+(t)]$ represents a left-handed plane wave, $[\underline{\varphi}_-(t)]$ represents a right-handed plane wave, both circularly polarized. Values of λ_0^{car} chosen are as follows: 430, 516 and 600 nm.

The aforementioned algorithm was implemented, using the Fortran 90 computing language and single-precision arithmetic, on a Sun Microsystems computer. The chosen spatiotemporal domain was discretized with $\Delta z = 5$ nm and $\beta = 0.9$, so that $\Delta t = 0.015$ fs. Snapshots of the axial component

$$P_z(z,t) = \underline{u}_z \bullet [\underline{E}(z,t) \times \underline{H}(z,t)] \tag{35}$$

of the instantaneous Poynting vector are shown at $t = 12.0$ fs in Figure 1 for the incident pulses at each selected carrier wavelength. The pulse duration is $\simeq 8$ fs, and $P_z(z,t)$ is clearly independent of the handedness of the carrier plane wave. Parenthetically, as the choice (31) of initial condition implies that $D_z(z,t) \equiv 0\,\forall\, t$, we tested our computer program to ensure that the latter requirement was met.

3.1 Chiral STF half-space

Let us begin by exploring the reflection and refraction[1] of the chosen NEPs at the first interface $z = z_\ell$. For this purpose, we simply removed z_r outside the domain $\{i \in [0,\, 3000]\,,\, n \in [0,\, 3431]\}$ of calculation – about the largest possible domain allowed by the capabilities of our computer for this problem – while $z_\ell = 7500$ nm. Thus, the launched NEP takes 25.0 fs to arrive at the vacuum/STF interface $z = z_\ell$.

Snapshots of $P_z(z,t)$ at $t = 49.5$ fs are shown in Figure 2 for LH carrier waves, and in Figure 3 for RH carrier waves. Ample time elapsed so that the incident pulse... can not be in evidence in both figures. Figure 4 gives a magnified view of $P_z(z,t)$ near the boundary of the chiral STF when the carrier wavelength is 516 nm. The data in these figures is normalized to the peak value of $P_z(z,t)$ attained by the incident pulse with $\lambda_0^{\mathrm{car}} = 516$ nm.

Examining the results in Figures 2 and 3, we observe that the reflected pulse contains more energy for RH carrier waves than for LH carrier waves. This observation is further substantiated by the plots in Figure 5 of the instantaneous energy per unit transverse area

$$U_\ell(t) = \frac{1}{2}\int_0^{z_\ell} [\epsilon_0 \underline{E}(z,t) \bullet \underline{E}(z,t) + \mu_0 \underline{H}(z,t) \bullet \underline{H}(z,t)]\,\mathrm{d}z \tag{36}$$

in the left (*i.e.*, vacuous) half-space, computed for $t \in [0,\, 2z_\ell/c_0]$. The value of this integral was approximated with the simple Euler method [22]. In all cases, $U_\ell(t)$ rises with time over the temporal width of the incident pulse and then levels off until the incident pulse reaches the interface $z = z_\ell$ at $t = 25.0$ fs. Then it decreases precipitously, as much of the incident energy crosses over to the chiral STF half–space. For LH carrier waves, $U_\ell(t)$ levels off after the drop, indicating that the reflected pulse acquires constant energy.

The situation is quite different for RH carrier waves. The energy density $U_\ell(t)$ in the vacuous half-space continues to rise for $t \gtrsim 33$ fs, indicating that the reflected pulse continues to gain energy. The only source of energy available is the refracted pulse, which implies that energy flows from the chiral STF into the vacuum.

Indeed, in Figure 3, $P_z(z,t) < 0$ not only for $z < z_\ell$ but also in the part of the chiral STF closest to the interface $z = z_\ell$. A light pipe is formed across that interface, and the refracted pulse "bleeds" energy into the vacuous half-space. We observed the length of the light pipe to continue to increase with time over the entire domain of our simulation. The light pipe can be seen more clearly in Figure 4 when the carrier light is RH, while the light pipe is absent when the carrier is LH. The formation of the light pipe clearly means that the reflected pulse has a long wake.

Thus, when the carrier wave is RH, the refracted pulse loses energy for two reasons: (i) the chiral STF is an absorbing medium, so that the refracted pulse must attenuate as it propagates along the $+z$ axis; and (ii) the wake

[1] We reserve the term *transmission* for chiral STF slabs.

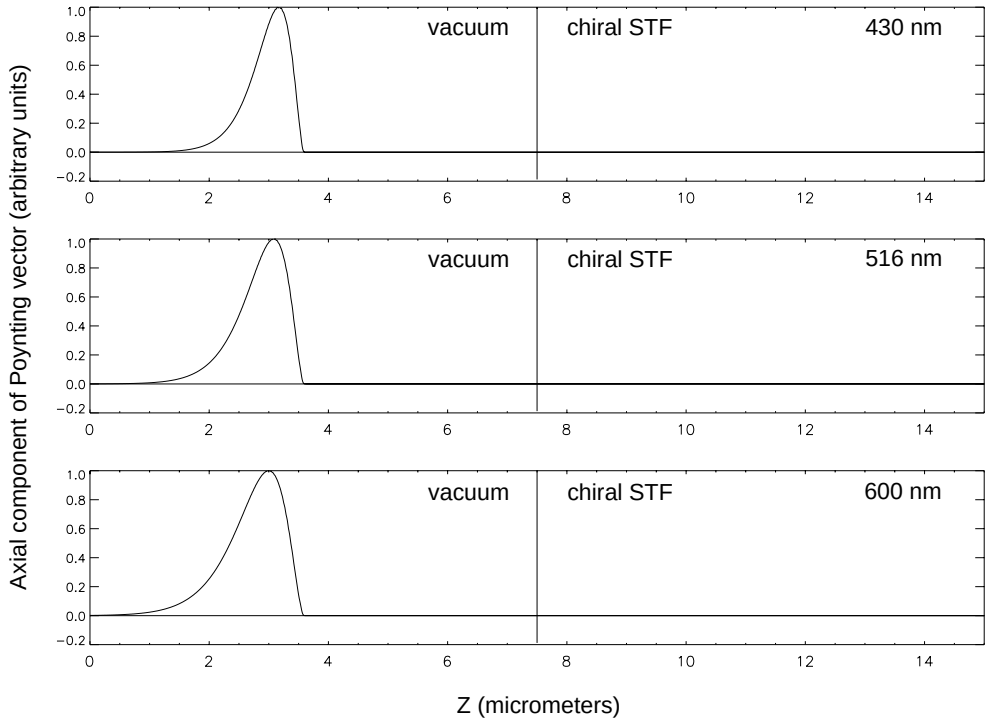

Fig. 1. Snapshots of the axial component $P_z(z,t)$ of the instantaneous Poynting vector at $t = 12.0$ fs. Only the incident pulses exist at this instant of time. Top: $\lambda_0^{\text{car}} = 430$ nm; middle: $\lambda_0^{\text{car}} = 516$ nm; bottom: $\lambda_0^{\text{car}} = 600$ nm. Data in all plots have been normalized to the peak value of the incident pulse with $\lambda_0^{\text{car}} = 516$ nm.

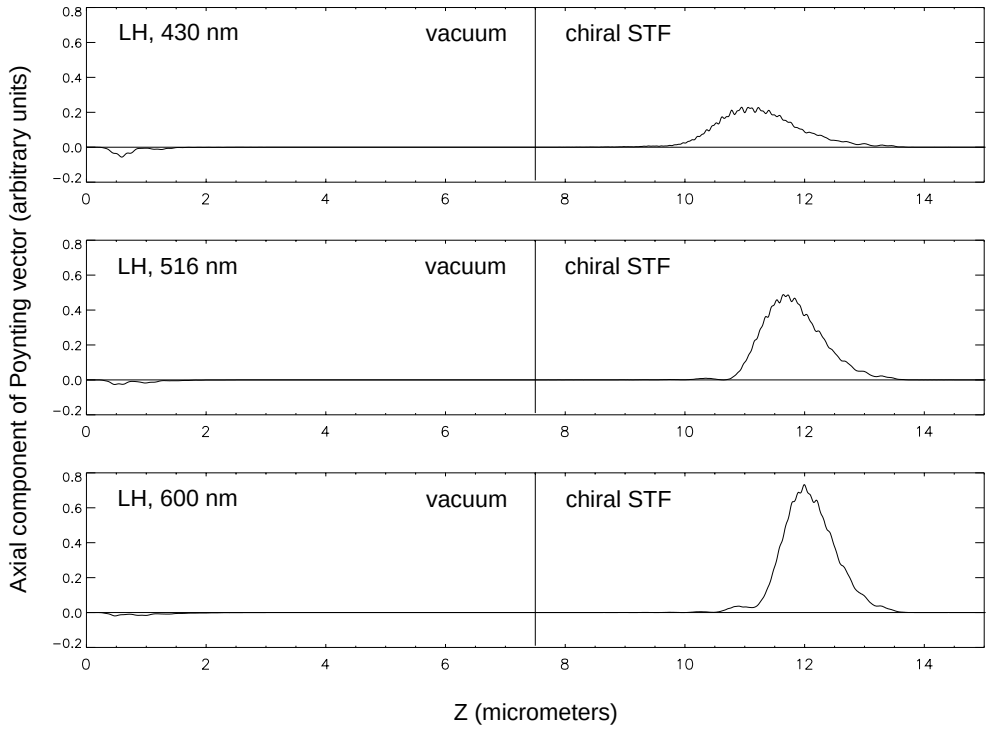

Fig. 2. Snapshots of the axial component $P_z(z,t)$ of the instantaneous Poynting vector at $t = 49.5$ fs across the interface of vacuous and chiral STF half-spaces, for LH carrier waves. Top: $\lambda_0^{\text{car}} = 430$ nm; middle: $\lambda_0^{\text{car}} = 516$ nm; bottom: $\lambda_0^{\text{car}} = 600$ nm. See Figure 1 for normalization details.

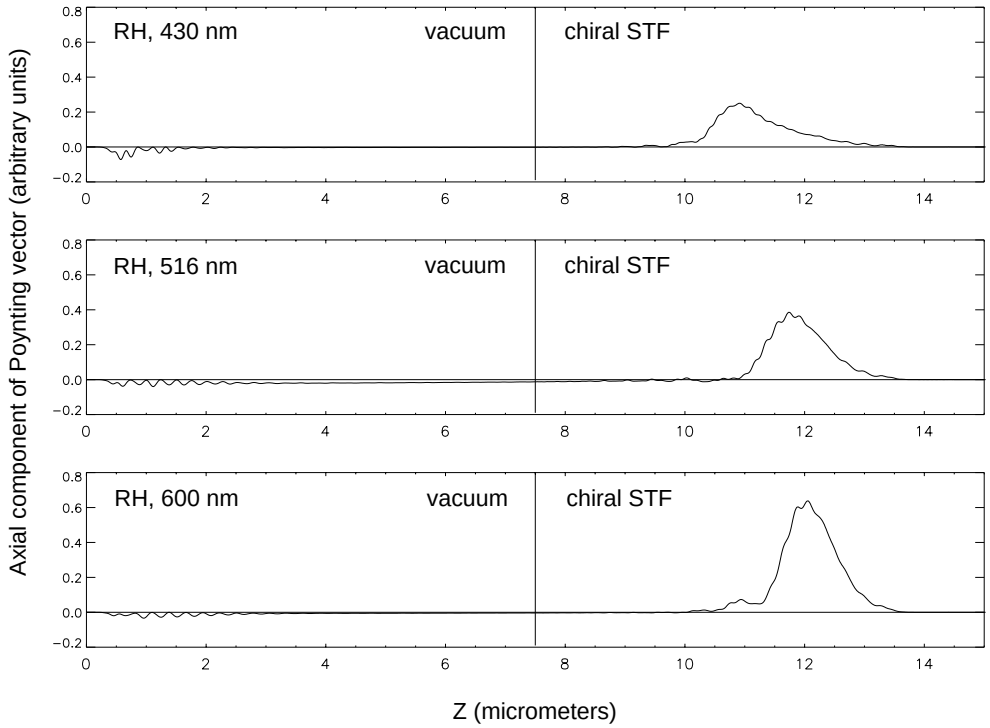

Fig. 3. Same as Figure 2, but for RH carrier waves. Notice the thick light pipe connecting the reflected and refracted pulses when the carrier has a wavelength of 516 nm. The presence of the light pipe is the mechanism behind the increased reflectivity of the half-space in the Bragg regime when the carrier wave is RH. See Figure 1 for normalization details.

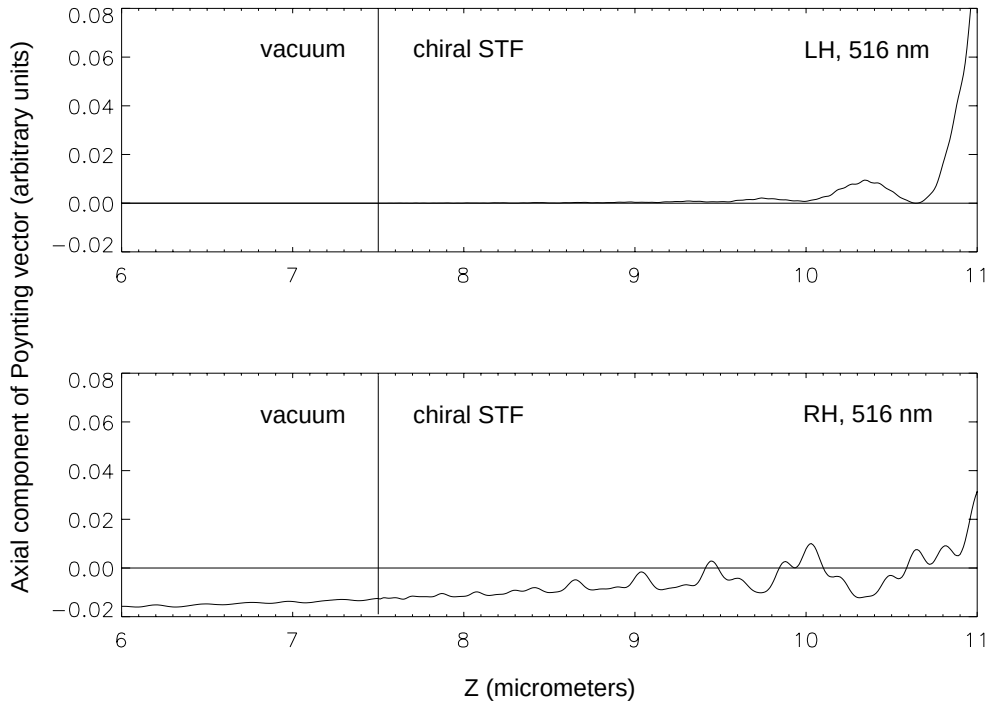

Fig. 4. Magnified view of the vacuum/chiral STF interface for LH (top graph) and RH (bottom) carriers with 516 nm wavelength, gleaned respectively from Figures 2 and 3.

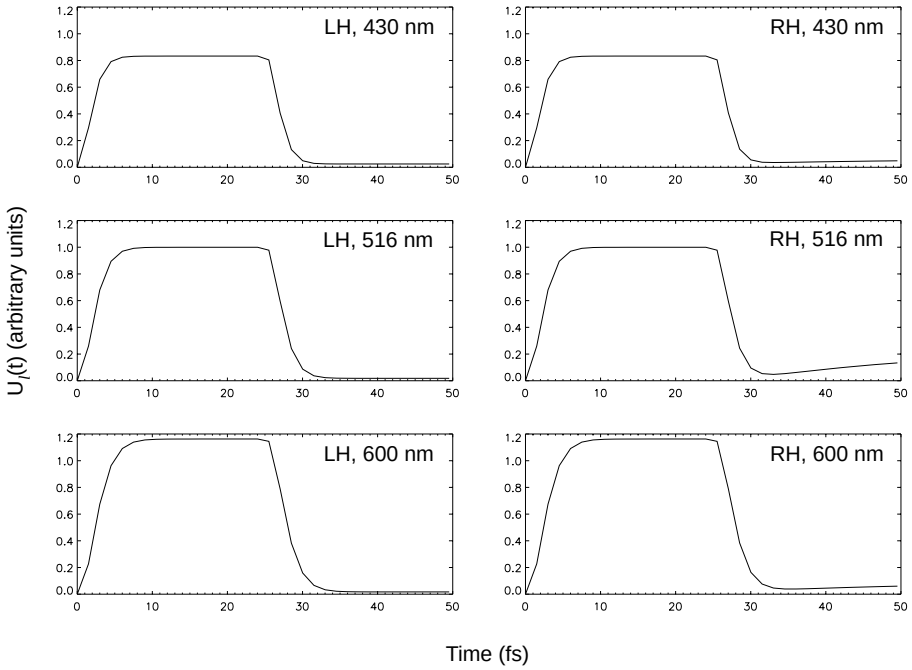

Fig. 5. Evolution of $U_\ell(t)$, the instantaneous energy per unit transverse area, with time in the vacuous half-space for LH (graphs on left) and RH (graphs on right) carrier waves. The plots have been normalized to the maximum value of $U_\ell(t)$ when $\lambda_0^{\text{car}} = 516$ nm.

of the refracted pulse continues to direct some energy towards the interface $z = z_\ell$. Further attenuation occurs during back-propagation, as does partial leakage into the vacuous half-space. Eventually, the reflected pulse will acquire its final shape and energy content, and the refracted pulse will die out, but our simulations did not span a long enough portion of spacetime to confirm that conclusion.

Significantly, the rate of growth of $U_\ell(t)$ for $t \gtrsim 33$ fs is the highest when the carrier wave is RH and $\lambda_0^{\text{car}} = \lambda_0^{\text{Br}}$. Furthermore, Fourier analysis of $[\underline{F}](z,t)$ for $t \gtrsim 33$ fs and $z < z_\ell$ shows that the reflected field spectrum has a very prominent maximum at λ_0^{Br} when the carrier wave is RH, the highest intensity recorded when λ_0^{car} equals λ_0^{Br}. The foregoing time-domain observations therefore constitute an exposition of the spatiotemporal anatomy of the circular Bragg phenomenon, which has been observed experimentally for continuous wave excitation of chiral STF slabs (of finite width) [13,16].

3.2 Chiral STF slab

Having established that the interaction of the handednesses of incident light and the chiral STF takes place in the vicinity of the first interface, we now proceed to scattering by a chiral STF occupying the region $z \in [11000, 15000]$ nm. This computation was performed over the domain $\{i \in [0, 4400], n \in [0, 4901]\}$, virtually the largest domain allowed by our computer.

In Figure 6, snapshots of $P_z(z,t)$ for the transmitted and reflected pulses carried by LH plane waves at $t = 72.0$ fs are given. Figure 7 displays similar plots for the pulses carried by RH plane waves. Only the primary reflected/transmitted pulses were captured in our simulation, while secondary pulses (arising from multiple transits within the slab) arriving at later times were excluded by the limited domain of our simulation. As, however, the primary pulses contain most of the energy, our results suffice for discussion.

The plots in Figures 6 and 7 show that the peak power densities of transmitted pulses are lower than those of the incident pulses, with the former increasing with λ_0^{car}. To a great extent, this increase can be explained by the fact that absorption bands in the chosen material are located at 280 and 290 nm wavelengths which lie in the ultraviolet regime. Consequently, absorption inside the chiral STF slab is lesser when λ_0^{car} is farther away from the absorption bands.

The longer wakes of the reflected pulses for RH rather than for LH carrier waves, as seen in Figures 6 and 7, are related to the light pipe described in the previous section. Pulse bleeding occurs inside the chiral STF slab, most prominently when $\lambda_0^{\text{car}} = \lambda_0^{\text{Br}}$. As a clear consequence of that phenomenon, the reflected pulse energy is the highest when the circularly polarized carrier wave has the same handedness as the chiral STF and $\lambda_0^{\text{car}} = \lambda_0^{\text{Br}}$. This statement is justified by the plots of $U_\ell(t)$ shown in Figure 8. The characteristics of these plots are similar to those for reflection by a chiral STF half-space in Figure 5.

The handedness of the carrier plane wave has a marked effect on the energy content of the transmitted pulse, according to Figures 6 and 7. The peak transmitted power density is higher, for all three values of λ_0^{car}, when the carrier wave is LH. This observation is corroborated by the

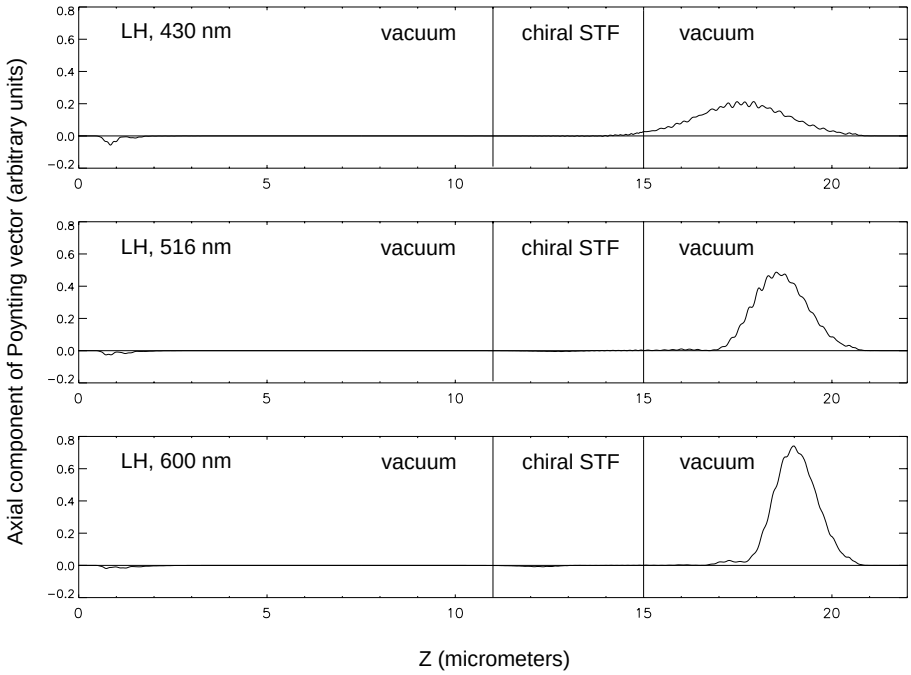

Fig. 6. Snapshots of the axial component $P_z(z,t)$ of the instantaneous Poynting vector at $t = 72.0$ fs across a chiral STF slab ($z \in [11000, 15000]$ nm), for LH carrier waves. Top: $\lambda_0^{\rm car} = 430$ nm; middle: $\lambda_0^{\rm car} = 516$ nm; bottom: $\lambda_0^{\rm car} = 600$ nm.

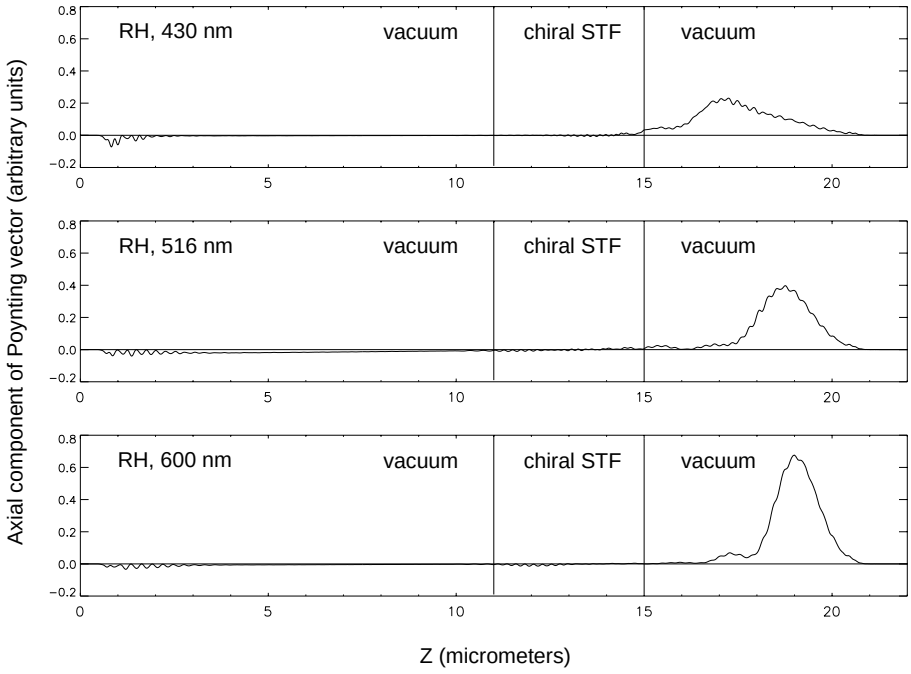

Fig. 7. Same as Figure 6, but the carrier waves are RH.

plots of the instantaneous energy per unit transverse area

$$U_r(t) = \frac{1}{2}\int_{z_r}^{z_{4400}} [\epsilon_0 \underline{E}(z,t) \bullet \underline{E}(z,t) + \mu_0 \underline{H}(z,t) \bullet \underline{H}(z,t)]\,\mathrm{d}z \tag{37}$$

in the right half-space. The transmitted pulse emerges from the chiral STF slab at $t \simeq 52$ fs. We note that $U_r(t)$ is significantly less thereafter with a RH carrier as compared to that with a LH carrier wave, when $\lambda_0^{\rm car} = \lambda_0^{\rm Br}$. Incidentally, both $U_\ell(t)$ and $U_r(t)$ in Figures 8 and 9, respectively, would increase slightly, after the arrival of secondary pulses.

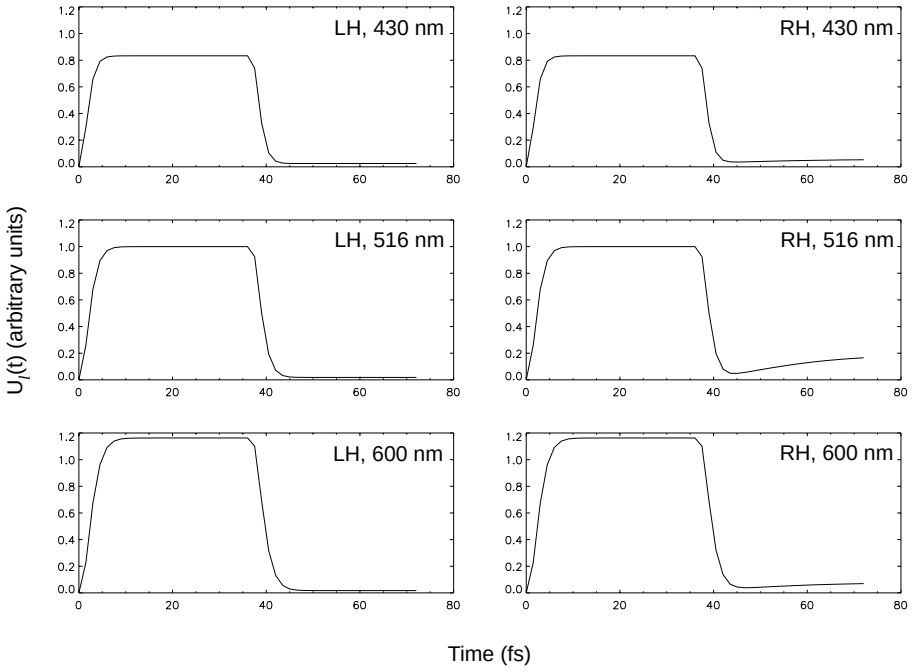

Fig. 8. Temporal evolution of $U_\ell(t)$ in the left half-space $z \leq z_\ell$ for LH (graphs on left) and RH (graphs on right) carrier waves incident on a chiral STF slab. The plots have been normalized to the maximum value of $U_\ell(t)$ when the carrier wavelength is 516 nm.

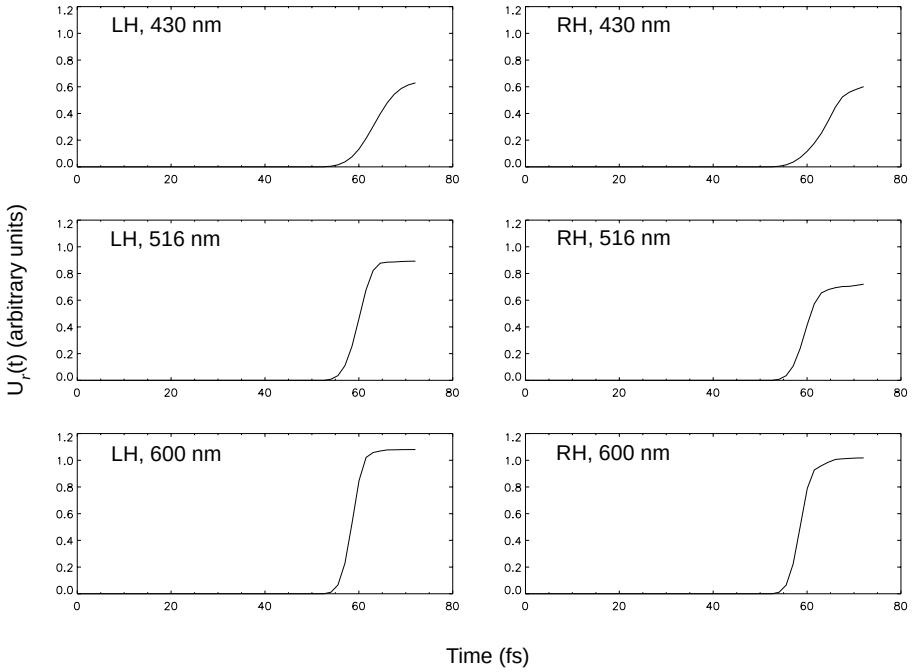

Fig. 9. Same as Figure 8, but for $U_r(t)$ evaluated in the right half-space $z \geq z_r$.

Several calculations show that the difference between the reflected/transmitted energy density for carrier waves of opposite handednesses is more pronounced for thicker chiral STF slabs. Certainly, the occurrence of pulse bleeding explains why the circular Bragg phenomenon is easier to observe in frequency–domain experiments for thicker chiral STF slabs [13, 23]. In thicker slabs, the electromagnetic field interacts with the material over a longer distance (and for a longer time), so that the light pipe transfers more energy to the reflected pulse when the conditions associated with the circular Bragg phenomenon exist.

Furthermore, Figures 6 and 7 indicate that the transmitted pulse has a more prominent wake for RH than for LH carrier waves, especially at the two higher values of $\lambda_0^{\rm car}$. Thus, the handedness of the carrier light in

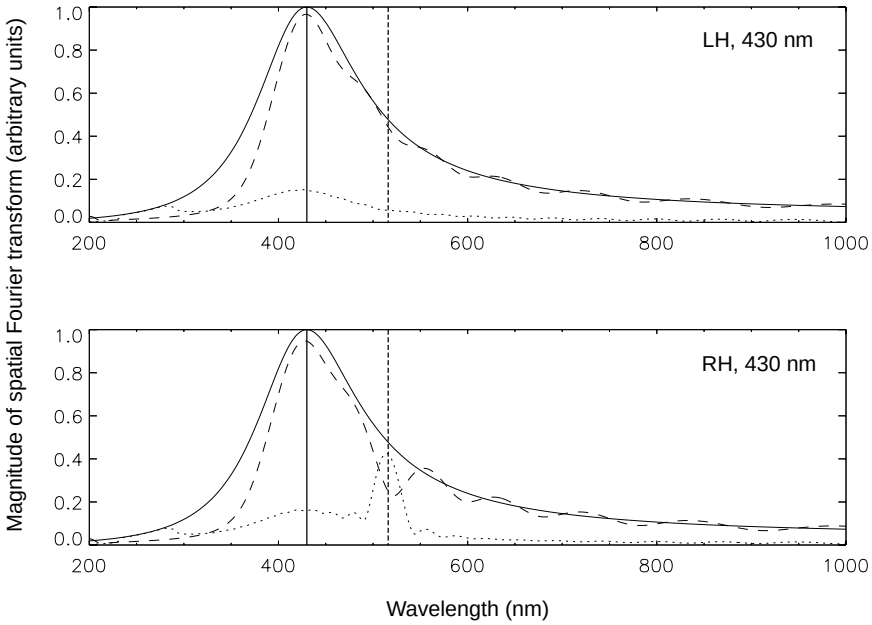

Fig. 10. Normalized spectrums of $\left[|\tilde{E}_x(t,\lambda_0)|^2 + |\tilde{E}_y(t,\lambda_0)|^2\right]^{1/2}$ for the incident (solid lines), the reflected (dotted lines), and the transmitted fields (dashed lines); $\lambda_0^{\text{car}} = 430$ nm. Top: LH carrier wave; bottom: RH carrier wave. Only the primary reflected and the primary transmitted pulses are captured here. The vertical lines on the graphs mark the locations of λ_0^{car} (solid) and λ_0^{Br} (dotted). The peak value of $\left[|\tilde{E}_x(t,\lambda_0)|^2 + |\tilde{E}_y(t,\lambda_0)|^2\right]^{1/2}$ for the incident pulse is normalized to unity. The calculated values for the transmitted pulses occasionally exceed those for the corresponding incident pulses due to discretization and truncation errors in evaluating the spectrums, but these errors are largely inconsequential as they occur outside the half–maximum bands of the incident pulses.

relation to that of the chiral STF slab affects pulse distortion, particularly when the conditions are right for the pulse bleeding phenomenon to appear.

Further light is shed on these issues by the spatial Fourier transforms[2] $\tilde{E}_x(t,\lambda_0)$ and $\tilde{E}_y(t,\lambda_0)$ of the sampled $E_x(z,t)$ and $E_y(z,t)$, respectively. These were computed as

$$\tilde{E}_{x,y}(t,\lambda_0) \approx \int_{z_a'}^{z_b'} \exp\left(\frac{2\pi j}{\lambda_0} z\right) E_{x,y}(z,t)\,\mathrm{d}z\,, \quad j = \sqrt{-1}\,. \tag{38}$$

Although the integral on the right side of (38) should ideally be evaluated over an infinite spatial domain, the finite interval $[z_a',\, z_b'] \equiv [0,\, z_\ell]$ at time $t = 15.01$ fs was sufficient to capture the incident pulse. The Fourier transforms of the primary reflected and transmitted pulses were taken at $t = 72.0$ fs over the spatial domains $[0,\, z_\ell]$ and $[z_r,\, z_{4400}]$, respectively. Secondary reflected/transmitted pulses have much smaller energies than their primary counterparts, and so were excluded from consideration.

Normalized spectrums of $\left[|\tilde{E}_x(t,\lambda_0)|^2 + |\tilde{E}_y(t,\lambda_0)|^2\right]^{1/2}$ for each selected value of λ_0^{car} are plotted in Figures 10–12. Reflection is noticeably weaker when the carrier wave is LH rather than RH, for all three values of λ_0^{car}. The effects of the pulse bleeding phenomenon are most evident in Figure 11, where a drop in transmission and increase in reflection at wavelengths near λ_0^{Br} can be seen. A smaller peak in the reflected spectrum at λ_0^{Br} can be observed for RH carrier in Figures 10 and 12 also; and this peak is accompanied by a corresponding dip in the transmitted spectrum, as expected [17,23].

Incidentally, the transmission spectral peaks for LH carrier waves in Figures 10–12 are located at wavelengths slightly greater than λ_0^{car}, the difference between the wavelength of peak transmission and λ_0^{car} being smaller for larger λ_0^{car}. This is due to the absorption characteristics of the chiral STF slab. The closer that λ_0^{car} is to the resonance wavelengths, the farther must the transmission spectral peak be from the incidence spectral peak, in agreement with the snapshots presented in Figures 6 and 7.

4 Concluding remarks

Solving the Maxwell curl equations explicitly in the time domain, we have shown that a chiral STF slab can drastically affect the shapes, amplitudes, and spectral components of femtosecond pulses. The wavelength and handedness of the plane wave carrying the incident pulse and the

[2] In vacuum, the spatial and the temporal Fourier transforms of any electromagnetic field component are isomorphic and simply related [24].

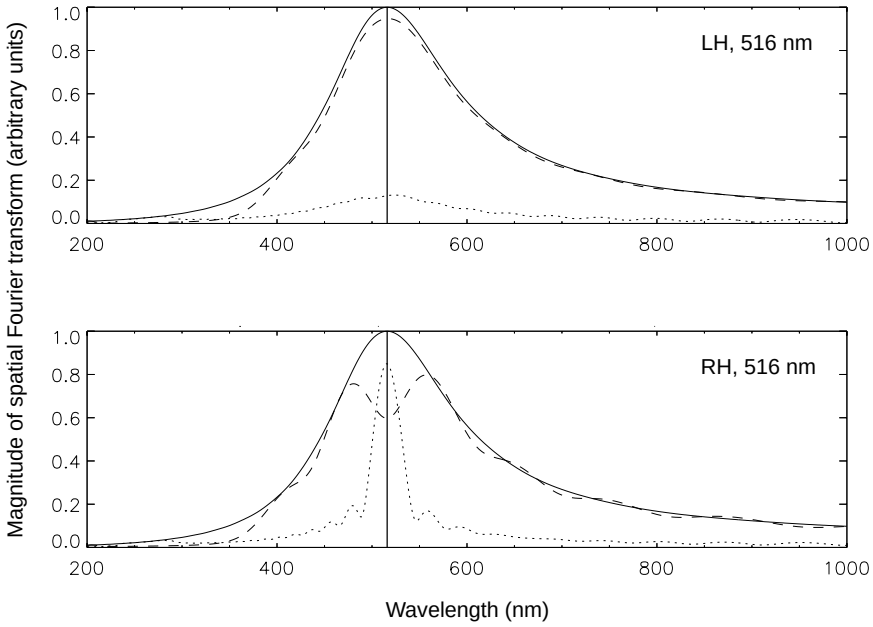

Fig. 11. Same as Figure 10, but $\lambda_0^{\rm car} = 516$ nm.

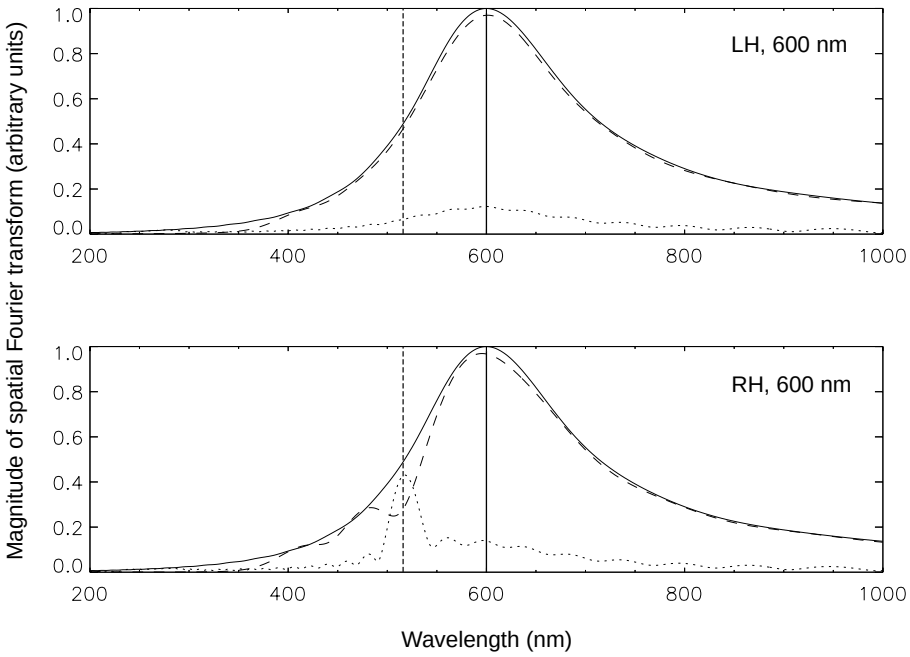

Fig. 12. Same as Figure 10, but $\lambda_0^{\rm car} = 600$ nm.

properties of the chiral STF determine the characteristics of the transmitted and reflected pulses.

The ability of chiral STF slabs to more strongly transmit or reflect a NEP depending on its carrier wavelength and handedness can find use in laser mirrors, optical filters, multiplexers, and other in-line optical telecommunication devices. The alteration in transmitted pulse shape is important in light recent work that suggests several bits of information may be encoded in a single femtosecond pulse [25]. When chiral STFs are to be used in optical circuits, pulse shaping may be needed to offset distortion by them as well as to either avoid or exploit the handedness-sensitive filtering action of the circular Bragg phenomenon. Furthermore, as diffusion of gaseous and liquid species into the porous microstructure of chiral STFs can alter their electromagnetic properties [6,26], these materials are strong candidates for incorporation into optical sensing systems based on pulse propagation.

J.B. Geddes III gratefully acknowledges support by a Proctor and Gamble Summer Undergraduate Research Scholarship.

References

1. P.G. de Gennes, J. Prost, *The Physics of Liquid Crystals* (Clarendon Press, Oxford, UK, 1993).
2. S.D. Jacobs, *Selected Papers on Liquid Crystals for Optics* (SPIE, Bellingham, WA, USA, 1992).
3. A. Lakhtakia, R. Messier, Mater. Res. Innov. **1**, 145 (1997).
4. V.C. Venugopal, A. Lakhtakia, Proc. Roy. Soc. London A **454**, 1535 (1998); errata: **455**, 4383 (1999).
5. V.C. Venugopal, A. Lakhtakia, Proc. Roy. Soc. London A **456**, 125 (2000).
6. R. Messier, A. Lakhtakia, Mater. Res. Innov. **2**, 217 (1999).
7. A. Lakhtakia, Sens. and Actuators B: Chem. **52**, 243 (1999).
8. A.T. Wu, M. Seto, M.J. Brett, Sens. and Mater. **11**, 493 (2000).
9. I. Hodgkinson, Q.H. Wu, A. Lakhtakia, R. Messier, OSA Opt. Photon. News **10**, 30 (December 1999).
10. Q.h. Wu, I.J. Hodgkinson, A. Lakhtakia, Opt. Eng. **39**, 1863 (2000).
11. I.J. Hodgkinson, Q.h. Wu, A. Lakhtakia, M.W. McCall, Opt. Commun. **177**, 79 (2000).
12. I.J. Hodgkinson, Q.H. Wu, Appl. Opt. **38**, 3621 (1999).
13. I. Hodgkinson, Q.h. Wu, B. Knight, A. Lakhtakia, K. Robbie, Appl. Opt. **39**, 642 (2000).
14. M. Schubert, Thin Solid Films **313/314**, 373 (1998).
15. A.K. Bhowmik, Optik **111**, 103 (2000).
16. J.C. Sit, D.J. Broer, M.J. Brett, Adv. Mater. **12**, 371 (2000).
17. A. Lakhtakia, Eur. Phys. J. AP **8**, 129 (1999).
18. A. Lakhtakia, V.C. Venugopal, Arch. Elektr. Über. **53**, 287 (1999).
19. A. Lakhtakia, Opt. Commun. **161**, 275 (1999).
20. T. Kamiya, *Femtosecond Technology: From Basic Research to Future Applications* (Springer, New York, NY, USA, 1999).
21. C. Kittel, *Introduction to Solid State Physics* (Wiley Eastern, New Delhi, India, 1974).
22. N. Gershenfield, *The Nature of Mathematical Modeling* (Cambridge Univ. Press, Cambridge, UK, 1999).
23. V.C. Venugopal, A. Lakhtakia, Opt. Commun. **145**, 171 (1998); errata: **161**, 370 (1999).
24. J.W. Goodman, *Introduction to Fourier Optics* (McGraw–Hill, New York, USA, 1968).
25. O. Sbanski, V.E. Roman, W. Kiefer, J. Popp, J. Opt. Soc. Am. A **17**, 313 (2000).
26. E. Ertekin, A. Lakhtakia, Eur. Phys. J. AP **5**, 45 (1999).

Eur. Phys. J. AP **16**, 247 (2001)

THE EUROPEAN PHYSICAL JOURNAL APPLIED PHYSICS

Erratum

Reflection and transmission of optical narrow-extent pulses by axially excited chiral sculptured thin films

J.B. Geddes III and A. Lakhtakia

CATMAS – Computational and Theoretical Materials Sciences Group, Department of Engineering Science and Mechanics, 212 Earth-Engineering Sciences Building, Pennsylvania State University, University Park, PA 16802-6812, USA

Eur. Phys. J. AP **13**, 3–14 (2001)

The same typographical error crept in the last term on the right sides of equations (19), (21) and (23) referred of the paper above. Please replace -1 by $-\delta(t)$. All other equations as well as our results are not affected. We regret any inconvenience caused by this error.

Eur. Phys. J. AP **14**, 97–105 (2001)

THE EUROPEAN PHYSICAL JOURNAL APPLIED PHYSICS

Time-domain simulation of the circular Bragg phenomenon exhibited by axially excited chiral sculptured thin films

J.B. Geddes III[a] and A. Lakhtakia[b]

CATMAS — Computational and Theoretical Materials Sciences Group, Department of Engineering Science and Mechanics, 212 Earth-Engineering Sciences Building, Pennsylvania State University, University Park, PA 16802–6812, USA

Received: 11 December 2000 / Accepted: 9 February 2001

Abstract. We present simulations of the transmission and reflection of narrow-extent pulses incident upon a chiral sculptured thin film (STF) along its axis of spirality, when the circular Bragg phenomenon is excited. Even though the frequency-domain reflection and transmission spectrums of a sufficiently thick chiral STF slab acquire final shapes within the Bragg regime, the shape and the duration of the transmitted pulse change with slab thickness over the entire range of our simulations. The emergence of a multiple-hump structure in the transmitted pulse is relevant to the use of chiral STFs in digital optics communication.

PACS. 77.55.+f Dielectric thin films – 78.20.Bh Theory, models, and numerical simulation – 42.70.-a Optical materials

1 Introduction

Any helicoidal bianisotropic medium (HBM) will, in general, display the circular Bragg phenomenon when suitably excited along its axis of spirality, because it is periodically nonhomogeneous along that axis [1]. Chiral liquid crystals [2,3] as well as chiral sculptured thin films [4,5] exemplify HBMs and are therefore known to display that phenomenon. Briefly, a structurally right- (resp. left-) handed HBM slab only a few periods thick almost completely reflects axially incident, right (resp. left) circularly polarized light with wavelength lying in the so-called Bragg regime; while the reflection of axially incident, left (resp. right) circularly polarized light in the same regime is very little. The bandwidth and the peak reflectivity of the Bragg regime first increase with the thickness of the slab, and then saturate [3,6]. Once this saturation has occurred, further thickening of the slab has negligible effects on the reflection spectrum.

Investigations of the circular Bragg phenomenon have traditionally been conducted entirely in the frequency domain. Only recently did time-domain studies of optical pulse propagation in complex chiral mediums – including liquid crystals [7,8] and sculptured thin films (STFs) [9] – commence. This may be because time-domain studies require enormous computer memory resources in order to fully incorporate causal constitutive relations [8,9], while the computer memory requirements for the corresponding frequency-domain investigations are negligible in comparison.

[a] e-mail: JBG136@psu.edu

[b] e-mail: AXL4@psu.edu

The current explosive growth of digital optics communication [10] has made time-domain research for novel materials imperative. As liquid crystalline as well as thin-film versions of HBMs are extremely attractive for optical applications [11,12], particularly as polarization-discriminatory filters, the circular Bragg phenomenon must be studied in the time domain.

In our initial study in that vein [9], we showed that a light pipe emerges and a pulse bleeding phenomenon occurs in a chiral STF half-space, when (i) the handednesses of a normally incident, amplitude-modulated carrier wave and the chiral STF coincide, and (ii) the carrier wavelength is in the vicinity of the center-wavelength of the Bragg regime. We also showed that pulse bleeding inside a chiral STF slab is responsible for the long wakes of reflected pulses and the low energy contents of the transmitted pulses, when the incident pulse is wideband and the conditions are right for the circular Bragg phenomenon to be manifested. Thus, a chiral STF slab can directly affect the shapes, amplitudes, and spectral components of femtosecond pulses.

In continuation of our earlier work [9], we report here on the influence of the thickness of a chiral STF slab on the circular Bragg phenomenon in the time domain. Our formulation is sufficiently general so that our conclusions also apply to chiral liquid crystals. In Section 2, we briefly review our finite difference algorithm [9] to simulate the propagation of a narrow-extent (*i.e.*, wideband) pulse through a chiral STF slab. Then, assuming Lorentzian constitutive properties, we present a scheme to accelerate that algorithm. Section 3 contains the numerical results

we obtained and a discussion of the technological ramifications of our findings.

2 Theory

Suppose the region $z_\ell \le z \le z_r$, $(z_\ell > 0)$, is occupied by a chiral STF, while the half-spaces $z \le z_\ell$ and $z \ge z_r$ are vacuous. A carrier wave modulated by a pulse is launched from the plane $z = 0$ at time $t = 0$ in the $+z$ direction. It excites the chiral STF slab, and eventually transforms into a reflected pulse and a transmitted pulse.

2.1 Constitutive relations

The time-domain constitutive relations everywhere may be expressed as [9]

$$\underline{D}(\underline{r},t) = \epsilon_0 \left(\underline{\underline{\epsilon}} * \underline{E}\right)(\underline{r},t)\,, \quad \underline{B}(\underline{r},t) = \mu_0\, \underline{H}(\underline{r},t)\,, \tag{1}$$

where ϵ_0 and μ_0 are the permittivity and the permeability of free space, respectively, while the operation $*$ denotes convolution with respect to time. The relative permittivity dyadic is specified by

$$\underline{\underline{\epsilon}}(\underline{r},t) = \begin{cases} \underline{\underline{I}}\,\delta(t)\,, & z \notin [z_\ell,\, z_r] \\ \underline{\underline{S}}_z(z-z_\ell)\cdot\underline{\underline{S}}_y(\chi)\cdot\left[\epsilon_a(t)\,\underline{u}_z\underline{u}_z\right. & \\ \left.+\epsilon_b(t)\,\underline{u}_x\underline{u}_x+\epsilon_c(t)\,\underline{u}_y\underline{u}_y\right]\cdot & \\ \qquad\times\underline{\underline{S}}_y^{-1}(\chi)\cdot\underline{\underline{S}}_z^{-1}(z-z_\ell)\,, & z\in[z_\ell,\, z_r] \end{cases}, \tag{2}$$

where $\underline{\underline{I}}$ is the identity dyadic; $\delta(t)$ is the Dirac delta function; and $\underline{u}_x$, $\underline{u}_y$, and $\underline{u}_z$ are the Cartesian unit vectors. The rotation dyadic

$$\begin{aligned}\underline{\underline{S}}_z(z) = {} & \underline{u}_z\underline{u}_z + (\underline{u}_x\underline{u}_x + \underline{u}_y\underline{u}_y)\,\cos(\pi z/\Omega) \\ & + (\underline{u}_y\underline{u}_x - \underline{u}_x\underline{u}_y)\,\sin(\pi z/\Omega)\end{aligned} \tag{3}$$

captures the structural right-handedness of the chosen chiral STF, with 2Ω being the structural period. The tilt dyadic

$$\underline{\underline{S}}_y(\chi) = \underline{u}_y\underline{u}_y + (\underline{u}_x\underline{u}_x + \underline{u}_z\underline{u}_z)\,\cos\chi + (\underline{u}_z\underline{u}_x - \underline{u}_x\underline{u}_z)\,\sin\chi \tag{4}$$

is a function of the angle of rise χ.

Single-resonance Lorentzian characteristics are assumed for the dielectric response properties of the chiral STF; thus [13],

$$\begin{aligned}\epsilon_{a,b,c}(t) &= \delta(t) + \chi_{a,b,c}(t) \\ &= \delta(t) + p_{a,b,c}\left(\frac{2\pi c_0}{\lambda_0^{a,b,c}}\right)\,\sin\left(\frac{2\pi c_0}{\lambda_0^{a,b,c}}t\right) \\ &\quad\times\exp\left(-\frac{c_0 t}{N_{a,b,c}\lambda_0^{a,b,c}}\right)\,\mathcal{U}(t)\,,\end{aligned} \tag{5}$$

where $\mathcal{U}(t)$ is the unit step function, $c_0 = (\epsilon_0\mu_0)^{-1/2}$, the oscillator strengths are denoted by $p_{a,b,c}$, while $\lambda_0^{a,b,c}$ and $N_{a,b,c}$ delineate the resonant attributes of the chosen material.

2.2 Review of 5×5 matrix formulation

For axial excitation, all fields are independent of x and y. Let the column 5-vector

$$[\underline{F}(z,t)] = [E_x(z,t),\, E_y(z,t),\, H_x(z,t),\, H_y(z,t)\, E_z(z,t)]^{\mathrm{T}} \tag{6}$$

contain the five non-zero components of the electromagnetic field, the superscript $^{\mathrm{T}}$ indicating the transpose. Then, the Maxwell curl postulates may be written compactly as [9]

$$\left[\underline{\underline{J}}\right]\,\partial_z\,[\underline{F}(z,t)] = \left[\underline{\underline{Q}}\right]\cdot\partial_t\,[\underline{F}(z,t)] + \epsilon_0\partial_t\left\{\left(\left[\underline{\underline{A}}\right]*[\underline{F}]\right)(z,t)\right\}\,, \tag{7}$$

with $\partial_z \equiv \partial/\partial z$ and $\partial_t \equiv \partial/\partial t$. In (7), the constitutive properties are contained in the 5×5 matrix $\left[\underline{\underline{A}}\right](z,t)$ which is identically null-valued for $z \notin [z_\ell,\, z_r]$, while

$$\left[\underline{\underline{A}}\right](z,t) = \left[\begin{array}{ccccc} 0 & 0 & 0 & 0 & 0 \\ 0 & 0 & 0 & 0 & 0 \\ A_{31}(z,t) & A_{32}(z,t) & 0 & 0 & A_{35}(z,t) \\ -A_{41}(z,t) & -A_{31}(z,t) & 0 & 0 & -A_{45}(z,t) \\ A_{45}(z,t) & A_{35}(z,t) & 0 & 0 & A_{55}(z,t) \end{array}\right]\,, \quad z\in[z_\ell,\, z_r]\,, \tag{8}$$

with

$$\begin{aligned}A_{31} &= (\epsilon_a\sin^2\chi + \epsilon_b\cos^2\chi - \epsilon_c) \\ &\quad\times\sin\frac{\pi(z-z_\ell)}{\Omega}\,\cos\frac{\pi(z-z_\ell)}{\Omega}\,,\end{aligned} \tag{9}$$

$$\begin{aligned}A_{32} &= (\epsilon_a\sin^2\chi + \epsilon_b\cos^2\chi) \\ &\quad\times\sin^2\frac{\pi(z-z_\ell)}{\Omega} + \epsilon_c\cos^2\frac{\pi(z-z_\ell)}{\Omega} - 1\,,\end{aligned} \tag{10}$$

$$A_{35} = (\epsilon_b - \epsilon_a)\sin\chi\cos\chi\sin\frac{\pi(z-z_\ell)}{\Omega}\,, \tag{11}$$

$$\begin{aligned}A_{41} &= (\epsilon_a\sin^2\chi + \epsilon_b\cos^2\chi) \\ &\quad\times\cos^2\frac{\pi(z-z_\ell)}{\Omega} + \epsilon_c\sin^2\frac{\pi(z-z_\ell)}{\Omega} - 1\,,\end{aligned} \tag{12}$$

$$A_{45} = (\epsilon_b - \epsilon_a)\sin\chi\cos\chi\cos\frac{\pi(z-z_\ell)}{\Omega}\,, \tag{13}$$

$$A_{55} = \epsilon_a\cos^2\chi + \epsilon_b\sin^2\chi - 1. \tag{14}$$

The two other 5×5 matrixes appearing in (7) are as follows:

$$\left[\underline{\underline{J}}\right] = \mathrm{diag}\,[1,1,1,1,0]\,, \tag{15}$$

$$\left[\underline{\underline{Q}}\right] = \left[\begin{array}{ccccc} 0 & 0 & 0 & -\mu_0 & 0 \\ 0 & 0 & \mu_0 & 0 & 0 \\ 0 & \epsilon_0 & 0 & 0 & 0 \\ -\epsilon_0 & 0 & 0 & 0 & 0 \\ 0 & 0 & 0 & 0 & \epsilon_0 \end{array}\right]\,. \tag{16}$$

We also define the matrixes $\left[\underline{\underline{W}}(z,t)\right] = \epsilon_0\left[\underline{\underline{Q}}\right]^{-1}\left[\underline{\underline{A}}(z,t)\right]$ and $\left[\underline{\underline{V}}\right] = c_0^{-1}\left[\underline{\underline{Q}}\right]^{-1}\left[\underline{\underline{J}}\right]$ for convenience.

2.3 Accelerated finite-difference algorithm

Both space and time are discretized as $z_i = i\Delta z$, ($i = 0, 1, 2, 3, ...$), and $t_n = n\Delta t$, ($n = 0, 1, 2, 3, ...$); derivatives are replaced by central differences, and the leapfrog method is employed. Accordingly, (7) transforms to the matrix difference equation [9]

$$\begin{aligned}\left[\underline{F}\right]_i^{n+1} = \left[\underline{F}\right]_i^{n-1} + \beta\left[\underline{\underline{Y}}\right]\cdot\left(\left[\underline{F}\right]_{i+1}^{n} - \left[\underline{F}\right]_{i-1}^{n}\right) \\ - \left[\underline{q}\right]_i^{n} - \left[\underline{\underline{W}}\right]_i^{n}\cdot\left(\left[\underline{F}\right]_i^{1} - \left[\underline{F}\right]_i^{0}\right)\Delta t\,, \quad (17)\end{aligned}$$

wherein the shorthand notations

$$\left[\underline{F}\right]_i^n = \left[\underline{f}(z_i,\, t_n)\right]\,, \quad \left[\underline{\underline{W}}\right]_i^n = \left[\underline{\underline{W}}(z_i,\, t_n)\right] \quad (18)$$

have been used; and $\beta = c_0\Delta t/\Delta z < 1$ for stability [14]. The last two terms on the right side of (17) must be calculated only if $z_i \in [z_\ell,\, z_r]$.

The bulk of the convolution is contained in the term

$$\left[\underline{q}\right]_i^n = \sum_{m=1}^{n-1}\left[\underline{\underline{W}}\right]_i^m\cdot\left(\left[\underline{F}\right]_i^{n-m+1} - \left[\underline{F}\right]_i^{n-m-1}\right)\Delta t\,, \quad (19)$$

and its calculation requires most of the computational time. Any acceleration – even on a supercomputer – is desirable. If we ensure that $z_\ell > z_1$, the chosen Lorentzian properties (5) provide the following route:

Let us define the additional variables

$$\begin{aligned}\zeta_{a,b,c}(t) = p_{a,b,c}\left(\frac{2\pi c_0}{\lambda_0^{a,b,c}}\right)\cos\left(\frac{2\pi c_0}{\lambda_0^{a,b,c}}t\right) \\ \times\exp\left(-\frac{c_0 t}{N_{a,b,c}\lambda_0^{a,b,c}}\right)\mathcal{U}(t) \quad (20)\end{aligned}$$

in analogy with $\chi_{a,b,c}(t)$, as well as the constants

$$\left.\begin{aligned}\bar{\chi}_{a,b,c} = \sin\left(\tfrac{2\pi c_0}{\lambda_0^{a,b,c}}\Delta t\right)\exp\left(-\tfrac{c_0\Delta t}{N_{a,b,c}\lambda_0^{a,b,c}}\right) \\ \bar{\zeta}_{a,b,c} = \cos\left(\tfrac{2\pi c_0}{\lambda_0^{a,b,c}}\Delta t\right)\exp\left(-\tfrac{c_0\Delta t}{N_{a,b,c}\lambda_0^{a,b,c}}\right)\end{aligned}\right\}\,. \quad (21)$$

Likewise, let us also define the following 5×5 matrix functions:

$$\left.\begin{aligned}\left[\underline{\underline{Y}}\right](z,t) = \left[\underline{\underline{W}}\right](z,t)\Big|_{\chi_{a,b,c}(t)\,\to\,\zeta_{a,b,c}(t)} \\ \left[\bar{\underline{\underline{W}}}\right](z) = \left[\underline{\underline{W}}\right](z,t)\Big|_{\chi_{a,b,c}(t)\,\to\,\bar{\chi}_{a,b,c}} \\ \left[\bar{\underline{\underline{Y}}}\right](z) = \left[\underline{\underline{W}}\right](z,t)\Big|_{\chi_{a,b,c}(t)\,\to\,\bar{\zeta}_{a,b,c}}\end{aligned}\right\}\,. \quad (22)$$

All of the foregoing definitions are to be used only for $z \in [z_\ell,\, z_r]$, and yield the temporal recurrence relations

$$\left.\begin{aligned}\left[\underline{\underline{W}}\right]_i^{m+1} = \left[\bar{\underline{\underline{Y}}}\right]_i\left[\underline{\underline{W}}\right]_i^m + \left[\bar{\underline{\underline{W}}}\right]_i\left[\underline{\underline{Y}}\right]_i^m \\ \left[\underline{\underline{Y}}\right]_i^{m+1} = -\left[\bar{\underline{\underline{W}}}\right]_i\left[\underline{\underline{W}}\right]_i^m + \left[\bar{\underline{\underline{Y}}}\right]_i\left[\underline{\underline{Y}}\right]_i^m\end{aligned}\right\}\,, \quad (23)$$

with $\left[\bar{\underline{\underline{W}}}\right]_i = \left[\bar{\underline{\underline{W}}}\right](z_i)$ and $\left[\bar{\underline{\underline{Y}}}\right]_i = \left[\bar{\underline{\underline{Y}}}\right](z_i)$. Next, defining the column vector

$$\left[\underline{k}\right]_i^n = \sum_{m=1}^{n-1}\left[\underline{\underline{Y}}\right]_i^m\cdot\left(\left[\underline{F}\right]_i^{n-m+1} - \left[\underline{F}\right]_i^{n-m-1}\right)\Delta t\,, \quad (24)$$

as well as making use of (23), we obtain the twin recurrence relations

$$\left.\begin{aligned}\left[\underline{q}\right]_i^{n+1} = \left[\underline{\underline{W}}\right]_i^1\cdot\left(\left[\underline{F}\right]_i^{n+1} - \left[\underline{F}\right]_i^{n-1}\right)\Delta t \\ + \left[\bar{\underline{\underline{Y}}}\right]_i\left[\underline{q}\right]_i^n + \left[\bar{\underline{\underline{W}}}\right]_i\left[\underline{k}\right]_i^n \\ \left[\underline{k}\right]_i^{n+1} = \left[\underline{\underline{Y}}\right]_i^1\cdot\left(\left[\underline{F}\right]_i^{n+1} - \left[\underline{F}\right]_i^{n-1}\right)\Delta t \\ - \left[\bar{\underline{\underline{W}}}\right]_i\left[\underline{q}\right]_i^n + \left[\bar{\underline{\underline{Y}}}\right]_i\left[\underline{k}\right]_i^n\end{aligned}\right\} \quad (25)$$

from the definitions (19) and (24).

The constant matrixes $\left[\underline{\underline{W}}\right]_i^1$, $\left[\underline{\underline{Y}}\right]_i^1$, $\left[\bar{\underline{\underline{W}}}\right]_i$ and $\left[\bar{\underline{\underline{Y}}}\right]_i$ corresponding to all $z_i \in [z_\ell,\, z_r]$ are computed in the beginning and stored. Thereafter, the accelerated solution algorithm proceeds as follows:

$\forall\, i > 0\,,$

knowing $\left\{\left[\underline{q}\right]_i^{n-1},\, \left[\underline{k}\right]_i^{n-1},\, \left[\underline{F}\right]_i^{0,1,n,n-1,n-2},\, \left[\underline{F}\right]_{i\pm1}^n\right\}$,

compute

$$\left\{\begin{aligned}\left[\underline{q}\right]_i^n = \left[\underline{\underline{W}}\right]_i^1\cdot\left(\left[\underline{F}\right]_i^n - \left[\underline{F}\right]_i^{n-2}\right)\Delta t \\ + \left[\bar{\underline{\underline{Y}}}\right]_i\left[\underline{q}\right]_i^{n-1} + \left[\bar{\underline{\underline{W}}}\right]_i\left[\underline{k}\right]_i^{n-1}\,, \\ \left[\underline{k}\right]_i^n = \left[\underline{\underline{Y}}\right]_i^1\cdot\left(\left[\underline{F}\right]_i^n - \left[\underline{F}\right]_i^{n-2}\right)\Delta t \\ - \left[\bar{\underline{\underline{W}}}\right]_i\left[\underline{q}\right]_i^{n-1} + \left[\bar{\underline{\underline{Y}}}\right]_i\left[\underline{k}\right]_i^{n-1}\,, \\ \left[\underline{F}\right]_i^{n+1} = \left[\underline{F}\right]_i^{n-1} + \beta\left[\underline{\underline{Y}}\right]\cdot\left(\left[\underline{F}\right]_{i+1}^n - \left[\underline{F}\right]_{i-1}^n\right) \\ - \left[\underline{q}\right]_i^n - \left[\underline{\underline{W}}\right]_i^n\cdot\left(\left[\underline{F}\right]_i^1 - \left[\underline{F}\right]_i^0\right)\Delta t\,.\end{aligned}\right. \quad (26)$$

3 Numerical results and discussion

The foregoing algorithm was implemented with the following constitutive properties: $p_a = 0.40$, $p_b = 0.52$, $p_c = 0.42$, $\chi = 20°$, and $\Omega = 200$ nm. These parameters fixed the center-wavelength of the Bragg regime at 516 nm, with a full-width half-maximum (FWHM) bandwidth of approximately 27 nm [4,9]. In order to keep absorption negligible at visible wavelengths so that the transmitted pulse possesses sufficiently high energy, we chose $\lambda_0^{a,c} = 280$ nm, $\lambda_0^b = 290$ nm, and $N_{a,b,c} = 10^5$. Setting $z_\ell = 60$ μm, we varied the thickness $z_r - z_\ell$ of the chiral STF from $5\,\Omega$ to $100\,\Omega$; hence, z_r ranged from 61 μm to 80 μm in our simulations. The domain $\{i \in [0, 30\,000]\,, n \in [0, 31\,681]\}$ was the same for each calculation, and the resolution of our grid was defined by setting $\Delta z = 4$ nm and $\beta = 0.9$, so that $\Delta t = 0.012$ fs. We chose the initial condition $\left[\underline{F}\right]_i^0 = \left[\underline{0}\right]\ \forall\, i$, thereby asserting the absence of the electromagnetic field anywhere at time $t = 0$. The boundary condition $\left[\underline{F}\right]_0^n = g(t_n)\left[\underline{\varphi}(t_n)\right]$ used by us describes a carrier wave represented by the column

vector $[\underline{\varphi}(t)]$ that is amplitude-modulated by the pulse function $g(t)$. For all numerical results reported here,

$$\left[\underline{\varphi}_{\pm}(t)\right] = \left[\cos\left(\frac{2\pi c_0}{\lambda_0^{\mathrm{car}}}t\right), \pm\sin\left(\frac{2\pi c_0}{\lambda_0^{\mathrm{car}}}t\right), \mp\eta_0^{-1}\sin\left(\frac{2\pi c_0}{\lambda_0^{\mathrm{car}}}t\right), \eta_0^{-1}\cos\left(\frac{2\pi c_0}{\lambda_0^{\mathrm{car}}}t\right), 0\right]^{\mathrm{T}}, \tag{27}$$

$$g(t) = \frac{c_0 t}{2\lambda_0^{\mathrm{car}}}\exp\left(\frac{-c_0 t}{\lambda_0^{\mathrm{car}}}\right). \tag{28}$$

Whereas $[\underline{\varphi}_+(t)]$ represents a left circularly polarized (LCP) plane wave, $[\underline{\varphi}_-(t)]$ represents a right circularly polarized (RCP) plane wave. The carrier wavelength was set to lay squarely in the Bragg regime, so that $\lambda_0^{\mathrm{car}} = 516$ nm. With this choice, the duration of the pulse was approximately 8 fs; and the pulse bandwidth completely contained the Bragg regime. Computations were performed on a Cray T3E supercomputer with a program written in FORTRAN 90.

Snapshots of the axial component of the Poynting vector $P(z,t) = \underline{u}_z \cdot [\underline{E}(z,t) \times \underline{H}(z,t)]$ for each slab thickness chosen are presented in Figures 1–6 at $t =$ 115.3, 230.6, 288.2, and 380.4 fs. The initial pulse can be seen to the left of the chiral STF slab in the top panel of each figure. Subsequent snapshots detail the evolution of the incident pulse in time as it propagates from left to right, encounters the chiral STF slab, and transforms into a transmitted pulse and a reflected pulse. The snapshot at $t = 380.4$ fs is presented in magnified view as the bottom panel of each figure. The carrier wave is RCP, so that the conditions are right for the circular Bragg phenomenon to occur.

When the thickness $z_r - z_\ell = 5\Omega$, the transmitted pulse is endowed with virtually the same shape and most of the energy of the incident pulse; see Figure 1. Suitably coded information in the duration and shape of the incident pulse is retained upon transmission through the chiral STF slab, although a slight distortion is possible.

A decrease in peak intensity and a temporal broadening of the transmitted pulse occur as the thickness $z_r - z_\ell$ increases to 20Ω (Fig. 2). As the thickness increases further to 40Ω in Figure 3, the transmitted pulse is dilated further in time, and takes on a dromedary-like shape with several distinct humps. These results indicate that measurements of the duration of the transmitted pulse might be complicated by the presence of multiple humps.

At thicknesses of 60Ω, 80Ω and 100Ω, Figures 4–6 respectively show that the overall transmitted pulse duration continues to increase and more distortion is evident. Although the transmitted pulses in the final panels of Figures 3–6 all possess the multiple-hump structure, each pulse has a different shape. This fact suggests that the transmitted pulse shape and duration continue to evolve, even though the transmission spectrum saturates [6] with respect to the slab thickness.

The duration of the reflected pulse increases as the slab thickness rises from 5Ω to 40Ω, even though the peak intensity does not change significantly (Figs. 1–3). This is in accord with the observation of the light pipe in the predecessor paper [9]. For $z_r - z_\ell > 40\Omega$ or so, the total energy of the reflected pulse does not change very much with increasing film thickness. This is reasonable because the incident pulse's spectral components lying within the Bragg regime together carry a finite amount of energy, and it is these spectral components that are largely reflected by the chiral STF slab. Hence, once the circular Bragg phenomenon deepens and saturates, the energy of the reflected pulse will not undergo large increases with increasing film thickness.

The foregoing time-domain observations are borne out by comparison with their frequency-domain counterparts, a task we accomplished by taking the Fourier transforms of the incident, reflected, and transmitted pulses using the formula

$$\tilde{E}_{x,y}(z,\lambda_0) = \int_{t_a}^{t_b} E_{x,y}(z,t)\exp\left(-\mathrm{j}\frac{2\pi c_0 t}{\lambda_0}\right)\mathrm{d}t\,, \quad \mathrm{j} = \sqrt{-1}\,. \tag{29}$$

The parameters z, t_a, and t_b were chosen to capture as much of the pulse as possible; $z = 14\,000\Delta z$ was chosen for the incident and reflected pulses, while $z = z_r + 50\Delta z$ for the transmitted pulse. We selected $t_a = 15\,000\Delta t$, $17\,500\Delta t$, and $16\,000\Delta t$, respectively, for the incident, reflected, and transmitted pulses; $t_b = 17\,000\Delta t$ for the incident pulse; and $t_b = 31\,680\Delta t$ for the reflected and transmitted pulses. Although our simulations would not capture all of the secondary pulses arising from multiple transits within the chiral STF slab, the secondary pulses may be neglected since most of the energy resides in the primary reflected and transmitted pulses.

The quantity $\tilde{E}(z,\lambda_0) = [|\tilde{E}_x(z,\lambda_0)|^2 + |\tilde{E}_y(z,\lambda_0)|^2]^{1/2}$ is plotted in Figure 7 for several values of $z_r - z_\ell$. As the slab thickness increases, the transmission at Bragg-regime wavelengths drops, and there is a corresponding increase in reflection. For $z_r - z_\ell > 40\Omega$ the transmission and reflection spectrums in the Bragg regime change very little with increasing slab thickness; this effect is the saturation of the circular Bragg phenomenon, and it vindicates our time-domain simulations.

Thus, even though the reflected and transmitted pulse spectrums may acquire final shapes (in the frequency domain) for a sufficiently thick chiral STF slab, evidently the transmitted pulse shape and duration are always influenced by the slab thickness, while the energy content of the reflected pulse is governed by the overlap of the spectrum of the incident pulse with the Bragg regime.

We have shown that pulse is broadened and distorted as it propagates through the chiral STF slab, when the conditions are right for the occurrence of the circular Bragg phenomenon – a fact which must be remembered when designing devices employing such films. A chiral STF slab must be thick enough to exhibit the desired filtering properties associated with the circular Bragg phenomenon, but thin enough to allow the transmitted pulse to retain appropriately coded information. The appearance of the multiple-hump structure may garble certain

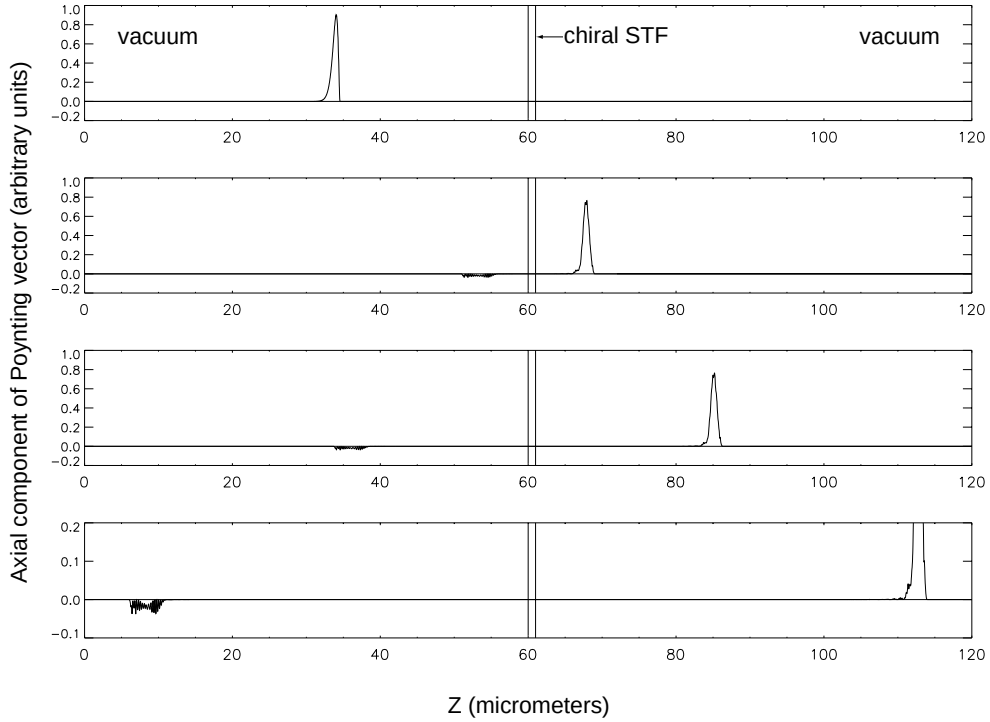

Fig. 1. Snapshots of $P(z,t) = \underline{u}_z \cdot [\underline{E}(z,t) \times \underline{H}(z,t)]$ at $t = 115.3$, 230.6, 288.2, and 380.4 fs – detailing the evolution of a narrow-extent pulse modulating a RCP carrier plane wave. The incident pulse impinges on a right-handed chiral STF slab of thickness $z_r - z_\ell = 5\Omega$ from the left, and metamorphoses into a reflected pulse (left of the slab) and a transmitted pulse (right of the slab). See the text for values of all parameters used. Multiply all values by 0.0001 $\mathrm{W\,m^{-2}}$ to obtain the original data.

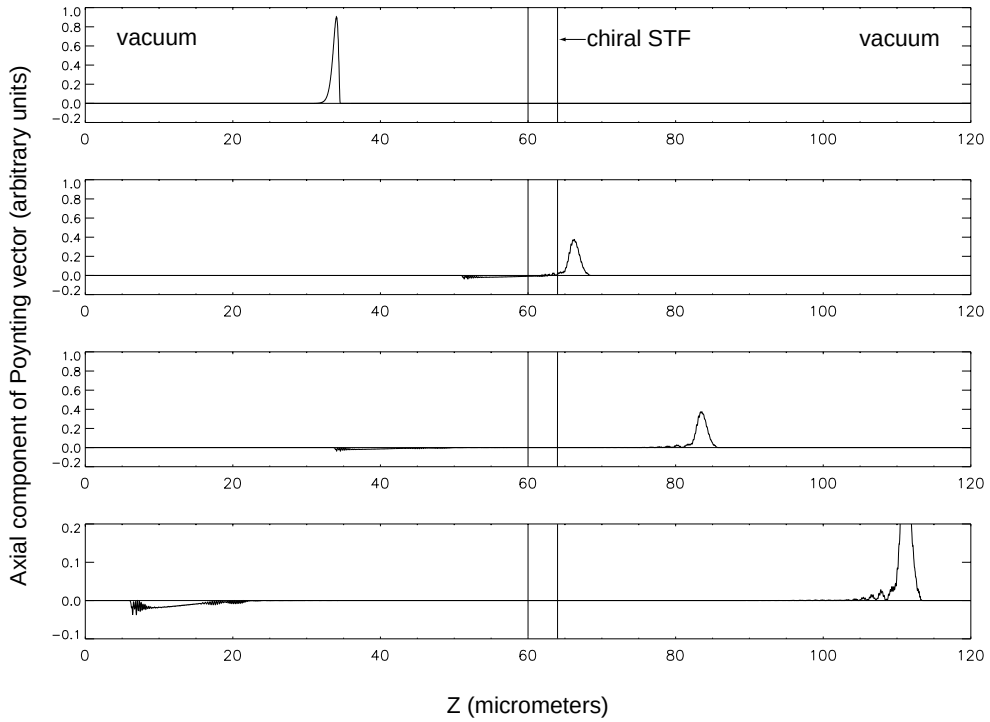

Fig. 2. Same as Figure 1, but the slab thickness $z_r - z_\ell = 20\Omega$.

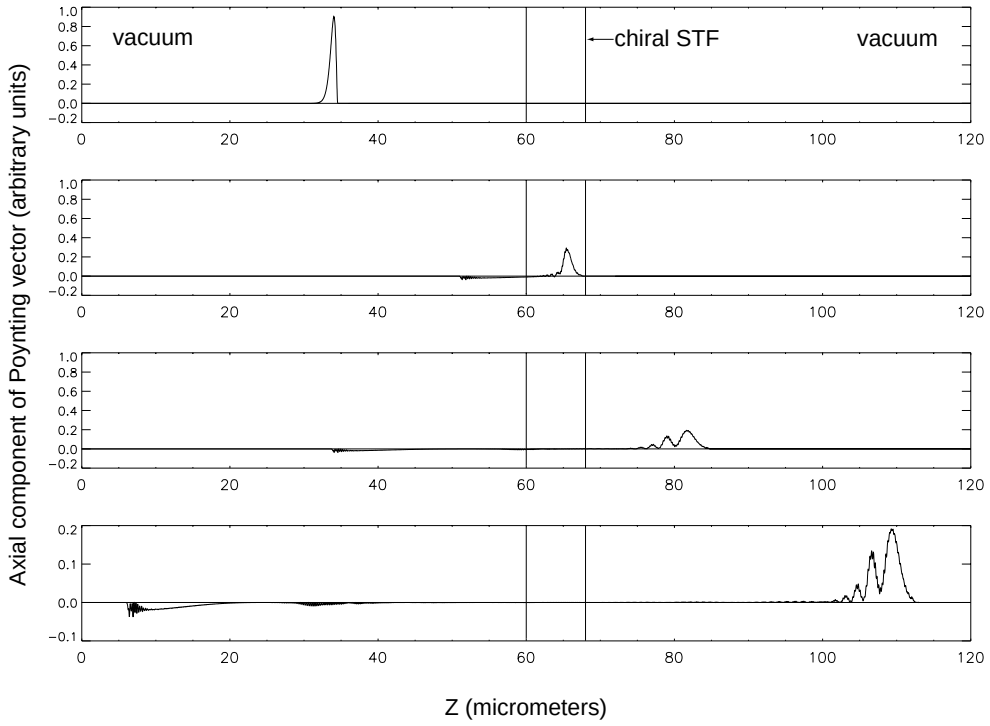

Fig. 3. Same as Figure 1, but the slab thickness $z_r - z_\ell = 40\Omega$.

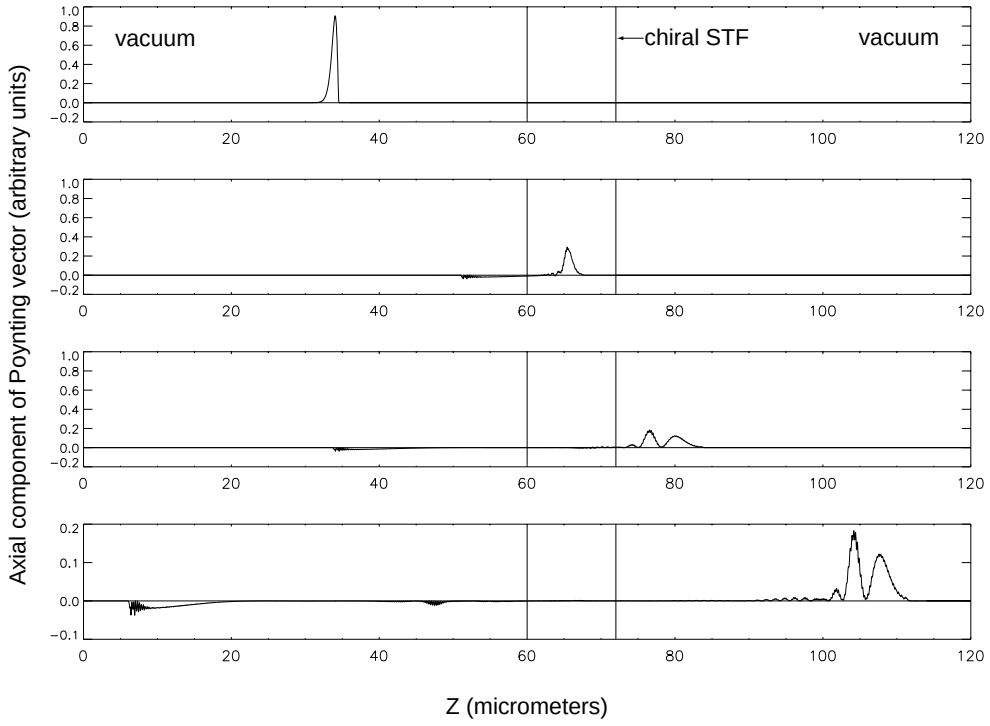

Fig. 4. Same as Figure 1, but the slab thickness $z_r - z_\ell = 60\Omega$.

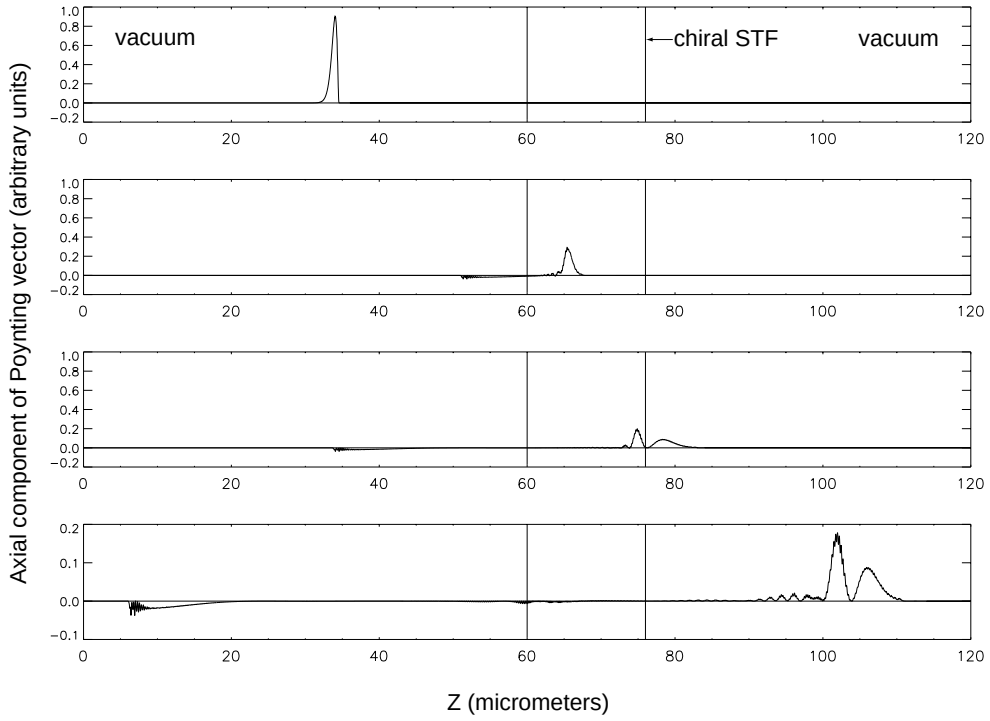

Fig. 5. Same as Figure 1, but the slab thickness $z_r - z_\ell = 80\Omega$.

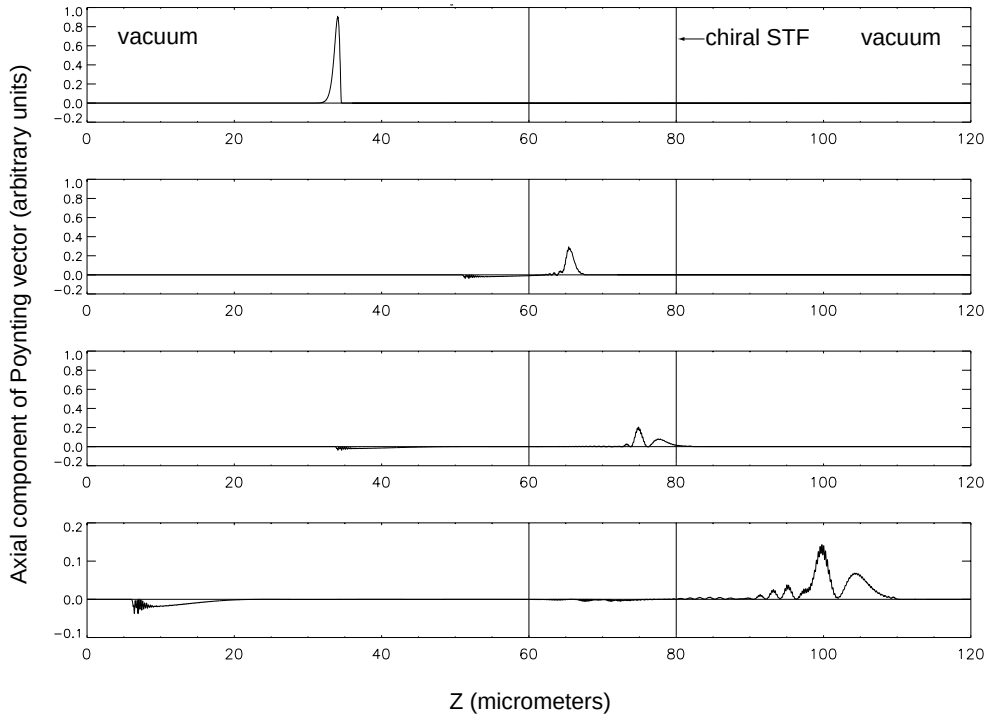

Fig. 6. Same as Figure 1, but the slab thickness $z_r - z_\ell = 100\Omega$.

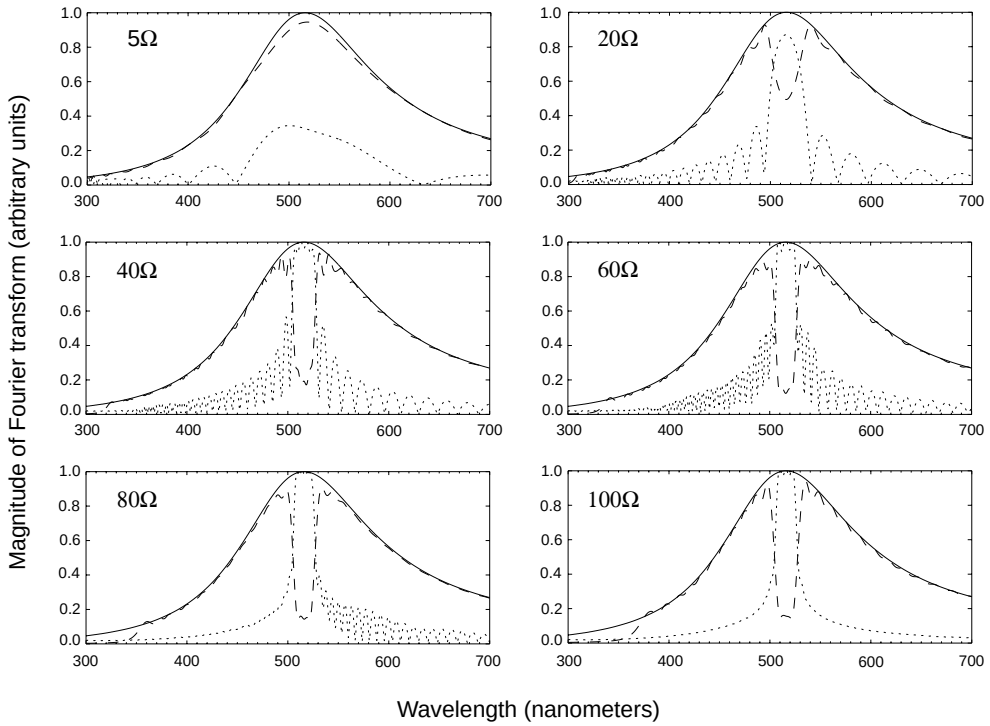

Fig. 7. Plots of $\tilde{E}(z,\lambda_0) = \left[|\tilde{E}_x(z,\lambda_0)|^2 + |\tilde{E}_y(z,\lambda_0)|^2\right]^{1/2}$ for the incident (solid lines), reflected (dotted lines), and transmitted (dashed lines) pulses and increasing values of $z_r - z_\ell$. The deepening of the circular Bragg phenomenon (in the frequency domain) is evident as the thickness $z_r - z_\ell$ of the chiral STF slab increases. The data have been normalized to the peak value of $\left[|\tilde{E}_x(z,\lambda_0)|^2 + |\tilde{E}_y(z,\lambda_0)|^2\right]^{1/2}$ taken by the incident pulse modulating a RCP carrier wave. See the text for the parameter values used to calculate these results.

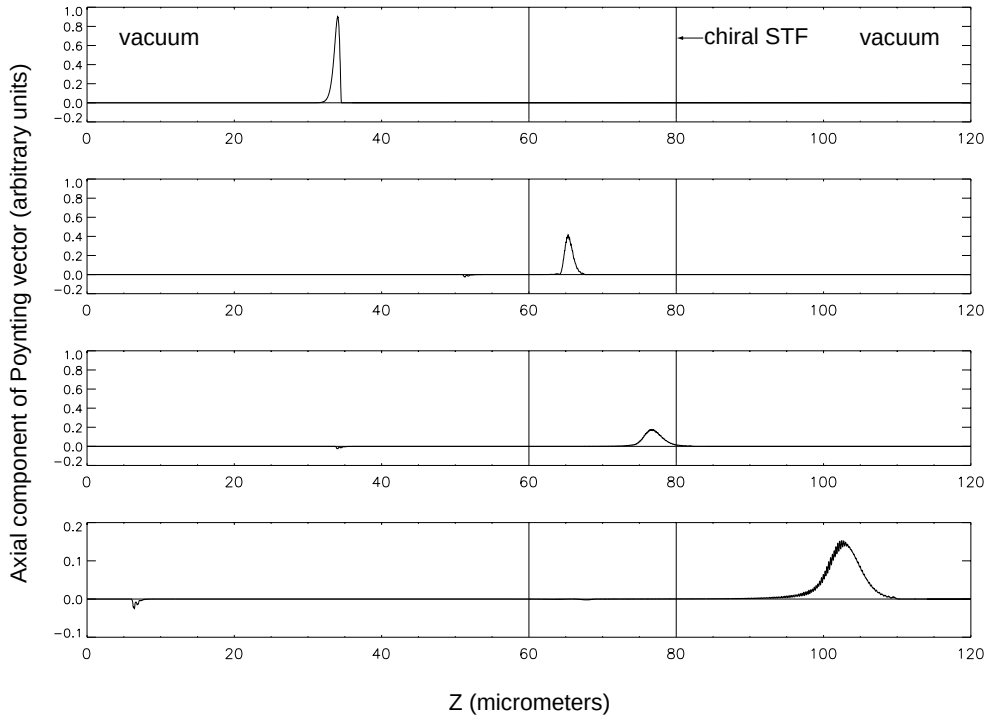

Fig. 8. Same as Figure 6, but the carrier plane wave is LCP.

information, if the effects of slab thickness are not properly taken into account. But the multiple-hump structure is also valuable in that it may be exploited for pulse-shaping, as has been done with scalar Bragg gratings [16].

Although the circular Bragg phenomenon does not occur when the carrier wave is LCP [15], and the transmission is high through even a 100 Ω-thick slab, significant broadening of the transmitted pulse can be observed, as may be gleaned from Figure 8. Of note here is that the multiple-hump structure does not appear for pulses carried by LCP carrier waves across thick slabs, indicating that pulse distortion of that kind is a function of the relative handedness of the chiral STF and the carrier wave. Broadening of transmitted pulses travelling on LCP carrier waves may be technologically significant, depending on the specific application at hand.

This research was supported in part by the Pittsburgh Supercomputing Center.

References

1. A. Lakhtakia, V.C. Venugopal, Arch. Elektr. Über. **53**, 287 (1999).
2. P.G. de Gennes, J. Prost, *The Physics of Liquid Crystals* (Clarendon Press, Oxford, UK, 1993).
3. W.D. St.John, W.J. Fritz, Z.J. Lu, D.-K. Yan, Phys. Rev. E **51**, 1191 (1995).
4. A. Lakhtakia, Eur. Phys. J. AP **8**, 129 (1999).
5. I.J. Hodgkinson, Q.h. Wu, B. Knight, A. Lakhtakia, K. Robbie, Appl. Opt. **39**, 642 (2000).
6. V.C. Venugopal, A. Lakhtakia, Opt. Commun. **145**, 171 (1998); erratum, **161**, 370 (1999).
7. E.E. Kriezis, S.J. Elston, Opt. Commun. **177**, 69 (2000).
8. J.B. Geddes III, M.W. Meredith, A. Lakhtakia, Opt. Commun. **182**, 45 (2000).
9. J.B. Geddes III, A. Lakhtakia, Eur. Phys. J. AP **13**, 3 (2001).
10. National Research Council, *Condensed-Matter and Materials Physics* (National Academy Press, Washington, DC, USA, 1999).
11. *Selected Papers on Liquid Crystals in Optics*, edited by S.D. Jacobs (SPIE, Bellingham, WA, USA, 1992).
12. *Electromagnetic Fields in Unconventional Materials and Structures*, edited by O.N. Singh, A. Lakhtakia (Wiley, New York, NY, USA, 2000).
13. C. Kittel, *Introduction to Solid State Physics* (Wiley Eastern, New Delhi, India, 1974).
14. N. Gershenfeld, *The Nature of Mathematical Modeling* (Cambridge University Press, Cambridge, UK, 1999).
15. M.W. McCall, A. Lakhtakia, J. Mod. Opt. **47**, 973 (2000).
16. P.C. Chou, H.A. Haus, J.F. Brennan III, Opt. Lett. **25**, 524 (2000).

Eur. Phys. J. AP **16**, 247 (2001)

THE EUROPEAN PHYSICAL JOURNAL
APPLIED PHYSICS

Erratum

Time-domain simulation of the circular Bragg phenomenon exhibited by axially excited chiral sculptured thin films

J.B. Geddes III and A. Lakhtakia

CATMAS – Computational and Theoretical Materials Sciences Group, Department of Engineering Science and Mechanics, 212 Earth-Engineering Sciences Building, Pennsylvania State University, University Park, PA 16802-6812, USA

Eur. Phys. J. AP **14**, 97–105 (2001)

A transcription error crept in the last term on the right sides of equations (10), (12) and (14) of the referred paper above. Please replace -1 by $-\delta(t)$. All other equations as well as our results are not affected. We regret any inconvenience caused by this error.

ground plane, becomes a planar rectangular monopole antenna when the bottom ground plane is removed. A parametric study of the rectangular monopole antenna has been carried out to optimize the bandwidth. We obtained a measured broad bandwidth from 1.220 to 3.550 GHz (1:2.9). The radiation pattern at various frequencies in the *E*- and *H*-planes of these antennas is similar to that of a thin monopole of equivalent height.

REFERENCES

1. S. Honda, M. Ito, H. Seki, and Y. Jingo, A disc monopole antenna with 1:8 impedance bandwidth and omnidirectional radiation pattern, Proc ISAP, Sapporo, Japan, 1992, pp. 1145–1148.
2. Hammoud, P. Poey, and F. Colomel, Matching the input impedance of a broadband disc monopole, Electron Lett 29 (1993), 406–407.
3. N.P. Agarwall, G. Kumar, and K.P. Ray, Wide-band planar monopole antennas, IEEE Trans Antennas Propagat 46 (1998), 294–295.
4. J.R. James and P.S. Hall, Handbook of microstrip antennas, Peter Peregrinus Ltd., London, 1989, vol. 1.
5. IE3D 6.0, Zeland Software Inc., Fremont, CA.

PULSE-CODED INFORMATION TRANSMISSION ACROSS AN AXIALLY EXCITED CHIRAL-SCULPTURED THIN FILM IN THE BRAGG REGIME

Joseph B. Geddes, III[1] and Akhlesh Lakhtakia[1]
[1] CATMAS — Computational and Theoretical Materials Sciences Group
Department of Engineering Science and Mechanics
Pennsylvania State University
University Park, Pennsylvania 16802-6812

Received 13 July 2000

ABSTRACT: *Although a monochromatic plane wave of a certain circular polarization state and wavelength may be almost completely reflected by a chiral sculptured thin film, we show here that information coded in rectangular pulses can still be transmitted across the film—provided the rise and fall times of the pulses are sufficiently small and the pulse widths are sufficiently large.* © 2001 John Wiley & Sons, Inc. Microwave Opt Technol Lett 28: 59–62, 2001.

Key words: *chiral-sculptured thin films; circular Bragg phenomenon; pulse-code modulation*

1. INTRODUCTION

Chiral-sculptured thin films (STFs) are solid dielectric examples of the so-called helicoidal bianisotropic media [1]. A class of nanoengineered materials, chiral STFs behave as unidirectionally nonhomogeneous, periodic, anisotropic, dielectric continuua in the visible and infrared regimes. Their periodicity allows them the ability to display the Bragg phenomenon on axial excitation. Their structural handedness (or chirality) makes the Bragg phenomenon polarization sensitive. Thus, virtually no reflection occurs when a structurally right-handed chiral STF of finite thickness is axially excited by monochromatic left circularly polarized (LCP) light, whereas virtually perfect reflection of incident right circularly polarized (RCP) light occurs—provided the film is sufficiently thick and the wavelength lies in the so-called Bragg regime. The described *circular* Bragg phenomenon has been theoretically as well as experimentally established [2, 3], and is the basis of several actual and potential applications in optics [1].

Optical communication systems employ monochromatic light for carrying information coded in rectangular pulses [4]. Typical pulse widths have been in the subpicosecond range for quite a while [5], and continue to get shorter. If an optical device fabricated with a chiral STF were used, and if the carrier wavelength were to lie in the Bragg regime of that chiral STF, the circular polarization state of the carrier wave can be expected to have a major effect on the pulse transmission characteristics of the device.

This thought provided the motivation for the present communication. We set up an initial-boundary value problem for the axial excitation of a chiral STF by a circularly polarized carrier plane wave that is amplitude modulated by a rectangular pulse. The time-domain constitutive relations of the chiral STF were chosen to be Lorentzian, with resonance wavelengths in the ultraviolet regime and modest absorption in the visible regime [2, 6]. The Bragg regime of the chiral STF was arranged to lie in the visible regime as well. Finite-difference calculus was used to solve the time-domain Maxwell equations in order to determine the interaction of a rectangular pulse with a chiral STF.

A brief description of the theoretical treatment is provided in the next section, followed by a discussion of the obtained results. Vectors are single underlined, dyadics are double underlined, while $\underline{u}_x$, $\underline{u}_y$, and $\underline{u}_z$ denote Cartesian unit vectors. The wavelength in free space is denoted by λ_0.

2. THEORY IN BRIEF

The chosen pulse is launched into the half space $z \geq 0$ from the plane $z = 0$ at time $t = 0$. A chiral STF fills the region $z_l \leq z \leq z_r$ ($z_l \geq 0$), while the half spaces $z \leq z_l$ and $z \geq z_r$ are vacuous.

In the constitutive relations

$$\underline{D}(\underline{r},t) = \epsilon_0(\underline{\underline{\epsilon}} * \underline{E})(\underline{r},t), \qquad \underline{B}(\underline{r},t) = \mu_0 \underline{H}(\underline{r},t) \quad (1)$$

ϵ_0 and μ_0 are the permittivity and permeability of free space, while $*$ denotes convolution with respect to time [7, 8]. The relative permittivity dyadic is given by

$$\underline{\underline{\epsilon}}(\underline{r},t) = \begin{cases} \underline{\underline{I}}\delta(t), & z \notin [z_l, z_r] \\ \underline{\underline{S}}_z(z - z_l) \cdot \underline{\underline{S}}_y(\chi) \cdot \underline{\underline{\epsilon}}^0_{\text{ref}}(t) \cdot \underline{\underline{S}}_y^{-1}(\chi) \cdot \underline{\underline{S}}_z^{-1}(z - z_l), & z \in [z_l, z_r] \end{cases} \quad (2)$$

wherein $\underline{\underline{I}}$ is the identity dyadic and $\delta(t)$ is the Dirac delta function; the rotation dyadic

$$\underline{\underline{S}}_z(z) = \underline{u}_z\underline{u}_z + (\underline{u}_x\underline{u}_x + \underline{u}_y\underline{u}_y)\cos\frac{\pi z}{\Omega} + (\underline{u}_y\underline{u}_x - \underline{u}_x\underline{u}_y)\sin\frac{\pi z}{\Omega} \quad (3)$$

denotes the structural right-handedness of the chiral STF with 2Ω as the structural period along the z-axis; and the tilt

Contract grant sponsor: Pittsburgh Supercomputing Center
Contract grant sponsor: Proctor & Gamble Summer Undergraduate Research Fellowship

dyadic

$$\underline{\underline{S}}_y = \underline{u}_y\underline{u}_y + (\underline{u}_x\underline{u}_x + \underline{u}_z\underline{u}_z)\cos\chi + (\underline{u}_z\underline{u}_x - \underline{u}_x\underline{u}_z)\sin\chi \tag{4}$$

involves the angle of rise $\chi > 0°$. The chiral STF is assumed to have Lorentzian response properties as follows [2, 6]:

$$\underline{\underline{\epsilon}}^{0}_{\mathrm{ref}}(t) = \epsilon_a(t)\underline{u}_z\underline{u}_z + \epsilon_b(t)\underline{u}_x\underline{u}_x + \epsilon_c(t)\underline{u}_y\underline{u}_y \tag{5}$$

with

$$\epsilon_{a,b,c}(t) = \delta(t) + p_{a,b,c}\left(\frac{2\pi c_0}{\lambda_0^{a,b,c}}\right)\sin\left(\frac{2\pi c_0}{\lambda_0^{a,b,c}}t\right) \times \exp\left(-\frac{c_0 t}{N_{a,b,c}\lambda_0^{a,b,c}}\right)\mathscr{U}(t). \tag{6}$$

In the foregoing expression, $c_0 = 1/\sqrt{\epsilon_0\mu_0}$ is the speed of light in vacuum; $p_{a,b,c}$ are the oscillator strengths; $\lambda_0^{a,b,c}$ and $N_{a,b,c}$ determine the resonance wavelengths and linewidths; while $\mathscr{U}(t)$ is the Heaviside function.

The launched rectangular incident pulse

$$g(t) = \frac{1}{\sqrt{2}}[\mathscr{U}(t) - \mathscr{U}(t - t_p)] \tag{7}$$

modulates the amplitude of a circularly polarized carrier wave. Whereas t_p is the pulse width, the carrier wavelength is denoted by λ_0^{car}. The signal propagates in the $+z$-direction until it encounters the chiral STF at $z = z_r$. Subsequently, a reflected pulse arises in the half space $z \le z_l$, and a (transmitted) pulse *may* eventually exist in the half space $z \ge z_r$.

The initial-boundary value problem thus described may be treated using finite-difference calculus, as has been done previously for cholesteric liquid crystals [9]. First, $\partial/\partial x \equiv 0$ and $\partial/\partial y \equiv 0$ are set in order to consider only axial propagation; and then, z and t are discretized with Δz and Δt as the relevant increments. Derivatives in the time-domain Maxwell equations are replaced by central differences, and the leapfrog method is employed [10]. For the sake of brevity, further details of the solution algorithm thus obtained are not given here.

3. NUMERICAL RESULTS AND DISCUSSION

The devised algorithm was implemented on a Cray T3E supercomputer, with the space increment $\Delta z = 4$ nm and the time increment $\Delta t = 0.012$ fs. The boundaries of the chiral STF were demarcated as $z_l = 50{,}000$ nm and $z_r = 54{,}000$ nm; and the following parameters were chosen for its dielectric properties: $p_a = 0.40$, $p_b = 0.52$, and $p_c = 0.42$; $\lambda_0^a = \lambda_0^c = 280$ nm and $\lambda_0^b = 290$ mn; and $N_a = N_b = N_c = 100$. Setting $\Omega = 200$ nm and $\chi = 20°$, we fixed the center wavelength of the Bragg regime at $\lambda_0^{\mathrm{Br}} = 516$ nm with a full-width half-maximum (FWHM) bandwidth of 27 nm [11]. Thus, $502.5 \le \lambda_0 \le 529.5$ nm is the Bragg regime.

The pulse duration was set at $t_p = 90.1$ fs, and the following values were chosen for the carrier wavelength λ_0^{car}: 430, 500, 516, 530, and 600 nm. The FWHM bandwidth of the incident signal is ~ 9 nm. Both LCP and RCP carrier plane waves were considered.

The computed axial component of the Poynting vector $P_z(z,t) = \underline{u}_z \cdot [\underline{E}(z,t) \times \underline{H}(z,t)]$ was recorded as a function of time for the incident and reflected pulses at $z = 35{,}000$ nm (to the left of the chiral STF), and for the transmitted pulse at $z = 55{,}000$ nm (to the right of the chiral STF). The

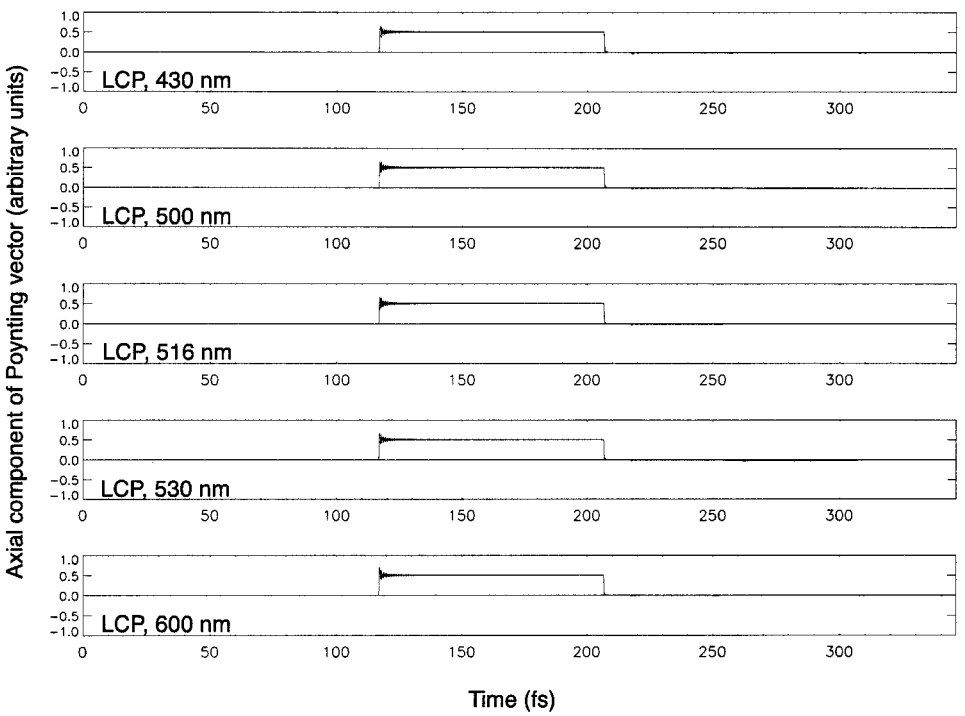

Figure 1 Temporal record of $P_z(z,t) = \underline{u}_z \cdot [\underline{E}(z,t) \times \underline{H}(z,t)]$ at $z = 35{,}000$ nm $< z_l$ when an incident rectangular pulse is carried by an LCP plane wave; $\lambda_0^{\mathrm{car}} = 430$, 500, 516, 530, and 600 nm (from top to bottom). Multiply all values of $P_z(z,t)$ by 0.0026 W/m^2 to obtain the unscale data

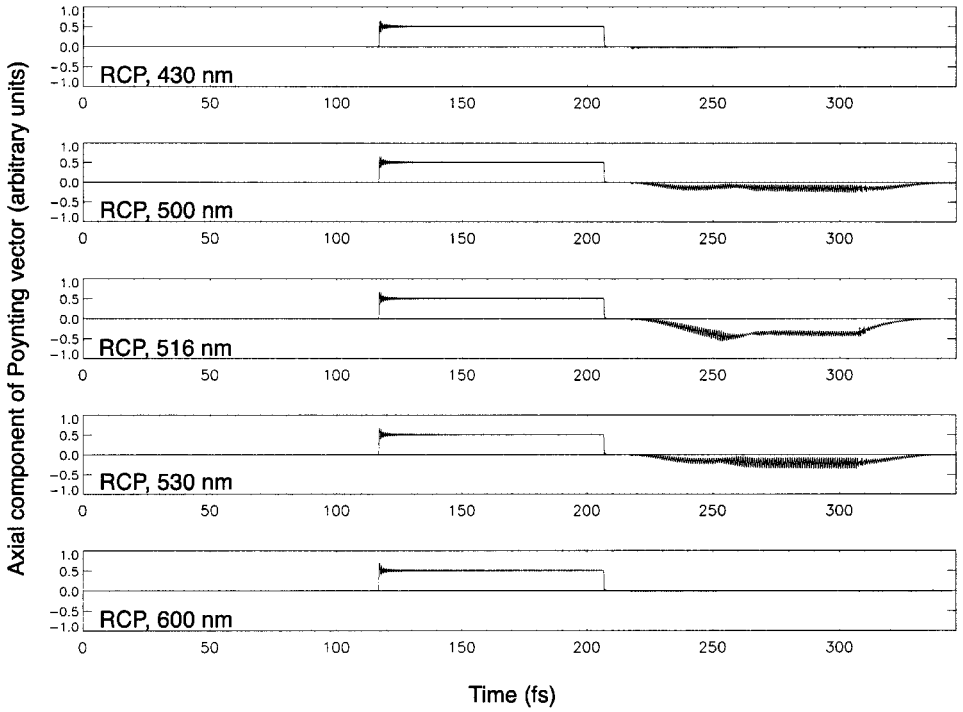

Figure 2 Same as Figure 1, except that the carrier wave is RCP

results for the incident and reflected pulses are plotted in Figures 1 and 2 for LCP and RCP carrier waves, respectively. In these figures, the signature of the circular Bragg phenomenon is clearly evident. The incident pulse is visible in the interval $115 \lesssim t \lesssim 205$ fs, and the reflected pulse begins to appear at $t \simeq 215$ fs. The carrier wave is LCP in Figure 1, and the energy content of the reflected pulse is minimal, regardless of the carrier wavelength. When the carrier wave is RCP and λ_0^{car} lies outside the Bragg regime, there is minimal reflection in Figure 2 also. However, when the bandwidth of the incident pulse overlaps the Bragg regime, the reflected pulse contains more energy; indeed, the reflected pulse is most energetic in Figue 2 when λ_0^{car} coincides with λ_0^{Br}.

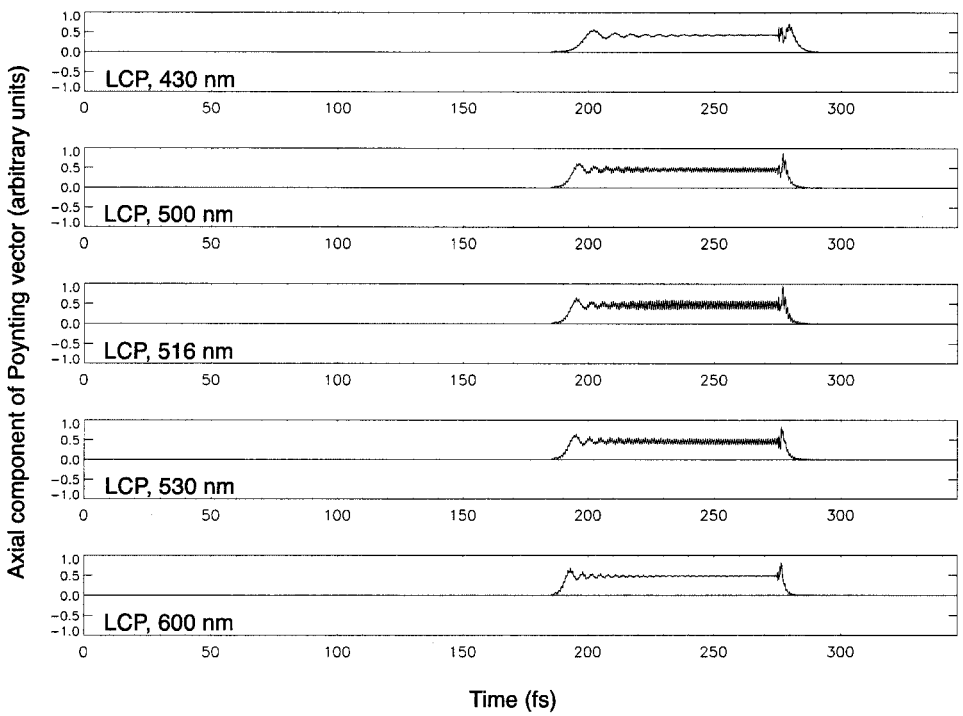

Figure 3 Same as Figure 1, but for $z = 55{,}000$ nm $> z_r$

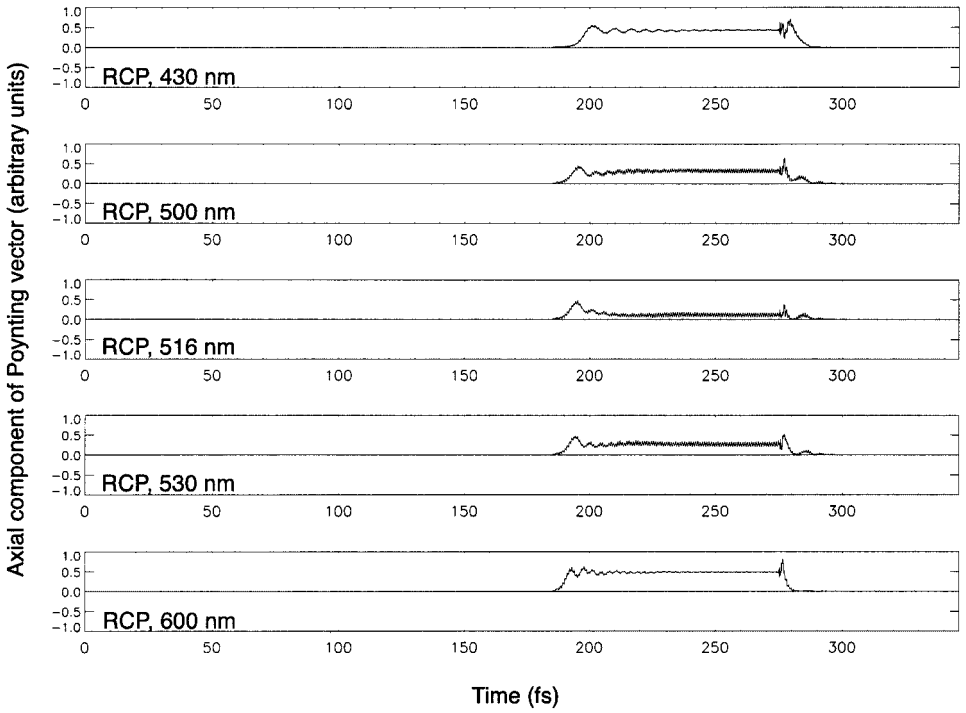

Figure 4 Same as Figure 3, except that the carrier wave is RCP

The results for the transmitted pulse, presented in Figures 3 and 4, corroborate the foregoing observations. Aside from a small amount of absorption, most of the incident pulse energy is transmitted into the right half space when either: 1) the carrier wave is LCP, or 2) the carrier wave is RCP and λ_0^{car} lies outside the Bragg regime. However, when the handedness of the carrier wave matches the structural handedness of the chiral STF and the carrier wavelength lies within the Bragg regime, the transmitted pulse is quite weak.

There is another—and a more significant—observation to be made in Figures 3 and 4: even when the transmission is weak, two spires remain at the leading and trailing edges of the transmitted pulse. That is, although most of the energy of an incident pulse is reflected when the circular Bragg phenomenon is excited by virtue of the wavelength and the circular polarization state of the carrier wave, a *ghost* of the pulse passes through the chiral STF. This ghost contains information about the width of the pulse, which is of fundamental importance to any optical communication system employing a pulse-width modulation scheme [4, 12]. In addition, the spire at the leading edge of each pulse is particularly prominent, meaning that the time interval between the arrivals of two consecutive pulses may be measured. Thus, chiral STFs may be used for optical devices employed in pulse-position modulation systems [12].

The spires fore and aft of each transmitted pulse can be attributed to the spectral components outside the Bragg regime that are transmitted by the slab. Although the FWHM bandwidth of the incident pulse ($\sim$ 9 nm) is less than that of the Bragg regime (27 nm), there are spectral components of the pulse that lie outside the Bragg regime, even when $\lambda_0^{car} = \lambda_0^{Br}$. These components are due to the steep edges of the incident pulse, and those sufficiently removed from the ultraviolet resonances at 280 and 290 nm do not pass through the chiral STF without excessive absorption. Thus, the rise and fall times of rectangular pulses must be sufficiently small, and the pulse widths must be sufficiently large, for ghost transmission to occur in opposition to the circular Bragg phenomenon.

REFERENCES

1. V.C. Venugopal and A. Lakhtakia, "Sculptured thin films: Conception, optical properties, and applications," Electromagnetic fields in unconventional materials and structures, O.N. Singh and A. Lakhtakia (Editors), Wiley, New York, 2000, pp. 151–216.
2. V.C. Venugopal and A. Lakhtakia, On absorption by non-axially excited slabs of dielectric thin-film helicoidal bianisotropic mediums, Eur Phys J Appl Phys 10 (2000), 173–184.
3. Q. Wu, I.J. Hodgkinson, and A. Lakhtakia, Circular polarization filters made of chiral sculptured thin films: Experimental and simulation results, Opt Eng 39 (2000), 1863–1868.
4. R.J. Hoss, Fiber optic communications design handbook, Prentice-Hall, Englewood Cliffs, NJ, 1990.
5. R.L. Fork, B.I. Greene, and C.V. Shank, Generation of optical pulses shorter than 0.1 psec by colliding pulse modelocking, Appl Phys Lett 38 (1981), 671–672.
6. C. Kittel, Introduction to solid state physics, Wiley Eastern, New Delhi, India, 1974.
7. E.J. Post, Formal structure of electromagnetics, Dover, New York, 1997.
8. W.S. Weiglhofer and A. Lakhtakia, On causality requirements for material media, AEU 50 (1996), 389–391.
9. J.B. Geddes, III, M.W. Meredith, and A. Lakhtakia, Circular Bragg phenomenon and pulse bleeding in cholesteric liquid crystals, Opt Commun 182 (2000), 45–57.
10. N. Gershenfeld, The nature of mathematical modeling, Cambridge University Press, Cambridge, England, 1999.
11. A. Lakhtakia, Spectral signatures of axially excited slabs of dielectric thin-film helicoidal bianisotropic mediums, Eur Phys J Appl Phys 8 (1999), 129–137.
12. B.P. Lathi, Modern digital and analog communication systems, Prism Books, Bangalore, India, 1993.

Eur. Phys. J. AP **17**, 21–24 (2002)
DOI: 10.1051/epjap:2001007

THE EUROPEAN PHYSICAL JOURNAL APPLIED PHYSICS

Videopulse bleeding in axially excited chiral sculptured thin films in the Bragg regime

J.B. Geddes III and A. Lakhtakia[a]

CATMAS – Computational & Theoretical Materials Sciences Group, Department of Engineering Science and Mechanics, Pennsylvania State University, University Park, PA 16802-6812, USA

Received: 10 May 2001 / Accepted: 24 September 2001

Abstract. The reflection and transmission of optical videopulses incident axially upon a slab of a chiral sculptured thin film (STF) is studied using a finite-difference simulation in the time domain. Videopulse bleeding is shown to occur when the handedness of the carrier plane wave matches the structural handedness of the chiral STF and the carrier wavelength lies in the Bragg regime.

PACS. 77.55.+f Dielectric thin films – 78.20.Bh Theory, models, and numerical simulation – 42.70.-a Optical materials

1 Introduction

The propagation of ultrashort optical pulses is of scientific as well as technical interest. Scientifically, such pulses are used to probe atomic, molecular, and material systems at short time scales [1,2]. Ultrashort optical pulses have potential practical utility in communications, sensors, and medicine. Although most recent experimental research has investigated pulses that contain multiple optical cycles (*i.e.*, cycles of the carrier light wave), pulses so short that they comprise about one optical cycle or less are possible. These entities, known as videopulses [3–5], are among the closest approximations of an impulse function that have yet been created.

Previous research on the interaction of femtosecond-duration pulses with chiral sculptured thin films (STFs) and cholesteric liquid crystals (CLCs) – materials that may be useful for manipulating ultrashort optical pulses – revealed the spatiotemporal anatomy of the *circular Bragg phenomenon* exhibited by these materials as a consequence of their helicoidally periodic microstructure [6,7]. In the frequency domain, the circular Bragg phenomenon is manifested as polarization-dependent reflection: monochromatic, right circularly polarized (RCP) light is largely reflected from a structurally right-handed material of little absorbance, while left circularly polarized (LCP) light is reflected very little, when the wavelength of the incident light lies within a wavelength band called the Bragg regime. In the time domain, upon entering a structurally right-handed chiral STF, an optical pulse modulating a RCP (but not a LCP) carrier plane wave undergoes a protracted, reflective transfer of energy out of the structurally chiral material in addition to experiencing any absorption. This polarization-selective reflection of energy, dubbed *pulse bleeding*, accounts for the increased reflection associated with the circular Bragg phenomenon in the frequency domain, and explains other effects such as the long duration of reflected pulses when the conditions for the circular Bragg phenomenon are present.

The previously studied pulses were of multiple optical cycles in duration. Our aim here is to show that polarization-dependent bleeding can occur even for videopulses. We solved the time-domain Maxwell equations on a Cray T3E supercomputer for the propagation of videopulses through a chiral STF of finite thickness, and examine the reflection and transmission of videopulses. The constitutive relations employed for the unidirectionally nonhomogeneous film are causal [9], and display the characteristic helicoidal variation of dielectric anisotropy with local orthorhombic symmetry [7]. CLCs can be accommodated in our formalism, being simplifications of chiral STFs in macroscopic electromagnetic terms. The reader is referred to two papers [7,8] for details of the algorithm employed by us.

2 Results and discussion

The region $z_\ell \leq z \leq z_r$, $(z_\ell > 0)$, is occupied by a chiral STF, while the half-spaces $z \leq z_\ell$ and $z \geq z_r$ are vacuous. A carrier plane wave amplitude-modulated by a videopulse is launched from the plane $z = 0$ at time $t = 0$ in the $+z$ direction. It excites the chiral STF slab, and eventually transforms into a reflected pulse and a transmitted pulse.

[a] e-mail: AXL4@psu.edu

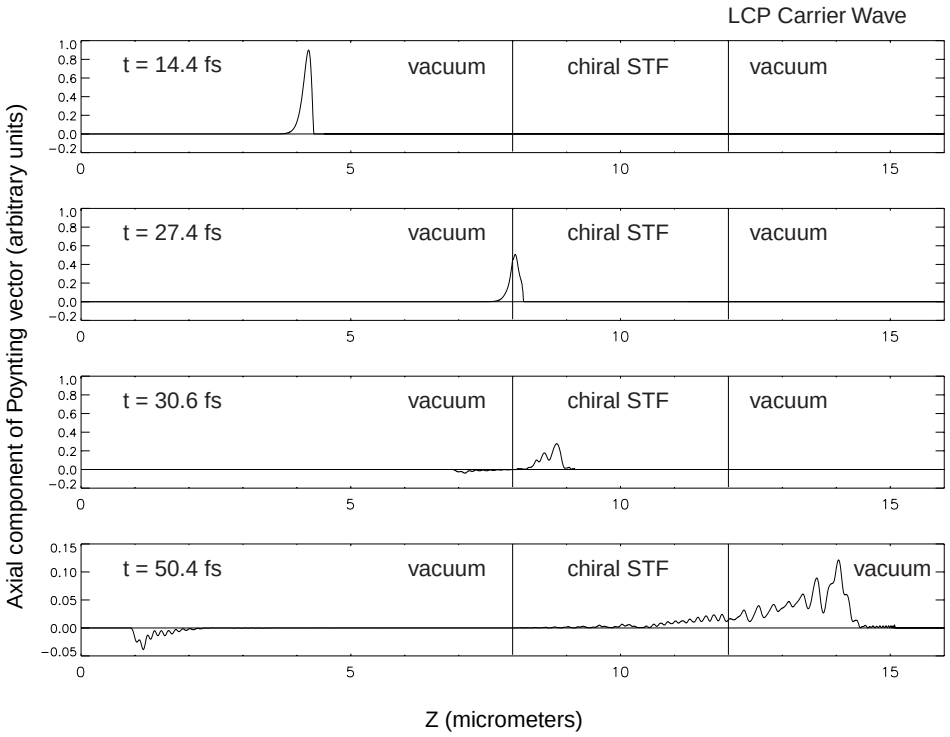

Fig. 1. Snapshots of the axial component of the instantaneous Poynting vector at four different instants of time (from top to bottom, $t = 14.4, 27.4, 30.6, 50.4$ fs) when the carrier plane wave is LCP. Multiply all values on the ordinates by 4.0×10^{-6} W m^{-2} to obtain the actual data.

The relative permittivity dyadic is specified as a function of position vector $\underline{r} = x\underline{u}_x + y\underline{u}_y + z\underline{u}_z$ and time t by

$$\underline{\underline{\epsilon}}(\underline{r},t) = \begin{cases} \underline{\underline{I}}\,\delta(t)\,, & z \notin [z_\ell,\, z_r] \\ \underline{\underline{S}}_z(z-z_\ell)\bullet\underline{\underline{S}}_y(\chi)\bullet\left[\epsilon_a(t)\,\underline{u}_z\underline{u}_z\right. & \\ \quad +\epsilon_b(t)\,\underline{u}_x\underline{u}_x+\epsilon_c(t)\,\underline{u}_y\underline{u}_y\left.\right]\bullet & \\ \quad \underline{\underline{S}}_y^{-1}(\chi)\bullet\underline{\underline{S}}_z^{-1}(z-z_\ell)\,, & z \in [z_\ell,\, z_r] \end{cases} , \quad (1)$$

where $\underline{\underline{I}}$ is the identity dyadic; $\delta(t)$ is the Dirac delta function; and $\underline{u}_x$, $\underline{u}_y$, and $\underline{u}_z$ are the Cartesian unit vectors. The rotation dyadic

$$\underline{\underline{S}}_z(z) = \underline{u}_z\underline{u}_z + (\underline{u}_x\underline{u}_x + \underline{u}_y\underline{u}_y)\,\cos(\pi z/\Omega) + (\underline{u}_y\underline{u}_x - \underline{u}_x\underline{u}_y)\,\sin(\pi z/\Omega) \quad (2)$$

captures the structural right-handedness of the chosen chiral STF, with 2Ω being the structural period. The tilt dyadic

$$\underline{\underline{S}}_y(\chi) = \underline{u}_y\underline{u}_y + (\underline{u}_x\underline{u}_x + \underline{u}_z\underline{u}_z)\,\cos\chi + (\underline{u}_z\underline{u}_x - \underline{u}_x\underline{u}_z)\,\sin\chi \quad (3)$$

is a function of the angle of rise χ. As single-resonance Lorentzian characteristics are assumed for the dielectric response properties of the chiral STF,

$$\epsilon_{a,b,c}(t) = \delta(t) + p_{a,b,c}\left(\frac{2\pi c_0}{\lambda_0^{a,b,c}}\right)\,\sin\left(\frac{2\pi c_0}{\lambda_0^{a,b,c}}t\right) \times\exp\left(-\frac{c_0 t}{N_{a,b,c}\lambda_0^{a,b,c}}\right)\,\mathcal{U}(t)\,,$$

where $\mathcal{U}(t)$ is the unit step function; c_0 is the speed of light in vacuum; the oscillator strengths are denoted by $p_{a,b,c}$; while $\lambda_0^{a,b,c}$ and $N_{a,b,c}$ delineate the resonant attributes of the chosen material.

For the numerical results presented here, we set $z_\ell = 8$ μm, $z_r = 12$ μm, $p_a = 0.40$, $p_b = 0.52$, $p_c = 0.42$, $\lambda_0^{a,c} = 280$ nm, $\lambda_0^b = 290$ nm, $N_{a,b,c} = 10^5$, $\chi = 20°$, and $\Omega = 200$ nm. The Bragg regime therefore is centered at 516 nm free-space wavelength, with a full-width half-maximum bandwith of approximately 27 nm [10].

The incident signal is either a RCP or LCP carrier plane wave whose amplitude is modulated by the pulse function

$$g(t) = \frac{c_0 t}{2\lambda_0^{\rm car}}\exp\left(\frac{-c_0 t}{0.2\lambda_0^{\rm car}}\right), \quad (4)$$

where $\lambda_0^{\rm car}$ is the carrier wavelength in vacuum. The videopulse in this paper is roughly 2 fs in duration, which translates to approximately $1\frac{1}{2}$ optical cycles of the carrier wave when $\lambda_0^{\rm car} = 516$ nm.

Snapshots of the axial component of the instantaneous Poynting vector are presented at four instants of time in the panels of Figures 1 and 2. In each case, the carrier wavelength $\lambda_0^{\rm car} = 516$ nm, but the carrier wave in Figure 1 is LCP while the carrier wave in Figure 2 is RCP. The videopulse traverses the space $0 < z < z_\ell$ and enters the chiral STF slab, whereupon part of it is reflected and part transmitted. It is evident in both figures that the transmitted pulse is considerably longer than the incident pulse, regardless of the carrier plane wave's handedness.

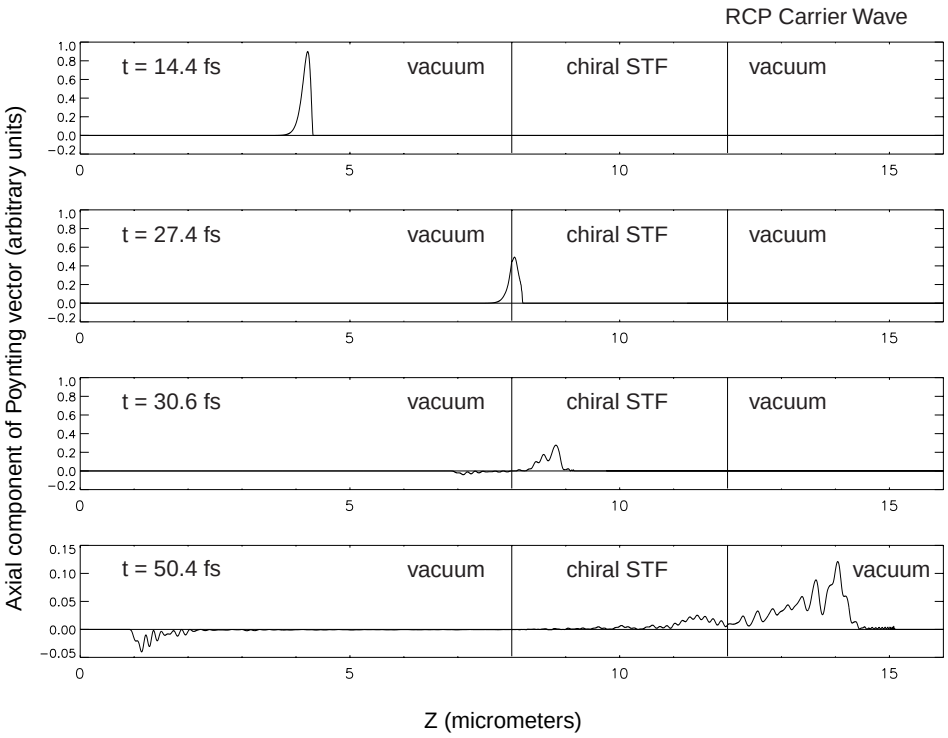

Fig. 2. Same as Figure 1, except the carrier plane wave is RCP.

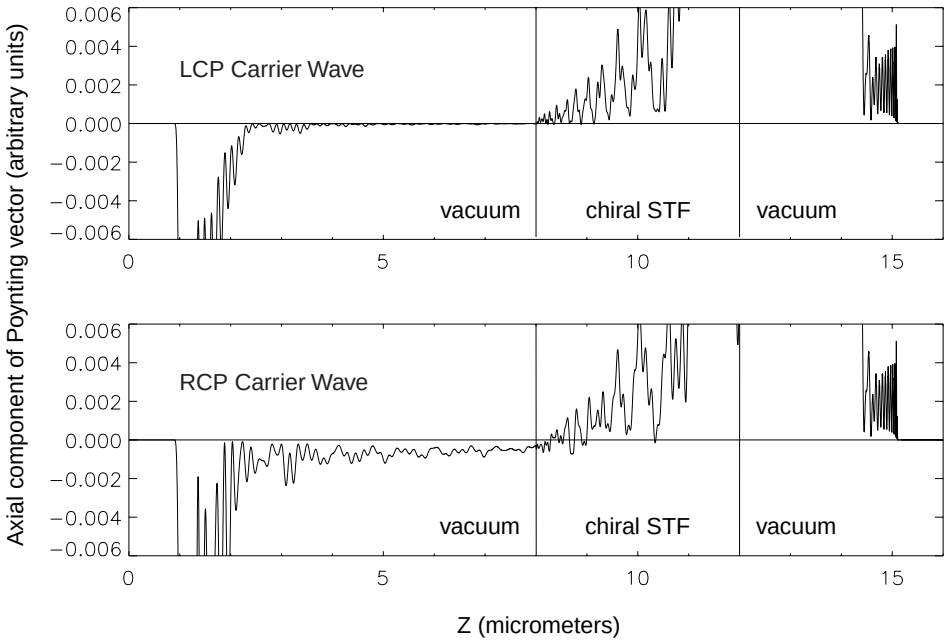

Fig. 3. Magnified views of the fourth panels ($t = 50.4$ fs) of Figures 1 and 2 (top and bottom, respectively).

Magnified views of the fourth panels of Figures 1 and 2 are given in Figure 3. From that figure, we see that the reflected pulse is much longer when the carrier wave is RCP than LCP, and the reflected and transmitted pulses are joined by a light pipe that ferries energy across the first vacuum/chiral STF interface. Thus, videopulse bleeding occurs in the case where the carrier wave is RCP. Frame-by-frame examination shows that although the videopulse modulating the LCP carrier wave also undergoes some bleeding, the light pipe across the first vacuum/chiral STF interface ferries much less energy and exists for a much shorter duration than with the RCP carrier wave. It is not clear whether the short-duration, low-energy light pipe for videopulses carried by LCP carrier waves is physically possible or simply a numerical artifact due to the extremely brief durations of videopulses. From these observations, we

conclude that pulse bleeding does not require the presence of many optical cycles in the incident pulse to occur.

Thus, we have shown the occurrence of *videopulse bleeding* in an axially excited chiral STF when the handedness of the carrier plane wave matches the structural handedness of the film and the carrier wavelength lies in the Bragg regime. The same conclusion follows for CLCs.

This research was supported in part by the Pittsburgh Supercomputing Center.

References

1. S. Nolte, G. Kamlage, F. Korte, T. Bauer, T. Wagner, A. Ostendorf, C. Fallnich, H. Welling, Adv. Eng. Mater. **2**, 23 (2000).
2. W.H. Knox, IEEE J. Sel. Topics Quantum Electron. **6**, 1273 (2000).
3. S.V. Sazonov, E.V. Trifonov, J. Phys. B: At. Mol. Opt. Phys. **27**, L7 (1994).
4. S.V. Sazonov, L.S. Yakupova, J. Phys. B: At. Mol. Opt. Phys. **27**, 369 (1994).
5. E.V. Kazantseva, A.I. Maimistov, B.A. Malomed, Opt. Commun. **188**, 195 (204).
6. J.B. Geddes III, M.W. Meredith, A. Lakhtakia, Opt. Commun. **182**, 45 (2000).
7. J.B. Geddes III, A. Lakhtakia, Eur. Phys. J. AP **13**, 3 (2001); erratum: **16**, 247 (2001).
8. J.B. Geddes III, A. Lakhtakia, Eur. Phys. J. AP **14**, 97 (2001); erratum: **16**, 247 (2001).
9. W.S. Weiglhofer, A. Lakhtakia, Arch. Elektr. Über. **50**, 389 (1996).
10. A. Lakhtakia, Eur. Phys. J. AP **8**, 129 (1999).

Optik 113, No. 5 (2002) 213–221

http://www.urbanfischer.de/journals/optik

Optik Optics
International Journal for Light and Electron Optics

Multiple Bragg regimes exhibited by a chiral sculptured thin film half-space on axial excitation

Jianwei Wang[1], Akhlesh Lakhtakia[1], Joseph B. Geddes III[2]

[1] CATMAS – Computational and Theoretical Materials Sciences Group, Department of Engineering Science and Mechanics, 212 Earth-Engineering Sciences Building, Pennsylvania State University, University Park, PA 16802-6812, USA
[2] Applied Science and Technology Graduate Group, University of California, Berkeley, CA 97420, USA

Abstract: Axially excited chiral sculptured thin films (STFs) are shown to display the circular Bragg phenomenon in more than one wavelength-regime, owing to the dispersion inherent in their dielectric susceptibilities. With the assumption of the one-resonance Lorentz model for the constitutive parameters in a frequency-domain investigation, two Bragg regimes emerge: one pre-resonant, and the other post-resonant. A wavelength-regime of perfect reflection also appears. The pulse-bleeding mechanism previously shown to underlie the pre-resonant Bragg regime turns out to be responsible also for the post-resonant Bragg regime. Femtosecond pulse propagation in the post-resonant regime would be very likely affected by the existence of multiple Bragg and perfectly reflecting regimes.

Key words: Bragg regime – chiral thin film – circular Bragg phenomenon – femtosecond pulse – Lorentz model – pulse propagation – sculptured thin film

1. Introduction

Owing to the periodic and rotational variation of its constitutive properties along a fixed axis, any helicoidal bianisotropic medium (HBM) must display the so-called circular Bragg phenomenon upon axial excitation by a plane wave [1]. This statement is supported by observations on both chiral liquid crystals [2, 3] and chiral sculptured thin films [4].

The circular Bragg phenomenon is polarization-selective, which is easy to conclude from frequency- as well as time-domain results. Let a circularly polarized plane wave with free-space wavelength λ_0 axially excite a chiral sculptured thin film (STF) of finite thickness. Provided the film thickness is sufficiently large and λ_0 lies within a certain wavelength-regime (determined by the periodicity and the relative permittivity dyadic of the chiral STF), the reflectance is much higher if the handedness of the incident plane wave matches the structural handedness of the chiral STF than if otherwise [4]. Grating theory provides an explanation of this phenomenon [5]: A plane wave of matching handedness effectively encounters a Bragg grating, while that of the other handedness does not.

In the time domain, upon entering a structurally right/left-handed chiral STF, an optical pulse modulating a right/left (but not a left/right) circularly polarized carrier plane wave undergoes a protracted, reflective transfer of energy out of the structurally chiral material in addition to experiencing absorption. This polarization-selective back-flow of energy, dubbed *pulse bleeding*, accounts for the increased reflection associated with the circular Bragg phenomenon in the frequency domain, and also explains other effects – such as the long duration of reflected pulses when the conditions for the circular Bragg phenomenon are present [6, 7].

The center-wavelength as well as the bandwidth of the Bragg regime can be easily predicted, provided the constitutive properties are taken to be frequency-dependent (in a relevant part of the electromagnetic spectrum) [4]. But the frequency-domain constitutive properties of linear materials must be dispersive, which is a requirement mandated by causality [8,9]. This leads to the speculation that more than one Bragg regime may be displayed on axial excitation.

This paper presents the results of our frequency-domain as well as time-domain investigations. With the assumption that dielectric properties of a chiral STF can be satisfactorily described by the single-resonance Lorentz model [10, 11], our emphasis is on the short-wavelength side of the material resonances in the electromagnetic spectrum. We show via frequency- and time-domain investigations that multiple Bragg regimes are indeed possible for axially excited chiral STFs, because of dispersion. Although the problems we address here involve only chiral STF half-spaces for the sake of simplicity, experience [6, 12] informs us that the results would be applicable to the more realistic chiral STF slabs as well. Mathematical isomorphism guarantees the potential applicability of the

Received 8 March 2002; accepted 15 May 2002.

Corresponding to: A. Lakhatkia
Fax: ++1-814-863-796
E-mail: AXL4@psu.edu

understanding derived here to chiral liquid crystals [13] too.

2. Theoretical preliminaries

The geometry of the problems addressed here comprises two half-spaces. While the half-space $z \leq z_\ell$ is vacuous, the half-space $z \geq z_\ell$ is occupied by a structurally right-handed chiral STF whose axis of nonhomogeneity is parallel to the z axis. The actual value of z_ℓ is irrelevant for frequency-domain, but not for time-domain, calculations.

2.1 Frequency-domain constitutive relations

For frequency-domain research, all electromagnetic fields are assumed to have an $\exp(-i\omega t)$ time-dependence, with ω as the angular frequency, t as the time, and $i = \sqrt{-1}$. The constitutive relations between the various electromagnetic field phasors, applicable everywhere, may be stated as follows:

$$\left.\begin{aligned} \tilde{\boldsymbol{D}}(\boldsymbol{r}, \lambda_0) &= \varepsilon_0 \, \tilde{\boldsymbol{\epsilon}}(\boldsymbol{r}, \lambda_0) \, \tilde{\boldsymbol{E}}(\boldsymbol{r}, \lambda_0) \\ \tilde{\boldsymbol{B}}(\boldsymbol{r}, \lambda_0) &= \mu_0 \tilde{\boldsymbol{H}}(\boldsymbol{r}, \lambda_0) \end{aligned}\right\} . \tag{1}$$

Here and hereafter, ε_0 and μ_0 are the permittivity and the permeability of free space (i.e., vacuum), respectively; $\eta_0 = \sqrt{\mu_0/\varepsilon_0}$ and $c_0 = 1/\sqrt{\varepsilon_0 \mu_0}$; while $\lambda_0 = 2\pi c_0/\omega$ is the free-space wavelength. The position vector is denoted by $\boldsymbol{r} = x\boldsymbol{u}_x + y\boldsymbol{u}_y + z\boldsymbol{u}_z$, with $\boldsymbol{u}_x$, $\boldsymbol{u}_y$ and $\boldsymbol{u}_z$ as the unit cartesian vectors.

The relative permittivity dyadic $\tilde{\boldsymbol{\epsilon}}(\boldsymbol{r}, \lambda_0)$ is conveniently and compactly expressed as [4]

$$\tilde{\boldsymbol{\epsilon}}(\boldsymbol{r}, \lambda_0) = \begin{cases} \boldsymbol{I} , & z < z_\ell \\ \boldsymbol{S}_z(z - z_\ell) \cdot \boldsymbol{S}_y(\chi) \\ \cdot \left[\tilde{\varepsilon}_a(\lambda_0) \, \boldsymbol{u}_z \boldsymbol{u}_z + \tilde{\varepsilon}_b(\lambda_0) \, \boldsymbol{u}_x \boldsymbol{u}_x + \tilde{\varepsilon}_c(\lambda_0) \, \boldsymbol{u}_y \boldsymbol{u}_y \right] & \\ \cdot \boldsymbol{S}_y^{-1}(\chi) \cdot \boldsymbol{S}_z^{-1}(z - z_\ell) , & z > z_\ell \end{cases} . \tag{2}$$

In these expressions, $\boldsymbol{I}$ is the identity dyadic; while $\tilde{\varepsilon}_{a,b,c}(\lambda_0)$ are complex-valued scalar functions of the wavelength. The rotation dyadic

$$\boldsymbol{S}_z(z) = \boldsymbol{u}_z \boldsymbol{u}_z + (\boldsymbol{u}_x \boldsymbol{u}_x + \boldsymbol{u}_y \boldsymbol{u}_y) \cos \frac{\pi z}{\Omega} + (\boldsymbol{u}_y \boldsymbol{u}_x - \boldsymbol{u}_x \boldsymbol{u}_y) \sin \frac{\pi z}{\Omega} \tag{3}$$

captures the helicoidal periodicity of the chiral STF, with 2Ω being the structural period. The tilt dyadic

$$\boldsymbol{S}_y(\chi) = \boldsymbol{u}_y \boldsymbol{u}_y + (\boldsymbol{u}_x \boldsymbol{u}_x + \boldsymbol{u}_z \boldsymbol{u}_z) \cos\chi + (\boldsymbol{u}_z \boldsymbol{u}_x - \boldsymbol{u}_x \boldsymbol{u}_z) \sin\chi \tag{4}$$

represents the locally aciculate microstructure of the chiral STF, with χ as the angle of tilt.

2.2. Time-domain constitutive relations

With the electromagnetic phasors related to the electromagnetic fields via the *temporal* Fourier transform as

$$\tilde{\boldsymbol{E}}(\boldsymbol{r}, \lambda_0) = \int_{-\infty}^{\infty} \boldsymbol{E}(\boldsymbol{r}, t) \exp(i\omega t) \, dt , \tag{5}$$

the time-domain counterparts of (1) are expressed as

$$\left.\begin{aligned} \boldsymbol{D}(\boldsymbol{r}, t) &= \varepsilon_0 (\epsilon * \boldsymbol{E})(\boldsymbol{r}, t) \\ \boldsymbol{B}(\boldsymbol{r}, t) &= \mu_0 \boldsymbol{H}(\boldsymbol{r}, t) \end{aligned}\right\} . \tag{6}$$

The operation $*$ denotes convolution with respect to time; thus,

$$(\epsilon * \boldsymbol{E})(\boldsymbol{r}, t) = \int_0^{\infty} \epsilon(\boldsymbol{r}, \tau) \, \boldsymbol{E}(\boldsymbol{r}, t - \tau) \, d\tau . \tag{7}$$

The counterpart of (2) in the time domain is the dyadic function

$$\epsilon(\boldsymbol{r}, t) = \begin{cases} \boldsymbol{I} \, \delta(t) , & z < z_\ell \\ \boldsymbol{S}_z(z - z_\ell) \cdot \boldsymbol{S}_y(\chi) & \\ \cdot \left[\varepsilon_a(t) \, \boldsymbol{u}_z \boldsymbol{u}_z + \varepsilon_b(t) \, \boldsymbol{u}_x \boldsymbol{u}_x + \varepsilon_c(t) \, \boldsymbol{u}_y \boldsymbol{u}_y \right] & \\ \cdot \boldsymbol{S}_y^{-1}(\chi) \cdot \boldsymbol{S}_z^{-1}(z - z_\ell) , & z > z_\ell \end{cases} , \tag{8}$$

where $\delta(t)$ is the Dirac delta function, while $\varepsilon_{a,b,c}(t)$ are real-valued functions of time.

2.3 Single-resonance Lorentz model

We chose the single-resonance Lorentz model [10] for the dielectric susceptibility functions

$$\tilde{\chi}_{a,b,c}(\lambda_0) = \tilde{\varepsilon}_{a,b,c}(\lambda_0) - 1 \tag{9}$$

and

$$\chi_{a,b,c}(t) = \varepsilon_{a,b,c}(t) - \delta(t) . \tag{10}$$

Accordingly,

$$\tilde{\chi}_{a,b,c}(\lambda_0) = \frac{p_{a,b,c}}{1 + (N_{a,b,c}^{-1} - i\lambda_0^{a,b,c}/\lambda_0)^2} \tag{11}$$

and

$$\chi_{a,b,c}(t) = p_{a,b,c} \left(\frac{2\pi c_0}{\lambda_0^{a,b,c}} \right) \sin \left(\frac{2\pi c_0}{\lambda_0^{a,b,c}} \, t \right) \times \exp \left(- \frac{c_0 t}{M_{a,b,c} \lambda_0^{a,b,c}} \right) \mathcal{U}(t) \tag{12}$$

constitute a matched pair with respect to the temporal Fourier transform. In these expressions, $\mathcal{U}(t)$ is the unit step function; $p_{a,b,c}$ denote the so-called oscillator strengths; while $N_{a,b,c} = 2\pi M_{a,b,c}$ and $\lambda_0^{a,b,c}$ determine the resonance wavelengths and linewidths.

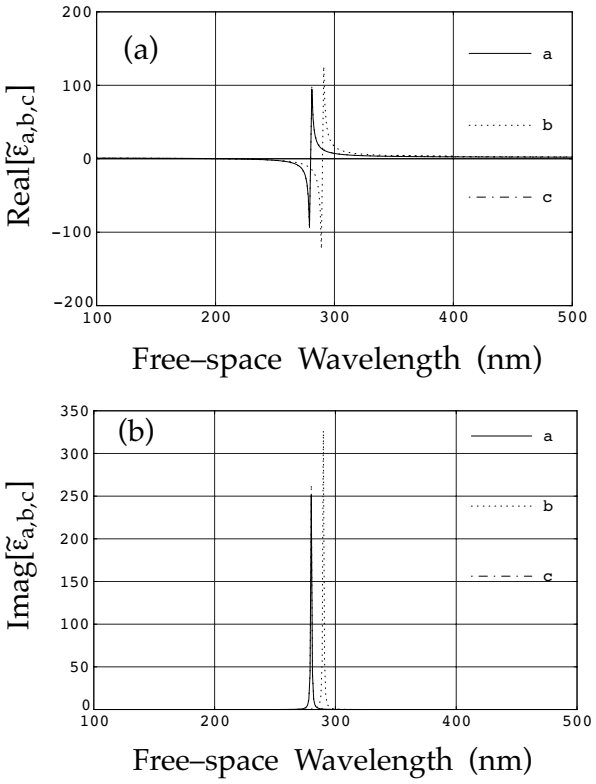

Fig. 1. a) Real and b) imaginary parts of $\tilde{\varepsilon}_{a,b,c}$ as functions of the free–space wavelength λ_0, when $p_a = 0.80$, $p_b = 1.04$, $p_c = 0.84$, $\chi = 20^\circ$, $\lambda_0^{a,c} = 280$ nm, $\lambda_0^b = 290$ nm, and $M_{a,b,c} = 100$ in (11). The plots of $\tilde{\varepsilon}_a(\lambda_0)$ and $\tilde{\varepsilon}_c(\lambda_0)$ are virtually indistinguishable.

For all calculations reported in this paper, we chose $p_a = 0.80$, $p_b = 1.04$, $p_c = 0.84$, $\chi = 20^\circ$, $\lambda_0^{a,c} = 280$ nm, $\lambda_0^b = 290$ nm, $M_{a,b,c} = 100$, and $\Omega = 90$ nm. The spectrums of $\tilde{\varepsilon}_{a,b,c}$ are shown in figure 1.

3. Planewave response of a chiral STF half-space

Suppose an arbitrarily polarized plane wave is normally incident on the chiral STF half-space from the vacuous half-space $z \leq z_\ell$. As a result, a plane wave is reflected into free space, while refraction into the chiral STF also occurs.

3.1. Boundary value problem

For axial excitation, all fields are independent of x and y, so that $\partial/\partial x \equiv 0$ and $\partial/\partial y \equiv 0$. The electric field phasor associated with the two plane waves in the vacuous half-space is stated as

$$\begin{aligned}\tilde{\boldsymbol{E}}(z,\lambda_0) = {} & [a_L(\lambda_0)\,\boldsymbol{u}_+ + a_R(\lambda_0)\,\boldsymbol{u}_-]\exp[\mathrm{i}k_0(z-z_\ell)] \\ & + [r_L(\lambda_0)\,\boldsymbol{u}_- + r_R(\lambda_0)\,\boldsymbol{u}_+]\exp[-\mathrm{i}k_0(z-z_\ell)]\,, \\ & z \leq z_\ell\,. \end{aligned} \tag{13}$$

Here, $k_0 = 2\pi/\lambda_0$ is the wavenumber in free space; the complex unit vectors $\boldsymbol{u}_\pm = (\boldsymbol{u}_x \pm \mathrm{i}\boldsymbol{u}_y)/\sqrt{2}$; $a_L(\lambda_0)$ and $a_R(\lambda_0)$ are the known amplitudes of the left- and the right-circularly polarized (LCP and RCP) components of the incident plane wave; while $r_L(\lambda_0)$ and $r_R(\lambda_0)$ are the unknown amplitudes of the reflected planewave components. The magnetic field phasor corresponding to (13) is then easily determined from the Faraday equation.

The electromagnetic field phasors induced in the chiral STF half-space are given as [14, 15],

$$\begin{aligned}&\tilde{\boldsymbol{E}}(z,\lambda_0) \\ &= \sum_{m=1}^{4}{}' \, a_m(\lambda_0)\exp[\mathrm{i}g_m(z-z_\ell)] \\ &\quad\times\left\{\boldsymbol{u}_x\left[e_{m1}\cos\frac{\pi(z-z_\ell)}{\Omega} - e_{m2}\sin\frac{\pi(z-z_\ell)}{\Omega}\right]\right. \\ &\quad\left.+\,\boldsymbol{u}_y\left[e_{m1}\sin\frac{\pi(z-z_\ell)}{\Omega} + e_{m2}\cos\frac{\pi(z-z_\ell)}{\Omega}\right] + \boldsymbol{u}_z e_{m3}\right\}, \\ &\qquad\qquad z \geq z_\ell\,, \end{aligned} \tag{14}$$

and

$$\begin{aligned}&\tilde{\boldsymbol{H}}(z,\lambda_0) \\ &= \sum_{m=1}^{4}{}' \, a_m(\lambda_0)\exp[\mathrm{i}g_m(z-z_\ell)] \\ &\quad\times\left\{\boldsymbol{u}_x\left[h_{m1}\cos\frac{\pi(z-z_\ell)}{\Omega} - h_{m2}\sin\frac{\pi(z-z_\ell)}{\Omega}\right]\right. \\ &\quad\left.+\,\boldsymbol{u}_y\left[h_{m1}\sin\frac{\pi(z-z_\ell)}{\Omega} + h_{m2}\cos\frac{\pi(z-z_\ell)}{\Omega}\right]\right\}, \\ &\qquad\qquad z \geq z_\ell\,. \end{aligned} \tag{15}$$

The (un-normalized) cartesian components of the modal field phasors, given by

$$\left.\begin{aligned} e_{m1}(\lambda_0) &= \omega\mu_0\left[g_m^2 - k_0^2\tilde{\varepsilon}_c + \left(\frac{\pi}{\Omega}\right)^2\right] \\ e_{m2}(\lambda_0) &= 2i\omega\mu_0\,\frac{\pi}{\Omega}\,g_m \\ e_{m3}(\lambda_0) &= e_{m1}(\lambda_0)\,\frac{\tilde{\varepsilon}_a - \tilde{\varepsilon}_b}{\tilde{\varepsilon}_a\tilde{\varepsilon}_b}\,\tilde{\varepsilon}_d\cos\chi\sin\chi \\ h_{m1}(\lambda_0) &= -\mathrm{i}\,\frac{\pi}{\Omega}\left[g_m^2 + k_0^2\tilde{\varepsilon}_c - \left(\frac{\pi}{\Omega}\right)^2\right] \\ h_{m2}(\lambda_0) &= g_m\left[g_m^2 - k_0^2\tilde{\varepsilon}_c - \left(\frac{\pi}{\Omega}\right)^2\right] \end{aligned}\right\}, \quad 1 \leq m \leq 4\,, \tag{16}$$

contain the four modal wavenumbers

$$\begin{aligned} g_1(\lambda_0) = -\,g_3(\lambda_0) = +\,2^{-1/2}\left\{k_0^2\,(\tilde{\epsilon}_c + \tilde{\varepsilon}_d) + 2\left(\frac{\pi}{\Omega}\right)^2\right. \\ \left. + k_0\left[k_0^2(\tilde{\epsilon}_c - \tilde{\varepsilon}_d)^2 + 8\left(\frac{\pi}{\Omega}\right)^2(\tilde{\epsilon}_c + \tilde{\varepsilon}_d)\right]^{1/2}\right\}^{1/2} \end{aligned} \tag{17}$$

and

$$g_2(\lambda_0) = -g_4(\lambda_0) = +2^{-1/2}\left\{k_0^2\,(\tilde{\varepsilon}_c+\tilde{\varepsilon}_d) + 2\left(\frac{\pi}{\Omega}\right)^2 - k_0\left[k_0^2(\tilde{\varepsilon}_c-\tilde{\varepsilon}_d)^2 + 8\left(\frac{\pi}{\Omega}\right)^2(\tilde{\varepsilon}_c+\tilde{\varepsilon}_d)\right]^{1/2}\right\}^{1/2}. \tag{18}$$

The quantity

$$\tilde{\varepsilon}_d(\lambda_0) = \frac{\tilde{\varepsilon}_a\,\tilde{\varepsilon}_b}{\tilde{\varepsilon}_a\cos^2\chi + \tilde{\varepsilon}_b\sin^2\chi} \tag{19}$$

is defined for convenience, the difference between $\tilde{\varepsilon}_c$ and $\tilde{\varepsilon}_d$ quantifying the degree of anisotropy relevant to an axially excited chiral STF [16]. We assume here that Ω is finite and exclude the possibility of the excitation of axially propagating Voigt waves [17].

The summation symbols in (14) and (15) are primed to indicate that two of the four modal coefficients $a_m(\lambda_0)$, $1 \le m \le 4$, must be identically null-valued in the present context. The determination of which two requires computation of the z-directed components of the modal time-averaged Poynting vectors $\tilde{\boldsymbol{P}}_m(z,\lambda_0)$, $1 \le m \le 4$; thus,

$$\begin{aligned}\tilde{P}_{mz}(z,\lambda_0) &= \boldsymbol{u}_z \cdot \tilde{\boldsymbol{P}}_m(z,\lambda_0) \\ &= \tfrac{1}{2}\,|a_m|^2 \exp\{-2\,\mathrm{Im}\,[g_m]\,z\} \\ &\quad \times \mathrm{Re}\left[e_{m1}h_{m2}^* - e_{m2}h_{m1}^*\right], \quad 1 \le m \le 4\,,\end{aligned} \tag{20}$$

where the asterisk denotes the complex conjugate. Because $\tilde{P}_{1z} > 0$ and $\tilde{P}_{3z} < 0$, in general [18], we must have $a_1 \neq 0$ and $a_3 \equiv 0$. The quantities $\tilde{P}_{2z}$ and $\tilde{P}_{4z}$ are always opposite in sign; hence, either $a_2 \equiv 0$ when $\tilde{P}_{2z}/|a_2|^2 < 0$, or $a_4 \equiv 0$ when $\tilde{P}_{4z}/|a_4|^2 < 0$.

The boundary value problem is formulated by ensuring the continuity of the tangential components of the electric and the magnetic field phasors across the plane $z = z_\ell$. Four simultaneous algebraic equations emerge [14], whose solution yields the four unknown coefficients appearing in (13), (14) and (15).

Our attention is focussed in this section on the four reflection coefficients entering the 2×2 matrix in the following relation:

$$\begin{bmatrix} r_L(\lambda_0) \\ r_R(\lambda_0) \end{bmatrix} = \begin{bmatrix} r_{LL}(\lambda_0) & r_{LR}(\lambda_0) \\ r_{RL}(\lambda_0) & r_{RR}(\lambda_0) \end{bmatrix} \cdot \begin{bmatrix} a_L(\lambda_0) \\ a_R(\lambda_0) \end{bmatrix}. \tag{21}$$

These coefficients are doubly subscripted: those with both subscripts identical refer to co-polarized, while those with two different subscripts denote cross-polarized, reflection. The square of the modulus of a reflection coefficient is called a reflectance.

3.2. Numerical results

Computed values of the four reflectances $R_{LL} = |r_{LL}|^2$, etc., as functions of λ_0 are plotted in fig. 2. The constitutive properties of the chiral STF used are specified in section 2.3.

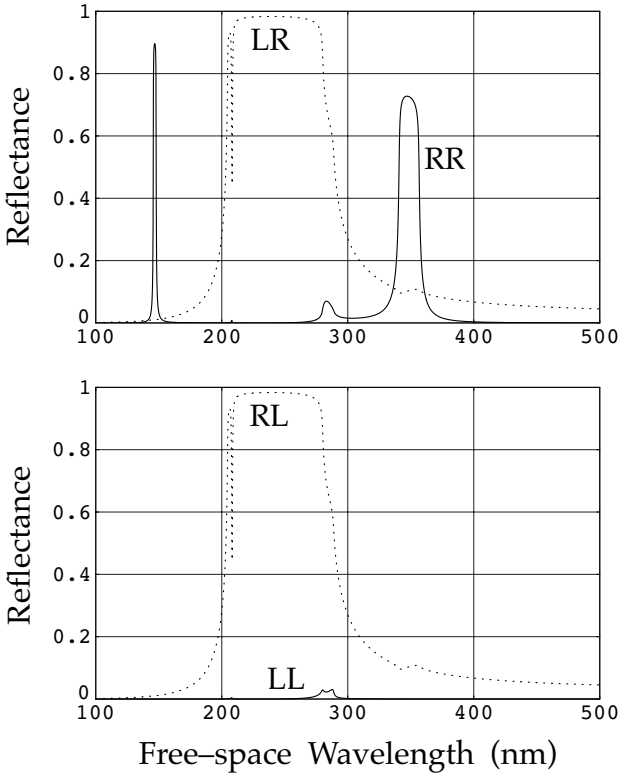

Fig. 2. Calculated reflectances $R_{RR} = |r_{RR}|^2$, etc., as functions of the free–space wavelength λ_0, when $p_a = 0.80$, $p_b = 1.04$, $p_c = 0.84$, $\chi = 20°$, $\lambda_0^{a,c} = 280$ nm, $\lambda_0^b = 290$ nm, and $M_{a,b,c} = 100$ in (13).

Five characteristics of the plots in fig. 2 are remarkable:

A. In the pre-resonant regime $\lambda_0 > 290$ nm, the circular Bragg phenomenon is evident in the neighborhood of 349 nm. In this Bragg regime, roughly of 20 nm bandwidth, the co-polarized reflectance R_{RR} is very high while the co-polarized reflectance R_{LL} is very low. Both cross-polarized reflectances R_{LR} and R_{RL} are very small. These characteristics are, of course, well-known [4] and have already been exploited technologically [19, 20].

B. In the post-resonant regime $\lambda_0 < 280$ nm, another circular Bragg phenomenon is evident in the neighborhood of 147 nm. It has the same characteristics as the one in the pre-resonant regime, except that it has a much narrower bandwidth. This is not surprising since $\tilde{\varepsilon}_c(\lambda_0)$ and $\tilde{\varepsilon}_d(\lambda_0)$ are likely to be much closer to each other in the post- than in the pre-resonant regimes, by virtue of the high-frequency behavior of the Lorentz model. The multiplicity of Bragg regimes exhibited by an axially excited HBM has thus been demonstrated for the first time, to our knowledge.

C. Extremely high cross-polarized and negligibly small co-polarized reflectances are evident for λ_0

lying roughly between 220 nm and 280 nm. This is because $\mathrm{Re}\,[\tilde{\varepsilon}_c(\lambda_0)] < 0$ and $\mathrm{Re}\,[\tilde{\varepsilon}_d(\lambda_0)] < 0$ in this regime. The chiral STF is insensitive to the handedness of the incident plane wave, because it reflects like a metal does at microwave frequencies. This corroborates a preliminary finding wherein dispersion had been neglected [21].

D. Two other features can be seen at wavelengths for which $\mathrm{Re}\,[\tilde{\varepsilon}_c(\lambda_0)]$ and $\mathrm{Re}\,[\tilde{\varepsilon}_d(\lambda_0)]$ are of opposite signs – in the neighborhoods of 220 nm and 285 nm. These are polarization-insensitive and do not appear to be technologically significant.

E. A general decline in reflectance at very low wavelengths is indicative of the fact that $\tilde{\varepsilon}_{a,b,c}(\lambda_0) \to 1$ as $\lambda_0 \to 0$, which is a feature of the Lorentz model [11].

4. Pulse response of a chiral STF half-space

Let $z_\ell > 0$, and a carrier wave modulated by a pulse be launched from the plane $z = 0$ at time $t = 0$ in the $+z$ direction. It excites the chiral STF half-space, and eventually transforms into a reflected pulse and a refracted pulse.

4.1. Initial-boundary value problem

The initial-boundary value problem for the pulse response of the chosen half-space is best formulated in terms of the column 5-vector [6]

$$[\boldsymbol{F}(z,t)] = [E_x(z,t),\, E_y(z,t),\, H_x(z,t),\, H_y(z,t)\, E_z(z,t)]^T\,, \tag{22}$$

which contains the five non–zero components of the electromagnetic field, the superscript ^{T} indicating the transpose. After substituting the constitutive relations (6) and (8) into the Maxwell curl postulates, $\nabla \times \boldsymbol{E}(\boldsymbol{r}, t) = -(\partial/\partial t)\, \boldsymbol{B}(\boldsymbol{r}, t)$ and $\nabla \times \boldsymbol{H}(\boldsymbol{r}, t) = (\partial/\partial t)\, \boldsymbol{D}(\boldsymbol{r}, t)$, the matrix differential equation

$$[\boldsymbol{J}] \cdot \frac{\partial}{\partial z}\,[\boldsymbol{F}(z,\,t)] = [\boldsymbol{Q}] \cdot \frac{\partial}{\partial t}\,[\boldsymbol{F}(z,\,t)] + \varepsilon_0\, \frac{\partial}{\partial t}\,\{([\boldsymbol{A}] * [\boldsymbol{F}])\,(z,\,t)\} \tag{23}$$

emerges. In (23), the constitutive properties are contained in the 5×5 matrix $[\boldsymbol{A}]\,(z,\,t)$ which is identically null-valued for $z < z_\ell$, while

$$[\boldsymbol{A}](z,\,t) = \begin{bmatrix} 0 & 0 & 0 & 0 & 0 \\ 0 & 0 & 0 & 0 & 0 \\ A_{31}(z,t) & A_{32}(z,t) & 0 & 0 & A_{35}(z,t) \\ -A_{41}(z,t) & -A_{31}(z,t) & 0 & 0 & -A_{45}(z,t) \\ A_{45}(z,t) & A_{35}(z,t) & 0 & 0 & A_{55}(z,t) \end{bmatrix}, \quad z > z_\ell\,, \tag{24}$$

with

$$A_{31}(z,t) = [\varepsilon_a(t)\sin^2\chi + \varepsilon_b(t)\cos^2\chi - \varepsilon_c(t)] \times \sin\frac{\pi(z-z_\ell)}{\Omega}\cos\frac{\pi(z-z_\ell)}{\Omega}\,, \tag{25}$$

$$A_{32}(z,t) = \left[\varepsilon_a(t)\sin^2\chi + \varepsilon_b(t)\cos^2\chi\right] \times \sin^2\frac{\pi(z-z_\ell)}{\Omega} + \varepsilon_c(t)\cos^2\frac{\pi(z-z_\ell)}{\Omega} - \delta(t)\,, \tag{26}$$

$$A_{35}(z,t) = [\varepsilon_b(t) - \varepsilon_a(t)]\,\sin\chi\,\cos\chi\,\sin\frac{\pi(z-z_\ell)}{\Omega}\,, \tag{27}$$

$$A_{41}(z,t) = \left[\varepsilon_a(t)\sin^2\chi + \varepsilon_b(t)\cos^2\chi\right] \times \cos^2\frac{\pi(z-z_\ell)}{\Omega} + \varepsilon_c(t)\sin^2\frac{\pi(z-z_\ell)}{\Omega} - \delta(t)\,, \tag{28}$$

$$A_{45}(z,t) = [\varepsilon_b(t) - \varepsilon_a(t)]\,\sin\chi\,\cos\chi\,\cos\frac{\pi(z-z_\ell)}{\Omega}\,, \tag{29}$$

$$A_{55}(z,t) = \varepsilon_a(t)\,\cos^2\chi + \varepsilon_b(t)\,\sin^2\chi - \delta(t)\,. \tag{30}$$

The two other 5×5 matrixes appearing in (23) are as follows:

$$[\boldsymbol{J}] = \mathrm{diag}[1,1,1,1,0]\,, \tag{31}$$

$$[\boldsymbol{Q}] = \begin{bmatrix} 0 & 0 & 0 & -\mu_0 & 0 \\ 0 & 0 & \mu_0 & 0 & 0 \\ 0 & \varepsilon_0 & 0 & 0 & 0 \\ -\varepsilon_0 & 0 & 0 & 0 & 0 \\ 0 & 0 & 0 & 0 & \varepsilon_0 \end{bmatrix}. \tag{32}$$

Eq. (23) requires initial as well as boundary conditions. As the electromagnetic field is absent everywhere at $t = 0$, we set the initial condition

$$[\boldsymbol{F}(z,0)] \equiv [0,\,0,\,0,\,0,\,0]^T\,. \tag{33}$$

The chosen boundary condition

$$[\boldsymbol{F}(0,t)] = g(t)\,[\boldsymbol{\varphi}(t)] \tag{34}$$

describes a carrier wave represented by the column vector $[\boldsymbol{\varphi}(t)]$ that is amplitude-modulated by the pulse function $g(t)$. For all numerical results reported here,

$$[\boldsymbol{\varphi}_\pm(t)] = \left[\cos\left(\frac{2\pi c_0}{\lambda_0^{\mathrm{car}}}\,t\right),\ \pm\sin\left(\frac{2\pi c_0}{\lambda_0^{\mathrm{car}}}\,t\right),\ \mp\eta_0^{-1}\sin\left(\frac{2\pi c_0}{\lambda_0^{\mathrm{car}}}t\right),\ \eta_0^{-1}\cos\left(\frac{2\pi c_0}{\lambda_0^{\mathrm{car}}}\,t\right),\ 0\right]^T \tag{35}$$

and

$$g(t) = \frac{c_0 t}{2\lambda_0^{\mathrm{car}}}\,\exp\left(\frac{-c_0 t}{\lambda_0^{\mathrm{car}}}\right), \tag{36}$$

were used. Whereas $[\boldsymbol{\varphi}_+(t)]$ represents a LCP plane wave, $[\boldsymbol{\varphi}_-(t)]$ represents a RCP plane wave, of free-space wavelength λ_0^{car}.

A central difference scheme converts the partial differential equation (23) into a set of recursive algebraic equations [6]. Our interest lying in the zone $\{z \geq 0,\, t \geq 0\}$, space and time are discretized as $z_j = j\,\Delta z, \quad (j = 0, 1, 2, 3, \ldots)$, and $t_n = n\,\Delta t$, $(n = 0, 1, 2, 3, \ldots)$; derivatives are replaced by central differences, and the leapfrog method is employed. Accordingly, (28) transforms to the matrix difference equation [6]

$$[\boldsymbol{F}]_j^{n+1} = [\boldsymbol{F}]_j^{n-1} + \beta c_0^{-1} [\boldsymbol{Q}]^{-1} \cdot [\boldsymbol{J}] \cdot \left([\boldsymbol{F}]_{j+1}^{n} - [\boldsymbol{F}]_{j-1}^{n} \right) - \varepsilon_0 [\boldsymbol{Q}]^{-1} \cdot \sum_{m=1}^{n-1} [\boldsymbol{A}]_j^m \cdot \left([\boldsymbol{F}]_j^{n-m+1} - [\boldsymbol{F}]_j^{n-m-1} \right) \Delta t - \varepsilon_0 [\boldsymbol{Q}]^{-1} \cdot [\boldsymbol{A}]_j^n \cdot \left([\boldsymbol{F}]_j^1 - [\boldsymbol{F}]_j^0 \right) \Delta t \,, \tag{37}$$

wherein the shorthand notations

$$[\boldsymbol{F}]_j^n = [\boldsymbol{F}(z_j,\, t_n)] \,, \qquad [\boldsymbol{A}]_j^n = [\boldsymbol{A}(z_j,\, t_n)] \tag{38}$$

have been used; and $\beta = c_0\,\Delta t / \Delta z < 1$ for stability [22]. The last two terms on the right side of (37) must be calculated only if $z_j > z_\ell$. The calculation of $[\boldsymbol{F}]_j^{n+1}$ on the left side of (37) was greatly accelerated by a computational scheme that exploited the structure of the single-resonance Lorentz model, as detailed elsewhere [7].

4.2. Numerical results

The duration of the chosen pulse function $g(t)$ is directly proportional to the carrier wavelength λ_0^{car}. As a reference, the pulse duration is ~ 3.1 fs when $\lambda_0^{\text{car}} = 200$ nm. The constitutive properties of the chiral STF used for time-domain calculations are specified in Section 2.3. We set $z_\ell = 7500$ nm, $\Delta z = 5$ nm and $\Delta t = 0.015$ fs. Calculations were performed using a Fortran 90 program implemented on an IBM RS 6000 AIX workstation over the domain $\{j \in [0, 3000], n \in [0, 3431]\}$. Computed values of $\boldsymbol{E}(z, t)$, $\boldsymbol{H}(z, t)$ and the axial component of the instantaneous Poynting vector

$$P_z(z, t) = \boldsymbol{u}_z \cdot [\boldsymbol{E}(z, t) \times \boldsymbol{H}(z, t)] \tag{39}$$

were stored and analyzed for many values of the carrier wavelength $\lambda_0^{\text{car}} \in [50, 600]$ nm.

As shown in section 3.2, our choice of the chiral STF parameters produces two distinct Bragg regimes – one for plane waves on the long-wavelength side of the material resonances (the pre-resonant regime), and the other on the short-wavelength side of those resonances (the post-resonant regime). If λ_0^{car} lies in either of the two regimes, the time-domain signature of the circular Bragg pheneomenon must be clearly evident in the reflected pulse. The same signature ought to be present if the pulse spectrum substantially overlaps a Bragg regime.

The pre-resonant Bragg regime has been thoroughly investigated [6, 7, 23]. Specifically, when an optical pulse modulating a RCP (but not a LCP) plane wave axially excites a structurally right-handed chiral STF, a protracted, reflective transfer of energy ensues. This polarization-selective pulse bleeding explains the circular Bragg phenomenon in the frequency domain, and will gather importance as chiral STFs are incorporated in femtosecond communication technology [19, 20, 24].

The post-resonant Bragg regime is likely to have a narrower bandwidth than its pre-resonant counterpart. This is because the permittivity of any material, at very high frequencies, tends towards that of free space [11], which would tend to decrease the degree of anisotropy and, in turn, the bandwidth of the Bragg regime. This is, of course, evident in figure 2.

In view of the focus of the predecessor reports [6, 7, 23] on the pre-resonant regime, we decide to confine the numerical results presented in the section to the post–resonant regime. Snapshots of $P_z(z, t)$ at $t = 12$ fs are shown in fig. 3 for $\lambda_0^{\text{car}} = 87$, 147, and 207 nm. As the electromagnetic field is confined to the vacuous half-space at that instant, $P_z(z, t)$ is independent of the handedness of the carrier plane wave.

At a later time, a reflected pulse and a refracted pulse emerge. Corresponding to those selected for fig. 3, snapshots of $P(z, t)$ at $t = 45$ fs are shown in figs. 4 and 5, for RCP and LCP carrier plane waves, respectively. Clearly, the reflected pulse appears to be much more distorted when the carrier wave is RCP than when it is LCP, which means that the interaction between the carrier wave and the chiral STF is more pronounced when the handedness of the former coincides with the structural handedness of the latter.

Most importantly, pulse bleeding is evident in fig. 4 but not in fig. 5, when $\lambda_0^{\text{car}} = 147$ nm. This is even

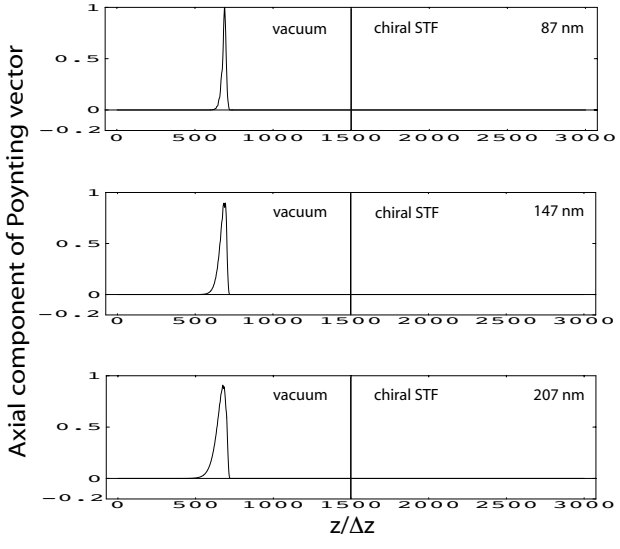

Fig. 3. Snapshots of the axial component $P_z(z, t)$ of the instantaneous Poynting vector at $t = 12$ fs. Only the incident pulse exists at this instant of time. Top: $\lambda_0^{\text{car}} = 87$ nm; middle: $\lambda_0^{\text{car}} = 147$ nm; bottom: $\lambda_0^{\text{car}} = 207$ nm. Data in all plots of figs. 3–6 are normalized to the peak value of the incident pulse when $\lambda_0^{\text{car}} = 87$ nm.

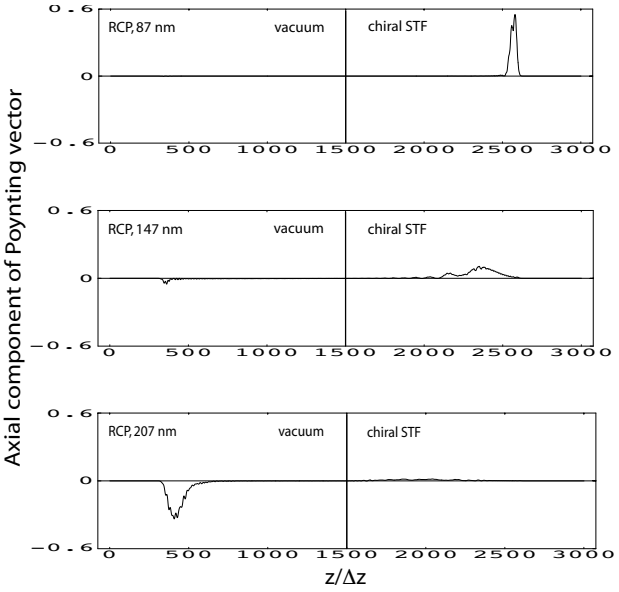

Fig. 4. Snapshots of the axial component $P_z(z, t)$ of the instantaneous Poynting vector at $t = 45$ fs, when the carrier plane wave is RCP. Top: $\lambda_0^{\text{car}} = 87$ nm; middle: $\lambda_0^{\text{car}} = 147$ nm; bottom: $\lambda_0^{\text{car}} = 207$ nm.

more clearly shown in the magnified plots of fig. 6, wherein a pipe of backward flowing electromagnetic energy across the interface $z = z_\ell$ has been identified. The refracted pulse energy must continue to diminish and the reflected pulse energy must continue to grow, therefore, until the refracted pulse has been substantially drained by reverse bleeding and forward attenuation – when the carrier handedness matches the structural handedness and the carrier wavelength lies

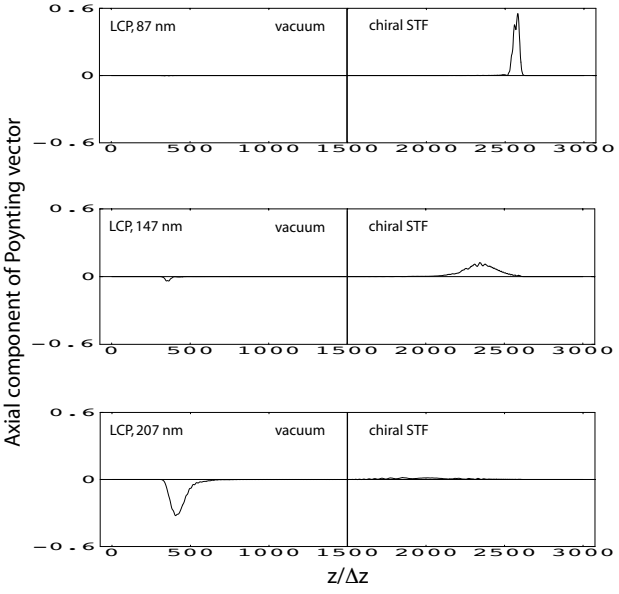

Fig. 5. Same as fig. 4, except that the carrier plane wave is LCP.

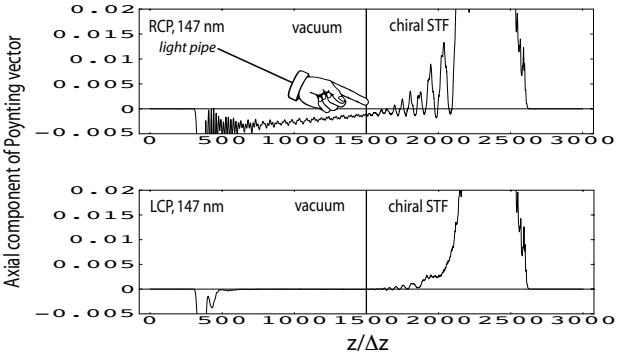

Fig. 6. Magnified snapshots of the axial component $P_z(z, t)$ of the instantaneous Poynting vector at $t = 45$ fs, when $\lambda_0^{\text{car}} = 147$ nm. Top: RCP carrier plane wave; bottom: LCP carrier plane wave.

in the post-resonant Bragg regime. This situation has already been encountered for the pre-resonant Bragg regime [6].

The incident pulse is of $\sim$2.3 fs duration when $\lambda_0^{\text{car}} = 147$ nm. Such short-duration pulses have been routinely produced now for about two decades [25, 26], and even attosecond pulses are nowadays possible [27]. They have very wide bandwidths. Conceivably, ultrawide-bandwidth pulses could cover more than one Bragg regimes. This is demonstrated in fig. 7, which was computed from the data collected for pulses launched on carrier waves with $\lambda_0^{\text{car}} = 147$ nm.

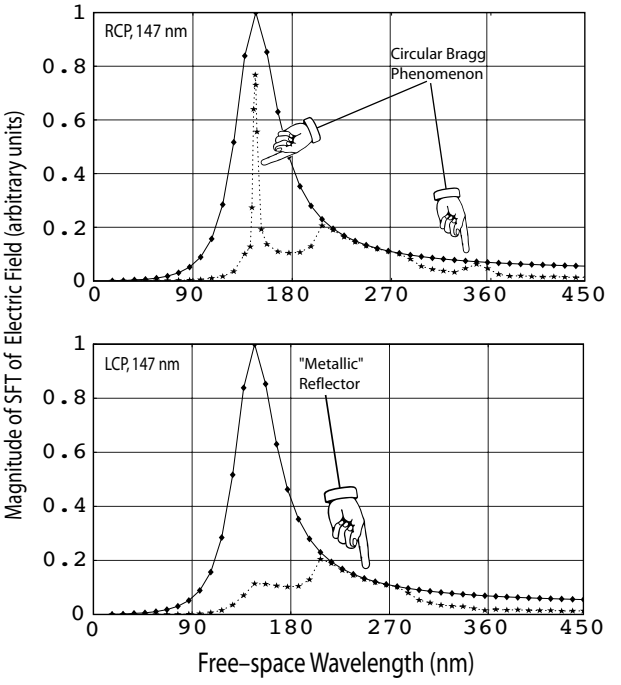

Fig. 7. Magnitude of $\mathcal{E}(\lambda_0, t)$ at $t = 22.5$ fs (solid lines) and $t = 45$ fs (dashed lines), when $\lambda_0^{\text{car}} = 147$ nm. Top: RCP carrier plane wave; bottom: LCP carrier plane wave.

The quantity plotted in fig. 7 is the magnitude of

$$\mathcal{E}(\lambda_0, t) = \int_0^{z_\ell} \boldsymbol{E}(z, t) \exp(-ik_0 z)\, \mathrm{d}z\,, \qquad (40)$$

which is a truncated *spatial* Fourier transform of $\boldsymbol{E}(z, t)$. The plots for $t = 22.5$ fs encompass the incident pulse (which is about to impinge on the interface $z = z_\ell$ at that instant), and those for $t = 45.0$ fs capture enough information about the reflected pulse to be meaningful.

Vacuum being non-dispersive, the spatial and the temporal Fourier transforms of any electromagnetic field therein are isomorphic and simply related [28]. Not surprisingly therefore, the plots in fig. 7 have the same information as in fig. 2. The post-resonant Bragg regime is clearly observable around 147 nm wavelength, and so is the pre-resonant Bragg regime around 349 nm wavelength, polarization-sensitivity being the distinguishing feature. The latter regime is not strongly manifested in fig. 7, only because the pulse energy is mostly confined to wavelengths around 147 nm.

Also, a polarization-insensitive, high-reflectance regime is present roughly between 220 nm and 280 nm in fig. 7; see item C of section 3.2. Finally, the declining reflectances at very short wavelengths – as identified in item E of section 3.2 – are also in evidence in fig. 7.

5. Concluding remarks

As real materials exhibit dispersive behavior due to the dictates of causality [8, 9], axially excited chiral sculptured thin films can be expected to display the circular Bragg phenomenon more than once in the electromagnetic spectrum. This expectation was borne out by our frequency-domain investigation on the planewave response of an axially excited chiral STF half-space, for whose dielectric properties we assumed the one-resonance Lorentz model [10, 11]. A long-wavelength (or pre-resonant) and a short-wavelength (or post-resonant) Bragg regimes emerged. In addition, our results showed that a chiral STF would act as a perfect reflector in a post-resonant wavelength-band.

These conclusions were confirmed by our time-domain investigation of the femtosecond-pulse response of the same half-space. The pulse-bleeding mechanism underlying the pre-resonant Bragg regime [6] was also shown to hold for the post-resonant Bragg regime. Furthermore, we concluded that the reflection of a femtosecond pulse carried by a plane wave in the post-resonant regime would be very likely affected by all Bragg regimes and perfectly reflecting regimes. As the understanding gleaned could be easily applied to transmission across chiral STF slabs, the potential of chiral STFs for the shaping of femtosecond pulses [29] is promising.

To conclude, all our results could also apply to cholesteric liquid crystals [12, 30], provided our assumptions regarding constitutive parameters hold.

Acknowledgement. Akhlesh Lakhtakia thanks Prof. Richard P. McNitt, Head, Department of Engineering Science and Mechanics, Pennsylvania State University, for his ongoing support of research on sculptured thin films.

References

[1] Lakhtakia A, Venugopal VC: On Bragg reflection by helicoidal bianisotropic mediums. Arch. Elektr. Über. **53** (1999) 287–290
[2] Nityananda R: On the theory of light propagation in cholesteric liquid crystals. Mol. Cryst. Liq. Cryst. **21** (1973) 315–331
[3] Parodi O: Light propagation along the helical axis in chiral smectics C. J. Phys. Colloq. C1 (Paris) **36** (1975) 325–326
[4] Venugopal VC, Lakhtakia A: Sculptured thin films: Conception, optical properties, and applications. In: Singh ON, Lakhtakia A (eds): Electromagnetic Fields in Unconventional Materials and Structures, Chap. 5. Wiley, New York 2000
[5] McCall MW: Axial electromagnetic wave propagation in inhomogeneous dielectrics. Math. Comput. Model. **34** (2001) 1483–1497
[6] Geddes III JB, Lakhtakia A: Reflection and transmission of optical narrow–extent pulses by axially excited chiral sculptured thin films. Eur. Phys. J. Appl. Phys. **13** (2001) 3–14; erratum: **16** (2001) 247
[7] Geddes III JB, Lakhtakia A: Time–domain simulation of the circular Bragg phenomenon exhibited by axially excited chiral sculptured thin films. Eur. Phys. J. Appl. Phys. **14** (2001) 97–105; erratum: **16** (2001) 247
[8] Scharf G: From Electrostatics to Optics, pp. 162–163. Springer, Berlin 1994
[9] Weiglhofer WS, Lakhtakia A: On causality requirements for material media. Arch. Elektr. Über. **50** (1996) 389–391
[10] Kittel C: Introduction to Solid State Physics, Chap. 13. Wiley Eastern, New Delhi 1974
[11] Bohren CF, Huffman DR: Absorption and Scattering of Light by Small Particles, Chap. 9. Wiley, New York 1983
[12] Geddes III JB, Meredith MW, Lakhtakia A: Circular Bragg phenomenon and pulse bleeding in cholesteric liquid crystals. Opt. Commun. **182** (2000) 45–57
[13] de Gennes PG, Prost J: The Physics of Liquid Crystals, Chap. 6. Clarendon Press, Oxford UK 1993
[14] Lakhtakia A: On percolation and circular Bragg phenomenon in metallic, helicoidally periodic, sculptured thin films. Microw. Opt. Technol. Lett. **24** (2001) 239–244 [Two typographical errors need correction: (i) $a_4 \equiv 0$ (but not $a_3 \equiv 0$) when $P_{4z}/|a_4|^2 < 0$; and $r_L - r_R$ should be replaced by $r_L + r_R$ in eq. (17).]
[15] Lakhtakia A, McCall MW: Simple expressions for Bragg reflection from axially excited chiral sculptured thin films. J. Mod. Opt. **49** (2002) at press
[16] Lakhtakia A: Local inclination angle: a key structural factor in emission from chiral sculptured thin films. Opt. Commun. **202** (2002) 103–111; erratum: **203** (2002) 447
[17] Lakhtakia A: Anomalous axial propagation in helicoidal bianisotropic media. Opt. Commun. **157** (1998) 193–201
[18] Lakhtakia A: Energy flows in axially excited, locally biaxial, dielectric, helicoidal bianisotropic media (HBMs), Opt. Commun. **161** (1999) 275–286
[19] Hodgkinson I, Wu Qh: Inorganic chiral optical materials. Adv. Mater. **13** (2001) 889–897
[20] Lakhtakia A: Sculptured thin films: accomplishments and emerging uses. Mater. Sci. Eng. C **19** (2002) 427–434

[21] Lakhtakia A, Moyer JT: Post- versus pre-resonance characteristics of axially excited chiral sculptured thin films. Optik **113** (2002) 97–99
[22] Gershenfeld N: The Nature of Mathematical Modeling, Chap. 7. Cambridge University Press, Cambridge, UK 1999
[23] Geddes III JB, Lakhtakia A: Videopulse bleeding in axially excited chiral sculptured thin films in the Bragg regime. Eur. Phys. J. Appl. Phys. **17** (2002) 21–24
[24] McCall MW, Lakhtakia A: Integrated optical polarization filtration *via* sculptured-thin-film technology. J. Mod. Opt. **48** (2001) 2179–2184
[25] Corkum P: Experimental attosecond science makes its debut. Physics World **13**(2) (2000) 23–24
[26] Nolte S, Kamlage G, Korte F, Bauer T, Wagner T, Ostendorf A, Fallnich C, Welling H: Microstructuring with femtosecond lasers. Adv. Eng. Mater. **2** (2000) 23–27
[27] Papadogiannis NA, Witzel B, Kalpouzos C, Charalambidis D: Observation of attosecond light localization in higher order harmonic generation. Phys. Rev. Lett. **83** (1999) 4289–4292 [See also the correspondence on this paper: (i) Tempea G, Scrinzi A, Krausz F, Brabec T: Phys. Rev. Lett. **87** (2001) 109401; (ii) Papadogiannis NA, Witzel B, Kalpouzos C, Charalambidis D: Phys. Rev. Lett. **87** (2001) 109402]
[28] Goodman JW: Introduction to Fourier Optics, Chap. 1. McGraw–Hill, New York 1968
[29] Schreier F, Bryngdal O: Femtosecond pulse shaping with a stratified diffractive structure. Opt. Commun. **185** (2000) 227–231
[30] Meredith MW, Lakhtakia A: Time-domain signature of an axially excited cholesteric liquid crystal. Part I: Narrow-extent pulses. Optik **111** (2000) 443–453

Available online at www.sciencedirect.com
SCIENCE DIRECT®
Optics Communications 225 (2003) 141–150
OPTICS COMMUNICATIONS
www.elsevier.com/locate/optcom

Effects of carrier phase on reflection of optical narrow-extent pulses from axially excited chiral sculptured thin films

Joseph B. Geddes III*, Akhlesh Lakhtakia

CATMAS – Computational and Theoretical Materials Sciences Group, Department of Engineering Science and Mechanics, The Pennsylvania State University, University Park, PA 16802-6812, USA

Received 12 June 2003; received in revised form 12 June 2003; accepted 7 August 2003

Abstract

Using a numerical time-domain method, we studied the reflection and refraction of optical narrow-extent pulses by linear and cubically nonlinear chiral sculptured thin films (STFs). The incident signal consisted of a carrier plane wave whose amplitude was modulated by a pulse envelope. The carrier phase and the nonlinearity of the chiral STF were found to have significant effects on both the shape and magnitude – as described by the instantaneous Poynting vector – of the reflected pulses, particularly with respect to the circular Bragg phenomenon exhibited by chiral STFs. The provided results point towards uses of the nanoengineered STFs in optical communication and sensing devices.

PACS: 77.55.+f; 78.20.Bh; 42.70−a

Keywords: Chirality; Circular Bragg phenomenon; Nonlinearity; Optical pulses; Phase; Sculptured thin films; Sensors

1. Introduction

When any number of materials are evaporated or sputtered in vacuum onto a relatively cool substrate that can rotate about the axes normal and tangential to its surface plane, sculptured thin films (STFs) are created [1–4]. These nanoengineered materials are characterized by a columnar microstructure that is twisted and bent at the nanoscale into many possible shapes, depending on the pattern of rotations. Rotation about an axis tangent to the substrate plane gives rise to sculptured nematic thin films (SNTFs). Column shapes possible for SNTFs include chevrons, C-shapes, and S-shapes. Rotation of the substrate about the axis normal to its surface gives rise to chiral STFs comprising nanohelixes [2]. Rotation about both axes simultaneously creates hybrid architectures, and multisection STFs can also be fabricated [5]. In the past several years, STF-based circular polarization filters, handedness inverters, and spectral hole filters have been fabricated and tested [6–8].

* Corresponding author. Tel.: +1-814-8638284; fax: +1-814-8659974.
E-mail address: jbg136@psu.edu (J.B. Geddes III).

0030-4018/$ - see front matter © 2003 Published by Elsevier B.V.
doi:10.1016/j.optcom.2003.08.002

In this paper, we concern ourselves with chiral STFs, the nanohelixes of which have constant pitch. Being periodically nonhomogeneous normal to the substrate plane, such STFs display the circular Bragg phenomenon [1,4]. When monochromatic, circularly polarized light whose wavelength lies in the so-called the Bragg regime encounters a chiral STF, it is:

- largely reflected if the circular polarization state of the incident light matches the structural handedness of the film, but
- largely refracted into the film if otherwise.

The circular Bragg phenomenon is a key characteristic of chiral STFs that makes many of their potential optical applications – such as laser mirrors and spectral hole filters – possible [1]. Its time-domain manifestation is a pulse-bleeding phenomenon described as follows.

Suppose that an optical signal, described as a carrier plane wave whose amplitude is modulated by a pulse envelope, is incident on a structurally right-handed chiral STF. If the carrier wave is left circularly polarized (LCP), the reflected pulse carries little energy as compared to the incident pulse. In contrast, if the carrier wave is right circularly polarized (RCP) and the signal bandwidth substantially overlaps the Bragg regime of the chiral STF, a much greater proportion of the incident energy is reflected. Moreover, when the carrier wave is RCP, the reflected pulse has a much longer duration than when the carrier wave is LCP – which phenomenon has been dubbed as pulse-bleeding. As a refracted pulse with RCP carrier wave propagates in the chiral STF, a portion of its energy in the Bragg regime is continually bled back out of the film to join the reflected pulse. The pulse-bleeding phenomenon is the time-domain manifestation of the circular Bragg phenomenon, and it was first investigated for cholesteric liquid crystals [9]. The investigation continued with time-domain studies of the circular Bragg phenomenon exhibited by chiral STFs, which yielded evidence suggesting that these nanoengineered materials could be useful in manipulating both narrow- and wide-extent pulses [10–14].

The technology to produce ultrashort light pulses of ever more fleeting duration has advanced since the advent of the laser to the present time, and femtosecond pulses are now routinely created. There are a multitude of uses for such pulses, including ultrafast interrogation of chemical reactions, lidar, communications, and materials processing [15,16]. Due to the relative ease with which their microstructure can be controlled during fabrication, STFs present a promising technology for manipulating these pulses. We expect chiral STFs to be especially useful in shaping and filtering ultrashort pulses.

In this paper, we study two heretofore unexplored parameters that impact the shapes of optical pulses reflected from chiral STFs – specifically, the effects of carrier phase and material nonlinearity. We calculated how pulses having different carrier wavelengths, phase, and circular polarization state are reflected from a chiral STF. The carrier wavelengths were chosen to be either in the Bragg regime or on either side of it. Moreover, since the power, and hence the electric field magnitude, of ultrashort pulses can be high [15,16], we expect nonlinear effects to be potentially significant when such pulses are incident on chiral STFs. Hence, we studied the reflection of pulses from both linear and cubically nonlinear chiral STF halfspaces.

The plan of this paper is as follows. In Section 2 of this paper, we set up the initial-boundary problem to be solved, including a mathematical description of the optical properties of chiral STFs and the incident pulses. We present our results in Section 3 and discuss their ramifications. In the mathematical development that follows, vectors are underlined once and dyadics twice.

2. Problem description

The spatial domain of the initial-boundary value problem is separated into two halfspaces. The halfspace $z < z_\ell$ ($z_\ell > 0$), is vacuous, while a chiral STF occupies the other halfspace $z > z_\ell$. An optical signal is launched at time $t = 0$ from the plane $z = 0$. It impinges normally upon the chiral STF halfspace, and portions of it are reflected and refracted.

2.1. Constitutive properties of chiral STFs

The constitutive relations of a linear dielectric STF are

$$\underline{D}(\underline{r},t) = \underline{\underline{\epsilon}}(\underline{r},t) * \underline{E}(\underline{r},t), \tag{1}$$

$$\underline{B}(\underline{r},t) = \mu_o \underline{H}(\underline{r},t), \tag{2}$$

where $*$ denotes convolution with respect to time. The permittivity dyadic operator of a chiral STF is defined as [10–14]

$$\underline{\underline{\epsilon}}(\underline{r},t) = \epsilon_o \underline{\underline{S}}_z(z-z_\ell) \cdot \underline{\underline{S}}_y(\chi) \cdot \underline{\underline{\epsilon}}^o_{\rm ref}(t) \cdot \underline{\underline{S}}_y^{-1}(\chi) \cdot \underline{\underline{S}}_z^{-1}(z-z_\ell), \tag{3}$$

where ϵ_o is the permittivity scalar of free space (i.e., vacuum), the tilt dyadic

$$\underline{\underline{S}}_y(\chi) = (\underline{u}_x\underline{u}_x + \underline{u}_z\underline{u}_z)\cos\chi + (\underline{u}_z\underline{u}_x - \underline{u}_x\underline{u}_z)\sin\chi + \underline{u}_y\underline{u}_y, \tag{4}$$

the rotation dyadic

$$\underline{\underline{S}}_z(z) = (\underline{u}_x\underline{u}_x + \underline{u}_y\underline{u}_y)\cos\left(\frac{\pi z}{\Omega}\right) + h(\underline{u}_y\underline{u}_x - \underline{u}_x\underline{u}_y)\sin\left(\frac{\pi z}{\Omega}\right) + \underline{u}_z\underline{u}_z, \tag{5}$$

where $\chi \in (0, \pi/2]$ is the so-called angle of rise, and 2Ω is the pitch (or the structural period). The vectors $\underline{u}_x$, $\underline{u}_y$, and $\underline{u}_z$ define a Cartesian coordinate system, with the z axis being the axis of periodic nonhomogeneity. The choice $h = +1$, used for the calculations reported here, holds for a structurally right-handed chiral STF; and the choice $h = -1$ indicates structural left-handedness. The local orthorhombic symmetry of chiral STFs [1] at macroscopic length scales mandates the representation

$$\underline{\underline{\epsilon}}^o_{\rm ref}(t) = \epsilon_a(t)\,\underline{u}_z\underline{u}_z + \epsilon_b(t)\,\underline{u}_x\underline{u}_x + \epsilon_c(t)\,\underline{u}_y\underline{u}_y. \tag{6}$$

We assumed single-resonance Lorentzian characteristics [17] with weak cubic nonlinearity for $\epsilon_{a,b,c}$, i.e.,

$$\epsilon_{a,b,c}(t) = \delta(t) + p_{a,b,c}\left[1 + p_{\rm nl}|\underline{E}(t)|^2\right]\omega_{a,b,c}\sin(\omega_{a,b,c}t) \times \exp\left(-\frac{\omega_{a,b,c}t}{2\pi N_{a,b,c}}\right)\mathscr{U}(t), \tag{7}$$

where $\delta(t)$ is the Dirac delta function; $\mathscr{U}(t)$ is the unit step function; $c_o = 1/\sqrt{\epsilon_o\mu_o}$ is the speed of light in free space; μ_o is the permeability of free space; $\omega_{a,b,c} = 2\pi c_o/\lambda_{a,b,c}$ are the angular frequencies of the material resonances; $\lambda_{a,b,c}(1 + N_{a,b,c}^{-2})^{-1/2}$ are the resonance wavelengths; $p_{a,b,c}$ are the oscillator strengths; and $p_{\rm nl}$ is the cubic nonlinearity parameter.

When $p_{\rm nl} \neq 0$, convolutions of the form $\epsilon_{a,b,c}(t) * \underline{E}(\underline{r},t)$ are to be interpreted as follows:

$$\epsilon_{a,b,c}(t) * \underline{E}(\underline{r},t) = \underline{E}(\underline{r},t) + p_{a,b,c}\omega_{a,b,c} \times \int_0^t \sin(\omega_{a,b,c}\tau)\exp\left(-\frac{\omega_{a,b,c}\tau}{2\pi N_{a,b,c}}\right) \times (1 + p_{\rm nl}|\underline{E}(\underline{r},t-\tau)|^2) \times \underline{E}(\underline{r},t-\tau)\,{\rm d}\tau.$$

2.2. Incident narrow-extent optical pulses

All fields in this problem are independent of y and z. The electric field $\underline{E}(z,t)$ and the magnetic field $\underline{H}(z,t)$ are adequately captured in free space by the 4-vector $\underline{F}(z,t) = \left[E_x, E_y, H_x, H_y\right]^{\rm T}$, wherein the superscript T indicates the transpose. The incident signal is described by a pulse envelope function that modulates the amplitude of either a LCP or a RCP carrier plane wave.

We employed the function

$$g(t) = A\left(\frac{t}{\tau_{\rm p}}\right)\exp\left(-\frac{2t}{\tau_{\rm p}}\right). \tag{8}$$

for the pulse envelope. The quantity $\tau_{\rm p}$ suffices to set the pulse duration, and the variable A determines the strength of the launched signal. The carrier wave is denoted by the 4-vector

$$\underline{\varphi}_{\pm}(t) = [\cos(\omega_{\rm car}t. + \phi), \pm\sin(\omega_{\rm car}t + \phi), \mp\eta_0^{-1}\sin(\omega_{\rm car}t + \phi), \eta_0^{-1}\cos(\omega_{\rm car}t + \phi)]^{\rm T}, \tag{9}$$

wherein $\omega_{\rm car} = 2\pi c_o/\lambda_{\rm car}$; $\lambda_{\rm car}$ is the carrier wavelength; ϕ denotes the carrier phase; while $\eta_0 = \sqrt{\mu_o/\epsilon_o}$ is the intrinsic impedance of free space. The upper/lower sign in (9) denotes LCP/RCP for propagation in the $+z$ direction, but RCP/LCP for propagation in the $-z$ direction. Thus, the field 4-vector in the launch plane $z = 0$ is given by

$$\underline{F}(0,t) = g(t)\,\underline{\varphi}_{\pm}(t), \quad t \geqslant 0. \tag{10}$$

2.3. Calculation parameters

We solved the time-domain Maxwell equations for the initial-boundary problem with a finite difference technique, the basics of which are described elsewhere [10–14]. For the presented results, we set $z_\ell = 20$ μm and $\tau_p = 3.44$ fs. The constitutive parameters of the chiral STF halfspace were chosen as follows: $p_a = 0.40$, $p_b = 0.52$, $p_c = 0.42$; $\lambda_a = \lambda_c = 280$ nm, $\lambda_b = 290$ nm; $N_{a,b,c} = 100$; $\chi = 20°$ and $\Omega = 200$ nm. Whereas $p_{nl} = 0$ for linear STFs, we set $p_{nl} = 10^{-11}$ m^2 V^{-2} for the chosen nonlinear STFs. The choice $A = 10^6$ V m^{-1} sufficed to allow significant nonlinear effects to be observed when p_{nl} took the nonzero value. The carrier phase ϕ was chosen equal to either 0 or $\pi/2$ for maximum contrast in elucidating the effects of this signal-launch parameter. The center wavelength of the Bragg regime for the linear case is 516 nm, and the Bragg regime has a bandwidth of approximately 27 nm [18].

3. Results and discussion

The z-component of the instantaneous Poynting vector

$$P_z(z,t) = \underline{u}_z \cdot [\underline{E}(z,t) \times \underline{H}(z,t)] \tag{11}$$

is plotted in Fig. 1 at time $t = 30.1$ fs. At that instant of time, the launched signal is still some distance from the interface $z = z_\ell$; and so Fig. 1 shows just the incident pulse. The pulse shape is independent of the incident carrier's wavelength, phase, and polarization state. However, the reflected pulse shape is dependent on those parameters, as well as on the nonlinearity of the chiral STF. Such effects are evident in Figs. 2–5, which depict the reflected pulses at $t = 132$ fs. Figs. 2 and 3 display the reflected pulses from linear and nonlinear chiral STFs, respectively, when the incident carrier wave is LCP. Figs. 4 and 5 present the results of the analogous situation when the incident carrier wave is RCP. The refracted pulses for the situations corresponding to Figs. 2–5 are presented in Figs. 6–9.

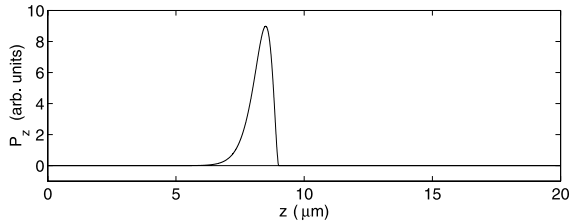

Fig. 1. Plot of the Poynting vector $P_z(z,t)$ for the incident pulse at $t = 30.1$ fs.

The effects of pulse bleeding in linear STFs become evident by comparing the reflected pulses in Fig. 2 with those in Fig. 4. Relatively little energy is reflected and the reflected pulse duration is short, when the incident carrier wave is LCP as opposed to RCP. In the latter case, the reflected pulses have long tails as a result of pulse-bleeding, irrespective of their carrier phase or wavelength. Even the signals with carrier wavelengths outside the Bragg regime ($\lambda_{car} = 430$ or 600 nm) undergo pulse-bleeding – because the short duration of an incident signal endows it with a large bandwidth, a portion of which overlaps the Bragg regime. Hence, all the pulses in Figs. 4 and 5 have long tails; but the tails with the greatest energy belong to the signals with carrier wavelengths in the center of the Bragg regime (i.e., $\lambda_{car} = 516$ nm; note that the Bragg wavelength may shift slightly from that value when $p_{nl} \neq 0$). That the foregoing effects are also observed on comparison of Figs. 3 and 5 indicates that the circular Bragg phenomenon also occurs in the nonlinear chiral STFs also, at least for the chosen type of nonlinearity.

The smaller the carrier wavelength, the greater the energy content of the leading edges of the reflected pulses – irrespective of other factors. We surmise that this effect is due to the closer proximity of shorter carrier wavelengths to the absorption resonances at 280 and 290 nm. The impedance mismatch between vacuum and the chiral STF increases as the carrier wavelength approaches the material resonance regimes. The impedance mismatch does not depend on the handedness of the carrier wave with respect to the structural handedness of the film. The greatest effects of the impedance mismatch are seen at the leading edges of the reflected pulses, but not at later times – since the energy content and length of their tails are governed mostly by the circular Bragg phenomenon, which takes some time to develop inside the chiral STF [11].

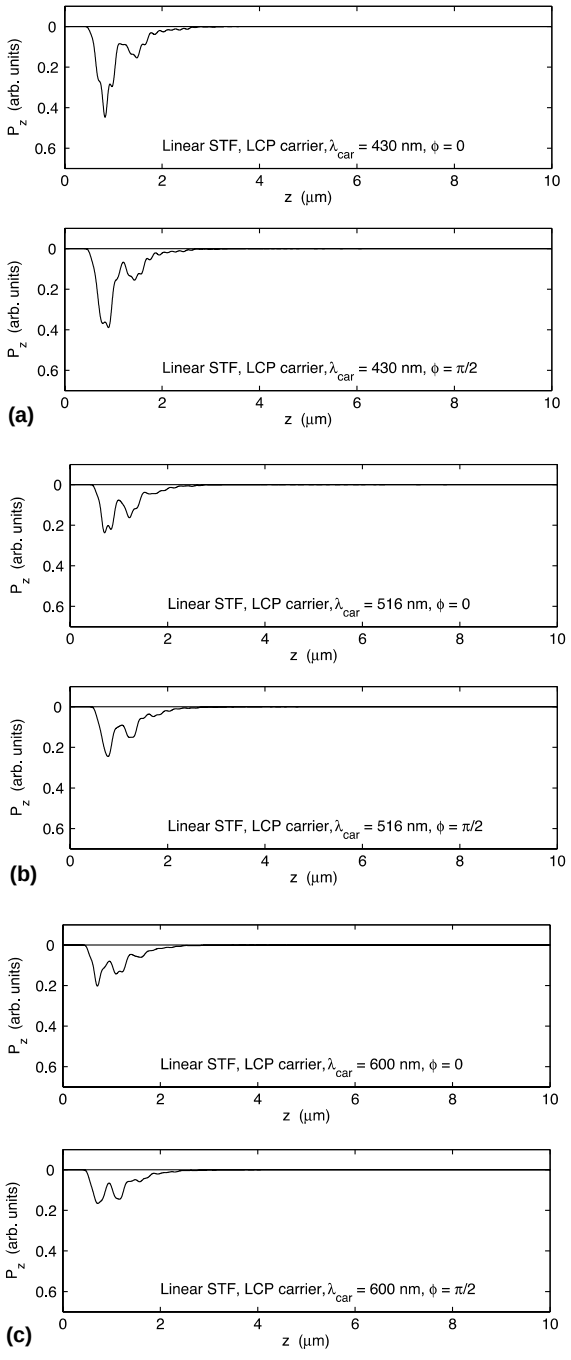

Fig. 2. Plots of the Poynting vector component $P_z(z,t)$, at $t = 132$ fs, of the pulses reflected by a linear chiral STF. The carrier phase is either $\phi = 0$ or $\phi = \pi/2$; and the carrier wavelength is $\lambda_{\text{car}} = 430$ nm (a), $\lambda_{\text{car}} = 516$ nm (b), or $\lambda_{\text{car}} = 600$ nm (c). The carrier plane wave is LCP. The vacuum/STF boundary at $z_\ell = 20$ μm is not shown. See the text for the values of other parameters.

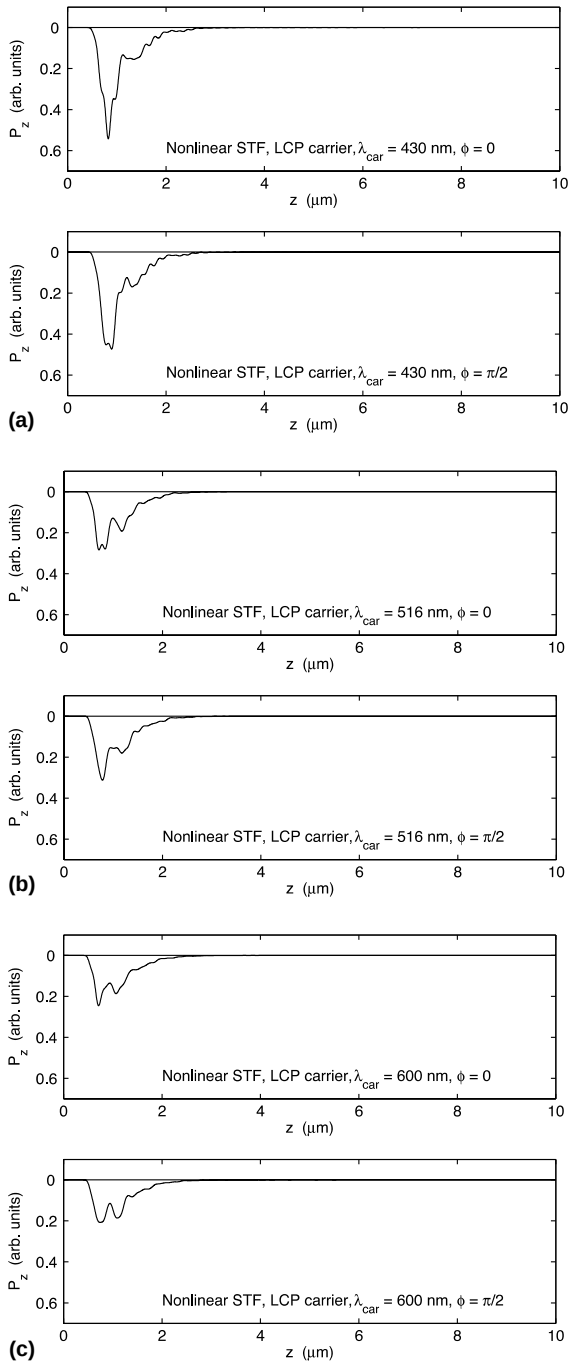

Fig. 3. Same as Fig. 2, except that the chiral STF is nonlinear.

The effects of nonlinearity are apparent on comparing Fig. 2 with Fig. 3, and Fig. 4 with Fig. 5. Pulses reflected from nonlinear STFs tend

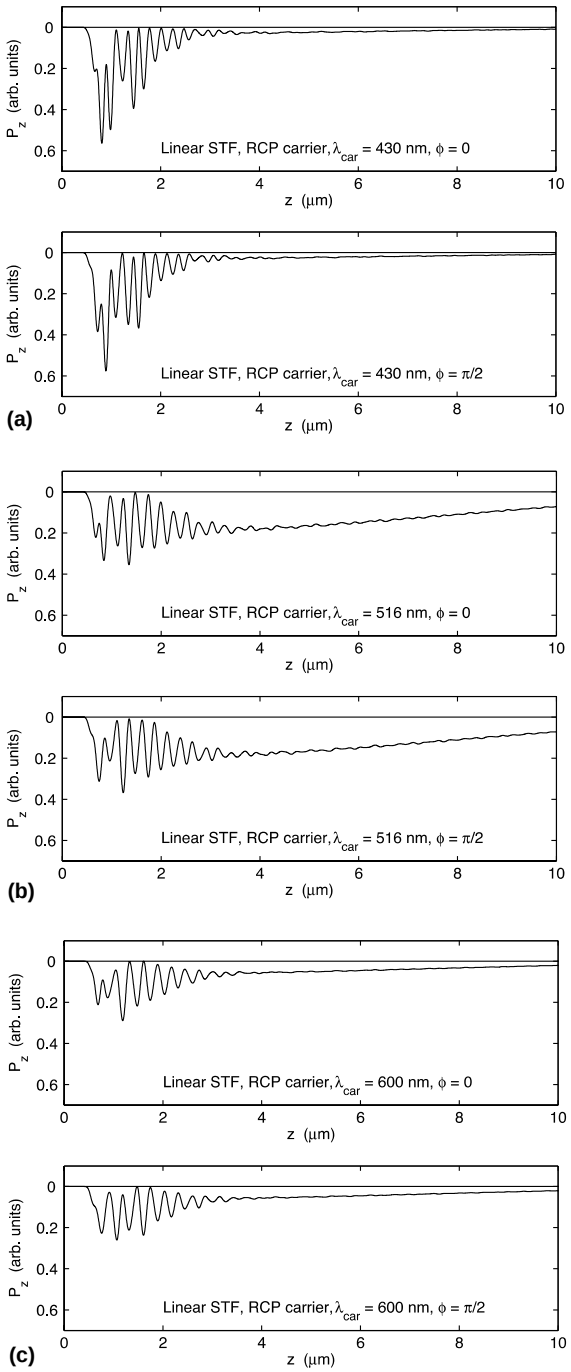

Fig. 4. Same as Fig. 2, except that the carrier plane wave is RCP.

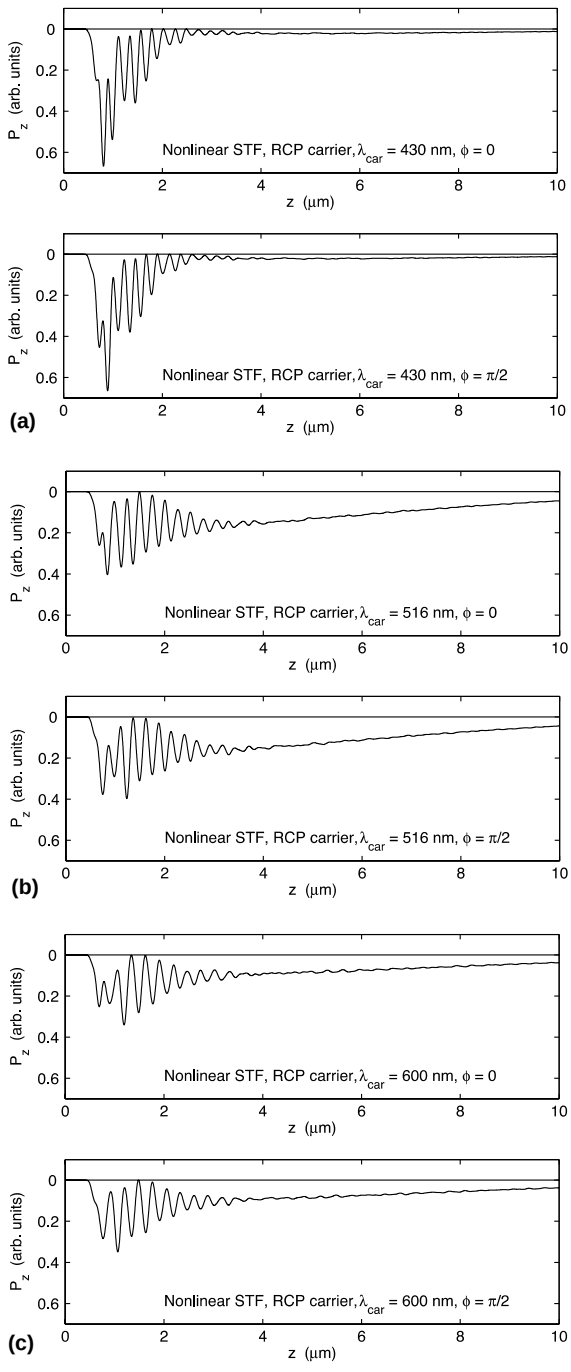

Fig. 5. Same as Fig. 4, except that the chiral STF is nonlinear.

to carry more energy at their leading edges than pulses reflected from linear STFs. This conclusion holds regardless of the carrier phase, wavelength, or polarization state. Once again, this follows from

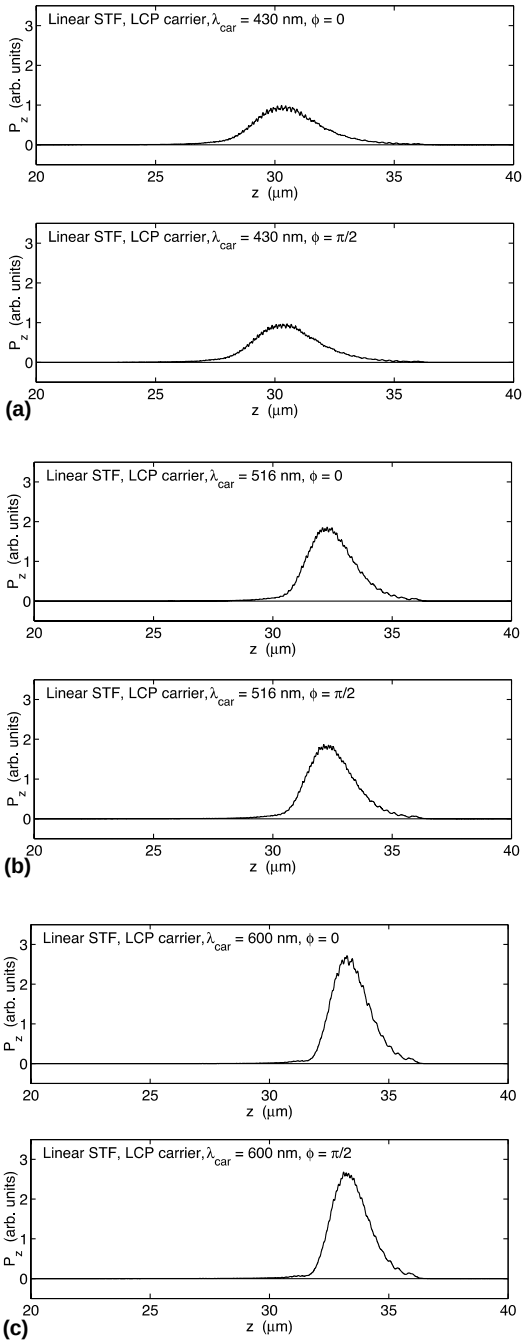

Fig. 6. Plots of the Poynting vector component $P_z(z,t)$, at $t = 132$ fs, of the pulses refracted into a linear chiral STF. The carrier phase is either $\phi = 0$ or $\phi = \pi/2$; and the carrier wavelength is $\lambda_{\text{car}} = 430$ nm (a), $\lambda_{\text{car}} = 516$ nm (b), or $\lambda_{\text{car}} = 600$ nm (c). The carrier plane wave is LCP. The vacuum/STF boundary at $z_\ell = 20$ μm is not shown. See the text for the values of other parameters.

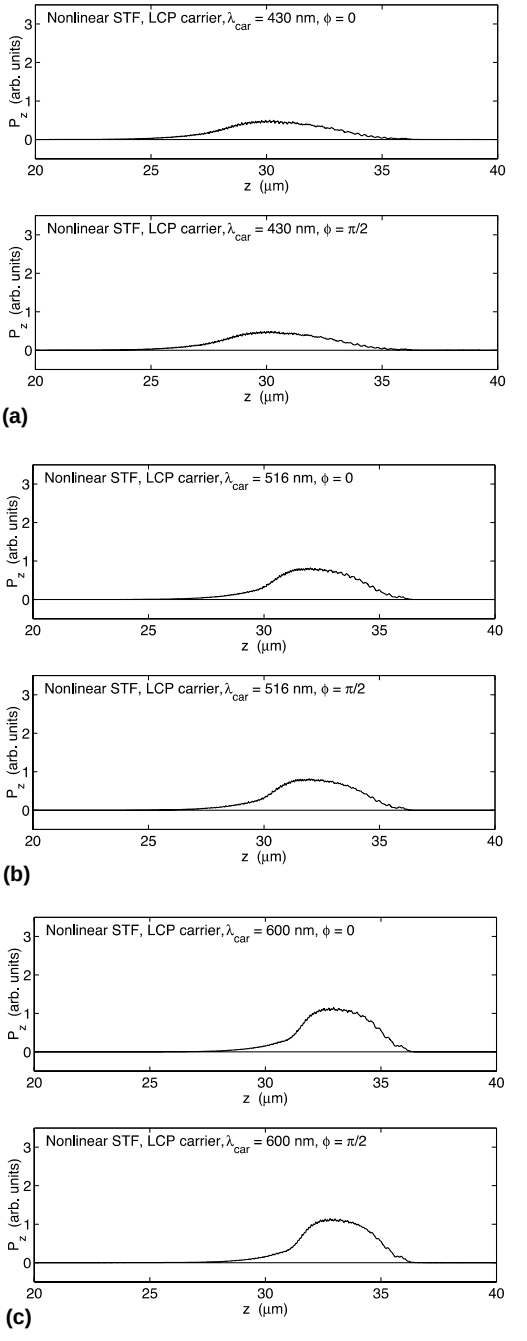

Fig. 7. Same as Fig. 6, except that the chiral STF is nonlinear.

the greater impedance mismatch at the interface $z = z_\ell$ when the chiral STF is nonlinear, because of the multiplicative nature of nonlinearity in (7).

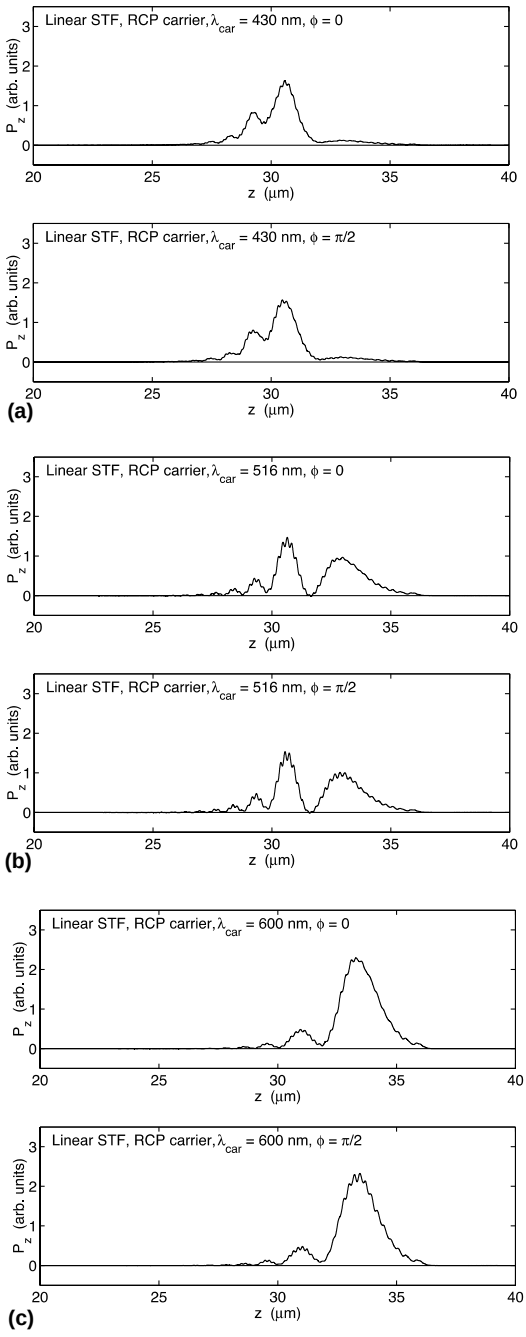

Fig. 8. Same as Fig. 6, except that the carrier plane wave is RCP.

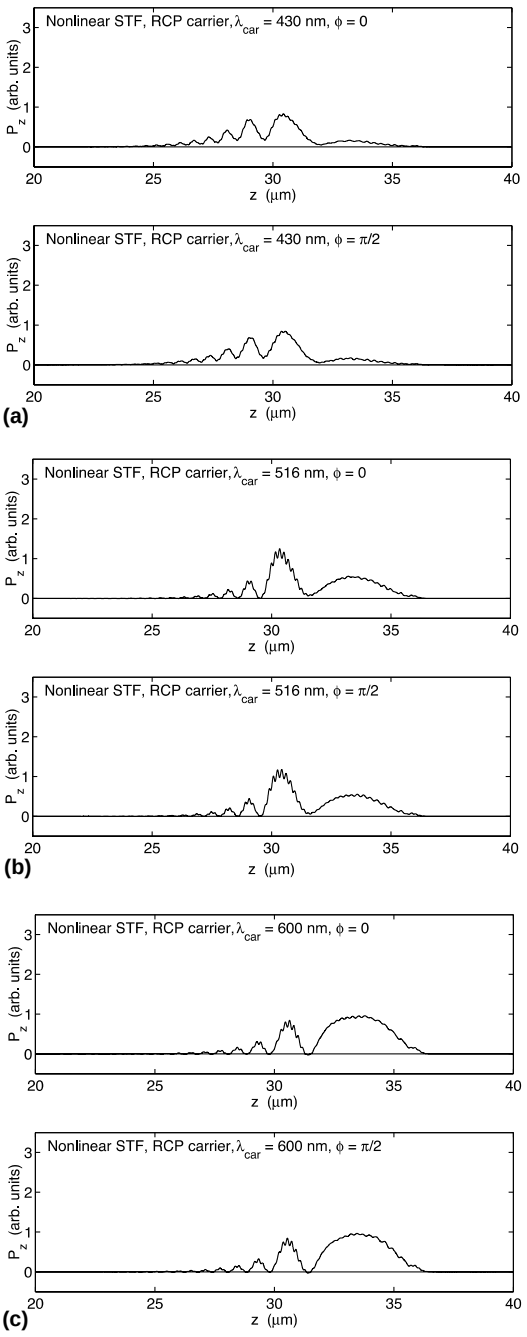

Fig. 9. Same as Fig. 8, except that the chiral STF is nonlinear.

The reflected signal from a chiral STF is a superposition of LCP and RCP components. Specifically, the reflected field $\underline{F}_{\mathrm{r}}(t)$ observed at a point in the vacuous halfspace long after the incident signal has passed must be of the form:

$$\underline{F}_{\mathrm{r}}(t) = g_{\mathrm{LCP}}(t)\underline{\varphi}_{-}(t) + g_{\mathrm{RCP}}(t)\underline{\varphi}_{+}(t). \tag{12}$$

The functions $g_{\mathrm{LCP}}(t)$ and $g_{\mathrm{RCP}}(t)$ describe the envelopes for the LCP and RCP components of the reflected signal, respectively. The Poynting vector $P_{\mathrm{r}}(t)$ of the reflected signal is

$$P_{\mathrm{r}}(t) = \frac{1}{\eta_0}\left[g_{\mathrm{LCP}}^2(t) + g_{\mathrm{RCP}}^2(t) + 2g_{\mathrm{LCP}}(t)g_{\mathrm{RCP}}(t)\cos(2\omega_{\mathrm{car}}t + 2\phi)\right]. \quad (13)$$

Hence, we expect to observe the effects of carrier phase when LCP and RCP components of the reflected signal interfere with each other. We do observe the effects of ϕ in the leading portions of the reflected pulses – the regions within about $2c_o\tau_{\mathrm{p}} = 2.06$ μm of their leading edges – in Figs. 2–5. When the incident carrier wave is RCP, distinctive oscillations occur, and the minimums and maximums (peaks and valleys) of the reflected pulse shift with respect to one another as the carrier phase changes. Specifically, the oscillations occur at a frequency of about $2c_o/\lambda_{\mathrm{car}}$; and a minimum when $\phi = 0$ corresponds to a maximum when $\phi = \pi/2$, as predicted by (13). The shapes in the reflected pulse tails are not much affected by changes in ϕ because they consist mostly of RCP light with wavelengths in the Bragg regime. Hence, the product $2g_{\mathrm{LCP}}(t)g_{\mathrm{RCP}}(t)$ in (13) is small. The third term on the right side of (13) – the only one that depends on the carrier phase – is then insignificant compared with the first two, and consequently the tails of those reflected pulses are largely unaffected by ϕ.

The effects of carrier phase are not very significant in the refracted pulses shown in Figs. 6–9. At the time of the snapshots, most of the energy at wavelengths in the Bragg regime in those pulses has been either absorbed by the chiral STF or bled back to the reflected pulse. We note that absorption is higher in the nonlinear STFs, a result of the enhancement of the oscillator strength $p_{a,b,c}$ by the nonlinearity parameter p_{nl} in (7).

4. Concluding remarks

Clearly, the effects of carrier phase shall have repercussions on the design of STF devices meant for shaping pulses. Indeed, measurement of the reflected pulse power as a function of time yields information about the carrier phase of the incident pulse, especially when the shape of the incident pulse is known initially. The carrier phase can carry information in a pulse independently of its duration, carrier polarization, spectral content, and proximity in time to other pulses (used, for example, in pulse position modulation [21]). Reflection and transmission of pulses through chiral STFs can independently tease out the bits encoded by several of these methods – including carrier phase – simultaneously. Hence, we expect chiral STFs to find some uses in optical communication systems.

Moreover, due to their porosity, the properties of STFs change when fluids are allowed to enter their interstices [19,20], thereby changing their linear and nonlinear optical properties. Hence, by monitoring the reflected pulse shape, spectral content, and duration one can deduce changes in the STF optical properties due to fluid infiltration. From that information one may infer the types and concentrations of fluids present in the film. We expect that interrogation of chiral STF sensors with optical pulses of varying carrier phase will provide even more information about the analyte than is possible simply by sticking to more traditional methods.

Finally, because of the mathematical isomorphism between the dielectric properties of chiral liquid crystals [22,23] and chiral STFs, we expect the results of our calculations to hold for the former types of materials.

Acknowledgements

This work was funded, in part, by the Pittsburgh Supercomputing Center. J.B. Geddes III gratefully acknowledges the support of an NSF Graduate Fellowship.

References

[1] V.C. Venugopal, A. Lakhtakia, in: O.N. Singh, A. Lakhtakia (Eds.), Electromagnetic Fields in Unconventional Materials and Structures, Wiley, New York, USA, 2000.

[2] K. Robbie, M.J. Brett, A. Lakhtakia, Nature 384 (1996) 616.
[3] R. Messier, V.C. Venugopal, P.D. Sunal, J. Vac. Sci. Technol. A 18 (2000) 1538.
[4] I.J. Hodgkinson, Q.H. Wu, Adv. Mater. 13 (2001) 889.
[5] M. Suzuki, Y. Taga, Jpn. J. Appl. Phys. Part 2 40 (2001) L358.
[6] Q.H. Wu, I.J. Hodgkinson, A. Lakhtakia, Opt. Eng. 39 (2000) 1863.
[7] I.J. Hodgkinson, A. Lakhtakia, Q.H. Wu, Opt. Eng. 39 (2000) 2831.
[8] I.J. Hodgkinson, Q.H. Wu, A. Lakhtakia, M.W. McCall, Opt. Commun. 177 (2000) 79.
[9] J.B. Geddes III, M.W. Meredith, A. Lakhtakia, Opt. Commun. 182 (2000) 45.
[10] J.B. Geddes III, A. Lakhtakia, Eur. Phys. J. Appl. Phys. 13 (2001) 3;
Erratum 16 (2001) 247.
[11] J.B. Geddes III, A. Lakhtakia, Eur. Phys. J. Appl. Phys. 14 (2001) 97;
Erratum 16 (2001) 247.
[12] J.B. Geddes III, A. Lakhtakia, Microwave Opt. Technol. Lett. 28 (2001) 59.
[13] J.B. Geddes III, A. Lakhtakia, Eur. Phys. J. Appl. Phys. 17 (2002) 21.
[14] J. Wang, A. Lakhtakia, J.B. Geddes III, Optik 113 (2002) 213.
[15] N. Bloembergen, Rev. Mod. Phys. 71 (1999) S283.
[16] T.R. Gosnell, A.J. Taylor (Eds.), Selected Papers on Ultrafast Laser Technology, SPIE Press, Bellingham, WA, USA, 1991.
[17] C. Kittel, Introduction to Solid State Physics, Wiley Eastern, New Delhi, India, 1974.
[18] A. Lakhtakia, Eur. Phys. J. Appl. Phys. 8 (1999) 129.
[19] I.J. Hodgkinson, Q.H. Wu, K.M. McGrath, Proc. SPIE 3790 (1999) 184.
[20] A. Lakhtakia, M.W. McCall, J.A. Sherwin, I.J. Hodgkinson, Q.H. Wu, Opt. Commun. 194 (2001) 33.
[21] B.P. Lathi, Modern Digital and Analog Communication Systems, Oxford University Press, New York, USA, 1998.
[22] P.G. de Gennes, J. Prost, The Physics of Liquid Crystals, Clarendon Press, Oxford, UK, 1993.
[23] S. Chandrasekhar, Liquid Crystals, Cambridge University Press, Cambridge, UK, 1992.

Available online at www.sciencedirect.com
SCIENCE DIRECT®
Optics Communications 252 (2005) 307–320
OPTICS COMMUNICATIONS
www.elsevier.com/locate/optcom

Numerical investigation of reflection, refraction, and diffraction of pulsed optical beams by chiral sculptured thin films

Joseph B. Geddes III *, Akhlesh Lakhtakia

Computational and Theoretical Materials Science Group, Department of Engineering Science and Mechanics, The Pennsylvania State University, University Park, PA 16802–6812, USA

Received 11 March 2005; accepted 1 April 2005

Abstract

We study the scattering of pulsed optical beams from chiral sculptured thin films (STFs). The spatiotemporal anatomy of the circular Bragg phenomenon (CBP) exhibited by chiral STFs is examined in two spatial dimensions, and we comment on its implications for pulsed beam shaping by STF-based devices. We highlight several differences between the time-domain manifestation of the CBP for pulsed plane waves and pulsed beams; and we present the reflection, refraction, and diffraction of a pulsed beam when it impinges upon the corner of a chiral STF.

Keywords: Beam shaping; Circular Bragg phenomenon; Optical pulse; Pulsed beam; Pulse shaping; Sculptured thin film; Structural chirality

1. Introduction

The practice of intentionally and precisely controlling the nanoscale morphology of solid thin films most probably began in 1959 [1]. In that year, Young and Kowal reported their measured values of optical rotation by fluorite films that had been evaporated onto a rotating substrate. They created, perhaps, the first thin films with helical morphology sculptured at the nanoscale. Although an unambiguous determination of the nanostructure of the resulting films was not made, the researchers measured the optical activity and found it in qualitative accord with predictions. Several decades later, with the discovery and direct imaging of the morphology of structurally chiral thin films [2], and the coalescence of a theoretical framework to guide their fabrication and application [3–5],

* Corresponding author. Tel.: +1 814 278 1235.
E-mail addresses: jbgeddes3@psu.edu (J.B. Geddes III), akhlesh@psu.edu (A. Lakhtakia).

0030-4018/$ - see front matter © 2005 Elsevier B.V. All rights reserved.
doi:10.1016/j.optcom.2005.04.001

intensive studies of sculptured thin films (STFs) began.

STFs are nanoengineered materials [6]. Even though the benefits of nanotechnology – better device performance, possibilities for novel material properties, and prospects for reduction of the uses of toxic materials – must ultimately be balanced against concerns about its (potential) effects on human and environmental health [7], and abuse [8], such technology is here to stay; and so we continue our investigations into the electromagnetic properties of STFs.

Every STF is an assemblage of parallel, bent nanowires affixed to a substrate. The nanowires comprise clusters that are $\approx$1–3 nm in size [6]. The equipment required to deposit STFs is simple, consisting of a vacuum chamber, a crucible containing the material to be deposited, and a substrate mounted to a stepper motor. The material is either evaporated or sputtered onto the rotating and/or translating substrate [5,6,9–12]. In this report, we focus on chiral STFs which consist of parallel helical nanowires of constant pitch whose axis of spirality lies normal to the substrate plane. Fig. 1 shows the scanning electron micrograph of a chiral STF.

Due to their unidirectionally periodic nonhomogeneity and helical morphology, chiral STFs exhibit the circular Bragg phenomenon (CBP) [6]. The effect, in essence, is a circular-polarization-sensitive photonic band gap. Circularly polarized light in a certain wavelength band, called the Bragg regime, is largely reflected if its handedness matches the structural handedness of the chiral STF; but is reflected little, if otherwise. This phenomenon is exploitable for many purposes.

The course of theoretical research on chiral STFs began with studies of planewave reflection and transmission, first at normal incidence (i.e., parallel to the axis of spirality) whereby chiral STFs can be excited axially. From those investigations, devices such as circular polarization filters, polarization-handedness inverters, and spectral hole filters were proposed; they were subsequently fabricated and tested [13–15]. The CBP plays a central role in the operation of these devices. Frequency-domain investigations of oblique incidence were then undertaken [16], and also studies of guided wave propagation within STFs, or space-guiding [17]. Frequency-domain analysis of nonlinear chiral STFs, specifically on second harmonic generation and STF lasers, yielded several device proposals as well [18–21].

A focus on communication systems led to the development of time-domain analysis of electromagnetic fields in chiral STFs. Time-domain analysis offers the advantage of allowing for the complete spatiotemporal evolution of a pulse to be examined, though at the cost of introducing computationally expensive convolutions into the material constitutive relations [22]. The time-domain analysis of chiral STFs is following a similar development as frequency-domain analysis, and has already yielded results beyond that

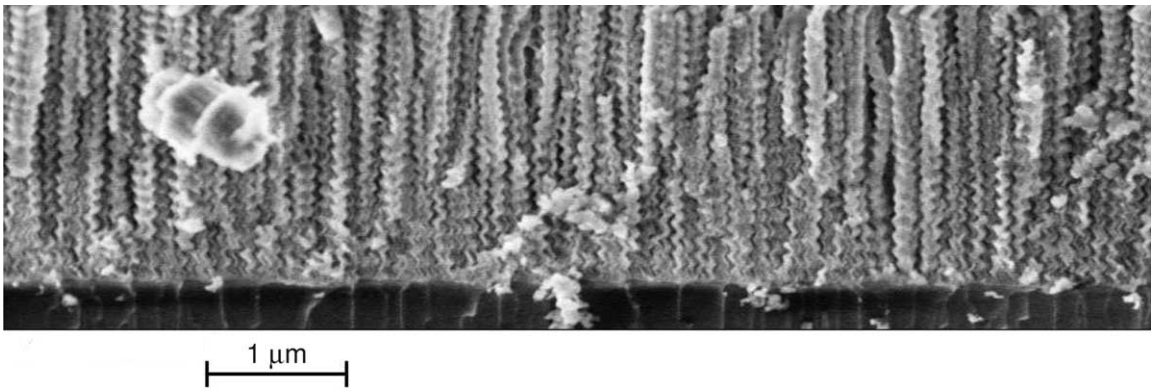

Fig. 1. Scanning electron micrograph of a chiral STF of silicon oxide (Courtesy: M.W. Horn, Pennsylvania State University).

attainable easily with the latter. In particular, examination of the axial excitation of chiral STFs by pulses modulating the amplitudes of normally incident, circularly polarized, carrier plane waves elucidated the time-domain signature of the CBP, dubbed as pulse bleeding [23,24]. In the time domain, energy is *continually* bled back from the refracted pulse to the reflected pulse, if the handedness of the carrier plane wave matches the structural handedness of the chiral STF; but not, if otherwise. Of course, the spectrum of the incident pulse must substantively overlap the Bragg regime for pulse bleeding to occur [25]. Therefore, chiral STFs are capable of selectively manipulating the shapes, amplitudes, and durations of optical pulses – depending on the pulse amplitude, as well as the phase and the circular polarization state of the carrier plane wave [23,24,26].

Analysis of pulsed beams incident normally on STFs is the next logical step, all the more so because of advances in experimental techniques that have motivated the analysis of that problem. Already device research with STFs has moved beyond axial-excitation designs and toward general STF architectures. Indeed, chiral STFs with periodic nonhomogeneities in three directions have recently been fabricated [27,28]. These advances in fabrication techniques call for a concerted program of theoretical work to guide the development of STF pulse- and/or beam-shaping devices.

In addition, chiral STFs have been infiltrated with liquid crystals, which alters their optical properties in a manner that is tunable by application of an electric field [29]. Piezoelectric manipulation of STF optical properties has also been suggested [19,30]. Such advances raise the possibility of tunable pulsed-beam-shapers. Nonlinear dyes could be diffused into STFs [20], which also might be useful in pulsed-beam-shaping. The determination of the advantages and disadvantages of STF shapers with respect to their homogeneous isotropic counterparts will require experimental as well as theoretical analyses.

In this paper, we take the first steps towards the design of STF pulsed-beam-shaping devices by building a framework to analyze their operation. The plan of our exposition is as follows. In Section 2, we outline the mathematics necessary to analyze the reflection, refraction, and diffraction of normally incident pulsed beams by chiral STFs. First, we describe the geometry of the problem and constitutive relations of the chosen STF; then we derive a matrix partial differential equation (MPDE), describing the propagation of pulsed beams parallel to the axis of spirality. We present a finite-difference algorithm to solve the MPDE. Section 3 contains the results of several illustrative calculations; and in Section 4, we sum up our main conclusions.

2. Problem description and solution method

A chiral STF occupies the region $\mathscr{R}_{\mathrm{STF}} : \{(x,y,z) \mid -d_{y0} \leqslant y \leqslant d_{y1}, d_{z0} \leqslant z \leqslant d_{z0} + d_z\}$ depicted in Fig. 2, while the remaining space is vacuous. A pulsed beam launched in vacuum propagates parallel to the z-axis and eventually encounters the chiral STF, whereupon part is reflected and part is transmitted. In the development that follows, vectors are underlined once and dyadics [31] twice; the matrix representation of a dyadic is indicated by enclosing the symbol for the dyadic within square brackets;

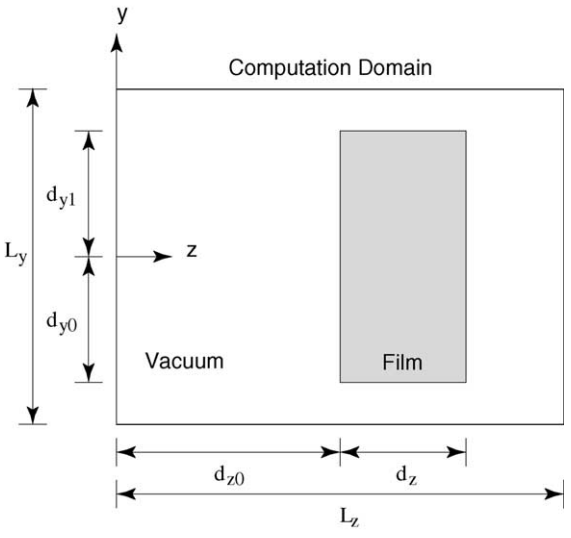

Fig. 2. Schematic of the region $\mathscr{R}$: $\{(x,y,z) \mid -L_y/2 \leqslant y \leqslant L_y/2, 0 \leqslant z \leqslant L_z\}$ of computation. The chiral STF occupies the region $\mathscr{R}_{\mathrm{STF}} : \{(x,y,z) \mid -d_{y0} \leqslant 4y \leqslant d_{y1},\ d_{z0} \leqslant z \leqslant d_{z0} + d_z\}$.

the real-valued vectors $\underline{E}$ and $\underline{D}$ denote the electric field and electric flux density, respectively, whereas $\underline{B}$ and $\underline{H}$ denote the corresponding magnetic variables. The set of three cartesian unit vectors is denoted as $\{\underline{u}_x,\underline{u}_y,\underline{u}_z\}$.

2.1. Constitutive relations

The constitutive relations of the linear chiral STF are:

$$\left.\begin{aligned}\underline{D}(\underline{r},t) &= \varepsilon_0(\underline{\underline{\varepsilon}} * \underline{E})(\underline{r},t)\\ \underline{B}(\underline{r},t) &= \mu_0\underline{H}(\underline{r},t)\end{aligned}\right\}, \quad \underline{r}\in\mathscr{R}_{\mathrm{STF}}, \tag{1}$$

where $\underline{\underline{\varepsilon}}(\underline{r},t)$ is the relative permittivity dyadic; t denotes time; $\underline{r} = x\underline{u}_x + y\underline{u}_y + z\underline{u}_z$ is the position vector; while ε_0 and μ_0 denote the permittivity and permeability of free space (i.e., vacuum), respectively. The symbol $*$ denotes convolution with respect to time as follows:

$$(\underline{\underline{\varepsilon}} * \underline{E})(\underline{r},t) = \int_0^\infty \underline{\underline{\varepsilon}}(\underline{r},t')\cdot\underline{E}(\underline{r},t-t')\,\mathrm{d}t'. \tag{2}$$

The relative permittivity dyadic is conveniently written as

$$\underline{\underline{\varepsilon}}(\underline{r},t) = \delta(t)\underline{\underline{I}} + \underline{\underline{\chi}}(\underline{r},t), \tag{3}$$

where $\delta(t)$ is the Dirac delta function and $\underline{\underline{I}}$ is the identity dyadic, while the anisotropic and nonhomogeneous electromagnetic properties of the chiral STF are contained in the dielectric susceptibility dyadic

$$\begin{aligned}\underline{\underline{\chi}}(\underline{r},t) = {}& \underline{\underline{S}}_z(z-d_{z0})\cdot\underline{\underline{S}}_y(\alpha)\cdot\underline{\underline{\chi}}^0_{\mathrm{ref}}(t)\cdot\underline{\underline{S}}_y^{\mathrm{T}}(\alpha)\\ &\cdot\underline{\underline{S}}_z^{\mathrm{T}}(z-d_{z0}), \quad \underline{r}\in\mathscr{R}_{\mathrm{STF}},\end{aligned} \tag{4}$$

wherein the superscript T denotes the transpose. The tilt dyadic

$$\begin{aligned}\underline{\underline{S}}_y(\alpha) = {}& (\underline{u}_x\underline{u}_x + \underline{u}_z\underline{u}_z)\cos\alpha + (\underline{u}_z\underline{u}_x - \underline{u}_x\underline{u}_z)\\ &\times\sin\alpha + \underline{u}_y\underline{u}_y\end{aligned} \tag{5}$$

depends solely on the angle of rise $\alpha > 0$. The material nonhomogeneity along the z-axis is captured in the rotation dyadic

$$\begin{aligned}\underline{\underline{S}}_z(z) = {}& (\underline{u}_x\underline{u}_x + \underline{u}_y\underline{u}_y)\cos\left(\frac{\pi z}{\Omega}\right)\\ &+ h(\underline{u}_y\underline{u}_x - \underline{u}_x\underline{u}_y)\sin\left(\frac{\pi z}{\Omega}\right) + \underline{u}_z\underline{u}_z,\end{aligned} \tag{6}$$

where Ω is the structural half-period, and h is the structural handedness parameter. We set either $h = +1$ for a structurally right-handed chiral STF, or $h = -1$ for structural left-handedness. As chiral STFs are deemed to possess local orthorhombic symmetry [6], the representation

$$\underline{\underline{\chi}}^0_{\mathrm{ref}}(t) = \chi_a(t)\underline{u}_z\underline{u}_z + \chi_b(t)\underline{u}_x\underline{u}_x + \chi_c(t)\underline{u}_y\underline{u}_y \tag{7}$$

is appropriate at visible and infrared wavelengths. We assumed a single-resonance Lorentzian model for the dispersion in the film [32]; hence

$$\chi_{a,b,c}(t) = p_{a,b,c}\omega_{a,b,c}\sin(\omega_{a,b,c}t)\exp\left(-\frac{\omega_{a,b,c}t}{2\pi N_{a,b,c}}\right)\mathscr{U}(t), \tag{8}$$

where $\mathscr{U}(t)$ is the unit step function; while the parameters $p_{a,b,c}$ are the oscillator strengths, $\omega_{a,b,c} = 2\pi c_0/\lambda_{a,b,c}$ are angular frequencies related to the material resonances, and $\lambda_{a,b,c}(1+N_{a,b,c}^{-2})^{-1/2}$ are the resonance wavelengths; $c_0 = 1/\sqrt{\varepsilon_0\mu_0}$ is the speed of light in vacuum.

2.2. Derivation of matrix partial differential equation

In the absence of sources, the Faraday and Ampere–Maxwell equations are:

$$\nabla\times\underline{E}(\underline{r},t) = -\partial_t\underline{B}(\underline{r},t), \tag{9}$$

$$\nabla\times\underline{H}(\underline{r},t) = \partial_t\underline{D}(\underline{r},t), \tag{10}$$

respectively, where ∂_q denotes partial differentiation with respect to q, which stands for any space or time variable. On substitution of (1)–(8) into (9) and (10), we obtain:

$$\left.\begin{aligned}\nabla\times\underline{E}(\underline{r},t) &= -\mu_0\partial_t\underline{H}(\underline{r},t)\\ \nabla\times\underline{H}(\underline{r},t) &= \varepsilon_0\left[\partial_t\underline{E} + \left(\underline{\underline{\chi}} * \partial_t\underline{E}\right)\right](\underline{r},t)\end{aligned}\right\}, \quad \underline{r}\in\mathscr{R}_{\mathrm{STF}}. \tag{11}$$

These can be rearranged in matrix form as

$$\begin{aligned}&[\underline{\underline{A}}_y]\partial_y[\underline{F}] + [\underline{\underline{A}}_z]\partial_z[\underline{F}]\\ &\quad = [\underline{\underline{B}}]\partial_t[\underline{F}] + \left([\underline{\underline{C}}] * \partial_t[\underline{F}]\right), \quad \underline{r}\in\mathscr{R}_{\mathrm{STF}},\end{aligned} \tag{12}$$

where

$$[\underline{\underline{A}}_y] = \begin{bmatrix} 0 & 0 & 1 & 0 & 0 & 0 \\ 0 & 0 & 0 & 0 & 0 & 0 \\ -1 & 0 & 0 & 0 & 0 & 0 \\ 0 & 0 & 0 & 0 & 0 & 1 \\ 0 & 0 & 0 & 0 & 0 & 0 \\ 0 & 0 & 0 & -1 & 0 & 0 \end{bmatrix}, \tag{13}$$

$$[\underline{\underline{A}}_z] = \begin{bmatrix} 0 & -1 & 0 & 0 & 0 & 0 \\ 1 & 0 & 0 & 0 & 0 & 0 \\ 0 & 0 & 0 & 0 & 0 & 0 \\ 0 & 0 & 0 & 0 & -1 & 0 \\ 0 & 0 & 0 & 1 & 0 & 0 \\ 0 & 0 & 0 & 0 & 0 & 0 \end{bmatrix}, \tag{14}$$

$$[\underline{\underline{B}}] = \begin{bmatrix} [\underline{0}] & -\mu_0[\underline{I}] \\ \varepsilon_0[\underline{I}] & [\underline{0}] \end{bmatrix}, \tag{15}$$

$$[\underline{\underline{C}}(y,z,t)] = \varepsilon_0 \begin{bmatrix} [\underline{0}] & [\underline{0}] \\ [\underline{\chi}] & [\underline{0}] \end{bmatrix}, \tag{16}$$

$$[\underline{F}(y,z,t)] = [E_x \quad E_y \quad E_z \quad H_x \quad H_y \quad H_z]^{\mathrm{T}}, \tag{17}$$

$[\underline{0}]$ indicates the null 3×3 matrix, and $[\underline{I}]$ the identity 3×3 matrix. The electromagnetic field is independent of x here.

Premultiplying both sides of (12) by $[\underline{\underline{B}}]^{-1}$, we obtain the MPDE

$$\begin{aligned} \partial_t[\underline{F}] = {} & [\underline{\underline{V_y}}]\partial_y[\underline{F}] + [\underline{\underline{V_z}}]\partial_z[\underline{F}] \\ & - [\underline{\underline{W}}] * \partial_t[\underline{F}], \quad \underline{r} \in \mathscr{R}_{\mathrm{STF}}, \end{aligned} \tag{18}$$

wherein the shorthand notation:

$$\left.\begin{aligned} \left[\underline{\underline{V_y}}\right] &= \left[\underline{\underline{B}}\right]^{-1}\left[\underline{\underline{A}}_y\right] \\ \left[\underline{\underline{V_z}}\right] &= \left[\underline{\underline{B}}\right]^{-1}\left[\underline{\underline{A}}_z\right] \\ \left[\underline{\underline{W}}\right] &= \left[\underline{\underline{B}}\right]^{-1}\left[\underline{\underline{C}}\right] \end{aligned}\right\}, \tag{19}$$

has been used for convenience. The derived MPDE (18) has to be solved numerically.

2.3. Finite-difference algorithm

Eq. (18) also describes pulse propagation in vacuum when $[\underline{\underline{W}}] = [\underline{0}]$. This equation is therefore extended to the half-space $z > 0$ by setting $p_{a,b,c} = 0$ in those regions that are not occupied by the chiral STF. We confine our calculations to the region $\mathscr{R}$: $\{(x,y,z) \mid -L_y/2 \leqslant y \leqslant L_y/2,\ 0 \leqslant z \leqslant L_z\}$ shown in Fig. 2.

In order to solve the extended Eq. (18) over $\mathscr{R}$ and time $t > 0$, we first discretize space and time. Thus,

$$y_i = i\Delta y, \quad i = 0, \pm 1, \pm 2, \ldots, \pm N_y, \tag{20}$$

$$z_j = j\Delta z, \quad j = 0, 1, 2, \ldots, N_z, \tag{21}$$

$$t_n = n\Delta t, \quad n = 0, 1, 2, \ldots, N_t, \tag{22}$$

where Δy and Δz are the space increments; Δt is the time increment; and $N_y = L_y/2\Delta y$, $N_z = L_z/\Delta z$, and N_t are the numbers of space and time increments used in the calculation.

On approximating derivatives with finite differences using the leapfrog method [33], we obtain

$$\begin{aligned} [\underline{F}]_{i,j}^{n+1} = {} & [\underline{F}]_{i,j}^{n-1} + \frac{\beta_y}{c_0}\left[\underline{\underline{V_y}}\right]\left([\underline{F}]_{i+1,j}^{n} - [\underline{F}]_{i-1,j}^{n}\right) \\ & + \frac{\beta_z}{c_0}[\underline{\underline{V_z}}]\left([\underline{F}]_{i,j+1}^{n} - [\underline{F}]_{i,j-1}^{n}\right) \\ & - \sum_{m=1}^{n-1}[\underline{\underline{W}}]_{i,j}^{m}\left([\underline{F}]_{i,j}^{n-m+1} - [\underline{F}]_{i,j}^{n-m-1}\right)\Delta t \\ & - \left[\underline{\underline{W}}\right]_{i,j}^{n}\left([\underline{F}]_{i,j}^{1} - [\underline{F}]_{i,j}^{0}\right)\Delta t. \end{aligned} \tag{23}$$

In this equation, we have used the shorthand notation:

$$\left.\begin{aligned} [\underline{F}]_{i,j}^{n} &= \left[\underline{F}(y_i, z_j, t_n)\right] \\ [\underline{M}]_{i,j}^{n} &= \left[\underline{\underline{M}}(y_i, z_j, t_n)\right] \end{aligned}\right\}, \tag{24}$$

with $[\underline{\underline{M}}]$ denoting any arbitrary matrix; while the stability parameters $\beta_y = c_0\Delta t/\Delta y$ and $\beta_z = c_0\Delta t/\Delta z$. For all calculations reported here, we kept $\Delta y = \Delta z$; hence, $\beta_y = \beta_z = \beta > 0$. We set β to values less than unity to keep the finite-difference algorithm stable [34]. The last term on the right side of (23) is null-valued, because $[\underline{F}(y,z,0)] = [\underline{0}]$ for the initial conditions to be described later.

2.4. Simplification of the convolution term

The computational expense incurred due to the convolution sum

$$[\underline{\underline{U}}]^n_{i,j} = \sum_{m=1}^{n-1} [\underline{\underline{W}}]^m_{i,j} \left([\underline{\underline{F}}]^{n-m+1}_{i,j} - [\underline{\underline{F}}]^{n-m-1}_{i,j} \right) \Delta t \tag{25}$$

on the right side of (23) can be reduced considerably, because Lorentzian constitutive properties have been assumed for the chiral STF [24,35]. This reduction is accomplished as follows; similar recursive techniques for simpler materials have been used in the past [36,37].

Our task is to find $[\underline{\underline{U}}]^{n+1}_{i,j}$ for given $[\underline{\underline{U}}]^n_{i,j}$. We begin by defining the matrixes

$$[\underline{u}]_j = \left[\underline{\underline{S}}_z (z_j - d_{z0}) \right] \cdot [\underline{\underline{S}}_y(\alpha)] \cdot \begin{bmatrix} \frac{\chi_b(\Delta t)}{p_b \omega_b} & 0 & 0 \\ 0 & \frac{\chi_c(\Delta t)}{p_c \omega_c} & 0 \\ 0 & 0 & \frac{\chi_a(\Delta t)}{p_a \omega_a} \end{bmatrix} \cdot \left[\underline{\underline{S}}_y(\alpha) \right]^{\mathrm{T}} \cdot \left[\underline{\underline{S}}_z (z_j - d_{z0}) \right]^{\mathrm{T}}, \tag{26}$$

$$\left[\underline{\underline{v}} \right]_j = \left[\underline{\underline{S}}_z (z_j - d_{z0}) \right] \cdot [\underline{\underline{S}}_y(\alpha)] \cdot \begin{bmatrix} \frac{\chi_b(\Delta t)\cot(\omega_b \Delta t)}{p_b \omega_b} & 0 & 0 \\ 0 & \frac{\chi_c(\Delta t)\cot(\omega_c \Delta t)}{p_c \omega_c} & 0 \\ 0 & 0 & \frac{\chi_a(\Delta t)\cot(\omega_a \Delta t)}{p_a \omega_a} \end{bmatrix} \cdot [\underline{\underline{S}}_y(\alpha)]^{\mathrm{T}} \cdot \left[\underline{\underline{S}}_z (z_j - d_{z0}) \right]^{\mathrm{T}}, \tag{27}$$

where $[\underline{\underline{S}}_y(\cdot)]$ is a 3×3 matrix equivalent to the dyadic $\underline{\underline{S}}_y(\cdot)$, etc. Then

$$[\underline{\underline{U}}]^{n+1}_{i,j} = [\underline{v}]_j [\underline{\underline{U}}]^n_{i,j} + [\underline{u}]_j [\underline{\underline{V}}]^n_{i,j} + [\underline{\gamma}]_j [\underline{u}]_j \left([\underline{\underline{F}}]^{n+1}_{i,j} - [\underline{\underline{F}}]^{n-1}_{i,j} \right) \Delta t, \tag{28}$$

where $[\underline{\underline{V}}]^n_{i,j}$ is defined recursively as

$$[\underline{\underline{V}}]^{n+1}_{i,j} = [\underline{v}]_j [\underline{\underline{V}}]^n_{i,j} - [\underline{u}]_j [\underline{\underline{U}}]^n_{i,j} + [\underline{\gamma}]_j [\underline{v}]_j \left([\underline{\underline{F}}]^{n+1}_{i,j} - [\underline{\underline{F}}]^{n-1}_{i,j} \right) \Delta t \tag{29}$$

and

$$[\underline{\gamma}]_j = \left[\underline{\underline{S}}_z (z_j - d_{z0}) \right] \cdot [\underline{\underline{S}}_y(\alpha)] \cdot \begin{bmatrix} p_b \omega_b & 0 & 0 \\ 0 & p_c \omega_c & 0 \\ 0 & 0 & p_a \omega_a \end{bmatrix} \cdot [\underline{\underline{S}}_y(\alpha)]^{\mathrm{T}} \cdot \left[\underline{\underline{S}}_z (z_j - d_{z0}) \right]^{\mathrm{T}}. \tag{30}$$

Finally, we note that $[\underline{\underline{U}}]^0_{i,j} = [\underline{\underline{V}}]^0_{i,j} = [\underline{\underline{0}}]$, while $[\underline{u}]_j$ and $[\underline{v}]_j$ are null-valued for $(y_i, z_j) \in \mathscr{R} - \mathscr{R}_{\mathrm{STF}}$.

2.5. Representation of the incident pulsed beam

With $\eta_0 = \sqrt{\mu_0/\varepsilon_0}$ denoting the intrinsic impedance of free space, we chose the field of the pulsed beam to have the form

$$[\underline{F}(y,0,t)] = \sqrt{\frac{\eta_0 \sqrt{2}}{\pi \tau w_0}} \exp\left(-\frac{(t-t_{\mathrm{d}})^2}{2\tau^2} \right) \exp\left(\frac{-k_{\mathrm{car}} y^2}{2 z_{\mathrm{R}}} \right) \times \begin{bmatrix} \cos\left(2\pi v_{\mathrm{car}} t + \varphi^{(s)}\right) \\ -\left[1 + \frac{y^2}{2 z_{\mathrm{R}}^2}\right] \cos\left(2\pi v_{\mathrm{car}} t + \varphi^{(p)}\right) \\ \left[\frac{y}{z_{\mathrm{R}}}\right] \sin\left(2\pi v_{\mathrm{car}} t + \varphi^{(p)}\right) \\ \frac{1}{\eta_0} \cos\left(2\pi v_{\mathrm{car}} t + \varphi^{(p)}\right) \\ \frac{1}{\eta_0}\left[1 + \frac{y^2}{2 z_{\mathrm{R}}^2}\right] \cos\left(2\pi v_{\mathrm{car}} t + \varphi^{(s)}\right) \\ -\frac{1}{\eta_0}\left[\frac{y}{z_{\mathrm{R}}}\right] \sin\left(2\pi v_{\mathrm{car}} t + \varphi^{(s)}\right) \end{bmatrix} \mathscr{U}(t) \tag{31}$$

on the plane $z = 0$ when $|y| \leqslant N_{\mathrm{ap}} \Delta y$, where the integer N_{ap} dictates the width of an aperture through which the pulsed beam must pass to enter the domain of computation; thus $[\underline{F}(y,0,t)] = [0,0,0,0,0,0]^{\mathrm{T}}$ for $|y| > N_{\mathrm{ap}} \Delta y$. The focal plane of the pulsed beam is $z = 0$, and z_{R} is the Rayleigh range (i.e., a measure of the collimation) of the carrier beam, while v_{car} is the carrier frequency, $k_{\mathrm{car}} = 2\pi/\lambda_{\mathrm{car}}$ is the carrier wavenumber, and λ_{car} is the carrier wavelength in free space. The carrier phases $\varphi^{(s)}$ and $\varphi^{(p)}$ correspond to the s- and p-polarized components of the beam, respectively. The waist w_0 of the carrier beam is related to the Rayleigh range by the relation $2 z_{\mathrm{R}} = k_{\mathrm{car}} w_0^2$. The time delay t_{d} and time constant τ fix the properties of the temporal pulse envelope.

The boundary value (31) was derived under the approximations $\lambda_{\mathrm{car}}/w_0 \ll 1$ (i.e., the paraxial approximation) and $1/(v_{\mathrm{car}}\tau) \ll 1$; when these approximations are satisfied, the pulsed beam is separable into factors that depend only on space or time [38]. We nulled the electromagnetic field at the other boundaries of $\mathscr{R}$; i.e., when either $y_i = \pm N_y \Delta y$ or $z_j = N_z \Delta z$ or both, then $[\underline{F}(y,z,t)] = [0,0,0,0,0,0]^{\mathrm{T}}$.

3. Results and discussion

We performed our computations, coded in Fortran 90, on the HP GS1280 system at the Pittsburgh Supercomputing Center. For the calculated results shown in Figs. 3–12, we set $N_y = 1502$, $N_z = 1002$, $N_t = 2002$, $\beta = 0.5$, and $\Delta y = \Delta z = 10$ nm. When the difference between the carrier phases is $\varphi^{(p)} - \varphi^{(s)} = \pi/2$, the incident beam is predominantly left circularly polarized (LCP); when that difference equals $-\pi/2$, the incident beam is predominantly right circularly polarized (RCP). Note that optical beams, in general, do not possess a pure polarization state [39], unlike plane waves. For all calculations presented in this section, we chose $\varphi^{(p)} - \varphi^{(s)} = \pi/2$, so that the incident pulsed beams are predominantly LCP.

The properties of the chiral STF were chosen as follows: we set $p_a = 0.40$, $p_b = 0.52$, $p_c = 0.42$; the choices $\lambda_a = \lambda_c = 280$ nm, $\lambda_b = 290$ nm, and $N_{a,b,c} = 100$ place the resonance wavelengths in the ultraviolet regime. We chose $\Omega = 200$ nm and $\alpha = 20°$, and hence the Bragg wavelength – the center wavelength of the Bragg regime – for the film is about 516 nm.

We chose $\lambda_{car} = 516$ nm – and so the carrier period $T_{car} = 1/\nu_{car} = 1.72$ fs – and set $\tau = 2T_{car} = 3.44$ fs. Furthermore, we set the time delay $t_d = 2.5\tau = 8.61$ fs. Thus, the computation domain is about $58\lambda_{car} \times 19\lambda_{car}$ in spatial size.

3.1. Reflection and refraction of pulsed beams by STFs

Figs. 3 and 4 show the electric field magnitude $|\underline{E}| = (E_x^2 + E_y^2 + E_z^2)^{\frac{1}{2}}$, for pulsed beams incident on three different STFs, at two different times

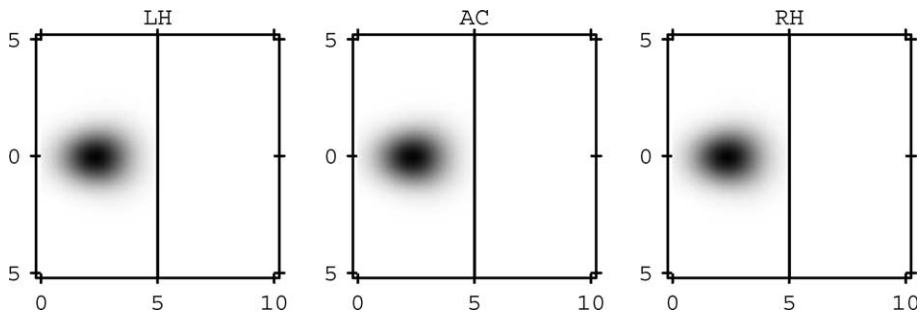

Fig. 3. Snapshots of $|\underline{E}|$ (in arbitrary units) of a pulsed beam at time $t = 16.7$ fs. The STF is either structurally left-handed (LH, at left), achiral (AC, in center), or right-handed (RH, at right), and the carrier beam of the incident pulse is predominantly left circularly polarized (LCP). The axes of each plot are labeled in μm, and the line bisecting each plot marks the left boundary of $\mathscr{R}_{STF}$. Note that only a portion of $\mathscr{R}$ is shown.

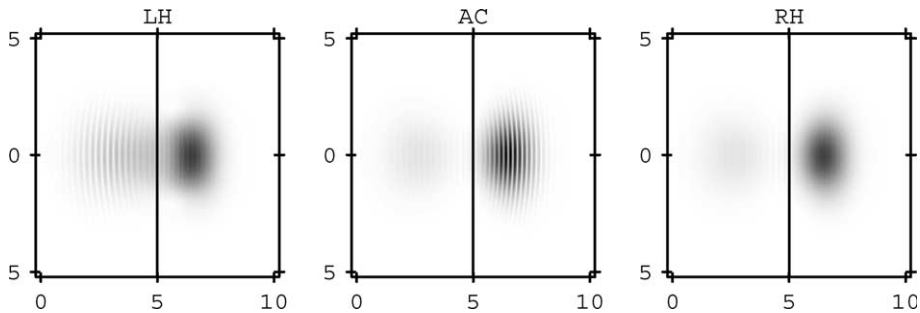

Fig. 4. Same as Fig. 3, except at time $t = 33.4$ fs. Note that when the STF is LH, the reflected pulse is longer in duration and apparently wider in the y-direction than when the STF is either AC or RH.

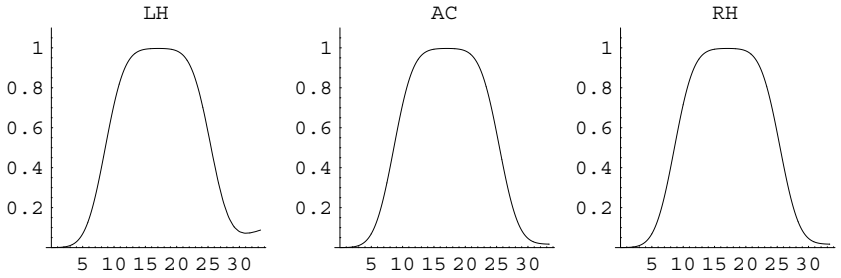

Fig. 5. Energy $U(t_n)$ (ordinate; in arbitrary units) as function of time (abcissa; in fs) in the vacuous region $0 \leqslant z < d_{z0}$ for the pulses in Figs. 3 and 4. Note the upward turn in $U(t_n)$ at $t_n \approx 31$ fs when the STF is structurally LH. This upward turn is due to the bleeding of energy from the refracted pulse to the reflected pulse.

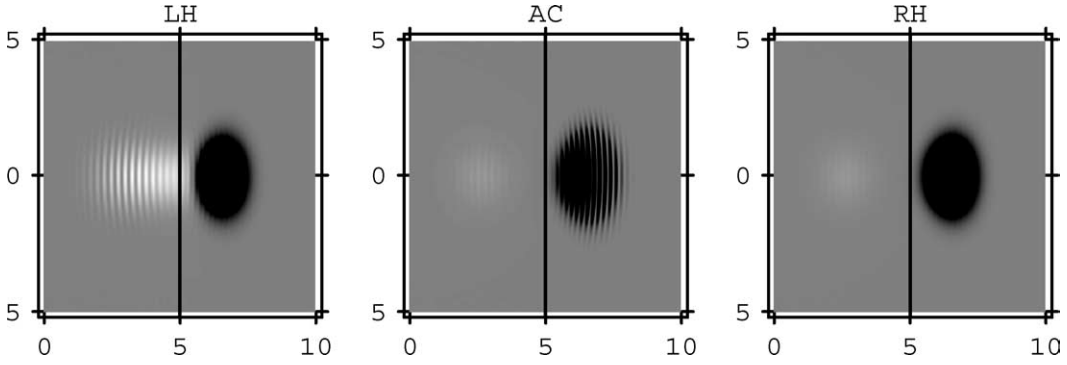

Fig. 6. Snapshot of the z-component of the Poynting vector $\underline{P}(\underline{r},t) = \underline{E}(\underline{r},t) \times \underline{H}(\underline{r},t)$ at time $t = 33.4$ fs. Black areas of the plots indicate regions where energy is flowing in the $+z$-direction, and white areas of the plots indicate regions where energy is flowing in the $-z$-direction. The plots have been scaled to increase the contrast between regions where $\underline{P} \cdot \underline{u}_z > 0$ and where $\underline{P} \cdot \underline{u}_z < 0$. Note the long region of backward-going ($-z$) energy, dubbed the light pipe, when the STF is structurally LH.

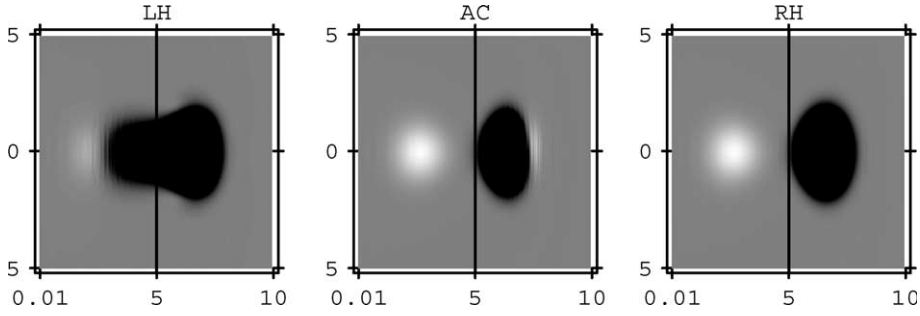

Fig. 7. Snapshot of electric field helicity $\underline{E}(\underline{r},t) \cdot (\nabla \times \underline{E}(\underline{r},t))$ at time $t = 33.4$ fs. White areas indicate regions where the helicity is negative (RCP), and black areas indicate regions where the helicity is positive (LCP). The leading portion of the reflected pulse has a net negative helicity, while its tail has a net positive helicity, when the CBP occurs.

$t = 1000\Delta t = 16.7$ fs and $t = 2000\Delta t = 33.4$ fs. The incident pulsed beams have $w_0 = 2\lambda_{car}$, and they consist of largely LCP light. We chose $N_{ap} = 207$, so that $N_{ap}\Delta y \approx 2w_0$. The STFs are either structurally left-handed (LH, $h = -1$), achiral (AC, $\Omega \to \infty$), or structurally right-handed (RH,

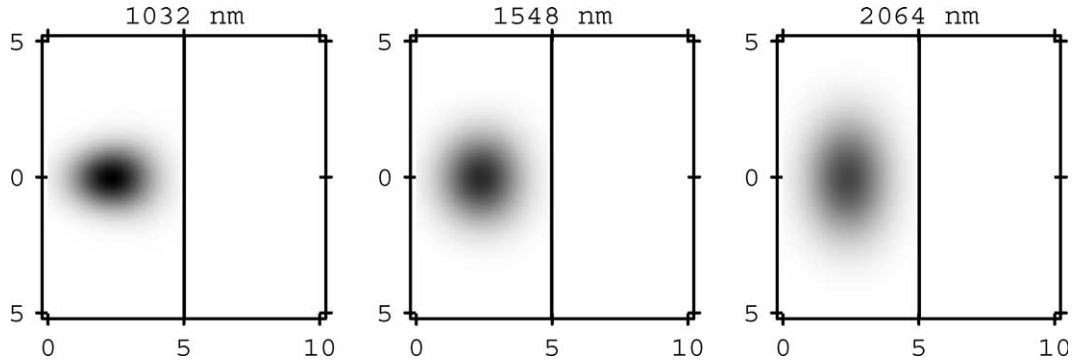

Fig. 8. Snapshots of $|\underline{E}|$ (in arbitrary units) of a pulsed beam with $w_0 = 2\lambda_{car}$ (1032 nm, at left), $3\lambda_{car}$ (1548 nm, in center), or $4\lambda_{car}$ (2064 nm, at right) at time $t = 16.7$ fs. The chiral STF is structurally LH, and the incident pulsed beam is predominantly LCP. The scaling of the plots is different than in Figs. 3 and 4.

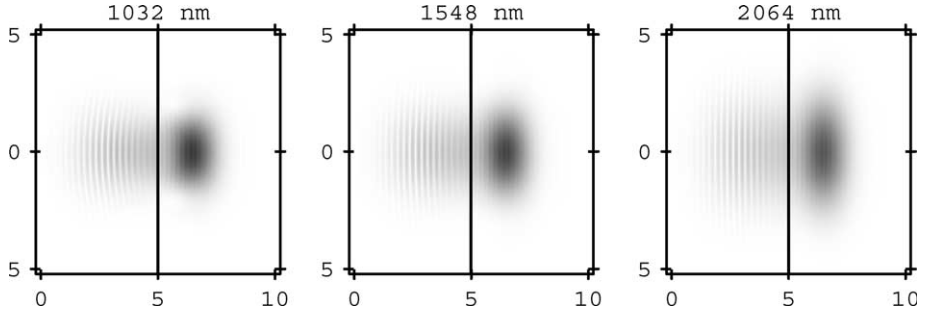

Fig. 9. Same as Fig. 8, except at time $t = 33.4$ fs. The width of the reflected pulses in the y-direction increases as w_0 increases.

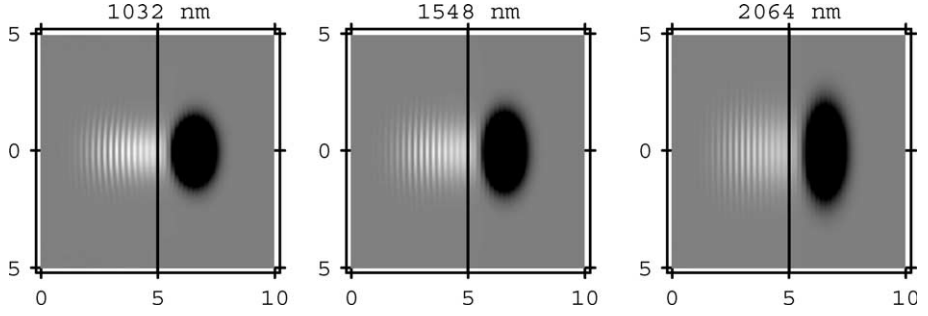

Fig. 10. Snapshots of $\underline{P}(\underline{r},t) \cdot \underline{u}_z$ (in arbitrary units) of a pulsed beam with $w_0 = 2\lambda_{car}$ (1032 nm, at left), $3\lambda_{car}$ (1548 nm, in center), or $4\lambda_{car}$ (2064 nm, at right) at time $t = 33.4$ fs. The chiral STF is structurally LH and the incident pulse is largely LCP. The contrast between regions where $\underline{P} \cdot \underline{u}_z > 0$ and regions where $\underline{P} \cdot \underline{u}_z < 0$ has been enhanced, but the scaling is different than in Fig. 6. The light pipe widens in the y-direction as w_0 increases.

$h = 1$), and their boundaries are located at $d_{z0} = 500\Delta z = 5$ μm and $d_{z0} + d_z = 1000\Delta z = 10$ μm; we set $d_{y0} = d_{y1} = 1500\Delta y = 15$ μm.[1] These choices mean that the right, upper, and lower boundaries of $\mathscr{R}_{STF}$ lie just inside $\mathscr{R}$. In Fig. 3, at $t = 16.7$ fs, the pulsed beams have almost reached the films. In Fig. 4, at $t = 33.4$ fs, the pulsed beams have suffered reflection and refraction at the left boundary of $\mathscr{R}_{STF}$.

[1] The achiral STF is simply a columnar thin film [6,40], and therefore, does not display any Bragg phenomenon.

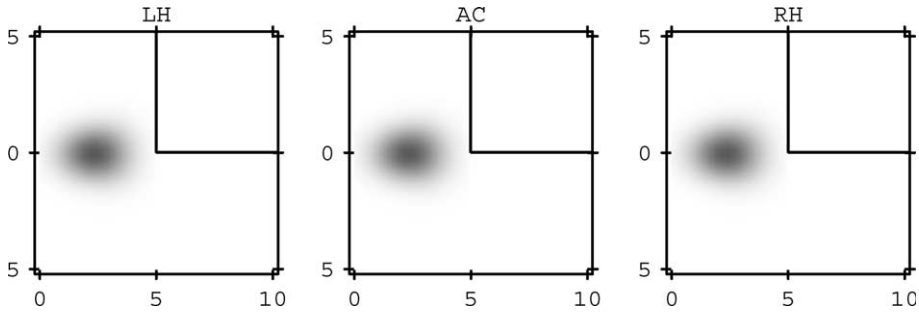

Fig. 11. Snapshots of $|\underline{E}|$ (in arbitrary units) at time $t = 16.7$ fs for a largely LCP incident pulsed beam with $w_0 = 2\lambda_{car}$. The pulsed beam impinges on the corner of an STF, which occupies most of the upper right quadrant of each plot. The STF is either structurally LH (at left), achiral (at center), or structurally RH (at right). The incident pulsed beam is predominantly LCP. The z-coordinate of the left boundary of $\mathscr{R}_{STF}$ and the y-coordinate of the lower boundary of $\mathscr{R}_{STF}$ are delineated. The scaling of these plots is different than in Figs. 3, 4, 8, and 9.

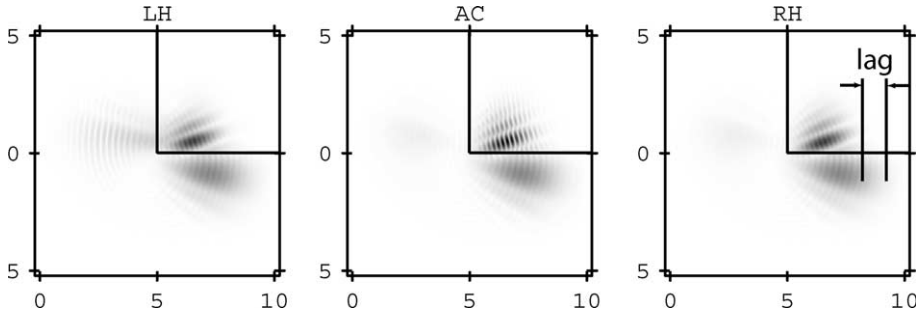

Fig. 12. Same as Fig. 11, but at time $t = 33.4$ fs. Refracted and diffracted pulses are visible in all three plots, but pulse bleeding creates a longer and more intense reflected pulse when the STF is structurally LH. The lag between the refracted and diffracted pulses (of $\approx$1 μm) is present in all three cases; it is marked in the rightmost plot.

In Fig. 4, when the predominant circular polarization state of the incident light matches the structurally handedness (if present) of the STF – as is the case for the leftmost plot – the reflection of the incident pulsed beam is greater than if otherwise. When the STF is achiral (middle plot) or the predominant handedness of the incident light and the structure of the STF are opposite (rightmost plot), then the reflection from the STF is not as prominent. Notice too that the duration (which is proportional to its length in the z-direction) and apparent width (in the y-direction) of the reflected pulse are also greater in the former case than in the latter two cases.

The observation of greater reflection when the criterions for the CBP are satisfied is clarified by plots of the energy

$$U(t_n) = \frac{1}{2}\sum_{i=-N_y}^{N_y}\sum_{j=0}^{(d_{z0}/\Delta z)-1}\left\{\varepsilon_0\left|\underline{E}(y_i,z_j,t_n)\right|^2 + \mu_0\left|\underline{H}(y_i,z_j,t_n)\right|^2\right\}\Delta y\Delta z \tag{32}$$

in the vacuous region $0 \leqslant z < d_{z0}$ presented in Fig. 5. In all three plots in that figure, $U(t_n)$ rises to a maximum value as the pulse enters the vacuous region $0 \leqslant z < d_{z0}$, and then falls as the pulse begins to refract into the STF. When the CBP does not occur, $U(t_n)$ continues to fall. However, in the leftmost plot $U(t_n)$ falls for a time and then increases once more. Hence, when the CBP occurs, there must be a bleeding of energy from the refracted pulse inside the film back into the vacuous region.

That bleeding is evident in Fig. 6, where the z-component of the Poynting vector $\underline{P}(\underline{r},t) = \underline{E}(\underline{r},t) \times \underline{H}(\underline{r},t)$ at $t = 33.4$ fs is plotted. The black

areas of the plots indicate regions where energy is flowing in the $+z$-direction, while the white areas of the plots indicate regions where energy is flowing in the $-z$-direction. The plots have been scaled to increase the contrast between forward-going ($+z$) and backward-going ($-z$) energy flows. In the case when the CBP occurs – i.e., when the STF is structurally LH – the reflected pulse is much longer than in the cases when the CBP does not occur. Also in that case, there is a region where $\underline{P} \cdot \underline{u}_z < 0$ that connects the tail of the reflected pulse to the refracted pulse across the boundary between vacuum and the film. This connection, called the light pipe, is not present in the other two cases, when the STF is structurally AC or RH. The light pipe, and the bleeding of energy from the refracted pulse to the reflected pulse it entails, is the time-domain fingerprint of the CBP.

An analogous phenomenon for pulsed plane waves has already been found and described [23,24]. There are, however, important differences between the cases of pulsed plane waves and pulsed beams. In the case of a two-dimensional pulsed beam, the film shapes the distribution of energy in the pulse in two spatial dimensions and time. For a pulsed plane wave, the distribution of energy is affected by the film in only one spatial dimension and time. Hence, the pulse bleeding phenomenon in two dimensions can be used to shape pulsed beams. For instance, notice that the apparent widths (in the y-direction) of the reflected pulse in Figs. 4 and 6 is greater when the CBP occurs than otherwise.

The incident pulse comprises almost wholly LCP light. What polarization(s) are present in the reflected and refracted pulses? To answer that question, we plotted the computed helicity of the electric field, i.e., $\underline{E}(\underline{r},t) \cdot (\nabla \times \underline{E}(\underline{r},t))$, as shown in Fig. 7 at $t = 33.4$ fs. The plots have been scaled to more clearly show regions of positive (i.e., LCP, indicated by black) and negative (i.e., RCP, indicated by white) helicity. As in Figs. 4 and 6, the reflected pulses are much shorter in duration when the CBP does not occur than when it does. In Fig. 7, the reflected pulse consists mostly of light having net negative helicity when the STF is structurally RH or AC. However, when the STF is structurally LH, only the leading portion of the reflected pulse has net negative helicity. Reflection from near the interface between vacuum and film is responsible for the leading portion of the pulse. The circular polarization state of the incident light is inverted upon this initial reflection, which is due to the impedance mismatch between the vacuum and film. The tail portion of the reflected pulse, that part created by pulse bleeding, has a net positive helicity. The interference between LCP and RCP components has been offered as an explanation of spatial oscillations in $\underline{P}$ for pulsed plane waves reflected from chiral STFs [26]. Similar oscillations are evident in Fig. 6.

This is one example of the connections between phase, length, and time in nanotechnology, a framework for which has been described elsewhere [41]. Phase, length, and time have always been interconnected in electromagnetics, but in that work they were shown to be intertwined in new ways when the microstructured geometry is a significant fraction of λ_{car}. The implications of these ideas for nanotechnology were expressed via several examples using planewave arguments. Therefore, it is no surprise that these interconnections should also appear for pulsed beams, since such beams can be thought of as combinations of plane waves with proper wavelengths, directions, and phase shifts [42].

Another difference between the case of pulsed plane waves and pulsed beams is that of diffraction. The shapes of pulsed plane waves do not change as they propagate through vacuum. The shape and intensity (but not the total energy) of a pulsed beam in vacuum *do* change as a function of the distance away from the focus of the beam – a phenomenon due to diffraction. In addition, the shapes of pulsed beams reflected from an STF slab of sufficiently large thickness change as they propagate away from the film, and their energy densities decrease. Hence, if a certain pulsed-beam shape or intensity is desired for a given application, and an STF-based device is in the optical path, designers must be careful to position the STF at the proper distance from the focus of the pulsed beam (because the properties of the pulsed-beam that the STF will shape depends on that distance). This phenomenon could be used to make a tunable pulsed-beam-shaping device. Such a device could be realized, for example, by mounting the STF on a piezoelectric stage. Then the distance between

the STF and the focus of the pulsed beam could be increased and decreased easily, causing concominant changes in the shapes and intensities of reflected and transmitted pulsed beams. This concept is a good candidate for further study with our numerical methods.

The Bragg wavelength of a chiral STF, and its absorption, reflection, and transmission properties in general, change with the angle of plane wave incidence [43]. Even though we consider normal incidence of a pulsed beam in this problem, that observation is relevant to the situation here, because diffraction of the incident beam means that some of its constituent plane waves strike the film at an oblique angle. The portion of the incident pulsed beam energy that strikes obliquely is determined in part by the beam waist. The effects of changing the beam waist are shown in Figs. 8 and 9. We chose the beam waist w_0 equal to $2\lambda_{car}$, $3\lambda_{car}$, or $4\lambda_{car}$, and we set $N_{ap}\Delta y \approx 2w_0$ – i.e., $N_{ap} = 207$, 310, or 413, respectively. The incident light is predominantly LCP, the chiral STFs are structurally LH, and the carrier wavelength lies within the Bragg regime; so the criterions for the CBP are satisfied. Snapshots of $|\underline{E}|$ are shown in Figs. 8 and 9, and of $\underline{P}(\underline{r},t)\cdot\underline{u}_z$ in Fig. 10. The boundaries of the chiral STF remain the same as for Figs. 3–7.

For all three values of w_0, the reflected pulse is of long duration. The apparent width of the reflected pulse in the y-direction increases as w_0 increases, as is evident from Fig. 9. The reason for this widening is due to the widening of the light pipe, as seen in Fig. 10. More of the pulse energy tends to hit the film obliquely when w_0 is smaller, so more of the light may tend not to fulfill the Bragg condition for normal incidence and be reflected. This comparison is apt only when the focuses of all pulsed beams lie at the same distance from the chiral STF. We expect the latter effect to exhibit itself through reduced pulse bleeding at the edges of the reflected pulse. The previous three sentences are not true without qualification, however. Chiral STFs can exhibit Bragg reflection at oblique angles, too, and the first-order Bragg wavelength changes with angle of incidence (approximately, the Bragg wavelength is proportional to $\cos^{1/2}\theta$, where θ is the angle of incidence measured with respect to the normal [43]). Calculations that allow the reflected pulse to develop more fully over a longer period of time will be needed to test these assertions.

3.2. Diffraction from an STF corner

We also examined diffraction of a pulsed beam from an STF corner. Plots of the electric field magnitude at $t = 16.7$ fs and $t = 33.4$ fs can be found in Figs. 11 and 12. In this case, $\mathscr{R}_{STF}$ is $\{x,y,z|0 \leqslant y \leqslant 1500\Delta y,\ 500\Delta z \leqslant z \leqslant 1000\Delta z\}$, i.e., $d_{y0} = 0$ μm, $d_{y1} = 15$ μm, $d_{z0} = 5$ μm, and $d_{z0} + d_z = 10$ μm. The film is either structurally LH, RH, or AC. The beam waist $w_0 = 1032$ nm, and the aperture width is dictated by our choice $N_{ap} = 207$.

In Fig. 11, the pulsed beams are shown as they traverse vacuum en route to the chiral STF corner, which occupies most of the upper right quadrant of each plot. The effects of the STF on the pulsed beam can be seen in Fig. 12. The reflection from the STF is most pronounced when it is structurally LH, as we expect from the previous calculations in this work. In all three cases, part of the incident pulse is diffracted from the edge of the STF; these diffracted parts, found in the vacuous lower right quadrants of the plots, are quite similar in appearance, irrespective of the microstructure of the STF. Thus, the incident pulse is split into at least two significant parts in all three cases. When the CBP occurs, there is a reflected pulse, a refracted pulse, and a diffracted pulse. When the CBP does not occur, there is a refracted pulse and a diffracted pulse, but the reflected pulse has little energy. In addition, the STF slows the propagation of the refracted pulse, and in so doing creates a lag in space and time between the diffracted pulse and the refracted pulse. This lag, of about 1 μm, is evident in all three plots of Fig. 12; it is marked in the rightmost plot. Therefore, chiral STFs have potential applications as circular-polarization-sensitive beamsplitters and time-delay elements.

4. Concluding remarks

We investigated the reflection, refraction, and diffraction of pulsed optical beams by chiral and

achiral STFs. Based on the results obtained, we consider the following points to be those of most technological relevance.

- Since pulsed beams undergo diffraction, the position of an STF-based device with respect to the beam source will influence any spatiotemporal pulse shaping that takes place. Of course, this effect will apply to any optical element operating on a pulsed beam. However, due to the inhomogeneous, anisotropic structure of chiral STFs, positioning is especially important in light of new relationships that connect phase, length, and time at a *confluence* of optical wavelengths and nanoscale morphology [41].
- Some of the results from time-domain studies of pulsed plane wave shaping by STFs carry over to our studies of pulsed beams. The CBP in the two-dimensional case, as in the one-dimensional case, manifests itself as a continuous bleeding of energy from the refracted pulse (inside the STF) to the reflected pulse (in vacuum). When the CBP occurs, the reflected pulse consists of a leading portion with predominant circular polarization opposite that of the structural handedness of the film, and a tail portion with predominant circular polarization identical to that of the incident pulse.
- The beam waist could have a significant influence on the shapes of pulses reflected from and transmitted through chiral STFs, though more quantitative measures of pulse shape are needed to explore this possibility fully.
- The corner of a chiral STF could be used as a circular-polarization-sensitive beamsplitter. Depending on its predominant polarization, an incident pulsed beam would either be split into a reflected pulse, refracted pulse, and diffracted pulse (the latter two of which would become transmitted pulses on leaving the device), or into two transmitted pulses. The transmitted pulses would be separated in space by the effects of diffraction and the slowing of the refracted pulse inside the STF. We expect the position of the STF edge – with respect to the center of the pulsed beam on the y-axis and with respect to the location of the beam focus on the z-axis – to affect splitting.

We hope that this information will be of use in designs of STF-based pulsed beam shaping devices.

Acknowledgments

This work was supported, in part, by grants of computing resources on the HP GS1280 system at the Pittsburgh Supercomputing Center. J.B.G. gratefully acknowledges the support of a National Science Foundation Graduate Research Fellowship and an SPIE Educational Scholarship.

References

[1] N.O. Young, J. Kowal, Nature 183 (1959) 104.
[2] K. Robbie, M.J. Brett, A. Lakhtakia, Nature 384 (1996) 616.
[3] A. Lakhtakia, R. Messier, M.J. Brett, K. Robbie, Innov. Mater. Res. 1 (1996) 165.
[4] A. Lakhtakia, R. Messier, Mater. Res. Innov. 1 (1997) 145.
[5] R. Messier, A. Lakhtakia, Mater. Res. Innov. 2 (1999) 217.
[6] A. Lakhtakia, R. Messier, Sculptured Thin Films: Nanoengineered Morphology and Optics, SPIE, Bellingham, WA, USA, 2005.
[7] Y. Gogotsi, Mater. Res. Innov. 7 (2003) 192.
[8] A. Mnyusiwalla, A.S. Daar, P.A. Singer, Nanotechnology 14 (2003) R9.
[9] I.J. Hodgkinson, Q.h. Wu, Adv. Mater. 13 (2001) 889.
[10] M. Suzuki, Y. Taga, Jap. J. Appl. Phys. Part 2 40 (2001) L358.
[11] Y.-P. Zhao, D.-X. Ye, G.-C. Wang, T.-M. Lu, Nano Lett. 2 (2002) 351.
[12] R. Messier, V.C. Venugopal, P.D. Sunal, J. Vac. Sci. Technol. A 18 (2000) 1538.
[13] Q. Wu, I.J. Hodgkinson, A. Lakhtakia, Opt. Eng. 39 (2000) 1863.
[14] I.J. Hodgkinson, A. Lakhtakia, Q.h. Wu, Opt. Eng. 39 (2000) 2831.
[15] I.J. Hodgkinson, Q.h. Wu, A. Lakhtakia, M.W. McCall, Opt. Commun. 177 (2000) 79.
[16] V.C. Venugopal, A. Lakhtakia, Proc. Roy. Soc. Lond. A 456 (2000) 125.
[17] E. Ertekin, A. Lakhtakia, Proc. Roy. Soc. Lond. A 457 (2001) 817.
[18] V.C. Venugopal, A. Lakhtakia, Proc. Roy. Soc. Lond. A 454 (1998) 1535, Errata: 455 (1999) 4383.
[19] F. Wang, A. Lakhtakia, R. Messier, Sens. Act. A 102 (2002) 31.
[20] E.E. Steltz, A. Lakhtakia, Opt. Commun. 216 (2003) 139.
[21] V.I. Kopp, Z.-Q. Zhang, A.Z. Genack, Progr. Quantum Electron. 27 (2003) 369.

[22] W.S. Weiglhofer, in: W.S. Weiglhofer, A. Lakhtakia (Eds.), Introduction to Complex Mediums for Electromagnetics and Optics, SPIE, Bellingham, WA, USA, 2003.
[23] J.B. Geddes III, A. Lakhtakia, Eur. Phys. J. Appl. Phys. 13 (2001) 3, Erratum: 16 (2001) 247.
[24] J.B. Geddes III, A. Lakhtakia, Eur. Phys. J. Appl. Phys. 14 (2001) 97, Erratum: 16 (2001) 247.
[25] J. Wang, A. Lakhtakia, J.B. Geddes III, Optik 113 (2002) 213.
[26] J.B. Geddes III, A. Lakhtakia, Opt. Commun. 225 (2003) 141.
[27] M.W. Horn, M.D. Pickett, R. Messier, A. Lakhtakia, Nanotechnology 15 (2004) 303.
[28] M.W. Horn, M.D. Pickett, R. Messier, A. Lakhtakia, J. Vac. Sci. Technol. B 22 (2004) 3426.
[29] K. Robbie, D.J. Broer, M.J. Brett, Nature 399 (1999) 764.
[30] F. Wang, A. Lakhtakia, R. Messier, J. Mod. Opt. 50 (2003) 239.
[31] H.C. Chen, Theory of Electromagnetic Waves, McGraw-Hill, New York, NY, USA, 1983.
[32] C. Kittel, Introduction to Solid State Physics, Wiley Eastern, New Delhi, India, 1974.
[33] W.H. Press, S.A. Teukolsky, W.T. Vetterling, B.P. Flannery, Numerical Recipes in FORTRAN, Cambridge, Cambridge, UK, 1992.
[34] M. Celuch-Marcysiak, W.K. Gwarek, Int. J. Numer. Model 12 (1999) 23.
[35] J.B. Geddes III, A. Lakhtakia, Optik 112 (2001) 62.
[36] R. Luebbers, F.P. Hunsberger, K.S. Kunz, R.B. Standler, M. Schneider, IEEE Trans. Electromagn. Compat. 32 (1990) 222.
[37] R.J. Luebbers, F. Hunsberger, K.S. Kunz, K.S. Kunz, IEEE Trans. Electromagn. Compat. 39 (1991) 29.
[38] M.A. Porras, Phys. Rev. E 58 (1998) 1086.
[39] J. Lekner, J. Opt. A: Pure Appl. Opt. 5 (2003) 6.
[40] I.J. Hodgkinson, Q.h. Wu, Birefringent Thin Films and Polarizing Elements, World Scientific, Singapore, 1997.
[41] A. Lakhtakia, J.B. Geddes III, Opt. Eng. 43 (2004) 2410.
[42] J.W. Goodman, Introduction to Fourier Optics, McGraw-Hill, New York, NY, USA, 1968.
[43] V.C. Venugopal, A. Lakhtakia, Eur. Phys. J. Appl. Phys. 10 (2000) 173.